Method development in Fluorescence Spectroscopy

Inaugural-Dissertation

zur Erlangung des Doktorgrades
der Mathematisch-Naturwissenschaftlichen Fakultät
der Heinrich-Heine-Universität Düsseldorf

vorgelegt von

Nicolaas Tette Midas van der Voort
aus Hilversum

Düsseldorf, 4th January 2024

Institute of Molecular Physical Chemistry
Heinrich-Heine-University Düsseldorf

Printed with the permission of
Department of Mathematics and Natural Sciences
Heinrich-Heine-University Düsseldorf

Referees:

1. Prof. Dr. Claus A.M. Seidel
2. Prof. Dr. Cornelia Monzel

Date of oral examination: 12 October 2023

Contents

Abstract

Although orders of magnitude more modest, this thesis attempts to follow the example of the invention of the microscope by Anthony van Leeuwenhoek [49] leading to the discovery of the microbiome which ultimately led to improvements in the human conditions by means of public sanitation. It does so by developing new methods that enables the user to glean information previously inaccessible. Specifically, 1) FRET-nanoscopy accesses the Ångström level using fluorescent imaging, and thus can study biomolecules under physiological conditions at the highest resolution on a single-molecule basis. This method was applied to obtain the length of the activated hGBP protein at 28 nm and perform precise measurements of the 3D position of fluorescent dyes on origamis to enable isotropic 3D resolution. 2) Cell Lifetime FRET Image Spectroscopy (CELFIS) is used to measure the abundance of molecular species to a 1% level in live cells under a large range of input conditions, such as concentration and cell phenotype. This method is of general use to unravel the complex input-response machinery, which is pivotal information for understanding cells. The method is applied to elucidate the signaling response of CD95 and to obtain the dimerization constant of CTLA4. 3) Contributions were made to existing methods, including robust photobleaching step analysis in live cells, extraction of quantitative data on molecular species from gated STED data and optimized acquisition procedures for live-cell FCS. Methods 1) and 2) are elaborated upon below.

FRET-nanoscopy The ultimate goal of nanoscopy is to deliver molecular resolution compatible with live systems at a single-molecule level. Fluorophore-fluorophore interactions via FRET is a well-established method to achieve structural resolution below the diffraction limit, but poses a challenge for single-nanometer nanoscopy as it leads to ambiguities of the fluorophore position if not properly treated. FRET-nanoscopy takes a step towards the ultimate goal of nanoscopy by providing Ångström resolution based on localizing single emitters in aberration-free STED data (colocalization STED (cSTED)) and by providing an experimental method and theoretical framework to calculate FRET distances under STED conditions, harnessing the potential of FRET. Synergistically, the information from FRET and cSTED is combined to make the transition from 2D to 3D at a molecular scale using Optical Pythagoras (OP). The method works as follows. FRET-nanoscopy requires a donor and acceptor FRET pair that can be depleted by the same STED laser. Alexa 568, Alexa 594 or Atto 594 are used as donors whereas Atto 643 or Atto 647N are used as acceptors. By localizing all emitters on a two-channel STED image, the fluorophore xy-position is resolved with high precision (<4 nm) at any length scale, achieving seamless resolution from 4 nm and upwards. Using a self-built particle averaging routine, broken or misfolded samples can be separated from intact samples with high fidelity yielding high purity data. When multiple molecular species are present in the ensemble, such as upside-up and upside-down origami platforms, these can be isolated and clustered separately. For each molecular species, the average particle is calculated to increase our precision to 0.4 nm. We use the breadboard property of DNA-origamis to confirm that our measurements match the predicted position within this precision. As the depletion laser changes the fluorescence lifetime decay of the dyes, we develop new analysis procedures to obtain accurate intensity-

and lifetime-based FRET indicators for accurate distances <0.5 nm under STED conditions. Uniquely, FRET measures distances independent of molecular orientation with respect to the imaging plane (hypotenuse), whereas localization measures the projected *xy*-distance (adjacent side), using Pythagoras' theorem they synergistically combine to determine the angle of the protein (OP). Lastly, we apply our approach to the protein hGBP1 *in vitro*, which undergoes a conformational change to an extended state upon activation, inaccessible to either STED or FRET alone. Using cSTED, we measure the most likely donor and acceptor distance to be 28 nm.

CELFIS The field of molecular biology is rapidly evolving from studying binary yes/no relationships to probing complex signal transduction mechanisms. To study a system where the outcome depends quantitively on the concentration of input signaling molecules, a method is required that can measure interactions with high sensitivity, cover large concentration ranges and gather sufficient statistics to study the natural variability in live cells. CELFIS fulfills these conditions by analyzing the change in donor lifetime decay due to FRET from live cell data, $\epsilon(t)$, to detect changes in FRET fractions as low as 0.2 %. The FRET fraction is transformed into the fraction of oligomers by 1) using Accessible Volume Simulations (AV) to calculate the portion of the time where donor and acceptor are close enough and 2) accounting for the abundance of donor-acceptor species in addition to donor-donor or non-matured species. CELFIS gathers high statistics using our highly automated acquisition and data processing pipeline, measuring >3000 cells in one experiment while obtaining phenotype information such as cell fate and protein expression level. We apply CELFIS to detect oligomerization of CD95 in response to addition of CD95L to reveal that 12 % oligomer formation in median is sufficient to trigger apoptosis. Furthermore, we study dimerization of the CTLA4 membrane receptor protein and find that the dimerization fraction depends on concentration, enabling us to obtain the dimerization constant K_{dimer}. An upper limit in the concentration accessible by FRET is posed by unspecific interaction due to proximity FRET. By using three independent monomer controls, we quantify and correct for proximity FRET, allowing us to measure quantitative oligomer fractions up to concentrations ∼10 000 receptors/µm^2. CELFIS is easily transferable to measure molecular interaction <10 nm in any cellular organelle.

Scientific contributions

Published works and manuscripts

All manuscripts and published works are included as appendices. Note that the page numbers from the original manuscripts have been replaced with the thesis page numbering for the ease of the reader.

1. **Nicolaas TM van der Voort**, Jan-Hendrik Budde et al., "FRET nanoscopy enables seamless imaging of molecular assemblies with sub-nanometer resolution", status: *in revision*, a preprint is available at *arXiv:2108.00024*, 2021*.

2. **Nicolaas TM van der Voort**, Nina M Bartels et al., "Quantifying the Spatio-temporal Evolution of Protein Interactions using Cell Lifetime FRET Image Spectroscopy (CELFIS)", status: *Manuscript sent to coauthors**.

3. **Nicolaas TM van der Voort**, Nina M Bartels et al., "Determining Concentrations of Fluorescently Labelled Membrane Protein in live Cells using a Confocal Microscope", *experimental Protocol*, status: *Manuscript sent to coauthors**.

4. Nina M Bartels, **Nicolaas TM van der Voort** et al., "A Minimal Model of CD95 Signal Initiation Revealed by Advanced Super-resolution and Multiparametric Fluorescence Microscopy", status: *submitted*, a preprint is available at *bioRxiv 2022.11.29.51837*, 2022*.

*first author contributions

Oral presentations

1. Nicolaas van der Voort, Jakub Kubiak, "SFB1208, project A08 progress report: method development at HHU - CD95 FRET studies and development of STED-FRET", in *SFB1208 weekly seminar series*, 2020.

2. Nicolaas van der Voort et al., "FRET-nanoscopy: A hybrid approach with Ångström resolution", in *Focus on Microscopy*, 2021, abstract url: `https://www.focusonmicroscopy.org/past/2021/PDF/1100_van_der_Voort.pdf`

3. Nicolaas van der Voort et al., "A hybrid approach with Ångström resolution", in *PicoQuant 26th Single-Molecule Workshop*, 2021.

4. Nicolaas van der Voort, Jakub Kubiak, "A08 FRET-nanoscopy & spectroscopy: Unlocking molecular mechanisms", in *SFB1208 retreat*, 2021.

5. Nicolaas van der Voort et al., "Towards interactomics with TRACE-FRET", in *GBM Fall Conference 2022 Molecular Basis of Life*, 2022.

Poster presentations

1. Nicolaas van der Voort et al., "Resolution on all scales: protein clusters with FRET to cells with STED", in *Picoquant 25th Single Molecule-Workshop*, 2019.

2. Nina M Bartels, Nicolaas van der Voort et al., "Elucidating cluster formation in CD95 signaling using multiparametric image spectroscopy", in *DGZ Life In Between - The Cell Biology of Interfaces*, 2021.

3. Nicolaas van der Voort et al., "A hybrid approach with Ångström resolution", in *EMBL Seeing is Believing 2021*, 2021.

4. Nicolaas van der Voort et al., "FRET-nanoscopy: a correlative approach with Ångström resolution", in *GBM Fall Conference 2022 Molecular Basis of Life*, 2022.

5. Nicolaas van der Voort et al., "CELFIS: a new tool for interactomics reveals spatial, temporal and concentration dimensions of oligomerization in single cells", in *EMBO Workshop From functional genomics to systems biology*, 2022.

Chapter 1

Introduction

Biomolecules assemble into biomolecular machines that drive the fundamental processes of life. Yet biomolecules are highly diverse, dynamic in nature and nanometer sized, such that the information researchers obtain is limited by the methods available to them. Among the plethora of available methods, Förster Resonance Energy Transfer (FRET) image spectroscopy is unique due to its biocompatibility while giving information on a truly molecular scale.

Fluorescent labeling of the biomolecules offers the unique advantage of studying one component of the complex biomolecular machinery at a time in living systems. Confocal fluorescence microscopy provides spatial information of the organization in living cells down to the diffraction limit of ∼200 nm [63]. With the advent of super-resolution microscopy or nanoscopy, the diffraction limit has been overcome. Stimulated Emission Depletion (STED) reaches typically ∼40 nm [26] while being compatible with live cells at the cost of increased photo-toxicity and photobleaching. Single-Molecule Localization Microscopy (SMLM) typically resolves ∼20 nm [46], but only works on fixed cells. Image reconstruction methods such as Structured Illumination Microscopy (SIM), array detector methods and re-scan confocal microscopy, are also live-cell compatible and have low photobleaching and photo-toxicity, but deliver a more modest resolution improvement down to 100 nm to 150 nm. All of these methods as of yet fail to capture the nanometric features of biomolecular machines.

Fluorescence-based methods are complemented by atomic-resolution methods, such as X-ray diffraction crystallography, cryo-Electron Microscopy or Nuclear Magnetic Resonance (NMR), where the latter is also capable of sensing molecular dynamics. While their resolution is unprecedented, none of them have single-molecule sensitivity or are compatible with live samples. Uniquely, FRET can quantitatively measure distances <12 nm and hence provides information on molecular structure as well as delivering a direct readout for molecular proximity due to binding. Then, the combination of microscopic or nanoscopic imaging with FRET spectroscopy synergistically resolves the spatial organization within the cell, while also measuring proximity at the molecular level. Both analyses can be made from a single dataset obtained using a microscope modified with Time-Correlated Single Photon Counting (TCSPC) readout electronics and polarization sensitized detection.

Hence, the overarching goal of the doctoral work presented in this thesis is to develop image spectroscopic methodologies for investigating biomolecular interactions, especially the stoichiometry and composition of biomolecular assemblies. I approach this task from two perspectives. The first perspective is method focused and its goal is to resolve any distance with the highest possible accuracy using image spectroscopy. Using STED microscopy, we achieved seamless resolution by localizing each fluorophore individually for the donor and acceptor channel with colocalization STED (cSTED). We subsequently reach sub-nanometer precision and

accuracy by averaging over many structures of the same species using Particle Averaging cSTED (PA-cSTED). From the spectroscopic side, we obtained quantitative FRET information under STED conditions for two FRET pair species with an interpair separation of only 75 nm. Here, we used well-defined *in vitro* samples with STED compatible dyes to calibrate the performance of the method, giving rise to the FRET-nanoscopy method discussed in chapter 2. An interesting opportunity arises as FRET reports on the absolute donor-acceptor distance, whereas particle-averaged cSTED data reports on the projection on the xy-plane. Following Pythagoras' formula, this has the potential to resolve isotropic distance information $<$12 nm. As the distances obtained from FRET and particle-averaged cSTED must match precisely for this to work, we performed an unpublished calibration project described in chapter 3.

In the second perspective, the application was central for directing research efforts. The system of interest, Cluster of Differentiation 95, also known as Fas, FasR or TNFRSF6 (CD95), showed only a very small increase in the oligomeric fraction, resulting in the development of CELFIS discussed in chapter 4. Serendipitously, CELFIS also yielded new insights on the oligomeric state of Cytotoxic T-Lymphocyte-Associated protein 4, also known as CD152 (CTLA4). To learn more about the CD95 oligomeric state, improvements in existing methods were needed, specifically: 1) establishment of robust confocal Photobleaching Step Analysis (cPBSA) in live cells to count the number of units in the CD95 oligomer, 2) optimization of acquisition procedures for live-cell Fluorescence Correlation Spectroscopy (FCS) and 3) extraction of quantitative data on molecular species from gated STED data. Additionally, Multiparameter Fluorescence Image Spectroscopy (MFIS) was used. The novel insights in the oligomeric state of CD95 as well as the developments in the latter methods are presented in chapter 5.

After summarizing the main result, I include a comprehensive overview of know-how, detailed method description and supporting materials in the appendices. Specifically, many important results were obtained on the Abberior Expert Line microscope and I include practical know-how on instrument alignment, operating modes and optimal acquisition settings in chapter 6. The works in this thesis were made possible due to self-written programs described in chapter 7. Next, the manuscripts for FRET-nanoscopy manuscript (appendix A.3), CELFIS (appendix B.3) and CD95 (appendix D) are included. Lastly, the protocol for determining the fluorescent protein concentration via their brightness is included in appendix C.

Note that I use both the 'I' and 'we' form throughout the thesis depending on whether the action was mostly a team effort or not. The author contributions are clarified in the corresponding sections in each chapter. I would like to conclude by thanking the reader for taking the time to read this work. I hope that you find its results insightful and its ideas inspiring.

Chapter 2

FRET-nanoscopy

In this paper, a new method that combines FRET with super-resolution STED microscopy, called FRET-nanoscopy, is introduced. The method can localize dyes on *in vitro* samples with Ångström precision while simultaneously obtaining quantitative FRET information. The work is currently submitted to arXiv [8].

2.1 Author contribution

Concerning the FRET-nanoscopy, the author of this thesis was responsible for the following content. **DNA origami** Optimization of the measurement protocol including setup alignment, optimization of recording settings and optimizing the dye preservation buffer. Measurement of the origami samples. **Software development** Origami data was analyzed in the self-written software *Seidel* (see software sections) capable of Maximum Likelihood Estimation (MLE) fitting of up to three emitters, calculation of FRET indicators and particle averaging. Seidel inspired similar features to be added to AnI, the MFIS program maintained by Suren Felekyan. **DNA Rulers** While originally the responsibility of Jan-Hendrik Budde (JHB), the author helped with acquiring data and developing models for fitting the distance distribution. Inspired by Claus Seidel, the author led the effort to explain aberrant ruler distances by surface roughness by posing research questions and analyzing AFM data recorded by Julian Sindram on samples prepared by Michelle Rademacher and Laura Vogel. **hGBP** Helping JHB, the author analyzed FRET-nanoscopy data from hGBP rings in *Seidel*. The author developed the model accounting for randomly oriented DA pairs in the distance distribution of the hGBP fiber in python with significant help from Anders Barth (AB) and Oleg Opanasyuk. **Manuscript** The author made figures 2 & 3 and panels for figures 1, 5 & 6. The author wrote sections for the results on the origami platform, edited by AB, and provided extensive input on all other sections. **Supplementary Information** The author wrote all sections relating to the above information, roughly half of the total SI content.

2.2 Motivation

The driving force behind this work was to close the so-called resolution gap: STED microscopy can reach resolutions down to ∼50 nm whereas FRET for our dye pairs can reach up to 12 nm. The area in between is referred to as the resolution gap - inaccessible to any method that can also measure single-molecules in their native liquid environments. Closing the resolution gap is relevant for the study of molecular complexes of 10 nm to 60 nm size, where several

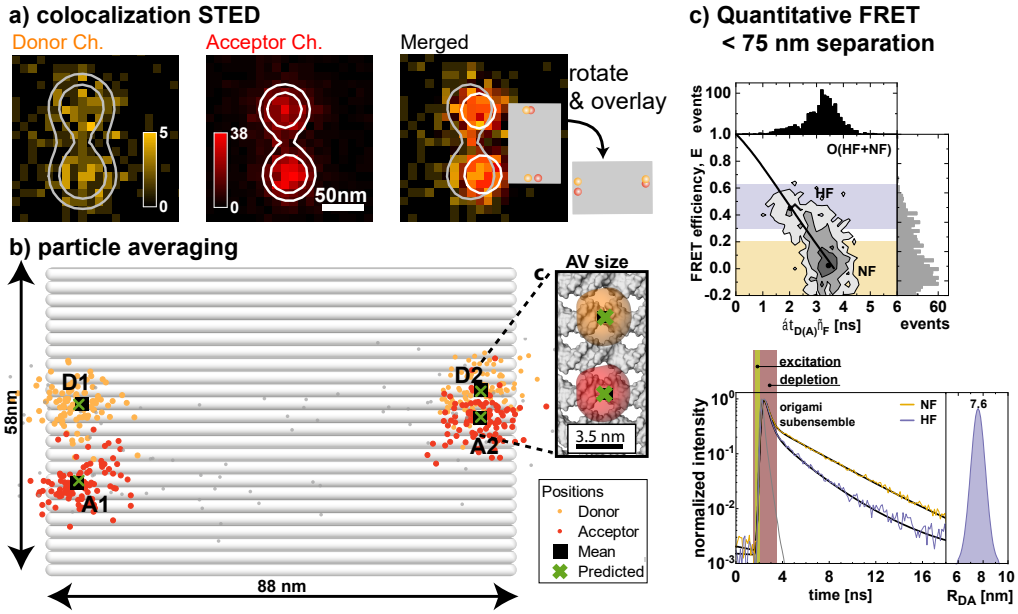

Figure 2.1: **graphical abstract a)** colocalization STED: Aberration free localization on STED images achieves ~ 5 nm precision. **b)** Resolution enhancement using particle averaging achieves 4 Ångström precision. **c)** Quantitative FRET on STED data resolves two FRET species at 75 nm separation shown in MFD (top) and lifetime analysis (bottom).

biomolecules assemble to fulfil cellular functions, such as signal transduction (e.g., the CD95-DISC complex [35, 37], pumps such as ATP synthase [54], channels such as the Type 1 Secretion system, hemolysin A [32] or membrane shapes such as cristae membranes folded by the MICOS complex [2]. Additionally, due to the fundamental nature of the work, the method may be applied in new innovative ways unimagined by the initial inventors.

2.3 Key results

2.3.1 Bayesian two color multi-Gauss spot fitting closes resolution gap

Our FRET-nanoscopy setup consists of a STED microscope with Alternating Line Excitation (ALEX) and TCSPC. This combination gives access to lifetime-based FRET as well as intensity-based FRET and enables increased resolution by gating the STED data after acquisition. As a sample, constructs labeled with STED-compatible dyes can be used. The dyes must be separated by at least the STED resolution of $\sim$50 nm if they emit in the same channel, but may be placed arbitrarily close if they are in different channels, wherein lies the strength of the method. Mimicking a molecular assembly, we use a model system of a DNA origami platform labeled with two FRET pairs at $\sim$75 nm distance, where the pairs are separated by 5 nm (high-FRET) and 14 nm (no-FRET) based on AV simulations.

Spatial information is obtained by localizing the position of each emitter individually. The fluorophores can be localized most accurately on gated STED data as it has the highest resolution and the Point Spread Function (PSF) resembles a Gaussian closely. MLE is used to localize up to three emitters simultaneously using Gaussian model functions, yielding the number of emitters and their location in each channel. By fortunate accident, the multi-Gauss fit model

yielded the number of spots in each spectral channel, dubbed spot stoichiometry, enabling a better data quality and simplification of the sample preparation by separating fully-labeled constructs in good condition from partially labeled or aggregated ones. While two emitters in the same spectral channel can be distinguished from a single bright emitter only if they are sufficiently far apart, two emitters from different spectral channels can be localized at any arbitrary distance, closing the resolution gap, provided FRET and chromatic aberration between the channels are accounted for. This benefit comes at no additional complexity as two detection channels are already required for measuring FRET.

2.3.2 Aberration free localizations

To study molecular assemblies, a method is required that can localize the position of each individual fluorophore. As a potential candidate, SMLM localizes each emitter by making them blink stochastically, but suffers from aberration-induced localization errors and drift limiting the resolution to ∼20 nm and prompting extensive efforts to overcome this limitation [27, 43]. A serendipitous outcome of our approach is that the STED depletion laser negates optical aberrations between the two detection channels. To see how a depletion beam negates chromatic aberrations, consider that only fluorophores close to the center of the depletion donut emit light for gated STED at typical depletion powers (∼40 µW measured at the objective), by Taylor expansion the depletion beam profile close to the center can be reliably modelled using a parabola, yielding $I_{\mathrm{STED}} = ax^2$, where a represents the power of the depletion laser. As the STED PSF is much smaller than the confocal PSF, the latter is roughly constant close to the depletion beam center. The probability for the fluorophore to be in the excited state is exponentially decreases with depletion power $p_{\mathrm{fl}} = \exp(-I_{\mathrm{STED}}/I_{\mathrm{s}})$, with I_{s} the STED saturation intensity, a combined dye and setup characteristic [26]. This yields $p_{\mathrm{fl}} = \exp(-ax^2/I_{\mathrm{s}})$, a Gaussian for the donor and acceptor channels centered on the same point, with slightly different width as I_{s} varies for the donor and acceptor dye (see figure 2.2). While the depletion beam is also subject to aberrations, any effect is negated by considering the difference between two emitters.

2.3.3 Particle alignment enables high purity *in silico* grouping

By considering the positions of all emitters simultaneously, one can calculate an average structure by aligning all available structures using PA-cSTED. Additionally, one can identify classes of similar structures based on their overall likeness. The particle alignment and averaging works as follows. First only fully labeled origami platforms with two donors and two acceptors are selected using the spot stoichiometry. Second, each emitter is assigned to a position based on the known geometry of the platform. For the origami data, this was either donor high-FRET, acceptor high-FRET, donor no-FRET or acceptor no-FRET. Third, the platforms were rotated and aligned to a reference platform chosen from among the dataset (see paper main text and section 2.3.4), using Root Mean Square Displacement (RMSD) as a score for how well the structure aligns overall. Molecular species can be identified by selecting groups of structures that show good alignment between them. For the origami data, molecular species can be identified that differ as few as 6 nm RMSD spread over 4 positions (see section 3.5). One of the main hurdles for obtaining precise molecular distances is the ability to filter impurities from the object of interest. Impurities are likely to occur due to partial labeling, incomplete folding or aggregation. These impurities tend to accumulate as sample complexity increases. Thus, a good filtering procedure of the methods helps increasing signal clarity as well as alleviating the demands on sample purity. Particle alignment provides high purity filtering by rejecting

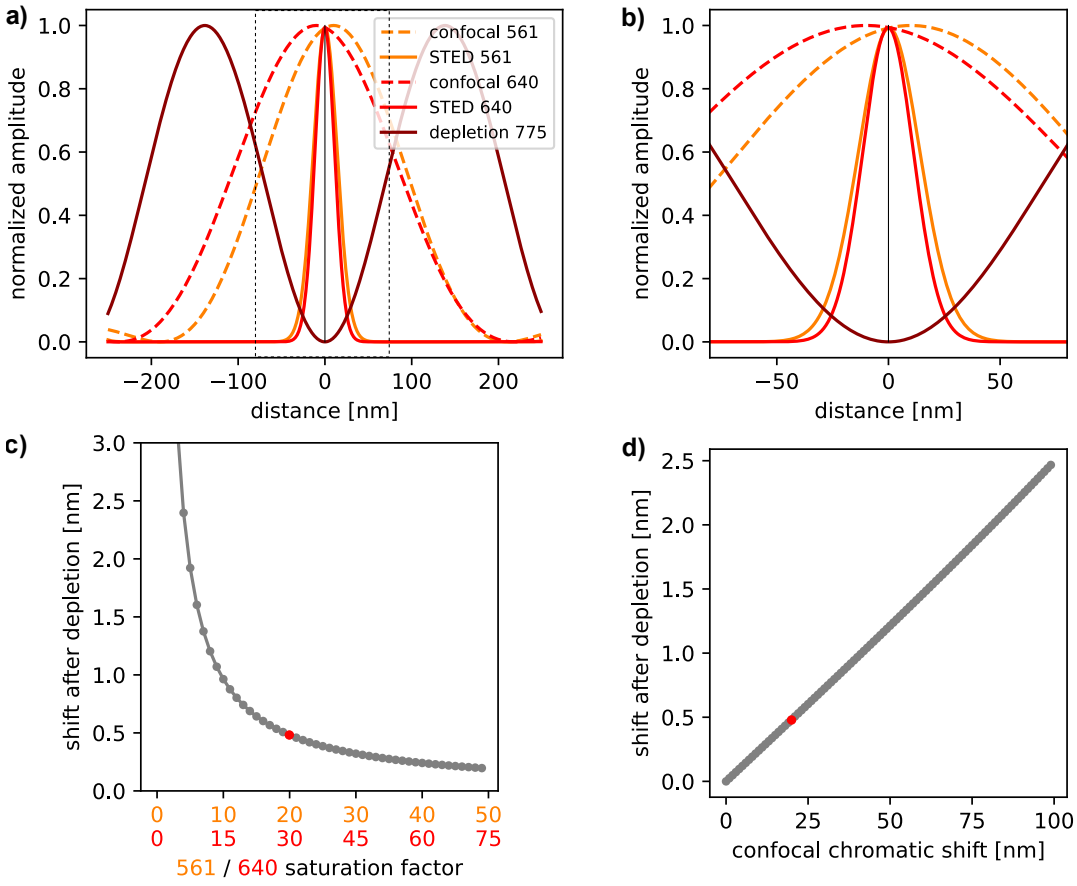

Figure 2.2: **Chromatic shifts disappear after depletion a)** full range and **b)** zoom. Ideal PSFs are calculated using a 1.4 numerical objective and respectively 561 nm, 640 nm and 775 nm wavelengths. Confocal PSFs calculated according to [12]. 775 depletion PSF as well as 561 and 640 STED PSFs calculated according to [26]. STED PSFs for 561 nm and 640 nm are calculated using a depletion factor of 20 and 30, respectively. To simulate the chromatic shifts, the confocal PSFs have each been shifted 10 nm with respect to the center, yielding a total displacement of 20 nm. After depletion, the shifts are reduced to 0.5 nm. **c)** Dependency of the shift reduction on the depletion laser power as indicated by the STED saturation factor. A fixed ratio for the 561 and 640 saturation factor of 1.5 has been assumed to reflect the different depletion efficiencies for the respective dyes. **d)** Dependency of the shift reduction on the chromatic shift between the channels. The red point in c) and d) reflects common measurement conditions shown in a) and b).

structures with high RMSD. The RMSD score provides a very sensitive readout as it considers information from all positions simultaneously. Notably, defects are more likely to be detected for dye pairs at large distances, such as the acceptor-acceptor distance. Hence, by considering the information of long distances, the accuracy for measuring short distances, such as a FRET pair, is improved as well. In addition, particle alignment can also be used to identify different molecular conformations, provided they are slow compared to the measurement time. For a well-defined molecular species, the structures vary less than 5 nm RMSD summed over all four positions (figure 3.9). Hence, a molecular conformation that causes a root-mean-squared shift >5 nm can be theoretically identified. As an example, origami structure were identified to be either top-up or bottom-up depending on an individual molecule basis (figure 3.2).

2.3.4 Particle averaging enables Ångström precision

Now that all constructs are aligned and defects have been filtered out, I calculate the average structure, increasing the precision and accuracy of the dye positions down to 4 Å standard deviation (see also manuscript main text on page 84 and Supplementary Method section *Alignment and Particle Averaging* on page 138). Particle averaging outperforms fitting the distance distribution pairwise using a non-centered-χ (n.c.-χ) distribution as the other labels act as fiducial markers, helping to filter aberrant structures and imposing an orientation on the two dyes. The localization precision is fundamentally constrained by FRET, which quenches the donor completely if the acceptor is closer than ∼4 nm. Reliable localization for these very small distances can nevertheless be obtained by relying on donor-recovery after acceptor photobleaching. Therefore, the power of the acceptor excitation laser was chosen such that the acceptor was likely to bleach before the donor. This experimental condition was instrumental in obtaining accurate donor-dye localizations for the high-FRET sample.

2.3.5 Optical Pythagoras

Ideally, an experiment can report on the precise *x,y,z* displacement of a FRET pair. FRET-nanoscopy has the potential to measure the 3D displacement vector <12 nm, the upper limit where FRET is detectable for a Förster radius of 69 Å to 72 Å, based on OP. The principle behind OP is that cSTED measures the distance projected on the *x,y*-plane, whereas FRET measures the absolute distance, or the hypothenuse of the triangle formed by the FRET pair and the coverslip surface. Hence, by applying Pythagoras' theorem, the z-information can be recovered. Comparison of the distances from cSTED and FRET showed a distance of 53 ± 7 Å and 72 ± 7 Å respectively, indicating a z-displacement of 50 ± 12 Å. Further investigations showed that the acceptors in the initial origami platform have a high anisotropy (figure 3c of the manuscript). This indicates sticking of the Atto 647N acceptor to either the glass surface or the DNA origami, which is a known property of this dye. Furthermore, the dye was linked to the phosphate groups of the DNA backbone via a C3 linker and an appended thymidine nucleotide, resulting in a comparatively large linker length of 31 Å. Thus, the z-displacement is likely to originate from the dye linkers pointing in opposite directions. The high anisotropy further points to an uncertainty in the Förster radius induced by preferred dipole orientations impacting the κ^2factor, which has been accounted for in the error estimate of the FRET distance.

Yet, to demonstrate the feasibility of optical Pythagoras as a means of measuring molecular displacement in *x,y,z*, a calibration sample with known *z*-position of all dyes is needed. Chapter 3 is dedicated to the design and characterization of such a platform.

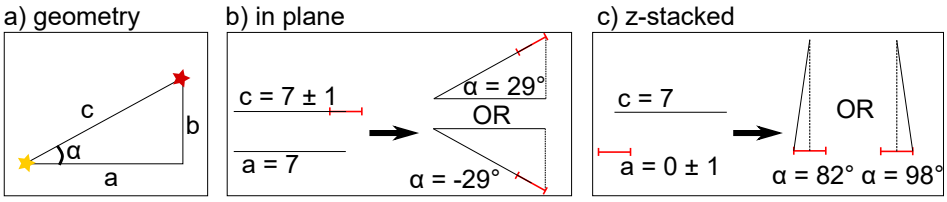

Figure 2.3: Sketch illustrating the difference in sensitivity for a z-stacked configuration ($\alpha = \pm 8°$) versus a planar configuration ($\alpha = \pm 29°$) for exemplary values of 7 nm length and 1 nm error. Note that in b) the error in a and in c) the error in c have been left out for simplicity.

2.3.6 Sensitive regime of optical Pythagoras

The accuracy with which the angle can be determined from optical Pythagoras is not uniform. In this section, I derive the error propagation for the angle α and illustrate the result for the cases of $\alpha = 0°$ and $\alpha = 90°$, showing that the sensitivity to obtain the z-information is highest when the dyes are on top of one another and decreases for more planar configurations (see figure 2.3). For a right triangle with the hypotenuse c, adjacent side a and opposite side b, we obtain the expression for α and the partial derivatives to a and c.

$$\alpha = \arccos(a/c), \tag{2.1}$$

$$\frac{\partial \alpha}{\partial a} = \frac{1}{\sqrt{c^2 - a^2}} = \frac{1}{b}, \tag{2.2}$$

$$\frac{\partial \alpha}{\partial c} = \frac{-a}{c\sqrt{c^2 - a^2}} = \frac{-a}{bc}, \tag{2.3}$$

where the expression for b has been inserted from their geometric relation. Then using the generic formula for error propagation

$$\sigma_\alpha^2 = \sigma_a^2 |\frac{\partial \alpha}{\partial a}|^2 + \sigma_c^2 |\frac{\partial \alpha}{\partial c}|^2 \tag{2.4}$$

$$\sigma_\alpha = \frac{1}{b}\sqrt{\sigma_a^2 + \frac{a^2}{c^2}\sigma_c^2}, \tag{2.5}$$

where the covariance between a and c is left out as they are obtained from independent experiments. We note the limiting states for 0° ($b = 0$) and 90° ($b = c, a = 0$):

$$\lim_{b \downarrow 0} \sigma_\alpha = +\infty \tag{2.6}$$

$$\lim_{b \to c} \sigma_\alpha = \frac{\sigma_a}{b} \tag{2.7}$$

2.4 Limitations

To sharpen the applicability of the new method, I discuss inherent limitations of the approach and how they may be alleviated.

2.4.1 Immobile samples with STED compatible labels

To enable highly accurate localizations, the sample must be static during the acquisition time of several seconds, which is achieved by immobilizing biomolecules on the surface of a microscope glass slide, often using a DNA-origami system to shield from surface contaminations. To study molecular assemblies, the samples must be prevented from rotating as well as moving, requiring at least two anchor points that must not restrict biologically relevant movement. Other ways of sample preparation include membrane bound systems that can be studied in cellular environments, where the cells must be either fixed, or the object of interest must be part of a larger molecular assembly such that it is sufficiently immobile. Furthermore, Giant Unilamellar Vesicles (GUVs) allow for immobilizing the object of interest by choosing saturated lipids with long carbon tails to increase the membrane viscosity, provided the lipid composition does not disturb the system. As the addition of a no-FRET dye pair acting as a fiducial marker highly improves the accuracy of the result, strategies to label molecular assemblies at multiple defined positions would be very beneficial. In-vitro reconstruction of molecular assemblies or in-vivo labeling with STED compatible dyes remains biochemically challenging, posing a limitation for the broad adoption of the method. Yet, such samples are required by all methods that wish to study biomolecular complexes at physiological conditions using fluorescence. Hence, the wish to study molecular complexes provides a driving force to generate such samples regardless of the development of FRET-nanoscopy.

2.4.2 System requirements

To advance a method from inception to maturity, it is vital that several labs are actively developing it. The basic requirements for FRET-nanoscopy are 1) a two-channel STED setup depleted by a single depletion laser and 2) the appropriate analysis software. Such a STED system can be readily obtained from commercial parties and is nowadays present in many labs all over the world. Analysis software was developed by the author and is available on GitHub[1]. While the analysis software is generic and publicly available[2], the acquisition software interfaces only with microscopes using Imspector[3] as operating software. Fortunately, many modern microscopes come with automation modules that make the implementation of such a program straightforward. A two-color STED system gives full access to the cSTED and subsequent PA-cSTED as well as intensity-based FRET determination. Additional modules may be added to enhance the readout, which I list here. The Abberior system is equipped with TCSPC which enables obtaining lifetime-based FRET, image gating in post-processing and performing sub-ensemble Time-Correlated Single Photon Counting (seTCSPC) analysis. As this unlocks the powerful framework of single-molecule FRET, it is arguably the most useful addition available. Furthermore, the system is equipped with polarization-sensitive detection, which is useful to add anisotropy information to the FRET system. Lastly, our system is equipped with 488 and 518 excitation lines with matching 595 depletion laser, in addition to the mostly used 561 and 640 excitation lines with matching 775 depletion, offering greater flexibility to work with fluorophores in different spectral ranges. In summary, FRET-nanoscopy can be performed on commercially available two-color STED system equipped with TCSPC. Software can be obtained from the author.

[1] `https://github.com/Fluorescence-Tools/Seidel`
[2] `https://github.com/Fluorescence-Tools/Abberior-Tools`
[3] `https://imspectordocs.readthedocs.io/en/latest/intro.html`

2.4.3 Limited photon budget

Intrinsically, the photons available for FRET analyses is limited as excited states depleted by the STED laser are discarded. We may quantify the fraction of discarded photons by interpreting the STED saturation factor as the reduction in surface area of a x,y PSF. I.e., at typical saturation factors of ~ 50, only 1 in 50 excited states relax via emission of fluorescence. To mitigate the limited number of photons, a single platform is imaged until nearly all fluorophores have photobleached. Furthermore, FRET-measurements under STED conditions are often benchmarked against other fluorescence spectroscopic methods, such as single-molecule Multiparameter Fluorescence Detection (sMFD).

Chapter 3

Calibration studies on DNA-origamis using FRET-nanoscopy

3.1 Introduction

The FRET-nanoscopy work [8] showed that the very high accuracy of PA-cSTED (<0.4 nm) can be combined with FRET data to yield isotropic 3D information <12 nm using OP. As a requirement, the distances from PA-cSTED must be calibrated against FRET data. The initial design of the DNA origami platform labeled with high-FRET and no-FRET dye pairs (O(HF+NF)) was not suitable for this purpose, as the extra thymine in the dye linker created an uncertainty in the position of the dye. Furthermore, the acceptor (Atto 647N) was shown to have a high anisotropy, indicating dye-sticking and an ill-defined κ^2 factor. In this project, we intend to show the feasibility of OP using a revised origami design where the dyes are attached directly on the base of the DNA.

The status of the project is currently ongoing. Hence, this chapter summarizes the available information at the time of writing. Currently, the revised origami platform has been synthesized, measured and analyzed using four different combinations of donor-acceptor pairs. Additionally, coarse-grained MD simulations have been done to model this system. To obtain a calibration sample where the donor-acceptor pair has a defined angle, a second origami was designed consisting of a cube attached to a platform. The materials for this second design have been ordered, but it has not yet been measured due to problems in the purification step of the synthesis.

An excellent earlier summary of this work is given by the master thesis of Michelle Rademacher [51], to which I also contributed materials (see section 3.2 below). To avoid duplication, I will here focus on what is new and what is significant for the main results. Specifically, I will discuss the main spectroscopic results, the results from MD simulations and the updated results from particle averaging, followed by a conclusion. For the origami designs, single-molecule measurements and n.c.-χ distribution fits I refer the reader to [51].

3.2 Author contributions

This project was initiated as the master thesis work of Michelle Rademacher (MR) under my supervision. Afterwards, it was continued by Noah Salama (NS) under my guidance. In both cases, I was involved in problem-solving on a daily basis, training them in FRET-nanoscopy, and performing analyses. Specifically, I did the analyses and figure generation for the FRET-

nanoscopy analyses, where NS helped separating the two species in the particle averaging analysis and MR did the TCSPC analysis under my supervision. NS and MR did single-molecule measurements. Christian Hanke performed coarse grained Molecular Dynamics Simulations (cgMD), on which I did AV simulations and further analyses. Lea Wasserman advised in synthesizing origami platform and synthesized the origami-cube construct. She was supervised by Amelie Heuer-Jungemann. Claus Seidel initiated the project and supervised on a PI level. I am thankful to all my co-authors for this pleasant and productive collaboration.

3.3 Coarse grained Molecular Dynamics simulations

3.3.1 Methods

A molecular model based on the DNA origami model is generated using caDNAno2 [15] and transformed to generate the input topology for coarse-grained simulations using tacoxDNA [57]. Coarse-grained MD simulations were performed using the oxDNA2 software package [55]. First the energy of the system is minimized to relax any unrealistic bond lengths. Then, the MD simulation is run to let the platform explore its thermodynamically accessible configurations. The first 99 frames of the MD simulation were not analyzed to eliminate any after-effects of the energy minimization. The simulations ran at least 300 frames, such that at least 200 frames could be analyzed, providing a good sampling of the available thermodynamic states. Subsequently, AV simulations were done using a linker of 20 Å length, 2 Å width and assuming a spherical dye of 3.5 Å radius (type AV1). Labels were attached to molecules on the major groove of the DNA, being atom N7 for guanine, atom C5 for cytosine, atom C7 for thymine and atom N7 for adenine referring to the standard atom labeling convention for DNA-nucleotides. A single donor position and two acceptor positions were used to simulate the high-FRET and no-FRET position. Four additional acceptors were simulated at one, three, four and five helices separation to probe all distances for interconversion of R_{mp}, $\langle R_{\mathrm{DA}} \rangle$ and $\langle R_{\mathrm{DA}} \rangle_E$.

3.3.2 Salt dependence

The DNA-origami relies on bivalent magnesium cations to shield the negative charges from the phosphate groups in the DNA-backbone, thus allowing the helices to approach each other closely. The oxDNA2 package calculates electrostatic interactions using the Debye-Hückel model. This model incorporates electrostatic shielding by salt ions via the Debye length $\lambda_{\mathrm{DH}}(T, I)$:

$$\lambda_{\mathrm{DH}}(T, I) = \sqrt{\frac{\epsilon_0 \epsilon_{\mathrm{r}} k_{\mathrm{B}} T}{2 N_{\mathrm{A}} e^2 I}}, \tag{3.1}$$

where the ϵ_0 and ϵ_{r} are the vacuum and relative permittivity, k_{B} is the Boltzmann constant, T is the temperature, N_{A} is the Avogadro constant, e is the fundamental electric charge and I is the ionic strength. The ionic strength is calculated by

$$I = \frac{1}{2} \sum_{i=1}^{n} c_i z_i^2, \tag{3.2}$$

where c_i and z_i are the concentration and charge numbers of the ions in the buffer, which are listed in table 3.1, yielding an ionic strength of ∼35 mM.

Taken at face value, the model predicts that 35 mM NaCl would be able to replace the Magnesium-based buffer, but this overlooks the higher local charge density of Magnesium and

buffer component	cations	anions	ionic strength
5 mM Tris-HCL	2.5 mM $TrisH^+$	-	1.25 mM
⋮	2.5 mM H^+	-	0 mM
⋮	-	5 mM Cl^-	2.5 mM
10 mM $MgCl_2$	9 mM Mg^{2+}	-	18 mM
⋮	-	20 mM Cl^-	10 mM
1 mM Na_2H_2EDTA	2 mM Na^+	-	1 mM
⋮	2 mM H^+	-	0 mM
⋮	-	1 mM $MgEDTA^{2-}$	2 mM
total	-	-	34.8 mM

Table 3.1: **Ionic strengths of DNA-origami imaging buffer components** Tris-HCl is assumed to be deprotonated at 50% at pH 8.0 and EDTA is assumed to completely complex magnesium [3]. The shielding activity of hydroxide and hydronium has been ignored as their concentrations are negligible at pH 8.0.

its complexation property. Indeed, experimental evidence shows that a NaCl concentration in the 1 M range is needed to replace the ∼10 mM $MgCl_2$ normally used to ensure correct folding of origamis [41]. Considering the clear discrepancy between model and experiment, we will test a series of salt concentrations to find the appropriate simulation equivalent to the experimental condition.

3.3.3 Simulation results

Representative depictions of the DNA origami simulation for several salt concentrations are shown in figure 3.1. The corresponding time-evolution of R_{mp} for high-FRET and no-FRET distances is shown in figure 3.2A, B. First, we consider theoretical ionic strength equivalent of the measurement buffer of 35 mM. Clearly, this concentration is incorrect as the platform looks severely strained and the obtained distances for high-FRET and no-FRET (table 3.2) are far from the experimentally measured variables. Proceeding to higher salt concentrations, 150 mM ionic strength still overestimates the no-FRET distance at 19.6 nm, rather than the experimentally observed range of 15 nm to 16.5 nm. At 500 mM, 1000 mM and 2000 mM ionic strength the R_{mp} distance stabilizes, indicating that the electrostatic repulsions are sufficiently shielded at 500 mM and that increasing the salt concentration further does not change the geometry. To obtain a unitary measure where high-FRET and no-FRET distances can be directly compared, the distances have been transformed into the interhelical distance (see figure 3.2C), yielding an interhelical distance of 2.6 nm to 2.9 nm. Note that the error bars indicate the inherent distribution of the distance due to thermal fluctuations, σ_{mp}. Interestingly, the thermal fluctuations are ∼1.0 nm for both high-FRET and no-FRET distances, indicating that the movement of individual helices is the dominant contribution to the thermal variance of R_{mp} and that expansion of the platform as a whole change plays a minor role. Further note that the high-FRET and no-FRET distances at 1000 mM are lower than their neighboring values, which can be traced back to the anomalously lower R_{mp} at frame 200 (compare figure 3.2A-4 to 3.2A-3), indicating that shorter distances are thermally accessible but that the simulation run-time is too short to sufficiently average over these unlikely events. Hence, this data point will be treated separately in further analyses.

property \ionic strength	35 mM	150 mM	500 mM	1000 mM	2000 mM
$\langle R_{\mathrm{mp,HF}} \rangle$ [nm]	10.8	6.6	5.8	5.0	5.6
$\langle R_{\mathrm{mp,NF}} \rangle$ [nm]	30.9	19.6	16.9	15.9	16.2
$\sigma_{\mathrm{mp,HF}}$ [nm]	0.8	0.9	0.9	0.9	0.9
$\sigma_{\mathrm{mp,NF}}$ [nm]	1.0	0.9	1.1	1.0	1.2

Table 3.2: **Time-averaged mean positions from cgMD** Distances shown for high-FRET, $\langle R_{\mathrm{mp,HF}} \rangle$, and no-FRET, $\langle R_{\mathrm{mp,NF}} \rangle$, positions and their variation due to thermal fluctuations expressed as the σ of the gaussian distribution. Data also graphically shown in figure 3.2C-1.

conversion	a_0 [nm]	a_1	a_2 [nm^{-1}]	a_3 [nm^{-2}]	a_4 [nm^{-3}]
$R_{\mathrm{mp}} \rightarrow \langle R_{\mathrm{DA}} \rangle$	9.6×10^{-1}	6.9×10^{-1}	4.5×10^{-2}	-3.0×10^{-3}	7.5×10^{-5}
$R_{\mathrm{mp}} \rightarrow \langle R_{\mathrm{DA}} \rangle_E$	1.56	9.1×10^{-1}	-5.6×10^{-2}	6.9×10^{-3}	-2.2×10^{-4}

Table 3.3: **Polynomial coefficients for listed interconversions** according to equation 3.3 shown in figure 3.2D.

A few further gains can be had from the simulation. As mentioned, we obtain an interconversion between the distances measured by cSTED, R_{mp}, the distances measured by lifetime FRET, $\langle R_{\mathrm{DA}} \rangle$, and the distances measured by efficiency-based FRET, $\langle R_{\mathrm{DA}} \rangle_E$, by also simulating AVs on other helices (white AVs in figure 3.1). This interconversion is very similar to the one used in the FRET-nanoscopy paper (section A.3.4, page 176), but differs slightly due to different linker lengths and anchor positions. The relation is fitted with the fourth order polynomial

$$\langle R_{\mathrm{DA}} \rangle_{(E)}(R_{\mathrm{mp}}) = \sum_{i=0}^{4} a_i R_{\mathrm{mp}}^i, \tag{3.3}$$

whose coefficients are listed in table 3.3. As another gain, we may verify that our simulations of a DNA origami platform in solution is also representative of platforms anchored to the surface. Our simulation reproduces the well-documented tendency of the origami platforms to curl in solution [5], which is not likely to occur when the platform is anchored to a surface. The curling is no problem for our interpretation as its effect is negligible at distances of ∼15 nm (compare figure 3.1a,b). Another difference occurs as the overall breathing of the structure is more restricted in surface-bound origamis due to the several anchor points compared to origamis in solution, which may affect the thermal fluctuations of R_{mp}. However, we have seen that single-helix displacement is the dominant source of R_{mp} fluctuations, such that the simulations still provide a reliable prediction.

Summarizing, the mean high-FRET distances from AV simulations are in the range 5.6 nm to 5.8 nm with thermal fluctuations of 0.9 nm standard deviation from the ionic strengths of 500 mM and 2000 mM. For no-FRET the mean distance was found to be in the range 15.9 nm to 16.9 nm with thermal fluctuations of ∼1.1 nm for the ionic strengths of 500 mM, 1000 mM and 2000 mM.

3.4 Spectroscopic distances

To obtain FRET-based distances, I investigate the spectroscopic information obtained from O(HF+NF) under STED conditions. All data was analyzed according to the methods described

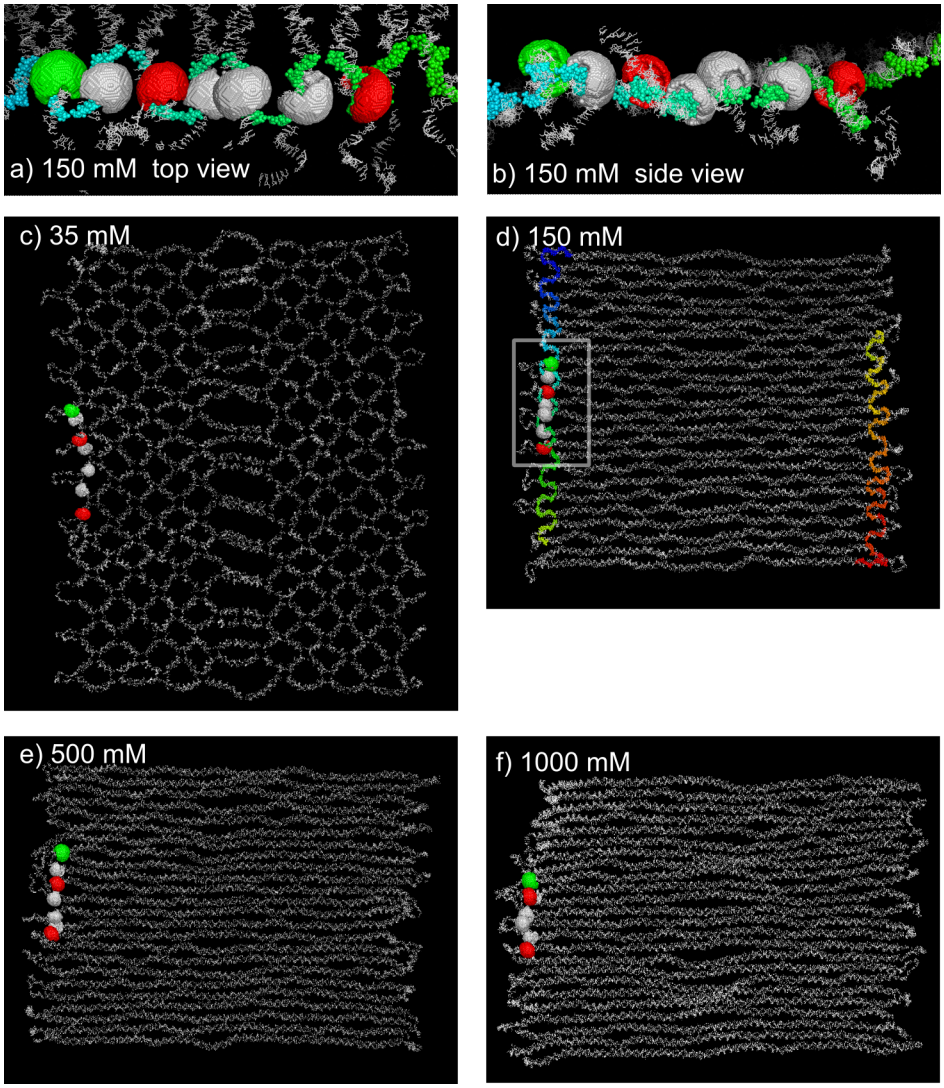

Figure 3.1: **cgMD simulations of origami platform** Coarse-grained data has been transformed back into a full molecular representation for display purposes. **a)** Top view of six labeling positions with the donor shown in green and the acceptors shown in red for the no-FRET and high-FRET positions. White colored positions have no experimental equivalent, but are used to generate extra data points to interconvert R_{mp}, $\langle R_{\mathrm{DA}} \rangle$ and $\langle R_{\mathrm{DA}} \rangle_{\mathrm{E}}$. **b)** Side view of positions show that the local geometry can be approximated well using a planar geometry. Single-stranded overhangs of the scaffold strand are visible. **c-f)** snapshots of the origamis show a relaxation of the structure corresponding to smaller helix-to-helix distances with increasing salt concentrations. Note that the two sides of the platform are equivalent, such that no-FRET and high-FRET positions may be modelled on the same side of the platform for simplicity.

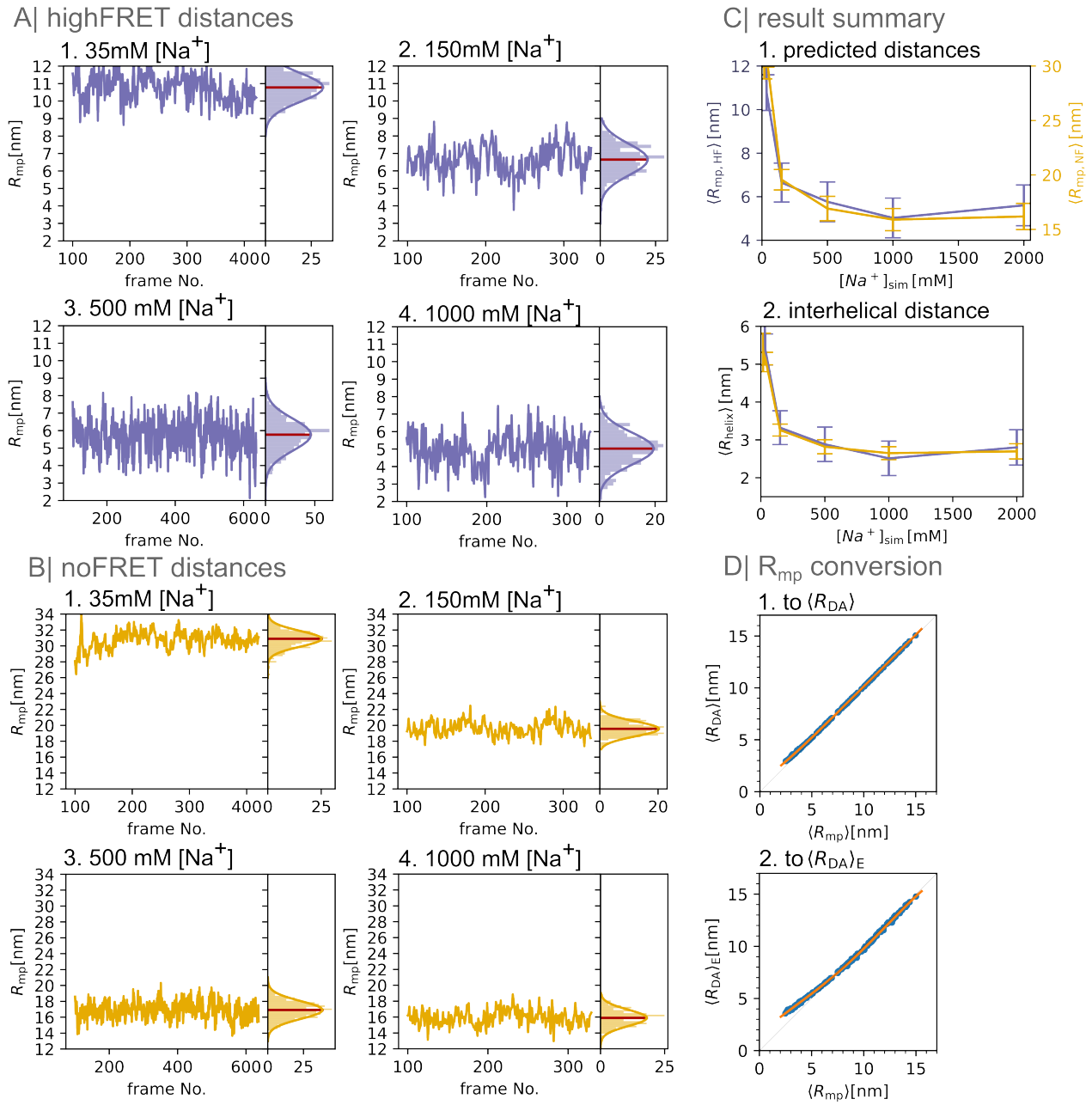

Figure 3.2: **Analyses of cgMD simulations for predicting distances depending on salt concentrations A** The time evolution of R_{mp} shows a decreasing distance with increasing salt concentration for the high-FRET pair and **B** the no-FRET pair. **C** Summary of the MD simulations showing **1.** the average mean distance and variation around the mean distance due to the thermal fluctuations as depicted by the error bars. **2.** The average interhelical distance calculated from the distance divided by the number of interhelical spacings, being two and six for high-FRET and no-FRET respectively. **D** Interconversion of R_{mp}, $\langle R_{\mathrm{DA}} \rangle$ and $\langle R_{\mathrm{DA}} \rangle_E$, polynomial coefficients of the fit given in table 3.3.

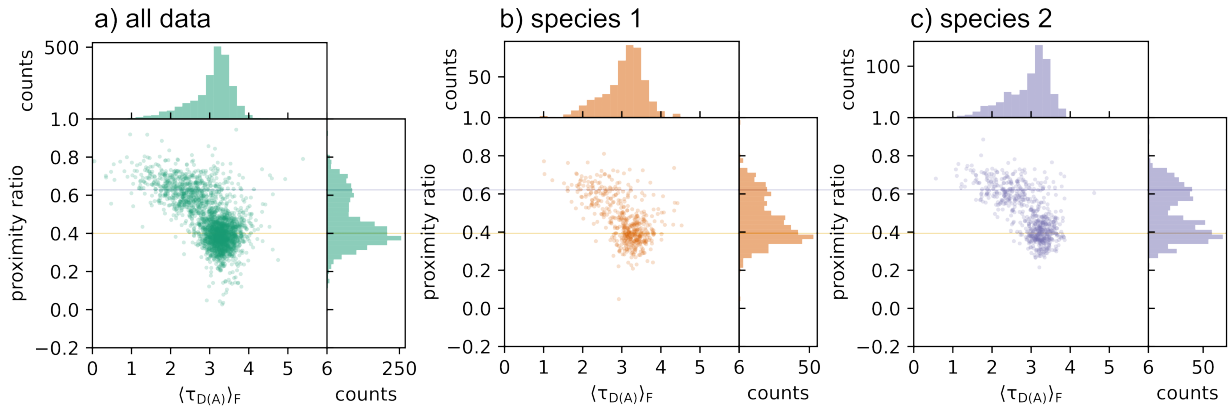

Figure 3.3: **Effect of platform orientation in $E-\tau$ diagrams** The uncorrected FRET efficiency, proximity ratio, is plotted against the donor lifetime of the O(HF+NF)-Alexa 594-Atto 643 sample for three different selections: **a)** all data, **b)** origami platforms labeled with two acceptors and two donors of species 1 and **c)** species 2, where the two species are differentiated by which side is up (see section 3.5). No difference between the selections is observed.

in the FRET-nanoscopy Supplementary Methods on page 130 and onwards. As we shall see more elaborately in the next section, some of the origami platforms were flipped, potentially leading to platform-orientation mediated dye-surface effects. To investigate this, we plotted the proximity ratio, the uncorrected FRET efficiency, against the donor lifetime for the O(HF+NF) labeled with Alexa 594-Atto 643 sample and its flipped and non-flipped subsets (figure 3.3). No change in efficiency or lifetime was observed, indicating that the photophysical properties of the dyes in the flipped and non-flipped subsets are identical.

Moving to quantitative distances, I first calculate the corrected Efficiency-donor lifetime diagrams shown in figure 3.4 using the correction factors given in table 3.4. Overall, obtained distance estimates agree closely between the four measurements. The centers of the high-FRET populations also show a good agreement with the static FRET line, where samples with Alexa 594 as donor lie slightly above and samples with Alexa 568 as donor lie slight below the static FRET line. As before, a band is visible from the high-FRET position to the no-FRET position due to bleaching and intermittent blinking induced by the depletion beam.

The corresponding seTCSPC decays have been fitted according to the model described in equation S19 on page 132 and are shown in figure 3.5. Intensity-based and lifetime-based FRET indicators are converted to R_{mp} using the conversion shown in figure 3.2D using equation 3.3 and the coefficients listed in table 3.6. Interestingly, the overall distances from lifetime-based FRET are lower than the distances obtained from spot-integrated FRET. A key difference between the two analyses is that the seTCSPC model can correctly attribute photons arriving during acceptor dark-states as being no-FRET, whereas spot-integrated FRET indicators measure the average state over the entire detection period. In this regard, spot-integrated FRET can be treated in the same way as burst-wise FRET from solution single-molecule experiments. Hence, the spot-integrated FRET distances may overestimate the real distances by averaging over intermittent no-FRET states caused by acceptor blinking. Such blinking effects may occur as the STED depletion beam opens up new dark states that are not rescued by Trolox [44]. For a discussion on dark states in presence of STED and the effect of photo-buffers, see section 6.2.2.

In conclusion, both spot-integrated and lifetime-based FRET distances show consistent result among the four samples indicating a good robustness of the result. Spot-integrated

	Al594-At647N	Al594-At643	Al568-At647N	Al568-At643
Surface	NHS-PEG	NHS-PEG	NHS-PEG	NHS-PEG
G	0.909	0.894	0.894	0.894
α	0.480	0.480	0.266	0.266
β	0.68	0.61	1.00	1.21
γ	2.41	2.27	2.53	2.38
δ	0.080	0.064	0.080	0.064
γ'	1.72	1.61	2.06	1.62
x_{D}^{0}	0.230	0.200	0.202	209
x_{A}^{0}	0.164	0.142	0.125	0.142
$x_{\mathrm{D}}^{\mathrm{d}}$	0.770	0.800	0.798	0.791
$x_{\mathrm{A}}^{\mathrm{d}}$	0.836	0.858	0.836	0.858
$\Phi_{\mathrm{F,D}}^{0}$	0.573	0.571	0.596	612
$\Phi_{\mathrm{F,A}}^{0}$	0.657	0.606	0.657	0.600
$\Phi_{\mathrm{F,D}}^{\mathrm{d}}$	0.041	0.031	0.031	0.038
$\Phi_{\mathrm{F,A}}^{\mathrm{d}}$	0.027	0.024	0.023	0.020
$I_{\mathrm{Dem\|Dex}}^{(\mathrm{BG})}$ [kHz]	0.60	0.60	0.60	0.60
$I_{\mathrm{Aem\|Dex}}^{(\mathrm{BG})}$ [kHz]	0.55	0.55	0.55	0.55
$I_{\mathrm{Aem\|Aex}}^{(\mathrm{BG})}$ [kHz]	0.72	0.72	0.72	0.72
$\frac{g_{\mathrm{D\|D}}}{g_{\mathrm{A\|A}}}$	0.477	0.464	0.431	0.419

Table 3.4: **Correction factors for quantitative efficiency-based FRET under STED conditions** Definitions given in Supplementary Information for FRET-nanoscopy, specifically page 128 onwards.

FRET distances are slightly higher (7.2 nm to 7.3 nm R_{mp}) compared to lifetime based distances (6.2 nm to 6.9 nm R_{mp}) which may be due to incorrect treatment of acceptor dark states of the former, hence the latter most reliably represents the real high-FRET distance.

3.5 Particle averaging distances

Particle alignment was applied to the origami platforms with a spot stoichiometry of two donors and two acceptors according to the method outlined in FRET nanoscopy manuscript on page 138 and onwards. Surprisingly, two species were identified during the coarse alignment step that were each other's mirror image (figure 3.6). This result indicated that the platforms have a roughly equal chance to bind with one or the other side to the glass slide, here referred to as species 1 and species 2. Note that the original origami dataset discussed in the FRET nanoscopy manuscript (chapter 2) consisted wholly of species 1. The origami platform is designed to have a defined binding orientation via eight biotin anchors sticking out on the opposite side of the fluorescent labels. Yet, experimental evidence indicates that the biotin anchors do not work as intended. I will lay out several considerations to direct future experimental investigation. Firstly, I have confirmed in the lab the common observation that DNA-origamis stick to the glass surface due to charge interaction in absence of any surface preparation. While incubation with BSA-biotin in absence of Neutravidin causes no DNA-origamis to bind to the surface, as tested by N.S., this has not yet been tested for NHS-PEG-biotin surface preparations used here. AFM-studies on surfaces (FRET-nanoscopy supplementary figure 23 on page 198) have shown

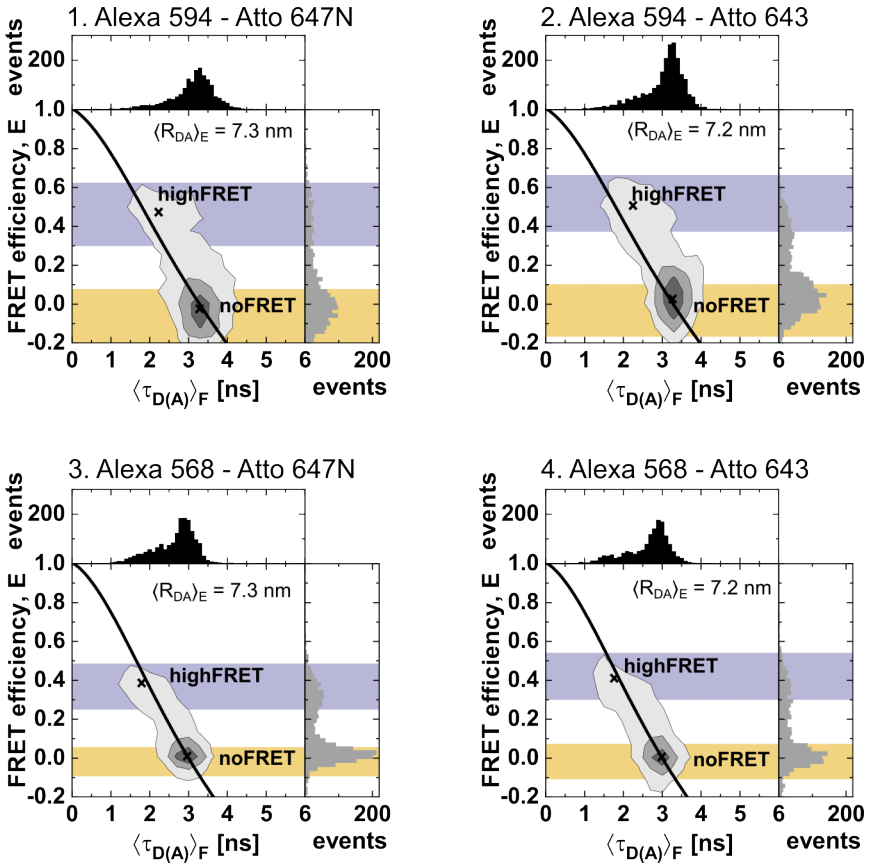

Figure 3.4: **Quantitative FRET efficiencies under STED conditions** for each sample corrected according to FRET-nanoscopy Supplementary Method section Accurate intensity-based FRET efficiencies under STED conditions on page 130. A list of correction factors is given in table 3.4. Crosses provide a guide to the eye for the center of each population. Mean intensity-based FRET distances for the high-FRET pair are reported in each graph. Shaded areas indicate subsensemble selection for TCSPC analysis of high-FRET (purple) and no-FRET (dark yellow). All spot stoichiometries are shown, no data selection has been applied.

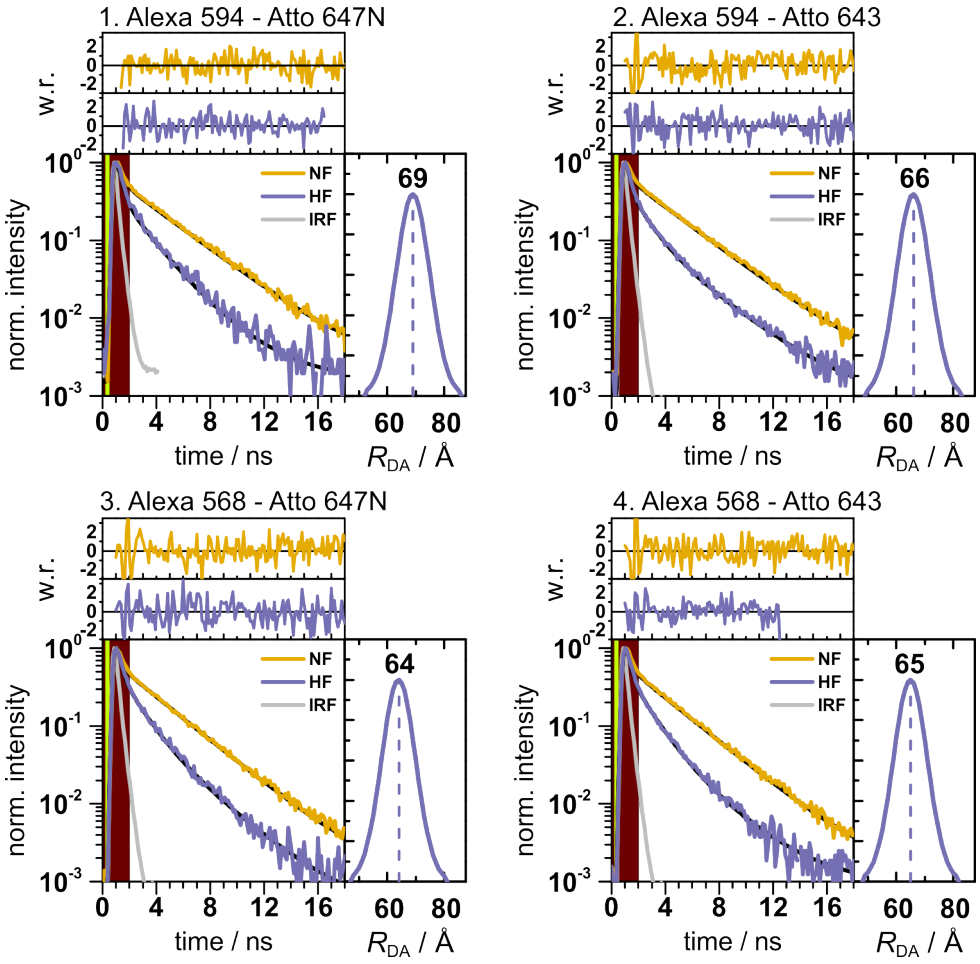

Figure 3.5: **seTCSPC under STED conditions** The figure is slightly modified from [51], fit parameters can be found there as well.

that PEG surfaces have a higher hardness than BSA-surfaces. Hence, the PEG-preparation may incompletely shield the electrostatic interactions with the surface, causing interaction with either side of the platform to occur. This option can be straightforwardly tested by adding DNA-origami platforms to PEG-surfaces in absence of Neutravidin. As a second option, the biotin anchors may not be uniformly on one side of the platform, but can freely thread through the DNA-origami platform. This option is likely when both species are observed in the absence of unspecific sticking of the platforms.

Regardless of the cause for the two species, we may investigate its effects on the localizations of the dye. Both species were analyzed separately for the fine alignment (figure 3.7) using an RMSD cutoff of 5 nm, showing excellent agreement between all four samples with deviations lying in the predicted error margins of ∼0.3 nm. The results show no systematic difference between the two species. Comparing different dye-pairs, a tilting for the high-FRET pair for Alexa 594 - Atto 647N and Alexa 594 - Atto 643 is visible for both species 1 and 2. As Alexa 594 is the common to all these samples, this indicates a pointing effect of the Alexa 594 dye and underlines the very high-accuracy of PA-cSTED. Note that we may exclude dye-DNA π-stacking as no increased anisotropy was found in single-molecule measurements (figure 35 from [51]). The high-FRET distances lie closely clustered around (6.0 ± 0.3) nm, matching to the predictions from simulations. As an exception, the data from Alexa 594 - Atto 643-species 1 and Alexa 568 - Atto 643-species 2 find lower distances being (5.0 ± 0.3) nm and (4.7 ± 0.3) nm respectively. As our data is of high quality and yields no indication for some measurement error, I conclude that these shorter distances represent reality.

The obtained distances are affected by the cutoff threshold of the RMSD alignment quality criterium. I investigated the effect of choosing a different RMSD cutoff on the high-FRET distance for all samples and dye pairs (figure 3.8), showing that the result varied ∼1 nm when the cutoff was varied between 1 nm to 10 nm. This result underlines the importance of motivating the RMSD cutoff, which I here do by choosing a single threshold for all samples that captures the main population of the RMSD distribution, while rejecting the tailing scores (see figure 3.9). Conceptually, this value optimally balances including structures that have minimal uncertainty sources, being photon shot noise and registration error, while rejecting structures with additional uncertainties such as origami misfolding. Equivalently, we may thus obtain the summed effects of registration and photon noise errors from the main population of RMSD scores, which is centered around ∼4 nm. Each fully labeled DNA origami has 8 Degrees of Freedom (DoF), two DoF for each dye position. The alignment procedures 2D shifts and rotates the platform, removing 3 DoF, leaving 5 DoF. As the errors add by the root-of-sum-of-squares, the error per degree of freedom is given by $4\,\text{nm}/\sqrt{5}$, yielding 1.8 nm, very close to the shot-noise limited error sources of ∼1.5 nm reported in table 3.5. This remarkable result shows that registration errors have a very tiny contribution to the overall localization error, highlighting once more that cSTED effectively eliminates any registration error.

In conclusion, all samples show excellent agreement with each other within the measurement error of ∼0.3 nm. Two species of DNA origami platforms were detected with different sides directed towards the glass surface, but no difference in localization result was found. The high-FRET distance was found to be $\sim(6.0 \pm 0.3)$ nm consistent over 6 datasets with two datasets giving a lower result, $\sim(4.85 \pm 0.30)$ nm. The choice of RMSD cutoff value was shown to be crucial for the overall outcome and I motivated the choice of 5.0 nm.

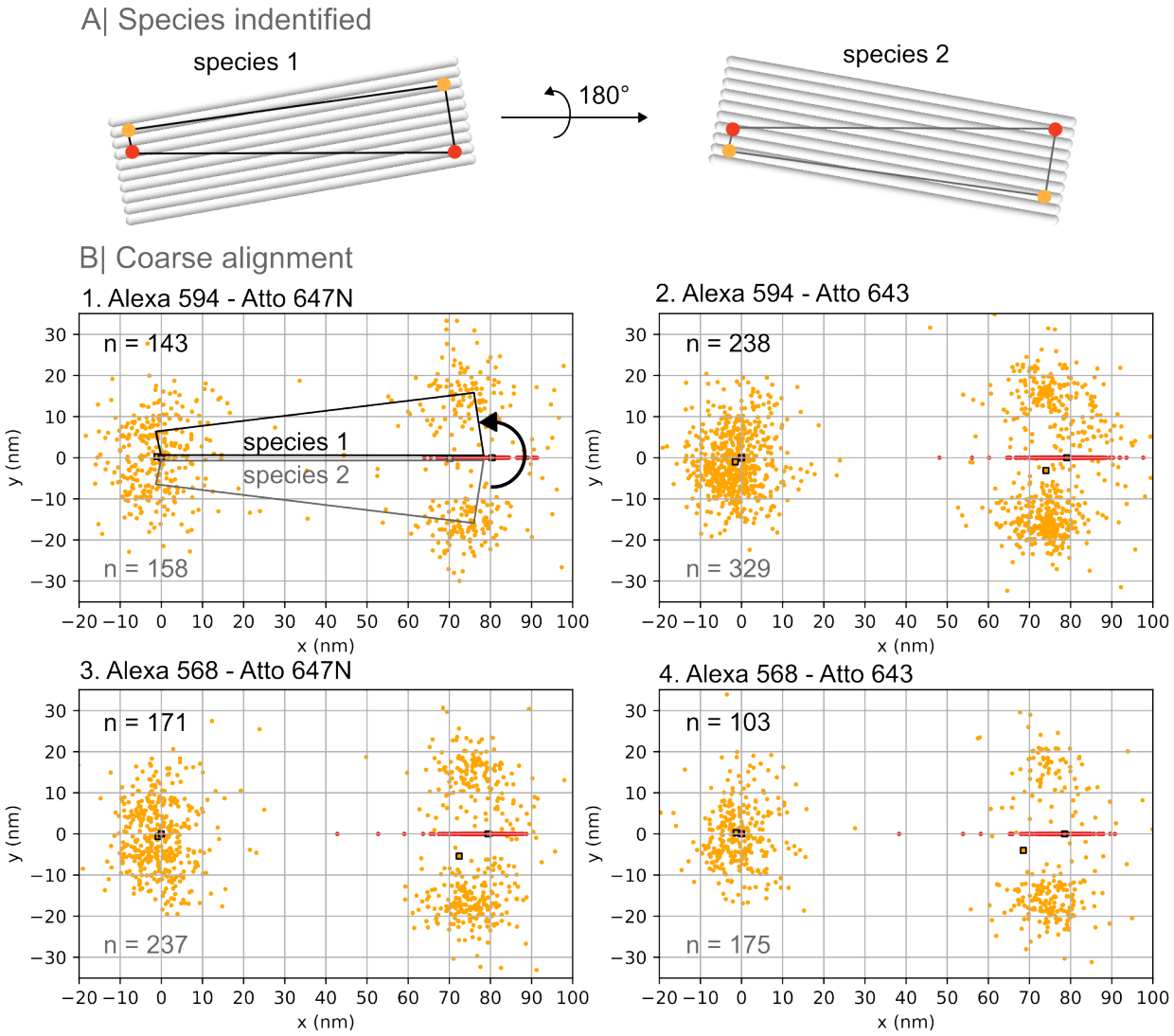

Figure 3.6: **Coarse Alignment of origami platforms reveal two species** The two species are flipped with respect to one another. **A** schematic sketches of the two species and their mirror symmetry. Note that only 10 out of 24 helices have been drawn. **B** Coarse alignment by positioning the high-FRET acceptor in the origin (all dots overlie) and the no-FRET acceptor along the positive x-axis. The number of structures are written on the top and bottom for species 1 and 2 respectively.

	Al594-At647N	Al594-At643	Al568-At647N	Al568-At643
$\langle\sigma_{\mathrm{loc,D}}\rangle$ [nm]	1.38	1.03	1.23	1.26
$\langle\sigma_{\mathrm{loc,A}}\rangle$ [nm]	1.06	0.82	0.81	1.02
$\langle\sigma_{\mathrm{loc}}\rangle$ [nm]	1.73	1.32	1.47	1.62

Table 3.5: **Localization errors from photon shot noise** Population average errors for the donor and acceptor channels and their combined effect. Calculated according to equation S29 on page 137.

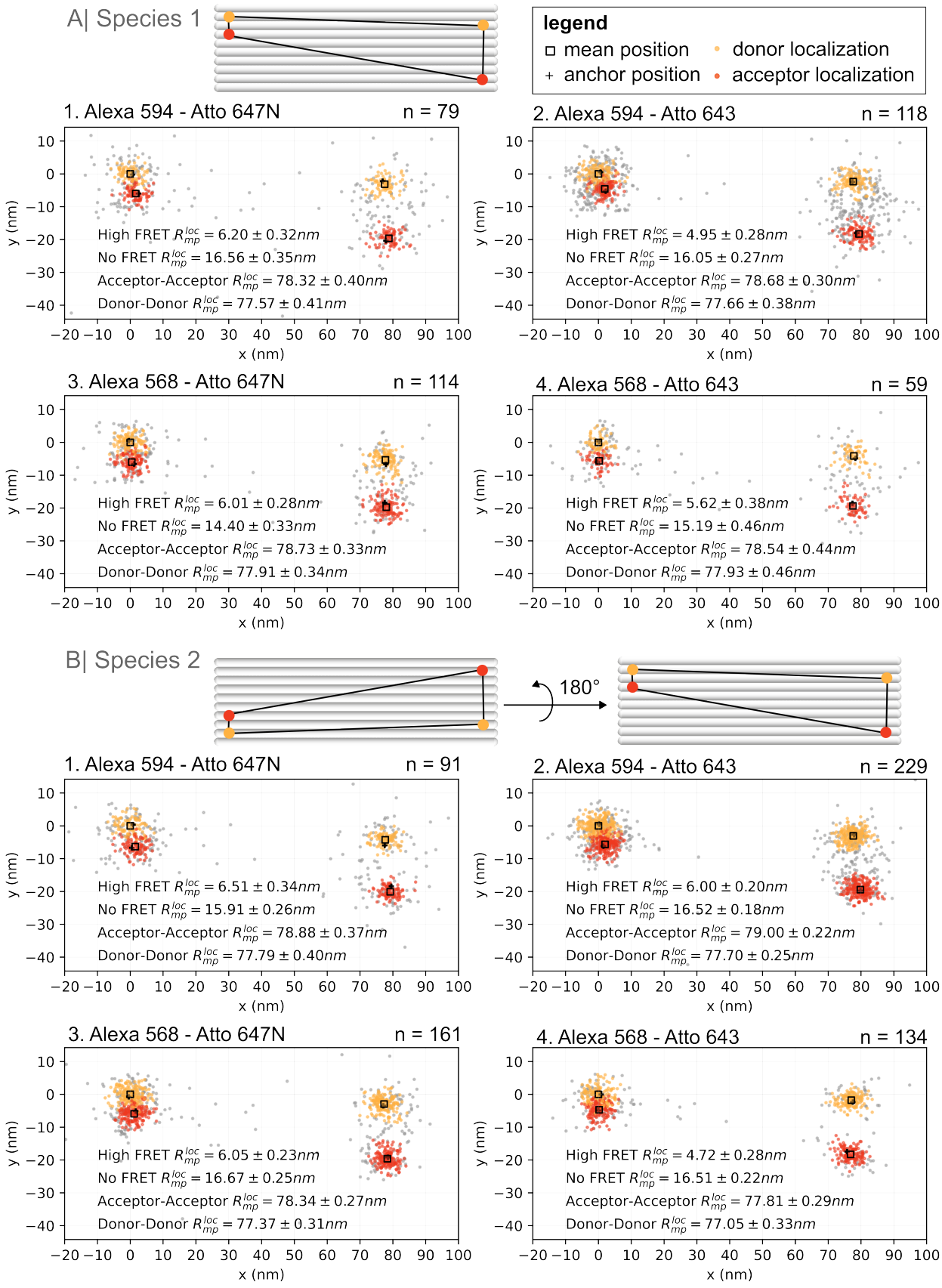

Figure 3.7: Caption on next page.

Figure 3.7: **Fine alignment of origami structures using RMSD minimization** Only structures with RMSD <5 nm are colored and used to calculate R_{mp} and its error via the standard error of the mean. Data points with a higher RMSD are shown in grey and are not considered for further analysis. The data has been rotated to align the helix direction with the x-axis. Distances are calculated from mean positions (equation S32 of the FRET-nanoscopy Supplementary Methods on page 139) and the error of the distance has been calculated by propagating the standard error of the mean (equation S33 of the FRET-nanoscopy Supplementary Methods on page 139). **A** Species 1 is shown. **B** Species 2 has been flipped *in silico* to facilitate comparison to species 1.

	Al594-At647N	Al594-At643	Al568-At647N	Al568-At643
$\langle R_{\mathrm{mp}}^{\mathrm{cg,AV}} \rangle$ [nm][1]	5.7 ± 0.1	5.7 ± 0.1	5.7 ± 0.1	5.7 ± 0.1
$\langle R_{\mathrm{mp}}^{\mathrm{sm,bw}} \rangle$ [nm]	7.64 ± 0.25	7.07 ± 0.15	7.30 ± 0.16	7.79 ± 0.23
$\langle R_{\mathrm{mp}}^{\mathrm{FN,bw}} \rangle$ [nm][2]	7.3 ± 0.3	7.3 ± 0.3	7.2 ± 0.2	7.2 ± 0.2
$\langle R_{\mathrm{mp}}^{\mathrm{sm,seTCSPC}} \rangle$ [nm]	6.92 ± 0.07	6.99 ± 0.07	6.86 ± 0.07	6.84 ± 0.21
$\langle R_{\mathrm{mp}}^{\mathrm{FN,seTCSPC}} \rangle$ [nm]	6.74 ± 0.74	6.44 ± 0.35	6.23 ± 0.35	6.33 ± 0.32
$\langle R_{\mathrm{mp}}^{\mathrm{FN,PA,species1}} \rangle$ [nm]	6.20 ± 0.32	4.95 ± 0.28	6.01 ± 0.28	5.62 ± 0.38
$\langle R_{\mathrm{mp}}^{\mathrm{FN,PA,species2}} \rangle$ [nm]	6.51 ± 0.34	6.00 ± 0.20	6.05 ± 0.23	4.72 ± 0.28

Table 3.6: **Overview of high-FRET distances**. Abbreviations: FN - FRET-nanoscopy data, sm - solution single-molecule, cg - coarse-grained simulations, bw - burst-wise analysis ($E-\tau$ histograms). This table represents an updated status compared to the table shown in [51]. All distances were converted to R_{mp} as described in the text. [1]Errors from averaging several salt concentrations. [2]Error from dynamic shift.

3.6 Conclusion and discussion

We have now gathered comprehensive information from various orthogonal methods, including burst-wise- and seTCSPC-based FRET information on solution single-molecule data as well as FRET-nanoscopy data, PA-cSTED data and cgMD simulations. We have used these techniques to measure properties of the DNA-origami platform, especially to obtain a calibration between FRET and PA-cSTED data on the high-FRET distance. The key results for the high-FRET and no-FRET distances are listed in table 3.6 and table 3.7, respectively. Note that in the following discussion I will not consider results from the non-centered-χ distribution fits as their results are superseded by the particle-averaging cSTED data due to superior particle filtering properties of the latter. Similarly, Particle Distribution Analysis (PDA) on the solution single-molecule data is not considered as the simple single static distribution model fails to reproduce the distance from $E-\tau$ diagrams, indicating some issue with the former.

	Al594-At647N	Al594-At643	Al568-At647N	Al568-At643
$\langle R_{\mathrm{mp}}^{\mathrm{cg,AV}} \rangle$[1] [nm]	16.3 ± 0.4	16.3 ± 0.4	16.3 ± 0.4	16.3 ± 0.4
$\langle R_{\mathrm{mp}}^{\mathrm{FN,PA,species1}} \rangle$ [nm]	16.6 ± 0.4	16.1 ± 0.3	14.1 ± 0.3	15.2 ± 0.5
$\langle R_{\mathrm{mp}}^{\mathrm{FN,PA,species2}} \rangle$ [nm]	15.9 ± 0.3	16.5 ± 0.2	16.7 ± 0.3	16.5 ± 0.2

Table 3.7: **overview of no-FRET distances**. [1]Errors from averaging several salt concentrations.

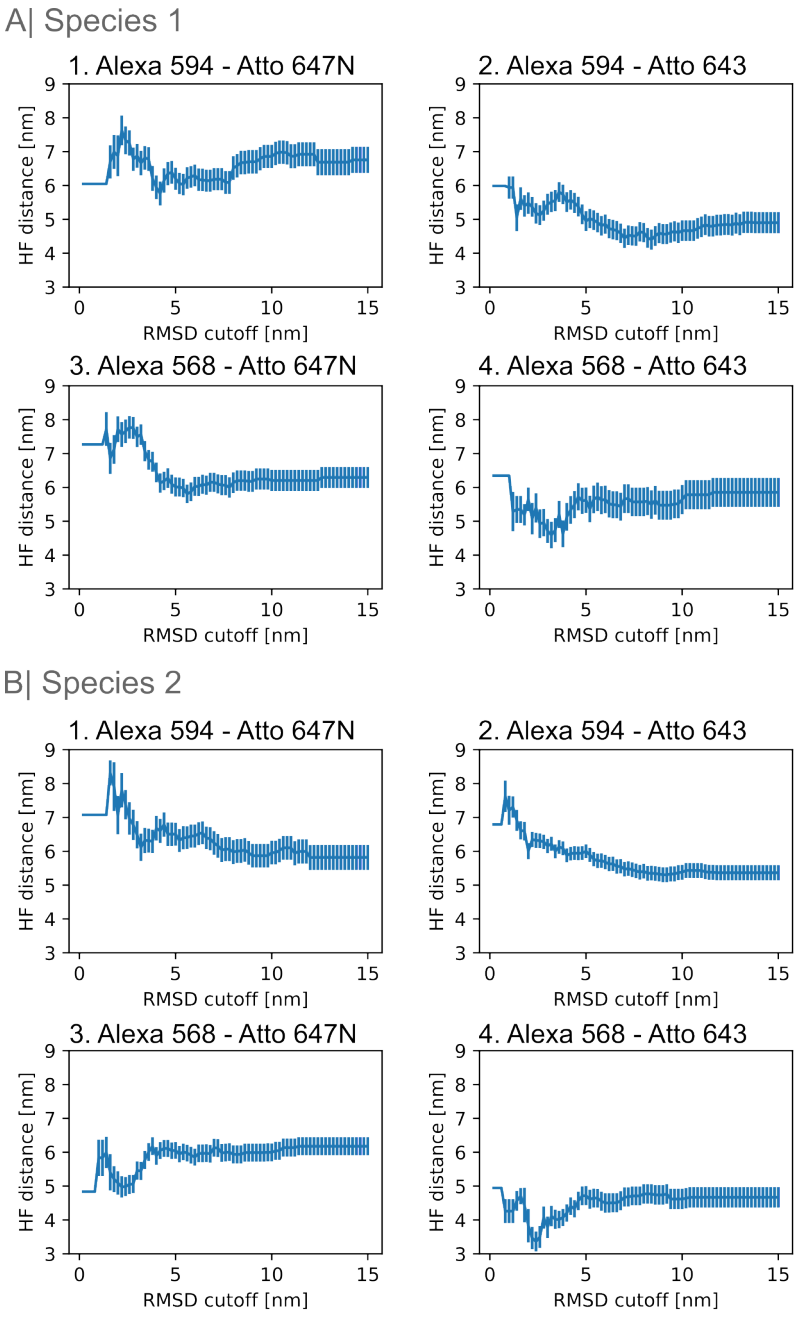

Figure 3.8: **high-FRET distance from particle averaging for different RMSD cutoff values** The mean distance changes as more structures with a higher RMSD value are considered (compare figure 3.9). The error on the average distance is calculated from standard error of the means. For an increasing smaller RMSD cutoff, the error remains approximately constant as fewer datapoints are compensated by tighter clustering. All samples shown for **A** species 1 and **B** species 2.

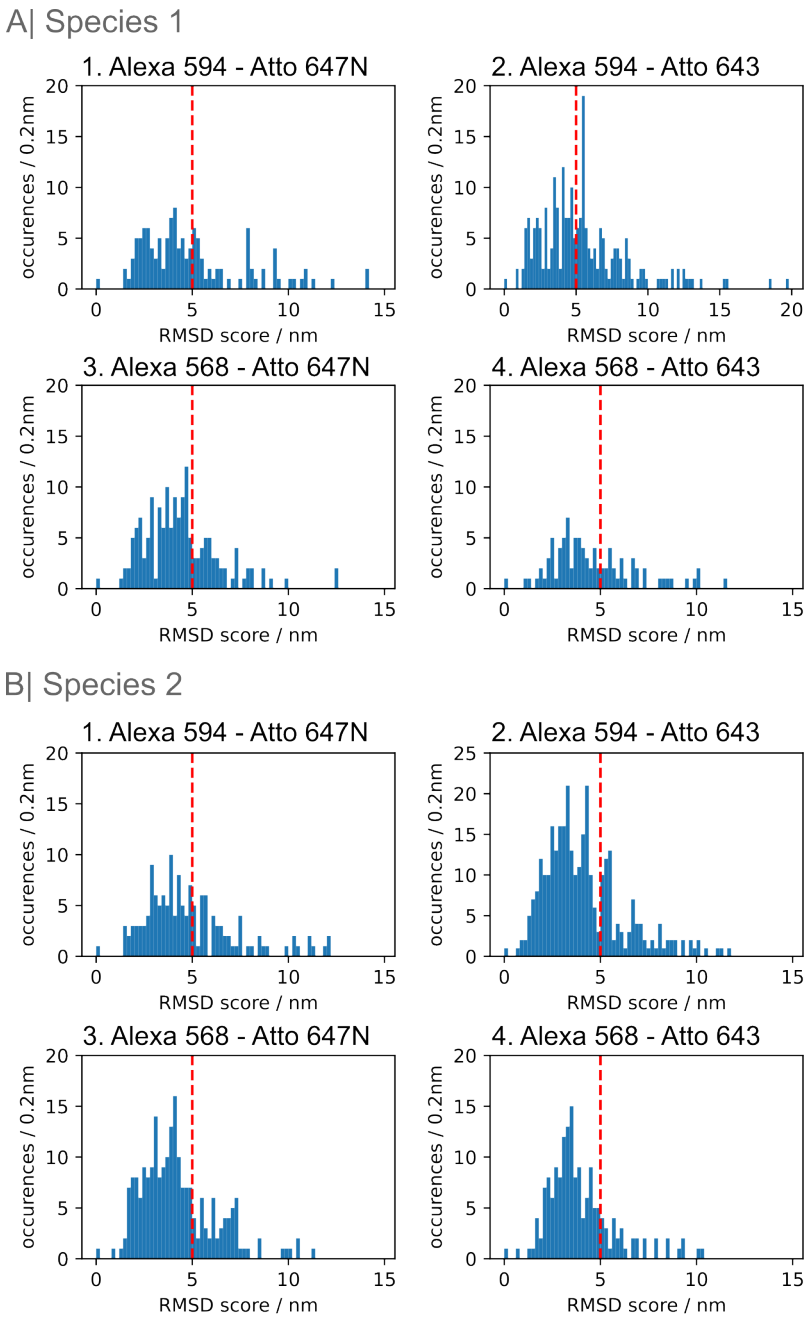

Figure 3.9: **RMSD score distributions A** All samples shown for species 1 and **B** species 2. The red dashed line indicates the RMSD cut used in figure 3.7.

The results from the cgMD simulations show that a ionic strength between 500 mM to 2000 mM is sufficient to relax the electrostatic interactions in the DNA origami platform. The physiological ionic strength of 35 mM clearly does not represent good simulation conditions due to the coarse-grained simulations not accounting for the higher local charge density of Magnesium or its ability to coordinate complexes. This observation matches experimental measurements [41] where a ∼10 mM Mg^{2+} concentrations needed to be replaced with 200 mM to 2000 mM Na^{+} concentrations to ensure proper origami folding. I argue that the simulations results in this ionic strength range is comparable to experimental results as the structure is electrostatically relaxed. Further, the platform shows no significant curvature on the ∼15 nm length scale, making it comparable to surface bound platforms where curvature would be absent. Comparison of the cgMD results to PA-cSTED data shows excellent agreement for both high-FRET and no-FRET distances. The measurements at different salt concentrations and for different dye pairs can be considered as repeats for the respective measurement method. Both methods show similar variability between repeats, indicating that the repeats preferentially probe different thermodynamically accessible states of the platform, such that the variability may be considered an inherent to the structure. This also matches the observation that the high-FRET distance changes when the RMSD cutoff is changed (figure 3.8. Additionally, we see a tilting of the high-FRET pair for all constructs with the Alexa 594 donor, potentially indicating a pointing effect. The high-FRET and no-FRET distances for the cgMD and PA-cSTED are consistent and lie in the range 5.3 nm to 6.2 nm and 15.0 nm to 16.5 nm respectively.

Turning towards the FRET information, we see that seTCSPC yields similar results between FRET-nanoscopy and solution single-molecule, being (6.5 ± 0.3) nm and (6.8 ± 0.1) nm respectively. The results from burst-integrated analysis yields slightly higher distances, being (7.3 ± 0.3) nm and (7.4 ± 0.4) nm respectively. The longer distances for burst-integrated analyses can be explained by considering intermittent acceptor dark states shorter than ∼200 µs duration, which would be correctly treated as no-FRET by TCSPC-based analysis, but would result in an elongation of the FRET population and an overestimation of the distance by burst-integrated analyses. Acceptor dark states of >1 ms can be excluded as they would be found in PDA analyses (figures 39-40 from [51] and would cause a the two limiting states in the $E - \tau$ diagram to be well-defined. The existence of such an acceptor dark state could be tested using solution-FCS on acceptor only and donor only origamis. Due to the more refined nature of seTCSPC analyses, I will consider its distances to be closest to the truth.

We may now consider how well PA-cSTED based measurements agree with FRET-based distances and assess the feasibility of Optical Pythagoras. Considering that these two methods are orthogonal and rely on completely different measurement principles, the agreement between both methods is impressive and place this study among the highest precision and accuracy single-molecule and fluorescence microscopy studies known to the author [27, 24, 21]. Nevertheless, seTCSPC-based distances are consistently 0.5 nm to 1 nm larger than PA-cSTED measurements, which may be due to several reasons. Firstly, the limited movement of the dyes in the major groove of the DNA may affect κ^2 and hence the Förster radius. Secondly, all localization-based distances scale with the pixel size which relies on the calibration of the microscope scanner. This calibration can be straightforwardly verified by obtaining a calibration slide, for example from[1] if budget allows. Thirdly, as this is the first direct comparison between the two methods, there may be other unidentified scaling factors that affect the entire method. I do not consider z-displacement of the dyes as a potential cause for the discrepancy as our AV simulations indicate there is no z-displacement. Regardless of the cause, the difference is consistent after all known effects have been discussed and accounted for and thus may be corrected.

[1] https://argolight.com/argo-hm-v2/

Turning to PA-cSTED, the analysis revealed two species that were each others mirror image, indicating that the platform may bind to the surface on either side. Despite this, no difference in the cSTED distances or the FRET signatures could be found, indicating that the dyes are not affected. The two species and four different dye pairs effectively generated 8 repeats for PA-cSTED, hence, I obtain an average value with error of (5.75 ± 0.60) nm to represent the variability between repeats. In conclusion, by considering the difference between seTCSPC and PA-cSTED as a consistent difference that can be calibrated, the variability between repeats forms the fundamental noise floor for determining the information content of Optical Pythagoras. For an exemplary total distance of 6 nm and requiring a minimum of twice the repeat standard deviation (1.2 nm) to resolve states, roughly 5 different angles, corresponding to projected distances of 0.6 nm, 1.8 nm, 3.0 nm, 4.2 nm and 5.4 nm can quantitatively be distinguished. Note that this maps non-uniformly to the corresponding angles (see section 2.3.6 and that more angles could be distinguished for larger distances.

Chapter 4

Quantifying the Spatio-temporal Evolution of Protein Interactions using Cell Lifetime FRET Image Spectroscopy (CELFIS)

In this work I establish a new method called CELFIS that can resolve changes in cellular oligomeric fraction with 1 % accuracy in living cells as a function of concentration, time and spatial localization. The method is crucial in elucidating the stoichiometry of CD95 after ligand addition as well as discovering a concentration dependent monomer to dimer transition for CTLA4. This chapter summarizes the manuscript appended in appendix B, which is very close to submission. The analysis software used in this manuscript is publicly available at [1].

4.1 Author contribution

This work was designed by the author and executed by N.B. and the author under supervision of C.M. and C.S. The author was solely responsible for writing the python analysis pipeline. Many thanks to Mykola Dimura for helping with AV simulations. This method was developed in response to the need for measuring the oligomeric state of CD95, but was found to be generically applicable. Oleg Opanasyuk developed the polarization-sensitized fit used in a later iteration of this work. All co-authors from this work generated essential contributions without which this work would not have been possible. I am especially grateful for previous work done on FRET sensitized donor decays in live cells by C.S. and colleagues.

4.2 Motivation

Molecular interactions constitute a dynamic network in space and time that drive cellular decision making and homeostasis. For example, the concentration of a membrane-bound homodimer depends on the concentration of its constituent monomers as well as the concentration of any co-factors and ligands located in the membrane, cytoplasm or extracellular domain. In principle, unravelling the precise spatio-temporal interdependence of molecular interactions allows predicting the evolution of a cell if the initial conditions are known. This is a highly sought-after goal with relevance for clinical applications, as it vastly increases our ability to

[1] `https://github.com/Fluorescence-Tools/Seidel`

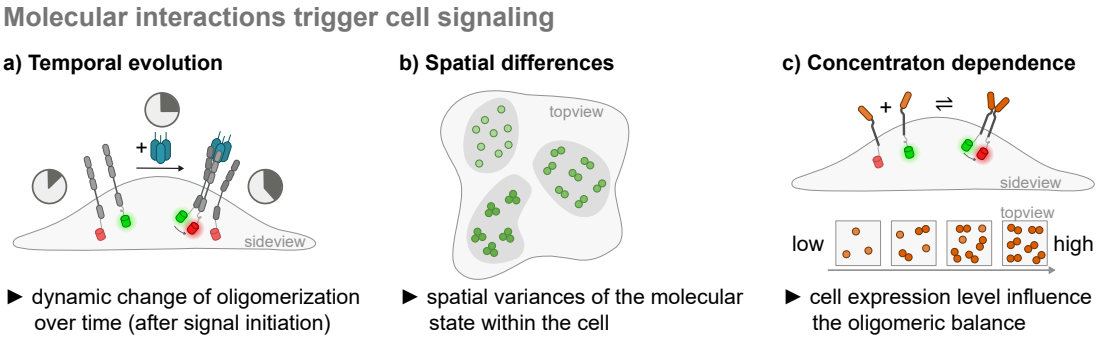

Figure 4.1: **The applications of CELFIS** By quantifying the oligomeric fraction in living cells, CELFIS can be used to monitor **(a)** temporal evolution of oligomerization, **(b)** differential oligomerization in subcellular compartments or **(c)** to measure the concentration dependence of oligomerization processes by measuring cells with different expression levels.

intervene in signaling pathways to the benefit of the patient. Clearly, the rate at which we approach this goal is limited by the power of the methods available. Commonly used methodologies like co-immunoprecipitation western-blot [38], Yeast two-Hybrid system (Y2H) [19] or TAP-MS [10] are mostly used to obtain binary yes / no answers under a single set of conditions and are thus blind to effect of concentration, time and spatial dynamics. Furthermore, these methods do not study the proteins embedded in their native environment in live cells as western-blot or TAP-MS only work *in vitro*, whereas Y2H measures protein interactions at a Transcription Factor binding site predominantly in the yeast host organism, although other host systems have also been developed [58]. As a major step forward, CELFIS allows for studying the abundance of up to two proteins and their homo- or hetero-oligomerization as a function of concentration, space and time in live cells, thus providing vastly more information than was previously possible. The CD95 signaling pathway is an excellent example of a molecular switching mechanisms as it is known for its ability to induce apoptosis [4, 48, 37], but may also lead to proliferation [42] or activation of the NFκB pathway [36]. The efficacy with which it induced apoptosis, or the decision regarding which cellular pathway is activated depends on the concentration of co-stimulatory or inhibitory cofactors [36]. Here we apply CELFIS to study the evolution of CD95 oligomer formation upon ligand addition as a function of time, cellular localization and CD95 concentration in HeLa cells. In a further example we measure the concentration dependent monomer to dimer transition of CTLA4, whose oligomerization state is likely to affect its function as a T-cell activity regulator [62].

4.3 Main results

A CELFIS experiment can resolve spatio-temporal information on the oligomeric state of fluorescently labeled proteins with high statistics. CELFIS can be used to study homo-interaction by labeling the protein of interest with donor and acceptor. Although we do not show it here, it can be readily expanded to hetero-interaction between two different protein species by labeling the species with donor or acceptor respectively. Data acquisition occurs on a two-color confocal microscope with TCSPC readout. A FRET sensitized donor decay ($\epsilon(t)$) is used to determine the FRET fraction, x_{FRET}, and the FRET rate, k_{FRET}. After publication of this thesis, an iteration of the fitting routine was implemented and applied to all data. The new fitting routine provides a forward model including Instrument Response Function (IRF) convolution

and polarization sensitized readout. The IRF convolution enabled sensitivity to very fast-life time components as well as accounting for detector shifts, yielding improved precision of the fitting result. The polarization sensitized readout provides anisotropy information. The new fitting routine was unable to fit k_{FRET} stably. This shortcoming was resolved by determining τ_{x} from a secondary fit and obtaining k_{FRET} from there. Uniquely, The FRET fraction is transformed in an oligomer fraction and absolute number of receptors using a combination of AV simulations, calculating the abundance of hetero-dimers using combinatorics and accounting for the maturation fraction. Temporal resolution is obtained by repeatedly measuring the same cells in time, while spatial resolution down to cellular compartments is obtained by building fluorescent lifetime decays from areas of interest. Below I elaborate on the key contributions and results in this work.

4.3.1 Measurement and analysis automation

A high number of statistics is required to sample all relevant biological conditions. For example, the fraction of interacting molecules may differ depending on the concentration of the interaction partners and the presence of co-factors or ligands. Even when the aforementioned conditions are identical, cells display a natural variability due to cell cycle [29] or other cellular factors. The data acquisition is automated using self-written software for the Imspector software such that ∼10 min preparation time suffice to record 20 areas each with multiple cells for a single measurement or time series. Similarly, data analysis is automated using a self-written analysis pipeline attached to this manuscript. Global analysis settings must be set once taking ∼20 min, typically only changing after re-alignment of the system. For each dataset, a series of binary masks must be given by the user to segment the images, such that the setup time per dataset is ∼10 min after which the analysis runs automatically.

4.3.2 Surface concentration determination

The molecular surface or volume concentration can be obtained from the fluorescent brightness provided that the brightness of a single fluorophore has been calibrated. Although seemingly simple, experimental accuracy depends on 1) knowing the precise concentration of calibration solution 2) knowing the precise diffusion constant of the reference dye for determining the confocal volume and area and 3) correcting for the fluorescence intensity coming from the cytoplasm. A detailed description of the experimental procedure was prepared as a Nature Exchange Protocol and included in the Supplementary Information (appendix C).

4.3.3 AV simulations to determine the FRET signal of a pure FRET dimer

To transform the FRET fraction into the fraction of dimeric molecules, a reliable determination of the FRET signal corresponding to a pure dimer, $x_{\mathrm{FRET,max}}$, is crucial. Previous experimental work measured the effect of peptide linker length on FRET Efficiency [17], which was used to calibrate the average linker extension for different linker lengths [14]. Here, we additionally consider the exact anchoring positions of the biomolecules and their geometric restrictions posed by e.g. a membrane by including these elements in the AV-simulation. Our AV simulations yielded a FRET fraction, $x_{\mathrm{FRET,AV}}$, of 46 % for two anchor points separated by 22 Å each with a 51 amino acid linker and a geometry limited to an approximate half-sphere and assuming that FRET can be detected up to 80 Å for a Förster radius of 52 Å. The $x_{\mathrm{FRET,max}}$ is further affected

by the fraction of mCherry acceptor molecules that correctly mature to a state where they are able to absorb a photon, $p_{\mathrm{A,m}}$. We refer to previous experimental work [16] to obtain the fraction of mCherry molecules that have reached a fluorescent state. Yet, mCherry molecules may fold to a state that is capable of absorption, but where relaxation of the excited stated proceeds non-radiatively. Hence, the fraction of mCherry molecules capable of absorption must be higher than the fraction of molecules capable of fluorescence and we estimate it to be 80 %. This number and a similar maturation efficiency for mEGFP of 80 % [16, 60] was also used to correct the calculation of the total number of receptors in the cell, as the concentration determination is ultimately based on absorption. For homo-interactions studied here, $x_{\mathrm{FRET,max}}$ is further reduced due to the presence donor-donor dimers, which do not contribute to a reduction in the lifetime. Owing to the previous determination of donor- and acceptor-concentration, the fraction of donors in a donor-acceptor dimer is straightforwardly determined from binomial combinatorics to be p_{A}, the fraction of acceptor labeled receptors (see CELFIS methods, section *FRET dependency on A:D ratio* page 224). For hetero-interactions this step is not needed such that the maximum FRET fraction is determined solely by AV simulations and the maturation fraction. The final $x_{\mathrm{FRET,max}}$ in case of homo-dimers is given by:

$$x_{\mathrm{FRET,max}} = x_{\mathrm{FRET,AV}} \times p_{\mathrm{A}} \times p_{\mathrm{A,m}}. \tag{4.1}$$

A treatment of $x_{\mathrm{FRET,max}}$ in case of trimers is given in the manuscript. For a mixture of dimers and trimers, the $x_{\mathrm{FRET,max}}$ may be calculated using a species average. CD95 may form dimers or trimers depending on the cooperativity of its oligomerization. As the cooperativity is unknown at the time of writing, a dimeric state has been assumed as the simplest assumption that allows for robust biological insight.

4.3.4 Proximity FRET correction and CTLA4 concentration dependent dimerization

Transiently transfected cells can easily produce FRET labeled molecules on membranes in sufficient quantities such that a significant FRET signal occurs due to accidental proximity of labeled molecules. As this so-called bystander or proximity FRET obscures the interpretation of FRET signal due to specific interaction, a correction strategy is needed to study membrane proteins at high concentrations (>1000 receptors/µm^2. Here, we use monomer controls from the CD95, CD95(ΔDD) and CD86 proteins to calibrate the concentration-dependent FRET signal due to proximity FRET only (figure 4.2A). We fit our data to a previously established model [64, 9, 33] that depend on a single parameter,

$$x_{\mathrm{FRET,prox}} = 1 - \exp(-\frac{c_{\mathrm{A}}}{c_{\mathrm{prox}}}) \tag{4.2}$$

where c_{A} is the acceptor concentration and c_{prox} describes the acceptor concentration at which 63% FRET fraction occurs due to proximity FRET. Out of three monomeric controls, the CD95 control was chosen due to its good fit quality, yielding a c_{prox} of $(3.13\pm0.15)\times10^4$ receptors/µm^2. The proximity FRET correction is applied to the CTLA4 protein, which was established as a dimer in the 1990s and early 2000s [39, 22, 13] using Western Blot analysis at high concentration. Surprisingly, the concentration dependent FRET fraction of CTLA4 did not match a purely dimeric protein, but rather showed a monomer to dimer transition as a function of concentration. After correcting for proximity effects, the dimerization constant was found to be (123 ± 11) receptors/µm^2 (figure 4.2B-1) using the dimerization model

$$x_{\mathrm{dimer}}(K_{\mathrm{dimer}}, c_0) = \frac{K_{\mathrm{dimer}}}{c_0}\left(1 + \frac{4c_0}{K_{\mathrm{dimer}}} - \sqrt{1 + \frac{8c_0}{K_{\mathrm{dimer}}}}\right), \tag{4.3}$$

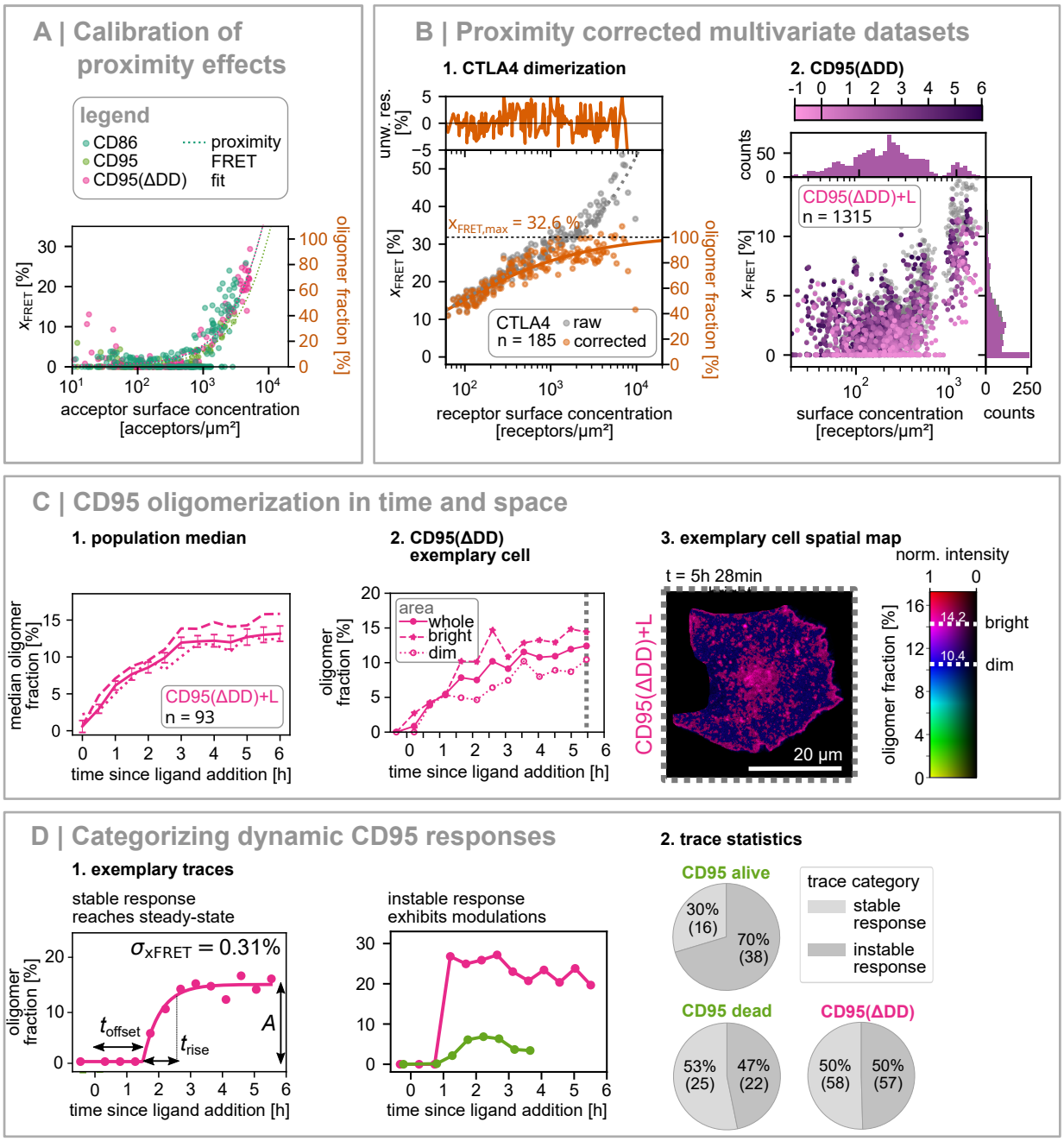

Figure 4.2: **Key results for CELFIS A|** FRET is observed in monomeric controls and fitted using equation 4.2 to obtain a calibration for proximity FRET. **B|** Proximity-corrected multivariate datasets for CTLA4 and CD95(ΔDD). The CTLA4 dimerization is fitted according to equation 4.3. The time dimension for CD95(ΔDD) is color-coded. **C|** The role of local receptor concentrations on the cell membrane were investigated by analyzing bright and dim domains separately. **1.** population median and **2.** an exemplary single-cell evolution. **3.** Exemplary cell colored with a 2D color map where the receptor concentration is encoded in the color brightness and the oligomer fraction in the color hue as indicated by the color bar. Data corresponding to full-length CD95 data for C| and D| is found in the manuscript. **D|** Time evolution of single-cell traces were categorized as being either stable or unstable for three data categories. The stable response traces were used to estimate the precision of the fit accuracy.

where K_{dimer} represents the dimerization constant and c_0 represents the total receptor concentration. In summary, our experimental approaches yield a robust calibration of the concentration dependent proximity FRET, allowing determination of the CTLA4 dimerization constant.

4.3.5 CELFIS applied to CD95

CELFIS was crucial to elucidate the oligomeric state of CD95 at rest and upon ligand addition, as discussed extensively in chapter 5. Here, we study the spatio-temporal ligand-induced evolution of CD95 oligomerization on the single cells and ensemble level, as well as correcting for proximity FRET. Temporal analysis on the ensemble level showed that oligomerization could occur at all concentrations (figure 4.2B-2) and that the oligomeric fraction increased in the first 3 hours after which the population median was constant (figure 4.2C-1). One outstanding research question was whether signaling occurs via specialized membrane areas. As a potential candidate, bright domains were found on the membranes indicating a local accumulation of receptors. Spatial analysis was performed by analyzing high and low receptor concentration domains on each cell, yielding that oligomerization occurred everywhere on the membrane, although a slightly larger oligomerization fraction occurred at higher receptor concentration (figure 4.2C). Following the same trend, cells with a higher overall CD95 concentration showed a larger oligomeric fraction after ligand addition (supplementary figure 10 of the CELFIS manuscript). Taken together, these results indicate that the fraction of oligomeric CD95 depends on the local concentration, consistent with a concentration-induced enhanced binding kinetics model.

Interestingly, the time evolution of single cells showed a variety of patterns not visible when considering only the population median. In a first category, selected cells showed an asymptotic approach to a new steady state corresponding to a purely kinetics driven response. The evolution of these traces could be well described by a simple model (Equation 12 and 13 in the manuscript), enabling us to distinguish fluctuations due to the measurement error from actual changes in the oligomer fraction, yielding a conservative estimate of the precision to be 0.22% x_{FRET} or 0.8% oligomer fraction. In a second category, modulation of the oligomeric fraction in time is indicative of cellular processes controlling the oligomeric state in a complex manner. The trends discussed in this section were observed for CD95 and CD95(ΔDD) variants. In summary, our spatio-temporal and concentration dependent analysis of CD95 and CD95(ΔDD) oligomerization has yielded quantitative insight into the nature of CD95 oligomerization. This study paves the way for quantifying other components of the CD95 signaling pathway, such as CD95 interaction with Fas-Associated Death Domain (FADD) and FADD interaction with procaspases 8 and 10.

4.4 Conclusion and significance

As our method is easily adoptable and widely applicable, I expect that it will open up new dimensions for studying molecular interactions quantitatively in the cell over time and space and as a function of concentration. By setting a new standard of quality and robustness for investigating molecular interactions, CELFIS will furthermore aid to address the current reproducibility crises. Several fields cite the hitherto lack of quantitative spatio-temporal information as a crucial limitation to the progress of their fields, including computational interaction modeling [50] or the study of the PI3K pathway [40]. The key components of CELFIS can be summarized as 1) measuring dimer concentrations down to 1% precision in live cells at endogenous expression levels, 2) providing the architecture to obtain and analyze large datasets of single-cells in time

and 3) providing new solutions to correcting proximity FRET at high concentration levels and determining the FRET signal corresponding a pure dimer signal, $x_{\mathrm{FRET,max,dimer}}$, or pure timer, $x_{\mathrm{FRET,max,trimer}}$. CELFIS benefitted from previous studies that developed fitting models [56, 23] or methods that took a different experimental approach [52]. The method is applied to reveal and quantify concentration dependent dimerization of CTLA4 and quantify the time dynamics of CD95 oligomerization as a function of local concentration. The method is easy to implement as it requires only a two-color confocal system with TCSPC readout, fluorescent protein-tagged proteins and analysis software that we provide. The results are robust, yet sophisticated due to the internal calibration using a donor-only probe and limited number of free variables in the fitting function. The method is applicable to a very wide class of biological problems, as it can be applied to elucidate the quantitative binding of any protein pair in life cells.

Chapter 5

The oligomeric state of CD95

The oligomeric state of the CD95 receptor was previously unknown due to experimental difficulty in measuring molecular stoichiometries. Here we develop confocal Photobleaching Step Analysis (cPBSA), quantitative STED imaging and CELFIS in addition to applying live-cell Fluorescence Correlation Spectroscopy (FCS) to scrutinize several proposed models and find that CD95 is monomeric at rest and that 8 % to 17 % oligomers form after ligand addition, either dimers or trimer, which is sufficient to efficiently induce apoptosis. Furthermore, our measurements yield information on the oligomerization and apoptosis dynamics as well as on CD95 diffusivity.

5.1 Author contribution

As part of a highly effective team, I was involved in performing measurements, developing and executing analyses, interpreting result, creating figures and writing texts. Notably, I designed and developed the cPBSA experiments and analyses with invaluable help from N.B. for optimized sample preparation. The development of CELFIS is discussed in chapter 4. As the two main authors on this publication, N.B. and I collaborated intensively in all aspects, where I emphasized on establishing methods and performing analyses and N.B. emphasized on sample preparation, performing experiments and creating beautiful figures. I am thankful for guidance from C.A.M.S. and C.M. in this project and extensive literature knowledge from C.M.

5.2 Motivation

The CD95 receptor pathway is a particularly interesting example to study signal initiation by means of molecular interactions as it is exclusively activated by the trimeric CD95 Ligand, also known as FasL (CD95L) and has several signaling outcomes depending on the presence of intracellular co-stimulatory proteins [34, 37]. CD95 signaling may either promote cell survival, induce an inflammatory response via the Nuclear Factor kappa-light-chain-enhancer of activated B cells (NFκB) pathway or, most prominently, induce apoptosis [30, 48, 4]. Due to its pivotal role in immune response, there is a great therapeutic interest in CD95 for patients with various diseases, including cancer, immunotherapy or infectious diseases [7]. As a Tumor Necrosis Factor Receptor (TNFR), its signaling pathway is further exemplary for other members of this super-family [6]. At a molecular level, signal activation is thought to occur via a change from one oligomeric state to another. Various models have been proposed, including the formation of a honeycomb network of trimers upon ligand addition [53, 61]. Yet, experimental validation

of these models in live cells has been lacking due to the difficulty in measuring oligomeric states in live cells. In this paper, I expanded existing methods to elucidate the oligomeric state of CD95 in presence and absence of ligand.

5.3 Photo Bleaching Step Analysis

Photobleaching Step Analysis (PBSA) measures the number of fluorophores in a diffraction limited spot by counting the number of bleaching steps (figure 5.1a). Typically, this method is applied using organic dyes on a TIRF setup. A crucial parameter for the interpretation of PBSA data is a known labeling efficiency of the object of interest. For example, labeling with organic fluorophores (monomeric Enhanced Green Fluorescent Protein (mEGFP)) ensures that each CD95 molecule is labeled with mEGFP, which has a folding efficiency of 80% [60]. By contrast, the CD95 antibody has unknown labeling efficiency and an unknown number of organic dyes attached, making antibody labeling strategies ill-suited for PBSA. Furthermore, I adjusted PBSA to work on a confocal setup (cPBSA), which has the potential to measure in any area of the cell. Analysis was performed using the Kalafut-Visscher (KV) algorithm [31] implemented in python [28].

Despite the good labeling efficiency, cPBSA on Fluorescent Proteins (FPs) remains challenging as the combined effects of mEGFP dark states, limited mEGFP photostability, autofluorescence and polarization dependent brightness prohibit interpreting the number of bleaching steps directly as the number of fluorophore. This issue was circumvented by introducing monomer (Cluster of Differentiation 86 also known as B7-2 (CD86)-mEGFP) and dimer (CD86-mEGFP-mEGFP and $CTLA4_{DA}$) controls which acted as an internal standard. Comparison of CD95 with the controls (figure 5.1b) showed that CD95 and its apoptosis-incompetent variant CD95(ΔDD) were indistinguishable from the CD86 monomer control before ligand addition and showed a ligand induced shift of $(16 \pm 7)\,\%$ and $(13 \pm 8)\,\%$ towards the dimeric control for CD95 and CD95(ΔDD) respectively. Molecular clusters consisting of many spots (>6), the fingerprint of a honeycomb lattice of trimers, were not observed.

Synergistically, I made cPBSA robust using simultaneous readout of Fluorescence Spectroscopy. Specifically, 1) I quantified the characteristic times of three dark states in mEGFP using auto-correlation of the intensity traces. 2) Using the dark states, I predicted the expected residual variance after identifying bleaching steps. This result matched the measured residual variance, justifying the analysis settings used. 3) I determined the polarization state of mEGFP to be ∼80 % freely moving and ∼20 % fixed using polarization sensitized detection.

5.4 CELFIS quantifies oligomeric fraction in time

A detailed image of the concentration and time-dependence of CD95 oligomer formation is provided by CELFIS (see also chapter 4). Cells were transfected with varying amount of transfection reagents to obtain expression levels ranging from 20 up to 1000 receptors/µm^2. In absence of ligand, CD95 and CD95(ΔDD) were monomeric independent of concentration. Upon ligand addition, a switch is visible from pure monomers in absence of ligand to a monomer/oligomer mixture independent of concentration (figure 5.2a). Repeated measurements of the same live cells showed the time dynamics of oligomer formation (figure 5.2), showing that the average CD95 oligomeric fraction increases during 2 hours after ligand addition, up to a concentration of 8 % to 17 % interquartile range just prior to apoptosis (figure 5.2c).

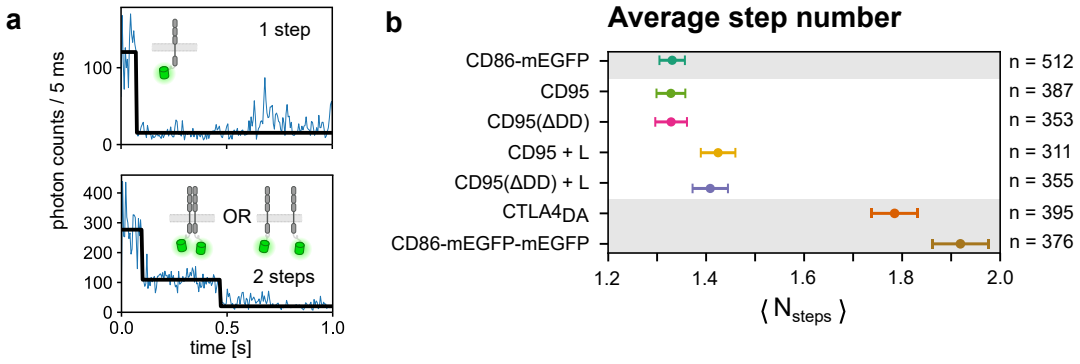

Figure 5.1: **Confocal Photo Bleaching Step Analysis a)** Exemplary intensity time traces of mEGFP on the surface and corresponding KV step analysis. Dual steps may be due to dimers or two monomers within a diffraction limited spot. **b)** Average number of steps per sample. Intensity time traces showing no steps were discarded. CD86 was used as monomer control, whereas $CTLA4_{DA}$ and CD86-mEGFP-mEGFP were used as dimer controls.

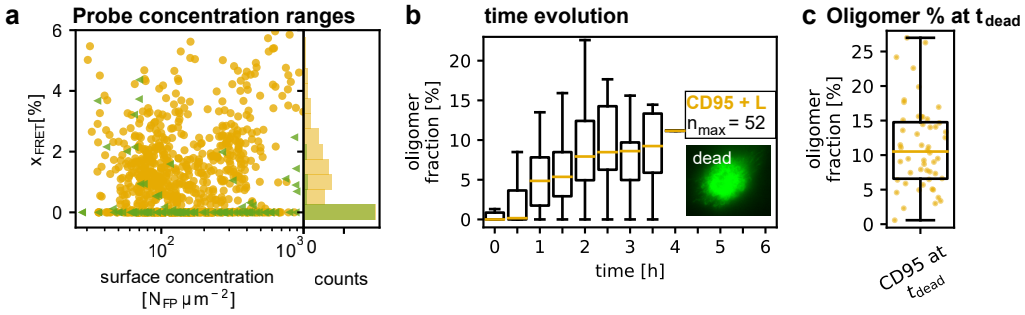

Figure 5.2: **Oligomerization state of CD95 studied with CELFIS a)** Concentration dependence of the x_{FRET}. CD95 is monomeric before ligand addition (green) and shows a small FRET fraction after ligand addition. **b)** The FRET fraction is transformed into the oligomer fraction and plotted against time. The data shows a gradual increase in oligomeric fraction, where vertical yellow lines represent medians. Note that cells progressively died during the observation time. **c)** Oligomer fraction of CD95 cells just prior to apoptosis. CD95 cells that remained alive during the observation time of 4 hours are not shown.

5.5 Live cell FCS, quantitative STED and apoptosis dynamics

Apoptosis dynamics were studied using Widefield microscopy for three different CD95 expression levels and three different ligand concentration levels, showing that the fraction of apoptotic cells increased and the average time until apoptosis decreased when either the receptor or ligand concentration increased.

To study the mobility of the CD95 receptor live cell FCS was performed. Considering the technical challenge of this method, a set of practical considerations was added to the Supplementary Information of the CD95 manuscript on page 301. The data showed that the CD95 protein has a diffusion coefficient of 0.21 µm^2/s to 0.24 µm^2/s, in a typical range for membrane proteins. No significant change in diffusion coefficient was observed after ligand addition, indicating that the small fraction of oligomers did not significantly alter the diffusion time.

Using super-resolution microscopy STED, the presence of a honeycomb lattice of trimers was investigated. Theoretically, a single hexagonal honeycomb unit would be 35nm in diameter and contain 18 CD95 molecules. Distinguishing it from trimers and monomers based on the size and especially the 18-fold brightness compared to monomers. Using quantitative imaging, deconvolution and object segmentation, the size and brightness distribution of the objects was analyzed and compared against monomer and dimer controls, showing that the mean brightness was between a monomer and a dimer, consistent with earlier results. Particularly, the tails of the brightness histograms were inspected for evidence of a honeycomb lattice of trimers visible as very bright spots, no significant change in the tail of the distribution compared to the dimer controls was found.

5.6 Conclusion: A minimal model for CD95 signaling

A minimal model for CD95 signaling is shown to consist of monomeric CD95 in absence of ligand and 8 % to 17 % oligomers just before apoptosis. This result is obtained for live cells from expression levels close to wild type, 20 receptors/µm^2, up to 1000 receptors/µm^2 (figure 5.3). As the oligomerization is comparable for wild type CD95 and the CD95(ΔDD) variant, the death domain does not play a role in oligomerization dynamics. Oligomerization is triggered by ligand addition, but may be stabilized by interaction of the transmembrane domains [20]. Other proposed models may occur for receptor concentrations higher than 1000 receptors/µm^2 or in *in vitro* experiments, but are not necessary for apoptosis signaling. This result also reflects on other members of the TNF family, who are structurally related. The methods developed and applied here are generally applicable to membrane proteins. Hence this work paves the way for similar studies on other members of the TNFR family.

5.7 Outlook

As CD95 is shown to build dimers or trimers in its signaling active state, attention shifts towards the stoichiometry of the Death Inducing Signaling Complex (DISC) [48]. For example, the stoichiometry, binding efficiency and recruitment speed of the death-domain binding FADD protein or its subsequent binding partners procaspase 8 and 10 [34].

For further experiments CELFIS and cPBSA are invaluable tools. The former is compatible with live cells, can measure from 20 up to 8000 receptors/µm^2 and has a higher sensitivity,

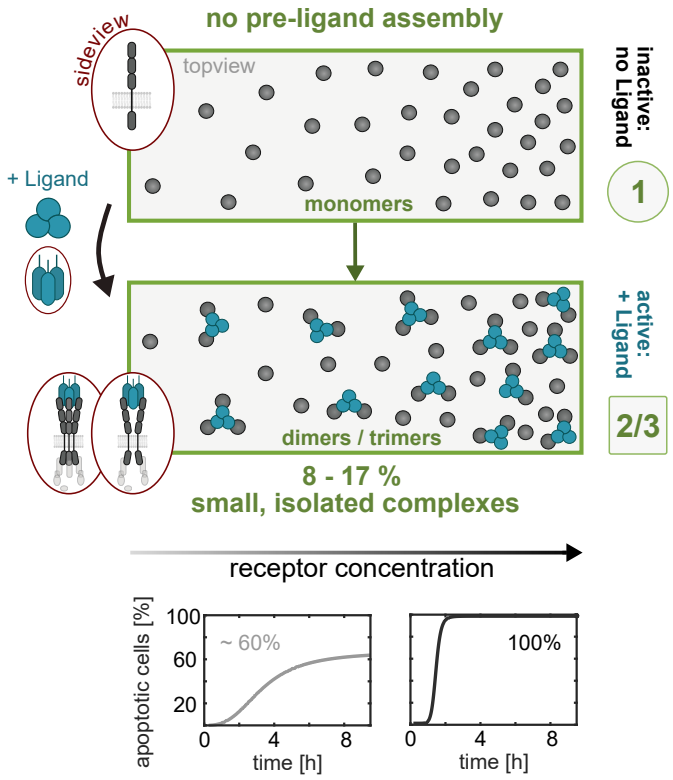

Figure 5.3: **Minimal model of CD95 signaling** CD95 is monomeric is absence of ligand (top) and forms dimers or trimers upon ligand addition (middle). For increasing receptor concentration, both apoptosis efficiency and speed increases (bottom).

whereas the latter works in fixed cells at receptor densities up to $\sim$20 receptors/µm^2. Based on different measurement principles, they consistently show a monomer to oligomer transition, indicating the robustness of the result. Yet, the nature of the oligomeric state remains unknown. Based on the enhanced effectivity of the trimeric ligand [6] and trimeric TNF family members [6, 61], one option is that CD95 may also form trimers. This is further supported by the presence CD95 trimers measured using western blot at high concentration [45]. One the other hand, one may predict the numbers of dimers and trimers based on kinetic theory when one assumes no cooperativity between the binding events. In this case, the low fraction of CD95 molecules in a cluster ($\sim$10 %) indicates that the oligomers are predominantly dimers. However, the cooperativity of CD95 must be determined before such deductions may be concluded with confidence. The methods presented in this manuscript have the potential to determine the fraction of dimers and trimers experimentally. CELFIS can provide an indirect measure based on the relation between k_{FRET} and the donor-acceptor ratio, but struggles to give quantitative information of oligomer species. As a promising alternative, cPBSA has the potential to measure dimers, trimers and higher oligomers quantitatively, provided the proteins may be labeled with organic dyes that have increased brightness, increased photostability and few nuisance photophysical state transitions, while also maintaining a 1:1 labeling stoichiometry and high labeling efficiency. A potential candidate that promises to fulfill all these conditions is labeling via genetically encoded Tags such as Halo- or Snap-Tag.

Chapter 6

Operating the Abberior Expert line microscope

The Abberior Expert line microscope has played a central role in all the work presented so far. Owing due to its unique and experimental character, it requires specific know-how to operate efficiently. This chapter contains the author's knowledge in aligning the instrument (section 6.1 and an amalgamation of theoretical knowledge, measurement data and practical experience for setting optimal experimental acquisition settings in section 6.2. Automated data acquisition was instrumental for obtaining high-quality datasets with high statistics, achieved using the program AbberiorControl, discussed in the software chapter (section 7.4).

6.1 Alignment of Abberior Expert line microscope

The Abberior expert line instrument is a uniquely modified system built by Abberior Instruments GmbH (Göttingen, Germany). Being a developmental system, it requires a decent amount of know-how to operate efficiently. In this section I will transfer the know-how necessary to keep the instrument well-aligned.

6.1.1 Beam-walking procedure

Aligning an optical beam requires control of the beam position and angle in the vertical and horizontal direction, creating for degrees of freedom. Four set screws are needed to adjust these parameters that are generally supplied by two mirrors (figure 6.1.2d). The two set screws controlling the vertical tilt on each mirror form a complementary pair that together control the vertical beam position and tilt. Analogously, the horizontal two set screws control the horizontal beam position and tilt. The beam walking procedure allows the experimentalist to change the complementary pair of screws in a coordinated fashion to arrive closer to the optimal global beam position. The procedure requires a goodness criterion, such as the brightness of the beam through two pinholes or the brightness of a fluorescent spot when imaging. The beam walking procedure works as follows:

1. Start with one axis, either vertical or horizontal.
2. Find the local maximum by changing the first set screw.
3. Move away from the local maximum using the second set screw. Now compensate with first set screw to re-find your local minimum.

4. In case your local maximum increases, repeat step 3 until you reach a maximum. In case it decreases, move the second set screw in the other direction and proceed accordingly.

5. After you've optimized one axes, switch to the other axes and repeat steps 2-4. Keep switching axes until you've reached the global maximum. You know you've reached it when your iterations no longer improve the end-result.

Note that a single set screw can be used to change the angle, whereas a complementary pair must be changed in a coordinated manner to change the position.

6.1.2 Alignment of excitation lasers

The alignment of the excitation lasers is stable provided that the lab temperature remains constant. Major realignments are rare and may only be needed after severe temperature fluctuations, as may occur in the summer during heat-waves. Minor re-alignment may be needed after more moderate temperature fluctuations or a few days after a major-realignment due to mechanical relaxation. As a coarse alignment step, a double pinhole can be mounted to the objective turret (figure 6.1.2a-c) to ensure that the beam is parallel and centered at the back focal plane. For a fine alignment, the effects of wavelength-specific chromatic shifts in the objective and alignment of the pinhole [47], must be included. This is done using a fluorescent sample such as TetraSpeck beads (ThermoFisher, Waltham, MA, USA), where the brightness of the PSF and its shape are used as a goodness criterion (6.1.2e-f). Note that for the excitation pathways the two adjustment mirrors are close together, but far from the back-focal plane of the objective. As a consequence, a change in beam angle causes a significant misplacement at the back focal plane, but a coordinated adjustment of two set screws changes the collimated beam position only slightly. Hence, most minor misalignments can be satisfactory resolved by tuning the beam angle on to the local optimum.

6.1.3 Alignment of STED laser

The position of the STED laser must be re-aligned on a daily basis. This can be done completely electronically by shaping the beam profile using a Spatial Light Modulator (SLM), increasing laser safety (figure 6.2c). For a good STED result, the STED beam must be symmetric and overlaid with the excitation lines. To ensure that the beam is symmetric, use gold beads to image the depletion PSF and use the aberration panel of the SLM to adjust any aberrations present (figure 6.2a-d). The beam profile typically remains stable over extended periods of time. For this setup, the apparent channel shift changes between imaging gold beads and fluorescent beads due to the different detection pathways used. As imaging fluorescent beads uses the normal fluorescence detection pathway, those beads are used to do the fine alignments. The depletion beam xy-position must be adjusted on a daily basis using the grating settings of the SLM (figure 6.2c,e).

6.1.4 Pinhole alignment

The pinhole alignment is typically stable over long periods negating any real necessity to change its alignment. If, for unforeseen reasons, the pinhole alignment must be changed still, use the following procedure:

1. place the pinhole in an open position, e.g. 2.5 Airy units.

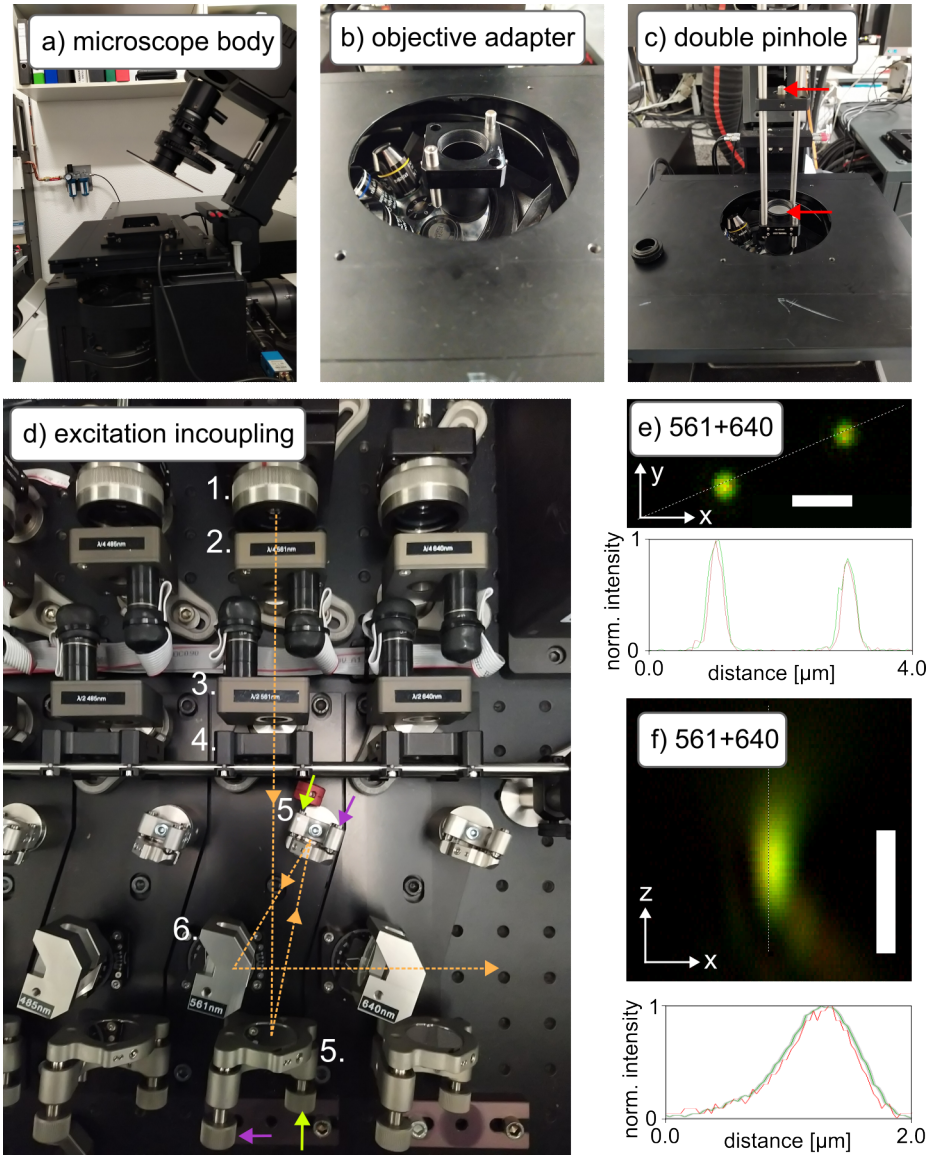

Figure 6.1: **Aligning the excitation pathway of the Abberior Expert Line Microscope** **a)** Side-view of the microscope body with condenser arm raised. The nano z-stage is visible. **b)** Front-view of the microscope stage with objective ring adapter used for mounting diagnostic tools. The nano z-stage as well as the condenser arm is removed to make room for the adapter. **c)** Concentric double pinhole (red arrows) is mounted on the objective ring to enable beam walking in case of severe misalignment. **d)** The beam path for the 561 excitation laser in coupling is shown. The in coupling for the 488, 561 and 640 excitation lines use the same schema. The path consists of the following elements: after exciting the fiber, the beam is collimated by a lens (1.) that can be adjusted to alter the collimation of the beam and therewith the z-position of the focus. Next, two $\lambda/4$ (2.) and $\lambda/2$ (3.) electronically controlled waveplates can be used to control the polarization of the beam (see section 6.1.6). Next, an excitation filter is used to reject spectrally shifted side-modes of the excitation laser. These side-modes are spectrally shifted by a few nanometers and also temporally shifted by a few 100 ps. Hence, rejection of these side-modes is necessary to obtain a clean TCSPC decay. The excitation alignment can be adjusted using two mirrors (5.). Complementary screws to adjust tilting and position in the vertical and horizontal position are shown in purple and green respectively. Finally, the beam is coupled in using an angle-tuned notch filter (6.). Caption continues on next page.

Figure 6.1: Caption continued **e)** Fluorescent image showing 561 and 640 channels of TetraSpeck beads showing good alignment between the channels. **f)** Gold beads are used to create a zx-image, used to inspect for z-alignment. Scale bar in e-f) 1 µm. Note that a shift along the x-axis is visible, which may disappear in the TetraSpeck image.

2. execute the beam walking procedure as outlined in section 6.1.1 using the PSF of fluorescent beads as a goodness criterion.
3. additionally, optimize the z-position as well.
4. Decrease the pinhole size and repeat steps 2-3. Repeat until 1 airy unit size.

6.1.5 Alignment of detector lenses

After changing detector filter cubes (figure 6.3b (1.)), the beam may be slightly displaced away from the sensitive area of the detector. To align the detectors, take a bright sample, such as an organic dye in solution and use the two alignment screws (2.) until the optimum is reached. The two alignment axes are independent and a wide global maximum can be easily found.

6.1.6 Setting the polarization of the excitation lasers

cPBSA benefits from circularly polarized light to reduce dipole induced brightness variations, whereas linearly polarized light enables anisotropy measurements. The Abberior expert line system is equipped with $\lambda/2$ and $\lambda/4$ motorized phase plates enabling full control over the polarization state of the light. Unfortunately, the control software does not know the absolute position of the motorized phase plates and will set the phase plates at a random position each time the software is started. As a workaround, the phase plates are disconnected under normal operation and a software configuration file is used that does not configure the phase plates. Changing the polarization state therefore requires temporary connecting the phase plates. Here follows a protocol to change the polarization state of the excitation light.

1. Connect the phase plate connectors to the correct socket for the desired wavelengths (figure 6.4a). Both the connectors and the sockets are labeled to make the right connection.
2. Enable the configuration file that configures the phase plates by 1) shutting down the Imspector software, the hardware may be left running. 2) in the Imspector library `C:\Imspector\`, back up the current configuration file and extract an existing backup copy of the configuration file with polarizers, e.g. `Configwithpols.7z`.
3. Mount the Polarization Analyzer (Schäfter+Kirchhoff GmbH, Hamburg, Germany) (figure 6.4b). When mounting it is crucial that the polarizer is mounted precisely at right angles with the microscope platform as shown in the picture.
4. Open the 'SKPolarizationAnalyzer' software, which should now give a current depiction of the polarization state of the beam.
5. Open controls for the electronic waveplates in the Imspector software. In case they are hidden, enable them under `Imspector>Window>LiveDialogs`. Tune the waveplates and inspect the current polarization state until the desired wavelength is reached. See figure 6.4c-d for vertical and left-circular polarization states.

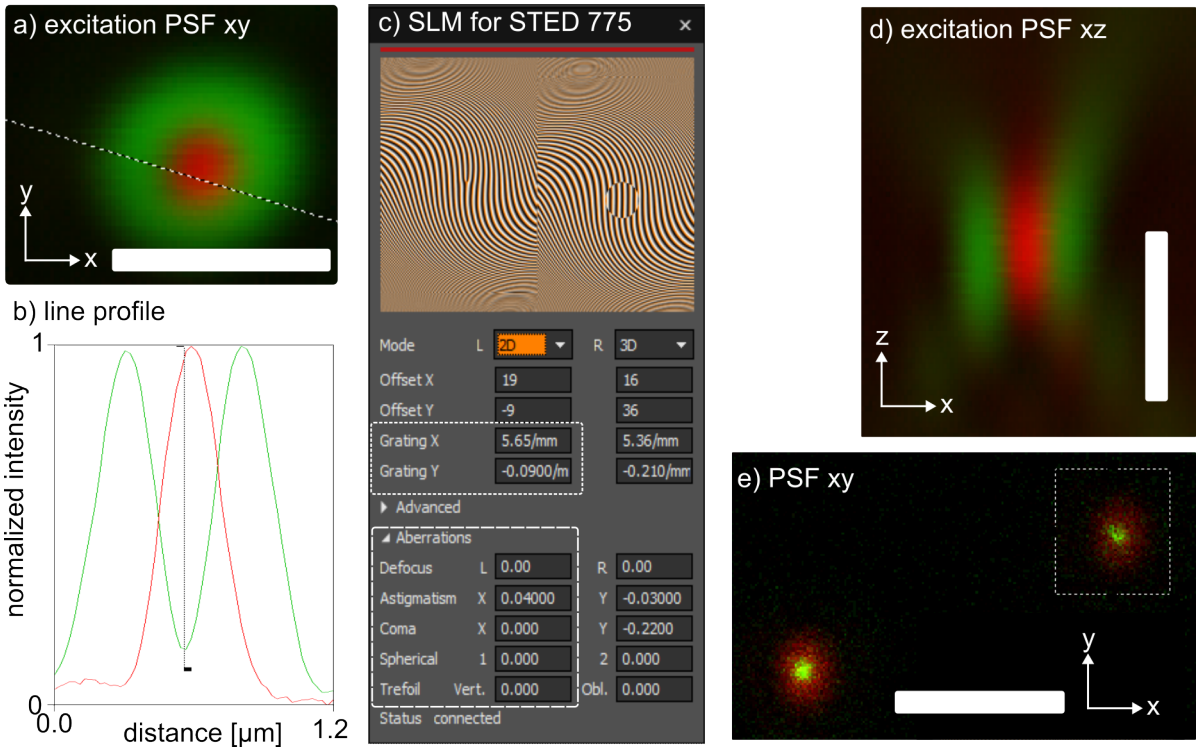

Figure 6.2: **Aligning the STED depletion beam a)** *xy*-image of gold beads showing good alignment between the 640 excitation and 775 depletion lasers. **b)** line profile corresponding to a). **c)** screenshot of the SLM for controlling the 775 depletion laser. Short dashes indicate the grating used to control the beam *xy*-position and long dashes indicate aberration correction for obtaining a symmetric beam profile. **d)** *xz* image of gold beads showing good alignment along the z axis. **e)** Fluorescent image of TetraSpeck beads showing 640 nm excitation in red and 640 nm excitation with 775 nm depletion in green. Data shows good alignment between excitation and depletion beams. Note that the size of the STED spot is limited by the bead size of 100 nm.

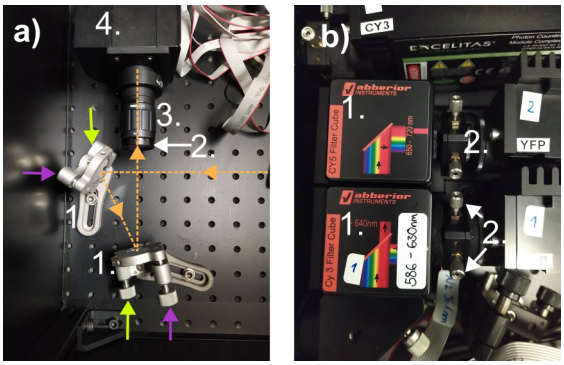

Figure 6.3: **Pinhole and detector alignment a)** Fluorescent light is focused onto the pinhole using two mirrors (1.), then it passes a shortpass filter (2.) necessary for filtering reflected infrared light from the autofocus system. The fluorescent bandpass filters in front of the detectors do not have high enough extinction coefficients at these wavelengths. Next it passes an adjustable lens array (3.) to control the focus position at the pinhole (4.). **b)** the fluorescent light is filtered (1.) via a long pass filter combined with a bandpass filter (bottom cube) or a mirror combined with a bandpass filter (top cube). After changing the fluorescent filter cubes, the beam may need to be realigned on the detector using the two set screws for each detector (2.). The perpendicular detectors are shown, the parallel detectors work identically.

6. Close the software, detach the phase plate connectors and reinitialize the configuration file that does not configure for polarizers.

6.1.7 ALEX and PIE operation

Full FRET information can be obtained using either ALEX or Pulsed Interleaved Excitation (PIE) for sequential excitation of the donor and acceptor. A limitation to setting the pulse delay is posed by the repetition rate of the 775 STED laser, which is fixed to 40 MHz. When operating in STED mode, the 775 STED laser must be used as a master oscillator, imposing a repetition time of 25 ns. This time window is too short to fit two sequential lifetime decays of all commonly used dyes, hence ALEX is used to sequentially excite both dyes and grant each fluorophore decay a time window of 25 ns. In cases where the excitation beam is static, such as cPBSA traces of FRET molecules, ALEX is not an option and hence PIE must be used. Here, another limitation is posed by inability of the Imspector control software to change the *TAC gain* parameter of the HydraHarp. As the HydraHarp has 32768 bins each 1 ps wide, the maximum width of the TCSPC decay is set to 32.7 ns. Nevertheless, in absence of a STED laser, the repetition time may be extended to 30 ns when using the internal oscillator operating at 33.3 MHz, sufficient to measure mEGFP-mCherry decays in PIE mode. A list of delay settings for ALEX and PIE mode are listed in the instrument logbook page 19.

6.2 Optimal acquisition setting for STED microscopy

STED microscopy gains resolution at the cost of photon statistics which is ultimately limited by photobleaching. Particularly, in combination with FRET, photon statistics must be sufficient to reliably determine FRET parameters. In this section, I discuss acquisition settings that provide the best performance.

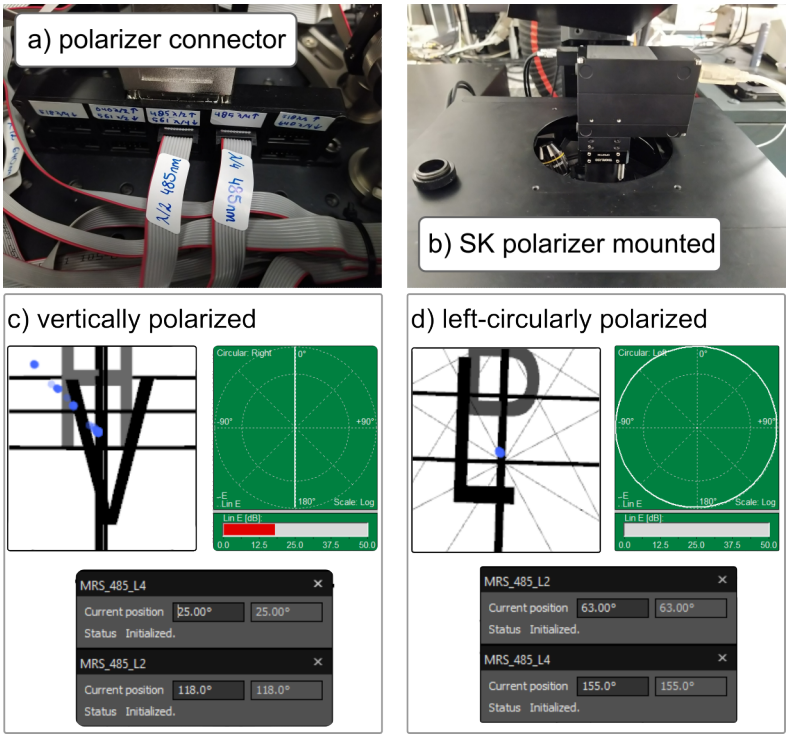

Figure 6.4: **Controlling the polarization of the excitation lasers a)** A picture of the phase plate connectors connected to their corresponding sockets. The 485 nm waveplates are connected. **b)** A picture of the polarization analyzer mounted using the adapter shown in figure 6.1.2b. **c)** polarization state of vertical and **d)** left circular polarized light is shown in the 'SKPolarizationAnalyzer' software. Note that the values for the waveplate position change each time the waveplates are initialized at Imspector startup.

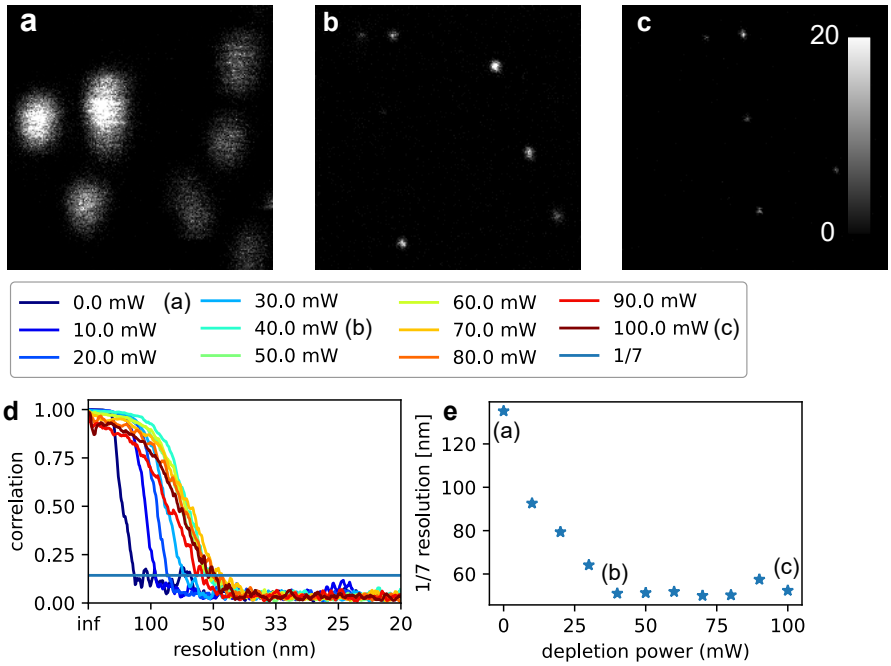

Figure 6.5: **STED resolution measured using Fourier Ring Correlation a)** Fluorescent images of 28 nm Crimson beads (Thermofisher, Waltham, MA, USA) are imaged in confocal mode, **b)** at 40 mW depletion power and **c)** at 100 mW depletion power. **d)** Fourier ring correlations for increasing depletion power are shown, the 1/7 cutoff criterion is included. **e)** The corresponding resolution according to the 1/7 criterion is shown.

6.2.1 STED resolution measured by Fourier Ring Correlation

In principle STED can achieve infinite resolution at sufficiently high depletion powers. In reality, however, at higher depletion powers the influence of shot noise and background deteriorate the image quality (figure 6.5a-c), such that a smaller PSF is traded against a worse Signal-to-Noise Ratio (SNR). One may eloquently determine the image resolution in the presence of noise by determining the signal to noise ratio for each k-vector in Fourier space using Fourier Ring Correlation (FRC) [59]. FRC requires two independent images of the same object, achieved here by recording a single object using 10 nm pixel size, 10 µm square image area, 50 µs dwell time, no line integration, 5 µW 640 excitation power and variable depletion power. Two independent images were subsequently created from a single image bs splitting on odd and even tac bins of 1 ps width. In Fourier space, when the amplitude for a k-vector is dominated by signal, the correlation between the two images is high and we consider the corresponding distance resolved. Conversely, when the amplitude of the k-vector is dominated by noise, there is no correlation and the corresponding distance is not resolved. As a cut-off, we choose the 1/7 criterion [59]. Figure 6.5d,e shows the FRC curves and corresponding resolution for increasing STED laser powers. The data shows an initial increase in resolution up to 40 mW depletion power down to 55 nm, after which the influence of noise starts to decrease the correlation at all distances. Similar findings are shown in [59]. As the resolution is limited by the size of objects in our image, I confirmed the bead size with the manufacturer (28 nm), which is not limiting to our obtained result of 55 nm. Further note that the resolution may be improved by taking brighter object or measuring longer. Yet, our probes of interest are typically single fluorophores that must yield sufficient photons to obtain FRET parameters. Hence, 40 mW depletion power was taken as an optimal tradeoff between resolution and photon statistics.

6.2.2 Anti-photobleaching buffers

Maximizing the number of photons that may be obtained from a single organic dye is crucial for obtaining good quality data. Hence, photoprotective buffers that increase the number of photons obtained from an organic dye before bleaching (photon yield) were studied as part of establishing the FRET-nanoscopy method. A prominent bleaching pathway occurs when an organic dye in the triplet state absorbs another photon exciting it to a highly energetic reactive state. When oxygen is present in the solution, the fluorophore can now be oxidized, quenching its fluorescence [25]. One popular strategy to reduce photobleaching is to add triplet quenchers to the solution, thus limiting the time spent in the triplet state and the probability of associated bleaching pathways. Here, Trolox (Tokyo Chemical Industry Co., Ltd., Tokyo, Japan) was successfully applied as a triplet quencher, being able to abolish intermittent dye blinking and increasing the overall brightness of the dye (figure 6.6). The molecular mechanism of triplet quenching by Trolox works by the combined action of Trolox and its reaction product Trolox-quinone [11], which together form a reducing oxidizing system (ROXS) capable of quenching the triplet state. The Trolox-quinone formation occurs under ambient conditions over approximately one day or may be accelerated by irradiating with UV-light (see also figure 23 from [51]). Pre-irradiating the Trolox solution with UV-light did not increase photon yield, indicating the presence of another oxidation agent, such as molecular oxygen. On the other hand, Trolox solutions from the day before clearly showed diminished effectiveness, which may be due to all Trolox having reacted to Trolox-quinone. Hence, all Trolox solution were created fresh daily by creating a 200X solution (50 mg Trolox in 1 ml ethanol) as an additive to the imaging buffer.

Oxygen is associated with photobleaching either by direct reaction of the fluorophore with oxygen radicals or reaction of a fluorophore in an excited state with molecular oxygen. Hence, another prominent photoprotection strategy is to deplete oxygen from the solution. However, oxygen itself has important triplet quenching activity, such that oxygen depletion without adding a triplet quencher causes greatly enhanced blinking behavior, as was seen using the oxygen scavenging system PCA with PCD [1] (figure 6.6). The PCA-PCD system was used as it causes no acidification as a by-product. When Trolox was added to create the PCA-PCD-Trolox (PPT) buffer, the triplet state was quenched, yet the overall photon yield did not improve significantly compared to using only Trolox (figure 6.6 and caption). Note that these measurements were performed under confocal conditions, and that high depletion laser powers under STED conditions may open additional bleaching pathways [44] not tested with these measurements. Nevertheless, based on our collected data, we conclude that simple Trolox addition was sufficient as a photoprotective strategy.

6.2.3 Further considerations for setting microscope acquisition parameters

Knowledge of the optical properties of the system and the photophysics of the organic dyes may be combined to optimize the acquisition settings. For example, the organic dye may be allowed to relax from long-lived dark states by setting a short dwell time. Here, the organic molecule is only illuminated during the short time period when the scanner moves over the fluorophore ($\sim$50 µs). There is a cost to very short dwell times, as the flyback time of the scanning beam creates an overhead for the total acquisition time. A good tradeoff was found for 5 µs dwell time.

Regarding excitation powers, best results were achieved using $\sim$5 µW, probably because this optimally balances high brightness, low triplet and low photobleaching. The pixel size

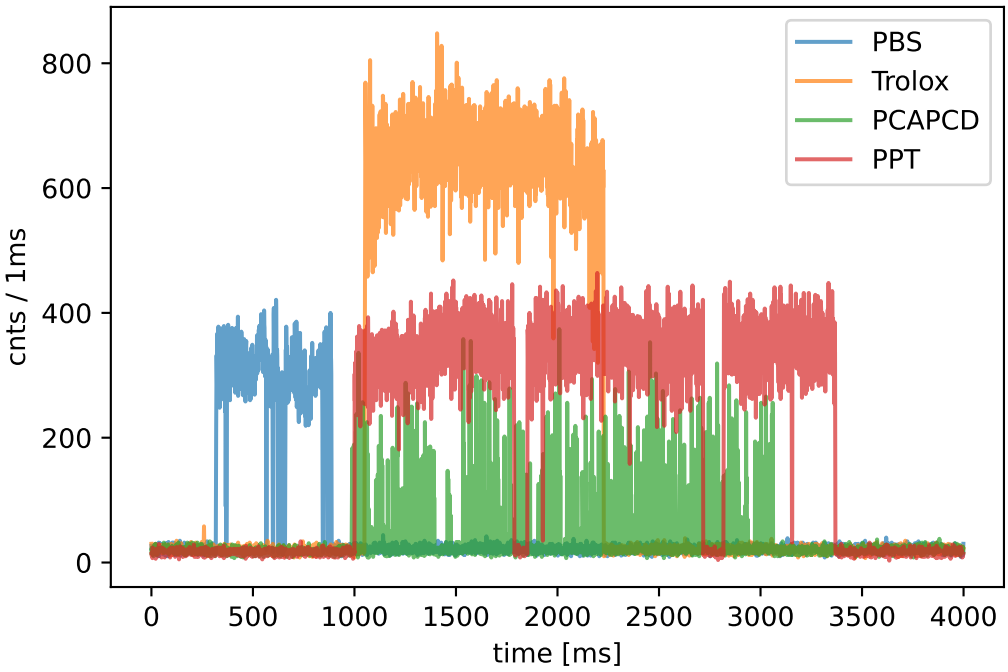

Figure 6.6: **Effect of photoprotection buffers** Single Atto 647N molecules were immobilized on the surface and irradiated with 640 nm light under several photoprotective buffers. Phosphate buffer Saline (PBS) showed dye blinking and yielded on average 79 kCnts (n = 5) before bleaching. Adding Trolox to PBS removed blinking and yielded on average 177 kCnts (n = 9) before bleaching. Adding the oxygen scavenging system PCA / PCD to PBS greatly increased blinking and yielded only 13 kCnts (n = 9) before bleaching. Adding both PCA / PCD and Trolox to PBS (PPT buffer) showed low blinking and yielded on average 180 kCnts (n = 12) before bleaching.

must be set according to the Nyquist criterion, which maximizes the information content of the image and may be calculated using the Nyquist calculator [1] (Scientific Volume Imaging B.V., Hilversum, the Netherlands). For STED and confocal data, 10 nm and 50 nm pixel size is recommended respectively. When z-sectioning is being used in the absence of 3D STED, 150 nm z-pixel size is recommended. Note that any shot noise incurred by the use of smaller pixels can be corrected by deconvolving the image.

[1] https://svi.nl/nyquistcalculator

Chapter 7

Software development

This chapter discussed the various programs that I developed during my PhD. I discuss the goal of the code, the code structure, input and output and dependencies required to run the program. A link to the relevant source code including embedded documentation is provided. Similarly, manuscript sections describing principles or equations relevant to the program are linked. Each program is discussed in its own section. Unless otherwise specified, the programs were written in their entirety by the author.

7.1 Seidel software for cSTED and super-resolved FRET

7.1.1 Goal

The *Seidel* program was developed to analyze FRET-nanoscopy measurements performed on origami labeled with multiple FRET pairs. It was developed in parallel to the program AnI by Dr. Suren Felekyan, which at the time could only analyze single FRET pairs. *Seidel* can localize up to three adjacent FRET pairs and extract FRET parameters. It also contains modules for localization analysis discussed in section 7.2 and 7.3. To limit program complexity and speed, *Seidel* does not consider anisotropy.

7.1.2 Input and output

Input Seidel takes lifetime image data as input in the form of .ptu (picoQuant) files. **Output** The output is a list of localizations and FRET parameters per image. An example of the output FRET data is shown in figure 3a of the FRET-nanoscopy manuscript (page 94. The localization data serves as input for further modules. The software was used for analysis of all origami and hGBP data in the FRET-nanoscopy manuscript (section A on page 84), in addition to origami analysis shown in chapter 3 and [51].

7.1.3 Code availability & method references

The code is available via my public git repository[1]. A usage example that guides the user through all analysis steps is given in the templates sub-folder[2]. The procedure for MLE Gauss

[1] `https://github.com/Fluorescence-Tools/Seidel`

[2] `https://github.com/Fluorescence-Tools/Seidel/blob/master/templates/20211103_template_v3.ipynb`

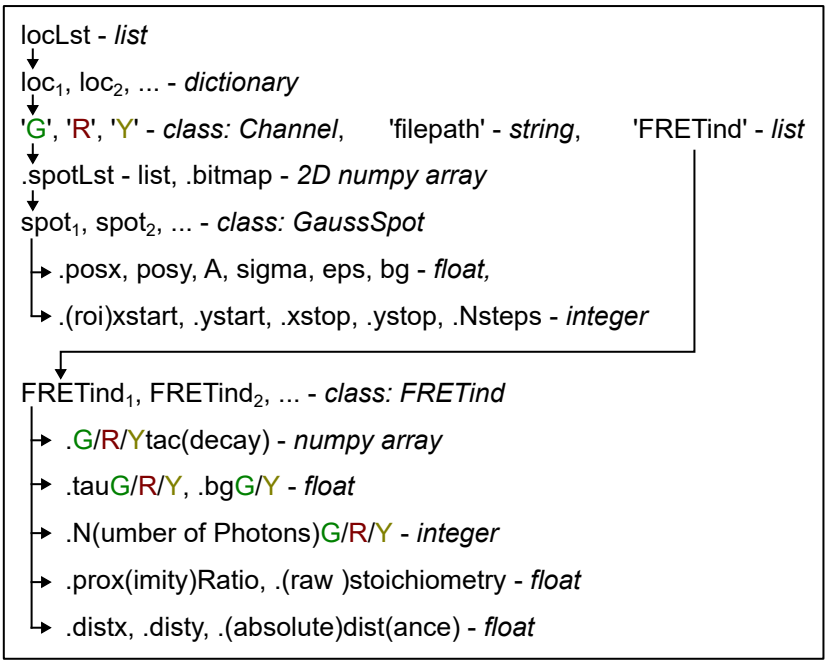

Figure 7.1: **Data structure of the Seidel software** Italic words describe a data type. Several classes are used as data containers. Normal type font indicate variable names, where text between parentheses '()' are used for clarification, and are not part of the variable name. FRET indicators are calculated for multiple channels, for example, G/R/Ytac(decay) is shorthand for three variables, containing the fluorescent decay for donor emission upon donor excitation, acceptor emission upon donor excitation and acceptor emission upon acceptor excitation respectively.

fitting is outlined in the FRET-nanoscopy methods section *colocalization of FRET pairs* on page 135.

7.1.4 Code structure

Seidel uses a hierarchical data structure to reflect the hierarchical nature of the data contained (figure 7.1). For example, multiple localizations, stored in spotLst, can be made on a single image, stored in bitmap, both are contained in a *Channel* object, which represents a channel in a multichannel fluorescent data file. FRET indicators are calculated for each donor and acceptor pair.

Seidel consists of functional units operating on a shared data structure with minimal interdependencies, making it Easy To Change (ETS) existing units or attaching new units as needed. This was necessary as the program goal was not known at inception and new features had to be continuously added as new ideas were tested. Hence, Seidel is a mixture of function-oriented and object-oriented programming, where units have a functional relation to one-another and classes are used within a functional unit to organize relevant function together.

The first analysis step (A, figure 7.2) consisted of reading the raw ptu data file using `PQ_PTU.dll` (PicoQuant) and transforming it into a 3D *xy, tac decay* image using the self-written `ProcessPhotonStream.dll`, both dll's were wrapped using the *ctypes* library. In the next step (B), the number of emitters was determined using up to three gauss fits using a MLE approach. Here, the computationally-intensive fit routine was written in c++ and compiled in a python binary called GaussFits using pybind11, whereas the supporting code was written in python.

Calculation of the FRET & localization indicators (C) as well as selecting subensembles (D) was implemented in python. The modules for localization analysis (E) are discussed in section 7.2 and 7.3. From the subensemble, seTCSPC decays can be generated for analysis in other programs (F).

7.1.5 Dependencies

Seidel was written in python 3.7 using package contained in the main-line anaconda package library. No packages from conda-forge were used. The dll's work on windows operating systems only and depend on basic windows dll's, tested on windows 10. GaussFits requires python 3.7, although it could be readily compiled for newer versions. Hence, Seidel requires a python 3.7 installation with anaconda packages on a windows pc, tested on windows 10. Upgrading to newer versions of python requires changing any deprecated syntax or functions and compiling GaussFits against a newer version. Making Seidel accessible for other operating systems requires compiled c-code for that operating system and ensuring the wrappers remain compatible.

7.2 Seidel module: Particle alignment for PA-cSTED

7.2.1 Goal

The particle alignment module of Seidel is aimed at 1) matching localizations to fluorophore positions 2) aligning the structures 3) calculating an average structure with higher accuracy than the individual structures.

7.2.2 Input and output

Input The locLst structure used in Seidel (see figure 7.1) can be used to directly initialize an instance for particle alignment. Note that this method of initialization conserves the original locLst with which it was initialized, so that the corresponding FRET parameters may be recovered after an alignment-based selection has been made. To facilitate interoperability, the particle instance may also be initialized using a list of coordinates generated using any program. The program supports structures with four fluorophores, although the program structure makes the program adaptable to support any number of fluorophores. **Output** The particle alignment module delivers an aligned set of localizations and their average structure as can be seen in figure 2 of the FRET-nanoscopy manuscript on page 91 and in figure 3.7 on page 32 for the Optical Pythagoras calibration measurements. Additionally, a Root-Mean-Square-Displacement (RMSD, see methods on page 138) score for alignment quality is generated.

7.2.3 Code availability & method references

The relevant code for this module can be found in the `AlignStructures.py` file, as part of Seidel accessible via the links given in subsection 7.1.3. Similarly, a usage example is part of the Seidel usage example. The principle of structure alignment is explained in the FRET-nanoscopy methods section *Alignment and particle averaging for origami measurements* on page 138.

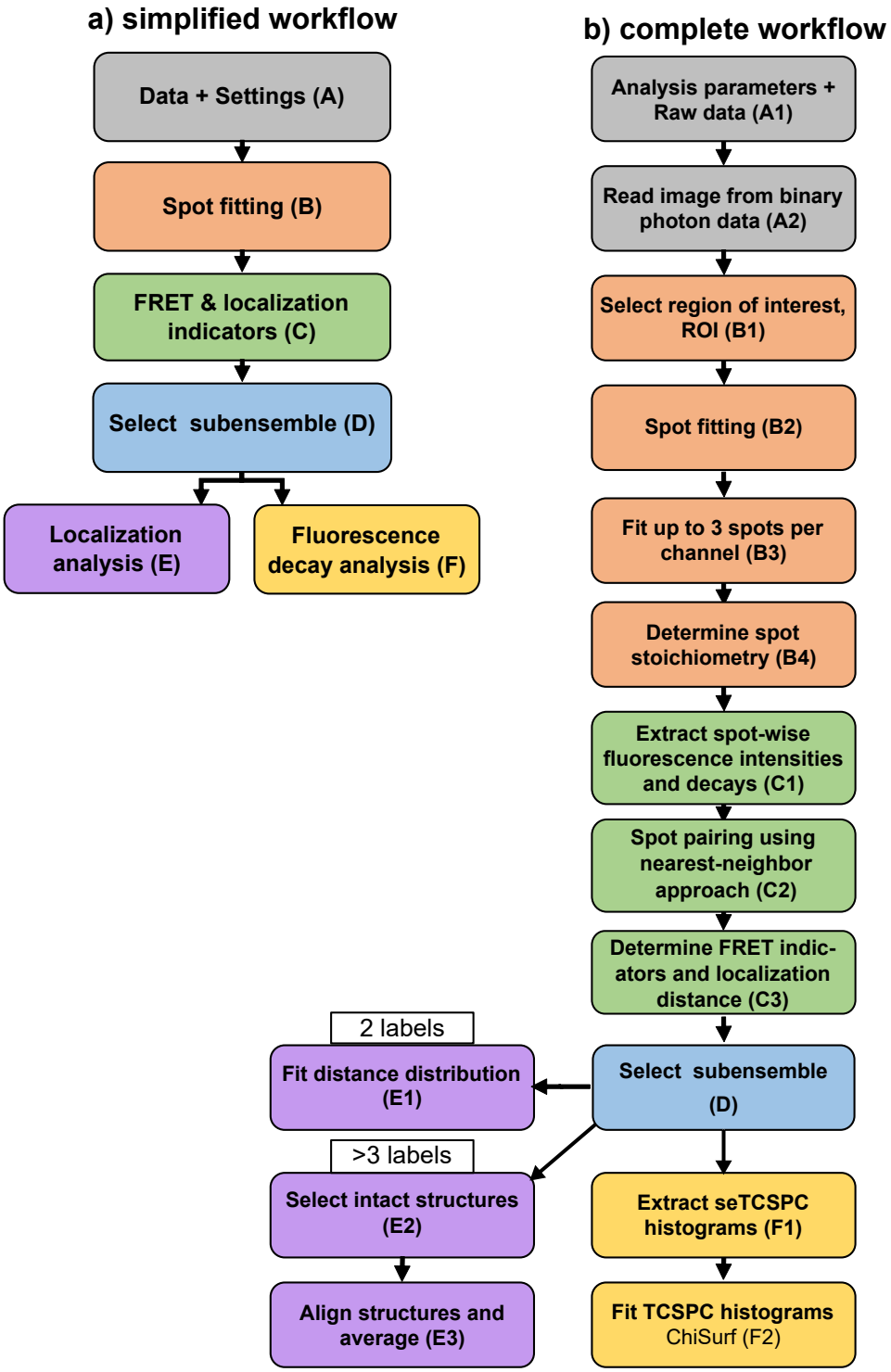

Figure 7.2: **Workflow of the Seidel software** Figure was adapted from supplementary figure 6 from the FRET-nanoscopy manuscript shown on page 177.

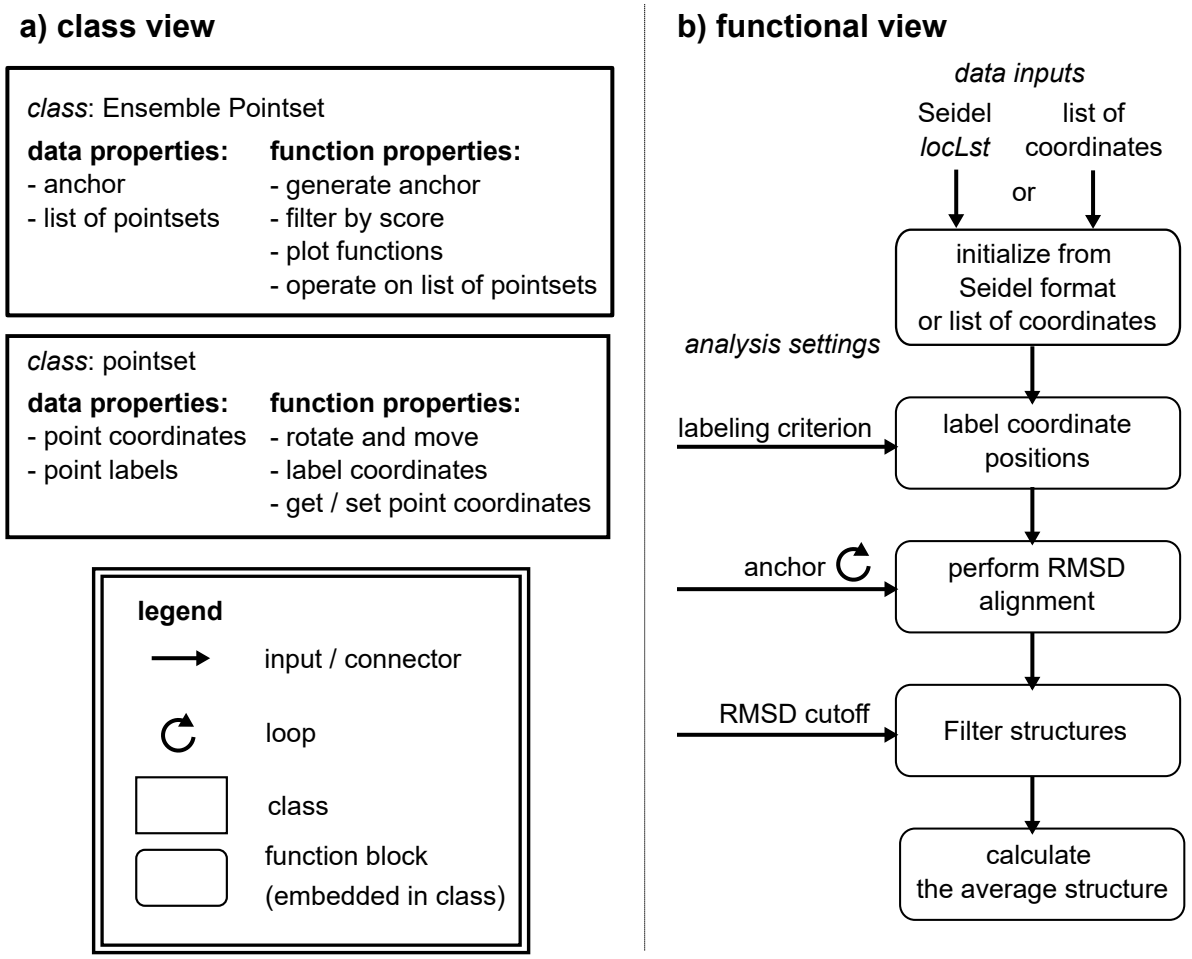

Figure 7.3: **Flowchart for particle alignment module in the Seidel software**

7.2.4 Code structure

A class structure has been adopted to organize the functions and data. The localizations of a single structure, e.g. origami platform, is saved in a pointset instance along with relevant functions (see figure 7.3a). The set of pointsets, e.g. belonging to a single measurement, are saved in an Ensemble Pointset instance along with the anchor to which they are aligned and a list of functions, including a mechanism to apply an operation on all constituent Pointsets. The class structure supports a functional sequence, shown in 7.3b. After initialization, the localization must be assigned a label. Currently two labeling criteria are implemented. Firstly, the labels may be assigned clockwise, provided all origamis are oriented with the same side to the bottom membrane. Secondly, the labels may be assigned based on donor-acceptor indicators, such as localization-based donor-acceptor distance or FRET efficiency. Donor-acceptor indicators should be used carefully as smears between populations may make a binary assignment difficult. After labeling, each structure is aligned to minimize the RMSD with respect to an anchor structure, after which structures with a bad RMSD score are discarded and the average structure is calculated from the remaining structures. Several anchors may be tested, for example from the ensemble of pointsets itself, where the best anchor is selected based on the lowest overall RMSD. Alternatively, structural sub-species may be identified by clustering species which have a low RMSD to a certain anchor.

7.2.5 Dependencies

This software module relies on the rmsd python package[3] in addition to standard anaconda dependencies. It is functionally independent from the rest of Seidel.

7.3 Seidel module: 1D histogram fitting

7.3.1 Goal

The goal of this Seidel sub-module is to fit histogrammed data with correct maximum likelihood description of the Poissonian statistics.

7.3.2 Input and output

Input Any one-dimensional dataset as a numpy array datatype may be used. **Output** The program returns a fit result along with its log-likelihood probability and Aikaike Information Criterion (AIC) and BIC scores. Additionally, a support plane for the fit may be generated. Examples of fit result and support planes may be found in the FRET-nanoscopy supplementary figure 13 on page 185 as well as in figures 44-52 from [51].

7.3.3 Code availability & method references

The link to the code repository and usage examples are given in subsection 7.1.3. The code relevant for this module is contained in the file `histogram_fitting.py`. A specialized model for fitting hGBP data is available in the corresponding analysis notebook[4], access outside of the Seidel group on request.

7.3.4 Code structure

The code consists of a simple functional structure shown in figure 7.4. Functions for creating N-Gaussian, N-n.c.-χ or N-Poisson models, in addition to functions providing initial parameter estimates are available. The code further contains functions for calculating and plotting support-planes.

7.3.5 Dependencies

Only python modules contained in the standard anaconda package library are needed. It is functionally independent from the rest of Seidel. As the most characteristic feature of the program is its Graphical User Interface (GUI), the program as a whole is sometimes also referred to as 'GUI', although its full name is AbberiorControl.

[3] `https://pypi.org/project/rmsd/`
[4] `https://github.com/NicolaasvanderVoort/analysis/blob/master/2020Q4/201112_hGBP.ipynb`

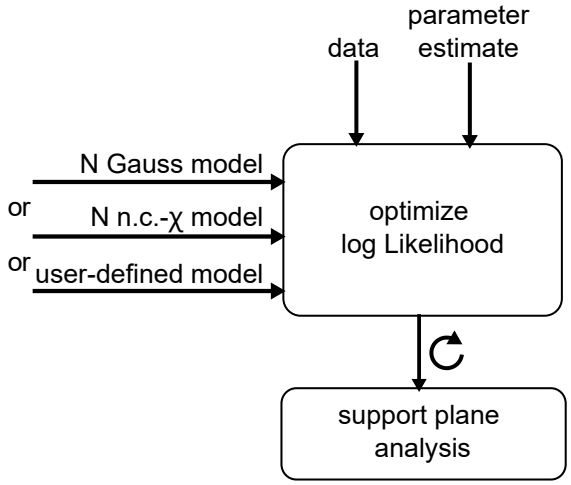

Figure 7.4: **Flowchart for histogram fitting module of Seidel** Legend same as in figure 7.3.

7.4 Automated data acquisition using the AbberiorControl ('GUI') software

7.4.1 Goal

The program is intended to automate data acquisition for FRET-nanoscopy, confocal Photobleaching Step Analysis, surface-based FRET measurements and CELFIS.

7.4.2 Author contributions

The first version of the program was written by Jan-Hendrick Budde. While being able to record data for FRET-nanoscopy, it had several issues as a result of non-adherence to good programming practices. I made the code run more reliably by restructuring the code. Additionally, I added the following features: 1) functionality to record fixed position time traces for cPBSA and surface FRET. 2) an option for selecting a set of manual positions for CELFIS 3) an abort function for user-friendliness 4) a timeout option for continuing data acquisition after a bug occurred in the Imspector layer.

7.4.3 Input and output

Input The user can set the data acquisition parameters using the corresponding tab of the GUI (figure 7.5a-(3)) and start the desired measurement using the button commands (2). **Output** A series of .ptu files is generated that can be analyzed in further analyses and the AbberiorControl acquisition settings are saved in a .txt file. Additionally, for fixed positions measurements, a preview of the data is printed to the python console.

7.4.4 Code availability & method references

The program is contained in the public Abberior-Tools repository[5]. A description for FRET nanoscopy data acquisition is found in the FRET nanoscopy methods *Data recording* on page 123.

[5] `https://github.com/Fluorescence-Tools/Abberior-Tools`

7.4.5 Code structure

The code may be understood from three perspectives: the GUI level, the architecture level and the functional level. The GUI (figure 7.5a) contains a window for showing an overview image (1), a series of buttons linked to commands (2), a series of settings that are read-out when commands are executed (3) and a text panel for displaying status messages (4), additionally, many outputs are displayed directly in the python console from which the code is run. The architecture of the program reflects the design of the GUI (figure 7.5b). The AbberiorControl class inherits from the tk.TK class, allowing it to generate the GUI. Additional variables to contain acquisition settings are added to the class, which are read out when the relevant button command is given. The program interfaces with the Imspector microscope control software via the specpy package[6].

From a functional perspective (figure 7.5c), the program first obtains a set of measurement positions and then measures those positions, either by a static confocal beam, or scanning to create an image. The measurement positions can be user-defined or automatically generated from an overview image. User defined positions are useful for measuring cells or subcellular phenomena. Positions of interest may be identified via the binoculars or via confocal imaging and the stage-center position can be saved using a single mouse-click. Alternatively, an overview image may be generated using the OVERVIEW button that reads the acquisition settings given in the OVERVIEW tab in GUI panel (3), where small capital letters are used to indicate GUI buttons or input fields. Upon pressing the FINDPEAK button, the overview image is smoothed with a gaussian filter of one pixel sigma and all local maxima are identified. These local maxima may then be filtered using the three sliders in the ROI_SELECT tab in GUI panel (3). Now that the measurement positions are known, a measurement is started using i) the TIMERUN button for fixed position measurements from automatic positions, using the laser power and time acquisition settings in the ROI_SELECT tab. ii) the RUN button for image measurements from automatic positions using ALEX and all acquisition settings in the left column of the ROI_SELECT tab. iii) the RUN POSITIONS button for image measurements from manually positions and the acquisition settings described in ii). The RUN button is typically used for FRET nanoscopy measurements with 1 µm ROI sizes and 10 nm pixel sizes. Conversely, the RUN POSITIONS button is typically used for CELFIS measurements with 60 µm image sizes and 100 nm pixel sizes. Each acquisition mode is also supplied with a looped implementation, indicated by the multi keyword. The #MULTI: acquisition setting sets the number of repeats. For MULTITIME and MULTIRUN, each iteration consists of moving the stage to a new area, recording an overview, identifying positions and running the respective measurement. For MULTI POSITIONS, the same set of stored positions is recorded multiple times, useful for recording the evolution of cells over time. Lastly, data acquisition is run in a separate thread, improving user-friendliness via the abort function. Multithreading also helped overcoming a bug that posed a significant practical limitation on the amount of data that could be collected. The bug consisted thereof that data acquisition would be stopped in the Imspector layer at a random time without giving feedback to AbberiorControl. As this would often happen during overnight measurements, those measurements would then need to be repeated. An effective work-around was implemented by setting a timeout in a parallel thread, where the timeout time is set using the acquisition setting AREA TIMEOUT [S].

[6] `https://imspectordocs.readthedocs.io/en/latest/specpy.html`

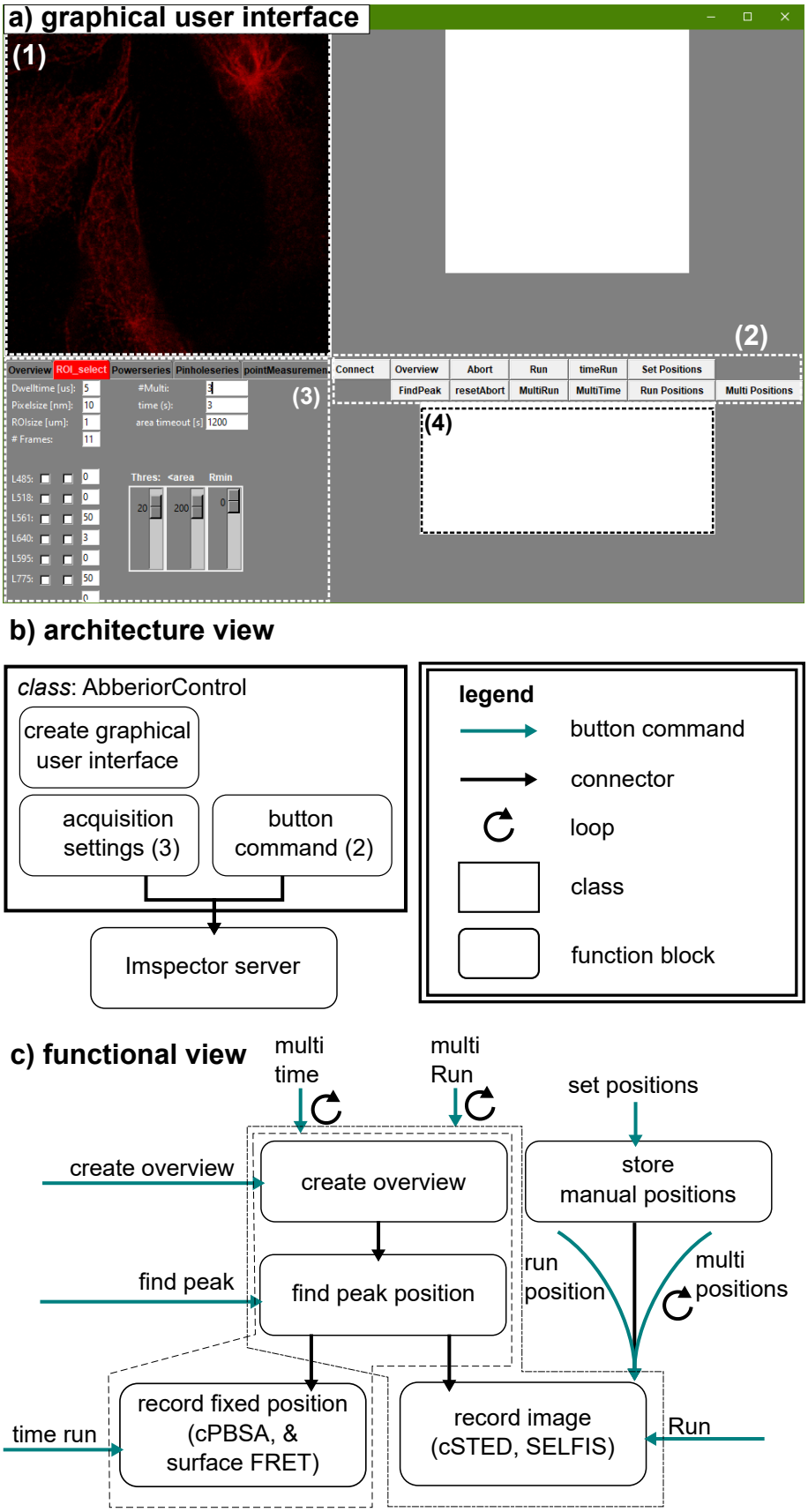

Figure 7.5: **Flowchart for the AbberiorControl software** for automated data acquisition on the Abberior microscope

7.4.6 Dependencies

In addition to packages contained in the anaconda package library, this program depends on the specpy package[7]. It also depends the cpp_wrappers.py file from Seidel with accompanying dll's (see section 7.1.5 to generate a live preview of static recordings. To run the program, simply run the main file called GUI_tkinter.py in a python 3.7 kernel.

7.5 Analysis software for CELFIS

7.5.1 Goal

The goal of this program is to automate data analysis for CELFIS experiments. The automation is important as one of the key benefits of CELFIS is its ability to obtain a large amount of statistics.

7.5.2 Input and output

The inputs and outputs are shown graphically in the software flowchart shown in figure 7.6. **Input** The primary input consists of ptu files and matching masks to identify areas of interest. For the analysis, settings must be provided for image reading parameters, building the magic angle decay and performing the fit. To transform the fluorescence brightness into a concentration map, the molecular brightness and the excitation laser power are needed. Further experimental information, such as a data batch identifier, cell identifier, cell phenotype and time of ligand addition may additionally be added. **Output** The fit outputs consist of the FRET fraction and the FRET rate. The image analysis outputs consist of the cell image area, the surface or volume concentration, time since ligand addition and derived variables. This program is used for all CELFIS measurements performed in the CELFIS and CD95 manuscripts on pages 210 and 267 respectively.

7.5.3 Code availability & method references

This code is currently interwoven with the image reading modules of the Seidel software, whose accessibility is described in section 7.1.3. It is soon to receive its dedicated repository and usage example. The methods underlying the analysis are described in the CELFIS methods on page 221. A protocol to determine the molecular brightness, an input parameter for the program, is appendix C.

7.5.4 Code structure

The CELFIS analysis software can be divided in functional units as shown in figure 7.6. The outputs are stored in a DataFrame data structure from the pandas python library. The first functional step in the analysis consists of creating a lifetime image from the ptu file, selecting the area of interest using a mask and extracting the fluorescence lifetime decay as well as the surface area and intensity. Multiple masks may be applied to a single image. This step utilizes the same image reading routines also used in Seidel (section 7.1). Then, in one branch of the program, the magic angle decay is constructed from the parallel and perpendicular (PS) decays and consequently fitted using a FRET sensitized donor decay fit. Note that the anisotropy

[7] `https://imspectordocs.readthedocs.io/en/latest/specpy.html`

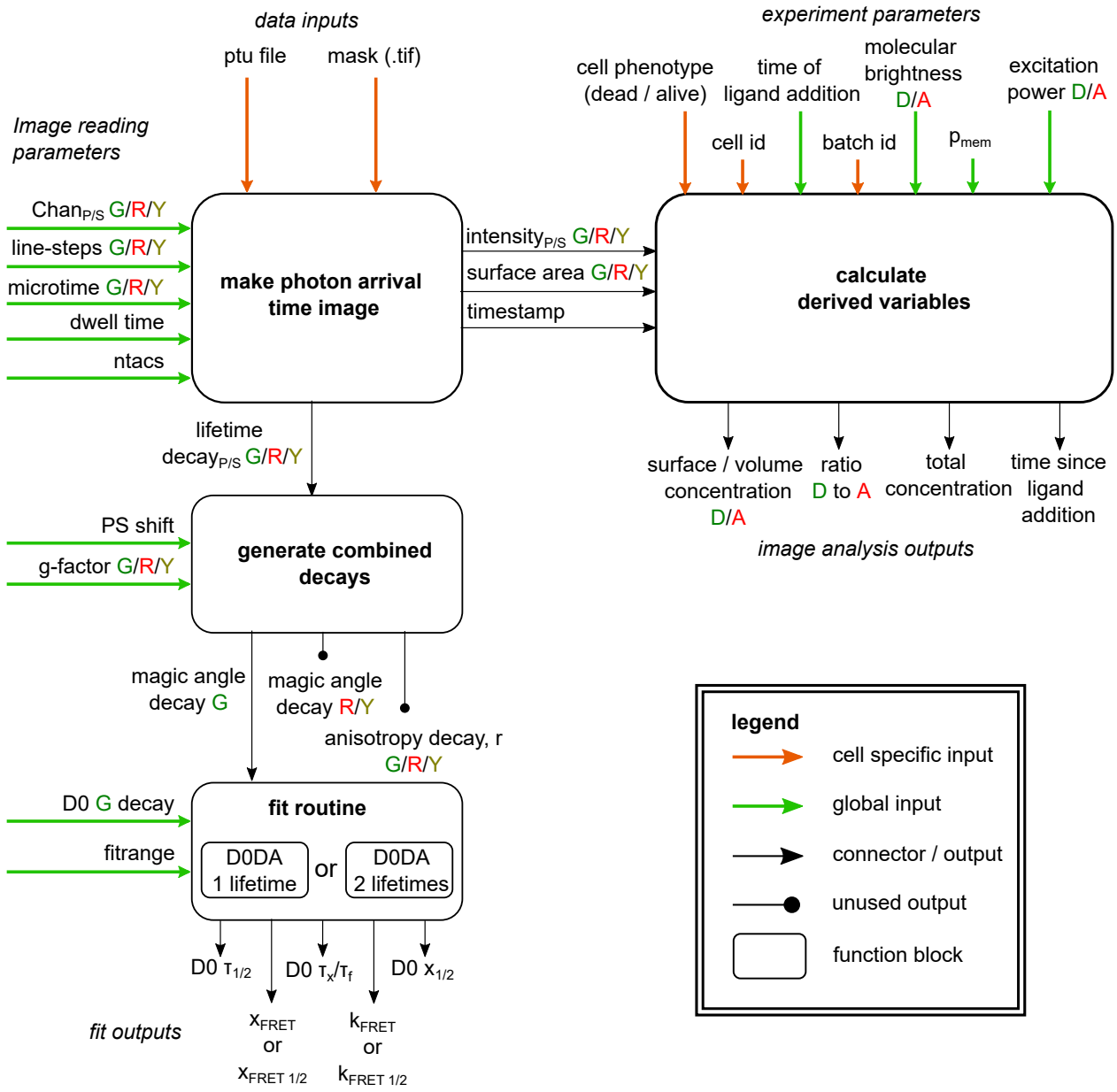

Figure 7.6: **Software flowchart for automated analysis of CELFIS data**

decay is also constructed from the PS decays, but currently not analyzed. At another branch of the program, the fluorescence intensity and the surface area are transformed into protein concentrations using the molecular brightness and the excitation power. A timestamp is derived from the ptu file name, which is combined with the time of ligand addition to yield the time since ligand addition.

7.5.5 Dependencies

The CELFIS analysis software relies on the same ptu reading and image formation routines that are used in Seidel (section 7.1.5). In addition to packages contained in the anaconda package library, the program depends on the tiffile package[8].

[8] https://pypi.org/project/tiffile/2018.10.10/

Summary

Coming to the end of the main matter of my doctoral thesis, I'd like to return to the two perspectives laid out in the introduction and judge how successful the tasks were fulfilled and what their current and potential future impact is. From the methods perspective, STED microscopy, single-molecule localization and FRET spectroscopy were each modified in order to combine them into the FRET-nanoscopy method. The results of which generously fulfill the goals we set out to obtain. We are able to measure any intramolecular distance, including the resolution gap of 10 nm to 45 nm with a standard deviation of ∼5 nm, which can be reduced to <0.5 nm by calculating the average particle. By checking internal consistency and controlling against known nanostructure dimensions, we've ascertained that these distances are both precise and accurate. Hence these distances provide real and useful information on the structures from which they are measured, where it should be noted that the variability between similar structures is likely to exceed the resolution of its averaged structure. The average particle resolution is on-par with the best fluorescence-based methods currently available [24, 27], while its simultaneous readout of FRET-based distances makes it unique among high-end fluorescence methods. FRET-nanoscopy provides so-far the most accurate base pair to base pair distance measurement within origami structures available. We also measure the extension of activated hGBP, which falls within the aforementioned resolution gap. Yet, the application of FRET-nanoscopy to a wider range of problem is limited due to its stringent demands on sample preparation, being high-efficiency labeling with STED compatible dyes, repetitive structures and preferentially a fixed orientation with respect to the lateral imaging plane. However, the impact of FRET-nanoscopy must be considered along another dimension, which is the innovations constituent to some of its parts. The first innovation is the application of localization on dual color-STED data, which effectively eliminates cross-channel aberrations. I serendipitously discovered this phenomenon, which may be further exploited in other applications where a depletion beam provides spatial information in two emission channels, being STED and Maximally Informative Luminescence Excitation Probing (MINFLUX). The second innovation is a quantitative description of the FRET signature under STED conditions. A failure to account for FRET creates a fundamental uncertainty in the position of the fluorophore, which becomes apparent as nanoscopy reaches down to the ∼10 nm resolution regime. By contrast, a quantitative description allows us to harness the effects of FRET to our benefit.

From the application perspective, the very low oligomerization fraction of CD95 (average ∼10 % dimers or trimers, corresponding to ∼3 % FRET fraction) prompted the development of the CELFIS method, capable of measuring such small changes. CELFIS constructs a lifetime decay from fluorescence lifetime images by selecting image features such as cells or cell organelles. Using a donor-only control as a reference, the lifetime decay is fitted using a FRET-sensitized donor decay tail fit, which we show to be precise up to 0.22% FRET fraction. Three additional features are added to the method. Firstly, the FRET fraction is transformed into the biologically-interpretable oligomer fraction using Accessible Volume simulations to account for the specific linker geometry and combinatorics to account for the fraction of hetero-oligos with

fully matured proteins. Secondly, an accurate fluorescence brightness calibration is performed to transform fluorescence intensity images into protein concentration images. Thirdly, data acquisition and analysis is automated using self-written software, enabling us to probe a wide variety of conditions with high statistics. The combination of accurate quantitative readout and high statistics make CELFIS a very timely tool to address several of biology's major ongoing challenges. The inherent complexity of biological systems makes that two similar experiments may have different findings if experimental conditions, such as concentration, differ. This is a contributing factor to what has been called the reproducibility crises [18]. Therefore, it is no longer sufficient to identify binary yes/no relationships valid in a single set of conditions, but complex biological systems must be understood in terms of quantitative relations valid in the complex environment of the cell. CELFIS provides a timely solution by providing tools to probe a large variety of experimental conditions with high statistics, furthermore it requires only ubiquitously available and minimally invasive FP-tagged biomolecules as a sample.

In addition to applying CELFIS to CD95, we serendipitously discovered the concentration-dependent monomer to dimer transition of CTLA4, which is relevant for understanding the role of CTLA4 in the immune response and which underlines the importance of probing a wide range of parameters. For CD95, CELFIS was used to measure the time-evolution of the oligomeric CD95 fraction on a single-cell basis. Additional information was provided by apoptosis dynamics measurements, quantitative STED imaging, live-cell FCS and cPBSA measurements. Taken together, we were able to clarify the ongoing debate on the stoichiometry of the CD95 state and propose a minimal model for signal initiation: CD95 is monomeric at rest and becomes dimeric or trimeric upon ligand addition. More complex models were not observed and are not necessary for signal activation. One remaining question is to quantify the abundance of dimers and trimers in the activated CD95 state. cPBSA provides a direct readout of the number of units in each cluster, however single-cluster stoichiometry determination was hindered by the poor signal-to-noise of mEGFP-based bleaching traces, enabling only the population mean to be determined reliably. I have proposed strategies for labeling CD95 with organic dyes, using which cPBSA promises to fully quantify the distribution of oligomeric states.

Concluding, both approaches were highly successful in their respective intent. I hope that future researchers find my work useful and that it will have a positive impact on society. I thank the reader for his patience.

Acknowledgement

I would like to thank everyone who accompanied me on this journey. It is certainly thanks to their help and inspiration that this work lies before you now. To start, I'd like to thank my supervisor, prof. Claus Seidel, for believing in me and providing me with the means needed to complete the tasks before me. Claus, you are extremely quick to identify the nucleus of an idea and consequently expose its unique advantages, from which I learned a lot. Cornelia, thank you for being my mentor throughout. Your acuity in literature and fairness in judgement was pleasant and very instructive. The FRET-nanoscopy project was certainly a team effort and I'd like to thank Jan for starting the project, Suren for help with software and analyses and Ralf for helping design the instrument. A special thanks to Anders, who suggested using DNA origamis and of whom I learned a great deal about scientific writing. I'd also like to thank the support team from Abberior instrument, who always provided immediate support when needed and Julian Sindram and Marius Otten from the research group of Matthias Karg for their help with AFM and TEM. It was very rewarding continuing the FRET-nanoscopy work on DNA origamis, first with Michelle and later with Noah. Thanks to Lea Wasserman for help in designing and synthesizing the origami structures used in this study and thanks to Christian for help with the cgMD simulations. I owe a great deal to Nina Bartels for intensively working with me on two major projects. It was a great moral support to talk to someone and spar about the daily research problems we had and I am rather proud of the work we did. Speaking about members of Cornelia's group, I'd also like to thank Xiaoyue Shang for working with me on measuring CD95 on origamis and Daniel Kuckla for lending me tools and cracking a joke. I'd like to thank all members of the Seidel group for comradery, scientific help and many a social evening. I would especially like to thank Alex for being knowledgeable on so many things, Folz for help with single-molecule measurements, Paul for his cheerful persona and our work on hGBPs, Julian Koch and Annemarie for help with cell-related issues, Jakub for advanced spectroscopic knowledge, Oleg for helping me crack some of the harder mathematical nuts and Mykola for great help in c++ programming. The lab can only run thanks to the silent actions of Bekir, Matthias, Veronika and Martin, thank you very much. In case I have forgotten to mention anyone, this is certainly due to my flawed memory.

Last, but not least, I'd like to thank Laura and my family for supporting me and making me better in innumerable ways.

Bibliography

[1] Colin Echeverría Aitken, R Andrew Marshall and Joseph D Puglisi. "An oxygen scavenging system for improvement of dye stability in single-molecule fluorescence experiments". In: *Biophysical journal* 94.5 (2008), pp. 1826–1835.

[2] Ruchika Anand, Andreas S Reichert and Arun Kumar Kondadi. "Emerging roles of the MICOS complex in cristae dynamics and biogenesis". In: *Biology* 10.7 (2021), p. 600.

[3] Giuseppe Arena, Salvatore Musumeci, Roberto Purrello and Silvio Sammartano. "Calcium- and magnesium-EDTA complexes. Stability constants and their dependence on temperature and ionic strength". In: *Thermochimica Acta* 61.1-2 (1983), pp. 129–138.

[4] Gülce S Gülcüler Balta et al. "3D cellular architecture modulates tyrosine kinase activity, thereby switching CD95-mediated apoptosis to survival". In: *Cell reports* 29.8 (2019), pp. 2295–2306.

[5] Kira Bartnik et al. "A DNA Origami Platform for Single-Pair Förster Resonance Energy Transfer Investigation of DNA–DNA Interactions and Ligation". In: *Journal of the American Chemical Society* 142.2 (2019), pp. 815–825.

[6] Jean-Luc Bodmer, Pascal Schneider and Jürg Tschopp. "The molecular architecture of the TNF superfamily". In: *Trends in biochemical sciences* 27.1 (2002), pp. 19–26.

[7] Edwin Bremer. "Targeting of the tumor necrosis factor receptor superfamily for cancer immunotherapy". In: *International Scholarly Research Notices* 2013 (2013).

[8] Jan-Hendrik Budde et al. "FRET nanoscopy enables seamless imaging of molecular assemblies with sub-nanometer resolution". In: *arXiv preprint arXiv:2108.00024* (2021).

[9] Lirong Chen et al. "Measuring the energetics of membrane protein dimerization in mammalian membranes". In: *Journal of the American Chemical Society* 132.10 (2010), pp. 3628–3635.

[10] Mark O Collins and Jyoti S Choudhary. "Mapping multiprotein complexes by affinity purification and mass spectrometry". In: *Current Opinion in Biotechnology* 19.4 (2008), pp. 324–330.

[11] Thorben Cordes, Jan Vogelsang and Philip Tinnefeld. "On the mechanism of Trolox as antiblinking and antibleaching reagent". In: *Journal of the American Chemical Society* 131.14 (2009), pp. 5018–5019.

[12] Ingemar J Cox, Colin JR Sheppard and Tony Wilson. "Improvement in resolution by nearly confocal microscopy". In: *Applied optics* 21.5 (1982), pp. 778–781.

[13] Peter J Darlington et al. "Hierarchical regulation of CTLA-4 dimer-based lattice formation and its biological relevance for T cell inactivation". In: *the Journal of Immunology* 175.2 (2005), pp. 996–1004.

[14] Mykola Dimura et al. “Automated and optimally FRET-assisted structural modeling”. In: *Nature communications* 11.1 (2020), pp. 1–14.

[15] Shawn M Douglas et al. “Rapid prototyping of 3D DNA-origami shapes with caDNAno”. In: *Nucleic acids research* 37.15 (2009), pp. 5001–5006.

[16] Valentin Dunsing et al. “Optimal fluorescent protein tags for quantifying protein oligomerization in living cells”. In: *Scientific reports* 8.1 (2018), pp. 1–12.

[17] Toon H Evers et al. “Quantitative understanding of the energy transfer between fluorescent proteins connected via flexible peptide linkers”. In: *Biochemistry* 45.44 (2006), pp. 13183–13192.

[18] Daniele Fanelli. “Is science really facing a reproducibility crisis, and do we need it to?” In: *Proceedings of the National Academy of Sciences* 115.11 (2018), pp. 2628–2631.

[19] Stanley Fields and Ok-kyu Song. “A novel genetic system to detect protein–protein interactions”. In: *Nature* 340.6230 (1989), pp. 245–246.

[20] Qingshan Fu et al. “Structural basis and functional role of intramembrane trimerization of the Fas/CD95 death receptor”. In: *Molecular cell* 61.4 (2016), pp. 602–613.

[21] Jonas J Funke and Hendrik Dietz. “Placing molecules with Bohr radius resolution using DNA origami”. In: *Nature nanotechnology* 11.1 (2016), pp. 47–52.

[22] JoAnne L Greene et al. “Covalent dimerization of CD28/CTLA-4 and oligomerization of CD80/CD86 regulate T cell costimulatory interactions”. In: *Journal of Biological Chemistry* 271.43 (1996), pp. 26762–26771.

[23] Annemarie Greife et al. “Structural assemblies of the di-and oligomeric G-protein coupled receptor TGR5 in live cells: an MFIS-FRET and integrative modelling study”. In: *Scientific reports* 6.1 (2016), pp. 1–16.

[24] Klaus C Gwosch et al. “MINFLUX nanoscopy delivers 3D multicolor nanometer resolution in cells”. In: *Nature methods* 17.2 (2020), pp. 217–224.

[25] Taekjip Ha and Philip Tinnefeld. “Photophysics of fluorescence probes for single molecule biophysics and super-resolution imaging”. In: *Annual review of physical chemistry* 63 (2012), p. 595.

[26] Benjamin Harke et al. “Resolution scaling in STED microscopy”. In: *Optics express* 16.6 (2008), pp. 4154–4162.

[27] Hamidreza Heydarian et al. “3D particle averaging and detection of macromolecular symmetry in localization microscopy”. In: *Nature communications* 12.1 (2021), pp. 1–9.

[28] Johan Hummert et al. “Photobleaching step analysis for robust determination of protein complex stoichiometries”. In: *Molecular biology of the cell* 32.21 (2021), ar35.

[29] DG Johnson and CL Walker. “Cyclins and cell cycle checkpoints”. In: *Annual review of pharmacology and toxicology* 39 (1999).

[30] David Kägi et al. “Fas and perforin pathways as major mechanisms of T cell-mediated cytotoxicity”. In: *Science* 265.5171 (1994), pp. 528–530.

[31] Bennett Kalafut and Koen Visscher. “An objective, model-independent method for detection of non-uniform steps in noisy signals”. In: *Computer physics communications* 179.10 (2008), pp. 716–723.

[32] Kerstin Kanonenberg, Sander HJ Smits and Lutz Schmitt. "Functional reconstitution of HlyB, a type I secretion ABC transporter, in saposin-A nanoparticles". In: *Scientific reports* 9.1 (2019), pp. 1–12.

[33] Christopher King et al. "The FRET signatures of noninteracting proteins in membranes: simulations and experiments". In: *Biophysical journal* 106.6 (2014), pp. 1309–1317.

[34] Frank C Kischkel et al. "Apo2L/TRAIL-dependent recruitment of endogenous FADD and caspase-8 to death receptors 4 and 5". In: *Immunity* 12.6 (2000), pp. 611–620.

[35] Frank C Kischkel et al. "Cytotoxicity-dependent APO-1 (Fas/CD95)-associated proteins form a death-inducing signaling complex (DISC) with the receptor." In: *The EMBO journal* 14.22 (1995), pp. 5579–5588.

[36] Sebastian Kreuz et al. "NFκB activation by Fas is mediated through FADD, caspase-8, and RIP and is inhibited by FLIP". In: *The Journal of cell biology* 166.3 (2004), pp. 369–380.

[37] IN Lavrik and PH Krammer. "Regulation of CD95/Fas signaling at the DISC". In: *Cell Death & Differentiation* 19.1 (2012), pp. 36–41.

[38] Jer-Sheng Lin and Erh-Min Lai. "Protein–protein interactions: co-immunoprecipitation". In: *Bacterial Protein Secretion Systems*. Springer, 2017, pp. 211–219.

[39] Peter S Linsley et al. "Binding Stoichiometry of the Cytotoxic T Lymphocyte-associated Molecule-4 (CTLA-4)". In: *Journal of Biological Chemistry* 270.25 (1995), pp. 15417–15424.

[40] Ralitsa R Madsen and Bart Vanhaesebroeck. "Cracking the context-specific PI3K signaling code". In: *Science Signaling* 13.613 (2020), eaay2940.

[41] Thomas G Martin and Hendrik Dietz. "Magnesium-free self-assembly of multi-layer DNA objects". In: *Nature communications* 3.1 (2012), pp. 1–6.

[42] Ana Martin-Villalba, Enric Llorens-Bobadilla and Damian Wollny. "CD95 in cancer: tool or target?" In: *Trends in molecular medicine* 19.6 (2013), pp. 329–335.

[43] Stefan Niekamp et al. "Nanometer-accuracy distance measurements between fluorophores at the single-molecule level". In: *Proceedings of the National Academy of Sciences* 116.10 (2019), pp. 4275–4284.

[44] Joanna Oracz et al. "Photobleaching in STED nanoscopy and its dependence on the photon flux applied for reversible silencing of the fluorophore". In: *Scientific reports* 7.1 (2017), pp. 1–14.

[45] Giuliana Papoff et al. "Identification and characterization of a ligand-independent oligomerization domain in the extracellular region of the CD95 death receptor". In: *Journal of Biological Chemistry* 274.53 (1999), pp. 38241–38250.

[46] Sri Rama Prasanna Pavani et al. "Three-dimensional, single-molecule fluorescence imaging beyond the diffraction limit by using a double-helix point spread function". In: *Proceedings of the National Academy of Sciences* 106.9 (2009), pp. 2995–2999.

[47] James Pawley. *Handbook of biological confocal microscopy*. Vol. 236. Springer Science & Business Media, 2006.

[48] M El Peter and PH Krammer. "The CD95 (APO-1/Fas) DISC and beyond". In: *Cell Death & Differentiation* 10.1 (2003), pp. 26–35.

[49] JR Porter. "Antony van Leeuwenhoek: tercentenary of his discovery of bacteria". In: *Bacteriological reviews* 40.2 (1976), pp. 260–269.

[50] Teresa M Przytycka, Mona Singh and Donna K Slonim. "Toward the dynamic interactome: it's about time". In: *Briefings in bioinformatics* 11.1 (2010), pp. 15–29.

[51] Michelle Paulina Rademacher. "Fluorescence Spectroscopic and Nanoscopic Studies Map Three-Dimensional DNA Origami Structures Using Optical Pythagoras". MA thesis. Düsseldorf, Germany: Heinrich Heine University Düsseldorf, Mar. 2022.

[52] Sarvenaz Sarabipour, Nuala Del Piccolo and Kalina Hristova. "Characterization of membrane protein interactions in plasma membrane derived vesicles with quantitative imaging Forster resonance energy transfer". In: *Accounts of chemical research* 48.8 (2015), pp. 2262–2269.

[53] Fiona L Scott et al. "The Fas–FADD death domain complex structure unravels signalling by receptor clustering". In: *Nature* 457.7232 (2009), pp. 1019–1022.

[54] Alan E Senior, Sashi Nadanaciva and Joachim Weber. "The molecular mechanism of ATP synthesis by F1F0-ATP synthase". In: *Biochimica et Biophysica Acta (BBA)-Bioenergetics* 1553.3 (2002), pp. 188–211.

[55] Benedict EK Snodin et al. "Introducing improved structural properties and salt dependence into a coarse-grained model of DNA". In: *The Journal of chemical physics* 142.23 (2015), 06B613_1.

[56] Yvonne Stahl et al. "Moderation of Arabidopsis root stemness by CLAVATA1 and ARABIDOPSIS CRINKLY4 receptor kinase complexes". In: *Current Biology* 23.5 (2013), pp. 362–371.

[57] Antonio Suma et al. "Tacoxdna: A user-friendly web server for simulations of complex DNA structures, from single strands to origami". In: *Journal of computational chemistry* 40.29 (2019), pp. 2586–2595.

[58] Bernhard Suter, Saranya Kittanakom and Igor Stagljar. "Two-hybrid technologies in proteomics research". In: *Current opinion in biotechnology* 19.4 (2008), pp. 316–323.

[59] Giorgio Tortarolo et al. "Evaluating image resolution in stimulated emission depletion microscopy". In: *Optica* 5.1 (2018), pp. 32–35.

[60] Maximilian H Ulbrich and Ehud Y Isacoff. "Subunit counting in membrane-bound proteins". In: *Nature methods* 4.4 (2007), pp. 319–321.

[61] Éva S Vanamee and Denise L Faustman. "Structural principles of tumor necrosis factor superfamily signaling". In: *Science Signaling* 11.511 (2018), eaao4910.

[62] Lucy SK Walker and David M Sansom. "The emerging role of CTLA4 as a cell-extrinsic regulator of T cell responses". In: *Nature Reviews Immunology* 11.12 (2011), pp. 852–863.

[63] Tony Wilson and Colin Sheppard. *Theory and practice of scanning optical microscopy*. Vol. 180. Academic press London, 1984.

[64] PK Wolber and Bruce S Hudson. "An analytic solution to the Förster energy transfer problem in two dimensions". In: *Biophysical journal* 28.2 (1979), pp. 197–210.

Acronyms

$\epsilon(t)$ FRET sensitized donor decay. 7, 39, 70

AIC Aikaike Information Criterion. 66

ALEX Alternating Line Excitation. 13, 55, 68

AV Accessible Volume Simulations. 7, 21, 40

CD86 Cluster of Differentiation 86 also known as B7-2. 46

CD95 Cluster of Differentiation 95, also known as Fas, FasR or TNFRSF6. 6, 7, 11, 38

CD95L CD95 Ligand, also known as FasL. 7, 45

CELFIS Cell Lifetime FRET Image Spectroscopy. 6, 7, 11, 38, 39, 43, 45–49, 72

cgMD coarse grained Molecular Dynamics Simulations. 21, 23–25, 33, 36, 81, 83

cPBSA confocal Photobleaching Step Analysis. 11, 45, 46, 48, 53, 55

cSTED colocalization STED. 6, 10, 11, 16, 18

CTLA4 Cytotoxic T-Lymphocyte-Associated protein 4, also known as CD152. 6, 11, 38, 41, 46

DISC Death Inducing Signaling Complex. 48

DoF Degrees of Freedom. 30

ETS Easy To Change. 62

FADD Fas-Associated Death Domain. 43, 48

FCS Fluorescence Correlation Spectroscopy. 6, 11, 45

FP Fluorescent Protein. 46, 73

FRC Fourier Ring Correlation. 57

FRET Förster Resonance Energy Transfer. 6, 7, 10, 16, 33, 55

GUI Graphical User Interface. 66, 68

GUV Giant Unilamellar Vesicle. 18

hGBP human Guanylate-Binding Protein. 6

IRF Instrument Response Function. 39, 40

KV Kalafut-Visscher. 46, 47

mEGFP monomeric Enhanced Green Fluorescent Protein. 46, 47

MFIS Multiparameter Fluorescence Image Spectroscopy. 11, 12

MINFLUX Maximally Informative Luminescence Excitation Probing. 72

MLE Maximum Likelihood Estimation. 12, 13, 61, 62

n.c.-χ non-centered-χ. 16, 20, 66

NFκB Nuclear Factor kappa-light-chain-enhancer of activated B cells. 45

NMR Nuclear Magnetic Resonance. 10

O(HF+NF) DNA origami platform labeled with high-FRET and no-FRET dye pairs. 20, 23, 26

OP Optical Pythagoras. 6, 7, 16, 20

PA-cSTED Particle Averaging cSTED. 11, 14, 18, 20, 30, 33, 36, 37

PBSA Photobleaching Step Analysis. 46

PIE Pulsed Interleaved Excitation. 55

PSF Point Spread Function. 13–15, 19, 57

RMSD Root Mean Square Displacement. 14, 16, 30, 34

seTCSPC sub-ensemble Time-Correlated Single Photon Counting. 18, 26, 29, 33, 36, 63, 81

SIM Structured Illumination Microscopy. 10

SLM Spatial Light Modulator. 51

sMFD single-molecule Multiparameter Fluorescence Detection. 19

SMLM Single-Molecule Localization Microscopy. 10, 14

SNR Signal-to-Noise Ratio. 57

STED Stimulated Emission Depletion. 6, 10, 72

TCSPC Time-Correlated Single Photon Counting. 10, 13, 18, 21, 28, 39, 44, 52, 55

TNFR Tumor Necrosis Factor Receptor. 45

Y2H Yeast two-Hybrid system. 39

List of Figures

List of Tables

FRET nanoscopy enables seamless imaging of molecular assemblies with sub-nanometer resolution

Nicolaas T.M. van der Voort[1,†], Jan-Hendrik Budde[1,†], Suren Felekyan[1], Julian Folz[1], Ralf Kühnemuth[1], Paul Lauterjung[1,2], Markus Köhler[3], Andreas Schönle[3], Julian Sindram[4], Marius Otten[4], Matthias Karg[4], Christian Herrmann[2], Anders Barth[1,a,*], Claus A. M. Seidel[1,*]

[1] Chair for Molecular Physical Chemistry, Heinrich-Heine-University Düsseldorf, Germany

[2] Physical Chemistry I, Ruhr-Universität Bochum, Germany

[3] Abberior Instruments GmbH, Hans-Adolf-Krebs-Weg 1, 37077 Göttingen, Germany

[4] Lehrstuhl für Kolloide und Nanooptik, Heinrich-Heine-Universität Düsseldorf, 40225 Düsseldorf, Germany

[a] Present address: Department of Bionanoscience, Kavli Institute of Nanoscience, Delft University of Technology, Delft, The Netherlands

[†] contributed equally

* Correspondence to: cseidel@hhu.de, anders.barth@hhu.de

Abstract

By circumventing the optical diffraction limit, super-resolved fluorescence microscopy techniques enable the study of larger cellular structures and molecular assemblies. However, fluorescence nanoscopy currently lacks the spatiotemporal resolution to resolve distances on the size of individual molecules and reveal the conformational fine structure and dynamics of molecular complexes. Here we establish FRET nanoscopy by combining colocalization STED microscopy with multiparameter FRET spectroscopy. We simultaneously localize donor and acceptor dyes of single FRET pairs at nanometer resolution down to molecular distances of 5 nm with a precision of 0.7 nm. FRET provides isotropic 3D distance information, while colocalization measures the projected distance onto the image plane. The combined information enables to determine the 3D orientation using Pythagoras's theorem. Studying two DNA model systems and the human guanylate binding protein hGBP1, we demonstrate how FRET nanoscopy unravels the interplay between their spatial organization and local molecular conformation in a complex environment.

Introduction

Fluorescence microscopy has made key contributions towards our understanding of biomolecular structures and dynamics at ambient conditions due to being minimally invasive and highly selective to the molecule of interest. An ideal microscope would provide seamless resolution from the dimensions of cells and cellular substructures to the molecular architecture of biomolecular assemblies. By circumventing the diffraction limit of optical microscopy, super-resolved fluorescence microscopy (nanoscopy) techniques have achieved a major step towards such a fluorescence "nanoscope"[1,2]. Established techniques for super-resolved imaging such as stimulated emission depletion (STED)[3], the various single-molecule localization microscopies (SMLM)[4-9] or cryogenic optical localization (COLD)[10] achieve theoretical resolutions of several nanometers. Practically achievable lateral resolutions at ambient conditions are often limited to about 20 nm, although the MINFLUX technique has recently pushed this limit to the single digit nanometer range[11-13]. While nanoscopy is hence well-suited to elucidate the spatial organization of larger cellular structures and molecular assemblies[14], it currently lacks the resolution to determine distances on the size of individual molecules that are required to address the conformation and fine structure of molecular complexes. Importantly, at interdye distances below 10 nm, dipole-dipole coupling leads to Förster resonance energy transfer (FRET) between fluorophores, posing a fundamental barrier for localization-based approaches due to accelerated photoblinking and bleaching[15]. Recently, colocalization microscopy has been shown to provide nanometer accuracy down to a distance of 8 nm[16], which required extensive corrections for optical aberrations and sample drift during the long acquisition times while still being limited by the occurrence of FRET at distances below ~12 nm.

Here, we unlock the sub-10-nm regime by introducing FRET nanoscopy. Our approach combines STED nanoscopy with multiparameter FRET spectroscopy to simultaneously localize single FRET pairs with nanometer resolution and quantitatively measure intramolecular distances with sub-nanometer precision (Fig. 1a-b). Different from previous approaches[17,18], we take full advantage of the potential of FRET to quantitatively resolve distances on the molecular scale with single-molecule resolution[19]. Importantly, the FRET information provides isotropic 3D distance information, while colocalization measures the projected distance onto the xy-plane. Combining these two observables, it is possible to determine the 3D orientation of the interdye vector using Pythagoras's theorem (Fig. 1b), without the need for more complex approaches such as tomographic reconstruction[10]. Multiparameter FRET nanoscopy combines three concepts (Fig. 1a-b). First, we apply STED nanoscopy to break the diffraction limit up to a resolution of ~40 nm to distinguish individual molecules. Second, we combine STED with single molecule

colocalization (cSTED) to take advantage of the high localization precision for single fluorescent molecules, providing nanometer accuracy down to 5 nm distances. The cSTED approach is fast (<10 s) as it does not rely on the accumulation of many localizations per molecule so that no drift correction is needed. Moreover, no corrections for chromatic and spherical aberrations are required because the point spread function (PSF) of the two spectral channels is dominated by the profile of the shared STED beam. Despite the lower photon budget compared to other SMLM techniques, cSTED reaches nanometer localization precisions due to the smaller size of the STED PSF and high scanning speed.

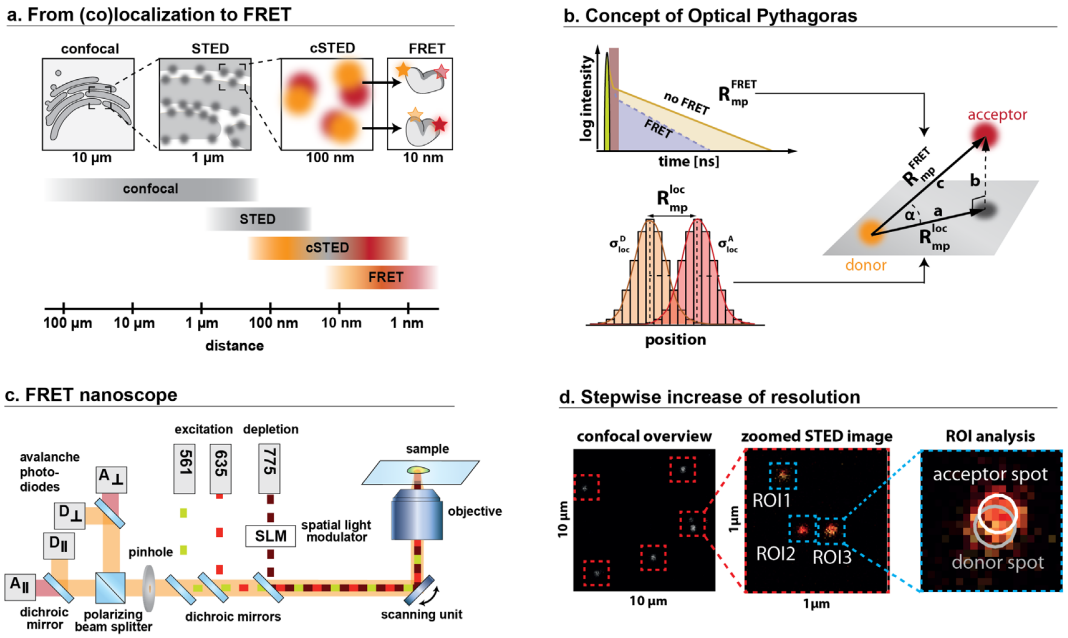

Figure 1: The concept of FRET nanoscopy. a) The combination of confocal and STED microscopy with colocalization-STED (cSTED) and FRET spectroscopy of a donor and acceptor dye enables seamless sub-nanometer resolution. **b)** Quantitative FRET-derived distances are obtained from the analysis of the donor fluorescence decay, providing the average donor acceptor distance $\langle R_{DA} \rangle$ that is converted to the FRET-based physical distance between the mean (center) dye positions R_{mp}^{FRET} (see Suppl. Tab. 8 and Suppl. Fig. 5)[19,20]. In addition, the positions of the donor and acceptor fluorophores are localized from the detected signal in each channel, providing the localization-based distance between the mean dye positions R_{mp}^{loc}. By comparing R_{mp}^{FRET} and R_{mp}^{loc}, information about the three-dimensional orientation of the molecule is obtained using Pythagoras's theorem. **c)** The experimental setup for FRET nanoscopy is based on a conventional STED setup with two excitation lasers and spectrally resolved detection. A single STED laser (775 nm) depletes both acceptor and donor fluorophores. Polarized excitation and detection provide the anisotropy information and allows to reconstruct the polarization-free fluorescence decay for accurate lifetime analysis (see Methods). **d)** The workflow of FRET nanoscopy. Small areas of 1x1 µm^2 are identified in a confocal overview and imaged under STED conditions. Regions of interest (ROIs) are identified and analyzed separately.

In the third aspect, we take advantage of the occurrence of FRET between a donor and an acceptor dipole at shorter distances as a natural extension of the cSTED approach, allowing us to address molecular distances in the range of 4-12 nm[19,21]. This approach is similar to the recently introduced metal-induced energy transfer (MIET) that provides sub-nanometer axial localization of fluorescence emitters using the distance-dependent quenching by metal[22] or graphene[23-25] over a range of up to 20 nm. However, by measuring the relative distance between two spectrally different fluorophores on the same molecule, FRET provides an internal reference that allows to directly measure the molecular conformation[20,26,27]. We implement FRET nanoscopy with multiparameter fluorescence imaging spectroscopy[28] to obtain spectral, time-resolved and polarization information, allowing us to classify localizations of single molecules using the intensity-based FRET efficiency as well as the fluorescence lifetimes and anisotropies of the donor and acceptor fluorophores. FRET nanoscopy thus combines spatial resolution on the molecular scale with ultimate sensitivity for molecular features by taking advantage of all dimensions of the fluorescence signal[29].

In this study, we benchmarked FRET nanoscopy using two model systems. First, we apply DNA origami nanotechnology to place two FRET pairs at a distance of ~75 nm. We show that FRET nanoscopy resolves the geometry of the four dyes on the origami with sub-nanometer precision, while simultaneously providing quantitative FRET information for the two FRET pairs. Second, we assess the accuracy of FRET-derived distances from the intensity and lifetime information using a set of DNA rulers that are immobilized on one or on both ends. The 3D information provided by FRET nanoscopy allows us to address the orientation of the DNA and resolve the roughness of the surface on the molecular scale. Finally, we use FRET nanoscopy to map the human guanylate binding protein 1 (hGBP1) which forms long fiber structures *in vitro* and live cells by oligomerization. Different to its closed conformation in the monomeric state, we show that hGBP1 adapts an extended conformation in the assembly, highlighting the potential of FRET nanoscopy to resolve molecular conformation in complex systems.

Concepts

Combining STED microscopy and multiparameter FRET spectroscopy. The multiparameter fluorescence detection STED microscope is based on a modified confocal microscope with pulsed excitation and depletion beams and polarization-resolved detection in two spectral channels (Fig. 1c and Supplementary Fig. 1). In total, we register four polarization resolved fluorescence decays, two for each spectral detection window. To probe both donor and acceptor fluorophores in rapid succession, we perform alternating line scans with direct donor and acceptor excitation. We deplete both fluorophores with the same STED pulse that is overlaid with the excitation and has 2 ns duration (Fig. 1c and Supplementary Fig. 1). Efficient depletion of both fluorophores by a single STED laser requires that both fluorophores show sufficient emission at the STED wavelength of 775 nm. Consequently, spectrally close fluorophores are needed. Here we use Atto594 or Alexa594 as FRET donors and Atto647N as FRET acceptor. We additionally apply time-gated detection to increase the spatial resolution for cSTED by discarding any photons that arrive during the depletion pulse[30-32], resulting in typical resolutions of 65 nm and 50 nm for the donor and acceptor channels, respectively (Supplementary Tab. 5). While higher resolutions are achievable with higher depletion power, these numbers represent a compromise to ensure that sufficient photons are detected for the FRET analysis.

FRET nanoscopy workflow with stepwise increased resolution. We first record a confocal overview image to determine the location of single molecules or molecular assemblies (Fig. 1d). For each location, a zoomed STED image (1x1 µm) is recorded, wherein regions of interest (ROI) are identified that contain a single dye or a closely spaced donor-acceptor dye pair. Each dye is identified as a 'spot' and the fluorescence signal in a spot pair is used to determine the spectroscopic parameters, i.e., the intensity-based FRET efficiency and the donor fluorescence lifetime and anisotropy. Additionally, the position of the emitters is localized by fitting with a 2D Gaussian function with a typical localization precision of ~3 nm. The localization precision σ_{loc} of the donor or acceptor fluorophore provides an additional criterion to distinguish single molecules and remove aggregates or multi-molecule events. The localization algorithm also identifies the most likely number of emitters based on a maximum likelihood criterion while penalizing for overfitting, allowing us to characterize each ROI by the number of active donor and acceptor fluorophores (spot stoichiometry, Supplementary Fig. 2). These parameters are used for filtering and to identify sub-populations within the ensemble of measured ROIs (Supplementary Fig. 3). For each FRET pair, the length of the projected inter-dye distance vector, d_{loc}, is determined. The distribution of d_{loc} depends on the distance between the mean positions of the dyes, $R_{\mathrm{mp}}^{\mathrm{loc}}$, and the

localization precision and is described by a non-central χ-distribution with two degrees of freedom (see methods eq. 15 and Supplementary Section 'Colocalization analysis')[16,33]. By calibrating the width parameter of the distribution, the mean-position distance $R_{\mathrm{mp}}^{\mathrm{loc}}$ can thus be determined with high precision despite the broad distribution of d_{loc}.

The time-resolved FRET nanoscopy experiment offers two approaches to determine the FRET efficiency and thus interdye distance: either from the detected intensities or the time-resolved fluorescence decays of the donor fluorophore. Due to the flexible dye linkers, a distribution of R_{DA} values is measured, so that the FRET efficiency is related to the FRET-averaged apparent donor-acceptor distance, $\langle R_{\mathrm{DA}} \rangle_{\mathrm{E}}$, by:

$$E = \frac{1}{1 + \left(\frac{\langle R_{\mathrm{DA}} \rangle_{\mathrm{E}}}{R_0} \right)^6}, \tag{1}$$

where R_0 is the Förster radius. For each spot pair, the FRET efficiency can be calculated from the corrected photon counts of the donor and acceptor fluorophores after donor excitation, $F_{\mathrm{D|D}}$ and $F_{\mathrm{A|D}}$, or the fluorescence lifetimes of the donor in the presence and absence of the acceptor, $\tau_{\mathrm{D(A)}}$ and $\tau_{\mathrm{D(0)}}$. In the absence of dynamics, the intensity-based and lifetime-based estimators of the FRET efficiency are equivalent, given by:

$$E = \frac{F_{\mathrm{A|D}}}{F_{\mathrm{D|D}} + F_{\mathrm{A|D}}} = 1 - \frac{\tau_{\mathrm{D(A)}}}{\tau_{\mathrm{D(0)}}}. \tag{2}$$

Slight deviations from this relation occur due to fast dynamics of the dye linkers (see eq. 10 in the Methods)[34,35], in which case the spot-integrated donor fluorescence lifetime corresponds to the fluorescence-weighted average, which we denote as $\langle \tau_{\mathrm{D(A)}} \rangle_{\mathrm{F}}$ in the following. To estimate accurate fluorescence lifetimes under STED conditions for each spot, we discard the initial part of the donor fluorescence decay during the depletion pulse and fit the tail to a single-exponential model function using a maximum likelihood estimator[36] (see Methods, Supplementary Section 'Determination of spot-integrated fluorescence lifetimes' and Supplementary Fig. 4). The determination of accurate intensity-based FRET efficiencies under STED conditions requires further corrections. A detailed description of the correction procedure for the intensities for crosstalk, direct excitation, differences in the quantum yield and detection efficiencies[19,37], as well as residual signal from partially depleted fluorophores is given in Supplementary Section 'Accurate intensity-based FRET efficiencies under STED conditions'. Additional information on the interdye distance distribution is obtained from the analysis of the sub-ensemble fluorescence decay. Different to the intensity-based approach, lifetime measurements report directly on the mean interdye distance $\langle R_{\mathrm{DA}} \rangle$ and

the width of the distance distribution (eq. S17). To utilize the complete fluorescence decay in the analysis, we account for the depletion part of the decay as a fast decay component with a lifetime of ~200 ps (Supplementary Tab. 9). Fluorescence decays of the donor in the absence and presence of the acceptor were analyzed globally to increase the robustness of the fit[38] (see Methods and Supplementary Section 'Sub-ensemble fluorescence decay analysis').

Results

FRET-nanoscopy resolves DNA origami nanostructures with single base pair resolution. We benchmarked the capabilities of FRET nanoscopy by imaging a single-layer rectangular DNA origami platform, O(HF+NF)[39,40], where we placed two FRET pairs (Atto594/Atto647N) with a high and zero FRET efficiency (high-FRET, HF and no-FRET, NF species), respectively (Supplementary Fig. 7). The distance between them amounts to ~75 nm, well below the diffraction limit (Fig. 2a-b). Using negative-stain transmission electron microscopy, we determined the mean dimensions of the origami as (88 ± 3) x (59 ± 4) nm (Supplementary Fig. 8). The DNA origami platforms were immobilized on a PEG-coated glass surface with neutravidin using eight biotin anchors on the lower side to ensure that the origamis are oriented in the xy-plane. We acquired zoomed STED images of 1824 origami platforms and localized individual emitters in the donor and acceptor channels (Fig. 2a). Using the spot stoichiometry of two donors and two acceptors as a filter criterion, we remove incompletely labelled origami platforms and retain only those containing two FRET dye pairs (N=137, Supplementary Fig. 2). To correct for the different orientations of the origamis in the xy-plane, we aligned the structures by rotation and translation of the dye coordinates using the Kabsch algorithm[41] (Fig. 2b, eq. 14). To provide an unbiased reference structure that requires no prior knowledge about the sample, we selected the structure from the dataset that optimizes the overall root mean squared deviation (RMSD) as a reference. Defect structures that showed a high RMSD after the alignment step were removed (see gray points in Fig. 2b and Supplementary Fig. 9). The overlay of all aligned structures allowed us to reconstruct the geometric arrangement of the dyes and estimate the mean dye positions and displacement vectors (Fig. 2b). From the standard error of the mean of the dye positions, we obtain a localization precision of < 4.5 Å. This high precision indicated to us that we could utilize our measurements to estimate the structural parameters of the origami platform. Due to the defined attachment points on the platform (Supplementary Fig. 7), the interdye distances can be expressed as the number of base pairs in the horizontal direction and the number of helices in the vertical direction (see eq. S35).

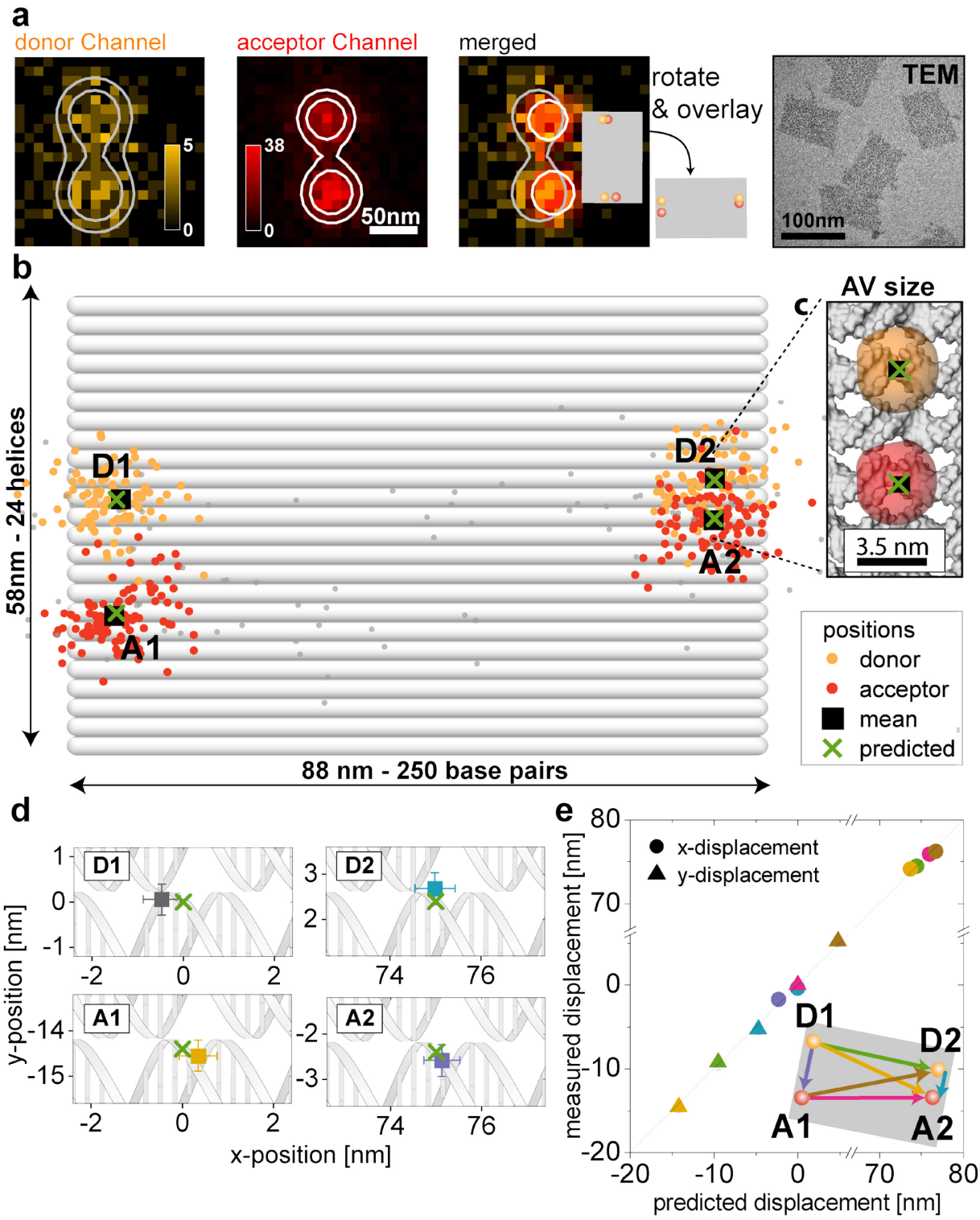

Figure 2: Colocalization STED (cSTED) analysis on rectangular DNA-origami nanostructures O(HF+NF). (a) Single origamis are recorded under gated STED conditions (see Supplementary Section 'Data acquisition' and Supplementary Tab. 14), yielding a median of 245 photons for the donor and 537 for the acceptor fluorophore. The position of the two dyes in each

channel is determined by fitting two Gaussian distributions with background. The set of four positions is then rotated and aligned to a common reference structure and each emitter is classified D1, D2, A1 or A2 based on its location and channel. Contour lines indicate one- and two sigma distances from the Gaussian centers. TEM images show intact origami platforms. **(b)** The estimated dye positions for a total of 137 origamis carrying all four dyes are overlaid on the DNA origami platform drawn to scale (gray rods represent DNA double strands). 36 structures had an overall RMSD > 10 nm and are disregarded for further analysis (grey points). The predicted structure is based on an interhelical distance of 2.4 nm and base pair extension of 3.16 Å (see text). The mean structure is overlaid with the predicted structure such that the center-of-mass and A1-A2 unit vector coincide. **(c)** Zoom-in on the D2-A2 dye pair. The clouds indicate the accessible volumes of the flexibly coupled fluorophore due to linker movement, yielding a structural prediction of 4.8 nm (green crosses). The average dye-dye displacement after particle alignment is in close agreement at 5.2 nm (black squares) **(d)** Zoom-in of the measured mean positions compared to the predicted values. Cartoon-DNAs are drawn to scale, placing the predicted position at the dye attachment point on the double helix (see main text and Supplementary Fig. 7). **(e)** The six interdye distances are compared to their predicted values. The cartoon structure is rotated such that the A-A vector lies on the x-axis. The values match within a precision of 7 Å over the range of -5 to 75 nm and are listed in Supplementary Tab. 18. Inset coloring matches the data markers. Data was collected on two measurement days on the same sample. A detailed description of analysis settings and corresponding sample numbers is found in Supplementary Table 14.

As an example, the distance between the two acceptor fluorophores is 236 base pairs in the x-direction and 5 helices along the y-direction, for which we measured a distance of 75.8 ± 0.6 nm (Supplementary Fig. 10). We find the best agreement between the structural model and the six measured interdye distances for a rise per base pair of 3.16 ± 0.03 Å and an inter-helical distance of 2.4 ± 0.1 nm (see Supplementary Note 2 and Supplementary Fig. 11). The predicted dye positions based on these model parameters are overlaid in Fig. 2b-d, showing the excellent agreement for all four dye positions. In Fig. 2d, we additionally overlay the estimated dye positions on a structural model of the DNA helices to highlight that our precision of 4.5 Å reaches the dimensions of a single base pair. A potential concern for the localization precision is given by the long linkage used to attach the dyes to the origami platform, allowing them to explore a large accessible volume (AV) on the origami surface as indicated in Fig. 2c (see Supplementary Section 'Accessible volume simulations'). Here, the linkage consists of two units: an unpaired nucleotide at the 3' end of a short staple strand and the usual flexible dye tether, resulting in a slightly increased linker length of ~29 Å (Supplementary Fig. 7 and Supplementary Tab. 6). However, as the movement of the dyes is fast compared to the acquisition time of the experiment, the localization approach measures the average position of the dye within its sterically accessible volume. Interestingly, the spread of the localizations of ~4.5 nm exceeds the theoretical limit based on photon statistics of 2 nm, which is unlikely to originate from registration error and suggests that we are sensitive to structural heterogeneities of the DNA origami constructs (see Supplementary Note 3). In summary, the cSTED approach resolves distances between individual fluorophores on

DNA origami nanostructures with a localization precision of < 5 Å over a wide range of displacements along the x and y direction from 5-80 nm (Fig. 2e).

The estimated average interhelical distance of 2.4 nm is well in the range of the experimental and theoretical observations. Due to the 'chicken-wire' structure of the DNA origami, the interhelical distance fluctuates between 1.85 nm at the junction and a maximum of 3.6 nm[42,43]. In our design, the dyes are placed 7 bp away from the nearest junction and thus half-way between the points of maximum and minimum interhelical distance. Our value agrees well with theoretical estimates from MD simulations[43,44] but is smaller than the values reported from cryoEM or small-angle X-ray scattering of 2.6-2.7 nm[42,45]. Interestingly, our estimate for the rise per base pair of 3.16 Å is slightly lower compared to values for individual double-stranded DNA (of ~3.32 ± 0.19 Å from crystallographic data[46] and 3.29 ± 0.07 Å from scattering interference measurements[47]). Different to these approaches, we measured the average rise per base pair over long distances of 237 bp across the origami nanostructure. Hence, the lower value indicates that the origami is slightly compressed along the long axis, potentially due to a breathing of the chicken-wire structure. A comparable deviation towards shorter distances has also been previously reported for interdye distances on DNA origami helix bundles measured by DNA-PAINT microscopy[48].

Resolving distinct FRET species within the diffraction limit. We then defined regions of interest of 70 x 70 nm containing single donor-acceptor FRET pairs for each DNA origami and computed two FRET indicators, the corrected intensity-based FRET efficiency E and the fluorescence-weighted average donor fluorescence lifetime $\langle\tau_{D(A)}\rangle_F$ (see Methods, spectroscopic analysis). Their correlation is shown in a two-dimensional frequency histogram of analyzed spots (Fig. 3a). Different to the colocalization analysis, we also included all constructs which contained at least one donor-acceptor dye pair in the FRET analysis to obtain higher statistics (N=1391). The E - $\langle\tau_{D(A)}\rangle_F$ diagram reveals two species with zero and high FRET efficiency that follow the expected relation given by the static FRET-line (solid line in Fig. 3a, see eq. 10 in the methods and Supplementary Table 19). Due to the low photon number in the donor channel for the high-FRET (HF) dye pair, we detect a larger fraction of no-FRET (NF) dye pairs. The tailing from the HF population towards the NF population is a result of photobleaching of the acceptor fluorophore during the acquisition time that is also evident in control measurements of the HF FRET-pair in the reference construct (Supplementary Fig. 13a). Consequentially, the FRET efficiency of the HF species (E=0.45) is slightly underestimated compared to solution-based single-molecule FRET control measurements of origamis carrying only one of the two dye pairs (E=0.53, Supplementary Fig. 12a). However, the intensity-based FRET efficiency is mainly used here for separating the

two species, and we show below that accurate FRET-derived distances are obtained from the sub-ensemble analysis of the fluorescence decays.

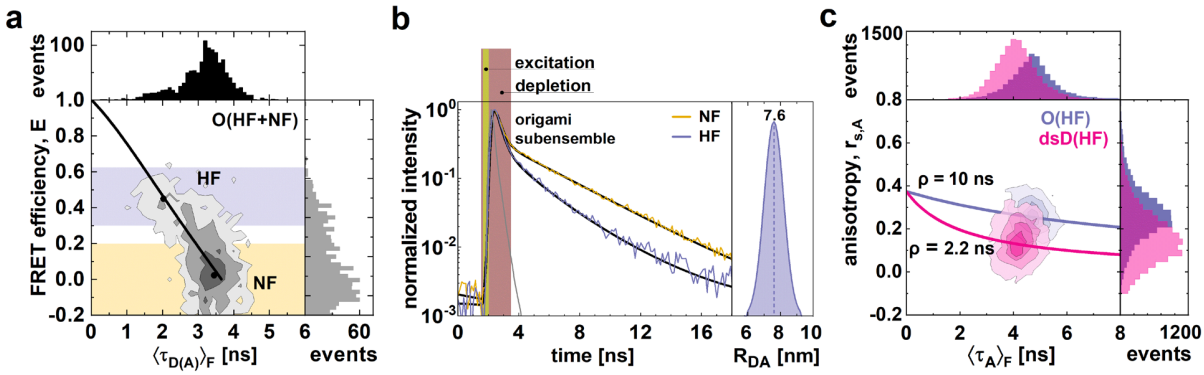

Figure 3: FRET nanoscopy distinguishes two FRET pairs for the O(HF+NF) sample within the diffraction limit. (a) Two-dimensional frequency histogram of the ROI-integrated intensity-based FRET efficiency, E, and the fluorescence-weighted average donor fluorescence lifetime, $\langle\tau_{D(A)}\rangle_F$. The static FRET-line (solid line, eq. 10 in the methods and Supplementary Table 19) shows the theoretic relation between lifetime and FRET efficiency. **(b)** Sub-ensemble fluorescence decays of the donor for the high and low FRET-efficiency species in **a** (see Supplementary Section 'Sub-ensemble fluorescence decay analysis')**.** Data for a-b same as in Figure 2. **(c)** Scatter corrected acceptor anisotropy, $r_{s,A}$, and acceptor fluorescence lifetime after direct excitation, $\langle\tau_A\rangle_F$, from solution-based single-molecule experiments are overlaid with the Perrin lines (see eq. S21c). The Perrin lines demonstrate that the mobilities of the acceptor dye is significantly decreased for O(HF+NF) compared to the DNA ruler dsD(HF), as characterized by the mean rotational correlation time, ρ (see Supplementary Fig. 14). Each sample was measured in a single experiment (object numbers see Supplementary Table 14)

We then selected dye pairs with a high or low FRET efficiency (HF: E>0.3, NF: E<0.2) and generated sub-ensemble decays of the donor fluorescence (Fig. 3b). For the fluorescence decay of the NF species, we obtained a donor fluorescence lifetime of 3.7 ± 0.1 ns. While the intensity-based FRET efficiency of the HF species was underestimated due to acceptor photobleaching, we can account for these artifacts by including a donor-only fraction in the lifetime analysis. Using a distance distribution model function (see Supplementary Section 'Sub-ensemble fluorescence decay analysis'), we obtain a distance between the average donor-acceptor positions $R_{\mathrm{mp}}^{\mathrm{FRET}}$ of 7.3 ± 0.3 nm, in good agreement with single-molecule measurements of freely diffusing molecules in solution ($R_{\mathrm{mp}}^{\mathrm{FRET}} = 7.3 \pm 0.1$ nm). As an additional control, we measured origamis that only contained the high-FRET or no-FRET dye pair and determined FRET-based distances using the lifetime and intensity information under single-molecule and STED conditions, which yielded

consistent mean-position distances in the range of 7.2-7.6 nm (Supplementary Fig. 13d and Supplementary Tabs. 9 and 10).

While we obtained consistent FRET-based distances under STED conditions, the FRET-derived mean position distance of 7.3 nm deviates significantly from the localization-based estimate of 5.2 nm and exceeds the expected distance for dyes that are placed two helices apart of ~4.8 nm. FRET measurements are additionally sensitive to the orientation of the transition dipole moments of the donor and acceptor fluorophores, expressed in the orientation factor κ^2 that enters the calculation of the Förster radius[19,49]. In the case of fast and free rotation of the fluorophores, an average value of $\langle\kappa^2\rangle$=2/3 is usually assumed[49]. Hübner et al. showed that the dye Atto647N, when linked to DNA origami structure, tends to position itself between two DNA helices, which restricts the diffusion and rotation of fluorophore[50,51]. Therefore, we use the available fluorescence anisotropy information to check the validity of this assumption for our sample. Indeed, confocal single-molecule control measurements show that the fluorescence lifetime and anisotropy of the positively charged Atto647N on the origami are significantly shifted to higher values as compared to the dsDNA, while the properties of the donor dye are unchanged (Fig. 3c and Supplementary Fig. 14, Supplementary Tab. 11). The restriction of the rotation induces an uncertainty of ~0.5 nm on the Förster radius (Supplementary Note 4), which is insufficient to explain the discrepancy. In addition, the interaction with the origami surface potentially displaces the acceptor dye with respect to the mean position within the AV (Fig. 2c). As our localization-based distance estimate of the interhelical distance is however in good agreement with previous reports, the displacement must occur predominantly in the axial (z) direction. Indeed, the rotational correlation times ρ determined from the fluorescence anisotropy indicate that the donor dye is mobile (ρ = 0.7 ns) while the acceptor dye is trapped (ρ = 10 ns, Supplementary Fig. 14a). Hence, a likely explanation for the larger FRET-derived distance is that the acceptor dye is trapped between two helices, moving it away from the donor dye, while the donor dye is pointing upwards away from the origami surface and remains mobile. Based on this model (Supplementary Note 4), we estimate a z-displacement between the dyes of 5.0 ± 1.2 nm, which is consistent with the combined length of the dye linkers, the additional unpaired nucleotide, and the thickness of the origami platform (Supplementary Note 4, Supplementary Figs. 7e and 15).

These results show that FRET-nanoscopy is not only capable of resolving different FRET species within a diffraction-limited spot, but also provides accurate FRET distances. Notably, the combined information of FRET and the localization distances together with Pythagoras's theorem (Fig. 1b) allows us to assess the 3D orientation of the interdye distance vector.

Accurate FRET measurements of dsDNA rulers. To test the accuracy of the FRET analysis under STED conditions, we performed measurements on short double-stranded DNA rulers (dsD) labeled with the dyes Alexa594 and Atto647N at distances from 7 to 15 nm. We verified that both dyes are freely moving in all dsD constructs to exclude a significant influence of specific dye orientations and positions on the FRET-based interdye distances (Supplementary Fig. 14b). The orientation of the interdye distance vector can be controlled by immobilizing the DNA rulers using biotin-neutravidin binding either with a single biotin (sb) at one end or doubly (db) with a biotin at each end (Fig. 4a). To control for surface effects, we performed the experiments using two surface preparation methods based on bovine serum albumin (BSA) or polyethylene glycol (PEG, see methods). A typical confocal overview image and zoomed STED images are shown in Figure 1c for an interdye distance of 15 nm (dsD(NF)) and double-biotin immobilization using BSA. Measuring the dsD constructs with increasing interdye distances on BSA (Fig. 4b) and PEG (Supplementary Fig. 19) surfaces, the recovered values of the two FRET indicators E and $\langle\tau_{D(A)}\rangle_F$ in the two-dimensional histograms follow the static FRET-line for decreasing FRET efficiency and increasing donor fluorescence lifetime. The experimental average FRET efficiencies of the populations match well with the predicted values based on AV simulations (black and red dashed lines, respectively, in Fig. 4b, Supplementary Tab. 13). To resolve the FRET rate directly and consider also photobleached dye species, we performed sub-ensemble TCSPC analysis using a distance distribution model function (Fig. 4c and Supplementary Fig. 21).

As the intensity-based and lifetime-based estimates of the interdye distance correspond to different averages over the accessible volume of the fluorophores, we convert both distance measures into a physical distance between mean dye positions $R_{\mathrm{mp}}^{\mathrm{FRET}}$ (Fig. 4d, Supplementary Fig. 5 and Supplementary Tab. 8)[20]. Within error, both methods agree well with the structural predictions based on a B-DNA structure. Notably, we obtained consistent results between single and double biotin samples and for the different surfaces, illustrating that FRET indeed measures the interdye distance independent of the orientation of the molecule.

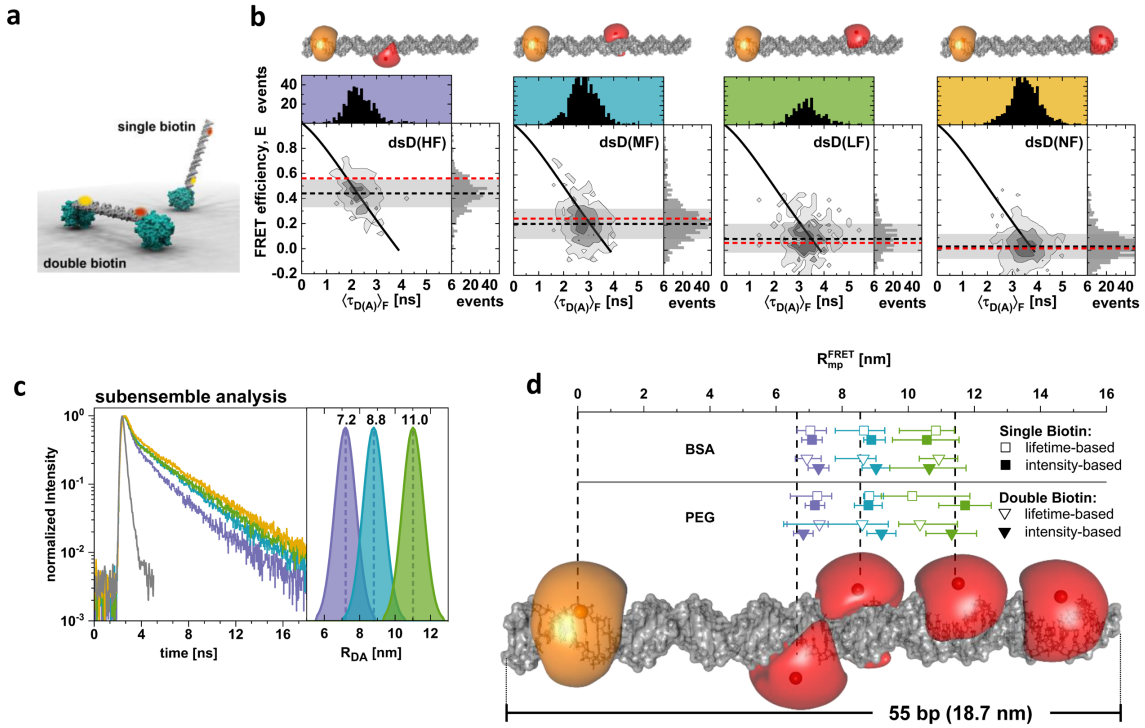

Figure 4: Accurate FRET analysis under STED conditions using DNA rulers. a) Cartoons of the double-stranded DNA rulers (dsD, 55 bp) labeled with Alexa594 and Atto647N on the functionalized glass surface. The DNA rulers are immobilized on one side (single biotin) or both sides (double biotin) by binding to immobilized avidin (turquoise, PDB-ID: 2AVI). The fluorophore positions are highlighted in orange and red. (details see Supplementary Tab. 1) **b)** Two-dimensional histograms of the FRET-efficiency, *E*, and fluorescence-weighted average donor fluorescence lifetime $\langle\tau_{D(A)}\rangle_F$ for the dsD(HF), dsD(MF), dsD(LF) and dsD(NF) DNA rulers using biotinylated BSA for immobilization. Measured mean FRET efficiencies are indicated by dashed black lines and predictions based on AV calculations by dashed red lines. The intensity-based FRET efficiency, *E*, was corrected for STED conditions (see Supplementary Section 'Accurate intensity-based FRET efficiencies under STED conditions'), placing it on the static FRET-line (black line, see eq. 10 in the methods and Supplementary Table 19). The selection of ROIs for sub-ensemble fluorescence decays of the donor in **c** is displayed as grey shaded area. Structural models for the different DNA rulers, indicating the accessible volumes (AV) of the fluorophores, are shown above. **c)** Sub-ensemble fluorescence decays of selected ROIs are shown in the colors corresponding to **b**. Decays were fitted to Gaussian distributed distances model with fixed width of σ_{DA} = 0.6 nm (eq. 6-7). The depletion part of the decay was described by a short lifetime component, as described in the Supplementary Section 'Sub-ensemble fluorescence decay analysis'. Each sample was measured on a single day. An extended overview of sample statistics and selection criteria is given in Supplementary Tab. 15. **d)** Comparison of intensity-based (filled symbol) and lifetime-based (open symbol) experimentally FRET-based distances between the mean dye positions, R_{mp}^{FRET} for immobilization under distinct conditions: (i) a single (square) and two (triangle) biotins, and (ii) BSA-layer (top), PEG-layer (bottom). Measured values are very close to the structural mean distances expected from AV simulations (vertical dashed lines). For **d**, the measured FRET-averaged distance, $\langle R_{DA}\rangle_E$ (from the intensities), and mean interdye distance,

$\langle R_{DA} \rangle$ (from the lifetime), are converted into the mean-position distance R_{mp}^{FRET} as described in Kalinin et al.[18] (see Methods, Supplementary Tab. 8 and Supplementary Fig. 5).

Colocalization analysis resolves surface heterogeneities. Next, we assessed whether distinct immobilization of the single- and double-biotin dsD samples result in characteristic features for localization distances d_{loc} between donor and acceptor positions that could be resolved by cSTED. The obtained probability densities of d_{loc} for the BSA surface in Fig. 5a (see Supplementary Fig. 18 for the PEG surface) clearly show that larger distances are observed for the double-biotin immobilization. Theoretically, the distribution of colocalization distances between two fixed emitters follows a χ-distribution whose width depends on the localization precision (see Supplementary Section 'Model-based analysis of localization-based distance distributions', eq. S30)[16,33]. However, all measured distance distributions showed excess broadening as they could not be described by a single component, which suggests a heterogeneous distribution of inclination angles (Supplementary Note 7 and Supplementary Tab. 12). To exclude that this heterogeneity is dynamic (e.g., caused by temporary sticking to the surface), we performed repeated localizations of the same molecule throughout the measurement. No large jumps were observed, and the standard deviation of the localization agreed with the localization precision (Supplementary Note 5 and Supplementary Fig. 22). This indicates a static heterogeneity wherein the DNA molecules experience distinct environments on the surface.

To describe the experimental d_{loc} distributions, we employed the maximum entropy method (MEM) that allows us to infer the distribution of the distance between the mean positions of the dyes based on the χ-distribution model function (Supplementary Note 6)[52]. The recovered distributions confirm the shift to larger distances for the double biotin samples (Fig. 5b). Interestingly, the analysis also reveals a visible peak for the single biotin low (dsD(LF)) and no FRET samples (dsD(NF)) at approximately half of the maximum R_{mp}^{loc} distance, implying that DNA is not randomly oriented on the surface. Similarly, the double-biotin sample does not lie flat on the surface as the peak distances are shorter than expected from AV simulations (dashed lines in Fig. 5b). The presence of a second peak at shorter distance for the double-biotin dsD(NF) sample is assigned to a residual population of single-bound molecules, which is also observed for the data measured on the PEG surface (Supplementary Fig. 18). The obtained fractions of doubly bound dsD correspond well to an estimate of 40 ± 10% based on the density of neutravidin molecules on the surface (Supplementary Note 8 and Supplementary Fig. 24). The consistent results for BSA and PEG surfaces (Supplementary Fig. 18), illustrate the reproducibility of the cSTED approach. Moreover, they suggest that the observed features are due to surface roughness associated with the biotin-neutravidin immobilization rather than specific interactions.

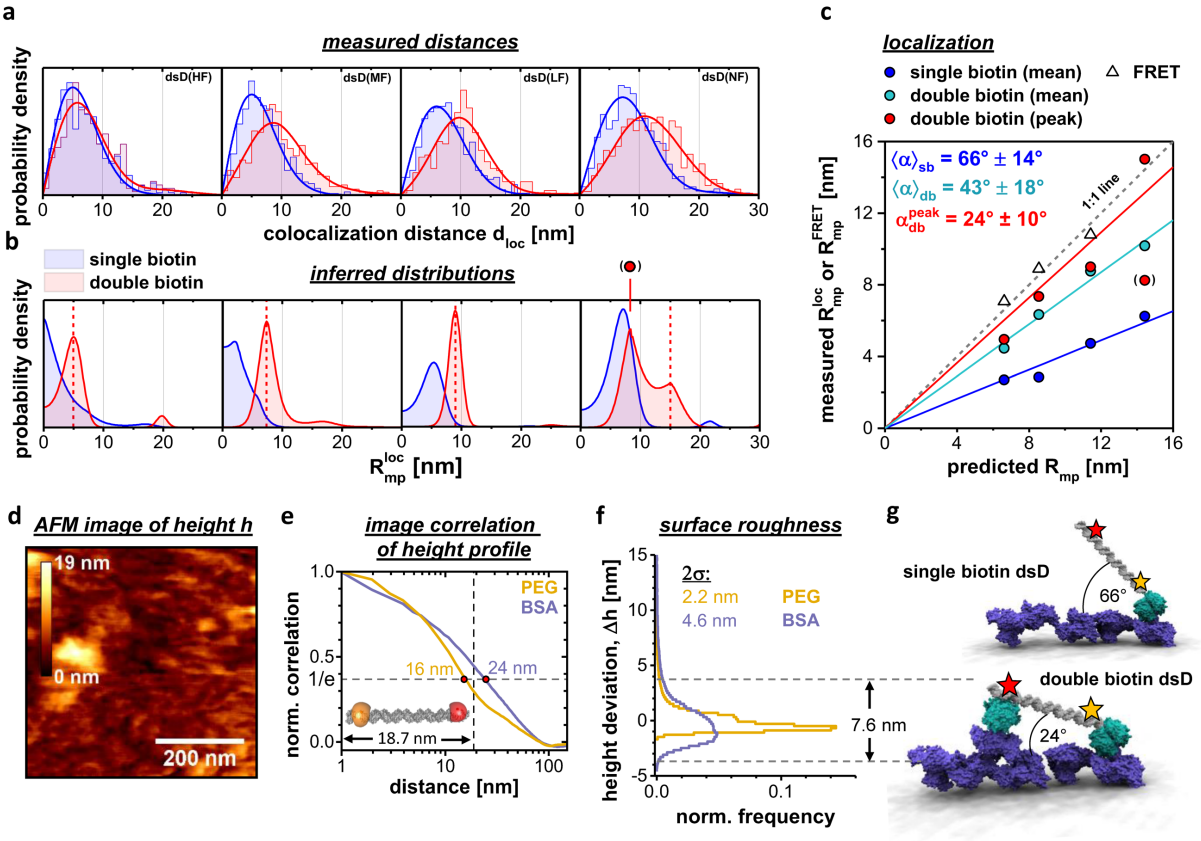

Figure 5: Colocalization analysis of DNA rulers. a) Distributions of the measured donor-acceptor distances from localization analysis for the single-biotin (blue) and double-biotin (red) samples (from left to right: dsD(HF), dsD(MF), dsD(LF), dsD(NF) on the BSA surface (see Supplementary Fig. 18 for the PEG surface). See Supplementary Tab. 15 for complete sample statistics. Fitted distributions based on maximum entropy analysis in **b** are shown as solid lines. Each dataset was obtained in a single experiment. **b)** We used MEM to infer the distribution of the center distance $R_{\mathrm{mp}}^{\mathrm{loc}}$ using a superposition of χ-distributions with fixed width $\sigma_\chi = 4.4$ nm to describe the measured distance distributions in **a**. The expected distances between the mean positions of the fluorophores based on the AV model are shown as red dashed lines. **c)** Distance-distance plots of the measured mean or peak (maximum) values (red dashed lines in b) of the inferred distance distributions against the predicted distances. Solid lines are linear fits to the data according to eq. S51 (Supplementary Note 9). The slopes of the fits define the inclination angle α which is calculated based on the mean, $\langle\alpha\rangle$, and width of the distance distribution, σ, or the peak value of the double-biotin population, $\alpha_{\mathrm{db}}^{\mathrm{peak}}$. For the FRET distances, the four estimates obtained for each sample (intensity- and lifetime-based, for single biotin and double biotin) were converted to R_{mp} and the average is reported (all four individual values were in overall agreement, see Supplementary Tab. 9 and 10). For the mean angles, the error is obtained by error propagation of the width of the obtained distance distribution (see Supplementary Note 9). The red circle (in brackets) indicates the second maximum of the dsD(NF) sample originating from DNA bound only with one biotin. **d)** AFM height images of BSA-neutravidin coated surfaces reveal an increased roughness at a molecular scale. The data was recorded using the QI mode and denoised using a

10-pixel median filter. The images for all conditions are shown in Supplementary Fig. 23. **e)** Normalized correlation curves of the height images were computed to provide estimates for the size of the elevated objects (see Supplementary Note 8). The observed characteristic decay constants are close to the size of our AFM tip of ~15 nm and the size of the DNA ruler. **f)** Normalized histograms of the roughness in the AFM height images for BSA (violet) and PEG (yellow) functionalized cover slides after addition of neutravidin. The roughness was computed by subtracting the average of the measured heights from the individual values. We characterized the histograms by the standard deviation 2σ (root-mean-square roughness). For comparison we depict the expected height difference between the ends of the double-immobilized DNA based on the inclination angle of $\alpha \approx 24°$ determined in **c**. **g)** Potential molecular cartoons for the orientation of DNA rulers on the molecular surface, where BSA and neutravidin are shown in purple and turquoise, respectively. DNA immobilized by a single anchor resulted a preferential orientation at an angle of ~60-70°. Immobilizing the dsDNA on both ends, a horizontal DNA orientation is expected, but height variations due to surface heterogeneities result in angles of up to ~24° between the attachment points.

Next, we applied our Optical Pythagoras procedure by studying the correlation between the mean distances of the inferred distribution for the single-biotin and double-biotin samples and the expected distance (Fig. 5c). While $R_{\mathrm{mp}}^{\mathrm{FRET}}$ follows the expected 1:1 line (open triangles in Fig. 5c), colocalization-based $R_{\mathrm{mp}}^{\mathrm{loc}}$ have slopes < 1, as expected for similar distributions of the inclination angle α for the different DNA rulers. From the slopes of the regression lines, we estimate an average inclination angle of 66° ± 14° for the single-biotin sample and 43° ± 18° for the double-biotin sample on the BSA surface, and 58° ± 19° and 44° ± 24° for the PEG surface (Supplementary Note 9). To describe the contribution of completely immobilized molecules in the double-biotin sample, we additionally determined the peak distances belonging to the double-bound fraction, yielding a small inclination angle of 24° ± 10° for the BSA surface and 20° ± 4° for the PEG surface. The corresponding height difference between the ends of the DNA of ~5-7 nm is similar to the molecular dimensions of BSA and neutravidin, indicating that the double-biotin DNA does not assume a perfectly horizontal orientation due to the roughness of the surface on the molecular scale. To test this hypothesis, we performed atomic force microscopy (AFM) of the functionalized surfaces (Fig. 5d and Supplementary Fig. 23) that revealed a heterogeneous height profile on a spatial scale of ~20 nm (Fig. 5e) with a root-mean-square roughness of 2-5 nm (Fig. 5f). It should be noted that most features on the molecular scale are smoothed over because they are smaller than the width of the AFM tip (~15 nm, see Supplementary Fig. 23e). Remarkably, the addition of neutravidin to the slide significantly increased the roughness and hardness of the surface (Supplementary Fig. 23).

Overall, the data obtained by AFM and FRET nanoscopy give a consistent view that the functionalized surfaces are rough on the scale of the DNA rulers. Moreover, FRET nanoscopy provides further detailed insights into the potential interactions of DNA with functionalized surfaces (Fig. 5g). For double-biotin DNA, we did not observe a fully flat configuration. The small angle of ~24° could be explained by the roughness on a molecular scale causing a height difference between the two attachment points (Fig. 5g). For the single-biotin DNA, the absence of a double-biotin like population indicates that there is no sticking of the unbound end. However, instead of assuming a standing-up conformation, the single-biotin DNA showed a preferred orientation of ~60-70° that remained constant over the acquisition time (Fig. 5g). A similar angle of 43 ± 1° was previously found for double-stranded DNA rulers anchored to a lipid membrane using cholesterol, which was attributed to steric hindrance at the attachment point preventing the ruler from lying down[25]. Similarly, we propose that the preferred orientation of the single-biotin DNA might originate from a preferential orientation of neutravidin on the surface that is propagated to the orientation of the single-biotin DNA via steric constraint at the biotin binding site.

FRET nanoscopy resolves the conformation hGBP1 in complex assemblies. Lastly, we applied FRET nanoscopy to study the conformational transitions of proteins upon oligomerization. A highly relevant system in the challenging research area of protein oligomers and assemblies is the human guanylate-binding protein 1 (hGBP1) that plays a major role in innate immunity[53,54] and belongs to the dynamin superfamily of large GTPases, with a molecular weight of ~67 kDa. In the monomer state of hGBP1, its three domains assume a compact formation of ~12 nm in length (Fig. 6a). Upon addition of the GTP analogue GDP-AlF_x, farnesylated hGBP1 polymerizes into fiber rings with disc-like assemblies of hGBP1 for which Shydlovskyi *et al.*[55] proposed that hGBP1 adopts an extended conformation. To image these assemblies, we randomly labeled hGBP1-wt on the native lysines and cysteines with reactive Alexa594 and Atto647N dyes, respectively (see Supplementary Section ‘hGBP1 expression and labeling’). After mixing the randomly labeled hGBP1-wt with unlabeled protein in a ratio of 1:10 and triggering oligomerization, we observed symmetric ring-like structures (Fig. 6b). To further improve the STED resolution, we applied a deconvolution algorithm (Supplementary Fig. 28 and Supplementary Section ‘Assessment of hGBP1 fiber diameter’). From the deconvolved images, we estimated a fiber diameter of 73 ± 4 nm, in agreement with previous reports (Fig. 6c)[55].

To gain insight into the structure of the assemblies and the conformation of hGBP1 in its oligomeric state, we site-specifically labeled hGBP1 on opposite ends of the protein at residues 18 and 577 (Fig. 6a). We reduced the fraction of labeled hGBP1 to 1:200 to localize single molecules in the images (Fig. 6b) and applied our FRET nanoscopy workflow. In contrast to the high FRET

efficiency observed for the monomer from free-diffusion single-molecule FRET experiments, we obtained a FRET efficiency close to zero for hGBP1 oligomers in agreement with an extended conformation of hGBP1 (Fig. 6d). As the interdye distance in the extended state is outside the FRET range, we can specify a lower boundary of ~12 nm and an upper boundary set by the dimensions of the extended protein of ~30 nm. To resolve the interdye distance in this range more accurately, we applied our established cSTED approach. As the colocalization measures the projected distance d_{loc}, it is necessary to consider the 3D orientation of the protein in the disc-like assemblies (Fig. 6e). By assuming a uniform distribution of the inclination angle α, the distribution of the projected mean-position distance $R_{\mathrm{mp}}^{\mathrm{loc}}$ is described by $P\left(R_{\mathrm{mp}}^{\mathrm{loc}}\right) = \frac{2}{\pi}\left(1 - \left(\frac{R_{\mathrm{mp}}^{\mathrm{loc}}}{R_{\mathrm{disc}}}\right)^2\right)^{-\frac{1}{2}}$, where R_{disc} is the disc radius (Fig. 6f and Supplementary Note 10). The experimentally observed localization distance d_{loc} is given by a non-central χ-distribution distribution of $R_{\mathrm{mp}}^{\mathrm{loc}}$ that is broadened due to the localization uncertainty defined by σ_{χ} (Supplementary eq. 30, Fig. 6g). The experimental distance distributions are well described by this model (Fig. 6h), yielding R_{disc} = 28 nm (68% confidence interval: 16–29 nm, Fig. 6i) with σ_{χ} ~11 nm. These results clearly support the model that oligomerized hGBP1 adopts an extended conformation as suggested by the absence of FRET.

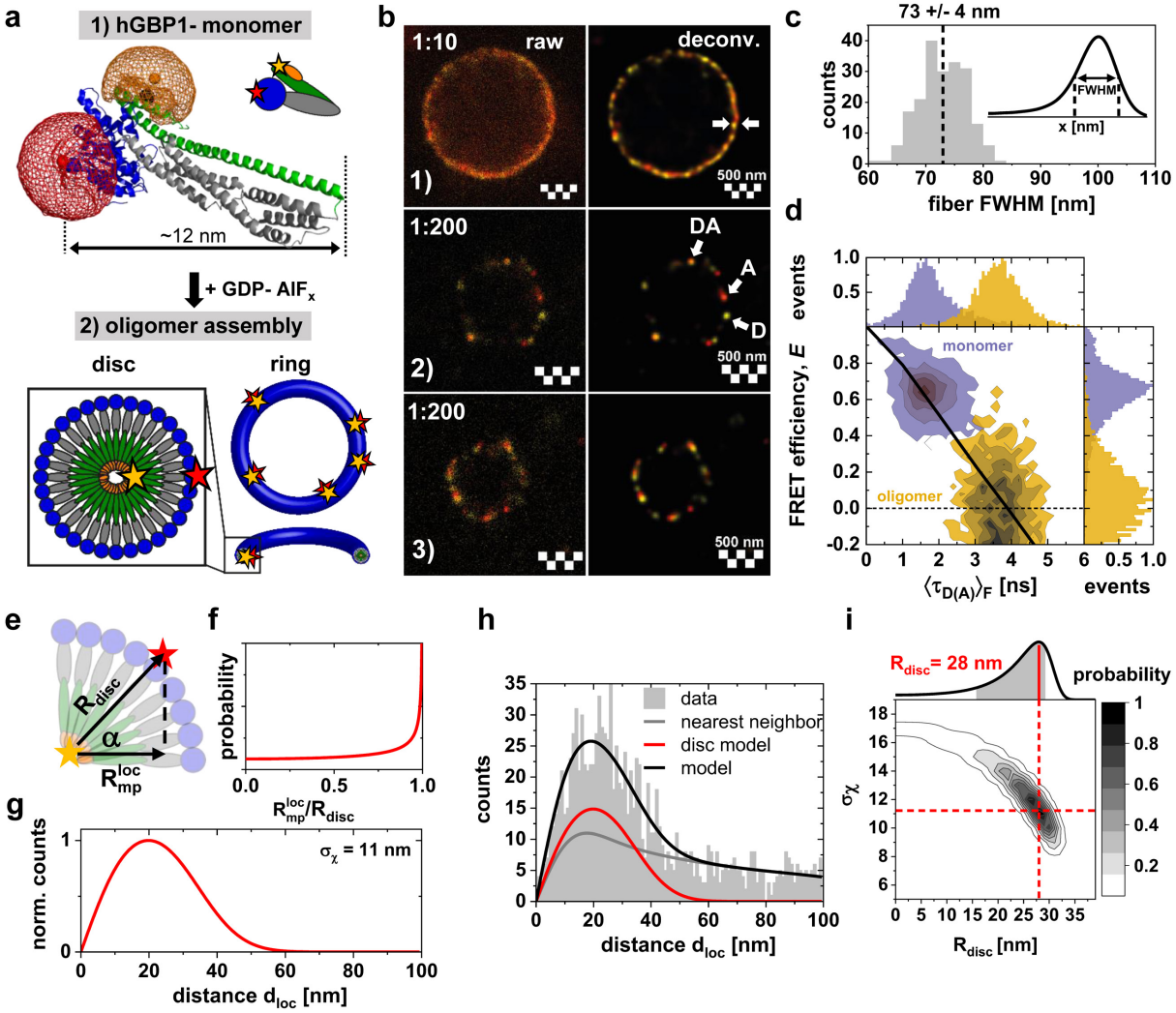

Figure 6: FRET nanoscopy reveals the conformation of hGBP1 in ring-like fibers. a) 1) The closed conformation of farnesylated hGBP1 in the apo state with fluorophores attached at residue 18 (Atto647N, red) and 577 (Alexa594, yellow) is displayed as cartoon of the crystal structure PDB-ID: 6K1Z[54]. The protein is divided into the large GTPase (LG) domain (blue), middle domain (MD, grey), helical GTPase effector domain (GED, green) and the farnesyl moiety (orange). 2) Upon activation with GDP-AlF$_x$, the protein polymerizes into ring-like fibers composed of discs of hGBP1 in an extended conformation[53,55]. **b)** STED measurements of hGBP1 polymers. Raw STED images are shown to the left and corresponding deconvolved STED images to the right. Single dyes are shown as yellow (Donor D, Alexa594) and red (Acceptor, A, Atto647N) spots. When both dyes colocalize they are shown as an orange spot (DA). 1) Measurement of 1:10 labeled to unlabeled hGBP1-wt. Wild type hGBP1 is randomly labelled with Atto647N on cysteines and Alexa594 on lysines to obtain a high labelling degree without mutation. 2-3) Measurements with 1:200 specifically labeled hGBP1 18-577 to unlabeled hGBP1-wt. Arrows indicate single donor-only (D), acceptor-only (A) and double-labeled (DA) molecules. Data recorded in a single experiment. **c)** Quantification of the fiber width of labeled hGBP1-wt. The full width at half maximum (FWHM) of the fibers was determined from line profile of the deconvolved images (see

pair of white arrows in B). Image data in b-c recorded using three independent experiments spread over 2 days. **d)** Two-dimensional frequency histograms of the FRET-efficiency, *E*, and fluorescence-weighted average donor fluorescence lifetime $\langle\tau_{D(A)}\rangle_F$ are shown for the hGBP1 18-577 monomer in purple (obtained from free-diffusion measurements, single experiment) and for GDP-AlF_x induced oligomers in yellow (obtained from FRET nanoscopy, six independent experiments). The static FRET-line is shown in black (see eq. 10 in the methods and Supplementary Table 19). **e)** Imaging in the xy-plane observes the mean-position distance R_{mp} of the projected disc radius R_{disc} for all angles α. **f)** The resulting probability distribution function of R_{mp} of the projected distance R_{disc} for the disc-like arrangement within the fibers. **g)** The distribution of the interdye distance d_{loc} experimentally observed by cSTED is related to R_{mp} (Supplementary Note 10, eq. S57), which is broadened by the localization uncertainty and sample heterogeneities (Supplementary Section 'Colocalization analysis', eq. S30). We display the disc model distribution of d_{loc} for a disc radius R_{disc} of 28 nm and a standard deviation of σ_χ of 11 nm. **h)** Experimental nearest-neighbor distances d_{loc} between donor and acceptor fluorophores in the fiber structures at 1:200 dilution (gray histogram). The overall model function (black) consists of the disc model shown in **g** and a baseline due to false-positive pairing in the nearest-neighbor algorithm due to randomly distributed donor- and acceptor-only molecules throughout the ring (gray line) (Supplementary Note 10, eq. S57). Data was collected from 10 independent experiments using freshly prepared samples spread over 6 days, yielding 1106 donor-acceptor distances < 100 nm. **i)** Parameter scan of the model R_{disc} and σ_χ fit parameters. The marginal probability density of the disc radius R_{disc} is shown at the top. The 68% confidence interval is indicated as grey shaded area.

Conclusions

In summary, we demonstrated that FRET nanoscopy provides seamless resolution from micrometers to the sub-nanometer range with a precision of < 7 Å. The combination of the colocalization and FRET derived distances provides 3D information by applying the Optical Pythagoras and the multiparametric fluorescence analysis, as demonstrated for the DNA origami and dsDNA samples. The achieved resolution is allows to resolve 3D orientation of single molecules in heterogeneous environments, such as functionalized surfaces or protein fibers.

While we obtained sufficient signal for single molecules to define the spectroscopic parameters and achieve a high localization precision of ~3 nm, the observation time for individual molecules is fundamentally limited by photobleaching. A promising approach that would allow the prolonged and repeated probing of a single molecule is the combination of DNA-PAINT with STED microscopy, utilizing the repeated hybridization of short labeled oligos to complementary sequences on the molecule of interest[56]. Notably and different to other SMLM techniques, our approach is fast (< 10 s imaging time) and instead relies on the consecutive imaging of many ROIs. Hence, it does not necessitate the fixation of the specimen and is potentially applicable to the study of transient assemblies in living cells. The high time resolution of the confocal time-

resolved detection[26,27] can further be utilized to resolve also fast molecular dynamics in a wide time range from nanoseconds to seconds by the workflow of multiparameter fluorescence imaging spectroscopy[28,57].

FRET nanoscopy is readily applicable to any biological system wherein molecules have a defined orientation. Further promising applications could be the study of the structural dynamics of membrane proteins, such as transmembrane receptors or transporters. We further envision that the combination of colocalization STED microscopy with particle alignment and averaging will provide novel insights into the nanoscale organization of higher-order, symmetric biological assemblies, such as the nuclear pore complex, centrosome, or chromatin fibers. FRET nanoscopy is ideally suited to determine the precise location of individual components within such systems, while simultaneously probing their conformation using the FRET information. Finally, we note that FRET nanoscopy can be implemented on any STED microscope with two color and time-resolved detection, which are available commercially and in microscope facilities around the world.

Methods

STED-FRET microscope

FRET-nanoscopy imaging was performed on a custom Abberior Instruments Expert Line system with polarization-sensitive readout and single-photon counting abilities. Briefly, linear polarized excitation lasers (561 nm and 635 nm, pulse width < 100 ps) and a circular polarized depletion laser (775 nm, pulse width 1.2 ns) are synchronized and overlaid using notch filters and focused by a 100x oil objective (Supplementary Figure 1). The fluorescence signal is separated by polarization and color and detected using avalanche photodiodes and single photon counting electronics. Alternating line excitation was used to sequentially excite the donor and acceptor fluorophores. More details are given in the Supplementary Section ‘Data acquisition – STED-FRET microscope’.

Sample preparation

Single-layer DNA origami nanostructures are based on published designs and were assembled as described in Schnitzbauer et al.[39,40]. Donor and acceptor fluorophores (Atto594, Atto647N) were attached to the 3’-end of the respective oligos with an additional thymine base pair as a spacer. All DNA strands are listed in Supplementary Table 2 and the origami design is illustrated in Supplementary Figure 7. DNA origami samples were immobilized on a PEG-biotin coated surface and measured in folding buffer containing 10 mM Tris, 1 mM EDTA, 12.5 mM $MgCl_2$ and

1 mM Trolox at pH 8.0. More details are given in the Supplementary Section ‘Sample preparation – DNA origami’.

For dsDNA rulers, the position of the donor dye (Alexa594) was kept fixed while the acceptor (Atto647N) position on the complementary strands was varied to achieve several interdye distances (Fig. 4b and d). For surface immobilization, the donor strands were labelled with a single biotin at the 5’ end (sb) or two biotins at the 3’ and 5’ ends (db). Samples were immobilized on either BSA-biotin or PEG-biotin surfaces and measured in PBS buffer containing 1 mM Trolox at pH 7.6. The DNA sequences are listed in Supplementary Table 1. More details are given in the Supplementary Section ‘Sample preparation – dsDNA’.

Wild-type hGBP1 was labeled with Alexa594 succinimidyl ester and Atto647N maleimide at the native lysines and cysteines, respectively. For site-specific labeling of hGBP1, first all native cysteine residues were mutated (i.e., C12A, C82A, C225S, C235A, C270A, C311S, C396A, C407S, C589S), as used before[58]. Reversal of the C-terminal C589S mutation allowed for site-specific farnesylation, and the residues N18 and Q577 were mutated to cysteines for fluorophore labeling. After farnesylation, hGBP1 was labeled with Alexa594 maleimide, purified by anion exchange chromatography and then labeled with Atto647N maleimide. Oligomerization was induced by the addition of 200 µM GDP in the presence of AlF_x in buffer containing 50 mM Tris-HCl, 150 mM NaCl, 5 mM $MgCl_2$, 300 µM $AlCl_3$ and 10 mM NaF at pH 7.9. Polymer structures were visible after 10-40 min after which they would remain stable for hours. The ratio of labelled Cys8 hGBP1-18-577 (or labelled hGBP1-wt) to unlabeled wild-type hGBP1 was adjusted depending on the desired labelling density in hGBP1 polymers. More information is given in the Supplementary Section ‘Sample preparation – hGBP1 expression and labeling’.

Image Spectroscopy.

Intensity-based spectroscopic parameters. Correction factors accounting for the spectral crosstalk of the donor fluorescence into the acceptor detection channel, the direct excitation of the acceptor by the donor excitation laser and the different detection efficiencies for the donor and acceptor were determined following the approach outlined in Lee et al.[37] and described in the Supplementary Section ‘Determination of intensity-based correction factors’. Quantum yields Φ_F of donor and acceptor were estimated from the fluorescence lifetime by comparison to a known reference. Correction of the detected signals was performed as described in the Supplementary Section ‘Intensity-based spectroscopic parameters’.

To estimate accurate intensity-based FRET efficiencies under STED conditions, we used the total intensity detected in the donor and acceptor channels without any time gating. The ungated signal contains contributions from both (partially) depleted and undepleted molecules, which exhibit different quantum yields. Donor and acceptor fluorophores are also generally depleted to a different extent. We assume the FRET efficiency of the depleted molecules to be zero due to the increased donor de-excitation rate through the depletion pulse. Under these assumptions, the accurate, distance-related FRET efficiency E is given by:

$$E = E' \cdot \left(1 + \frac{x_{\mathrm{D}}^{\mathrm{d}} \cdot \Phi_{\mathrm{F,D}}^{\mathrm{d}}}{x_{\mathrm{D}}^{0} \cdot \Phi_{\mathrm{F,D}}^{0}}\right), \tag{3}$$

where $x_{\mathrm{D}}^{\mathrm{d}}$ and x_{D}^{0} are the fractions of depleted and undepleted donor fluorophores and $\Phi_{\mathrm{F,D}}^{\mathrm{d}}$ and $\Phi_{\mathrm{F,D}}^{0}$ are the respective quantum yields. The modified FRET efficiency E' is related to the measured fluorescence signals as:

$$E' = \frac{F_{\mathrm{A|D}}}{\gamma' \cdot F_{\mathrm{D|D}} + F_{\mathrm{A|D}}}, \tag{4}$$

where $F_{\mathrm{D|D}}$ and $F_{\mathrm{A|D}}$ are the signals detected in the donor and acceptor channels after donor excitation and γ' is a factor that corrects for the relative detection yield if the donor and acceptor fluorophores and taking the fraction of undepleted molecules into account. See Supplementary Section ‘Accurate intensity-based FRET efficiencies under STED conditions’ for details and a general expression for non-zero FRET efficiency of the depleted species. The quantum yields and fractions under STED conditions are obtained from bi-exponential lifetime fits by assuming that the short lifetime component of ~200-400 ps originates from depleted fluorophores (see Supplementary Table 9). Error estimation was performed by propagating the uncertainty of all correction factors as described in Hellenkamp et al.[19]. The correction parameters of all measurements are compiled in Supplementary Table 3.

Sub-ensemble fluorescence decay analysis. To minimize polarization effects, the total fluorescence decay was approximated from the detected parallel and perpendicular signals (see Supplementary Section 'Sub-ensemble fluorescence decay analysis' eq. S15). We fit the fluorescence decay of the donor-only sample, $f_{\mathrm{D|D}}^{(\mathrm{D0})}(t)$, using a bi-exponential model to account for non-depleted and partially depleted molecules given by:

$$f_{\mathrm{D|D}}^{(\mathrm{D0})}(t) = x_{\mathrm{STED}}^{(\mathrm{D0})} \cdot e^{-t/\tau_{\mathrm{D0,STED}}} + \left(1 - x_{\mathrm{STED}}^{(\mathrm{D0})}\right) \cdot e^{-t/\tau_{\mathrm{D0}}}, \tag{5}$$

where t is the TCSPC delay time, $x_{\mathrm{STED}}^{(\mathrm{D0})}$ is the apparent fraction of undepleted donor fluorophores and τ_{D0} and $\tau_{\mathrm{D0,STED}}$ are the donor-only lifetimes of the undepleted and depleted donor fluorophore.

The FRET-induced donor fluorescence decay, $f_{\mathrm{D|D}}^{(\mathrm{DA})}(t)$, is described by a normal distribution of the interdye distance, R_{DA}, arising due to the flexible dye linkers[34], with the addition of a donor-only fraction to account for bleaching and photoblinking of the acceptor fluorophore:

$$f_{\mathrm{D|D}}^{(\mathrm{DA})}(t) = x_{\mathrm{STED}}^{(\mathrm{DA})} \cdot e^{-t/\tau_{\mathrm{D,STED}}} + \left(1 - x_{\mathrm{STED}}^{(\mathrm{DA})}\right) \cdot \left((1 - x_{\mathrm{D0}}) \cdot \int_0^\infty x_{\mathrm{FRET}}(R_{\mathrm{DA}}) \cdot e^{-\left(\tau_{\mathrm{D0}}^{-1} + k_{\mathrm{FRET}}(R_{\mathrm{DA}})\right)t} \mathrm{d}R_{\mathrm{DA}} + x_{\mathrm{D0}} \cdot e^{-t/\tau_{\mathrm{D0}}} \right), \quad (6)$$

where $x_{\mathrm{STED}}^{(\mathrm{DA})}$ and $\tau_{\mathrm{D,STED}}$ are the apparent fraction and lifetime of the depleted donor fluorophore in the presence of the acceptor, respectively. x_{D0} is the donor-only fraction and $x_{\mathrm{FRET}}(R_{\mathrm{DA}})$ is the fraction of molecules with interdye distance R_{DA}, corresponding to a FRET rate constant of $k_{\mathrm{FRET}}(R_{\mathrm{DA}}) = \frac{1}{\tau_{\mathrm{D(0)}}} \cdot \left(\frac{R_0}{R_{\mathrm{DA}}}\right)^6$. The distance distribution $x_{\mathrm{FRET}}(R_{\mathrm{DA}})$ is given by a normal distribution centered at the mean interdye distance $\langle R_{\mathrm{DA}} \rangle$ with width σ_{DA}:

$$x_{\mathrm{FRET}}(R_{\mathrm{DA}}) = \frac{1}{\sqrt{2\pi}\sigma_{\mathrm{DA}}} \cdot \exp\left(-\frac{(R_{\mathrm{DA}} - \langle R_{\mathrm{DA}} \rangle)^2}{2\sigma_{\mathrm{DA}}^2}\right). \quad (7)$$

Donor-only and FRET-sensitized decays are analyzed globally to improve the robustness of the fit. Error estimates are obtained from an analysis of the reduced χ^2 surface. For details, see Supplementary Sections ‘Sub-ensemble fluorescence decay analysis’ and ‘Error estimation of FRET-derived distances’.

Spot-integrated fluorescence lifetimes. To estimate accurate spot-integrated fluorescence lifetimes of the undepleted fluorophores, we fitted the tail of the spot-integrated fluorescence decay $f(t)$ to a single-exponential model according to:

$$f(t) = f_0 e^{-t/\tau} + bg, \quad (8)$$

where f_0 is the initial amplitude of the decay and bg is a constant background term. To accurately account for the polarized detection, a global fit of the parallel and perpendicular decays is performed that incorporates the depolarization of the fluorescence signal due to molecular rotation, polarization mixing by the objective and the polarization of the scattered background signal (Supplementary Section ‘Determination of spot-integrated fluorescence lifetimes’). The

optimization is performed using a maximum likelihood estimator that correctly accounts for the counting statistics by minimizing the $2I^*$ parameter defined by:[36]

$$2I^* = 2\sum_i n_i \ln\frac{n_i}{f_i}, \tag{9}$$

where n_i is the number of photons detected in TCSPC bin i and f_i is the average value of the model function in TCSPC bin i.

Linker-corrected relationship between the FRET efficiency and donor fluorescence lifetime. The static FRET-line as given in eq. 2 describes the ideal relation between the fluorescence-weighted average FRET efficiency E and the fluorescence-weighted fluorescence donor lifetime $\langle\tau_{\mathrm{D(A)}}\rangle_F$ in the absence of dynamics. Deviations from eq. 2 occur due to the flexibility of the dye linker, causing an apparent distance distribution width of 6 Å as determined from reference measurements of freely-diffusing DNA rulers[34]. Linker-corrected static FRET lines were approximated using fourth-order polynomials as described previously[34]:

$$E = 1 - \frac{\sum_{i=0}^{4} a_i \langle\tau_{\mathrm{D(A)}}\rangle_F^i}{\tau_{\mathrm{D(0)}}}, \tag{10}$$

where $\tau_{\mathrm{D(0)}}$ is the fluorescence lifetime of the donor in the absence of the acceptor and a_i are the polynomial coefficients. The polynomial coefficients used in this work are compiled in Supplementary Table 19.

Accessible volume (AV) simulations and distance conversion. The sterically accessible volumes (AVs) of the fluorophores were determined using the *FRET positioning and screening (FPS)* software[20]. From this the distance between the mean positions R_{mp}, the average distance $\langle R_{\mathrm{DA}}\rangle$, the average FRET efficiency $\langle E\rangle$ and the FRET-averaged distance $\langle R_{\mathrm{DA}}\rangle_E$, are obtained. See Supplementary Section 'Accessible volume simulations' for details and Supplementary Table 6 for the used parameters. Conversion of the measured distances $\langle R_{\mathrm{DA}}\rangle$ (from the lifetime information) and $\langle R_{\mathrm{DA}}\rangle_E$ (from the fluorescence intensities) into the FRET-based mean-position distance $R_{\mathrm{mp}}^{\mathrm{FRET}}$ was performed as described previously[20]. Briefly, AVs for the donor and acceptor fluorophores were calculated for dsDNA. By randomly orienting the AVs and calculating the parameters $R_{\mathrm{mp}}^{\mathrm{FRET}}$, $\langle R_{\mathrm{DA}}\rangle$ and $\langle R_{\mathrm{DA}}\rangle_E$, conversion functions based on a polynomial approximation are obtained (see Supplementary Table 8 and Supplementary Figure 5).

Image processing in FRET nanoscopy

Spot localization. The point spread function (PSF) of the STED microscope is modelled as a 2D Gaussian function. To account for multiple spots in origami and hGBP1 data, up to three 2D Gaussian functions were fitted. The model function where $G(x, y)$ at pixel (x, y) is given by:

$$G(x,y) = \sum_{i=1}^{3} A_i \cdot \exp\left[\frac{\left(x - x_{0,i}\right)^2 + \left(y - y_{0,i}\right)^2}{2\sigma_{\mathrm{PSF},i}^2}\right] + bg, \tag{11}$$

where A_i is the amplitude, $x_{0,i}$ and $y_{0,i}$ are the center coordinates and $\sigma_{\mathrm{PSF},i}$ is the width of spot i, and bg is a constant background term. To correctly account for the Poisson statistics of photon detection, spot localization is performed using a maximum likelihood estimator by maximizing the *2I** parameter given by:

$$2I^* = -2\sum_i n_i - G_i + n_i \ln\frac{G_i}{n_i}, \tag{12}$$

where n_i and G_i are the number of photons and the value of the model function in pixel i, respectively. To estimate the number of spots in a ROI, the fit with the lowest *2I** was chosen while adding a constant penalty for additional free parameters. See Supplementary Section 'Colocalization analysis of FRET pairs' for details. The theoretical localization precision was predicted based on the photon counting statistics as described in Mortensen et al.[59] (see Supplementary Section 'Colocalization analysis - Predicted localization precision').

Data filtering. Data filtering was performed based on imaging parameters (e.g., the spot width and the number of spots), as well as spectroscopic parameters (e.g., the donor fluorescence lifetime, FRET efficiency and stoichiometry). Origami data was filtered based on the number of spots detected in the donor and acceptor channels (spot stoichiometry) and a minimal number of photons per spot of 20 (see Supplementary Section 'Spectroscopic analysis - Filtering procedure for origamis' and Supplementary Table 14). dsDNA data was filtered by selecting spots with a width of less than 35 nm and am apparent stoichiometry, S_{app}, of 0.5 ± 0.1, defined by:

$$S_{\mathrm{app}} = \frac{I_{\mathrm{D|D}} + I_{\mathrm{A|D}}}{I_{\mathrm{D|D}} + I_{\mathrm{A|D}} + I_{\mathrm{A|A}}}, \tag{13}$$

where $I_{\mathrm{D|D}}$ and $I_{\mathrm{A|D}}$ are the detected signal in the donor and acceptor detection channels after donor excitation and $I_{\mathrm{A|A}}$ is the detected signal in the acceptor detection channel after acceptor excitation. For more details, see Supplementary Section 'Filtering procedure for DNA rulers' and Supplementary Table 15.

Alignment of DNA origami nanostructures. Particle averaging on origami sample was done in three steps. First, only fully labelled structures were selected using the spot stoichiometry. Second, each dye was characterized as being either D1, D2, A1 or A2 based on its position on the structure, as defined in Figure 2b. This is possible because all structures are bound to the surface with the same side due to the placement of the biotin anchors. Third, the Kabsch algorithm was used to align the structures with respect to a reference structure by translation and rotation by minimizing the root-mean-square displacement (RMSD):[41]

$$RMSD = \sqrt{\frac{1}{4}\sum_{j\in\{\mathrm{D1,D2,A1,A2}\}} \left(x_j - x_{\mathrm{ref},j}\right)^2 + \left(y_j - y_{\mathrm{ref},j}\right)^2}, \tag{14}$$

where x_j and y_j are the x- and y-coordinates of fluorophore j and the subscript 'ref' refers to the reference structure. A model-free reference structure was obtained by selecting the structure from the experimental dataset, which provided the lowest RMSD over all structures. Outliers in the RMSD score were removed as shown in Supplementary Figure S9. A complete description of the alignment procedure is given in the Supplementary Section 'Colocalization analysis - Alignment and particle averaging for origami measurements'.

Colocalization analysis. The uncertainty of the localization estimation is described by a normal distribution whose width is determined by the localization precision. The resulting distribution of the localization-based interdye distances d_{loc}, however, is not normally distributed but assumes an asymmetric form in the case that the interdye distance $R_{\mathrm{mp}}^{\mathrm{loc}}$ is comparable to the localization precision, which is the case in the cSTED analysis. It is given by a noncentral χ-distribution P_χ with two degrees of freedom, as has been described previously:[16,33]

$$P_\chi\left(d_{\mathrm{loc}}|R_{\mathrm{mp}}^{\mathrm{loc}},\sigma_\chi\right) = \left(\frac{d_{\mathrm{loc}}}{\sigma_\chi^2}\right)\cdot \exp\left(-\frac{d_{\mathrm{loc}}^2 + {R_{\mathrm{mp}}^{\mathrm{loc}}}^2}{2\sigma_\chi^2}\right)\cdot I_0\left(\frac{d_{\mathrm{loc}}R_{\mathrm{mp}}^{\mathrm{loc}}}{\sigma_\chi^2}\right), \tag{15}$$

where d_{loc} is the measured colocalization distance, $R_{\mathrm{mp}}^{\mathrm{loc}}$ is the mean-position distance, σ_χ is a width parameter and $I_0(x)$ is the modified Bessel function of zero-th order (for details, see Supplementary Section 'Model-based analysis of localization-based distance distributions' and Supplementary Note 7). The width parameter of the distribution, σ_χ, depends on the localization precisions for the donor and acceptor fluorophores ($\sigma_{\mathrm{loc,D}}$ and $\sigma_{\mathrm{loc,A}}$) and additional registration error (σ_{reg}):

$$\sigma_\chi = \sqrt{\sigma_{\mathrm{loc,D}}^2 + \sigma_{\mathrm{loc,A}}^2 + \sigma_{\mathrm{reg}}^2}. \tag{16}$$

Here, we estimate a typical width of $\sigma_\chi = 4.4$ nm based on the defined distribution of the acceptor-acceptor distance obtained for the DNA origami nanostructures (Supplementary Figure 10), which was fixed for the analysis of the distance distributions for the dsDNA rulers.

The maximum entropy method (MEM) is an approach to extract the most unbiased distribution of a given parameter that provides a satisfactory fit to the experimental data[60-62]. Instead of minimizing the reduced chi-square, χ_r^2, the following functional is maximized:

$$\Theta = vS - \chi_r^2 \tag{17}$$

where v is a constant scaling factor and S is the entropy functional of the parameter distribution. Without prior knowledge, the entropy *S* of a discrete probability distribution p_i is defined by:

$$S = -\sum_i p_i \log p_\mathrm{i}\,, \tag{18}$$

We subject the MEM analysis to the mean-position distance $R_\mathrm{mp}^\mathrm{loc}$ to extract the distribution $p\left(R_{mp}^{\mathrm{loc},(i)}\right)$. The experimental distribution of colocalization distances $H(d_\mathrm{loc})$ is described as superposition of non-central -distributions P_χ as defined in eq. 15 by:

$$H(d_\mathrm{loc}) = \sum_i p\left(R_\mathrm{mp}^{\mathrm{loc},(i)}\right)\, P_\chi\left(d_\mathrm{loc}\middle|R_\mathrm{mp}^{\mathrm{loc},(i)}, \sigma_\chi\right), \tag{19}$$

where the set of kernel functions $\left\{P_\chi\left(d_\mathrm{loc}\middle|R_\mathrm{mp}^{\mathrm{loc},(i)}, \sigma_\chi\right),\ i = 1 \ldots N\right\}$ is defined over a range of mean-position distance $R_\mathrm{mp}^\mathrm{loc}$ from 0 to 30 nm. The reduced chi-squared χ_r^2 is defined as:

$$\chi_r^2 = \frac{1}{K}\sum_k \frac{1}{w_k^2}\left(H\left(d_\mathrm{loc}^{(k)}\right) - M\left(d_\mathrm{loc}^{(k)}\right)\right)^2, \tag{20}$$

where M is the measured histogram, K is the number of bins on the histogram and w_k are the weights of data points given by $w_k = \sqrt{M\left(d_\mathrm{loc}^{(k)}\right)}$ for Poissonian counting statistics. Maximization of Θ is performed as described by Vinogradov and Wilson[52]. See Supplementary Note 6 for details.

Processing of STED images

hGBP1 images were deconvolved and analyzed in the Huygens software (Scientific Volume Imaging) using the CMLE algorithm with a signal to noise ratio of 10 and 40 iterations (see Supplementary Section 'Assessment of hGBP1 fiber diameter' and Supplementary Fig. 28).

TEM imaging of DNA origami nanostructures

Origami samples for transmission electron microscopy were negatively staining using uranyl acetate and imaged using a JEM-2100PLUS instrument (JEOL) at 80 kV acceleration voltage (see Supplementary Section 'Transmission electron microscopy' and Supplementary Fig. 8).

AFM imaging of functionalized surfaces

AFM images were recorded using a soft cantilever (k = 0.04 N/m) in the QI mode on a NanoWizard 4 instrument (JPK Instruments). See Supplementary Section 'Atomic force microscopy' for details.

Confocal single-molecule FRET measurements of freely diffusion molecules

Confocal single-molecule FRET measurements were performed on a two-color multiparameter fluorescence detection setup with pulsed-interleaved excitation as described previously[63]. See Supplementary Section 'Confocal single-molecule measurements' for details.

Data availability

The dataset for the O(HF+NF) sample is available on GitHub in an analyzed form for demonstration purposes. Further datasets of raw (Picoquant TTTR format) and processed data as well as the analysis are available from the corresponding authors on reasonable request.

Code availability

DNA origami and hGBP1 data was analyzed using the Python-based *Seidel* software, publicly available on https://github.com/Fluorescence-Tools/Seidel. cSTED analysis of dsDNA as well as single-molecule analyses were performed in the *MFIS_2021* software suite consisting of the programs *AnI-3SF*, *Margarita* and *Kristine*, available at https://www.mpc.hhu.de/en/software/mfis-2021. MEM analysis of dsDNA in Fig. 5 was performed using the *MEM toolbox*, available at https://github.com/AndersBarth/MEMtoolbox. Sub-ensemble TCSPC analyses were performed using the program *ChiSurf*, freely available on https://github.com/Fluorescence-Tools/chisurf. The workflow for FRET nanoscopy combines these software packages as shown in Supplementary Figure 6 and described in detail in Supplementary Section '*Spectroscopy and image analysis'.*

Acknowledgements

This work was funded in part by the German Research Foundation (DFG) within the Collaborative Research Center SFB 1208 “Identity and Dynamics of Membrane Systems - From Molecules to Cellular Functions” (T.P. A08 to C.S.) and by the European Research Council through the Advanced Grant 2014 hybridFRET (number 671208) to C.S. We acknowledge the DFG and the state NRW for establishing two microscopes within program Major Research Instrumentation as per Art. 91b GG that were essential for this study: (i) the FRET nanoscope with the funding ID (INST 208/741-1 FUGG) to C.S., and (ii) the cryo-TEM with the funding ID (INST 208/749-1 FUGG) to M.Ka. J.B. and J.F. acknowledge the support of the International Helmholtz Research School of Biophysics and Soft Matter (IHRS BioSoft). We thank Oleg Opanasyuk for help with theoretical modeling of distance distributions, and Laura Vogel and Michelle Rademacher for performing the sample preparation for AFM imaging. We thank Costanza Girardi (Dipartimento di Fisica "G.Occhialini”, Università di Milano Bicocca, Italy) for helping to test and establish measurement conditions and analysis procedures for dsDNA rulers with our STED nanoscope during her research stay for her master thesis funded within the Erasmus program. The DNA strands for the core DNA origami structure were a generous gift by Don C. Lamb, LMU Munich, Germany.

Author contributions

C.S., A.B. and C.H. designed research. C.S., R.K., S.F. and A.S. designed the multiparameter STED microscope. M.Kö. and A.S. realized the hardware and software and assisted in operation of multiparameter STED microscope. J.B., N.V. R.K. and S.F established the operation and measurement procedures for the STED nanoscope. N.V. performed and analyzed measurements of DNA origami nanostructures. A.B. designed and assembled the DNA origami nanostructures. J.B. and C.G. performed and analyzed experiments on DNA rulers. P.L. and J.B. performed and analyzed experiments on hGBP1. A.B., N.V. and J.B. contributed analytical tools and oversaw data analysis of experiments on DNA rulers and hGBP1. S.F. and N.V. developed software for molecule identification and localization. J.F. performed single-molecule FRET control experiments of DNA origami nanostructures and hGBP1. M.O. and M.Ka. performed TEM imaging of DNA origami nanostructures and analyzed TEM images. J.S. and M.Ka. performed AFM experiments of functionalized surfaces and analyzed AFM images. A.B., C.S., N.V. and J.B. discussed and prepared figures. A.B. wrote the initial draft of the manuscript with extensive input from N.V. and J.B. C.S. defined and expanded the initial draft, contributed extensively to the writing and revising

of the manuscript. All authors contributed to and approved the final version of the manuscript. C.S. initiated, supervised and coordinated the project.

Competing interests

Markus Köhler and Andreas Schönle, two of the authors are employees of Abberior Instruments GmbH (Hans-Adolf-Krebs-Weg 1, 37077 Göttingen, Germany) selling super-resolution microscopes. The FRET nanoscope used in this work and requested by Claus Seidel is a unique prototype research instrument developed by them for this project.

References

1. Hell, S. W. Far-field optical nanoscopy. *Science* **316**, 1153-1158 (2007).
2. Moerner, W. E. Microscopy beyond the diffraction limit using actively controlled single molecules. *J Microsc* **246**, 213-220 (2012).
3. Hell, S. W. & Wichmann, J. Breaking the diffraction resolution limit by stimulated emission: stimulated-emission-depletion fluorescence microscopy. *Opt Lett* **19**, 780-782 (1994).
4. Betzig, E. *et al.* Imaging intracellular fluorescent proteins at nanometer resolution. *Science* **313**, 1642-1645 (2006).
5. Rust, M. J., Bates, M. & Zhuang, X. Sub-diffraction-limit imaging by stochastic optical reconstruction microscopy (STORM). *Nat Methods* **3**, 793-795 (2006).
6. Hess, S. T., Girirajan, T. P. & Mason, M. D. Ultra-high resolution imaging by fluorescence photoactivation localization microscopy. *Biophys J* **91**, 4258-4272 (2006).
7. Heilemann, M. *et al.* Subdiffraction-resolution fluorescence imaging with conventional fluorescent probes. *Angew Chem Int Ed Engl* **47**, 6172-6176 (2008).
8. Sharonov, A. & Hochstrasser, R. M. Wide-field subdiffraction imaging by accumulated binding of diffusing probes. *Proc Natl Acad Sci U S A* **103**, 18911-18916 (2006).
9. Jungmann, R. *et al.* Single-molecule kinetics and super-resolution microscopy by fluorescence imaging of transient binding on DNA origami. *Nano Lett* **10**, 4756-4761 (2010).
10. Weisenburger, S. *et al.* Cryogenic optical localization provides 3D protein structure data with Angstrom resolution. *Nat Methods* **14**, 141-144 (2017).
11. Balzarotti, F. *et al.* Nanometer resolution imaging and tracking of fluorescent molecules with minimal photon fluxes. *Science* **355**, 606-612 (2017).
12. Gwosch, K. C. *et al.* MINFLUX nanoscopy delivers 3D multicolor nanometer resolution in cells. *Nat Methods* **17**, 217-224 (2020).
13. Masullo, L. A. *et al.* Pulsed Interleaved MINFLUX. *Nano Lett* **21**, 840-846 (2021).
14. Szymborska, A. *et al.* Nuclear pore scaffold structure analyzed by super-resolution microscopy and particle averaging. *Science* **341**, 655-658 (2013).
15. Helmerich, D. A. *et al.* Photoswitching fingerprint analysis bypasses the 10-nm resolution barrier. *Nat Methods* **19**, 986-994 (2022).
16. Niekamp, S. *et al.* Nanometer-accuracy distance measurements between fluorophores at the single-molecule level. *Proceedings of the National Academy of Sciences of the United States of America* **116**, 4275-4284 (2019).
17. Szalai, A. M. *et al.* Super-resolution Imaging of Energy Transfer by Intensity-Based STED-FRET. *Nano Lett* **21**, 2296-2303 (2021).
18. Deussner-Helfmann, N. S. *et al.* Correlative Single-Molecule FRET and DNA-PAINT Imaging. *Nano Lett* **18**, 4626-4630 (2018).
19. Hellenkamp, B. *et al.* Precision and accuracy of single-molecule FRET measurements-a multi-laboratory benchmark study. *Nat Methods* **15**, 669-676 (2018).
20. Kalinin, S. *et al.* A toolkit and benchmark study for FRET-restrained high-precision structural modeling. *Nat Methods* **9**, 1218-1225 (2012).
21. Förster, T. Zwischenmolekulare Energiewanderung und Fluoreszenz. *Annalen der Physik* **437**, 55-75 (2006).
22. Chizhik, A. I., Rother, J., Gregor, I., Janshoff, A. & Enderlein, J. Metal-induced energy transfer for live cell nanoscopy. *Nature Photonics* **8**, 124-127 (2014).
23. Ghosh, A. *et al.* Graphene-based metal-induced energy transfer for sub-nanometre optical localization. *Nature Photonics* **13**, 860-865 (2019).
24. Kaminska, I. *et al.* Distance Dependence of Single-Molecule Energy Transfer to Graphene Measured with DNA Origami Nanopositioners. *Nano Lett* **19**, 4257-4262 (2019).

25. Fullbrunn, N. *et al.* Nanoscopic anatomy of dynamic multi-protein complexes at membranes resolved by graphene-induced energy transfer. *Elife* **10** (2021).
26. Sanabria, H. *et al.* Resolving dynamics and function of transient states in single enzyme molecules. *Nat Commun* **11**, 1231 (2020).
27. Lerner, E. *et al.* FRET-based dynamic structural biology: Challenges, perspectives and an appeal for open-science practices. *Elife* **10** (2021).
28. Kudryavtsev, V. *et al.* Monitoring dynamic systems with multiparameter fluorescence imaging. *Anal Bioanal Chem* **387**, 71-82 (2007).
29. Widengren, J. *et al.* Single-molecule detection and identification of multiple species by multiparameter fluorescence detection. *Anal Chem* **78**, 2039-2050 (2006).
30. Moffitt, J. R., Osseforth, C. & Michaelis, J. Time-gating improves the spatial resolution of STED microscopy. *Opt Express* **19**, 4242-4254 (2011).
31. Vicidomini, G. *et al.* Sharper low-power STED nanoscopy by time gating. *Nat Methods* **8**, 571-573 (2011).
32. Vicidomini, G. *et al.* STED nanoscopy with time-gated detection: theoretical and experimental aspects. *PLoS One* **8**, e54421 (2013).
33. Churchman, L. S., Flyvbjerg, H. & Spudich, J. A. A non-Gaussian distribution quantifies distances measured with fluorescence localization techniques. *Biophys J* **90**, 668-671 (2006).
34. Kalinin, S., Valeri, A., Antonik, M., Felekyan, S. & Seidel, C. A. Detection of structural dynamics by FRET: a photon distribution and fluorescence lifetime analysis of systems with multiple states. *J Phys Chem B* **114**, 7983-7995 (2010).
35. Barth, A. *et al.* Unraveling multi-state molecular dynamics in single-molecule FRET experiments. I. Theory of FRET-lines. *J Chem Phys* **156**, 141501 (2022).
36. Maus, M. *et al.* An experimental comparison of the maximum likelihood estimation and nonlinear least-squares fluorescence lifetime analysis of single molecules. *Anal Chem* **73**, 2078-2086 (2001).
37. Lee, N. K. *et al.* Accurate FRET measurements within single diffusing biomolecules using alternating-laser excitation. *Biophys J* **88**, 2939-2953 (2005).
38. Peulen, T. O., Opanasyuk, O. & Seidel, C. A. M. Combining Graphical and Analytical Methods with Molecular Simulations To Analyze Time-Resolved FRET Measurements of Labeled Macromolecules Accurately. *J Phys Chem B* **121**, 8211-8241 (2017).
39. Rothemund, P. W. Folding DNA to create nanoscale shapes and patterns. *Nature* **440**, 297-302 (2006).
40. Schnitzbauer, J., Strauss, M. T., Schlichthaerle, T., Schueder, F. & Jungmann, R. Super-resolution microscopy with DNA-PAINT. *Nat Protoc* **12**, 1198-1228 (2017).
41. Kabsch, W. A solution for the best rotation to relate two sets of vectors. *Acta Crystallographica Section A* **32**, 922-923 (1976).
42. Bai, X. C., Martin, T. G., Scheres, S. H. & Dietz, H. Cryo-EM structure of a 3D DNA-origami object. *Proc Natl Acad Sci U S A* **109**, 20012-20017 (2012).
43. Yoo, J. & Aksimentiev, A. In situ structure and dynamics of DNA origami determined through molecular dynamics simulations. *Proc Natl Acad Sci U S A* **110**, 20099-20104 (2013).
44. Arbona, J. M., Aime, J. P. & Elezgaray, J. Modeling the mechanical properties of DNA nanostructures. *Phys Rev E Stat Nonlin Soft Matter Phys* **86**, 051912 (2012).
45. Fischer, S. *et al.* Shape and Interhelical Spacing of DNA Origami Nanostructures Studied by Small-Angle X-ray Scattering. *Nano Lett* **16**, 4282-4287 (2016).
46. Olson, W. K., Gorin, A. A., Lu, X. J., Hock, L. M. & Zhurkin, V. B. DNA sequence-dependent deformability deduced from protein-DNA crystal complexes. *Proc Natl Acad Sci U S A* **95**, 11163-11168 (1998).

47. Mathew-Fenn, R. S., Das, R. & Harbury, P. A. Remeasuring the double helix. *Science* **322**, 446-449 (2008).
48. Raab, M. *et al.* Using DNA origami nanorulers as traceable distance measurement standards and nanoscopic benchmark structures. *Sci Rep* **8**, 1780 (2018).
49. Sindbert, S. *et al.* Accurate distance determination of nucleic acids via Forster resonance energy transfer: implications of dye linker length and rigidity. *J Am Chem Soc* **133**, 2463-2480 (2011).
50. Mathur, D. *et al.* Can a DNA origami structure constrain the position and orientation of an attached dye molecule? *J. Phys. Chem. C* (2020).
51. Hübner, K. *et al.* Determining the in-plane orientation and binding mode of single fluorescent dyes in DNA origami structures. *ACS Nano* (2021).
52. Vinogradov, S. A. & Wilson, D. F. Recursive maximum entropy algorithm and its application to the luminescence lifetime distribution recovery. *Applied Spectroscopy* **54**, 849-855 (2000).
53. Kutsch, M. & Coers, J. Human guanylate binding proteins: nanomachines orchestrating host defense. *FEBS J* **288**, 5826-5849 (2021).
54. Ji, C. *et al.* Structural mechanism for guanylate-binding proteins (GBPs) targeting by the Shigella E3 ligase IpaH9.8. *PLoS Pathog* **15**, e1007876 (2019).
55. Shydlovskyi, S. *et al.* Nucleotide-dependent farnesyl switch orchestrates polymerization and membrane binding of human guanylate-binding protein 1. *Proc Natl Acad Sci U S A* **114**, E5559-E5568 (2017).
56. Spahn, C., Grimm, J. B., Lavis, L. D., Lampe, M. & Heilemann, M. Whole-Cell, 3D, and Multicolor STED Imaging with Exchangeable Fluorophores. *Nano Lett* **19**, 500-505 (2019).
57. Greife, A. *et al.* Structural assemblies of the di- and oligomeric G-protein coupled receptor TGR5 in live cells: an MFIS-FRET and integrative modelling study. *Sci Rep* **6**, 36792 (2016).
58. Peulen, T.-O. *et al.* Integrative dynamic structural biology unveils conformers essential for the oligomerization of a large GTPase. *arXiv*, arxiv.org/abs/2004.04229 (2020).
59. Mortensen, K. I., Churchman, L. S., Spudich, J. A. & Flyvbjerg, H. Optimized localization analysis for single-molecule tracking and super-resolution microscopy. *Nat. Methods* **7**, 377 (2010).
60. Livesey, A. K. & Skilling, J. Maximum-Entropy Theory. *Acta Crystallographica a-Foundation and Advances* **41**, 113-122 (1985).
61. Brochon, J. C. Maximum entropy method of data analysis in time-resolved spectroscopy. *Methods Enzymol* **240**, 262-311 (1994).
62. Skilling, J. & Bryan, R. K. Maximum-Entropy Image-Reconstruction - General Algorithm. *Monthly Notices of the Royal Astronomical Society* **211**, 111-+ (1984).
63. Sisamakis, E., Valeri, A., Kalinin, S., Rothwell, P. J. & Seidel, C. A. M. Accurate Single-Molecule Fret Studies Using Multiparameter Fluorescence Detection. *Methods in Enzymology, Vol 475: Single Molecule Tools, Pt B* **475**, 455-514 (2010).

Supporting Information

FRET nanoscopy enables seamless imaging of molecular assemblies with sub-nanometer resolution

Nicolaas T.M. van der Voort[1,†], Jan-Hendrik Budde[1,†], Suren Felekyan[1], Julian Folz[1], Ralf Kühnemuth[1], Paul Lauterjung[1,2], Markus Köhler[3], Andreas Schönle[3], Julian Sindram[4], Marius Otten[4], Matthias Karg[4], Christian Herrmann[2], Anders Barth[1,a,*], Claus A. M. Seidel[1,*]

[1] Chair for Molecular Physical Chemistry, Heinrich-Heine-University Düsseldorf, Germany

[2] Physical Chemistry I, Ruhr-Universität Bochum, Germany

[3] Abberior Instruments GmbH, Hans-Adolf-Krebs-Weg 1, 37077 Göttingen, Germany

[4] Lehrstuhl für Kolloide und Nanooptik, Heinrich-Heine-Universität Düsseldorf, 40225 Düsseldorf, Germany

[a] Present address: Department of Bionanoscience, Kavli Institute of Nanoscience, Delft University of Technology, Delft, The Netherlands

[†] contributed equally

* Correspondence to: cseidel@hhu.de, anders.barth@hhu.de

Table of contents

Materials and Methods

Data acquisition

STED-FRET microscope

FRET nanoscopy was performed on a custom-designed Abberior Instruments Expert Line microscope (Abberior Instruments, Göttingen, Germany) using an Olympus IX83 microscope body equipped with an '*easy 3D'* module based on a spatial light modulator (SLM), that is sketched in Supplementary Fig. 1a. The excitation lasers with wavelengths 561 nm and 640 nm pulse width < 100 ps) and the STED depletion laser (775 nm, pulse width 1.2 ns) were synchronized at 40 MHz and spatially overlaid by notch filters: N1 for 561 nm excitation (NF03-594E, Semrock, with tuned angle), N2 for 640 nm excitation (NF03-658E, Semrock, with tuned angle) and N3 for 775 nm STED depletion (Abberior). A combination of a λ/4 and λ/2 waveplate was used in the excitation and depletion pathways to create linearly and circularly polarized light, respectively. Both waveplates were needed for each line to compensate polarization mixing caused by the notch filters. The fluorescence signal was split by polarization and color using a broad-band polarizing beam splitter (PBS, Abberior) and two dichroic mirrors at 640 nm (DM1 & DM2, Abberior) and detected by four APDs (SPCM-AQRH-13-TR, Excelitas). Further spectral selection in the donor and acceptor channels was achieved by dye-specific band pass filters (BP1-4). The donor fluorescence was detected in the range 605-625 nm for dsDNA-Alexa594 and origami-Atto594 measurements (ET615/20, Semrock) and in the range 585-630 nm for hGBP1-Alexa594 (ET608/45, AHF, Germany). The acceptor fluorescence of the dye Atto647N was detected in the range 650-720 nm for all samples (ET685/70M, Abberior). The detected signal was split into parallel and perpendicular components using a polarizing beam splitter. Finally, photon arrival times were recorded with picosecond resolution on an external time-correlated single photon counting (TCSPC) unit (HydraHarp 400, PicoQuant GmbH, Berlin, Germany). All measurements were performed with an oil-immersion objective (NA 1.4, UPLSAPO 100XO, Olympus, Germany). The point-spread function was measured using 150 nm gold nanoparticles (Sigma-Aldrich, St. Louis, US, see Supplementary Fig. 1b-c for a characterization of the PSF), while the achievable STED resolution was determined using dye-filled polystyrene beads (crimson beads; 40 nm, Thermo Fisher Scientific, Waltham, US).

To further increase the achievable resolution, time-gated fluorescence detection was performed during data processing using a time gate from 0.9 -12.8 ns relative to the STED depletion pulse, resulting in an increase of the STED resolution by up to 20%[1]. While the instrument can achieve a higher resolution, this comes at the cost of fewer photons that are available for the spectroscopic analysis. Due to the high overlap of the emission spectra of the donor and acceptor dyes (Supplementary Fig. 1e for the dye spectra), the spectral crosstalk α of the donor fluorescence into the acceptor channels ranges between 0.49 and 0.56 (see Supplementary Tab. 3). To avoid crosstalk in the acceptor channel and to achieve alternating excitation of the donor and acceptor fluorophores, we performed line-interleaved donor and acceptor excitation. Because the movement in the y-direction of the scanner is constant over time, the acceptor emission upon acceptor excitation channel is shifted by half a pixel (corresponding to 5 nm) in the y direction. All acceptor localizations are corrected for this shift. No other corrections to the localization data are applied. To minimize the effects of spherical aberrations and drift, data was

recorded close to the optical axis (< 20 µm) in a small ROI (1 µm x 1 µm) for fast image acquisition (<20 seconds). The instrument response function (IRF), describing the timing response of the system, was determined under following conditions: (i) for excitation at 561 nm, an aqueous solution of erythrosine in 5 M potassium iodide as quencher[2] was used, (ii) for excitation at 640 nm, an aqueous solution of malachite green[3] was used (see Supplementary Fig. 1f for typical IRFs).

Data recording

To automate the acquisition of zoomed STED images of single molecules as depicted in Fig. 1d, we implemented a custom-written spot finding algorithm for the Imspector software (http://www.imspector.de), written in the Python programming language. First, we acquire an overview image (20 µm x 20 µm) by direct excitation of the acceptor (640nm, 13.6 µW, dwell time 100µs), allowing us to identify molecules with active acceptors. First, spot detection was performed using an intensity threshold and by requiring a minimal distance between spots. Second, the total number of detected acceptor-labeled spots per overview image was used to estimate the spot surface density and finally calculate the probability of single- and multi-spot events per image under assumption of randomly distributed spots on the surface. If the probability of multi events goes below 5%, the recorded overview image was taken for the acquisition of STED images of single spots After filtering, the positions of spots containing single molecules were stored. Consecutively, for each position a 1 µm x 1 µm image was then recorded for 61 frames and saved in the PicoQuant PTU file format.

To optimize the use of the available signal before photobleaching, different strategies were used for the extraction of the FRET parameters and the localization of the fluorophores. For the FRET signal, photobleaching of either donor or acceptor is a limiting factor. On the other hand, localization does not require both dyes to be active. In the case of high FRET, acceptor photobleaching even aides the donor localization precision as the donor signal is increased. Thus, only the first 100 µs or 20 frames (see Supplementary Tab 14) are used for the calculation of the FRET-related spectroscopic parameters, while the total collected signal is used to estimate the fluorophore position.

DNA origami and DNA ruler measurements

All data was recorded using a 1 µm x 1 µm image (100 x 100 pixel) with a 5 µs dwell time, amounting to a frame time of 300 ms including the delay caused by the resonant scanner. For the origami measurements, the excitation powers were 6.4 µW for the donor excitation (561 nm), 3.3 µW for the acceptor excitation (640 nm) and 35 mW for the STED depletion (775 nm) lasers, respectively. For the DNA ruler measurements, the excitation powers were 4.2 µW for the donor excitation (561 nm), 2.7 µW for the acceptor excitation (640 nm) and 42 mW for the STED depletion (775 nm) lasers, correspondingly. The analysis settings for the measurements of the different DNA origami constructs containing only the noFRET dye pair O(NF), only the highFRET dye pair O(HF), or both dye pairs O(HF+NF), are listed in Supplementary Tab. 14.

hGBP1 measurements

Super-resolved STED FRET measurements of Cys8 hGBP1-18-577 were performed with line-alternating excitation of donor (Alexa594) and acceptor (Atto647N) dyes, excited with 561 nm laser (5 µW) and 640 nm laser (2 µW), respectively, at a pulse rate of 40 MHz. Depletion was done by 775 nm STED laser at a power of 42 mW. Images of hGBP1 rings were taken at a distance of 300-500 nm above the surface to ensure minimal diffusion of the structures while reducing background signal from the surface. The analysis settings are summarized in Supplementary Fig. 29.

Sample preparation

dsDNA

To screen a broad range of FRET efficiencies, we designed highFRET (dsD(HF)), midFRET (dsD(MF)), lowFRET (dsD(LF)) and noFRET (dsD(NF)) samples of donor-acceptor pairs on dsDNA (Supplementary Tab. 1). All single DNA strands were synthesized and labeled by IBA GmbH (Göttingen, Germany), followed by HPLC purification. The position of the donor dye (Alexa594) was kept fixed while the acceptor (Atto647N) position on the complementary strands was varied. The dye derivatives with an activated NHS-ester were coupled to the amino group of C6-amino-linker connected a thymine (T) or cytosine (C). Additionally, a single or two biotin anchors were attached to the 3' and 5' ends of the donor strands (single biotin was attached to the 5' end only) for surface immobilization.

Hybridization of complementary single stranded DNA was performed inside a thermocycler (primus 96 advanced, pegLab, Erlangen). Donor only strands were mixed with reversed acceptor only strands in excess 1:3 in buffer (20mM $MgCl_2$, 100mM KCl, 20 mM KH_2PO_4/K_2HPO_4, pH 6.5) and quickly heated up to 85° C and fast cooled up to 52° C with 0.1° C/s. The solution was kept at this temperature for 2 hours, subsequently cooled down to 4° C and stored at this temperature. Detailed information about sample properties is listed in Supplementary Tab. 1.

DNA origami

We used single-layer DNA origami nanostructures are based on published designs and were assembled as described in Schnitzbauer et al[4]. The structural design is depicted in Supplementary Fig. 7. Folding of structures was performed in buffer containing 10 mM Tris, 12.5 mM $MgCl_2$ and 1 mM EDTA at pH 8.0 in a one-pot reaction containing 10 nM p7249 M13 single-stranded DNA scaffold (tilibit nanosystems, Munich, Germany); 100 nM core staple strands, 100 nM biotinylated staple strands and 1 µM fluorescently labeled staple strands in a total volume of 40 µl (the used sequences are listed in Supplementary Tab. 2). Unlabeled and biotinylated staple strands were purchased from Biomers (Ulm, Germany). Fluorescently labeled staple strands were purchased from IBA (Göttingen, Germany). Annealing was performed by heating the mixture to 80 °C and cooling it using a temperature gradient from 60 to 4 °C in steps of 3 min 12 s per °C. The correct assembly of the structures was checked by gel electrophoresis (2% agarose) and TEM imaging. Purification was performed by precipitating the origami nanostructures by adding one volume of buffer containing 15% PEG 8000 (w/v), 5 mM Tris,

1mM EDTA and 500 mM NaCl[5]. The sample was thoroughly mixed and centrifuged at 16.000 g for 25 min in a microcentrifuge at room temperature. After the supernatant was removed with a pipette, the pellet was dissolved in imaging buffer (10 mM Tris, 12.5 mM $MgCl_2$, 1 mM EDTA, pH 8.0) and the precipitation step was repeated one more time, after which the pellet was incubated in imaging buffer over night at room temperature to fully recover the structures.

Fluorophores were attached to the 3'-end of the respective oligos with an additional thymine base pair as a spacer. Fluorophore positions were determined with the Picasso software[4]. All strands are listed in Supplementary Tab. 2. The origami design as obtained from the caDNAno software and the chemistry of the dye linker are shown in Supplementary Fig. 7[6].

Surface preparation

dsDNA or DNA origami nanostructures were immobilized on the surface using biotinylated NHS-PEG (3145 g / mol, Iris Biotech GmbH) or biotinylated BSA (bovine serum albumin, biotin labeled, Sigma-Aldrich), see Supplementary Tab. 13 for a list of measurements and surface preparations. Both immobilization protocols start with a cleaning procedure of a single cover slide (Precision cover glasses thickness No. 1.5H, Marienfeld, Lauda-Königshofen, Germany). Cover slides were sonicated (RH510 H, Bandelin electronic) in 5% Hellmanex (Sigma-Aldrich) for 20 min, washed 10-times with water and dried under nitrogen flow. Cleaned cover slides were activated for 10 minutes in an oxygen plasma (FEMTO Plasma Cleaner, Diener electronic, Ebhausen, Germany; for AFM data only: PlasmaFlecto 10, plasma technology GmbH, Herrenberg-Gülstein, Germany).

NHS-PEG-Biotin. Cleaned cover slides were incubated with 3 M ethanolamine hydrochloride (Sigma-Aldrich) solved in DMSO (dimethyl sulfoxide, VWR Chemicals) for least 12 h at room temperature. After removal of remaining ethanolamine hydrochloride from the surface by washing with water and drying with nitrogen, 200 µl NHS-PEG-Biotin (IRIS Biotech GmbH, 6 mg/ml,) in chloroform (Sigma-Aldrich) was added and sandwiched between a second cover slide. After 1 h, the sandwiched cover slides were separated carefully, cleaned with acetonitrile (Methyl cyanide, Sigma-Aldrich), and again dried with nitrogen. Finally, the surface was incubated for 10 min with neutravidin (20 µg/ml in water, Thermo Scientific) and washed with PBS (GIBCO) to remove remaining/ unbound neutravidin molecules.

BSA-Biotin. After the cleaning procedure, the surface was incubated for 10 min with biotinylated BSA (Sigma-Aldrich, 3 mg/ml in PBS), washed up to 5 times with PBS, incubated for 10 min with neutravidin (Invitrogen, 20µg/ml in water), and washed again with buffer to remove unbound neutravidin molecules.

The overnight measurements of immobilized samples on the cover slide took up to 24 h. To reduce evaporation of the sample solution, the coated slides were glued to IBIDI sticky slides VI 0.4 (ibidi, Gräfelfing, Germany). Here 6 defined chambers are created with a volume of 60 µl. After sample injection, the chamber was washed 5 times with PBS before being filled with imaging buffer solution.

All measurements were performed under addition of 1 mM Trolox (6-Hydroxy-2,5,7,8-tetramethylchroman-2-carboxylic acid, Sigma Aldrich) prepared freshly for better photostability of the dyes (dissolve 50 mg Trolox in 1ml ethanol for a 200X buffer).

hGBP1 expression and labeling

Plasmids. The wild-type of hGBP1 (hGBP1-wt) harbors 9 cysteine residues with one being blocked by the farnesyl moiety after modification. To site-specifically attach fluorescence labels for FRET measurements, all wild-type cysteines were mutated in our previous work leading to the mutant termed Cys9 hGBP1 (i.e., C12A, C82A, C225S, C235A, C270A, C311S, C396A, C407S, C589S)[7]. The mutation C589S was reversed using the QuikChange site-directed mutagenesis kit with KOD Hot Start DNA polymerase (Merck, Millipore) resulting in so termed Cys8 hGBP1. This allows for the farnesylation of the C-terminus of the protein. To introduce two cysteine residues for FRET studies, residues N18 and Q577 were replaced by a cysteine. This mutant termed Cys8 hGBP1-18-577 is used throughout this study. The success of mutagenesis was verified by sequencing (3130xl sequencer, Applied Biosystems).

Protein expression and purification. Expression and purification of wild type and mutant hGBP1 was performed as described previously[8,9]. In brief, the DNA was expressed in E. coli strain Rosetta™ (DE3)pLysS using a pQE-80L vector (Qiagen). For affinity chromatography, Cobalt-NTA-Superflow was used followed by size exclusion chromatography with a Superdex 200 column. To ensure the stability of the protein, the buffer for size exclusion chromatography and storage included 2 mM DTT. This was removed prior to labelling reactions by applying the solutions to spin concentrators (Vivaspin™) in three repetitive cycles. Both non-farnesylated hGBP1-wt and the non-farnesylated mutant Cys8 hGBP1-18-577 were farnesylated using the protocol for enzymatic modification[8] leading to hGBP1-wt and Cys8 hGBP1-18-577, respectively. Protein absorption was measured at 280 nm using a NanoDrop™ 2000 spectrophotometer (ThermoFisher Scientific, USA) and the concentration was calculated with an extinction coefficient of 45000 $M^{-1}cm^{-1}$. Purity of the farnesylated protein was checked by SDS-PAGE and the activity of the protein was verified by the turbidity assay using standard conditions[8] which demonstrates both enzymatic activity and the formation of polymers.

Protein labelling. Human GBP1-wt was unspecifically labelled by mixing 100 µM protein with 150 µM Alexa594 succinimidyl ester (Life Technologies GmbH) on lysines and 150 µM Atto647N maleimide (ATTO TEC GmbH) on cysteines by incubation on ice for 30 minutes. Unbound dye was removed with spin concentrators (Vivaspin™). Cys8 hGBP1-18-577 was labelled by mixing 100 µM protein with 130 µM Alexa 594 C5 maleimide (Life Technologies GmbH) in buffer C_{Label} (50 mM Tris/HCl, 150 mM NaCl, 5 mM $MgCl_2$, pH 7.4) and by incubation for 60 min. The unbound dye was removed, and the buffer was exchanged to low salt buffer (50 mM Tris/HCl, 5 mM $MgCl_2$, pH 7.4) with spin concentrators (Vivaspin™). Different labelled species were isolated by anion exchange chromatography using a ResourceQ column (GE Healthcare) and running a gradient from 0-200 mM NaCl at pH 7.4. The labelled species with approximately 100 % labelling efficiency were mixed with 3 eq of Atto647N maleimide (ATTO TEC GmbH) and incubated for 90 min. The unbound dye was removed with a HiPrep 26/20 S25 desalting column. The labelling efficiencies for both dyes for labelled hGBP1-wt (Donor: 42%; Acceptor: 78%) and labelled Cys8 hGBP1-18-577 (Donor: 118%; Acceptor: 92%) were determined by using their respective extinction coefficients (Atto647N ε(646 nm) = 150000 $M^{-1}cm^{-1}$; Alexa594 ε(590 nm) = 92000 $M^{-1}cm^{-1}$), accounting for the spectral overlap and comparing the resulting dye

concentrations to the protein concentration. Afterwards, the protein was stored at concentrations of 10-30 µM in buffer C (50 mM Tris-HCl, 150 mM NaCl, 5 mM $MgCl_2$, pH 7.9) after addition of 2 mM DTT at -80°C.

Triggering hGBP1 oligomerization. A 10 µl sample containing a total of 10 µM protein was prepared in buffer C with AlF_x (50 mM Tris-HCl, 150 mM NaCl, 5 mM $MgCl_2$, 300 µM $AlCl_3$, 10 mM NaF, pH 7.9). The mixture of labelled Cys8 hGBP1-18-577 (or labelled hGBP1-wt) and hGBP1-wt varied depending on the desired labelling density in hGBP1 polymers. Most measurements where single fluorescence spots could be identified were taken at a Cys8 hGBP1-18-577 concentration of 0.05 µM and a hGBP1-wt concentration of 9.95 µM. To induce the polymerization reaction, 200 µM GDP was added and the reaction solution was incubated for 15 min. The reaction solution was mixed and 1 µl was diluted in 1 ml buffer C with AlF_x and 200 µM GDP. After mixing the diluted sample, 300 µl were transferred into a Nunc™ Lab-Tek™ II Chamber Slide™ (ThermoFisher Scientific), which was previously passivated with a 1 g/l BSA solution for 20 minutes. Polymer structures were visible after 10-40 min after which they would remain stable for hours.

Spectroscopy and image analysis

Filtering procedures

Filtering procedure for DNA rulers. The processed data file contains a list of parameters for each spot (see SI Supplementary Tab. 17). We distinguish between image parameters (such as the localization precision, spot symmetry and spot stoichiometry) and spectroscopic parameters (e.g., the intensity-based stoichiometry, the FRET efficiency and the fluorescence lifetimes of the donor and acceptor dyes). The filtering procedure is schematically illustrated in Supplementary Fig. 3. First, spots with a spot width larger than a given threshold were discarded (see SI Supplementary Tab. 15). Large spot widths occur for insufficient photon numbers (low localization precision) or if multiple donor or acceptor fluorophores are present in the ROI (multi-molecule events, aggregation). In the second step, double-labeled spots containing one donor and one acceptor were identified based on the intensity-based stoichiometry by selecting spots with $S \simeq 0.5$.

Filtering procedure for origamis. The origami datasets were fitted with multiple circular 2D Gaussians and filtering was performed based on the detected number of spots for each color (spot stoichiometry). Dim spots with less than 20 photons were discarded. Only completely labelled structures were used for particle averaging, whereas for spectroscopic analysis also ROIs with two or three spots for donor and acceptor were used (Supplementary Fig. 2) for better statistics. An additional cut in the acceptor brightness and spot stoichiometry was applied to the only data O(HF) to remove structures affected by acceptor photobleaching. For the particle averaging, we additionally used the RMSD with respect to the reference structure for filtering (Supplementary Fig. 9). For the analysis of sub-ensemble TCSPC decays, an additional cut of the FRET efficiency was performed. All filtering parameters are listed in Supplementary Tab. 16 and the settings are given in Supplementary Tab. 14.

Filtering procedure for hGBP1. For hGBP1, a manual pre-selection of data was done by visual inspection of the ring structures with respect to the labeling density and the definition of the spots (blurring). Analogous to the origami analysis, the hGBP1 data was fitted with multiple circular Gaussians. Dim spots with less than 20 photons were discarded. Only spots with at least one detected donor and acceptor spot (spot stoichiometry >0) and an uncorrected FRET efficiency (proximity ratio, PR) > 0.35 were selected for further analysis (Supplementary Fig. 29a). All filtering thresholds are given in Supplementary Tab. 14.

Determination of intensity-based correction factors

Spectral crosstalk of the donor fluorescence into the acceptor detection channel, α, the relative excitation flux, β, and the direct excitation of the acceptor by the donor excitation laser, δ, where calculated following the approach outlined in[10]. Briefly, α was determined from the ratio of signal in the donor and acceptor channel in the absence of an acceptor dye using confocal measurements of the noFRET origami sample. δ was determined under STED conditions by placing the acceptor-only population at zero stoichiometry and β was determined from each dataset directly by placing the double-labeled population at a stoichiometry of 0.5. Donor-only and acceptor-only constructs were selected based on the number of detected spots for each color (spot stoichiometry, see Supplementary Fig. 2). Spectra were obtained from the manufacturer[11] and combined with the transmission spectra of the dichroic mirrors, notch filters and emission filters to obtain estimated detection efficiencies using the homebuilt program *Detection Efficiencies*[12]. Quantum yields were estimated based on the fluorescence lifetimes of donor-only and acceptor-only samples. To estimate the lifetime of the undepleted fluorophores under STED conditions, the fluorescence decays were fitted with two lifetimes. In the model, the short lifetime accounts for the fast depletion by the STED pulsed, while the long lifetime is assigned to the fluorescence of the undepleted fluorophores. The quantum yield is determined from the measured lifetime τ by:

$$\Phi_{\mathrm{F}} = \Phi_{F,\mathrm{ref}} \frac{\tau}{\tau_{\mathrm{ref}}}\,, \qquad (S1)$$

where Φ_{F} is the quantum yield and the subscript *ref* refers to a known reference. Here, the reference values for both Atto594 and Atto647N are taken from reference[11]. The species fractions x_{D}^{0}, $x_{\mathrm{D}}^{\mathrm{d}}$, x_{A}^{0}, $x_{\mathrm{A}}^{\mathrm{d}}$ are obtained from the sub-ensemble lifetime fits for each dataset separately. See SI Supplementary Tab. 3 for an overview of the correction factors.

Intensity-based spectroscopic parameters

For a relative assessment of the FRET efficiency, it is not required to account for all correction parameters. Instead, the proximity ratio, E_{PR}, can serve as a qualitative estimate, defined by:

$$E_{\mathrm{PR}} = \frac{{}^{i}I_{\mathrm{Aem|Dex}}}{{}^{i}I_{\mathrm{Dem|Dex}} + {}^{i}I_{\mathrm{Aem|Dex}}}, \qquad (S2)$$

where ${}^{i}I$ are the uncorrected (raw) intensities in the donor channel after donor excitation (${}^{i}I_{\mathrm{Dem|Dex}}$) and the acceptor channel after donor excitation (${}^{i}I_{\mathrm{Aem|Dex}}$). To determine the accurate FRET efficiency, *E*, additional corrections are required. First, the uncorrected intensities need to be corrected as follow. As a first step, the signals are corrected for constant background $I^{(\mathrm{BG})}$:

$$\begin{aligned} {}^{ii}I_{\mathrm{Dem|Dex}} &= {}^{i}I_{\mathrm{Dem|Dex}} - I^{(\mathrm{BG})}_{\mathrm{Dem|Dex}} \\ {}^{ii}I_{\mathrm{Aem|Dex}} &= {}^{i}I_{\mathrm{Aem|Dex}} - I^{(\mathrm{BG})}_{\mathrm{Aem|Dex}} \\ {}^{ii}I_{\mathrm{Aem|Aex}} &= {}^{i}I_{\mathrm{Aem|Aex}} - I^{(\mathrm{BG})}_{\mathrm{Aem|Aex}} \end{aligned} \tag{S3}$$

Here, ${}^{i}I_{\mathrm{Aem|Aex}}$ describes the uncorrected measured intensity in the acceptor channel after acceptor excitation. It is assumed that the spectral properties of the fluorophores (extinction coefficient, absorption spectrum, emission spectrum) do not change under STED conditions. Corrections for spectral crosstalk of the donor into the acceptor detection channel and direct excitation of the acceptor by the donor excitation laser can thus be performed as for conventional FRET experiments[10,13], yielding the corrected acceptor fluorescence after donor excitation $F_{\mathrm{A|D}}$:

$$F_{\mathrm{A|D}} = {}^{ii}I_{\mathrm{Aem|Dex}} - \alpha\,{}^{ii}I_{\mathrm{Dem|Dex}} - \delta\,{}^{ii}I_{\mathrm{Aem|Aex}}, \tag{S4}$$

where α is the correction factor for crosstalk and δ for direct excitation. No further corrections are needed for the other two channels. For convenience, we change the notation to indicate that the intensities ${}^{ii}I$ are corrected fluorescence signals, F:

$$\begin{aligned} F_{\mathrm{D|D}} &= {}^{ii}I_{\mathrm{Dem|Dex}} \\ F_{\mathrm{A|A}} &= {}^{ii}I_{\mathrm{Aem|Aex}} \end{aligned} \tag{S5}$$

The uncorrected (apparent) ROI – stoichiometry, ${}^{i}S_{\mathrm{app}}$, is given by:

$${}^{\mathrm{i}}S_{\mathrm{app}} = \frac{I_{\mathrm{Aem|Dex}} + I_{\mathrm{Dem|Dex}}}{I_{\mathrm{Aem|Dex}} + I_{\mathrm{Dem|Dex}} + I_{\mathrm{Aem|Aex}}} \tag{S6}$$

Additionally, the observed intensities need to be corrected for different excitation intensities and absorption cross sections (β correction factor), donor and acceptor quantum yields ($\Phi^{0}_{\mathrm{F,D}}, \Phi^{0}_{\mathrm{F,A}}$) and detection efficiencies (γ correction factor). The β factor is determined by the excitation spectra of the donor and acceptor and the excitation intensity ratio as:

$$\beta = \frac{\sigma_{\mathrm{A|R}}}{\sigma_{\mathrm{D|G}}}\frac{I_{\mathrm{Aex}}}{I_{\mathrm{Dex}}} \tag{S7}$$

The γ factor is given by:

$$\gamma = \frac{g_{\mathrm{A|A}}}{g_{\mathrm{D|D}}}\frac{\Phi^{0}_{\mathrm{F,A}}}{\Phi^{0}_{\mathrm{F,D}}} \tag{S8}$$

Here, the detection efficiency ratio $\frac{g_{\mathrm{A|A}}}{g_{\mathrm{D|D}}}$ is calculated based on the emission spectra of the donor and acceptor and the transmission of the optical elements. The corresponding quantum yields of donor- and acceptor-only sample are determined under experimental conditions by sub-ensemble lifetime fitting. The fully corrected ROI stoichiometry is then explicitly given by:

$$S = \frac{\gamma F_{\mathrm{D|D}} + F_{\mathrm{A|D}}}{\gamma F_{\mathrm{D|D}} + F_{\mathrm{A|D}} + {}^{1}/_{\beta}\, F_{\mathrm{A|A}}} \tag{S9}$$

The FRET population should be symmetrically distributed at S = 0.5, the donor only population at S = 1 and the acceptor only population at S = 0. The correction parameters of all measurements are compiled in Supplementary Tab. 3.

Accurate intensity-based FRET efficiencies under STED conditions

To estimate accurate intensity-based FRET efficiencies, we used the total intensity detected in the donor and acceptor channels without time gating. This is necessary because otherwise the effective detection efficiency of the donor fluorescence (i.e., the fraction of the fluorescence decay that falls within the time gate) would depend on the fluorescence lifetime, which in turn depends on the rate of energy transfer. In addition, the use of the ungated signal allows us to maximize the available signal. However, without the application of time gating, the measured fluorescence signals contain contributions from both (partially) depleted and undepleted molecules, which exhibit different quantum yields. Donor and acceptor fluorophores are also generally depleted to a different extent. The measured fluorescence signals after donor excitation can be described by:

$$\begin{aligned} F_{\mathrm{D|D}} &= \sigma_{\mathrm{D|D}}\, I_{\mathrm{Dex}}\, g_{\mathrm{D|D}} \left[x_{\mathrm{D}}^{0}\, \Phi_{\mathrm{F,D}}^{0}\, (1 - E_0) + x_{\mathrm{D}}^{\mathrm{d}}\, \Phi_{\mathrm{F,D}}^{\mathrm{d}}\, (1 - E_{\mathrm{d}})\right] \\ F_{\mathrm{A|D}} &= \sigma_{\mathrm{D|D}}\, I_{\mathrm{Dex}}\, g_{\mathrm{A|A}} \left[x_{\mathrm{A}}^{0}\, \Phi_{\mathrm{F,A}}^{0}\, E_0 + x_{\mathrm{A}}^{\mathrm{d}}\, \Phi_{\mathrm{F,A}}^{\mathrm{d}}\, E_{\mathrm{d}}\right] \end{aligned} \tag{S10}$$

where $\sigma_{D|G}$ is the absorption cross-section of the donor at the donor excitation wavelength, I_{Dex} is the excitation intensity of the donor excitation laser, $g_{\mathrm{D|D}}$ and $g_{\mathrm{A|A}}$ are the detection efficiencies of the donor fluorophore in the donor detection channel and the acceptor fluorophore in the acceptor detection channel, x_{D}^{0} and x_{A}^{0} are the fractions of undepleted donor and acceptor molecules with respective quantum yields $\Phi_{\mathrm{F,D}}^{0}$ and $\Phi_{\mathrm{F,A}}^{0}$ and FRET efficiency E_0, and $x_{\mathrm{D}}^{\mathrm{d}}$ and $x_{\mathrm{A}}^{\mathrm{d}}$ are the fractions of depleted or partially depleted donor and acceptor molecules with respective quantum yields $\Phi_{\mathrm{F,D}}^{\mathrm{d}}$ and $\Phi_{\mathrm{F,A}}^{\mathrm{d}}$ and FRET efficiency E_{d}. Note that the FRET efficiency of the depleted molecules is expected to be reduced due to the increased donor de-excitation rate through the depletion pulse, resulting in a negligible FRET efficiency for depleted donors. Accordingly, we have not accounted for the possibility that a depleted donor might transfer its energy to a non-depleted acceptor. We also do not consider the rare event that a non-depleted donor might transfer its energy to a depleted acceptor.

In the lifetime analysis of sub-ensemble decays, we describe the contribution of depleted fluorophores with a short lifetime component. From the time-resolved information of donor- and acceptor- only molecules, we can thus obtain the species-fraction of the depleted and undepleted molecules, x^{d} and $x^{0} = 1 - x^{\mathrm{d}}$, and estimate the respective quantum yields from the fitted lifetimes, $\Phi_{\mathrm{F}}^{\mathrm{d}}$ and Φ_{F}^{0} for the donor and acceptor fluorophore. This allows us to solve for the FRET efficiency E_0 in the absence of depletion by taking the ratio of the measured fluorescence signals:

$$\frac{F_{\mathrm{A|D}}}{F_{\mathrm{D|D}}} = \frac{g_{\mathrm{A|A}}}{g_{\mathrm{D|D}}} \cdot \frac{x_{\mathrm{A}}^{0} \cdot \Phi_{\mathrm{F,A}}^{0} \cdot E_0 + x_{\mathrm{A}}^{\mathrm{d}} \cdot \Phi_{\mathrm{F,A}}^{\mathrm{d}} \cdot E_{\mathrm{d}}}{x_{\mathrm{D}}^{0} \cdot \Phi_{\mathrm{F,D}}^{0} \cdot (1 - E_0) + x_{\mathrm{D}}^{\mathrm{d}} \cdot \Phi_{\mathrm{F,D}}^{\mathrm{d}} \cdot (1 - E_{\mathrm{d}})}, \tag{S11}$$

from which we obtain

$$E_0 = E_0' \cdot \left(1 + \frac{x_{\mathrm{D}}^{\mathrm{d}} \cdot \Phi_{\mathrm{F,D}}^{\mathrm{d}}}{x_{\mathrm{D}}^{0} \cdot \Phi_{\mathrm{F,D}}^{0}}\right) - E_{\mathrm{d}} \cdot \left(E_0' \frac{x_{\mathrm{D}}^{\mathrm{d}} \cdot \Phi_{\mathrm{F,D}}^{\mathrm{d}}}{x_{\mathrm{D}}^{0} \cdot \Phi_{\mathrm{F,D}}^{0}} + (1 - E_0') \cdot \frac{x_{\mathrm{A}}^{\mathrm{d}} \cdot \Phi_{\mathrm{F,A}}^{\mathrm{d}}}{x_{\mathrm{A}}^{0} \cdot \Phi_{\mathrm{F,A}}^{0}}\right). \quad (S12)$$

Here, the modified FRET efficiency E_0' is related to the measured fluorescence signals as:

$$E_0' = \frac{F_{\mathrm{A|D}}}{\frac{x_{\mathrm{A}}^{0} \cdot g_{\mathrm{A|A}} \cdot \Phi_{\mathrm{F,A}}^{0}}{x_{\mathrm{D}}^{0} \cdot g_{\mathrm{D|D}} \cdot \Phi_{\mathrm{F,D}}^{0}} \cdot F_{\mathrm{D|D}} + F_{\mathrm{A|D}}} = \frac{F_{\mathrm{A|D}}}{\gamma' \cdot F_{\mathrm{D|D}} + F_{\mathrm{A|D}}}, \quad (S13)$$

where $\gamma' = \frac{x_{\mathrm{A}}^{0}}{x_{\mathrm{D}}^{0}} \cdot \overbrace{\frac{g_{\mathrm{A|A}} \cdot \Phi_{\mathrm{F,A}}^{0}}{g_{\mathrm{D|D}} \cdot \Phi_{\mathrm{F,D}}^{0}}}^{\gamma} = \frac{x_{\mathrm{A}}^{0}}{x_{\mathrm{D}}^{0}} \cdot \gamma$ is a modified γ-factor that corrects for the relative detection yield of the donor and acceptor fluorophores, taking the fraction of undepleted molecules into account.

We further assume that the FRET efficiency under depletion conditions is zero, as the de-excitation of the excited donor fluorophore is faster than the energy transfer, yielding the simplified equation as used in the main text:

$$E_0 = E_0' \cdot \left(1 + \frac{x_{\mathrm{D}}^{\mathrm{d}} \cdot \Phi_{\mathrm{F,D}}^{\mathrm{d}}}{x_{\mathrm{D}}^{0} \cdot \Phi_{\mathrm{F,D}}^{0}}\right). \quad (S14)$$

The correction parameters of all measurements are compiled in Supplementary Tab. 3.

Determination of average intensity-based FRET efficiencies

To estimate the average intensity-based FRET efficiency from single-molecule histograms, the one-dimensional FRET efficiency distribution was first fitted to a normal distribution. To reduce the influence of outliers, the average FRET efficiency was calculated based only on those spots that fell within one standard deviation of the mean. The estimated FRET efficiencies of all measurements are compiled in Supplementary Tab. 10.

Sub-ensemble fluorescence decay analysis

Selecting molecules with similar ROI-integrated spectroscopic properties (i.e., FRET efficiency or donor fluorescence lifetime) allows us to perform a quantitative analysis of the interdye distance distributions. Sub-ensemble fluorescence decays were generated by binning the microscopic arrival times of the donor photons of all selected spots. As we use polarization-resolved detection, the unpolarized total fluorescence decay $f(t)$ is constructed according to:

$$f(t) = f_{\parallel}(t) + 2 \cdot G \cdot f_{\perp}(t) \quad (S15)$$

where $f_{\parallel}(t)$ and $f_{\perp}(t)$ are the fluorescence decays measured in the parallel and perpendicular detection channels, respectively[39], and the polarization correction factor $G = \frac{\eta_{\parallel}}{\eta_{\perp}}$ accounts for the instrument's polarization dependent transmission where $\eta_{\parallel}$ and $\eta_{\perp}$ are the detection efficiencies of the parallel and perpendicular detection channels (see Supplementary Tab. 3). Note that this approach (eq. S15) is

applicable when the molecule can rotate freely. Minor inaccuracies might thus occur due to the contribution of immobilized and hence partially aligned molecules.

The energy transfer due to FRET increases the relaxation rate of the excited donor fluorophore and thus reduces the excited state lifetime. The rate of energy transfer due to FRET, k_{RET}, depends on the sixth power of the interdye distance R_{DA}[14]:

$$k_{\mathrm{RET}}(R_{\mathrm{DA}}) = \frac{1}{\tau_{D(0)}} \cdot \left(\frac{R_0}{R_{\mathrm{DA}}}\right)^6 \qquad (S16)$$

The interdye distance can thus be measured by the reduction of the fluorescence lifetime of the donor-acceptor labeled sample compared to a sample containing only the donor fluorophore (Donor-only, D0). In the absence of STED, the fluorescence decay of the donor in the presence of the acceptor $f_{D|D}^{(DA)}$ can then be described as:

$$f_{\mathrm{D|D}}^{(\mathrm{DA})}(t) = \int_0^\infty x_{\mathrm{FRET}}(R_{\mathrm{DA}}) \cdot e^{-\left(k_{\mathrm{D0}} + k_{\mathrm{RET}}(R_{\mathrm{DA}})\right)t}\, \mathrm{d}R_{\mathrm{DA}}, \qquad (S17a)$$

where k_{D0} is the deexcitation rate of the donor in the absence of the acceptor and $x_{\mathrm{FRET}}(R_{\mathrm{DA}})$ describes the fraction of molecules with interdye distance R_{DA}. Here, we assume that the dyes rotate fast ($\kappa^2 = 2/3$) but diffuse slowly compared to the fluorescence lifetime. The distribution of interdye distances arising due to the flexible dye linkers can then be described by a normal distribution with width σ_{DA}:

$$x_{\mathrm{FRET}}(R_{\mathrm{DA}}) = \frac{1}{\sqrt{2\pi}\sigma_{\mathrm{DA}}} \cdot \exp\left(-\frac{(R_{\mathrm{DA}} - \langle R_{\mathrm{DA}}\rangle)^2}{2\sigma_{\mathrm{DA}}^2}\right), \qquad (S17b)$$

where $\langle R_{\mathrm{DA}}\rangle = \frac{1}{NM}\sum_{i=1}^{N}\sum_{j=1}^{M} |R_{\mathrm{D,i}} - R_{\mathrm{A,j}}|$ is the mean interdye distance averaged over all possible donor and acceptor positions.

To utilize the full range of the fluorescence decay, we account for the signal from partially depleted molecules using a fast decay component. We describe the fluorescence decay of the donor-only sample $f_{\mathrm{D|D}}^{(\mathrm{D0})}$ with a bi-exponential model:

$$f_{\mathrm{D|D}}^{(\mathrm{D0})}(t) = \overbrace{x_{\mathrm{STED}}^{(\mathrm{D0})} \cdot e^{-k_{\mathrm{D0,STED}}t}}^{\text{Depletion}} + \overbrace{\left(1 - x_{\mathrm{STED}}^{(\mathrm{D0})}\right) \cdot e^{-k_{\mathrm{D0}}t}}^{\text{Donor only}}, \qquad (S18)$$

where k_{D0} is the deexcitation rate of the non-depleted molecules, and $k_{\mathrm{D0,STED}}$ and $x_{\mathrm{STED}}^{(\mathrm{D0})}$ are the de-excitation rate and fraction of partially depleted molecules in the donor-only sample. Analogously, we include a fast decay component in the description of the donor fluorescence decay in the presence of the acceptor:

$$f_{\mathrm{D|D}}^{(\mathrm{DA})}(t) = \overbrace{x_{\mathrm{STED}}^{(DA)} \cdot e^{-k_{\mathrm{D,STED}}t}}^{\text{Depletion}} + \left(1 - x_{\mathrm{STED}}^{(\mathrm{DA})}\right) \cdot$$
$$\left(\overbrace{(1 - x_{\mathrm{noFRET}}) \cdot \int_0^\infty x_{\mathrm{FRET}}(R_{DA}) \cdot e^{-\left(k_{D0} + k_{\mathrm{RET}}(R_{DA})\right)t} \mathrm{d}R_{DA}}^{\text{Gaussian distribution}} + \overbrace{x_{\mathrm{noFRET}} \cdot e^{-k_{D0}t}}^{\text{Donor only}} \right), \qquad (S19)$$

where $k_{\mathrm{D,STED}}$ and $x_{\mathrm{STED}}^{(\mathrm{DA})}$ are the de-excitation rate and fraction of partially depleted molecules in the double-labeled sample, and x_{noFRET} describes the fraction of molecules that lack the acceptor due to bleaching or blinking of ~5-10% (see Supplementary Tab. 9).

For a quantitative analysis, it is crucial to precisely know the de-excitation rate of the donor in the absence of the acceptor k_{D0}. In this work, we take the population of noFRET molecules for the origami and the noFRET sample for the DNA rulers as the donor-only reference. This choice of a reference is preferred to a pure donor-only reference as it allows us to select intact molecules by the presence of the acceptor that is placed outside of the FRET range. To further stabilize the fit, we globally analyzed the donor-only and FRET-induced donor decays by linking the donor-only de-excitation rate k_{D0} but optimizing the STED-related parameters individually. The width of the Gaussian distance distribution was fixed to a value of 6 Å that satisfies benchmark experiments on similar systems[15] and was confirmed for the solution-based FRET measurements of the DNA rulers.

Sub-ensemble fluorescence decays were analyzed with the ChiSurf software package (http://www.fret.at/tutorial/chisurf/)[16] using the iterative re-convolution approach. Model decays are convoluted with the experimental instrument response function (*IRF*). In addition, a constant number of background counts N_{bg} (offset) and contribution of scattered laser counts N_{sc} is considered, according to:

$$F_{\mathrm{exp}}(t) = N_0 \cdot IRF(t) \otimes f(t) + N_{sc} \cdot IRF(t) + N_{bg}, \qquad (S20)$$

where N_0 is the initial intensity of the decay.

The measured data and sub-ensemble fluorescence fits shown in Supplementary Figs. 12 (origami, confocal), 13 (origami, STED) and 20 (DNA ruler, STED), 21 (DNA ruler, confocal). The fit results are compiled in Supplementary Tab. 9.

Determination of spot-integrated fluorescence lifetimes

The intensity-weighted average fluorescence lifetime for single emitters was obtained from a single-exponential tail-fit of the spot-integrated fluorescence decays (part of the histogram after depletion pulse) using maximum likelihood estimation. In general, the measured fluorescence decay pattern is described by a convolution of the instrument response function (IRF) with an exponential decay model function, $f(t)$. In our particular case with an additional STED pulse, the rising and fast dropping parts of decays are not within fit range and, in order to reduce computation time of the model function, the IRF here is replaced by a δ-function (1 channel convolution).

Assuming a single depolarization process, the ideal model functions for the fluorescence decays detected on the parallel and perpendicular detectors are approximated by:

$$f_{\parallel}(t,\tau,\rho) = \frac{f_0}{3} e^{-t/\tau}\left[1 + r_0(2 - 3l_1)e^{-t/\rho}\right] \qquad (S21a)$$

$$f_{\perp}(t,\tau,\rho) = \frac{f_0}{3} e^{-t/\tau}\left[1 - r_0(1 - 3l_2)e^{-t/\rho}\right] \qquad (S21b)$$

where τ denotes the fluorescence lifetime, f_0 is the normalization factor, r_0 the fundamental anisotropy of the fluorophore, ρ is the rotational correlation time and the correction factors l_1, l_2 account for the mixing of the polarizations by the objective[40]. The rotational correlation time, ρ, is related to the steady state anisotropy $\langle r \rangle$, the fundamental anisotropy r_0 and the fluorescence lifetime τ by the Perrin equation:

$$\rho = \tau \left(\frac{r_0}{\langle r \rangle} - 1 \right)^{-1} \qquad (S21c)$$

The final model functions for the parallel and perpendicular signal, $F_\parallel$ and $F_\perp$, are constructed from ideal, area normalized patterns ($f_{\parallel,\mathrm{norm}}$, $f_{\perp,\mathrm{norm}}$) by accounting for the scatter fraction, x_{sc}, of the area normalized stacked scatter decay patterns ($S_{\parallel,\mathrm{norm}}$, $S_{\perp,\mathrm{norm}}$), the polarization correction factor G and the constant background fraction, x_{bg} (see eq. S20):

$$F_\parallel(t;\tau,\rho,\gamma_{sc}) = F_\parallel(0) \cdot \left\{ \left[(1 - x_{sc}) \cdot f_{\parallel,norm}(t;\tau,\rho) + x_{sc} \cdot S_{\parallel,norm}(t) \right] \cdot \left(1 - x_{bg}\right) + x_{bg} \right\} \qquad (S21d)$$

$$F_\perp(t;\tau,\rho,\gamma_{sc}) = F_\perp(0) \cdot \left\{ G \cdot \left[(1 - x_{sc}) \cdot f_{\perp,norm}(t;\tau,\rho) + x_{sc} \cdot S_{\perp,norm}(t) \right] \cdot \left(1 - x_{bg}\right) + x_{bg} \right\} \qquad (S21e)$$

Here, $F_\parallel(0)$ and $F_\perp(0)$ are initial amplitudes, respectively. By the polarization correction factor, G, the detection efficiencies differences in parallel and perpendicular channels were accounted as the fluorescence ratio of parallel channel to perpendicular one ($G = \frac{\eta_\parallel}{\eta_\perp}$ accounts for the instrument's polarization dependent transmission where $\eta_\parallel$ and $\eta_\perp$ are the detection efficiencies of the parallel and perpendicular detection channels). For a detailed model description, see Schaffer et al[39]. The fit function uses a maximum likelihood estimator for Poisson statistics as described previously[17].

As the fit model assumes a single-exponential decay, we obtain the intensity-weighted average fluorescence lifetime, $\langle \tau_{D(A)} \rangle_F$. This quantity, however, contains additional information on the shape of the fluorescence decay by means of the second moment of the lifetime distribution, which can be exploited to detect conformational dynamics on timescales faster that the imaging time[15].

Background photons originate from three sources: i) scattered photons of the excitation laser that leak through the emission filters, which mostly coincide with the rise term of our fluorescence decay; ii) background fluorescence, which can be reduced by working with clean surfaces and was negligible here; and iii) uncorrelated background noise, ***bg***, from detector dark counts or background photons, which is present in our data but predictable. The uncorrelated background signal expected amount scales linearly with the acquisition time and follows a flat pattern (constant x_{bg}).

We estimate the uncorrelated background amount based on the background count rate in an empty surface area (see Supplementary Tab. 14). Overall, the uncorrelated background contribution was low (<1%) for the donor channel and slightly higher (<5%) due to higher dark counts for the acceptor.

Accessible volume simulations

The model of the dsDNA is generated by the Nucleic Acid builder version 04/17/2017 of AmberTools[18]. The accessible volume (AV) is defined by modelling of the dye molecule by a geometrical approach that considers sterically allowed dye positions within a defined linker length from the attachment point with

equal probability (see Supplementary Tab. 6 for the used dye parameters). The AVs are generated using the *FRET positioning and screening (FPS)* software[19]. From the AVs of the donor and acceptor fluorophores, the distance between the mean positions, R_{mp}, the average distance $\langle R_{\mathrm{DA}} \rangle$, the average FRET efficiency $\langle E \rangle$ and the FRET-averaged distance $R_{\langle \mathrm{E} \rangle}$ are obtained (Supplementary Tab. 7 and 8 and Supplementary Fig. 5). We compared these values to the experimentally measured values of the dsDNA rulers.

Error estimation of FRET-derived distances

Fluorescence decay sub-ensemble analysis. To estimate the distance uncertainty of the sub-ensemble fluorescence decay analysis, we performed a parameter scan of the mean interdye distance $\langle R_{DA} \rangle$ while optimizing all other parameters ('support plane analysis'). To determine the confidence intervals, we performed an F-test that compares the best fit (null hypothesis) to the alternate model where $\langle R_{DA} \rangle$ is changed from the optimal value. The confidence interval is obtained from the reduced chi-squared value χ_r^2 where the change compared to the optimal value $\chi_{r,0}^2$ cannot be explained by the loss of a degree of freedom within a certain confidence. The threshold value is determined by the F-test as [20]:

$$\chi^2_{\mathrm{r,threshold}} = \chi^2_{\mathrm{r},0} \cdot \left(1 + \frac{p}{N-p} \cdot F(\alpha, p, v) \right) \qquad (S22)$$

where p is the number of parameters, N is the number of datapoints and $F(\alpha, p, N-p)$ is the inverse cumulative F-distribution with confidence level α, i.e., the value at which the cumulative F-distribution reaches the value α. If not specified otherwise, we report the 95% confidence intervals.

Intensity-based FRET efficiency. Error estimation for the distances obtained from intensity-based FRET efficiencies was performed by propagating the uncertainty of all correction factors as described in Hellenkamp et al.[13]. The assumed uncertainties of the correction factors are summarized in Supplementary Tab. 3.

Colocalization analysis of FRET pairs

The colocalization-STED analysis encompasses three main steps. Firstly, spots are identified and cropped from the larger taken zoomed STED image for the confocal overview image (Fig. 1d). Secondly, the spot is fitted with a single or multiple 2D Gaussians and the best fit is selected based on the likelihood quality criterion. Lastly, the Gaussian center is used to define a spot integration area from which spot intensity and spot lifetime-based FRET parameters are determined (see Supplementary Fig. 6).

Step 1: ROI identification. Spots are identified in the image based on an intensity threshold. First, the data is smoothed with a Gaussian filter to avoid shot noise artifacts. Average background counts range from 0.1 to 0.3 photons / pixel and a threshold of 1 photon / pixel is applied to separate background from signal areas and generate ROIs. The smoothing is only applied for ROI selection, while for further analysis the raw data is used. ROIs that touch image borders or overlay with other ROIs are discarded. ROI identification was done independently for the donor emission upon donor excitation and acceptor

emission upon acceptor excitation. The acceptor emission upon donor excitation was not used for localization as it contains additional signal originating from the donor dye due to crosstalk.

Step 2: Spot localization. The point spread function (PSF) of the STED microscope is modelled by a 2D Gaussian function:

$$G(x,y)_{\mathrm{x_0\ y_o},\sigma_{\mathrm{PSF}},\mathrm{A,bg}} = A \cdot \exp\left[\frac{(x-\ x_0)^2 + (y-y_0)^2}{2\sigma_{\mathrm{PSF}}^2}\right] + A_{bg}, \qquad (S23)$$

where A denotes the amplitude, x_0 and y_0 are the center coordinates of the emitter, σ_{PSF} is the width of the spot (determined by the PSF) and A_{bg} a constant background offset. To fit with a model with multiple spots, multiple single 2D Gaussian models are combined in sum while keeping the width identical for all spots:

$$G_n(x,y)_{\mathrm{x_0\ y_o},\sigma_{\mathrm{PSF}},\mathrm{A,bg}} = \sum_{i=1}^{n} A_i \cdot \exp\left[\frac{\left(x-\ x_{0,\mathrm{i}}\right)^2 + \left(y-y_{0,\mathrm{i}}\right)^2}{2\sigma_{\mathrm{PSF,i}}^2}\right] + A_{bg}, \qquad (S24)$$

where the subscript n indicates the number of 2D Gaussian functions. For the analysis of the double-stranded DNA sample, only a single 2D Gaussian function is fitted per ROI.

To correctly account for the Poissonian statistics of the single photon counting data, we employ a maximum likelihood estimator that provides an unbiased and accurate estimate for the center of a 2D Gaussian spot[21,22]. The probability that a pixel with expectation value λ counts n photons is given by the Poissonian distribution, $\mathcal{L}(n|\lambda) = \frac{\lambda^n}{n!}e^{-\lambda}$. The model function generates a set of expectation values λ_{i} for each pixel based on the model parameters θ, $\lambda_i = f(\theta)$. The likelihood that the model describes image is obtained from the product over all pixels

$$\mathcal{L}(\lambda_i|n_i) = e^{-\Sigma_i \lambda_i} \prod_{\mathrm{i}} \frac{{\lambda_{\mathrm{i}}}^{\mathrm{n_i}}}{n_{\mathrm{i}}!}, \qquad (S25)$$

where n_i is the number of counts in the i-th pixel. Rather than calculating the likelihood, the log-likelihood is easier to calculate:

$$\ell(\lambda_i|n_i) = \ln \mathcal{L}(\lambda_i|n_i) = \sum_i (-\lambda_i + n_i \ln \lambda_i - \ln(n_i!)). \qquad (S26)$$

The optimal model parameters are obtained by maximizing the objective function $\ell(\lambda_i|n_i)$. An implementation of the Broyden-Fletcher-Goldfarb-Shanno algorithm is used to find the best solution[23]. This algorithm is based on a quasi-Newtonian that handles many fit parameters well.

The absolute value of the likelihood or log-likelihood is usually not very informative to assess the goodness of the model. A more useful number is obtained by normalizing the likelihood with respect to the likelihood of the best possible model, which is given by the model that is equal to the data itself. This results in the $2I^*$ value[17,24]:

$$2I^* = -2 \ln\left(\frac{\mathcal{L}(\lambda_i|n_i)}{\mathcal{L}(n_i|n_i)}\right) = -2\left(\ell(\lambda_i|n_i) - \ell(n_i|n_i)\right). \qquad (S27)$$

Similar to the χ^2 value for Gaussian error distributions, the 2I* value is always positive, and a lower value is indicative of a better fit. For Gaussian errors, the 2I* value converges to the χ^2 value. The log-likelihood

can be used to obtain confidence intervals for model parameters θ, by calculating the normalized likelihood, or probability density function (pdf):

$$p(\theta) = \frac{\exp(l(\theta))}{\int \exp(l(\theta))\, d\theta}. \qquad (S28)$$

Step 3: Spot stoichiometry in the multi-spot analysis. For the DNA origami and hGBP1 measurements, we additionally estimated the spot stoichiometry by counting the number of emitters in the donor and acceptor channels (Supplementary Fig. 2). We consider up to three spots per ROI for the analysis of the donor and acceptor images. To estimate the most likely number of emitters, the best model is selected based on the 2I* value. An absolute 2I* penalty of 0.03 for each spot was imposed to account for the additional fitting parameters. For the DNA origami measurements, we selected only intact constructs carrying all four dyes to remove partially labelled or others dimerized/aggregated structures. For the hGBP1 measurements, only ROIs with at least one donor and acceptor spot were considered for further analysis.

Predicting the localization precision

MLE supplies an estimate for the uncertainty of the fit parameters. Importantly, the uncertainty in the spot location is given in detail by[21]:

$$Var(x_0) = Var(y_o) = \frac{{\sigma_a}^2}{N} \cdot \left(1 + \int_0^1 \frac{\ln t}{1 + t/\xi}\, dt\right)^{-1}, \qquad (S29)$$

where ${\sigma_a}^2 = \sigma_{PSF}^2 + a^2/12$ is the pixelation broadened spot width, a is the pixel size and σ_{PSF} the fitted width of the Gaussian PSF. ξ represents the signal to noise ratio and is given by $\xi = 2\,\pi\,{\sigma_a}^2 bg/(N\,a^2)$, where N is the total amount of photons in the spot. The first term is the general expression for the mean of a distribution sampled N times, while the second term in brackets adds a noise penalty. The computed and the experimental localization precisions are compiled in Supplementary Tab. 5. The experimental data (background and spot sizes) are shown in Supplementary Figs.17 (origami), 25 (DNA ruler) and 29 (hGBP1).

Model-based analysis of localization-based distance distributions

The distribution of interdye distances d_{loc} between two fluorophores D and A whose position follows a normal distribution with localization precisions $\sigma_{loc,D}$ and $\sigma_{loc,A}$, respectively, is given by a non-central χ-distribution with two degrees of freedom:

$$P_\chi\left(d_{\mathrm{loc}} | R_{\mathrm{mp}}^{\mathrm{loc}}, \sigma_\chi\right) = \left(\frac{d_{\mathrm{loc}}}{\sigma_\chi^2}\right) \cdot \exp\left(-\frac{d_{\mathrm{loc}}^2 + {R_{\mathrm{mp}}^{\mathrm{loc}}}^2}{2\sigma_\chi^2}\right) \cdot \mathrm{I}_0\left(\frac{d_{\mathrm{loc}} R_{\mathrm{mp}}^{\mathrm{loc}}}{\sigma_\chi^2}\right) \qquad (S30)$$

where $R_{\mathrm{mp}}^{\mathrm{loc}}$ is the mean-position distance between the fluorophores and $I_0(x)$ is the modified Bessel function of zero-th order[25,26]. The width parameter σ_χ is determined by the combined localization

precision and additional registration error, $\sigma_\chi = \sqrt{\sigma_{\mathrm{loc,D}}^2 + \sigma_{\mathrm{loc,A}}^2 + \sigma_{\mathrm{reg}}^2}$.[25] For large distances compared to the localization uncertainty (i.e., $R_{\mathrm{mp}}^{\mathrm{loc}} \gg \sigma_\chi$), the distribution approaches a normal distribution. However, if the mean-position distance is on the scale of the localization uncertainty ($R_{\mathrm{mp}}^{\mathrm{loc}} \approx \sigma_\chi$), the distribution becomes highly asymmetric. In addition, it becomes difficult to fit both the location parameter $R_{\mathrm{mp}}^{\mathrm{loc}}$ and the scale parameter σ_χ simultaneously because they are highly correlated. As a result, the shape of the distribution is mainly determined by the scale parameter σ_χ but becomes insensitive to $R_{\mathrm{mp}}^{\mathrm{loc}}$. Niekamp et al. propose that the σ_χ should be fixed to obtain meaningful results for the mean-position distance[25]. As the number of occurrences in a bin is governed by Poisson statistics, maximum likelihood estimation is used to find the optimal model fit parameters[24]. All data are compiled in Supplementary Tab. 12.

Alignment and particle averaging for origami measurements

Particle averaging is a powerful tool to enhance the precision of measurements. However, it requires that molecules from a single molecular species are selected, as the inclusion of other molecular species is detrimental to the result. Here, a single molecular species is obtained in two steps. Firstly, we select only molecular assemblies with two emitters in the donor channel and two emitters in the acceptor channel using the spot stoichiometry. Secondly, we align the four positions to a reference structure and select only those that have a good overall alignment with the reference structure, as described below.

All molecular assemblies were first rotated such that the two donors are at the top. This step enables to identify the NF pair (D1 and A1) on the left and the HF pair (D2 and A2) on the right. In addition, local minima in the fine alignment are avoided where the structures are rotated by 180 degrees. As the biotin anchors are situated on the opposite side of the fluorophores, the classification into the NF and HF pairs was unambiguous. Our alignment procedure can be classified as a case of Procrustes analysis, where the sample is translated and rotated, but not stretched. This problem is linear and can be solved directly using the Kabsch algorithm[27]. An implementation in the Python programming language was used (http://github.com/charnley/rmsd). The Kabsch algorithm minimizes the root-mean-square-displacement (RMSD), which is defined as

$$RMSD_i = \sqrt{\frac{1}{4}\sum_{\mathrm{j}\in\mathrm{S}} \left(x_{\mathrm{i,j}} - x_{\mathrm{ref,j}}\right)^2 + \left(y_{\mathrm{i,j}} - y_{\mathrm{ref,j}}\right)^2}\,;\; S = \{D1, D2, A1, A2\}, \qquad (S31)$$

where $x_{\mathrm{i,j}}$ and $y_{\mathrm{i,j}}$ indicate the position of dye j in construct i and $x_{\mathrm{ref,j}}$ and $y_{\mathrm{ref,j}}$ indicate the position of the dye in the reference structure. The RMSD is a useful criterion to assess how well the structures align overall (as used to filter outliers for the origami measurements, see Supplementary Fig. 9). It is possible to calculate the best possible RMSD when one considers photon noise as the only source of imprecision. For a single localization the precision can be calculated from spot brightness, spot width and signal-to-noise level (see section 'Predicted localization precision'). For completely labelled origamis, the average predicted localization precision for the donors was 1.7 nm and for the acceptors 1.1 nm. The RMSD score takes the Cartesian norm over all four positions, resulting in a lower estimate for the RMSD of 2.8 nm (see Supplementary Fig. 17 for an overview of the experimental localization precisions). The

higher experimental RMSD of ~4.5 nm is due to structural heterogeneities of the DNA origami platform, matching the variation in platform sizes observed in TEM imaging (Supplementary Fig. 8). In addition, simulations have shown a high flexibility of the DNA origami[28,29]. See Supplementary Note 3 for a detailed discussion of the localization precision for the DNA origami measurements and potential error sources.

If pre-knowledge of the structure of the molecular assembly is available, one could in principle enforce a given symmetry *a priori* by the choice of an external reference structure. Here, to avoid any *a priori* assumptions, we instead select an internal reference structure from the dataset itself. Here we consider all completely labelled origami platforms with two donor and two acceptor dyes as potential reference structures. For each reference structure, the mean RMSD was calculated over al structures that have RMSD lower than 20 nm and only reference structures where more than 80 structures have RMSD lower than 20 nm are considered. This is done to avoid broken structures polluting the interpretation of the mean RMSD. The lowest scoring candidate was selected as the best reference structure.

The average origami structure is calculated straightforwardly by taking the mean position of all measured structures:

$$\bar{x_j} = \frac{1}{N}\sum_{i=1}^{N} x_{i,j} \qquad \bar{y_j} = \frac{1}{N}\sum_{i=1}^{N} y_{i,j} \tag{S32}$$

where j indicates the dye label as before and the superscript bar denotes the average structure.

The uncertainty in the average structure is taken as the standard error of the mean (SEM):

$$SEM_{\bar{x}_j} = \sqrt{\frac{1}{N(N-1)}\sum_{i=1}^{N}(x_{i,j} - \bar{x_j})^2} \qquad SEM_{y_j} = \sqrt{\frac{1}{N(N-1)}\sum_{i=1}^{N}(y_{i,j} - \bar{y_j})^2} \tag{S33}$$

The origami model and the mean origami position are aligned such that their center-of-masses (COM) and acceptor-acceptor distance unit vector align. The center-of-mass is calculated by weighing each point equally:

$$x_{com} = \frac{1}{4}\sum_{j\in S} x_j\,; \qquad y_{com} = \frac{1}{4}\sum_{j\in S} y_j \tag{S34}$$

The coordinate system is rotated such that the x-axis matches the strands direction of the origami platform for Fig. 2a-d of the main text. For Fig. 2e, the mean acceptor-acceptor distance has been aligned with the x-axis such that the Cartesian distances are more spread out over the axis and can be represented in a single plot.

Assessing the diameter of hGBP1 fibers

To estimate the fiber diameter, we selected structures that showed uniform ring borders from measurements of labelled hGBP1-wt diluted with hGBP1-wt in a ratio of 1:10 (see Fig. 6b, c). Images were deconvolved with Huygens Professional version 20.04 (Scientific Volume Imaging, The Netherlands, http://svi.nl), using the CMLE algorithm, with SNR:10 and 40 iterations. To determine the

fiber width, multiple line profiles across the fiber were drawn and the full width at half maximum (FWHM) was measured. An average fiber diameter of 73 ± 4 nm was obtained (Supplementary Fig. 28). We observed similar fiber diameters for hGBP1 polymers constituted of labelled Cys8 hGBP1-18-577.

Transmission electron microscopy

Transmission electron microscopy was performed on a JEM-2100Plus (JEOL Ltd., Tokyo, Japan) operating in bright-field mode at 80 kV acceleration voltage. Samples were prepared by applying 7 microliters of the respective aqueous sample dispersion on carbon-coated copper grids (200 mesh, Science Services) for 1 minute. After blotting, grids were placed on a drop of 3% uranyl acetate solution and immediately blotted. Then, the grid was placed again on another drop of uranyl acetate solution, this time for 30 seconds. After blotting the grid was dried for 20 minutes. The dimensions of the DNA origamis were determined using the image analysis software ImageJ (see Supplementary Fig. 8 for exemplary TEM images of the DNA origami platform and the size estimation of the DNA origami by TEM).

Atomic force microscopy

AFM measurements were performed on a NanoWizard 4 (JPK Instruments AG, Germany) equipped with a temperature regulated liquid cell and using Sharp Nitrile Lever (Bruker, USA) probes. The softest of the four cantilevers (position D) was used. The spring constant was determined as k = 0.04 N/m using the thermal noise method in both air and PBS buffer. Samples were immersed in PBS buffer at 25 °C and equilibrated for 20 min before approaching the probe. The AFM was operated in the quantitative imaging (QI) mode[30], a high-resolution force mapping method, with a setpoint force of 0.5 nN. The standard scan size was 500 nm × 500 nm at a resolution of 512 × 512 px. To characterize the functionalized surfaces over a wide distance range, we took 5 representative images and logarithmic spacing with respect to the origin of the first image (0 µm) for BSA (1, 10, 40 1000 µm) and for PEG (10, 40 ,1000 and 1010 µm). The JPK SPM Data Processing software (v.6.1.142) was used to process the obtained force curves. Briefly, the curves were smoothed and adjusted for baseline offset and slope. The z-position at a force of 50 pN was defined as height and the slope of the last 4 nm of the extend segment was fitted for hardness information. The generated height and slope maps were flattened by 2nd order line levelling and single pixel outliers were removed by interpolation from the surrounding pixel values. Representative images for all conditions are shown in Supplementary Fig. 23.

Solution-based confocal single-molecule spectroscopy with multiparameter fluorescence detection

Single-molecule FRET experiments with pulsed interleaved excitation (PIE) [31] were performed on a homebuilt confocal fluorescence microscope as described previously[32]. The fluorescent donor molecules were excited by a pulsed white light laser source (SuperK Fianium FIU-15 with spectral filter SuperK Varia, NKT Photonics) at 530 nm, operated at 19.5 MHz using a power of 80 µW at the sample. The acceptor molecules are excited by a pulsed diode laser (LDH-D-C 640) operated at 19.5 MHz with

8 µW. The laser light is guided into the epi-illuminated confocal microscope Olympus IX71 (Olympus, Hamburg, Germany) by dichroic beam splitter F68-532_zt532/640NIRrpo (AHF, Germany) focused by a water immersion objective (UPlanSApo 60x/1.2W, Olympus Hamburg, Germany). The emitted fluorescence is collected through the objective, spatially filtered using a pinhole with 100 µm diameter, split into parallel and perpendicular components via a polarizing beam splitter cube (VISHT11, Gsänger Optoelektronik, Germany) and spectrally split into donor and acceptor channel by a dichroic mirror (T640LPXR, AHF, Germany). Fluorescence emission was filtered (donor: 47-595/50 ET, acceptor: HQ 730/140, AHF, Germany) and focused on avalanche photodiodes (SPCM-AQRH-14-TR, Excelitas). The detector outputs were recorded by a TCSPC module (HydraHarp 400, PicoQuant, Berlin, Germany), using a time resolution of 2 ps. All samples were measured in Nunc chambers (Lab-Tek, Thermo Scientific) with 500 µL sample volume and a concentration of ~50 pM.

Data analysis was performed using home-written LabView software that was developed in the Seidel lab and is described in[32]. It is available upon request on the homepage of the Seidel group (https://www.mpc.hhu.de/software.html). Single-molecule events were identified using a burst search algorithm according to[33] using a Lee filter, a threshold of 0.2 ms and a minimum of 60 photons per burst. Double labelled species were selected via a stoichiometry cut between S=0.3 to S=0.7. See Supplementary Fig. 12 for the measurements of the DNA origami sample, Supplementary Fig. 20 for the DNA ruler and Fig. 6 in the main text for the hGBP1 sample.

Supplementary Notes

Supplementary Note 1: Detailed analysis workflow

Image and fluorescence spectroscopy analysis was performed using home-built software (ANI software and SEIDEL software, respectively) that follows a joint workflow summarized in Supplementary Fig. 6 (the capital letter references in this note refer to the respective panels in the flowchart). In step A, the raw photon data is separated into the donor channel (detected signal in the donor channel after donor excitation), FRET-sensitized acceptor channel (detected signal in the acceptor channel after donor excitation) and acceptor channel after direct excitation (detected signal in the acceptor channel after acceptor excitation) (see Supplementary Fig. 1a and Supplementary Fig. 3)[34]. The images are then segmented into regions of interest (ROIs) for spot fitting (step B1). A Gaussian filter is applied to smooth shot noise and the image is segmented using an intensity threshold. Both an upper and lower threshold criterion can be applied to reject dirt (higher threshold) or increase sensitivity to weak signals (lower threshold). All further analysis is done using the raw data. Next, the intensity data of each ROI is fitted to 2D Gaussian functions (B2). In the single-spot analysis used for the dsDNA sample, spots are fitted to a single 2D Gaussian function (ANI software) and the spot width and localization precision are estimated (B3-4, left). In the multi-spot analysis, multiple 2D Gaussian functions (SEIDEL software) are fitted and the number of spots is determined based on the log-likelihood value while applying a penalty for overfitting (see section 'Spot stoichiometry', B3-4, right). For both approaches, spot centers are used to define the integration area to obtain the spot fluorescence decay and intensity (C1, see also Supplementary Fig. 4). Localization is performed on time-gated data, whereas FRET-informative photons are collected based on ungated data. Analysis settings for each step are reported in Supplementary Tab. 14 and 15. Spots of donors and acceptors are paired (C2) to gain access to intensity-based FRET indicators, such as the FRET efficiency, stoichiometry, and localization-based interdye distance (C3). Dyes are paired by first selecting the pair with the smallest distance and removing them from the available set. This is repeated until there are either no more donors or acceptors available. Supplementary Tab. 17 lists all available spectroscopic and localization parameters. Available FRET and localization-based indicators are used to select a sub-ensemble for further analysis in the filtering step (D and see *'Filtering procedures'*). For quantitative FRET analysis, the lifetime decay histogram is created by accumulating lifetime decays from spots in the sub-ensemble (F1) and fitted in the Chisurf software package (F2)[16]. For the single-spot analysis, the localization-based interdye distance distributions can be analyzed by two approaches: model-based maximum likelihood fitting (E1) or model-free analysis by the maximum-entropy method (MEM) (E2). For the multi-spot analysis, the structures of interest are aligned, and particle averaging is performed (E3). The advantage of the latter approach is that it uses both x- and y-coordinate, whereas the other two use only the norm of the distance vector.

Supplementary Note 2: Estimation of structural parameters of the DNA origami platform

The origami platform is modelled as a rectangular grid that is parametrized by the rise per base pair along the long axis (y) and the interhelical distance along the short axis (x). To avoid potential errors due to the rotation of the dye attachment point around the helical axis, the dyes are attached such that all of them are located at the same position along the helical turn (see Supplementary Fig. 7 for details on the dye attachment). Here, we assume no interaction of the dye with the origami platform. Hence, the mean positions of the dyes are assumed to correspond to the xy-positions of the attachment points. The distances between the dyes in terms of the structural parameters of the DNA origami platform can then be expressed as:

$$\mathrm{d}_{ij} = \sqrt{\left(n_{\mathrm{bp,ij}} d_{\mathrm{bp}}\right)^2 + \left(n_{\mathrm{h,ij}} d_{\mathrm{h}}\right)^2}; \quad i,j \in \{D1, D2, A1, A2\} \tag{S35}$$

where d_{ij} is the distance between dyes i and j, d_{bp} and d_{h} are the rise per base pair and the interhelical distance, and $n_{\mathrm{bp,ij}}$ and $n_{\mathrm{h,ij}}$ are the number of base pairs and helices between the dyes. In the global alignment procedure, we are not only measuring the distance between the dyes but instead resolve their relative displacement as xy-coordinate pairs. In the coordinate frame of the DNA origami nanostructure (Fig. 2b and Supplementary Fig. 7), the displacements are defined as:

$$x'_{\mathrm{ij}} = n_{\mathrm{bp,ij}} d_{\mathrm{bp}} \tag{S36}$$

$$y'_{\mathrm{ij}} = n_{\mathrm{h,ij}} d_{\mathrm{h}} \tag{S37}$$

As the rotation of the whole structure is arbitrary, for display purposes it may be either rotated such that the helices are perpendicular to the x-axis (fig 2b-d) or such that the A1A2 vector lies parallel to the x axis (fig 2e). The angle of rotation is given by the angle ξ of the A1A2 vector with respect to the helical axis (x-axis in the origami frame of reference):

$$\tan \xi = \frac{y_{\mathrm{A1A2}}}{x_{\mathrm{A1A2}}} \tag{S38}$$

The coordinate transformation to the experimental coordinate frame is then performed by counterclockwise rotation:

$$\begin{pmatrix} x \\ y \end{pmatrix} = \begin{pmatrix} \cos\xi & -\sin\xi \\ \sin\xi & \cos\xi \end{pmatrix} \begin{pmatrix} x' \\ y' \end{pmatrix} \tag{S39}$$

The measured distances, xy-displacements, their associated uncertainties, and the values for n_{bp} and n_{h} for the different dye pairs are given in Supplementary Tab. 18. The model parameters d_{bp} and d_h are fitted by minimizing the chi-squared value χ^2 assuming normally distributed errors in the x- and y-directions, σ_x and σ_y, defined by:

$$\chi^2 = \sum_{i,j} \frac{\left(x_{ij} - x_{ij,meas}\right)^2}{\sigma_x^2} + \frac{\left(y_{ij} - y_{ij,meas}\right)^2}{\sigma_y^2}; \quad i,j \in \{D1, D2, A1, A2\} \tag{S40}$$

To estimate the confidence intervals of the structural parameters, we performed a parameter scan of the χ^2 surface. The confidence interval was obtained by considering the χ^2 distribution. To this end, the

number of degrees of freedom in our fit must be determined. There are four average points, each having an x- and y-coordinate, totaling eight observables. During the alignment first the center of mass of the structure is set equal to the center of mass of the alignment anchor, using two degrees of freedom for (x,y). Next, the rotation of the structure is set to minimize the RMSD. The rotation is parametrized by a single value (i.e., the angle) and uses one degree of freedom. Thus, after the alignment procedure, five independent observables are left. As the fit has two parameters, three degrees of freedom are left. The reduced chi-squared value χ^2_{red} is then obtained as $\chi^2_{red} = \chi^2/3$.

Supplementary Fig. 11 shows the support plane describing the certainty for interhelical distance and average base pair extension. For three degrees of freedom the statistical variance of a good fit is very large (Supplementary Fig. 11b) such that a good model is 95% likely to have χ^2_{red} values within [0-2.60]. The χ^2_{red} value for the fit with the highest probability is 0.73, indicating that the model fits the data within the certainty interval. Consequently, the 95% confidence interval on model parameters is obtained from all models whose χ^2_{red} falls in the 95% likelihood range.

The obtained interhelical distance is 2.41 nm (68% conf. interval 2.30-2.55 nm) and the average extension of 236 base pairs is 75.0 nm (68% conf. interval 74.2-75.8 nm), corresponding to a rise per base pair of 0.318 nm. We also estimated the rise per base pair solely from the acceptor-acceptor distances (see Supplementary Fig. 10), which yielded a similar distance of 74.8 ± 0.3 nm for 236 base pairs and a corresponding rise per base pair of 0.317 nm.

Supplementary Note 3: Discussion on error sources in origami samples

We calculate the localization precision for the origami datasets based on photon statistics alone to be 2.0 nm for the O(HF+NF) sample, 3.0 nm for the O(NF) sample, and 4.6 nm for the O(HF) sample (see Supplementary Fig. 17 for the spot-wise histograms of the localization precision). The O(HF+NF) sample has the lowest uncertainty due to photon statistics as more frames were accumulated. The estimated localization precision is systematically found to be smaller than the width of the localization-based interdye distance distributions of 7.4 nm for the $O(HF+NF)_{NF\ cut}$ population, 3.4 nm for the $O(HF+NF)_{HF\ cut}$ population, 7.4 nm for the O(NF) sample, and 5.8 nm for the O(HF) sample (see Supplementary Fig. 13 e-h for the distance distributions). This could indicate an additional error contribution due to aberrations. However, we argue that the additional broadening is primarily caused by molecule-to-molecule variations and that the true experimental localization precision is close to the fundamental limit based on the photon statistics. This argument is supported by the occurrence of two distinct populations in the acceptor-to-acceptor distance distributions, which show a narrow and a broad peak centered around the same mean value (see Supplementary Fig. 10a), indicating that small structural defects occur for a fraction of the origami platforms. The same effect should be expected for smaller distances. However, as the distances are on the order of the localization precision, the structural heterogeneity shows mostly as a peak-broadening due to the properties of the χ-distribution (see section 'Model-based analysis of localization-based distance distributions' in the Supplementary Methods). Interestingly, we also occasionally observe very sharp sub-populations in the distance distributions (Supplementary Fig.

13g), which are unlikely to occur by chance and indicate that the localization precision is limited by the structural variation of the sample.

Supplementary Note 4: Discussion of discrepancy between localization and FRET distances for origamis

We observed a discrepancy between the localization-based and FRET-based estimates of the interdye distance for the high-FRET dye pair on the origami nanostructures. The R_{mp}^{FRET} for the origami O(HF) pair has been measured using confocal single-molecule spectroscopy and STED nanoscopy to be in the range 72-75 Å using the intensity and lifetime information (Supplementary Tab. 13). The high amount of consistency between solution-based FRET experiments and FRET nanoscopy indicates the capability of FRET nanoscopy to infer accurate distances from the spectroscopic information. On the other hand, the localization-derived distance R_{mp}^{loc} was found to be 53 ± 7 Å as obtained using the global alignment procedure (Supplementary Tab. 18). Additional localization-based distances can be obtained from fitting non-centered χ-distributions (Supplementary Fig. 13 g and h). However, this data provided much lower accuracy due to contribution of broken constructs which could be removed by the global alignment procedure using the RMSD criterion and the unfavorable properties of the χ-distribution. We thus do not consider these results for the further discussion. From the position of the dye attachment points on the origami structure (Supplementary Fig. 7), it is predicted that the interdye distance corresponds to twice the interhelical distance. Using the value obtained in this work, we thus expect an interdye distance of 48 ± 2 Å (Supplementary Fig. 11). This indicates a clear mismatch between the FRET-derived and the predicted distance.

Single-molecule studies revealed an increased acceptor anisotropy for the origami sample compared to the dsDNA rulers (see Supplementary Fig. 14 and Supplementary Tab. 11), which indicates sticking of the dyes due to specific interactions with DNA backbone or bases. Recently, Hübner et al[35]have shown that the dye Atto647N used in this work tends to stick between the helices of the DNA origami platform. Their study was performed on an origami platform identical to ours, with the only exception that our linker includes an additional unpaired thymine base. The increased anisotropy was only observed for the origami sample with a rotational correlation time of 10 ns, while for the DNA ruler a significantly shorter rotational correlation time of 2 ns was obtained that indicates the absence of sticking interactions (Supplementary Fig. 14). This suggests that the dye-DNA interaction is facilitated by the close proximity of the DNA helices in the origami nanostructure. On the other hand, the donor dye does not exhibit different anisotropies between the dsDNA and origami environment and free rotation can be assumed.

Accurate FRET distances are obtained under the assumption that dyes can freely rotate, such that the κ^2 value used for the calculation of the Förster radius equals 2/3. However, this assumption no longer holds when the dye is stuck in a specific orientation and the real distance can be larger or smaller depending on the mutual orientation of the transition dipole moments of the donor and acceptor dyes. It is possible to estimate the error on the FRET distance by computing minimal and maximal κ^2 values given anisotropy values for the donor and acceptor[36] and propagating this error into the uncertainty of R_{DA}. Here we integrate over the possible orientations of the donor and acceptor transition dipole moments subject to constraints given by the measured residual anisotropies (Supplementary Tab. 11)

to predict the mean and variance of the κ^2 distribution. These simulations were performed using the ChiSurf software package (https://github.com/Fluorescence-Tools/chisurf)[16]. κ^2 is found to be in the range [0.33, 1.03] with a mean of 0.63, resulting in an estimated Förster radius of 75.8 Å with an uncertainty of ± 6 Å. We propagate the uncertainty of the Förster radius to the FRET-derived mean positions distance based on the sub-ensemble fluorescence decay analysis of 73 ± 3 Å (Supplementary Fig. 13d, Supplementary Tabs 9 and 13), yielding a final estimate of $R_{\mathrm{mp}}^{\mathrm{FRET}}$ from the $\mathrm{O(HF+NF)_{highFRET}}$ cut sub-ensemble fit of 72 ± 7 Å.

Based on the measured mean-position distances from the localization of $R_{\mathrm{mp}}^{\mathrm{loc}}$ = 53 ± 7 Å and FRET of $R_{\mathrm{mp}}^{\mathrm{FRET}}$ = 72 ± 7 Å, corresponding to the projected distance in the xy-plane and the isotropic distance, respectively, we can estimate the corresponding z-displacement between the donor and acceptor fluorophore, R_z, using the Pythagorean theorem according to:

$$R_z = \sqrt{R_{\mathrm{mp,FRET}}^2 - R_{\mathrm{mp,loc}}^2} \qquad (S41)$$

We thus estimate a predicted z-displacement R_z of 50 ± 12 Å from the experimental measurements of the projected and isotropic distances.

The proposed three-dimensional arrangement of the dyes on the origami nanostructure is schematically displayed in Supplementary Fig. 15. The acceptor is positioned between the helices, while the donor is pointing upwards away from the origami surface. The acceptor fluorophore (red) is stuck between two helices pointing away from the donor fluorophore, while the donor fluorophore (orange) is free to diffuse and rotate. The mean position of the donor (orange circle) in its AV (light orange) is assumed to be slightly tilted towards the acceptor position to satisfy the localization-based distance $R_{\mathrm{mp}}^{\mathrm{loc}}$ of 53 Å, which is shorter than the distance expected for a distance of 2.5 helices of 60 Å based on an interhelical spacing of 24 Å as determined from the global alignment. The estimated z-displacement R_z between the fluorophores of 50 Å matches the length of the dye linker of ~29 Å plus the diameter of the DNA helix of ~20 Å. Correspondingly, the acceptor is assumed to penetrate through the interhelical space, placing its center on the lower side of the origami.

Supplementary Note 5: Assessment of sticking/unsticking dynamics of dsDNA rulers during acquisition

To assess the occurrence of sticking/unsticking dynamics during the acquisition time (i.e., “jumping” of one end of the DNA rulers), we performed repeated localizations over the course of the measurement. We used the single- and double-biotin dsD(NF) sample due to the absence of energy transfer between the dyes. We recorded 60 frames in total, split the measurement into four intervals 15 frames each, and selected only those molecules, which had sufficient signal in all frame intervals to exclude photobleaching by requiring at least 50 photons both in the donor and acceptor channels. In addition, only molecules with an interdye distance (as estimated from all 60 frames) of less than 30 nm were considered. Each frame interval was processed using the cSTED workflow, yielding the xy-coordinates of the center position of the donor and acceptor and the interdye distance. We visualize the distance

vector of each frame interval in a Cartesian plot (Supplementary Fig. 22a). No large jumps were observed and the localizations from the four frame intervals are found to cluster in one region of the plot, indicating that there are no “jumps” during the measurement for both the single-biotin and double-biotin samples.

We additionally quantify the fluctuations of the localization σ_{dyn} from the standard deviations of the localizations in the x- and y-directions ($\sigma_{\mathrm{dyn,x}}$ and $\sigma_{\mathrm{dyn,y}}$) as:

$$\sigma_{\mathrm{dyn}} = \sqrt{\sigma_{\mathrm{dyn,x}}^2 + \sigma_{\mathrm{dyn,y}}^2} \qquad (S42)$$

Similar distributions of σ_{dyn} are observed for the single-biotin and double-biotin samples, indicating that no large jumps occur for either immobilization strategy (Supplementary Fig. 22). If jumping were to occur during the measurement, a high value for σ_{dyn} should also be correlated with the observation of a seemingly shorter colocalization based interdye distance. However, no correlation is observed between the parameter σ_{dyn} and the colocalization-based interdye distance and identical distance distributions are obtained for large and small values of σ_{dyn}. In the absence of dynamics, σ_{dyn} effectively measures the localization precision for an acquisition time of 15 frames. Indeed, the estimated values for σ_{dyn} are close to the shot-noise limited localization precision of ~6 nm for the reduced number of photons collected over the shorter acquisition time, indicating that the spread of the repeated localizations is primarily caused by the localization error.

Supplementary Note 6: Analysis of dsDNA ruler distance distributions by the maximum entropy method

The maximum entropy method (MEM) is an approach to extract the most unbiased distribution of a given parameter that provides a satisfactory fit to the experimental data[37-39]. Instead of minimizing the reduced chi-square, χ_{r}^2, the following functional is maximized:

$$\Theta = vS - \chi_{\mathrm{r}}^2 \qquad (S43)$$

where v is a constant scaling factor and S is the entropy functional of the parameter distribution. The entropy is defined by:

$$S = -\sum_i p_i \log \frac{p_i}{m_i} \qquad (S44)$$

where p_i describes the distribution of the parameter of interest and m_i describes the prior knowledge of the distribution. Since we have no prior knowledge, we use a flat prior in the analysis.

We describe the experimental histograms of the colocalization distance $H(d_{loc})$ as a superposition of non-central χ-distributions P_χ as defined in the section ‘Colocalization analysis’ (eq. S30) with fixed width parameter σ_χ:

$$H(d_{\mathrm{loc}}) = \sum_i p\left(R_{\mathrm{mp}}^{\mathrm{loc,(i)}}\right) \cdot P_\chi\left(d_{loc} \middle| R_{\mathrm{mp}}^{\mathrm{loc,(i)}}, \sigma_\chi\right) \qquad (S45)$$

where the set of kernel functions $\left\{P_\chi\left(d_{\mathrm{loc}}\middle|R_{\mathrm{mp}}^{\mathrm{loc,(i)}},\sigma_\chi\right),\ i=1\ldots N\right\}$ is defined over the mean-position distance $R_{\mathrm{mp}}^{\mathrm{loc}}$. Here, we used a fixed value of σ_χ = 4.4 nm that was estimated from the distribution of acceptor-acceptor distances for the origami data (see Supplementary Fig. 10).

The reduced chi-squared χ_r^2 is then defined as:

$$\chi_{\mathrm{r}}^2=\frac{1}{K}\sum_k\frac{1}{w_k^2}\left(H\left(d_{\mathrm{loc}}^{(\mathrm{k})}\right)-M\left(d_{\mathrm{loc}}^{(\mathrm{k})}\right)\right)^2 \qquad (S46)$$

where M is the measured histogram, K is the number of bins on the histogram and w_k are the weights of data points given by $w_k=\sqrt{M\left(d_{\mathrm{dloc}}^{(\mathrm{k})}\right)}$ for Poisson counting statistics.

Maximization of Θ is performed as described in Vinogradov and Wilson[40] over a wide range of values for the regularization parameter v. The choice of the regularization parameter v was done by visual inspection of the L-curve plot of the negative entropy $-S$ against the reduced chi-squared χ_{r}^2, which provided a more robust selection of v compared to corner detection algorithms[41]. The visual analysis yielded a value of $v=0.1$ that was used for all analyses of the DNA ruler datasets (see Supplementary Fig. 18).

Supplementary Note 7: Model-based analysis of colocalization distance histograms of dsDNA rulers

In addition to the maximum entropy-based analysis, we also performed a model-based analysis of the distance distribution obtained for the dsDNA rulers (see section 'Colocalization analysis' in the Supplementary Methods). However, as no reliable distance estimates could be obtained, we preferred the model-free approach employing the maximum entropy method to infer the underlying distance heterogeneity.

Neither the single-biotin nor the double-biotin samples could be described by a single-component χ-distribution model function using the theoretically predicted localization precision based on the photon statistics, corresponding to a width parameter σ_χ of 4 nm. We thus reasoned that the single-biotin sample experiences excess heterogeneity due to partial sticking to the surface that would lead to a larger effective width of the distance distribution. Indeed, by letting the width σ_χ vary, we could achieve a good fit for all single-biotin samples (Supplementary Tab. 12), with mean-position distances R_{mp} close to zero as would be expected for a singly immobilized DNA ruler. We also tested a single-component model for the description of the broad distance distributions obtained for the double-biotin samples, which provided a poor fit but captured the trend of increasing distances with larger dye separation.

The observation of short colocalization-based distances for the double-biotin sample indicates a potential contamination by singly immobilized molecules, which could be as high as 60% as discussed in Supplementary Note 8. We thus assumed that a fraction of the molecules is immobilized only on one end and behaves like single-biotin molecules. The remaining fraction of molecules are assumed to be immobilized on both ends, thus lying flat on the surface and exhibiting shot-noise limited broadening of the distance distribution (σ_χ = 4.4 nm). While the fit provided a good description of the data, the

determined distances for the doubly immobilized population showed large deviations from the expected mean-position distances (Supplementary Tab. 12). We also considered an equivalent model where we allowed the width of the doubly immobilized population to vary, which was also unable to provide reliable distances.

Supplementary Note 8: Estimation of surface roughness and neutravidin density on functionalized surfaces

To immobilize molecules on the surface, we use BSA or PEG-functionalized surfaces and biotin-neutravidin linkage. In addition to the inherent roughness of the BSA or PEG surfaces, neutravidin itself has a size of ~4 nm, comparable to the length of the DNA rulers (18.7 nm, Fig. 4d). The density of neutravidin on the surface is also limited, such that not all doubly biotin labelled DNA rulers are bound on both ends. The DNA origami platforms, on the other hand, possess 8 biotin anchors on their lower side, increasing the chance that at least two biotins are bound, and are much larger and hence less sensitive to local height differences present on the surface. These effects are reflected in our data: while the dsDNA rulers showed shorter than expected distances, indicating that they are angled with respect to the surface, the dye-to-dye distances on the origami platform were found within the expected range, indicating that they lie flat on the surface.

PEG-3000 (average molecular weight of 3 kDa, corresponding to ~70 monomer units) is covalently bound to the surface on one side and functionalized with biotin on the other side. PEG is a flexible polymer chain and considerably smaller than a typical protein. BSA, on the other hand, is a large protein (66 kDa) with a high propensity to stick to glass surfaces. In principle it can build multi-layers of loosely associated proteins. Each BSA molecule is labelled with up to twelve biotin molecules, enabling potential BSA-biotin-BSA crosslinking. In this section, we will investigate the density of neutravidin on the surface using fluorescence and the surface roughness using AFM imaging.

We first estimated the neutravidin concentration on the PEG surface using fluorescently labeled biotin (Supplementary Fig. 24). To assess the fraction of single and double bound DNA molecules, we estimate the surface area that the unbound biotin can explore. To this end, the DNA ruler is considered as a rigid rod of 17 nm length with a flexible 1.5 nm linker with biotin on either side. The linker length is obtained from chemical bond lengths of a C6 linker attached to a nucleic acid[36,42] the size of biotin itself is excluded as it has a fixed conformation in the neutravidin binding pocket. The singly bound molecule can freely rotate around its anchor point. The maximal extension between the terminally attached biotins occurs when both linkers are pointing outward, resulting in 21 nm. The minimal extension occurs when both linkers are pointing inwards, resulting in 13 nm. The area accessible for the unbound biotin is thus:

$$A_{\mathrm{biot}} = \pi(21^2 - 13^2)\ \mathrm{nm}^2 = 6.4 \cdot 10^2\ \mathrm{nm}^2 \qquad (S47)$$

To estimate the neutravidin density on the surface, we add Atto647N-biotin in low concentrations to the surface (Supplementary Fig. 24a) to determine the brightness of individual molecules. Next, we titrate the Atto647N concentration until the surface is saturated. Individual spots are no longer visible, so the brightness is used to determine the number of fluorophores. The binding affinity of neutravidin to biotin is high (K_d = 10^{-15} M)[43], hence we assume that the number of fluorophores equals the number of

neutravidin binding sites, resulting in a characteristic area per neutravidin molecule A_{neutr} of $1.1 \cdot 10^3$ nm^2

The average number of neutravidin molecules in the accessible area can be calculated as:

$$N_{\mathrm{neutr}} = \frac{A_{\mathrm{biot}}}{A_{\mathrm{neutr}}} = \frac{6.4 \cdot 10^2\ nm^2}{1.1 \cdot 10^3\ nm^2} = 0.58 \qquad (S48)$$

When a DNA ruler is observed on the surface, it is given that it has at least a single bond. The probability to find at least one other (second) neutravidin molecule in the accessible area follows Poisson statistics and is given by:

$$p(\text{double bound}) = 1 - e^{-N_{\mathrm{neutr}}} = 44\ \% \qquad (S49a)$$

The standard error of the neutravidin surface density was estimated as 80 nm^2 from multiple independent surface preparations. We additionally consider an uncertainty of the effective linker length of 0.5 nm. By recalculating the accessible area for an effective linker of 1 and 2nm we obtain an estimated uncertainty of the accessible area of 210 nm^2. Using standard error propagation, we obtain for the error of the double-bound fraction:

$$\Delta p(\text{double bound}) = N_{\mathrm{neutr}} e^{-N_{\mathrm{neutr}}} \sqrt{\left(\frac{\Delta A_{\mathrm{biot}}}{A_{\mathrm{biot}}}\right)^2 + \left(\frac{\Delta A_{\mathrm{neutr}}}{A_{\mathrm{neutr}}}\right)^2} = 0.11 \qquad (S49b)$$

The likelihood that a DNA ruler is doubly bound is thus obtained as 44 ± 11 %. In the inferred distance distributions of the DNA rulers, however, we found a significant non-zero population also for single-biotin immobilization, and generally observed only a small fraction of short (zero) distances for the double-biotin samples (Fig. 5a-b and Supplementary Fig. 18a-b). This indicates that DNA rulers might also be bound to the surface by unspecific interactions (sticking).

Next, we assessed the surface roughness of the functionalized surfaces by AFM. The PEG-neutravidin surfaces showed height variations that are comparable to the size of individual neutravidin proteins (see Supplementary Fig. 23a for the AFM height images), causing the DNA rulers to be slightly angled with respect the surface as evidenced by the observed shorter distance in the colocalization analysis (see Supplementary Fig. 18 for inferred distance distributions and inclination angles). On BSA-functionalized surfaces, we observed height variations of 10-30 nm (see Supplementary Fig. 23b for the AFM height images), much larger than for the PEG surfaces. Indeed, we observed significantly reduced colocalization distances in the inferred distributions and determined a larger inclination angle of 25° compared to 20° for the PEG surfaces (see Fig 5a-c in the main text). For BSA surfaces, a variation of the height profile is observed over distances of 10 nm (see Fig. S23b, right column, for the height distributions). This indicates that the height profile varies between surface preparations and potentially explains why for some samples a larger difference between the observed and expected distance was found (compare, e.g., dsD(LF) and dsD(NF) in Fig. 5b of the main text). In absence of neutravidin the surfaces are very flat (compare Supplementary Fig. 23 a-c and b-d).

To get the average dimension of surface features, an autocorrelation of the surfaces for the PEG-Neutravidin and BSA-Neutravidin was done (see Fig. 5e and Supplementary Fig. 23e-f). Similar to the

image correlation spectroscopy (ICS) technique[44,45], first the fluctuations around the mean height were obtained as:

$$dIm\,(x,y) = Im(x,y) - \langle Im\rangle, \tag{50a}$$

where $Im(x,y)$ denotes the AFM image and $\langle Im\rangle$ is the average height. The autocorrelation is calculated as:

$$C(x,y) = \int\int dIm(x',y')dIm(x'-x,y'-y)dx'dy'\,. \tag{50b}$$

Taking x_c and y_c as the center of the correlation in the x- and y-dimensions and the distance from the center $r = \sqrt{(x-x_c)^2+(y-y_c)^2}$, we radially integrate to obtain the 1D correlation function:

$$C_{1D}^{\sim}(r) = \frac{1}{2\pi r}\int\int \delta(r^2-(x-x_c)^2-(y-y_c)^2)\,C(x,y)\,dx\,dy\,, \tag{50c}$$

where the division by $2\pi r$ is to divide out the Jacobian of the transformation. Finally, the correlation functions are normalized:

$$C_{1D}(r) = \frac{C_{1D}^{\sim}(r)}{\max\left(C_{1D}^{\sim}(r\neq 0)\right)}, \tag{50d}$$

where the value at $r = 0$ value is discarded as it is not indicative of the average feature size, but rather indicates the variance of the dataset. The characteristic distance is chosen at the point where the correlation function has decayed to a value of 1/e. The average feature size for PEG is found to be 16 nm and for BSA 24 nm. This matches the expectation that the resolution of the AFM images is limited by the AFM tip size, features smaller than this distance cannot be imaged.

Supplementary Note 9: Estimation of inclination angles of dsDNA rulers

To estimate the inclination angle α, we perform a linear regression of the measured localization-based mean-position distance, $R_{\mathrm{mp}}^{\mathrm{loc}}$, against the predicted distance between the dyes for a flat orientation of the dsDNA, $R_{\mathrm{mp}}^{(\mathrm{flat})}$, according to:

$$R_{\mathrm{mp}}^{\mathrm{loc}} = m\cdot R_{\mathrm{mp}}^{(\mathrm{flat})}. \tag{S51}$$

From the slope m, the inclination angle α is then estimated as:

$$\alpha = arcsin(m)\,, \tag{S52}$$

where $arcsin$ is the inverse sine function.

To reflect the broadening of the observed distance distribution, the uncertainties of the average inclination angles of the single biotin and double biotin samples ($\Delta\alpha$) are obtained by propagating the standard deviation of the distance distributions ΔR_{mp}^{loc} according to:

$$\Delta\alpha = \frac{d\alpha}{dR_{\mathrm{mp}}^{\mathrm{loc}}}\Delta R_{\mathrm{mp}}^{\mathrm{loc}} = \frac{\Delta R_{\mathrm{mp}}^{\mathrm{loc}}}{R_{\mathrm{mp}}^{(\mathrm{flat})}}\left(1-\left(\frac{R_{\mathrm{mp}}^{\mathrm{loc}}}{R_{\mathrm{mp}}^{(\mathrm{flat})}}\right)^2\right)^{-\frac{1}{2}}. \tag{S53}$$

$\Delta R_{\mathrm{mp}}^{(\mathrm{exp})}$ is calculated from the distance distribution $p(R_{\mathrm{mp}}^{\mathrm{loc}})$ obtained from the MEM analysis by:

$$\Delta R_{\mathrm{mp}}^{\mathrm{loc}} = \sqrt{\langle {R_{\mathrm{mp}}^{\mathrm{loc}}}^2 \rangle - \langle R_{\mathrm{mp}}^{\mathrm{loc}} \rangle^2}, \qquad (S54)$$

where $\langle {R_{\mathrm{mp}}^{\mathrm{loc}}}^2 \rangle = \sum p\left(R_{mp,i}^{loc}\right) {R_{mp,i}^{loc}}^2$ and $\langle R_{\mathrm{mp}}^{\mathrm{loc}} \rangle = \sum p\left(R_{\mathrm{mp,i}}^{\mathrm{loc}}\right) R_{\mathrm{mp,i}}^{\mathrm{loc}}$. For each measurement series (single or double biotin on BSA or PEG surface), the uncertainty $\Delta\alpha$ is estimated for each measurement of dsD(HF), dsD(MF), dsD(LF) and dsD(NF), and subsequently averaged to obtain the uncertainty of the reported inclination angle. For the estimates of the inclination angles of the double-biotin sample based on the peak distance of the double-biotin population, the reported standard error is obtained from the covariance matrix of the fit using the *curve_fit* function of the SciPy package for Python. See main Fig. 5 and Supplementary Fig. 18 for inferred distributions of $R_{\mathrm{mp}}^{\mathrm{loc}}$, the regression analysis and the estimated uncertainties of the angle, $\Delta\alpha$.

Supplementary Note 10: Colocalization analysis of hGBP1

In this section, we describe the model for the interdye distance distributions obtained by cSTED for hGBP1. Two effects need to be accounted for. First, due to arrangement of extended hGBP1 molecules in the ring-like assemblies, a distribution of the projected distance is observed even for a fixed interdye distance. Second, the random distribution of labeled hGBP1 molecules over the fiber rings leads to false-positive pairing of fluorophores attached to different hGBP1 molecules.

For the first part, we consider a uniform distribution of the inclination angle α, i.e., $P(\alpha) = const.$ The angle α defines the projected interdye distance, $R_{\mathrm{mp}}^{\mathrm{loc}}$, as a function of the radius of the disc, R_{disc}, by (see schematic in Fig. 6e of the main text):

$$R_{\mathrm{mp}}^{\mathrm{loc}} = R_{\mathrm{disc}} \cos\alpha\,. \qquad (S55)$$

The corresponding distribution of the projected distance in the disc is then obtained as:

$$P_{\mathrm{disc}}\left(R_{\mathrm{mp}}^{\mathrm{loc}} \,|R_{\mathrm{disc}}\right) = \mathrm{P}(\alpha) \frac{\mathrm{d}\alpha\left(R_{\mathrm{mp}}^{\mathrm{loc}}\right)}{\mathrm{d}R_{\mathrm{mp}}} = \frac{2}{\pi}\left(1 - \left(\frac{R_{\mathrm{mp}}^{\mathrm{loc}}}{R_{\mathrm{disc}}}\right)^2\right)^{-\frac{1}{2}}. \qquad (S56)$$

An example of the distribution $P_{\mathrm{disc}}\left(R_{\mathrm{mp}}^{\mathrm{loc}} \,|R_{\mathrm{disc}}\right)$ and the corresponding distribution of the localization-based interdye distance d_{loc} is shown in Fig. 6f-g of the main text.

The baseline due to random nearest-neighbor pairing of separate donor- or acceptor-only hGBP1 molecules is evaluated based on a Monte-Carlo approach. Considering the diameter and number of localizations of donor and acceptor dyes within each measured ring, the spots are randomly redistributed over the ring and nearest neighbor pairing is performed as for the data. To eliminate stochastic noise and obtain a smooth distribution, the simulation is performed 1000 times. See Supplementary Fig. 29b-c for the resulting distribution of the localization-based interdye distance d_{loc}.

To obtain the final model function for the colocalization analysis of hGBP1, one has to again consider the inherent distribution of the measured interdye distance d_{loc} due to the localization uncertainty, described by a χ-distribution. The model function is then given by:

$$M_{R_{\mathrm{disc}},\sigma_\chi}(d_{\mathrm{loc}}) = \int_0^\infty \left(A_{\mathrm{BL}} BL\left(R_{\mathrm{mp}}^{\mathrm{loc}}\right) + A_{\mathrm{disc}} P_{\mathrm{disc}}\left(R_{\mathrm{mp}}^{\mathrm{loc}} | R_{\mathrm{disc}}\right)\right) P_\chi(R_{\mathrm{loc}}, \sigma_\chi | R_{\mathrm{mp}}^{\mathrm{loc}}) dR_{\mathrm{mp}}^{\mathrm{loc}} \quad (S57)$$

where $BL(R_{mp})$ describes the shape of the baseline of randomly distributed spots on the ring, $P_\chi(R_{\mathrm{loc}}, \sigma_{chi} | R_{\mathrm{mp}}^{\mathrm{loc}})$ is the χ-distribution with two degrees of freedom with the central parameter R_{mp} and width parameter σ_χ , and A_{BL} and A_{disc} are the corresponding amplitudes.

To generate the reported histogram of the colocalization distances in Fig. 6h of the main text, only those spots with a proximity ratio (uncorrected FRET efficiency calculated from the raw signals) above 0.35 were selected (the selection threshold is shown in Supplementary Fig. 29a). The amplitude of the baseline was fitted only for long distances (> 50 nm) and fixed for the fit over the whole distance range using the full model function (see Fig. 6h, main text). 68% confidence intervals were determined from the marginal probability distribution of the disc radius R_{disc} obtained from a two-dimensional parameter scan of the fit parameters R_{disc} and σ_χ (see Fig. 6i).

Supplementary Tables

Sample information

Supplementary Tab. 1: Overview of DNA sequences for the DNA rulers (dsD). The donor strand (D-strand) is labeled with Alexa594 dye and acceptor strand (A-strand) with Atto647N dye (for details see the section 'Sample preparation, dsDNA' in the Supplementary Methods). The labeling sites of the donor and acceptor are shown in green and in red in the sequence, respectively.

Sample	Base position (Linker), strand	# Biotin-anchor	Dyes (Donor/Acceptor)	Sequence
dsD(HF)	T 6 (C6), D-strand C 30(C6), A-strand	1	Alexa594 / Atto647N	5´-Biotin - CGT ACT GAT TAA TCT CCG CAA ATG TGA ACG CGT ACT GAT TAA TCT CCG CAA ATG T - 3´ 5‘ - A CAT TTG CGG AGA TTA ATC AGT ACG CGT TCA CAT TTG CGG AGA TTA ATC AGT ACG - 3´
dsD(MF)	T 6 (C6), D-strand C 24(C6), A-strand	1	Alexa594 / Atto647N	5´-Biotin - CGT ACT GAT TAA TCT CCG CAA ATG TGA ACG CGT ACT GAT TAA TCT CCG CAA ATG T - 3´ 5‘ - ACA TTT GCG GAG ATT AAT CAG TAC GCG TTC ACA TTT GCG GAG ATT AAT CAG TAC G - 3´
dsD(LF)	T 6 (C6), D-strand T 19(C6), A-strand	1	Alexa594 / Atto647N	5´-Biotin - CGT ACT GAT TAA TCT CCG CAA ATG TGA ACG CGT ACT GAT TAA TCT CCG CAA ATG T - 3´ 5‘ – ACA TTT GCG GAG ATT AAT CAG TAC GCG TTC ACA TTT GCG GAG ATT AAT CAG TAC G - 3´
dsD(NF)	T 6 (C6), D-strand T 6 (C6), A-strand	1	Alexa594 / Atto647N	5´-Biotin - CGT ACT GAT TAA TCT CCG CAA ATG TGA ACG CGT ACT GAT TAA TCT CCG CAA ATG T - 3´ 5‘ – ACA TTT GCG GAG ATT AAT CAG TAC GCG TTC ACA TTT GCG GAG ATT AAT CAG TAC G - 3´
dsD(HF)	T 6 (C6), D-strand C 30(C6), A-strand	2	Alexa594 / Atto647N	5´-Biotin - CGT ACT GAT TAA TCT CCG CAA ATG TGA ACG CGT ACT GAT TAA TCT CCG CAA ATG T - 3´-Biotin 5‘ - A CAT TTG CGG AGA TTA ATC AGT ACG CGT TCA CAT TTG CGG AGA TTA ATC AGT ACG - 3´
dsD(MF)	T 6 (C6), D-strand C 24(C6), A-strand	2	Alexa594 / Atto647N	5´-Biotin - CGT ACT GAT TAA TCT CCG CAA ATG TGA ACG CGT ACT GAT TAA TCT CCG CAA ATG T – 3’-Biotin 5‘ - ACA TTT GCG GAG ATT AAT CAG TAC GCG TTC ACA TTT GCG GAG ATT AAT CAG TAC G - 3´
dsD(LF)	T 6 (C6), D-strand T 19(C6), A-strand	2	Alexa594 / Atto647N	5´-Biotin - CGT ACT GAT TAA TCT CCG CAA ATG TGA ACG CGT ACT GAT TAA TCT CCG CAA ATG T - 3´-Biotin 5‘ – ACA TTT GCG GAG ATT AAT CAG TAC GCG TTC ACA TTT GCG GAG ATT AAT CAG TAC G - 3´
dsD(NF)	T 6 (C6), D-strand T 6 (C6), A-strand	2	Alexa594 / Atto647N	5´-Biotin - CGT ACT GAT TAA TCT CCG CAA ATG TGA ACG CGT ACT GAT TAA TCT CCG CAA ATG T - 3´-Biotin 5‘ – ACA TTT GCG GAG ATT AAT CAG TAC GCG TTC ACA TTT GCG GAG ATT AAT CAG TAC G - 3´

Supplementary Tab. 2: Sequences for staple strands and scaffold of the DNA origami platform

Name	Sequence	Modification
A1	TTTTCACTCAAAGGGCGAAAAACCATCACC	
A2	GTCGACTTCGGCCAACGCGCGGGGTTTTTC	
A3	TGCATCTTTCCCAGTCACGACGGCCTGCAG	
A4	TAATCAGCGGATTGACCGTAATCGTAACCG	
A5	AACGCAAAATCGATGAACGGTACCGGTTGA	
A6	AACAGTTTTGTACCAAAAACATTTTATTTC	
A7	TTTACCCCAACATGTTTTAAATTTCCATAT T	3‘ Atto647N
A8	TTTAGGACAAATGCTTTAAACAATCAGGTC T	3‘ Atto594
A9	CATCAAGTAAAACGAACTAACGAGTTGAGA	
A10	AATACGTTTGAAAGAGGACAGACTGACCTT	
A11	AGGCTCCAGAGGCTTTGAGGACACGGGTAA	
A12	AGAAAGGAACAACTAAAGGAATTCAAAAAAA	
B1	CAAATCAAGTTTTTTGGGGTCGAAACGTGGA	
B2	CTCCAACGCAGTGAGACGGGCAACCAGCTGCA	
B3	TTAATGAACTAGAGGATCCCCGGGGGGTAACG	
B4	CCAGGGTTGCCAGTTTGAGGGGACCCGTGGGA	
B5	ACAAACGGAAAAGCCCCAAAAACACTGGAGCA	
B6	AACAAGAGGGATAAAAATTTTTAGCATAAAGC	
B7	TAAATCGGGATTCCCAATTCTGCGATATAATG	
B8	CTGTAGCTTGACTATTATAGTCAGTTCATTGA	
B9	ATCCCCCTATACCACATTCAACTAGAAAAATC	
B10	TACGTTAAAGTAATCTTGACAAGAACCGAACT	
B11	GACCAACTAATGCCACTACGAAGGGGGTAGCA	
B12	ACGGCTACAAAAGGAGCCTTTAATGTGAGAAT	
C1	AGCTGATTGCCCTTCAGAGTCCACTATTAAAGGGTGCCGT	
C2	ATTAAGTTTACCGAGCTCGAATTCGGGAAACCTGTCGTGC	5‘ biotin
C4	GTATAAGCCAACCCGTCGGATTCTGACGACAGTATCGGCCGCAAGGCG	
C5	TATATTTTGTCATTGCCTGAGAGTGGAAGATT	
C6	GATTTAGTCAATAAAGCCTCAGAGAACCCTCA	
C7	CGGATTGCAGAGCTTAATTGCTGAAACGAGTA	
C8	ATGCAGATACATAACGGGAATCGTCATAAATAAAGCAAAG	
C9	ATAAGGGAACCGGATATTCATTACGTCAGGACGTTGGGAA	5‘ biotin
C11	TTTATCAGGACAGCATCGGAACGACACCAACCTAAAACGAGGTCAATC	
C12	ACAACTTTCAACAGTTTCAGCGGATGTATCGG	
D1	AAAGCACTAAATCGGAACCCTAATCCAGTT	
D2	TGGAACAACCGCCTGGCCCTGAGGCCCGCT	
D3	TTCCAGTCGTAATCATGGTCATAAAAGGGG	
D4	GATGTGCTTCAGGAAGATCGCACAATGTGA	
D5	GCGAGTAAAAATATTTAAATTGTTACAAAG	
D6	GCTATCAGAAATGCAATGCCTGAATTAGCA	
D7	AAATTAAGTTGACCATTAGATACTTTTGCG	
D8	GATGGCTTATCAAAAAGATTAAGAGCGTCC	
D9	AATACTGCCCAAAAGGAATTACGTGGCTCA	
D10	TTATACCACCAAATCAACGTAACGAACGAG	
D11	GCGCAGACAAGAGGCAAAAGAATCCCTCAG	
D12	CAGCGAAACTTGCTTTCGAGGTGTTGCTAA	
E1	AGCAAGCGTAGGGTTGAGTGTTGTAGGGAGCC	
E2	CTGTGTGATTGCGTTGCGCTCACTAGAGTTGC	
E3	GCTTTCCGATTACGCCAGCTGGCGGCTGTTTC	
E4	ATATTTTGGCTTTCATCAACATTATCCAGCCA	
E5	TAGGTAAACTATTTTTGAGAGATCAAACGTTA	
E6	AATGGTCAACAGGCAAGGCAAAGAGTAATGTG	
E7	CGAAAGACTTTGATAAGAGGTCATATTTCGCA	
E8	TAAGAGCAAATGTTTAGACTGGATAGGAAGCC	
E9	TCATTCAGATGCGATTTTAAGAACAGGCATAG	
E10	ACACTCATCCATGTTACTTAGCCGAAAGCTGC	
E11	AAACAGCTTTTTGCGGGATCGTCAACACTAAA	
E12	TAAATGAATTTTCTGTATGGGATTAATTTCTT	
F1	CCCGATTTAGAGCTTGACGGGGAAAAAGAATA	
F2	GCCCGAGAGTCCACGCTGGTTTGCAGCTAACT	
F3	CACATTAAAATTGTTATCCGCTCATGCGGGCC	
F4	TCTTCGCTGCACCGCTTCTGGTGCGGCCTTCC	
F5	TGTAGCCATTAAAATTCGCATTAAATGCCGGA	
F6	GAGGGTAGGATTCAAAAGGGTGAGACATCCAA	
F7	TAAATCATATAACCTGTTTAGCTAACCTTTAA	
F8	TTGCTCCTTTCAAATATCGCGTTTGAGGGGGT	
F9	AATAGTAAACACTATCATAACCCTCATTGTGA	
F10	ATTACCTTTGAATAAGGCTTGCCCAAATCCGC	
F11	GACCTGCTCTTTGACCCCCAGCGAGGGAGTTA	

F12	AAGGCCGCTGATACCGATAGTTGCGACGTTAG	
G1	CCCAGCAGGCGAAAAATCCCTTATAAATCAAGCCGGCG	
G2	GCGATCGGCAATTCCACACAACAGGTGCCTAATGAGTG	5‘ biotin
G4	TAAATCAAAATAATTCGCGTCTCGGAAACCAGGCAAAGGGAAGG	
G5	GAGACAGCTAGCTGATAAATTAATTTTTGT	
G6	TTTGGGGATAGTAGTAGCATTAAAAGGCCG	
G7	GCTTCAATCAGGATTAGAGAGTTATTTTCA	
G8	CGTTTACCAGACGACAAAGAAGTTTTGCCATAATTCGA	
G9	TTGTGTCGTGACGAGAAACACCAAATTTCAACTTTAAT	5‘ biotin
G11	TGACAACTCGCTGAGGCTTGCATTATACCAAGCGCGATGATAAA	
G12	TCTAAAGTTTTGTCGTCTTTCCAGCCGACAA	
H1	TCAATATCGAACCTCAAATATCAATTCCGAAA T	
H2	GCAATTCACATATTCCTGATTATCAAAGTGTA	
H3	AGAAAACAAAGAAGATGATGAAACAGGCTGCG	
H4	ATCGCAAGTATGTAAATGCTGATGATAGGAAC	
H5	GTAATAAGTTAGGCAGAGGCATTTATGATATT	
H6	CCAATAGCTCATCGTAGGAATCATGGCATCAA	
H7	AGAGAGAAAAAAATGAAAATAGCAAGCAAACT	
H8	TTATTACGAAGAACTGGCATGATTGCGAGAGG	
H9	GCAAGGCCTCACCAGTAGCACCATGGGCTTGA	
H10	TTGACAGGCCACCACCAGAGCCGCGATTTGTA	
H11	TTAGGATTGGCTGAGACTCCTCAATAACCGAT	
H12	TCCACAGACAGCCCTCATAGTTAGCGTAACGA	
AA1	AACGTGGCGAGAAAGGAAGGGAAACCAGTAA	
AA2	TCGGCAAATCCTGTTTGATGGTGGACCCTCAA	
AA3	AAGCCTGGTACGAGCCGGAAGCATAGATGATG	
AA4	CAACTGTTGCGCCATTCGCCATTCAAACATCA	
AA5	GCCATCAAGCTCATTTTTTAACCACAAATCCA	
AA6	CAACCGTTTCAAATCACCATCAATTCGAGCCA	
AA7	TTCTACTACGCGAGCTGAAAAGGTTACCGCGC	
AA8	CCAACAGGAGCGAACCAGACCGGAGCCTTTAC	
AA9	CTTTTGCAGATAAAAACCAAAATAAAGACTCC	
AA10	GATGGTTTGAACGAGTAGTAAATTTACCATTA	
AA11	TCATCGCCAACAAAGTACAACGGACGCCAGCA	
AA12	ATATTCGGAACCATCGCCCACGCAGAGAAGGA	
BB1	TAAAAGGGACATTCTGGCCAACAAAGCATC	
BB2	ACCTTGCTTGGTCAGTTGGCAAAGAGCGGA	
BB3	ATTATCATTCAATATAATCCTGACAATTAC	
BB4	CTGAGCAAAAATTAATTACATTTTGGGTTA	
BB5	TATAACTAACAAAGAACGCGAGAACGCCAA	
BB6	CATGTAATAGAATATAAAGTACCAAGCCGT	
BB7	TTTTATTTAAGCAAATCAGATATTTTTTGT	
BB8	TTAACGTCTAACATAAAAACAGGTAACGGA	
BB9	ATACCCAACAGTATGTTAGCAAATTAGAGC	
BB10	CAGCAAAAGGAAACGTCACCAATGAGCCGC	
BB11	CACCAGAAAGGTTGAGGCAGGTCATGAAAG	
BB12	TATTAAGAAGCGGGGTTTTGCTCGTAGCAT	
CC1	TCAACAGTTGAAAGGAGCAAATGAAAAATCTAGAGATAGA	
CC2	ATTCATTTTTGTTTGGATTATACTAAGAAACCACCAGAAG	5‘ biotin
CC4	TCAAATATAACCTCCGGCTTAGGTAACAATTTCATTTGAAGGCGAATT	
CC5	GTAAAGTAATCGCCATATTTAACAAAACTTTT	
CC6	TATCCGGTCTCATCGAGAACAAGCGACAAAAG	
CC7	TTAGACGGCCAAATAAGAAACGATAGAAGGCT	
CC8	CGTAGAAAATACATACCGAGGAAACGCAATAAGAAGCGCA	
CC9	CACCCTCAGAAACCATCGATAGCATTGAGCCATTTGGGAA	5‘ biotin
CC11	GCGGATAACCTATTATTCTGAAACAGACGATTGGCCTTGAAGAGCCAC	
CC12	TCACCAGTACAAACTACAACGCCTAGTACCAG	
DD1	ACCCTTCTGACCTGAAAGCGTAAGACGCTGAG	
DD2	AGCCAGCAATTGAGGAAGGTTATCATCATTTT	
DD3	GCGGAACATCTGAATAATGGAAGGTACAAAAT	
DD4	CGCGCAGATTACCTTTTTTAATGGGAGAGACT	
DD5	ACCTTTTTATTTTAGTTAATTTCATAGGGCTT	
DD6	AATTGAGAATTCTGTCCAGACGACTAAACCAA	
DD7	GTACCGCAATTCTAAGAACGCGAGTATTATTT	
DD8	ATCCCAATGAGAATTAACTGAACAGTTACCAG	
DD9	AAGGAAACATAAAGGTGGCAACATTATCACCG	
DD10	TCACCGACGCACCGTAATCAGTAGCAGAACCG	
DD11	CCACCCTCTATTCACAAACAAATACCTGCCTA	
DD12	TTTCGGAAGTGCCGTCGAGAGGGTGAGTTTCG	
EE1	CTTTAGGGCCTGCAACAGTGCCAATACGTG	
EE2	CTACCATAGTTTGAGTAACATTTAAAATAT	
EE3	CATAAATCTTTGAATACCAAGTGTTAGAAC	
EE4	CCTAAATCAAAATCATAGGTCTAAACAGTA	

EE5	ACAACATGCCAACGCTCAACAGTCTTCTGA	
EE6	GCGAACCTCCAAGAACGGGTATGACAATAA	
EE7	AAAGTCACAAAATAAACAGCCAGCGTTTTA	
EE8	AACGCAAAGATAGCCGAACAAACCCTGAAC	
EE9	TCAAGTTTCATTAAAGGTGAATATAAAAGA	
EE10	TTAAAGCCAGAGCCGCCACCCTCGACAGAA	
EE11	GTATAGCAAACAGTTAATGCCCAATCCTCA	
EE12	AGGAACCCATGTACCGTAACACTTGATATAA	
FF1	GCACAGACAATATTTTTGAATGGGGTCAGTA	
FF2	TTAACACCAGCACTAACAACTAATCGTTATTA	
FF3	ATTTTAAAATCAAAATTATTTGCACGGATTCG	
FF4	CCTGATTGCAATATATGTGAGTGATCAATAGT	
FF5	GAATTTATTTAATGGTTTGAAATATTCTTACC	
FF6	AGTATAAAGTTCAGCTAATGCAGATGTCTTTC	
FF7	CTTATCATTCCCGACTTGCGGGAGCCTAATTT	
FF8	GCCAGTTAGAGGGTAATTGAGCGCTTTAAGAA	
FF9	AAGTAAGCAGACACCACGGAATAATATTGACG	
FF10	GAAATTATTGCCTTTAGCGTCAGACCGGAACC	
FF11	GCCTCCCTCAGAATGGAAAGCGCAGTAACAGT	
FF12	GCCCGTATCCGGAATAGGTGTATCAGCCCAAT	
GG1	AGATTAGAGCCGTCAAAAAACAGAGGTGAGGCCTATTAGT	
GG2	AACAATAACGTAAAACAGAAATAAAAATCCTTTGCCCGAA	5‘ biotin
GG4	GTGATAAAAAGACGCTGAGAAGAGATAACCTTGCTTCTGTTCGGGAGA	
GG5	GTTTATCAATATGCGTTATACAAACCGACCGT	
GG6	GCCTTAAACCAATCAATAATCGGCACGCGCCT	
GG7	GAGAGATAGAGCGTCTTTCCAGAGGTTTTGAA	
GG8	GTTTATTTTGTCACAATCTTACCGAAGCCCTTTAATATCA	
GG9	AGCCACCACTGTAGCGCGTTTTCAAGGGAGGGAAGGTAAA	5‘ biotin
GG11	CAGGAGGTGGGGTCAGTGCCTTGAGTCTCTGAATTTACCGGGAACCAG	
GG12	CCACCCTCATTTTCAGGGATAGCAACCGTACT	
HH1	CTTTAATGCGCGAACTGATAGCCCCACCAG	
HH2	CAGAAGATTAGATAATACATTTGTCGACAA	
HH3	CTCGTATTAGAAATTGCGTAGATACAGTAC	
HH4	CTTTTACAAAATCGTCGCTATTAGCGATAG T	3‘ Atto647N
HH5	CTTAGATTTAAGGCGTTAAATAAAGCCTGT	
HH6	TTAGTATCACAATAGATAAGTCCACGAGCA	
HH7	TGTAGAAATCAAGATTAGTTGCTCTTACCA T	3‘ Atto594
HH8	ACGCTAACACCCACAAGAATTGAAAATAGC	
HH9	AATAGCTATCAATAGAAAATTCAACATTCA	
HH10	ACCGATTGTCGGCATTTTCGGTCATAATCA	
HH11	AAATCACCTTCCAGTAAGCGTCAGTAATAA	
HH12	GTTTTAACTTAGTACCGCCACCCAGAGCCA	
Scaffold	TTCCCTTCCTTTCTCGCCACGTTCGCCGGCTTTCCCCGTCAAGCTCTAAATCGGGGGCTCCCT TTAGGGTTCCGATTTAGTGCTTTACGGCACCTCGACCCCAAAAAACTTGATTTGGGTGATGGTT CACGTAGTGGGCCATCGCCCTGATAGACGGTTTTTCGCCCTTTGACGTTGGAGTCCACGTTCT TTAATAGTGGACTCTTGTTCCAAACTGGAACAACACTCAACCCTATCTCGGGCTATTCTTTTGA TTTATAAGGGATTTTGCCGATTTCGGAACCACCATCAAACAGGATTTTCGCCTGCTGGGGCAA ACCAGCGTGGACCGCTTGCTGCAACTCTCTCAGGGCCAGGCGGTGAAGGGCAATCAGCTGTT GCCCGTCTCACTGGTGAAAAGAAAAACCACCCTGGCGCCCAATACGCAAACCGCCTCTCCCC GCGCGTTGGCCGATTCATTAATGCAGCTGGCACGACAGGTTTCCCGACTGGAAAGCGGGCAG TGAGCGCAACGCAATTAATGTGAGTTAGCTCACTCATTAGGCACCCCAGGCTTTACACTTTATG CTTCCGGCTCGTATGTTGTGTGGAATTGTGAGCGGATAACAATTTCACACAGGAAACAGCTAT GACCATGATTACGAATTCGAGCTCGGTACCCGGGGATCCTCTAGAGTCGACCTGCAGGCATG CAAGCTTGGCACTGGCCGTCGTTTTACAACGTCGTGACTGGGAAAACCCTGGCGTTACCCAA CTTAATCGCCTTGCAGCACATCCCCCTTTCGCCAGCTGGCGTAATAGCGAAGAGGCCCGCAC CGATCGCCCTTCCCAACAGTTGCGCAGCCTGAATGGCGAATGGCGCTTTGCCTGGTTTCCGG CACCAGAAGCGGTGCCGGAAAGCTGGCTGGAGTGCGATCTTCCTGAGGCCGATACTGTCGTC GTCCCCTCAAACTGGCAGATGCACGGTTACGATGCGCCCATCTACACCAACGTGACCTATCCC ATTACGGTCAATCCGCCGTTTGTTCCCACGGAGAATCCGACGGGTTGTTACTCGCTCACATTT AATGTTGATGAAAGCTGGCTACAGGAAGGCCAGACGCGAATTATTTTTGATGGCGTTCCTATT GGTTAAAAAATGAGCTGATTTAACAAAAATTTAATGCGAATTTTAACAAAATATTAACGTTTACA ATTTAAATATTTGCTTATACAATCTTCCTGTTTTTGGGGCTTTTCTGATTATCAACCGGGGTACA TATGATTGACATGCTAGTTTTACGATTACCGTTCATCGATTCTCTTGTTTGCTCCAGACTCTCAG GCAATGACCTGATAGCCTTTGTAGATCTCTCAAAAATAGCTACCCTCTCCGGCATTAATTTATC AGCTAGAACGGTTGAATATCATATTGATGGTGATTTGACTGTCTCCGGCCTTTCTCACCCTTTT GAATCTTTACCTACACATTACTCAGGCATTGCATTTAAAATATATGAGGGTTCTAAAAATTTTTA TCCTTGCGTTGAAATAAAGGCTTCTCCCGCAAAAGTATTACAGGGTCATAATGTTTTTGGTACA ACCGATTTAGCTTTATGCTCTGAGGCTTTATTGCTTAATTTTGCTAATTCTTTGCCTTGCCTGTA TGATTTATTGGATGTTAATGCTACTACTATTAGTAGAATTGATGCCACCTTTTCAGCTCGCGCC CCAAATGAAAATATAGCTAAACAGGTTATTGACCATTTGCGAAATGTATCTAATGGTCAAACTAA ATCTACTCGTTCGCAGAATTGGGAATCAACTGTTATATGGAATGAAACTTCCAGACACCGTACT TTAGTTGCATATTTAAAACATGTTGAGCTACAGCATTATATTCAGCAATTAAGCTCTAAGCCATC CGCAAAAATGACCTCTTATCAAAAGGAGCAATTAAAGGTACTCTCTAATCCTGACCTGTTGGAG TTTGCTTCCGGTCTGGTTCGCTTTGAAGCTCGAATTAAAACGCGATATTTGAAGTCTTTCGGGC	Note that the start of the sequence is according to the convention in the Picasso software [4,46].

	TTCCTCTTAATCTTTTTGATGCAATCCGCTTTGCTTCTGACTATAATAGTCAGGGTAAAGACCTG ATTTTTGATTTATGGTCATTCTCGTTTTCTGAACTGTTTAAAGCATTTGAGGGGGATTCAATGAA TATTTATGACGATTCCGCAGTATTGGACGCTATCCAGTCTAAACATTTTACTATTACCCCCTCTG GCAAAACTTCTTTTGCAAAAGCCTCTCGCTATTTTGGTTTTTATCGTCGTCTGGTAAACGAGGG TTATGATAGTGTTGCTCTTACTATGCCTCGTAATTCCTTTTGGCGTTATGTATCTGCATTAGTTG AATGTGGTATTCCTAAATCTCAACTGATGAATCTTTCTACCTGTAATAATGTTGTTCCGTTAGTT CGTTTTATTAACGTAGATTTTTCTTCCCAACGTCCTGACTGGTATAATGAGCCAGTTCTTAAAAT CGCATAAGGTAATTCACAATGATTAAAGTTGAAATTAAACCATCTCAAGCCCAATTTACTACTCG TTCTGGTGTTTCTCGTCAGGGCAAGCCTTATTCACTGAATGAGCAGCTTTGTTACGTTGATTTG GGTAATGAATATCCGGTTCTTGTCAAGATTACTCTTGATGAAGGTCAGCCAGCCTATGCGCCT GGTCTGTACACCGTTCATCTGTCCTCTTTCAAAGTTGGTCAGTTCGGTTCCCTTATGATTGACC GTCTGCGCCTCGTTCCGGCTAAGTAACATGGAGCAGGTCGCGGATTTCGACACAATTTATCAG GCGATGATACAAATCTCCGTTGTACTTTGTTTCGCGCTTGGTATAATCGCTGGGGGTCAAAGA TGAGTGTTTTAGTGTATTCTTTTGCCTCTTTCGTTTTAGGTTGGTGCCTTCGTAGTGGCATTAC GTATTTTACCCGTTTAATGGAAACTTCCTCATGAAAAAGTCTTTAGTCCTCAAAGCCTCTGTAG CCGTTGCTACCCTCGTTCCGATGCTGTCTTTCGCTGCTGAGGGTGACGATCCCGCAAAAGCG GCCTTTAACTCCCTGCAAGCCTCAGCGACCGAATATATCGGTTATGCGTGGGCGATGGTTGTT GTCATTGTCGGCGCAACTATCGGTATCAAGCTGTTTAAGAAATTCACCTCGAAAGCAAGCTGA TAAACCGATACAATTAAAGGCTCCTTTTGGAGCCTTTTTTTTGGAGATTTTCAACGTGAAAAAAT TATTATTCGCAATTCCTTTAGTTGTTCCTTTCTATTCTCACTCCGCTGAAACTGTTGAAAGTTGT TTAGCAAAATCCCATACAGAAAATTCATTTACTAACGTCTGGAAAGACGACAAAACTTTAGATC GTTACGCTAACTATGAGGGCTGTCTGTGGAATGCTACAGGCGTTGTAGTTTGTACTGGTGACG AAACTCAGTGTTACGGTACATGGGTTCCTATTGGGCTTGCTATCCCTGAAAATGAGGGTGGTG GCTCTGAGGGTGGCGGTTCTGAGGGTGGCGGTTCTGAGGGTGGCGGTACTAAACCTCCTGA GTACGGTGATACACCTATTCCGGGCTATACTTATATCAACCCTCTCGACGGCACTTATCCGCC TGGTACTGAGCAAAACCCCGCTAATCCTAATCCTTCTCTTGAGGAGTCTCAGCCTCTTAATACT TTCATGTTTCAGAATAATAGGTTCCGAAATAGGCAGGGGGCATTAACTGTTTATACGGGCACT GTTACTCAAGGCACTGACCCCGTTAAAACTTATTACCAGTACACTCCTGTATCATCAAAAGCCA TGTATGACGCTTACTGGAACGGTAAATTCAGAGACTGCGCTTTCCATTCTGGCTTTAATGAGGA TTTATTTGTTTGTGAATATCAAGGCCAATCGTCTGACCTGCCTCAACCTCCTGTCAATGCTGGC GGCGGCTCTGGTGGTGGTTCTGGTGGCGGCTCTGAGGGTGGTGGCTCTGAGGGTGGCGGTT CTGAGGGTGGCGGCTCTGAGGGAGGCGGTTCCGGTGGTGGCTCTGGTTCCGGTGATTTTGA TTATGAAAAGATGGCAAACGCTAATAAGGGGGCTATGACCGAAAATGCCGATGAAAACGCGCT ACAGTCTGACGCTAAAGGCAAACTTGATTCTGTCGCTACTGATTACGGTGCTGCTATCGATGG TTTCATTGGTGACGTTTCCGGCCTTGCTAATGGTAATGGTGCTACTGGTGATTTTGCTGGCTCT AATTCCCAAATGGCTCAAGTCGGTGACGGTGATAATTCACCTTTAATGAATAATTTCCGTCAAT ATTTACCTTCCCTCCCTCAATCGGTTGAATGTCGCCCTTTTGTCTTTGGCGCTGGTAAACCATA TGAATTTTCTATTGATTGTGACAAAATAAACTTATTCCGTGGTGTCTTTGCGTTTCTTTTATATGT TGCCACCTTTATGTATGTATTTTCTACGTTTGCTAACATACTGCGTAATAAGGAGTCTTAATCAT GCCAGTTCTTTTGGGTATTCCGTTATTATTGCGTTTCCTCGGTTTCCTTCTGGTAACTTTGTTCG GCTATCTGCTTACTTTTCTTAAAAAGGGCTTCGGTAAGATAGCTATTGCTATTTCATTGTTTCTT GCTCTTATTATTGGGCTTAACTCAATTCTTGTGGGTTATCTCTCTGATATTAGCGCTCAATTACC CTCTGACTTTGTTCAGGGTGTTCAGTTAATTCTCCCGTCTAATGCGCTTCCCTGTTTTTATGTTA TTCTCTCTGTAAAGGCTGCTATTTTCATTTTTGACGTTAAACAAAAAATCGTTTCTTATTTGGATT GGGATAAATAATATGGCTGTTTATTTTGTAACTGGCAAATTAGGCTCTGGAAAGACGCTCGTTA GCGTTGGTAAGATTCAGGATAAAATTGTAGCTGGGTGCAAAATAGCAACTAATCTTGATTTAAG GCTTCAAAACCTCCCGCAAGTCGGGAGGTTCGCTAAAACGCCTCGCGTTCTTAGAATACCGGA TAAGCCTTCTATATCTGATTTGCTTGCTATTGGGCGCGGTAATGATTCCTACGATGAAAATAAA AACGGCTTGCTTGTTCTCGATGAGTGCGGTACTTGGTTTAATACCCGTTCTTGGAATGATAAG GAAAGACAGCCGATTATTGATTGGTTTCTACATGCTCGTAAATTAGGATGGGATATTATTTTTCT TGTTCAGGACTTATCTATTGTTGATAAACAGGCGCGTTCTGCATTAGCTGAACATGTTGTTTATT GTCGTCGTCTGGACAGAATTACTTTACCTTTTGTCGGTACTTTATATTCTCTTATTACTGGCTCG AAAATGCCTCTGCCTAAATTACATGTTGGCGTTGTTAAATATGGCGATTCTCAATTAAGCCCTA CTGTTGAGCGTTGGCTTTATACTGGTAAGAATTTGTATAACGCATATGATACTAAACAGGCTTT TTCTAGTAATTATGATTCCGGTGTTTATTCTTATTTAACGCCTTATTTATCACACGGTCGGTATTT CAAACCATTAAATTTAGGTCAGAAGATGAAATTAACTAAAATATATTTGAAAAAGTTTTCTCGCG TTCTTTGTCTTGCGATTGGATTTGCATCAGCATTTACATATAGTTATATAACCCAACCTAAGCCG GAGGTTAAAAAGGTAGTCTCTCAGACCTATGATTTTGATAAATTCACTATTGACTCTTCTCAGC GTCTTAATCTAAGCTATCGCTATGTTTTCAAGGATTCTAAGGGAAAATTAATTAATAGCGACGAT TTACAGAAGCAAGGTTATTCACTCACATATATTGATTTATGTACTGTTTCCATTAAAAAAGGTAA TTCAAATGAAATTGTTAAATGTAATTAATTTTGTTTTCTTGATGTTTGTTTCATCATCTTCTTTTGC TCAGGTAATTGAAATGAATAATTCGCCTCTGCGCGATTTTGTAACTTGGTATTCAAAGCAATCA GGCGAATCCGTTATTGTTTCTCCCGATGTAAAAGGTACTGTTACTGTATATTCATCTGACGTTA AACCTGAAAATCTACGCAATTTCTTTATTTCTGTTTTACGTGCAAATAATTTTGATATGGTAGGT TCTAACCCTTCCATTATTCAGAAGTATAATCCAAACAATCAGGATTATATTGATGAATTGCCATC ATCTGATAATCAGGAATATGATGATAATTCCGCTCCTTCTGGTGGTTTCTTTGTTCCGCAAAAT GATAATGTTACTCAAACTTTTAAAATTAATAACGTTCGGGCAAAGGATTTAATACGAGTTGTCGA ATTGTTTGTAAAGTCTAATACTTCTAAATCCTCAAATGTATTATCTATTGACGGCTCTAATCTATT AGTTGTTAGTGCTCCTAAAGATATTTTAGATAACCTTCCTCAATTCCTTTCAACTGTTGATTTGC CAACTGACCAGATATTGATTGAGGGTTTGATATTTGAGGTTCAGCAAGGTGATGCTTTAGATTT TTCATTTGCTGCTGGCTCTCAGCGTGGCACTGTTGCAGGCGGTGTTAATACTGACCGCCTCAC CTCTGTTTTATCTTCTGCTGGTGGTTCGTTCGGTATTTTTAATGGCGATGTTTTAGGGCTATCA GTTCGCGCATTAAAGACTAATAGCCATTCAAAAATATTGTCTGTGCCACGTATTCTTACGCTTT CAGGTCAGAAGGGTTCTATCTCTGTTGGCCAGAATGTCCCTTTTATTACTGGTCGTGTGACTG GTGAATCTGCCAATGTAAATAATCCATTTCAGACGATTGAGCGTCAAAATGTAGGTATTTCCAT GAGCGTTTTTCCTGTTGCAATGGCTGGCGGTAATATTGTTCTGGATATTACCAGCAAGGCCGA TAGTTTG	

Results

Supplementary Tab. 3: Correction parameters for accurate intensity-based FRET efficiencies. List of correction factors for intensity-based FRET efficiencies, including the additional parameters required for the correction under STED conditions (see sections 'Determination of intensity-based correction factors', 'Intensity-based spectroscopic parameters' and 'Accurate intensity-based FRET efficiencies under STED conditions' in the Supplementary Methods).

			Correction Factor																
Sample	***Surface***	***G (eq. S15)***	***α***	***β***	***γ***	***δ***	***γ'***	x_D^0	x_A^0	x_D^d	x_A^d	$\Phi_{F,D}^0$	$\Phi_{F,A}^0$	$\Phi_{F,D}^d$	$\Phi_{F,A}^d$	$I_{Dem\|Dex}^{(BG)}$ (kHz)	$I_{Aem\|Dex}^{(BG)}$	$I_{Aem\|Aex}^{(BG)}$	$\frac{g_{D\|D}}{g_{A\|A}}$
Single Biotin dsD	BSA-Biotin	0.84	0.493 ±5	1.33 ±1	1.37 ±2	0.12 ±2	1.6 ± 1	0.14 ± 1	0.12± 1	0.86± 2	0.88± 2	0.84± 2	0.69± 2	0.06 ± 5	0.04 ±1	0.66±1	2.55± 10	2.35± 10	0.6
Double Biotin dsD	BSA-Biotin	0.84	0.493 ±5	1.33 ±1	1.37 ±2	0.12 ±2	1.6± 1	0.14 ± 1	0.12± 1	0.86± 2	0.88± 2	0.84± 2	0.69± 2	0.06 ± 5	0.04 ±1	0.67±1	2.05± 10	2.03± 10	0.6
Single Biotin dsD	NHS-PEG-Biotin	0.84	0.493 ±5	0.48 ±1	1.37± 2	0.23 ±2	1.6 ± 1	0.14± 1	0.12± 1	0.86± 2	0.88± 2	0.84± 2	0.69± 2	0.06 ± 5	0.04 ±1	0.65±1	1.63± 10	1.35± 10	0.6
Double Biotin dsD	NHS-PEG-Biotin	0.84	0.493 ±5	0.77 ±1	1.0 ±2	0.12 ±2	1.6 ± 1	0.14± 1	0.12± 1	0.86± 2	0.88± 2	0.84± 2	0.69± 2	0.06 ± 5	0.04 ±1	0.60 ±1	1.55± 10	1.41± 10	0.6
O(HF+NF)	NHS-PEG-Biotin	0.89	0.52 ± 2	1.2 ± 1	2.3 ± 2	0.07 ± 2	1.5 ± 1	0.21 ± 1	0.14 ± 1	0.80 ± 2	0.86 ± 2	0.81 ± 2	0.78 ± 2	0.060 ± 5	0.048 ± 5	0.20 ± 2	0.65 ± 10	0.54 ± 10	0.42 ± 6
O(NF)	NHS-PEG-Biotin	0.77	0.52 ± 2	2.1 ± 1	2.3 ± 2	0.07 ± 2	1.3 ± 1	0.29 ± 1	0.17 ± 1	0.71 ± 2	0.83 ± 2	0.81 ± 2	0.78 ± 2	0.060 ± 5	0.048 ± 5	0.20 ± 2	0.65 ± 10	0.54 ± 10	0.42 ± 6
O(HF)	NHS-PEG-Biotin	0.77	0.52 ± 2	1.5 ± 1	2.3 ±2	0.07 ± 2	2.8 ± 2	0.17 ± 1	0.20 ± 1	0.83 ± 2	0.80 ± 2	0.81 ± 2	0.78 ± 2	0.060 ± 5	0.048 ± 5	0.20 ± 2	0.65 ± 10	0.54 ± 10	0.42 ± 6
dsD (sm)	in solution	0.87	0.34	0.71	0.92	0.11	-	-	-	-	-	0.67	0.65	-	-				0.95
O (sm)	in solution	0.87	0.75	1.54	1.23	0.13	-	-	-	-	-	0.85	0.65	-	-				0.45
hGBP1		0.84	0.56 ±5	1.8± 1	1.13 ±2	0.12 ±2	1.6 ± 1	0.17± 1	0.12± 1	0.83 ± 2	0.88 ± 2	0.85± 2	0.69	0.69± 2	0.04 ±1	4.67	5.41	6.4	0.72

Supplementary Tab. 4: Parameters used for the determination of the Förster radius for dsD ,DNA origami and hGBP1. List of the parameters for two dye pairs for calculating the respective Förster radii, R_0. The absorption and fluorescence spectra as well as the spectral overlap spectrum *J* are shown in Supplementary Fig. 26. The fluorescence quantum yield of Atto594 is taken from the manufacturer[11].

Dye pairs	κ^2	n_{im}	$\Phi_{F,D}$	$\varepsilon_{A,max}$ [$M^{-1}cm^{-1}$]	J [$cm^{-1}M^{-1}nm^4$]	R_0 [Å]
Alexa594-Atto647N (for dsD and hGBP1)	2/3	1.40	0.80	150000	$1.008 \cdot 10^{16}$	71.0
Atto594-Atto647N (for DNA origami)	2/3	1.40	0.85	150000	$1.56 \cdot 10^{16}$	76.5

Supplementary Tab. 5: Microscope resolution and predicted precision. The theoretical precision was calculated using measured values for each dataset as described in section 'Predicting the localization precision' of the Supplementary Methods according to equation S29. The full width at half maximum of the point spread function was obtained from the average σ_{PSF} of all molecules. For the spot-wise distributions of the estimated localization precisions, see Supplementary Fig. 17 for the DNA origami measurements and Supplementary Fig. 25 for the DNA ruler measurements.

Sample	Immob.	# biotin anchors	Predicted localization precision [nm]	Donor FWHM [nm]	Acceptor FWHM [nm]
dsD(HF)	BSA	1	3.17	65	50
dsD(HF)	BSA	2	3.47	65	49
dsD(MF)	BSA	1	2.97	68	51
dsD(MF)	BSA	2	3.42	68	52
dsD(LF)	BSA	1	3.03	67	53
dsD(LF)	BSA	2	2.97	83	63
dsD(NF)	BSA	1	3.94	68	53
dsD(NF)	BSA	2	3.45	67	50
dsD(HF)	PEG	1	4.54	56	67
dsD(HF)	PEG	2	5.04	63	50
dsD(MF)	PEG	1	4.25	52	67
dsD(MF)	PEG	2	3.34	68	52
dsD(LF)	PEG	1	4.89	54	67
dsD(LF)	PEG	2	3.76	68	52
dsD(NF)	PEG	1	4.53	71	58
dsD(NF)	PEG	2	4.41	72	56
O(NF)	PEG	6	2.9	75	62
O(HF)	PEG	6	3.4	93	74
O(HF-NF)	PEG	6	2.0	70	56

Supplementary Tab. 6: Accessible volume parameters. Dye parameters for the AV simulations of Alexa594 and Atto647N on dsDNA with Förster radius R_0 = 71 Å, and of Atto594 and Atto647N on the origami nanostructures with a Förster radius R_0 = 76.5 Å. On the origami, an extension of the linker length due to the addition of an unpaired thymine base of 8.3 Å is considered based on the length of a phosphate-sugar-phosphate fragment in dsDNA. For detail, see the section '*Accessible Volume Simulations*' in the Supplementary Methods.

Dye	linker length [Å]	linker width [Å]	dye radius [Å]
Alexa594 (dsDNA)	20.5	4.5	3.5
Atto647N (dsDNA)	21.0	4.5	3.5
Atto594 (Origami)	28.8	4.5	3.5
Atto647N (Origami)	29.3	4.5	3.5

Supplementary Tab. 7: Expected FRET efficiencies and distances from accessible volume simulations for DNA rulers. FRET-based distances were calculated using a Förster radius of R_0 = 71 Å. See Supplementary Tab. 6 for the AV parameters and Supplementary Tab. 10 for the corresponding experimental data. The simulated FRET related distances were converted into $R_{\mathrm{mp}}^{\mathrm{FRET}}$ using a conversin functions as shown in Supplementary Fig. 5 using the parameters given in Supplementary Tab. S8.

Sample	$\langle E \rangle$	$\langle R_{\mathrm{DA}} \rangle_{\mathrm{E}}$ [Å]	$\langle R_{\mathrm{DA}} \rangle$ [Å]	R_{mp}^{FRET} [Å]
dsD(HF)	0.556	68.4	68.5	66.3
dsD(MF)	0.254	85.0	87.1	85.5
dsD(LF)	0.058	112.9	115.5	114.2
dsD(NF)	0.015	143.2	145.4	144.4

Supplementary Tab. 8: Conversion of FRET-related distances into mean-position distances. List of polynomial coefficients describing conversion into $R_{\mathrm{mp}}^{\mathrm{FRET}}$. The corresponding polynomials are given by $R_{\mathrm{mp}}^{\mathrm{FRET}} = a_0 + a_1\langle R_{\mathrm{DA}} \rangle_{\mathrm{E}} + a_2\langle R_{\mathrm{DA}} \rangle_{\mathrm{E}}{}^2 + a_3\langle R_{\mathrm{DA}} \rangle_{\mathrm{E}}{}^3 + a_4\langle R_{\mathrm{DA}} \rangle_{\mathrm{E}}{}^4 + a_5\langle R_{\mathrm{DA}} \rangle_{\mathrm{E}}{}^5$

and $R_{\mathrm{mp}}^{\mathrm{FRET}} = a_0 + a_1\langle R_{\mathrm{DA}} \rangle + a_2\langle R_{\mathrm{DA}} \rangle^2 + a_3\langle R_{\mathrm{DA}} \rangle^3 + a_4\langle R_{\mathrm{DA}} \rangle^4 + a_5\langle R_{\mathrm{DA}} \rangle^5$

The polynomials were determined based on AV simulations on dsDNA using a Förster radius of R_0 = 71 Å for the dye pair Alexa594-Atto647N and R_0 = 76.5 Å for dye pair Alexa594-Atto647N. The polynomials were determined as described in Kalinin et al.[19]. The corresponding graphs are shown in Supplementary Fig 5.

Conversion	sample	a_0	a_1	a_2	a_3	a_4	a_5
$\langle R_{\mathrm{DA}} \rangle_{\mathrm{E}} \rightarrow R_{\mathrm{mp}}^{\mathrm{FRET}}$	**Alexa594-Atto647N**	-68.1	4.48	-0.08	1.1E-03	-6.84E-06	1.67E-08
	Atto594-Atto647N	-153.4	8.09	-0.15	1.7E-03	-9.62E-06	2.09E-08
$\langle R_{\mathrm{DA}} \rangle \rightarrow R_{\mathrm{mp}}^{\mathrm{FRET}}$	**Alexa594-Atto647N**	-64.9	5.34	-0.15	1.4E-03	-8.76E-06	2.02E-05
	Atto594-Atto647N	-161.4	10.27	-0.21	2.3E-03	-1.23E-05	2.50E-08

Supplementary Tab. 9: Sub-ensemble fluorescence decay analysis. Fit parameters obtained from fluorescence decay analysis of single-molecule measurements acquired under STED (top) and confocal conditions (bottom). The fit model and parameters are described in section 'Sub-ensemble fluorescence decay analysis' of the Supplementary Methods (see equations S19 and S20). Superscript ***f*** indicates that the value was kept fixed during fitting. For each numerical superscripts ([1,2,3]) the corresponding parameters were optimized globally. The fluorescence decays and corresponding fits are shown Supplementary Fig. 13d for the DNA origami measurements and Supplementary Fig. 21 for the DNA ruler measurements.

Sample	Immob.	# biotin-anchors	x_{STED}	τ_{STED} [ns]	x_{FRET}	$\tau_{F,\,Donly}$ [ns]	R_0 [Å]	$\langle R_{DA} \rangle$ [Å]; σ = 6 Å	χ^2_r
FRET nanoscopy									
dsD(HF)	BSA	1	0.76	0.3	0.22	3.84	71	72.9+5 \ -4	1.18
dsD(HF)	BSA	2	0.77	0.3	0.22	3.84	71	71.9+4 \ -3	1.04
dsD(MF)	BSA	1	0.76	0.33	0.17	3.84	71	88.1+6 \ -8	1.07
dsD(MF)	BSA	2	0.72	0.35	0.28	3.84	71	87.9+4 \ -8	1.12
dsD(LF)	BSA	1	0.7	0.33	0.3	3.84	71	109.2+6 \ -11	1.09
dsD(LF)	BSA	2	0.75	0.33	0.25	3.84	71	110.1+ 6\ -6	1.09
dsD(NF)	BSA	1	0.67	0.34	0.33	3.84	71	115	0.99
dsD(NF)	BSA	2	0.69	0.38	0.31	3.84	71	124.5	1.04
dsD(HF)	PEG	1	0.74	0.36	0.26	3.84	71	74.9+4 \ -8	1.06
dsD(HF)	PEG	2	0.77	0.28	0.23	3.84	71	75.5+3 \ -10	1.01
dsD(MF)	PEG	1	0.69	0.39	0.31	3.84	71	89.6+4 \ -2	1.43
dsD(MF)	PEG	2	0.65	0.41	0.35	3.84	71	87.6+7 \ -22.6	1.09
dsD(LF)	PEG	1	0.67	0.34	0.33	3.84	71	102+18 \ -9	1.00
dsD(LF)	PEG	2	0.66	0.38	0.34	3.84	71	104.3+12 \ -6	1.3
dsD(NF)	PEG	1	0.72	0.36	0.28	3.84	71	107.8	1.04
dsD(NF)	PEG	2	0.69	0.38	0.31	3.84	71	115	1.17
O(NF)[1]	PEG	6	0.80	0.23 ± 5	-	3.69± 12[1]	76.5	-	1.02
O(HF)[1]	PEG	6	0.84	0.29	0.15	3.69± 12[1]	76.5	75+6 \ -6	1.59
O(HF-NF)$_{NF\ cut}$[2]	PEG	6	0.84	0.25 ± 3	0[f]	3.74 ± 10[2]	76.5	-	1.33
O(HF-NF)$_{HF\ cut}$[2]	PEG	6	0.88	0.27	0.1	3.74 ± 10[2]	76.5	76+3 \-3	1.00
Confocal single-molecule spectroscopy									
dsD(HF)	-	1	-	-	1	3.96	71	70	1.2
dsD(MF)	-	1	-	-	1	3.96	71	90; σ = 24 Å	1.2
dsD(LF)	-	1	-	-	1	3.96	71	115	1.5
dsD(NF)	-	1	-	-	1	3.96	71	133	1.1
O(NF)	-	6	-	-	0[f]	3.753	76.5	--	0.86
O(HF)	-	6	-	-	1[f]	3.753	76.5	78.3	1.2
O(HF-NF)	-	6	-	-	0.4	3.753	76.5	78.3	2.5

Supplementary Tab. 10: Intensity-based FRET efficiencies of all measurements. FRET efficiencies are determined from the center of the population in the two-dimensional histograms of the FRET efficiency versus fluorescence-weighted lifetime (see section 'Determination of average intensity-based FRET efficiencies') and are converted into interdye distances as described in section '*Accessible volume simulations*' (see Supplementary Tab. 8 for the conversion function). Two-dimensional histograms of the FRET efficiency versus fluorescence-weighted lifetime (*E*-τ plots) for DNA origami measurements are shown in Supplementary Figs. 12a and 13a for confocal single-molecule spectroscopy and FRET nanoscopy, respectively. The corresponding plots for the measurements of the dsDNA rulers are shown in Supplementary Figs. 19 and 20 for FRET nanoscopy and confocal single-molecule spectroscopy, respectively.

Sample	**Surface**	**# Biotin-anchor**	$\langle E \rangle$	$\langle R_{\mathrm{DA}} \rangle_E$ **[Å]**	R_{mp}^{FRET} **[Å]**
FRET nanoscopy					
dsD(HF)	BSA	1	0.47	72 ±2.6	71 ±3
dsD(HF)	BSA	2	0.44	74 ±2.6	73 ±3
dsD(MF)	BSA	1	0.22	88 ±3.8	89 ±4
dsD(MF)	BSA	2	0.21	89 ±3.8	89 ±4
dsD(LF)	BSA	1	0.1	103 ±9.8	106 ±10
dsD(LF)	BSA	2	0.09	104± 11.3	106 ±11
dsD(HF)	PEG	1	0.46	73 ±2.5	72 ±3
dsD(HF)	PEG	2	0.52	70 ±2.5	68 ±3
dsD(MF)	PEG	1	0.23	87 ±3.7	88 ±4
dsD(MF)	PEG	2	0.19	90 ±4.0	91 ±4
dsD(LF)	PEG	1	0.05	115 ±8.2	117 ±8
dsD(LF)	PEG	2	0.07	111 ±7.8	113 ±8
O(NF)	PEG	8	0.02± 0.02	>120	-
O(HF)	PEG	8	0.53± 0.02	76 ±2.0	74 ±2.0
O(HF-NF)$_{\text{NF cut}}$	PEG	8	0.02± 0.02	>120	-
O(HF-NF)$_{\text{HF cut}}$	PEG	8	0.45± 0.02	79 ±2.0	77 ±2.0
hGBP1	-	-	0	-	-
Confocal single molecule spectroscopy					
dsD(HF)	-		0.5	70	-
dsD(MF)	-		0.22	86	-
dsD(LF)	-		0.06	111	-
dsD(NF)	-		0.02	134	-
O(NF)	-	8	0	>120	-
O(HF)	-	8	0.53	75	73
O(HF-NF)	-	8	-	-	-
hGBP1	-	-	>0.5-	-	-

Supplementary Tab. 11: Steady state anisotropies for origami and dsDNA ruler. Donor (r_D) and acceptor steady state anisotropies (r_A) are determined from single-molecule measurements based on the Perrin plots of the scatter-corrected anisotropy against the intensity-weighted average fluorescence lifetime (see Supplementary Fig. 14). Only FRET-active molecules carrying both dyes were considered. The rotational correlation times for donor and acceptor (ρ_D, ρ_A), respectively, are obtained by a graphical fit to the Perrin equation using a fundamental anisotropy, $r_0 = 0.374$, for the donor and acceptor (see eq. S21c in section 'Determination of spot-integrated fluorescence lifetimes' of the Supplementary Methods).

Sample	r_D	ρ_D [ns]	r_A	ρ_A [ns]
O(HF+NF)	0.07	0.8	0.25	10
O(NF)	0.06	0.7	0.25	9
O(HF)	0.09	0.7	0.25	10
dsD(HF)	0.11	0.9	0.13	2.2
dsD(MF)	0.1	1.1	0.18	4
dsD(LF)	0.08	1.1	0.12	1.9
dsD(NF)	0.08	1.1	0.13	2.2

Supplementary Tab. 12: Model-based analysis of distance distributions of dsDNA rulers. Summary of fit results for surface immobilization by BSA-Biotin and NHS-PEG-Biotin. The procedure is described in Supplementary Note 7 and in the section 'Colocalization analysis' (see eq. S30). For each surface immobilization the single biotin distance distribution is fitted by single-component χ-distribution fit (I). For double biotin distribution two independent fit models were applied, assuming a single biotin component with fixed $\sigma_{\chi,1}$ from single biotin fit (II), and additional fixing of double biotin component $\sigma_{\chi,2}$ = 4 nm (III). Fixed values are highlighted in grey. Further parameters are described in the chapter 'Spectroscopy and Image analysis' in the section 'Model-based analysis of localization-based distance distributions'.

I. Single biotin – all parameters free									
Sample	**Surface**	**Number of biotin anchor**	**Model component**	**Amplitude A_1**	**$R_{\mathrm{mp},1}$ [nm]**	**$\sigma_{\chi,1}$**	**Amplitude A_2**	**$R_{\mathrm{mp},2}$ [nm]**	**$\sigma_{\chi,2}$**
dsD(HF)	BSA	1	1	1	0	5.21			
dsD(MF)	BSA	1	1	1	0	5.03			
dsD(LF)	BSA	1	1	1	4.95	4.41			
dsD(NF)	BSA	1	1	1	5.8	4.95			
II. Double biotin Single biotin parameters fixed, double biotin distance and sigma free									
dsD(HF)	BSA	2	2	0	0	5.21	1	4.13	5.17
dsD(MF)	BSA	2	2	0	0	5.03	1	7.54	5
dsD(LF)	BSA	2	2	0.29	4.95	4.41	0.71	10.4	3.59
dsD(NF)	BSA	2	2	0.12	5.8	4.95	0.88	10.72	6.03
III. Double biotin Single biotin parameters fixed, double biotin distance free, but sigma fixed									
dsD(HF)	BSA	2	2	0.73	0	5.21	0.27	8.89	4
dsD(MF)	BSA	2	2	0.29	0	5.03	0.71	9.61	4
dsD(LF)	BSA	2	2	0.18	4.95	4.41	0.82	9.7	4
dsD(NF)	BSA	2	2	0.48	5.8	4.95	0.52	13.99	4
I. Single biotin – all parameters free									
Sample	**Immob.**	**Number of biotin anchor**	**Model component**	**Amplitude A_1**	**$R_{mp,1}$ [nm]**	**$\sigma_{\chi,1}$**	**Amplitude A_2**	**$R_{mp,2}$ [nm]**	**$\sigma_{\chi,2}$**
dsD(HF)	PEG	1	1	1	0	5.77	1	0	5.77
dsD(MF)	PEG	1	1	1	0	6.33	1	0	6.33
dsD(LF)	PEG	1	1	1	0	7.08	1	0	7.08
dsD(NF)	PEG	1	1	1	7.18	4.99	1	7.18	4.99
II. Double biotin Single biotin parameters fixed, double biotin distance and sigma free									
dsD(HF)	PEG	2	2	0.27	0	5.77	0.73	0.03	7.7
dsD(MF)	PEG	2	2	0	0	6.33	1.0	7.2	6.2
dsD(LF)	PEG	2	2	0.5	0	7.08	0.5	12.92	3.36
dsD(NF)	PEG	2	2	0.67	7.18	4.99	0.33	15.62	3.86
III. Double biotin Single biotin parameters fixed, double biotin distance free, but sigma fixed									
dsD(HF)	PEG	2	2	0.77	0	5.77	0.23	12.01	4
dsD(MF)	PEG	2	2	0.64	0	6.33	0.37	12.4	4
dsD(LF)	PEG	2	2	0.43	0	7.08	0.57	12.26	4
dsD(NF)	PEG	2	2	0.66	7.18	4.99	0.34	15.47	4

Supplementary Tab. 13: Overview of estimated interdye distances. All distances are mean-position distances R_{mp}. Where applicable, the FRET-related distances were converted into R_{mp}^{FRET}, as described in section 'Accessible volume simulations' and shown in Supplementary Fig. 5, using the parameters given in Supplementary Tab. S8. The experimental origin of the distances is denoted as follows: FN: FRET nanoscopy, SM: confocal single-molecule spectroscopy, int: intensity-based ($\langle R_{DA} \rangle_E$ in Supplementary Tab. 10), lt: lifetime-based ($\langle R_{DA} \rangle$ in Supplementary Tab. 9) loc: localization-based (R_{mp}^{loc}). The localization-based distances represent the average of the distribution of R_{mp}^{loc} obtained from the MEM analysis for dsD. For the accessible volume simulations, we used an atomistic model of the origami generated by the CanDo software[47,48], based on an assumed inter-helical distance of 2.25 nm for the accessible volume simulations. The superscript [a] denotes those values obtained from aligned structures, which is in general more accurate due to the better filtering of broken constructs. For the intensity- and lifetime-based FRET analysis of the DNA origami, see Supplementary Fig. 13a-d, and for the dsDNA rulers, see Supplementary Figs. 19 and 21.

			R_{mp}^{loc} [Å]	R_{mp}^{FRET} [Å]				
Sample	**Surface**	**# Biotin-anchor**	**FN-loc**	**AV sim.**	**FN-int**	**FN-lt**	**SM-int**	**SM-lt**
O(NF)	PEG	8	165 ± 5	144	>120	>120	>120	>120
O(HF)	PEG	8	94 ± 10	48	74 ± 2	72 ± 6	73	75
O(HF-NF)$_{NF\ cut}$	PEG	8	147 ± 7[a]	144	>120	>120	--	>120
O(HF-NF)$_{HF\ cut}$	PEG	8	53 ± 7[a]	48	77 ± 2	73 ± 3	--	75
dsD(HF)	BSA	1	0	66.3	71 ± 3	70.5	70	70
dsD(HF)	BSA	2	49.5	66.3	73 ± 3	69.5	70	70
dsD(MF)	BSA	1	19.5	85.5	89 ± 4	88.9	86	90
dsD(MF)	BSA	2	73.5	85.5	89 ± 4	88.8	86	90
dsD(LF)	BSA	1	54	114.2	106 ± 10	108.3	111	115
dsD(LF)	BSA	2	90	114.2	106 ± 11	109.2	111	115
dsD(NF)	BSA	1	72	144.4	-	-	-	-
dsD(NF)	BSA	2	150	144.4	-	-	-	-
dsD(HF)	PEG	1	0	66.3	72 ±3	72.6	70	70
dsD(HF)	PEG	2	64.5	66.3	68 ±3	73.2	70	70
dsD(MF)	PEG	1	31.5	85.5	88 ±4	88.2	86	90
dsD(MF)	PEG	2	75	85.5	91 ±4	86.0	86	90
dsD(LF)	PEG	1	70.5	114.2	117 ±8	101.1	111	115
dsD(LF)	PEG	2	112.5	114.2	113 ±8	103.5	111	115
dsD(NF)	PEG	1	79.5	144.4	-	-	-	-
dsD(NF)	PEG	2	133.5	144.4	-	-	-	-

Filtering and analysis settings

Supplementary Tab. 14: Overview of used analysis settings. Values between square brackets indicate corresponding software settings as listed is Supplementary Tab. 16. Software settings that are not explicitly mentioned all have default values. The procedures are described in detail in Supplementary Note 1, in the chapter 'Spectroscopy and Image analysis' in the section 'Filtering procedures', and illustrated in Supplementary Figs. 3 and 6.

Parameter	**O(HF-NF)**	**O(NF)**	**O(HF)**	**dsD (all)**	**hGBP1**
Analysis workflow	**multi-spot**			**single-spot**	**multi-spot**
Localization analysis					
# images taken	2036 (100%)	1500 (100%)	2992 (100%)	--	258 (rings)
# frames for localization [Framestop_localization]	60	20	20	60	100
# frames for FRET [Framestop_FRET]	20	20	20	30	20
gate for localization [Ggate_loc, Rgate_loc, Ygate_loc]	3.7 ns - 19.2 ns	3.7 ns - 19.2ns	0.0 ns - 19.2 ns	3.8 ns -15.4 ns	3.8 ns -15.4 ns
gate for spot lifetime tail fit [Ggate_lt, Rgate_lt, Ygate_lt]	3.7 ns - 19.2 ns	3.7 ns - 19.2 ns	3.7 ns - 19.2 ns	3.8 ns -15.4 ns	3.2 ns -15.4 ns
ROI size [ROIsize]	30 x 30 pixels	20 x 20 pixels	20 x 20 pixels	21 x 21 pixels	17x17 pixels
absolute threshold [ROI_threshold_abs]	1	1	1	2	1
minimal brightness per spot [garbageBrightness]	20	20	20	--	40
# FRET pairs	1394 (67%)	724 (48%)	987 (33%)		1533 (spots)
Data filtering for particle averaging					
spot stoichiometry	2 Donors, 2 Acceptors	--	--	--	--
RMSD (alignment score)	< 10 nm	--	--	--	--
No. of platforms	101 (7%)	--	--	--	--
Data filtering for fluorescence spectroscopy					
spot stoichiometry	≥1 Donor, ≥1 Acceptor	≥1 Donor, ≥1 Acceptor	1 Donor, 1 Acceptor	--	≥1 Donor, ≥1 Acceptor
acceptor intensity	--	--	>150 counts	--	--
background for lifetime fitting [kHz]	0.1	0.5	0.6	--	0.4
# FRET pairs	1384 (68 %)	677 (45%)	327 (11%)	--	1533
Data filtering for sub-ensemble lifetime decay					
spot stoichiometry	1, 2 or 3 Donors and 1, 2 or 3 Acceptors			--	1, 2 or 3 Donors and 1, 2 or 3 Acceptors
efficiency for highFRET cut	E > 0.31	--	E > 0.31	--	-
# FRET pairs for highFRET cut	372 (18 %)	--	694 (23 %)	--	-
efficiency for noFRET cut	E < 0.2	E < 0.2	--	--	-
# FRET pairs for noFRET cut	729 (36 %)	450 (30%)	--	--	-
proximity ratio cut, PR					P > 0.35

Supplementary Tab. 15: Selection criteria for dsDNA rulers. The number of spots (# spots) corresponds to the remaining spots after each selection step. The procedures are described in Supplementary Note 1, the section 'Spectroscopy and Image analysis, Filtering procedures' in the Supplementary Methods, and illustrated in Supplementary Figs. 3 and 6.

				Image indicator			FRET indicator	
Sample	**Surface**	**# biotin anchors**	**Total number of spots**	**Selection: $\sigma_{PSF,D}$ [nm]**	**Selection: $\sigma_{PSF,A}$ [nm]**	**# spots**	**Selection: corrected stoichiometry *S***	**# spots**
dsD(HF)	BSA	1	2116	20- 35	15-30	1316	0.4-0.6	**583**
dsD(HF)	BSA	2	1461	20- 35	15-30	825	0.4-0.6	**346**
dsD(MF)	BSA	1	2044	20- 35	15-30	1360	0.4-0.6	**554**
dsD(MF)	BSA	2	2784	20- 35	15-30	1669	0.4-0.6	**705**
dsD(LF)	BSA	1	2064	20- 35	15-30	1337	0.4-0.6	**553**
dsD(LF)	BSA	2	3819	20- 35	15-30	882	0.4-0.6	**321**
dsD(NF)	BSA	1	2382	20- 35	15-30	1533	0.4-0.6	**652**
dsD(NF)	BSA	2	3246	20- 35	15-30	1800	0.4-0.6	**712**
dsD(HF)	PEG	1	2299	20- 35	15-30	1491	0.35-0.65	**1195**
dsD(HF)	PEG	2	1120	20- 35	15-30	708	0.35-0.65	**554**
dsD(MF)	PEG	1	1188	20- 35	15-30	858	0.35-0.65	**717**
dsD(MF)	PEG	2	653	20- 35	15-30	378	0.35-0.65	**233**
dsD(LF)	PEG	1	1082	20- 35	15-30	602	0.4-0.6	**428**
dsD(LF)	PEG	2	1410	20- 35	15-30	811	0.35-0.65	**495**
dsD(NF)	PEG	1	1151	20- 35	15-30	689	0.35-0.65	**520**
dsD(NF)	PEG	2	3884	20- 35	15-30	2450	0.35-0.65	**1845**

Supplementary Tab. 16: Complete description of all analysis parameters for the SEIDEL software. See section 'Spectroscopy and image analysis, Filtering procedures' and Supplementary Figs. 3 and 6.

Parameter	**Description**
Read/Write settings (A)	
File directory	Folder containing the raw photon (.ptu) files
Output folder	Location to save output files.
Lifetime image loading (B1)	
Ggate_loc, Rgate_loc, Ygate_loc	Donor, FRET sensitized acceptor, direct excited acceptor localization gate range. Localization may be performed on gated or ungated data.
Ggate_lt, Rgate_lt, Ygate_lt	Donor, FRET sensitized acceptor, direct excited acceptor lifetime gate range. The spot-wise lifetime is always fitted on gated data.
Ggate_I, Rgate_I, Ygate_I	Donor, FRET sensitized acceptor, direct excited acceptor intensity gate range. The spot-wise intensity is always obtained from ungated data.
Framestop_FRET	Starting from the first frame, how many frames are merged to collect statistics for FRET analysis. Not all frames are used to exclude bleaching which is more likely to occur as more frames are accumulated.
Ntacs	Number of TAC channels in lifetime decay. Default 256.
Rebin	If given, the image is rebinned by an integer factor. Default False.
Framestop_localization	How many frames to collect for localization. Default all frames are taken
Fit region Selection (B2)	
ROI_threshold_abs	Minimal amplitude for ROI selection. Default 1 count / pixel.
ROI_threshold_relative	Minimal amplitude for ROI selection relative to image max. Default 0.3 (norm. int.)
min_distance	Minimal distance between the centers of two ROIs in pixels. Default 15 pixels.
smoothIntensitySigma	Standard deviation of Gaussian filter to smooth the image and identify regions of interest. Default 2 pixels.
ROIsize	Side of square region of interest. Default 20 pixels
spot integration area	Integration area around a spot center used for spectroscopy information. Default 7 x 7 pixels.
Fit parameters (B3)	

DTwoIstar	Minimal improvement in 2I* after an additional spot has been added to the fit model for the fit to be accepted as better. Default 0.03 normalized likelihood)
garbageBrightness	Spots with a lower intensity are discarded. Default 20 counts integrated over a spot.
junkIstar	Pure-noise data sometime have very low 2I*. Fits with a 2I* below are not considered good. Default value 0.30 (normalized likelihood)
fitbg	fit background when fitting Gaussian spots. Default True
setbg	Initial estimate for background. Default 0.2 counts / pixel.
Ellipt_circ	If True, allows for elliptical spots. Default False.
Correction parameters (C)	
max_dist (post-processing)	All pair distances more than max_dist away from the mean displacement are considered junk and kicked out. Default 100nm.
Correction and selection parameters (D)	
Image_stoichiometry	Image stoichiometry lists the number of green and yellow spots that are located in an image. It is different from stoichiometry obtained from photon counts. One can chose to incorporate only images with e.g. 1 green and 1 yellow spot.
Channel shift correction	Correct for channel shift. Per default a (0nm, 5nm) shift in (x, y) is applied as the acceptor direct excitation image is shifted by half a pixel because of the line interleaved donor and acceptor direct excitation and constant scanner velocity in y.
Lifetime background	Background level for lifetime tail fits. Default: 0 kHz.

***Supplementary Tab. 17: List of filtering parameters*.** Some parameters are defined for a single spot and others are defined only for a donor-acceptor spot pair (multi-spot procedure). 'Acceptor (PIE)' is used to indicate acceptor under direct excitation, 'acceptor (FRET)' is used to indicate FRET sensitized acceptor. Additional intensity-derived parameters are also available but not listed explicitly. [1]Anisotropy is only available in AnI-3SF program. [2]Lifetime decay histogram is an array of values and therefore is separately exported (Supplementary Fig. 6, panel F1). [3]Correction parameters are used to calculate these values in a separate program (Margarita). See 'Spectroscopy and image analysis, Filtering procedures', Supplementary Figs 3 and 6.

FRET indicator	**Type**
Donor / acceptor (PIE) position	Single spot
Donor / acceptor (PIE) localization photons	Single spot
Donor / acceptor (PIE) spot width	Single spot
Donor / acceptor (PIE) spot ellipticity	Single spot
Donor / acceptor (PIE) background	Single spot
Number of donor / acceptor (PIE) spots	Single spot
Donor / acceptor (FRET) / acceptor (PIE) lifetime	Single spot
Donor / acceptor (FRET) / acceptor (PIE) intensity	Single spot
Anisotropy[1]	Single spot
Donor / acceptor (FRET) / acceptor (PIE) lifetime decay histogram[2]	Single spot
Localization distance	Spot pair
Proximity ratio (uncorrected Efficiency)	Spot pair
Stoichiometry[3]	Spot pair
Efficiency (corrected)[3]	Spot pair

Supplementary Tab. 18: Position of dyes on the origami platform determined by localization analysis. The estimated positions are shown in the main text in Fig. 2b and the respective interdye distances in Fig. 2e. The positions are aligned according to the origami frame of reference such that the D1 point is in the origin and that the x axis is parallel to the helical axis, as indicated by the superscript ^{D1}. The distribution of alignment scores is displayed in Supplementary Fig. 9. For the interdye distances, the experimental coordinate system is used which is rotated by an angle of 18 degrees with respect to the origami frame of reference such that both acceptor positions lie on the x axis, as indicated by the superscript ^{AA}. For the distances, the spacing between the dyes in terms of the structural parameters of the origami nanostructure (number of helices n_h and base pairs n_{bp}) is given in addition. x, y: measured x- and y-displacement; x model, y model: x- and y-displacement based on the structural model described in Supplementary Note 2 (eq. S35) with d: interdye distance, d model: interdye distance based on the modeled x- and y-displacements.

	x [nm]	x model [nm]	y [nm]	y model [nm]	d [nm]	d model [nm]	n_h	n_{bp}
D1 position	-0.5± 0.4	0^{D1}	0.1±0.3	0^{D1}				
D2 position	75.0±0.4	75	2.7±0.4	2.4				
A1 position	0.35±0.4	0^{D1}	-14.6±0.3	-14.4				
A2 position	75.1±0.4	75	-2.6±0.4	-2.4				
D1-A1 distance (NF)	-1.8±0.7	-2.3	14.5±0.7	14.2	14.6±0.7	14.4	-6	0
D1-D2 distance	74.5±0.7	74.0	9.3±1.0	9.5	75.1±0.7	74.6	1	236
D1-A2 distance	76.4±0.7	76.3	-5.3±0.7	-4.7	76.5±0.7	76.4	-1	236
A1-D2 distance	74.5±0.7	73.3	14.5±0.7	14.2	75.9±0.7	74.7	7	236
A1-A2 distance	75.9±0.6	75.6	0^{AA}±0	0^{AA}	75.9±0.6	75.6	5	236
D2-A2 distance (HF)	-0.3±0.7	-0.8	5.3±0.7	4.7	5.3±0.7	4.8	-2	0

Supplementary Tab. 19: Polynomial coefficients for linker-corrected static FRET line.

Linker-corrected static FRET–lines are approximated by a fourth-order polynomial as given in equation 10 in the main text. Static FRET-lines generated by the given parameters are used in Fig. 3a, Supplementary Fig. 12 and 13a for the DNA origami, and Fig. 4b, Supplementary Fig. 21 and 29 for the DNA rulers, and Fig. 6d for hGBP1.

	sample	$\tau_{D(0)}$ [ns]	a_1	a_2	a_3	a_4	a_5
Imaging	**dsDNA**	3.84	-0.0125	0.5910	0.3127	-0.0800	0.0069
	Origami	3.6500	-0.0067	0.7172	0.2383	-0.0678	0.0065
	hGBP1	3.9	-0.0126	0.5925	0.3070	-0.0773	0.0066
confocal sm spectr.	**dsDNA**	3.9	-0.0131	0.5815	0.3138	-0.0786	0.0066
	Origami	3.9	-0.0109	0.6352	0.2726	-0.0684	0.0058
	hGBP1	3.84	-0.0125	0.5910	0.3127	-0.0800	0.0069

Supplementary Figures

Method figures

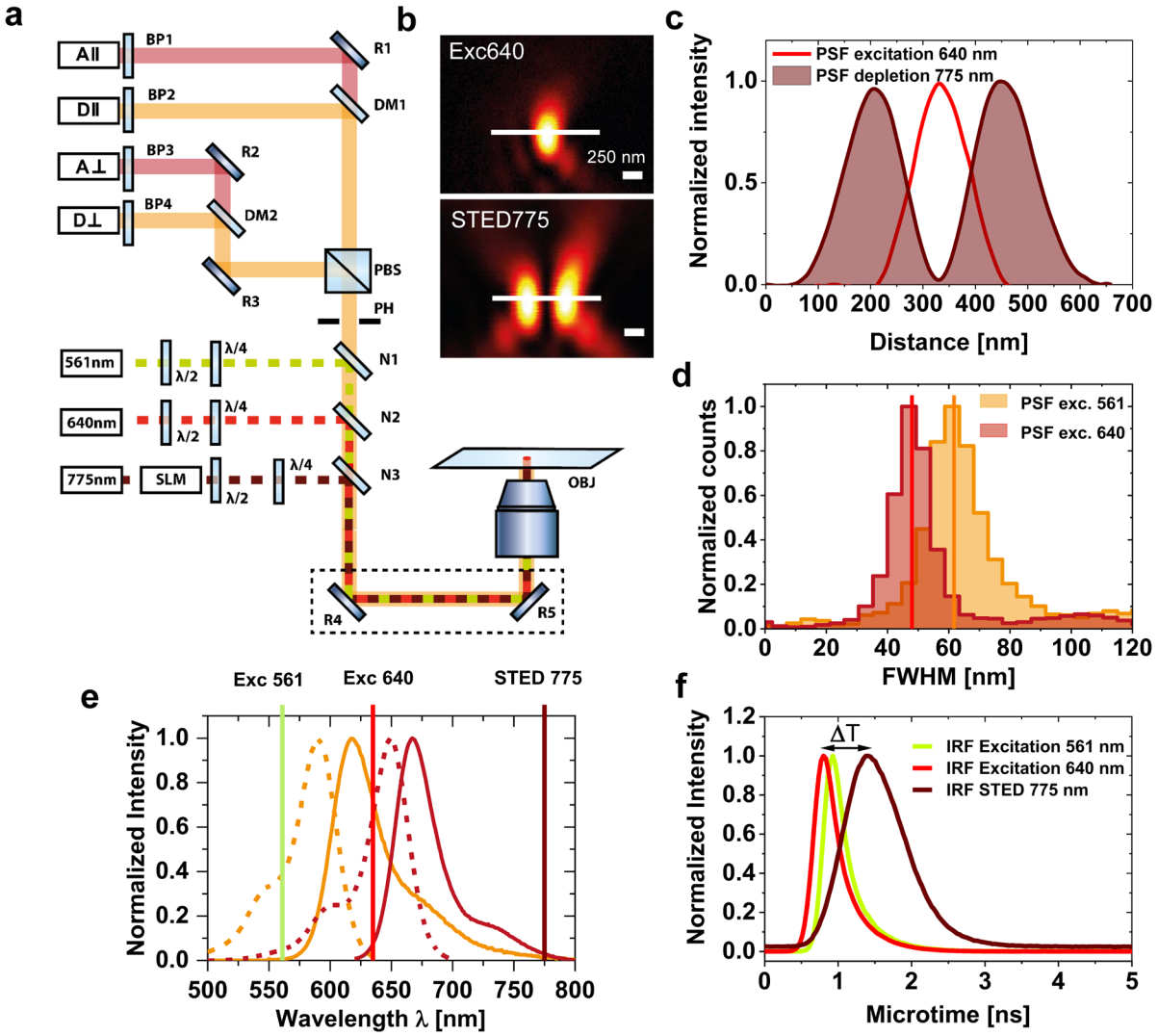

Supplementary Fig. 1: STED-FRET microscope. **a)** Scheme of the microscope with pulsed laser excitation at 561 nm and 635 nm, and depletion at 775 nm. The STED 775 laser is modulated by a spatial light modulator (SLM) to generate the 2D donut transverse mode. The excitation and depletion lasers are overlaid by notch filters (N1-N3). The emitted light is guided back through a pinhole (PH), split by polarization using a polarizing beam splitter (PBS), split spectrally by dichroic mirrors (DM), and filtered by band pass filters (BP) in front of the detectors. A detailed description is given in the Supplementary Methods in the section 'STED-FRET microscope'. **b-c)** Recorded point spread function (PSF) of excitation laser 640 nm and depletion laser 775 nm measured using gold beads of 150-nm. **d)** Histogram of determined full width at half maximum (FWHM) of PSF measured on single biotin dsD(NF) sample immobilized via BSA-Biotin. **e)** Excitation and emission spectra of the dyes Atto594 and Atto647N attached to dsDNA. Vertical lines illustrate the used excitation and depletion wavelength. **f)** Recorded instrument response functions (IRF) of used excitation/depletion lasers (561nm, 640nm and 775nm) showing the time delay of 0.5 ns for the depletion laser 775nm.

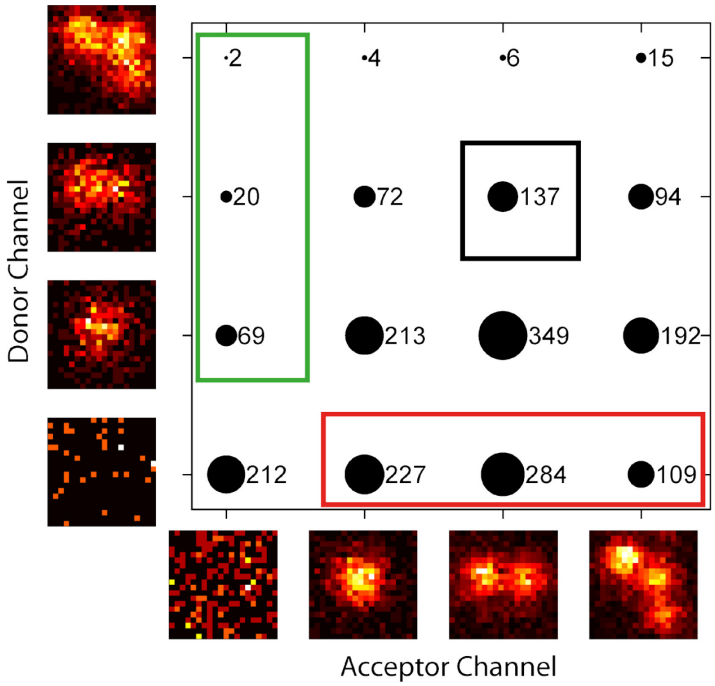

Supplementary Fig. 2: Spot stoichiometry for DNA origami. Data corresponds to the O(HF+NF) sample. Black circles with numbers indicate the number of constructs corresponding to that spot stoichiometry species. The green box indicates constructs without acceptors (donor-only), used to determine the crosstalk and donor only lifetime. Similarly, the red box indicates constructs without donors (acceptor-only), used to determine direct excitation and acceptor lifetime. The black box indicates fully labelled structures with two FRET pairs, which are used to obtain an average structure. Partially labelled structures (1 donor - 1 acceptor, 1 donor – 2 acceptors, 2 donors – 1 acceptor) each contain one FRET pair and all available FRET pairs are included in Fig. 2b of the main text. An emitter stoichiometry of >2 can occur due to crowding or aggregation. Overall, more acceptor spots than donor spots are detected, attributed to the weaker donor signal due to a lower detection efficiency and quenching by FRET. For a description of the filtering procedure, see 'Spectroscopy and image analysis, Filtering procedures' and Supplementary Fig. 3 and 6.

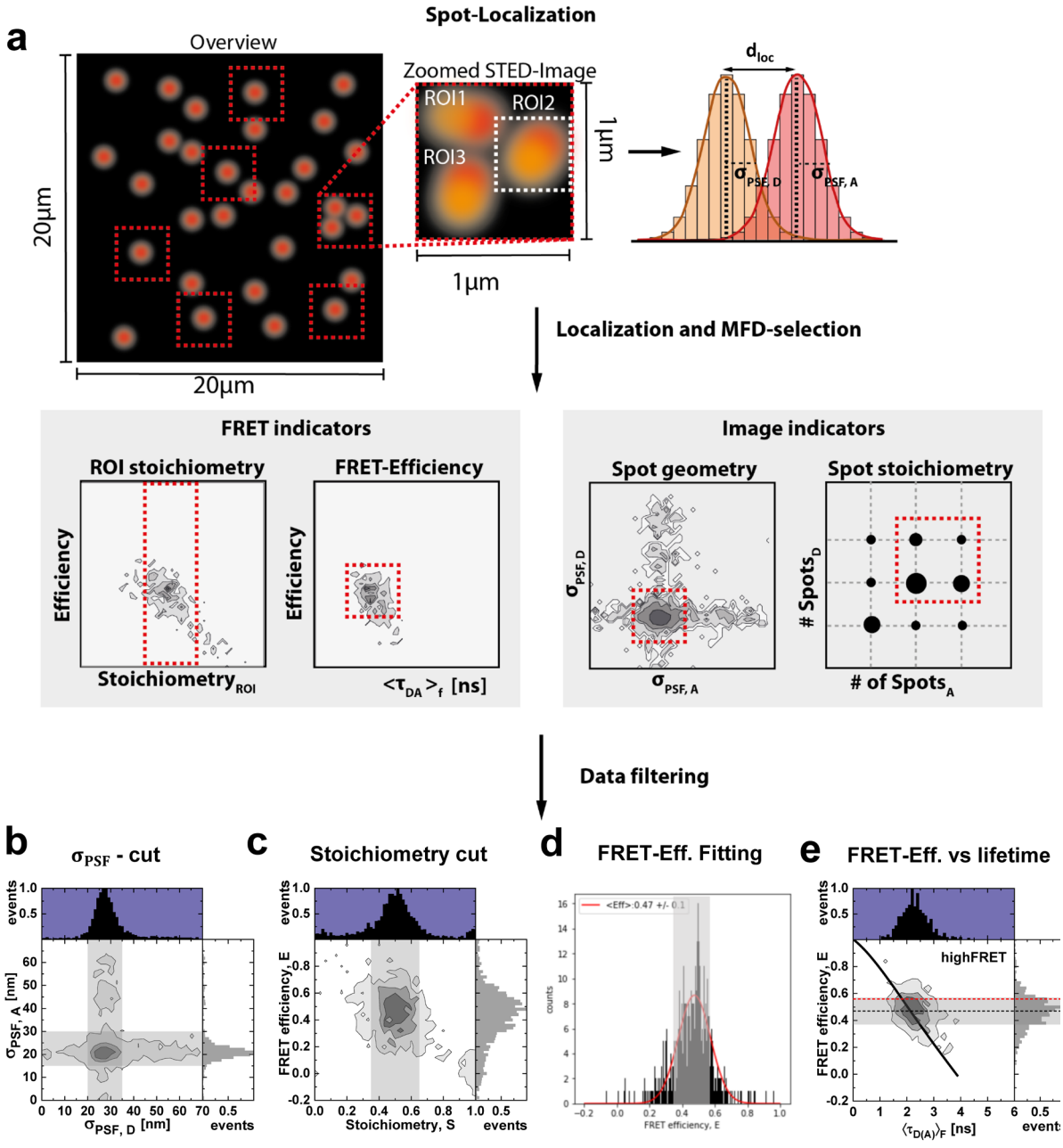

Supplementary Fig. 3: Schematic data filtering workflow. a) Schematic illustration of the filtering procedure for dsDNA (dsD) and origami samples (O). b-e) Applied data filtering shown using the single biotin labeled dsD(HF) sample. Intensity-based FRET-derived distances are determined by (b) filtering of 2D Gaussian fitted spots by sigma selection, (c) only donor acceptor pairs are selected with a stoichiometry around 0.5, and (d) the FRET efficiency histogram is fitted by a single Gaussian distribution to determine the mean and sigma (grey area in e). e) The resulting 2D histogram of FRET efficiency, E, vs the fluorescence weighted donor lifetime. The grey area marks the 1σ fitted FRET efficiency histogram and is used to calculate the mean FRET efficiency (black dotted line). The predicted FRET efficiency by AV simulation is shown as a red dotted line. See Supplementary Tab. 14, 15, 16 and 17 for an overview of the analysis settings and applied filterig parameters and

Supplementary Fig. 6 for a general overview of the analysis workflow, including the localization analysis.

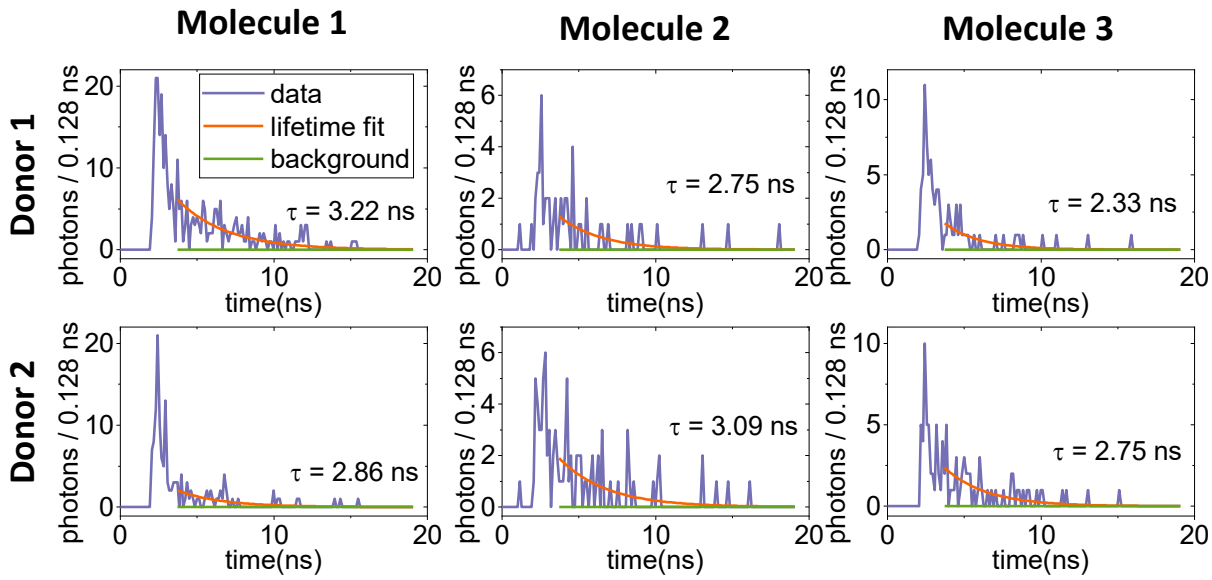

Supplementary Fig. 4: Exemplary ROI-wise donor fluorescence decay fits. Three origami molecules carrying two FRET pairs O(HF+NF) were randomly selected. See 'Spectroscopy and image analysis, Determination of spot-integrated fluorescence lifetimes' for a description of the procedure and fit model.

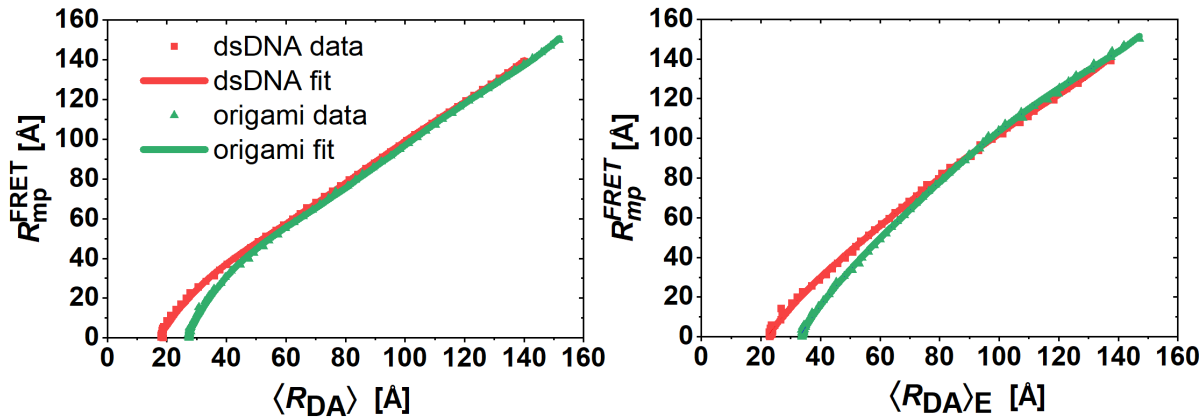

Supplementary Fig. 5: Conversion between FRET-averaged distances and mean-position distances. The conversion function is given for the two FRET pairs Alexa594-Atto647N (left, as used for the DNA rulers) and Atto594-Atto647N (right, used for the DNA origami). The legend is identical for both panels. The relation between the mean position distance $R_{\mathrm{mp}}^{\mathrm{FRET}}$ and the mean donor-acceptor distance $\langle R_{\mathrm{DA}} \rangle$ (left) or the FRET-averaged interdye distance $\langle R_{\mathrm{DA}} \rangle_E$ was approximated by a fifth-order

polynomial. The polynomial coefficients and the corresponding equation are given in Supplementary Tab. 8. The polynomials were determined as described in Kalinin et al.[19]

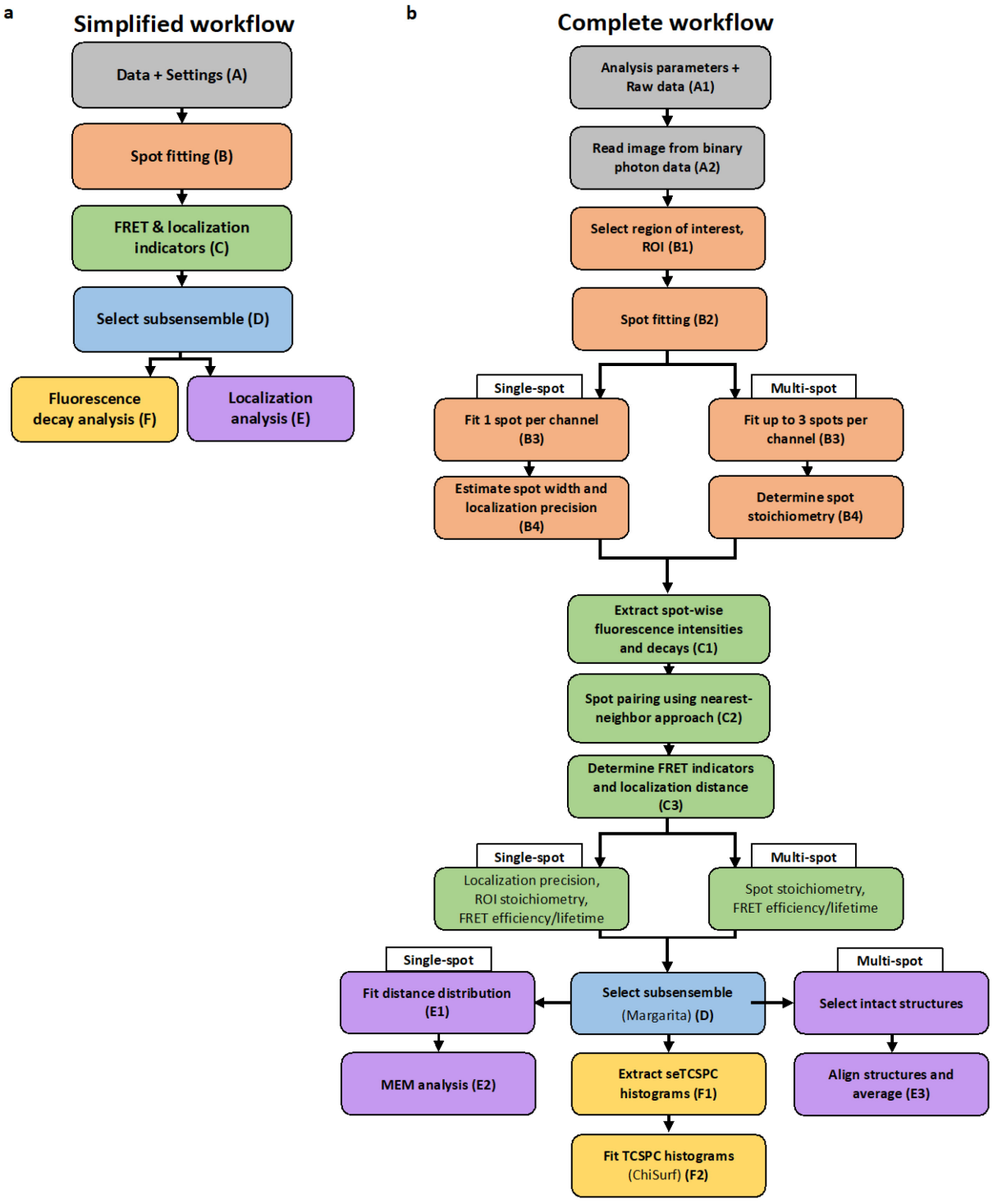

Supplementary Fig. 6: Analysis workflow. **a**) Simplified workflow. **b**) Complete workflow. See Supplementary Note 1 for a detailed description of the workflow.

Origami figures

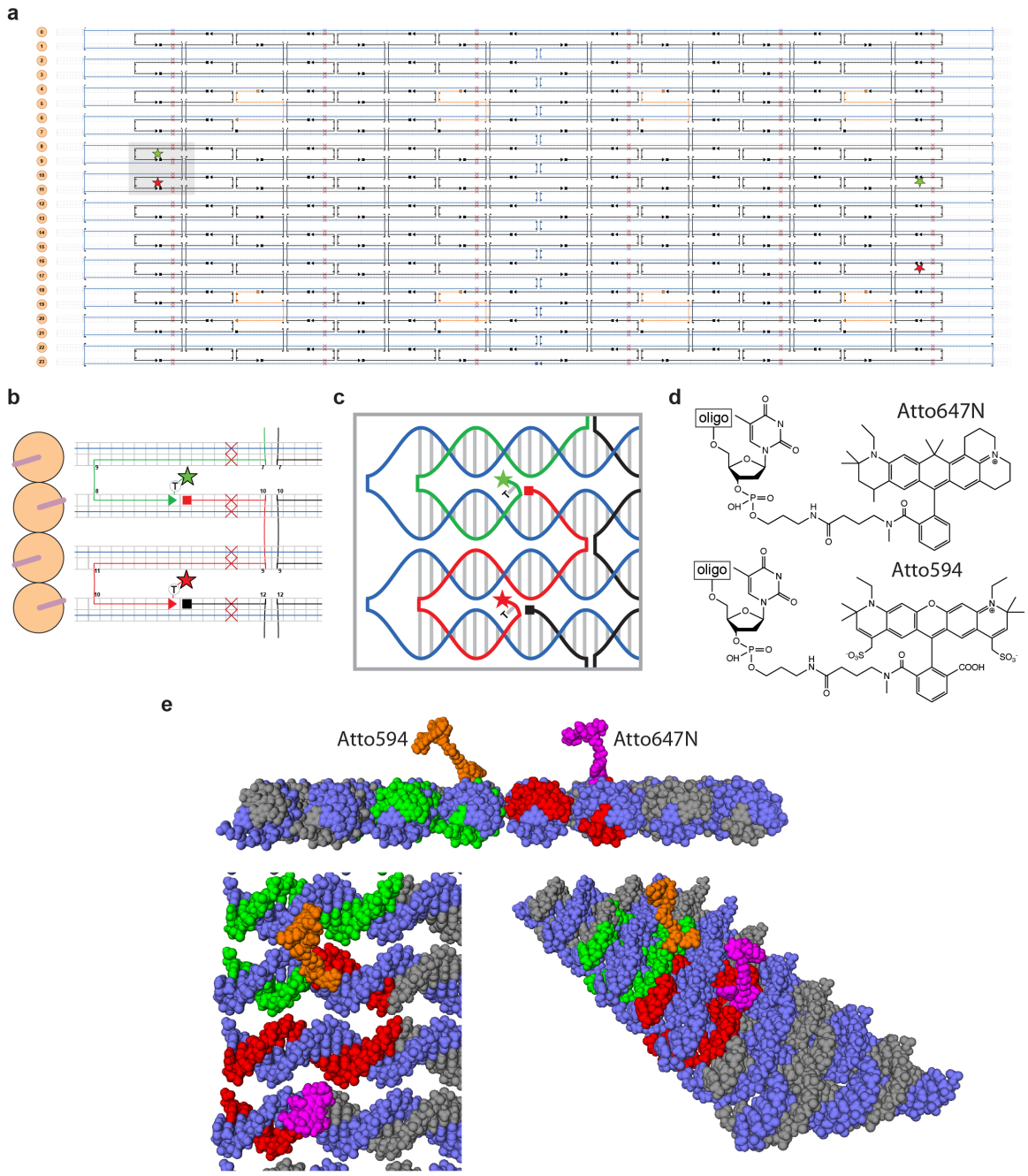

Supplementary Fig. 7: DNA origami design. **a)** Strand diagram of the single-layer DNA origami rectangle. Green and red stars indicate the labeling positions of the donor (Atto594) and acceptor (Atto647N) dyes, respectively. The schematic was generated using the caDNAno software[6]. Squares signify the 5' end and arrow heads the 3' end of the staple strands. **b)** Zoom-in of the high FRET dye pair (gray shaded area in panel a). The scaffold strand is colored in blue, staple strands in black and the strands carrying the donor and acceptor are colored green and red, respectively. 5' ends of staple strands are indicated by squares, 3' ends by arrow tips. The dyes are linked to the 3' end with an unpaired thymine base pair as a spacer. A side-view of the four displayed helices on the left indicates the orientation of the orange shaded base pairs. Base pairs used for the dye attachment point upwards

from the plane are defined by the origami rectangle. Red crosses indicate deletions in the structure used to reduce twisting of the single-layer sheet. **c)** Cartoon representation of the fragment shown in panel b, providing a more detailed view of the routing of the scaffold and staple strands. **d)** Chemical structures of the dyes and the labeling chemistry used for the attachment to the 3' end. A C3-aminolink group on the terminal phosphate is reacted with a N-hydroxysuccinimidyl residue on the dyes. **e)** 3D model of the dyes linked to the origami structure in a side view (top), top view (bottom left) and perspective view (bottom right). The strands are colored as in panels b and c. Dyes are colored orange (Atto594) and magenta (Atto647N). The single-stranded scaffold overhangs are not displayed. See Supplementary Tab. 2 for the list of DNA sequences.

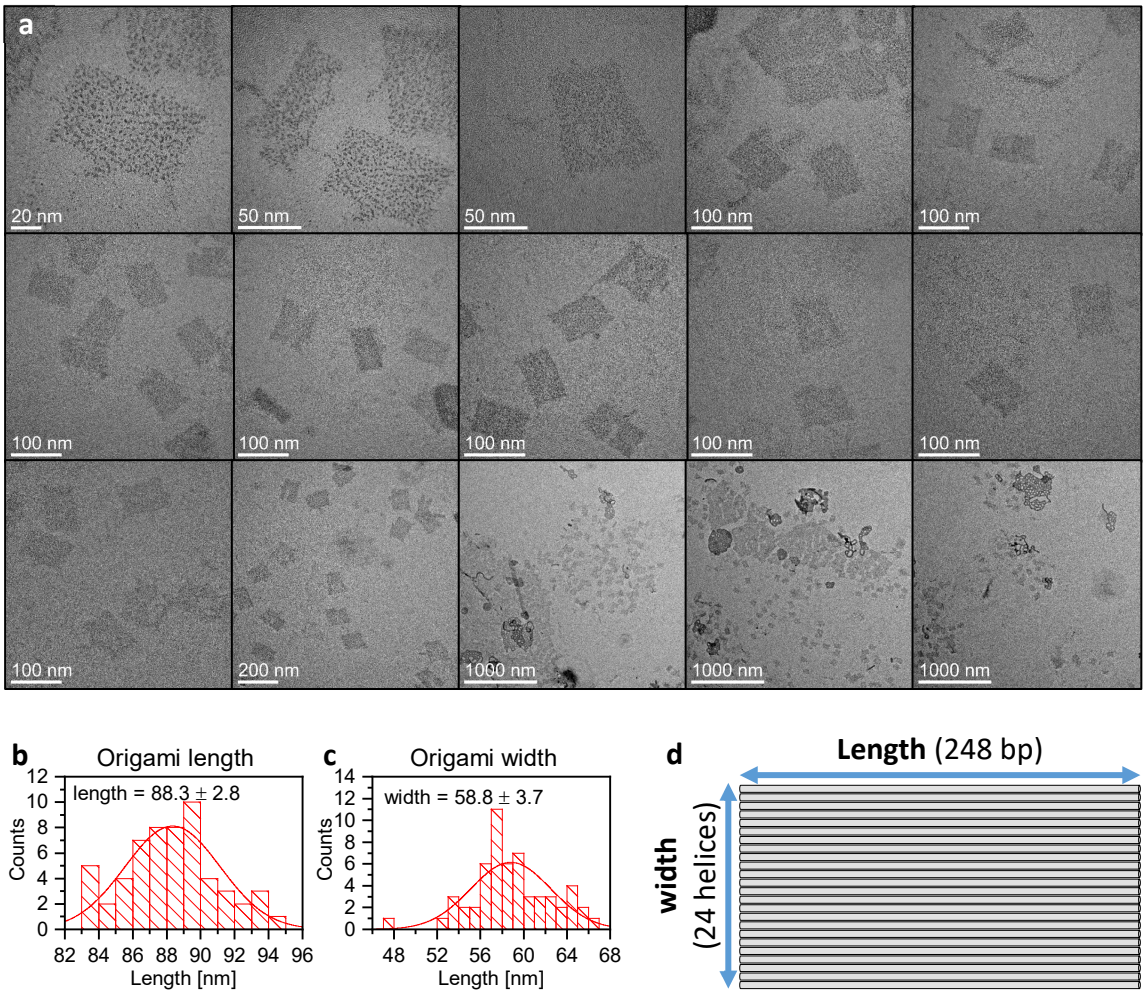

Supplementary Fig. 8: TEM imaging of DNA origami platforms. **a**) Overview of recorded TEM images. Images are sorted from higher magnification to lower magnification. **b**-**c**) The dimensions were measured manually using ImageJ image analysis software and fitted to Gaussian distribution to determine the mean and width. **d**) Schematic of the origami platform. The dimension of the origami platform is the same regardless which labels are attached to it. The applied procedures are described in the section 'Transmission electron microscopy' of the Supplementary Methods.

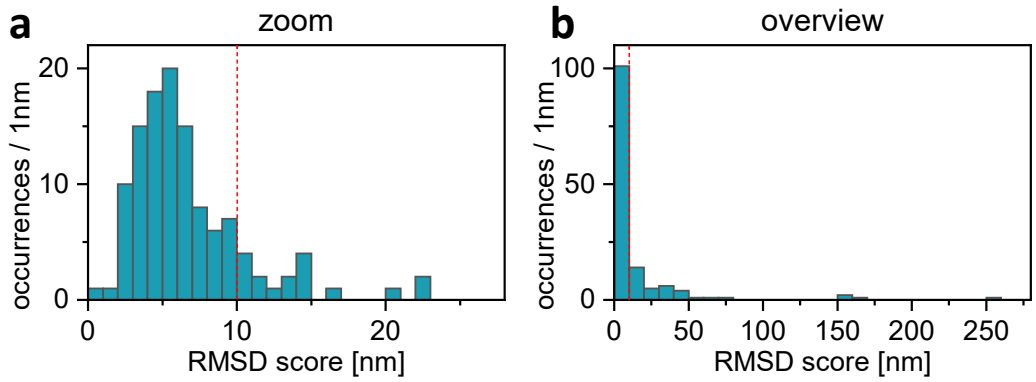

***Supplementary Fig. 9: Distribution of the alignment RMSD scores for the DNA origami*. a)** The distribution of the root-mean-square-displacement (RMSD) scores as calculated with respect to the best reference structure for the O(HF+NF) sample. It shows a single peak around 5 nm, close to the lowest possible localization precision based on photon statistics of 2.8 nm. Origamis with an RMSD score higher than 10 nm (red line) are discarded for further analysis. **b)** Extreme outliers (RMSD score > 100 nm) are attributed to aggregation or random placement of two partially labelled structure in close proximity. The DNA origami selection criteria are listed in Supplementary Tab. S14. For a complete description of the alignment procedure, see section 'Spectroscopy and image analysis, Alignment and particle averaging for origami measurements' in the Supplementary Methods.

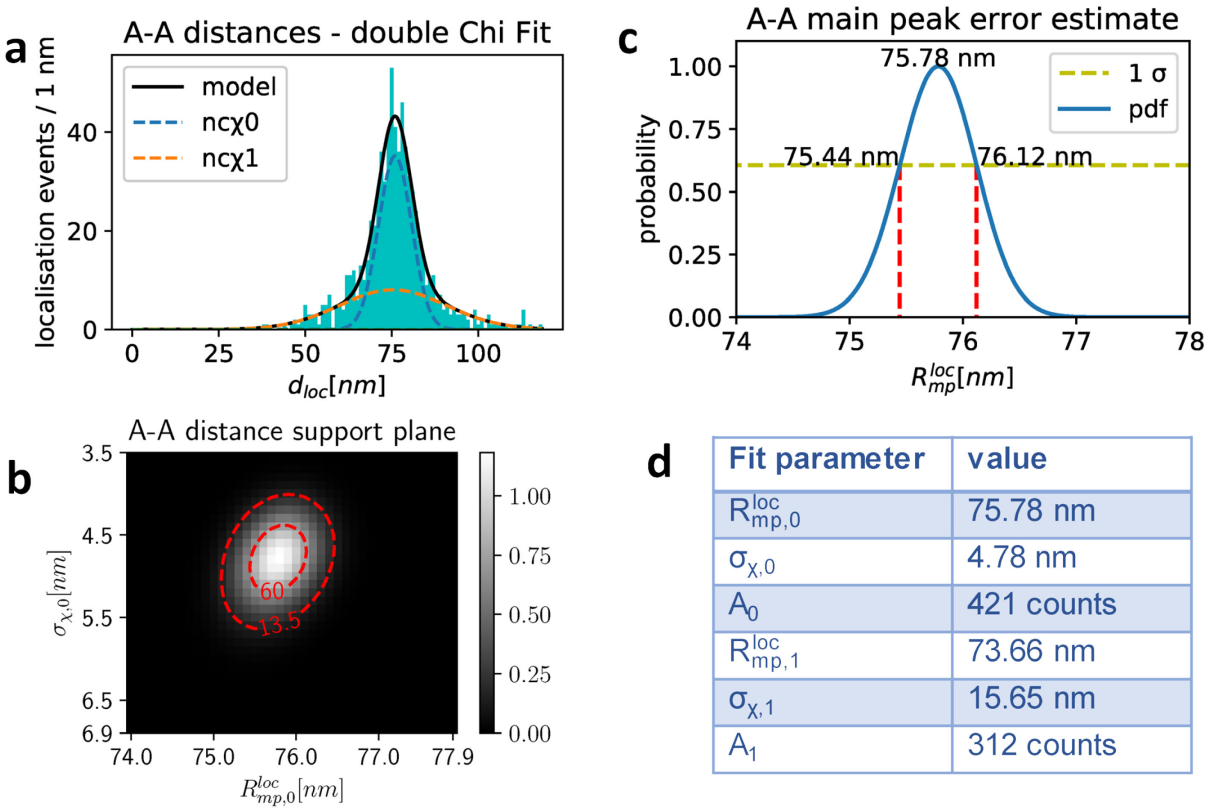

Fit parameter	value
$R^{loc}_{mp,0}$	75.78 nm
$\sigma_{\chi,0}$	4.78 nm
A_0	421 counts
$R^{loc}_{mp,1}$	73.66 nm
$\sigma_{\chi,1}$	15.65 nm
A_1	312 counts

Supplementary Fig. 10: Acceptor-to-acceptor distance distribution of DNA origamis. Constructs with two acceptors and 0, 1, 2 or 3 donor spots were selected from the O(HF+NF) sample. **a)** The colocalization distance histogram was fitted using maximum likelihood optimization and two non-central χ-distributions, each with amplitude A and fitting parameters $R^{\mathrm{loc}}_{\mathrm{mp}}$ and σ_χ (see eq. 30 in section 'Model-based analysis of localization-based distance distributions'). A single χ-distribution model was rejected based on the Aikaike information criterion (AIC=478, not shown), which was significantly better for the two-component fit (AIC=340). **b)** The probability density function (PDF) for $R^{\mathrm{loc}}_{\mathrm{mp}}$ and σ_χ calculated from the likelihood. The *p*-values (unit: nm^{-2}) are normalized such that they represent the probability over an area of 1 nm^2. Dashed lines indicate the 60% and 13.5% levels relative to the highest likelihood value. The optimum is well defined and no correlation between $R^{\mathrm{loc}}_{\mathrm{mp}}$ and σ_χ is observed, as is expected when R_{mp} / σ_χ >> 1. **c)** PDF for the mean-position distance of the narrow population, $R^{\mathrm{loc}}_{\mathrm{mp,0}}$, where the highest *p*-value is normalized to one. The distribution is Gaussian and the 60% *p*-values indicate the 1σ confidence interval, yielding an acceptor-acceptor distance of 75.8 ± 0.3 nm. Based on the DNA origami structure, the acceptors are separated by 5 helices, or 12 nm along the short direction based on an interhelical spacing of 2.4 nm, as estimated from the particle alignment procedure. Using the Pythagorean theorem, the distance between the two acceptors along the helical strands is estimated to be 74.8 ± 0.3 nm. **d)** Fit parameters corresponding of the fit shown in **a** (see eq. 30 in section 'Model-based analysis of localization-based distance distributions'). The presence of two peaks indicates two species of origamis. The defined population with narrow width (index 0) is attributed to correctly folded origamis as the width is close to the predicted localization precision (see Supplementary Tab. 5). The broad distribution (index 1) is attributed to incorrectly folded or broken origamis. For further details, see Supplementary Notes 2-3.

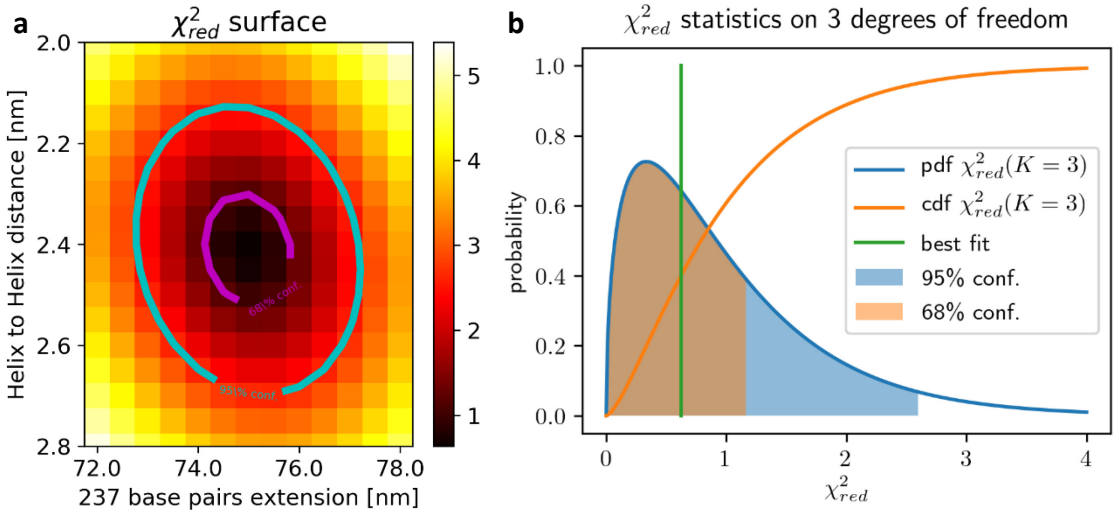

Supplementary Fig. 11: Error analysis on origami lattice constants. **a)** χ^2_{red} surface as a function of the base pair extension and average helix to helix distance. Confidence interval limits are reported in Supplementary Note 2. **b)** χ^2_{red} distribution for three free parameters. Limiting χ^2_{red} values for confidence intervals are obtained from integrating the curve from the left (shaded areas). For further details, see Supplementary Note 2.

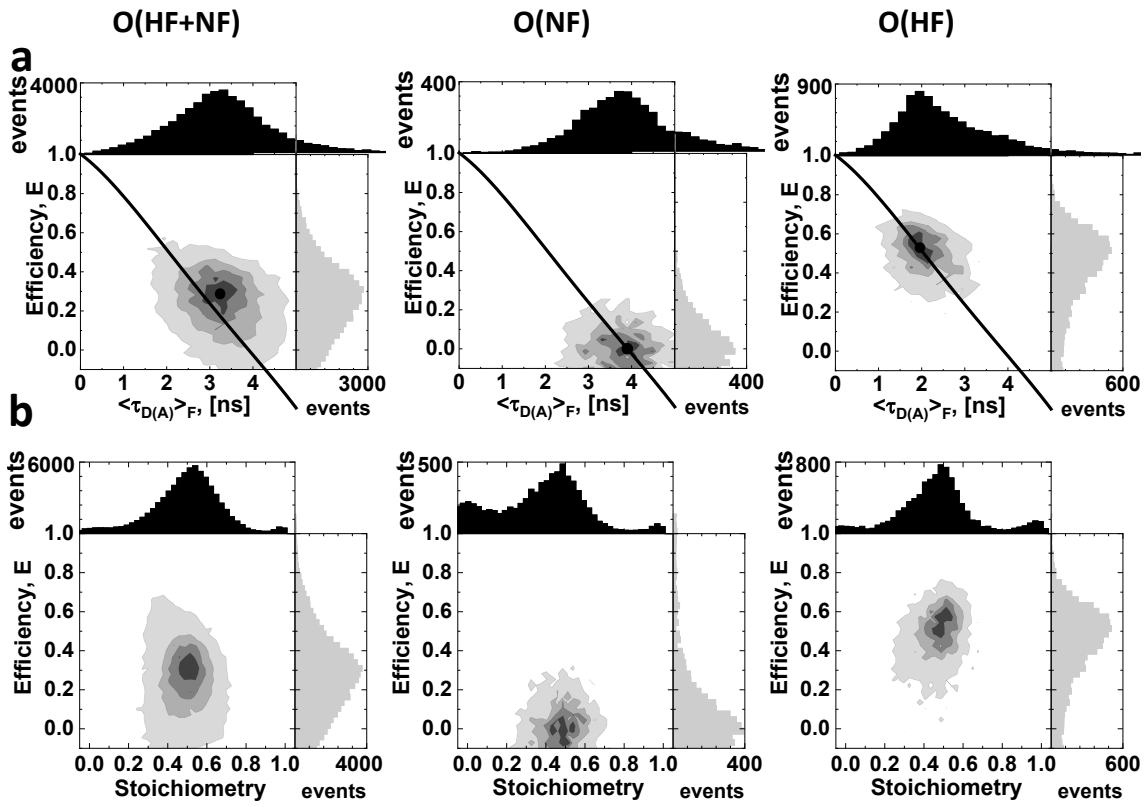

Supplementary Fig. 12: Solution-based confocal single-molecule FRET measurements of three origami samples: O(HF+NF), O(NF) and O(HF). Confocal single-molecule FRET measurements of freely diffusing molecules in solution using multiparameter fluorescence detection were performed to characterize the O(HF+NF), O(NF) and O(HF) samples. **a)** Two-dimensional frequency histogram of the intensity-based FRET efficiency, *E*, and the fluorescence-weighted average donor fluorescence lifetime, $\langle\tau_{D(A)}\rangle_F$. The populations lie on a static FRET line including the contribution of the flexible linker (solid line, given by eq.10 in the Methods section of the main text using the parameters in Supplementary Tab. 19). The population centers are reported in Supplementary Tab. 10. The sample O(HF+NF) contains a mixture of two FRET species and hence lies above the static FRET line. **b)** Two-dimensional frequency histogram of the intensity-based FRET efficiency, E, and stoichiometry. The necessary setup correction factors for the computation of the plotted corrected parameters are compiled in Supplementary Tab. 3. The stoichiometry histograms (b) show a shoulder towards lower a stoichiometry of 0.33, indicating constructs where two acceptors and a single donor is observed. This observation correlates with longer diffusion times (not shown), indicating dimerization/oligomerization of DNA origami platforms, e.g. via single strand loops protruding from the short side of the platform. For details, see section 'Solution-based confocal single-molecule spectroscopy with multiparameter fluorescence detection'.

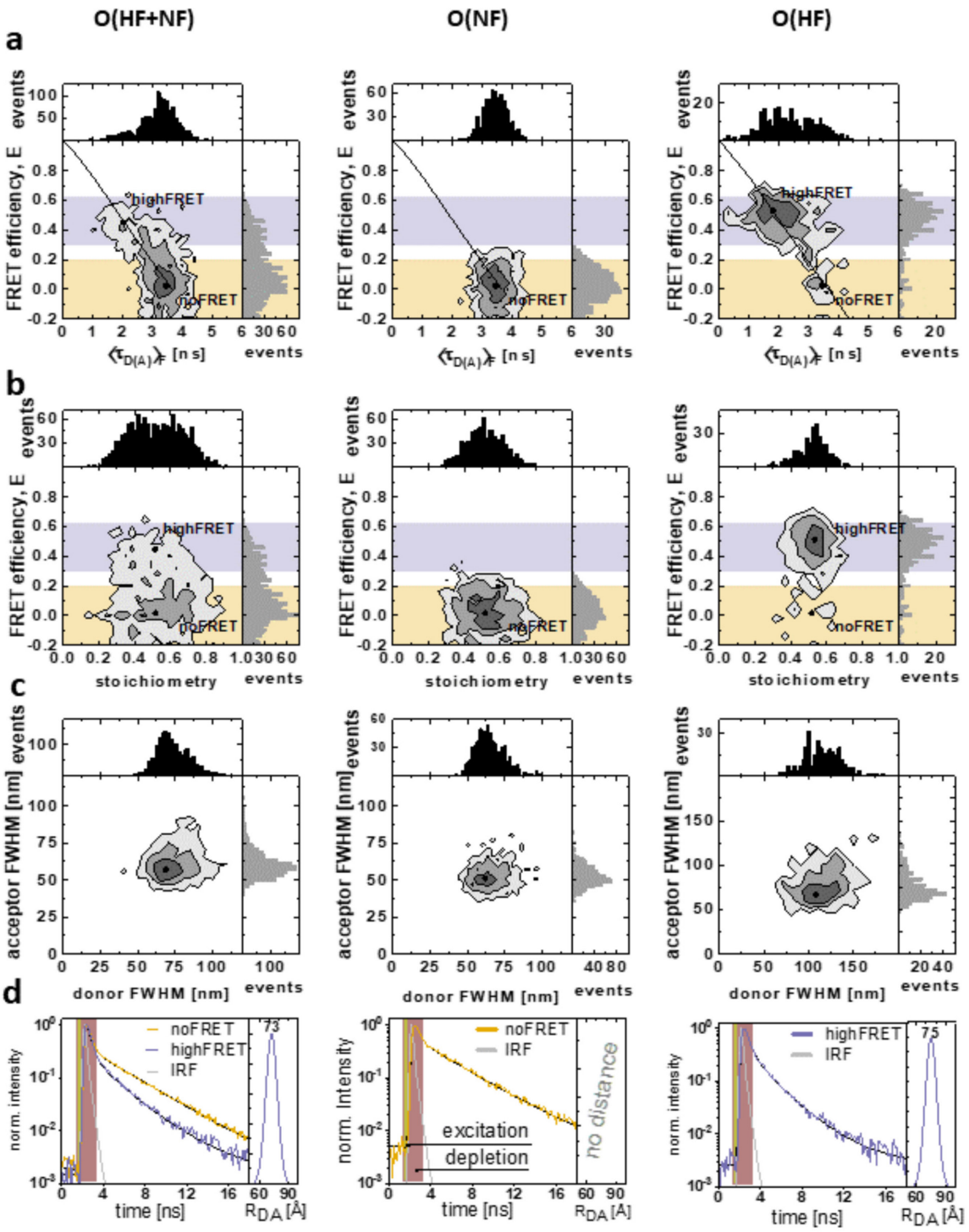
O(HF+NF)
O(NF)
O(HF)
a
b
c
d
events
FRET efficiency, E
highFRET
noFRET
⟨τD(A)⟩F [ns]
stoichiometry
acceptor FWHM [nm]
donor FWHM [nm]
norm. intensity
noFRET
highFRET
IRF
time [ns]
RDA [Å]
excitation
depletion
no distance

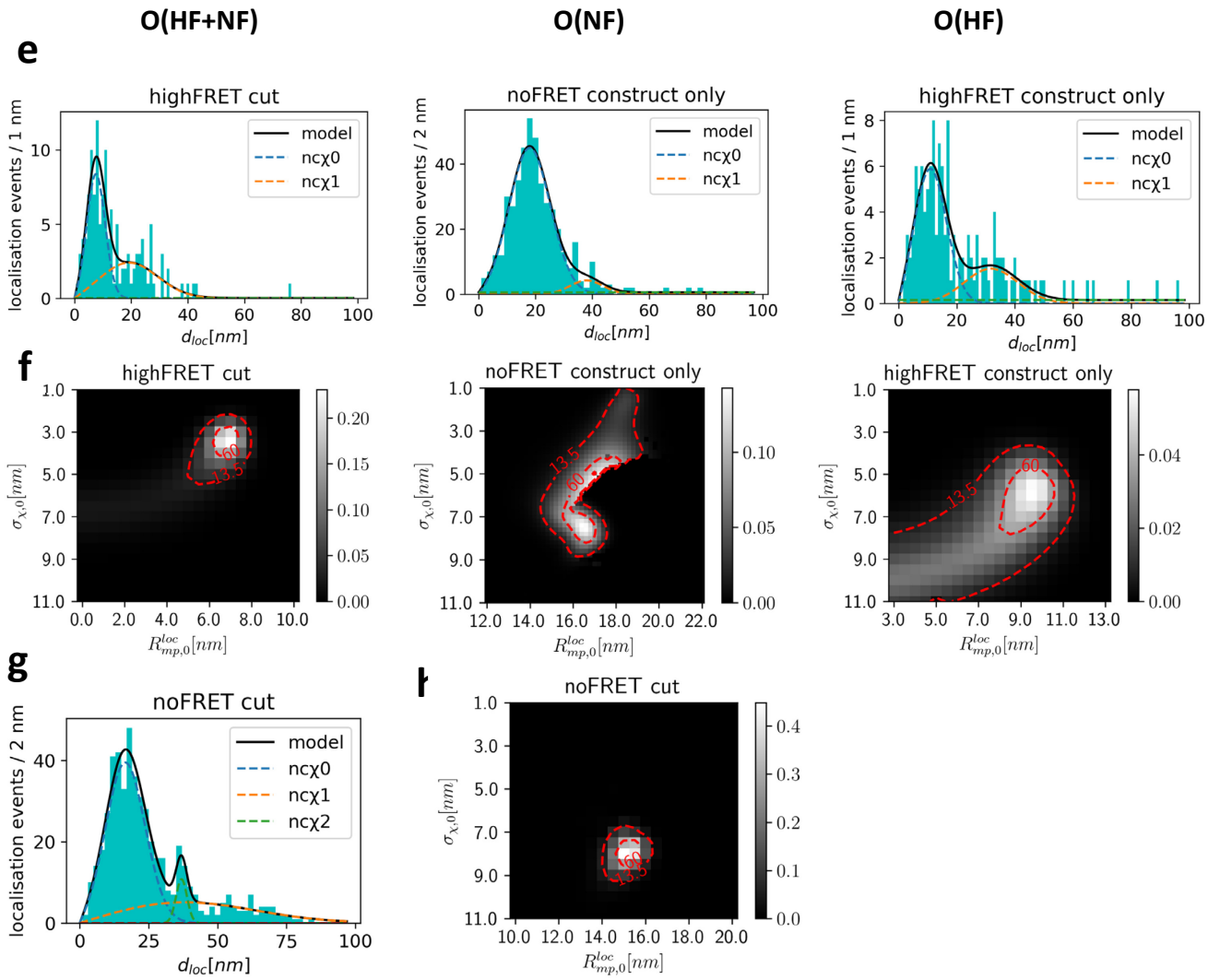

Supplementary Fig. 13: FRET nanoscopy of three origami constructs: O(HF+NF), O(NF) and O(HF). **a)** Two-dimensional frequency histogram of the spot-integrated intensity-based FRET efficiency, *E*, and the fluorescence-weighted average donor fluorescence lifetime, $\langle\tau_{D(A)}\rangle_F$. All spot populations lie on a static FRET line including the contribution of the flexible linker (solid line, given by eq. 10 in the Methods section of the main text using the parameters in Supplementary Tab. 19). Populations lie on the static FRET line. For the O(HF+NF) and O(HF), a tailing of the high FRET population is visible due to acceptor bleaching. Numeric values for the population centers are reported in Supplementary Tab. 10. **b)** Corresponding two-dimensional frequency histogram of the spot-integrated intensity-based FRET efficiency, E, and the fluorescence-stoichiometry. The stoichiometry for O(HF+NF) is broader as the dataset originates from two measurement days with different laser power. The FRET populations lie in the violet shaded areas. **c)** Full-width-at-half-max (FWHM) of the donor and acceptor as determined for Gaussian spot fitting. The resolution in the donor channel and acceptor channels are 60 nm and 50 nm for the O(NF) sample, 67 nm and 57 nm for the O(HF+NF) sample and 105 nm and 70 nm for the O(HF) sample, respectively. For the O(HF) data, the lifetime of the donor is shortened by FRET, reducing the number of photons available for localization in the gated data. Consequently, localization was done on ungated data to better identify spots and achieve a higher localization precision. **d)** Sub-ensemble donor decay histograms and fits with obtained distance

distributions (side panel). Yellow bar indicates the duration of the excitation pulse and light red bar indicates duration of the STED pulse. Fit models are described in the methods. All fit results are compiled in Supplementary Tab. 9. **e,g)** Localization histograms and fits. Localizations outside the main peak are attributed to incomplete filtering of broken structures and an additional χ-distribution (see eq. S30) was used to describe the data. The green line for O(NF) and O(HF) indicates a constant background offset. **f,h)** 2D Probability density functions (pdf) for the principal peak in (e, g). *p*-values are normalized to indicate the likelihood of the true value being in a 1 x 1 nm area. Dashed lines indicate 60% and 13.5% probability relative to the highest *p*-value. Purple and yellow areas in a, b indicate the FRET efficiency cuts used in d-h. Additional filtering criteria are reported in Supplementary Tab. 14. Comparison of columns in spectroscopic indicators (a, b, d) show that the O(HF+NF) parameters consist of the sum of O(NF) and O(HF), indicating that accurate spectroscopic parameters can be determined from the two dyes on the same platform (75 nm separation) as well as if they were isolated. This result is confirmed by comparison of localization histograms where main populations for O(HF+NF) (NF: 15.0 ± 0.7 nm, HF: 6.8 ± 1 nm) match the populations of O(NF) (NF: 16.5 ± 1 nm) and O(HF) (HF: 9.5 ± 1.5 nm). While the localization histograms can be used to determine any distance, incomplete filtering of broken constructs is detrimental to the accuracy, and it represents a challenge to improve filtering further in future work. In comparison, filtering by aligning structures can completely reject broken structures. The former is more widely applicable as it can used with two labels, whereas the latter is restricted to constructs with at least 3 labels.

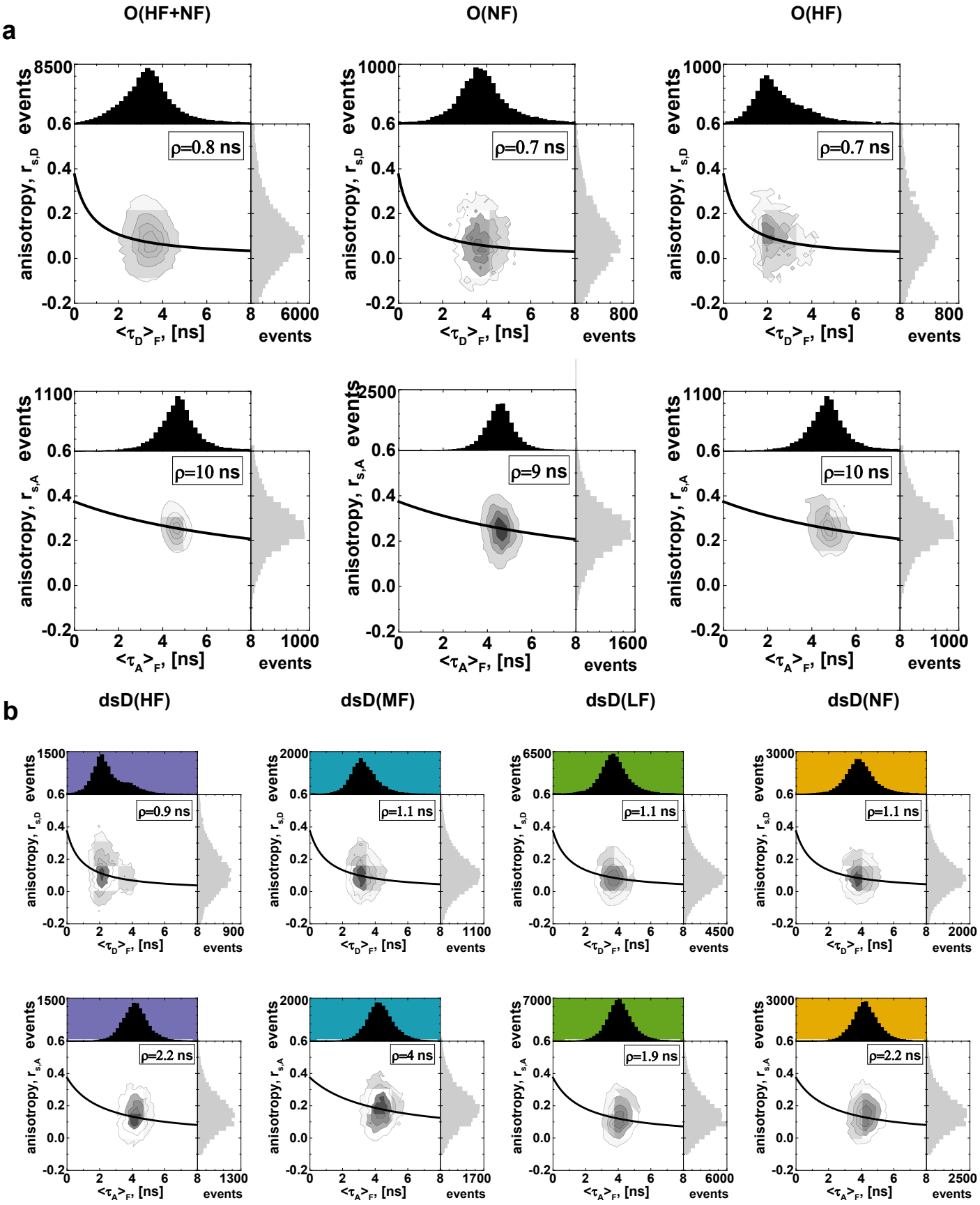

Supplementary Fig. 14: Solution-based confocal single-molecule measurements of anisotropies and fluorescence lifetimes for origami and dsDNA samples. **a)** Two-dimensional frequency histograms for the steady-state anisotropies of the Atto594 donor ($r_{s,D}$, top row) and Atto647N acceptor

($r_{s,A}$, bottom row) and the fluorescence lifetime for origami samples obtained by confocal single-molecule measurements. Each plot is overlaid with the Perrin equation (eq. S21c in section 'Determination of spot-integrated fluorescence lifetimes') using a fundamental anisotropy of r_0 = 0.374 for the donor and acceptor. The corresponding rotational correlation time is given in the graph. For the O(HF+NF) sample, the weighted averages of the two donors and two acceptor dyes are reported, respectively. The rotational correlation time for the acceptor Atto647N is high, indicating sticking. This effect was also observed by others[35,49]. The donor rotational correlation time is fast (< 2.5ns), indicating that the dye can move freely. **b)** Same as for a, but for the dsDNA ruler samples which are labelled with Alexa594 as donor and Atto647N as acceptor. All rotational correlation times are fast (<2.5ns) except for the medium FRET acceptor. This indicates that the sticking of the acceptor dye is specific to the origami sample. This observation matches the origami FRET distances, which overestimate the predicted distance due to κ^2 effects. As a control, dsDNA rulers yield the correct predicted distance. Values are reported in Supplementary Tab. 11. The procedures are described in the sections 'Determination of spot-integrated fluorescence lifetimes' and 'Solution-based confocal single-molecule spectroscopy with multiparameter fluorescence detection'.

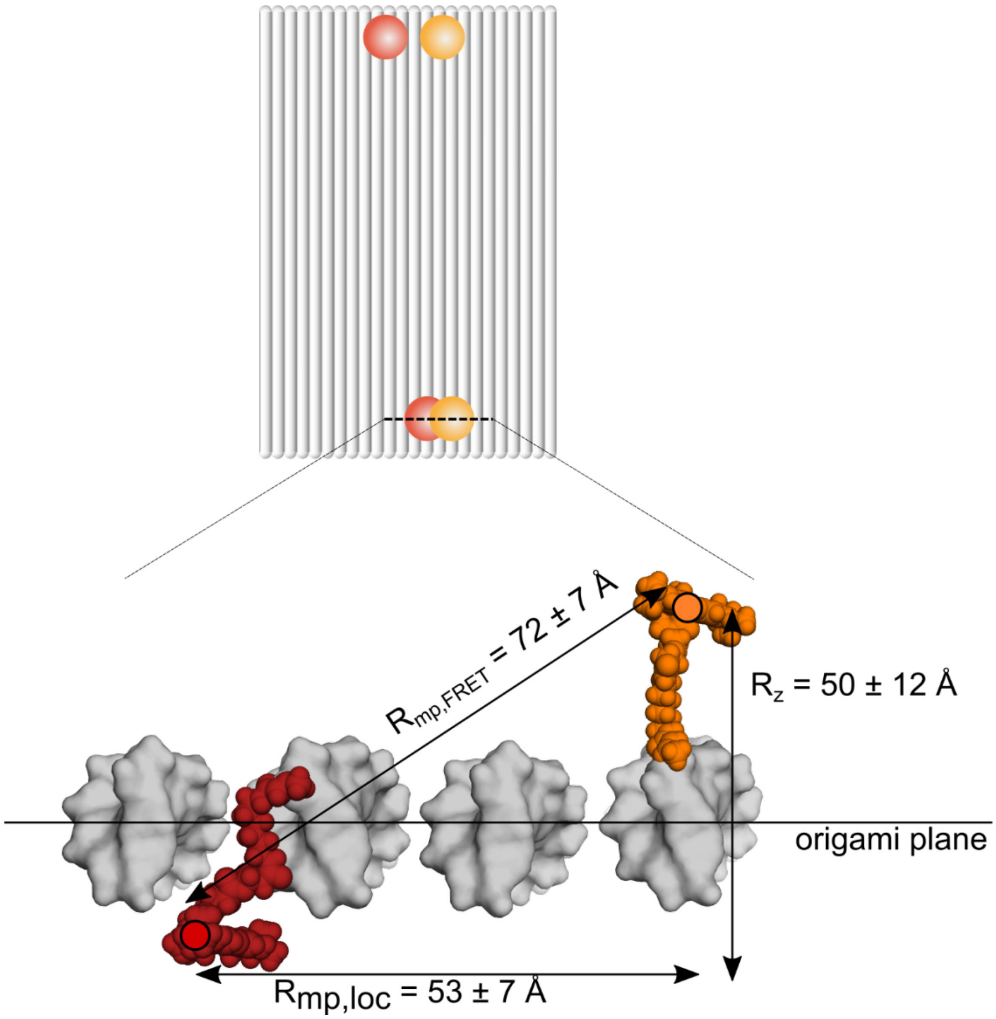

Supplementary Fig. 15: Proposed model for the three-dimensional positioning of the dyes on the origami platform.

The potential reasons for the discrepancy between localization and FRET distances for origami are discussed in Supplementary Note 4.

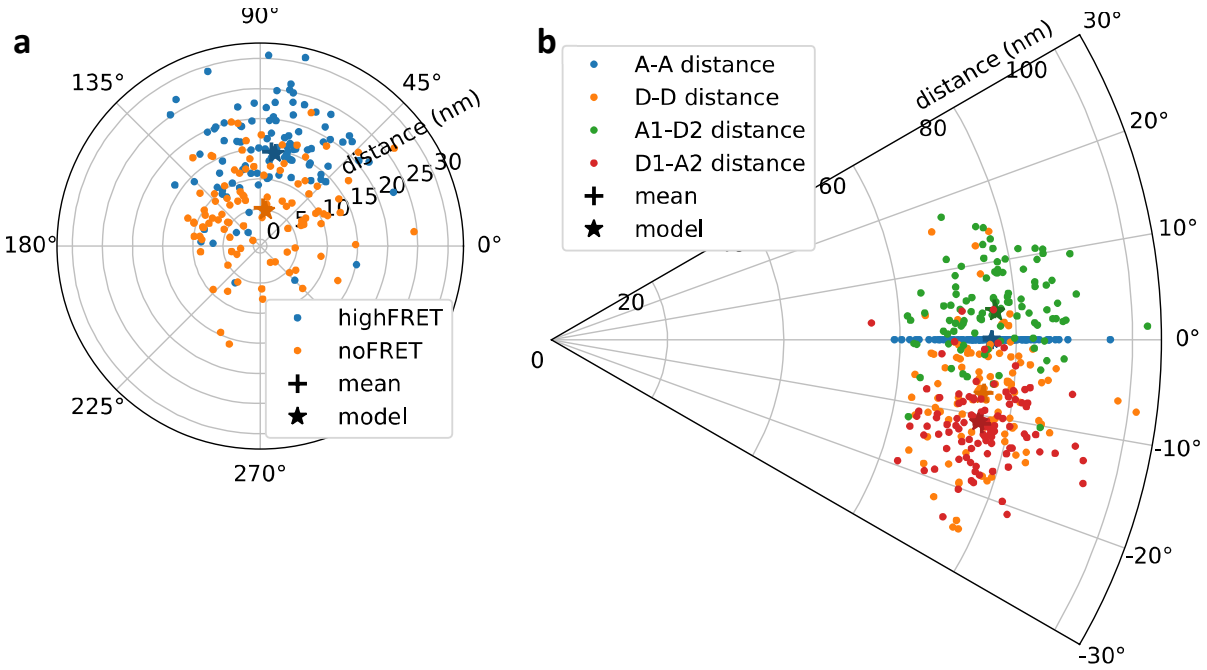

Supplementary Fig. 16: Alternative origami alignment based on acceptor-acceptor distance.

The origamis are aligned such that the acceptor-acceptor distance is oriented along the x-axis and the acceptor of the no-FRET (NF) dye pair is placed in the origin. **a)** Interpair distances **b)** Intrapair distances. This alignment approach is advantageous as one may use any sample that has two acceptors, for example 1 donor – 2 acceptors, and obtain better statistics. However, it does not use all information available and has sub-optimal alignment. We may rotate all structures without loss of information, hence it is natural to display distances in polar coordinates. The same dye labelling conventions as in Fig. 2 (main text) have been used. The mean and predicted distances match closely, such that the symbols overlap (refer to Fig. 2d of the main text for a zoomed figure).

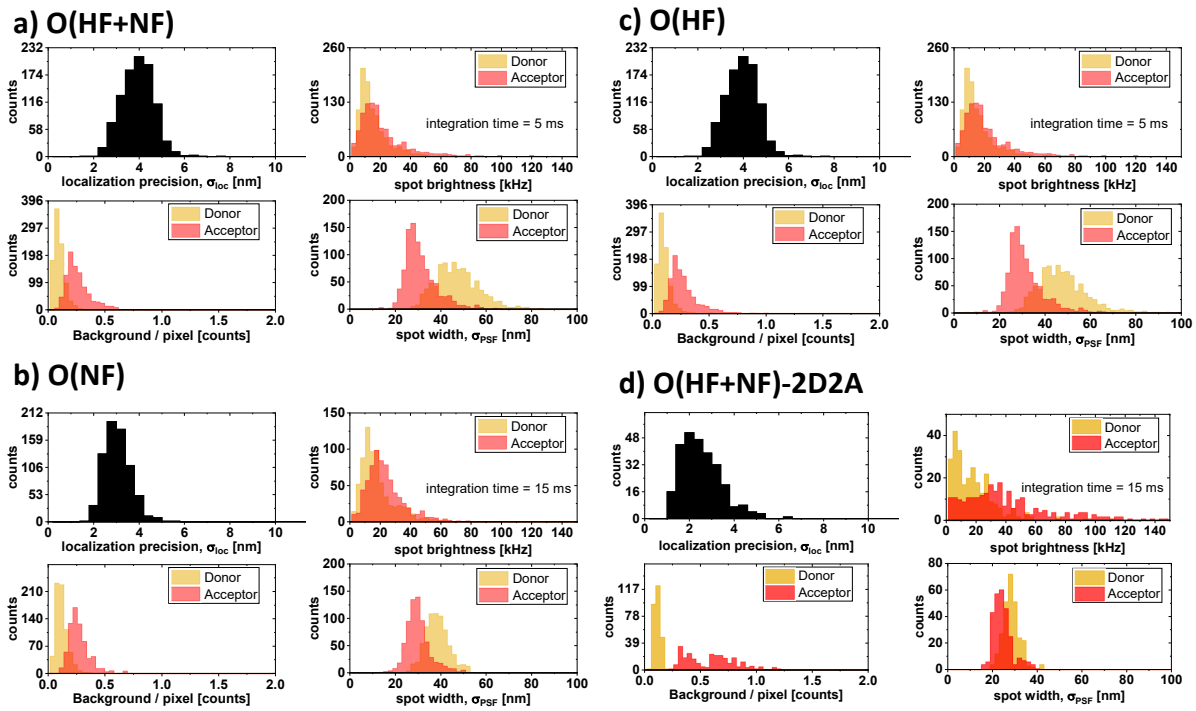

***Supplementary Fig. 17: Localization precision of origamis*. a)** Localization characteristics for the O(HF+NF) sample. The localization precision (top-left) is calculated from equation S29 in section 'Predicting the localization precision' and depends on the spot brightness (top-right), the background level (bottom-left) and the spot width (bottom-right). **b)** The same is shown for the O(NF) and the **c)** O(HF) sample. All FRET pairs were included in (a-c). **d)** Same as a), but only selecting spot stoichiometry of 2 donors and 2 acceptors, matching the dataset shown in main figure 2. No filtering based on the RMSD has been used (see Supplementary figure 9). All samples measured on PEG-prepared surfaces.

DNA ruler figures

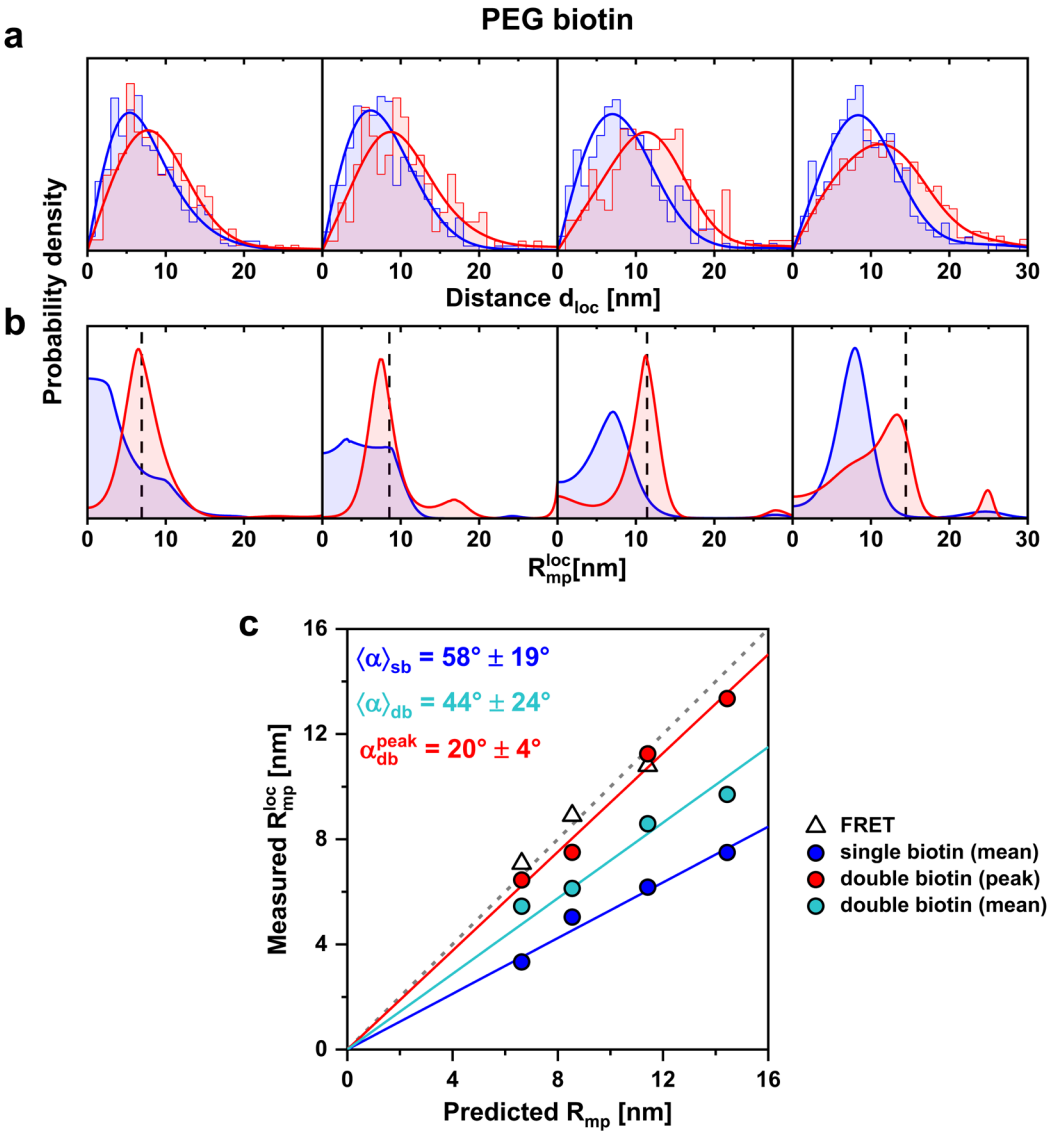

Supplementary Fig. 18: Colocalization analysis of DNA rulers on PEG surfaces. **a)** Distributions of the measured donor-acceptor distances from localization analysis for the single-biotin (blue) and double-biotin (red) samples (from left to right: dsD(HF), dsD(MF), dsD(LF), dsD(NF)) on the PEG surface. Fitted distributions based on maximum entropy analysis are shown as solid lines. **b)** The inferred distributions of the center distance of the χ-distribution from maximum entropy analysis of the distance distributions shown in **a** (from left to right: dsD(HF), dsD(MF), dsD(LF), dsD(NF). For the MEM analysis, the width of the χ-distributions was set to σ_χ = 4.4 nm. Expected distances between the mean positions of the fluorophores based on the AV model are shown as dashed lines. **c)** Distance-distance plots of the measured mean or peak (maximum) values of the inferred distance distributions against the predicted distances. Solid lines are linear fits to the data. The slopes of the fits define the inclination angle α which is calculated based on the mean and width of the distance distribution, $\langle\alpha\rangle$, or the peak value of the

double-biotin population, $\alpha_{\mathrm{db}}^{\mathrm{peak}}$. For the mean angles, the error is estimated from the width of the distance distribution. Compare Fig. 5a-c of the main text for the corresponding analysis of measurements performed on BSA-functionalized surfaces. See Supplementary Note 6 for a description of the MEM analysis and Supplementary Note 9 for a description of the procedure to estimate the inclination angles.

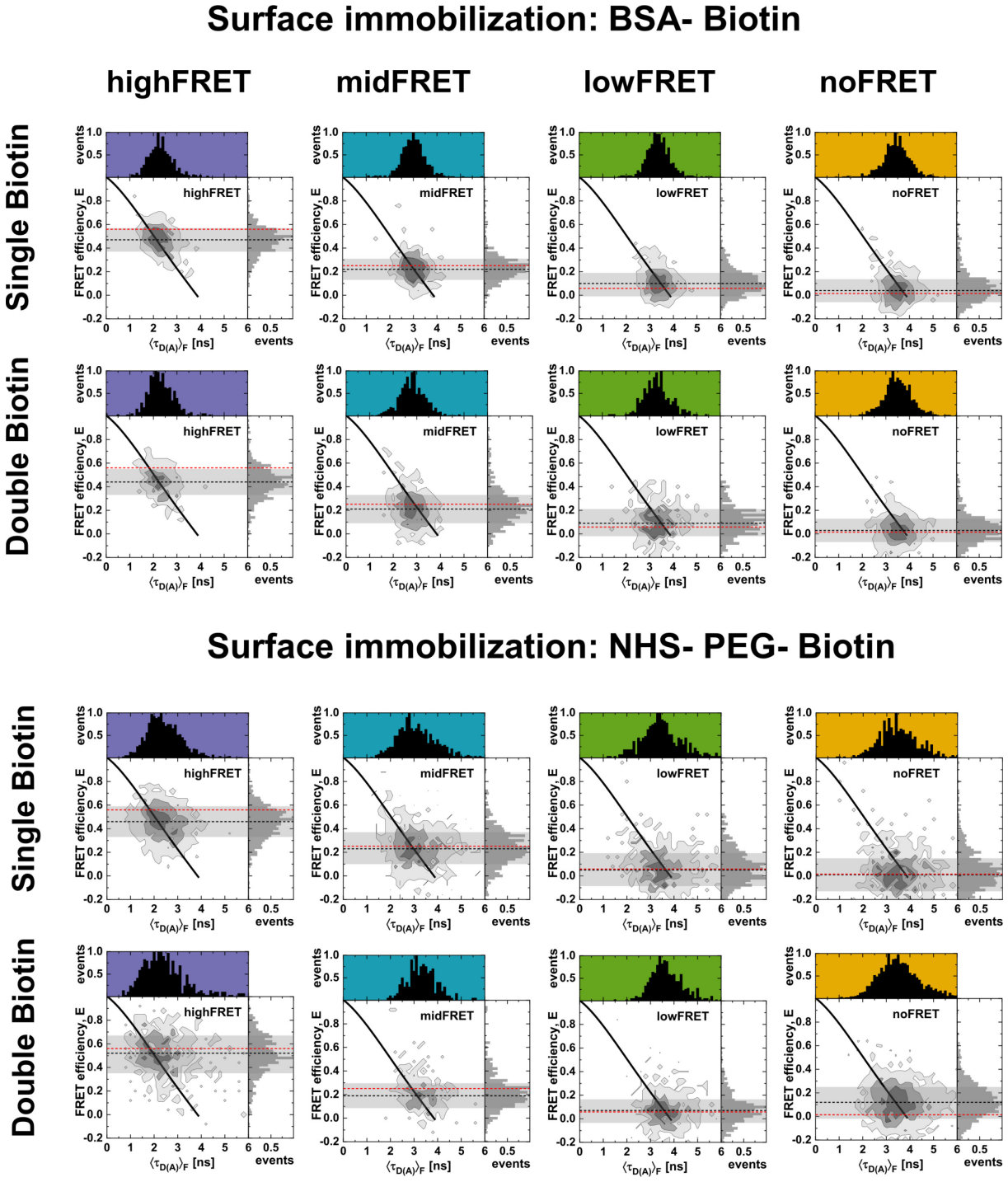

Supplementary Fig. 19: Two-dimensional frequency histograms of FRET efficiency and donor lifetime for FRET nanoscopy of dsDNA rulers. Two-dimensional frequency histograms of the ROI-integrated intensity-based FRET efficiency, *E*, and the fluorescence-weighted average donor fluorescence lifetime, $\langle\tau_{D(A)}\rangle_F$. The ROI populations lie on a static FRET line (solid line, given by eq.10

in the Methods section of the main text using the parameters in Supplementary Tab. 19). Single biotin and corresponding double biotin samples for each immobilization are colored equivalently (see Fig. 4 for a detailed description). The average FRET efficiencies are are reported in Supplementary Tab. 10.

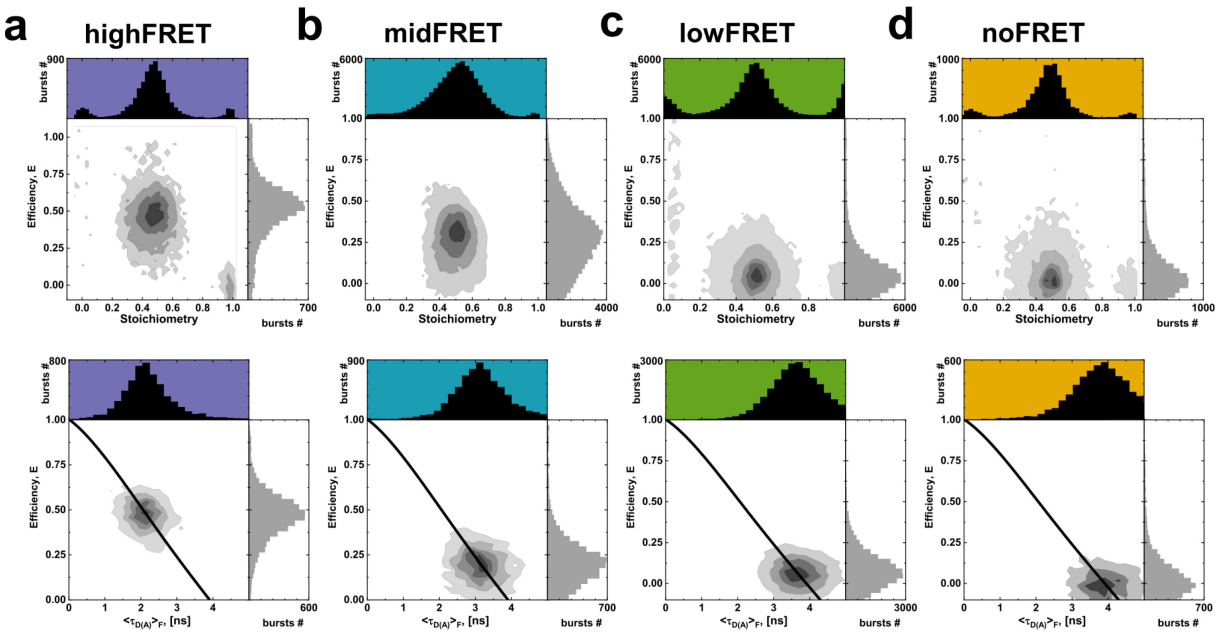

Supplementary Fig. 20: Two-dimensional frequency histograms of FRET efficiency and donor lifetime for solution-based confocal single-molecule FRET measurements of dsDNA rulers. Shown are the results for the samples dsD(HF) **(a)**, dsD(MF) **(b)**, dsD(LF) **(c),** and dsD(NF) **(d)**. Two-dimensional frequency histograms of single-molecule bursts for intensity-based FRET efficiency, E, and stoichiometry are plotted (first row). Double labeled species were selected via a stoichiometry cut between S = 0.3 and S = 0.7, leading to corresponding FRET efficiency versus fluorescence weighted lifetime plots (second row). For each sample, the FRET species lie on the static FRET line (black, given by eq.10 in the Methods section of the main text using the parameters in Supplementary Tab. 19). Sub-ensemble lifetime fits of the selected populations were performed and compiled in Supplementary Tab. 9. For details on the measurement procedure, see section 'Solution-based confocal single-molecule spectroscopy with multiparameter fluorescence detection'.

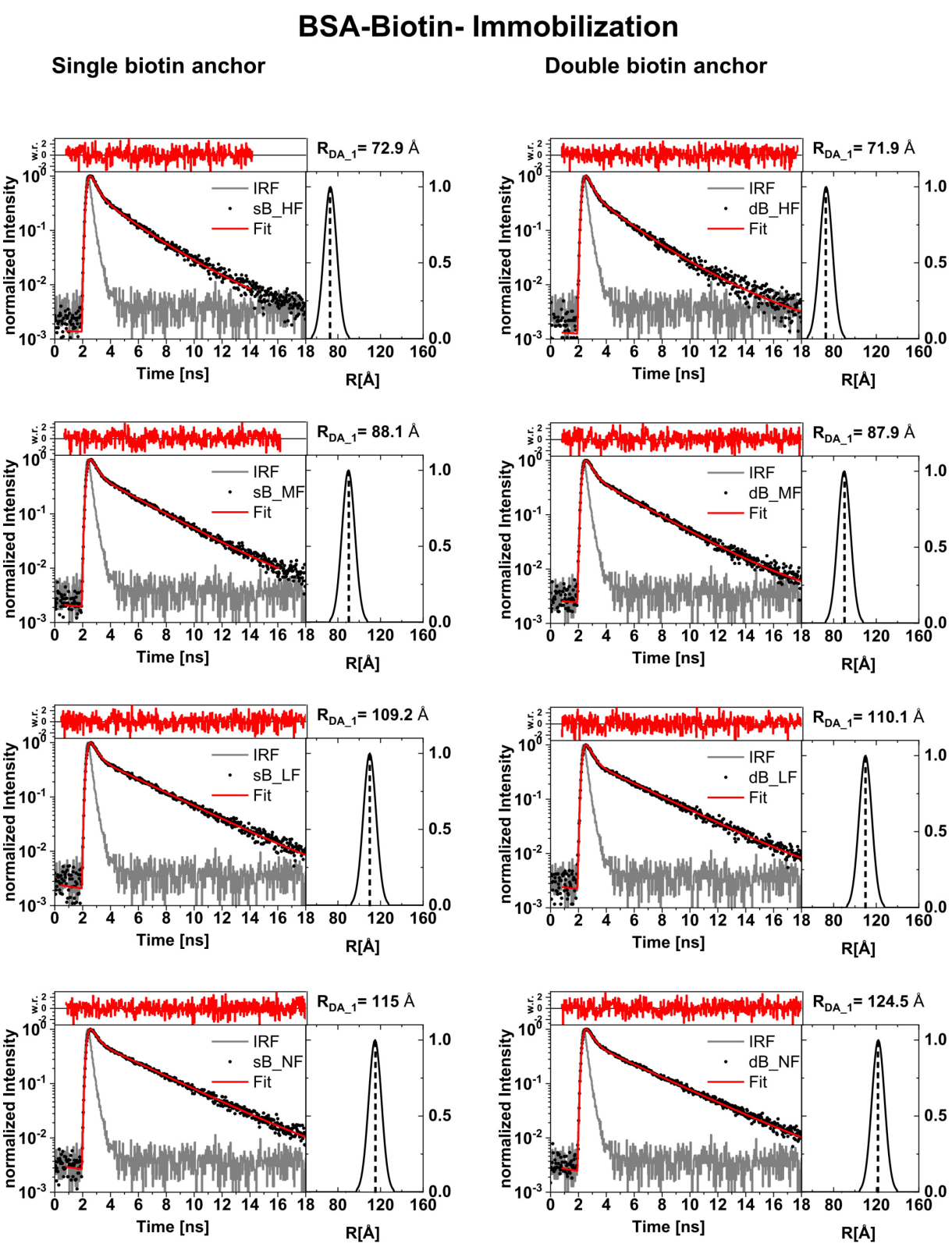
BSA-Biotin- Immobilization
Single biotin anchor
Double biotin anchor
R_DA_1= 72.9 Å
IRF
sB_HF
Fit
R_DA_1= 71.9 Å
dB_HF
R_DA_1= 88.1 Å
sB_MF
R_DA_1= 87.9 Å
dB_MF
R_DA_1= 109.2 Å
sB_LF
R_DA_1= 110.1 Å
dB_LF
R_DA_1= 115 Å
sB_NF
R_DA_1= 124.5 Å
dB_NF
normalized Intensity
Time [ns]
R[Å]
w.r.

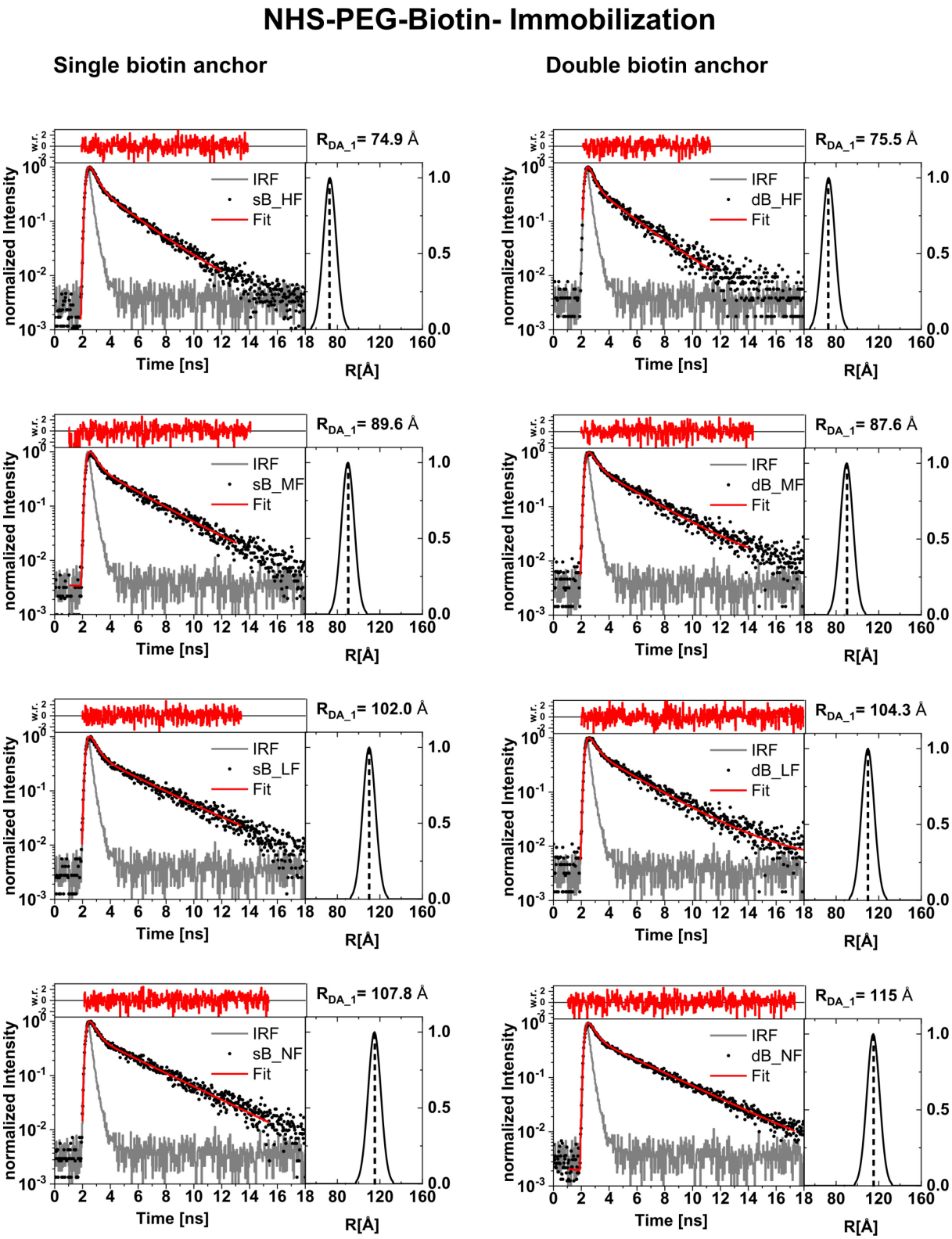

Supplementary Fig. 21: Sub-ensemble fluorescence decay analysis of dsDNA rulers. Summary of sub-ensemble lifetime fit with Gaussian distributed distances model (see section 'Spectroscopy and image analysis, Sub-ensemble fluorescence decay analysis', *eq. S19*). Bottom left: Sub-ensemble decay (scatter) convoluted with instrument response function (IRF, grey). Top left: weighted residuals. Bottom right: Gaussian model centered R_{DA} with σ = 0.6 nm. All fit results are compiled in Supplementary Tab. 9.

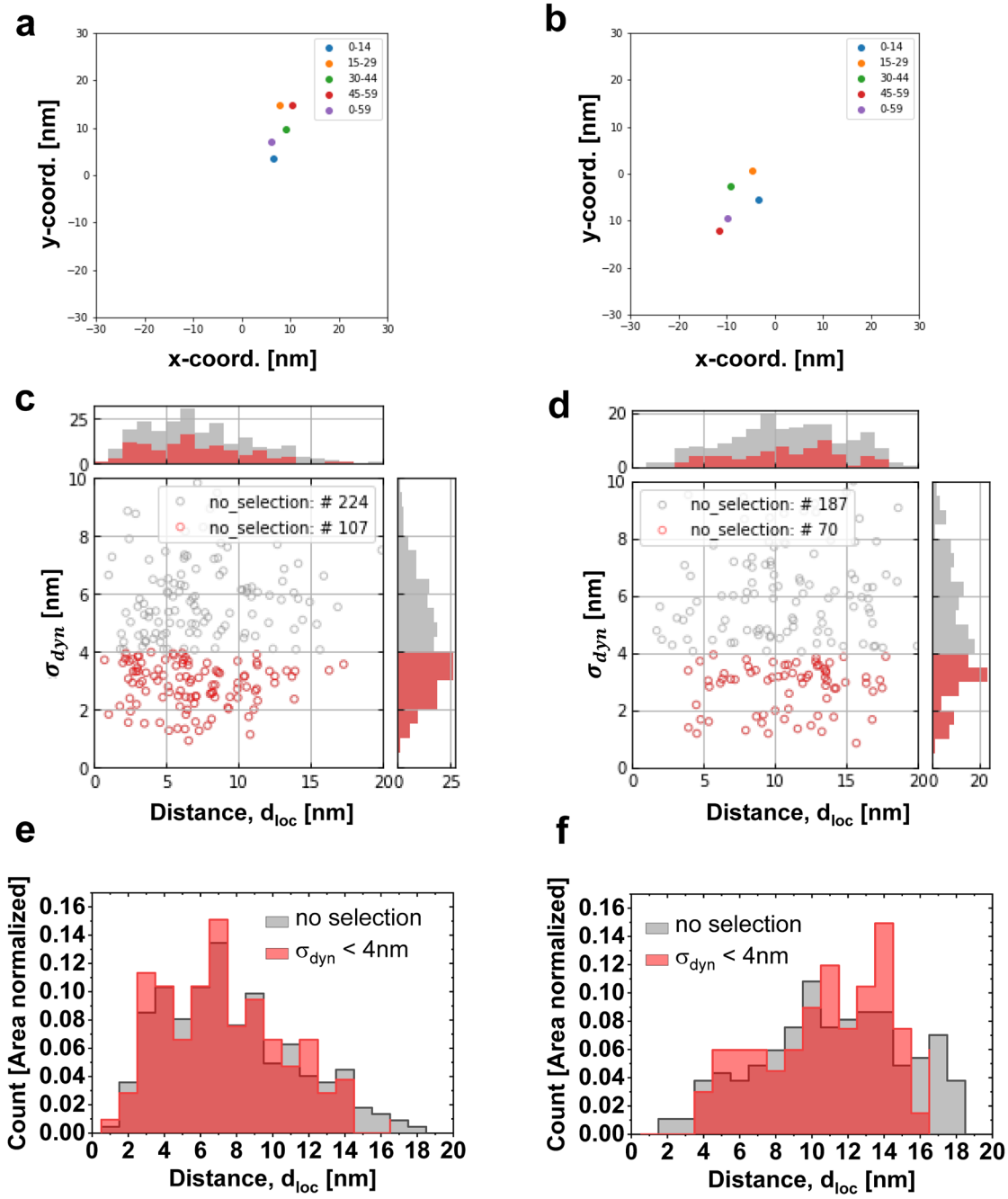

Supplementary Fig. 22: The position of dsDNA rulers remains constant during the acquisition time. a-b) Exemplary distance vector plots (three selected spots) of single (a) and double biotin (b) labeled dsD(NF) sample immobilized by BSA-biotin. Small displacement of colored spots indicates fast dynamic of dsDNA on the surface. **c-d)** Visualization of dynamic sigma selection for dsD(NF)T sample with single biotin (c) and double biotin (d) immobilization. The red colored selection corresponds to a dynamic sigma smaller than 4 nm. **e-f)** The corresponding distance histograms of the different selections are colored as in c-d. The procedures are described in Supplementary Note 5.

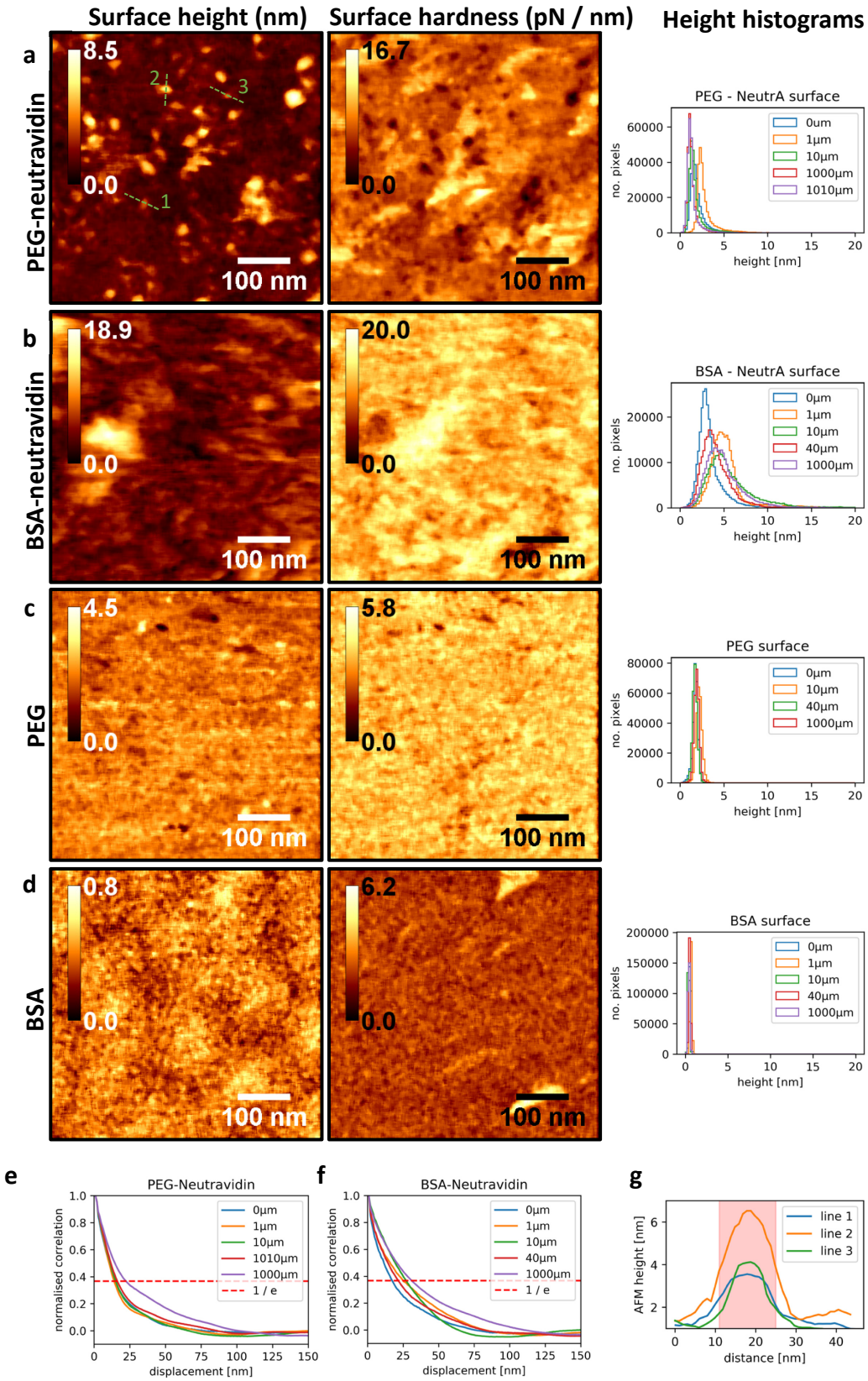

Supplementary Fig. 23: AFM imaging of functionalized surfaces. Biotin-functionalized surfaces using PEG and BSA after (**a-b**) and before (**c-d**) addition of neutravidin. The AFM was operated in QI mode [30] (see section 'Atomic force microscopy'). Height and hardness information was filtered using a median filter of 10x10 pixels and afterwards the zero-level was set to the lowest value in the image. For

each preparation, the surface was recorded on multiple locations so that the obtained images and analysis parameters in panels a, e and f were labelled according to their relative positions. **a**) PEG-neutravidin surfaces show elevated features that are identified as individual neutravidin molecules because the height matches the known height from neutravidin proteins (4 nm). The lateral (xy) resolution is limited by the dimension of the AFM tip. Green lines correspond to line profiles shown in **(g)**. Furthermore, elevated features (white) correlate with softer surfaces (black) indicating that these proteins are soft with respect to their surroundings. Additional hard features are visible in the hardness, but not in the height, indicating that they are either shallow or covered. **b**) BSA-neutravidin surfaces show higher features, typically 10 nm and up to 30 nm. This potentially indicates crosslinking of BSA and neutravidin, as each BSA protein has up to 12 biotins and neutravidin has four bindings sites. In addition, BSA might form aggregates. By comparing the surface roughness of (**c**) and (**d**), it is clear that our measurement setup is capable of resolving these height profiles and that additional heterogeneity is the consequence of surface roughness. **e-f)** Normalized image autocorrelation functions of the height profiles (see Supplementary Note 8, eq. S50a-d) for PEG-Neutravidin (e) and BSA-Neutravidin (f) surfaces. Autocorrelations in 2D were radially integrated to obtain a 1D profile. The first value in the autocorrelation function is skipped as it represents a constant offset, normalization is done on the second value. Fig. 5e in the main text shows the average of the 5 displayed BSA and PEG curves. The cross section with 1/e indicates the correlation length. **g)** Line profiles of the smallest features identified throughout are used to determine the lateral of the AFM images. Red box indicates the approximate half-width of the features to be 14 nm. Note that the feature size is not significantly affected by the median filter. See section ‘Atomic force microscopy’ in the Supplementary Methods and Supplementary Note 8 for details on the procedures.

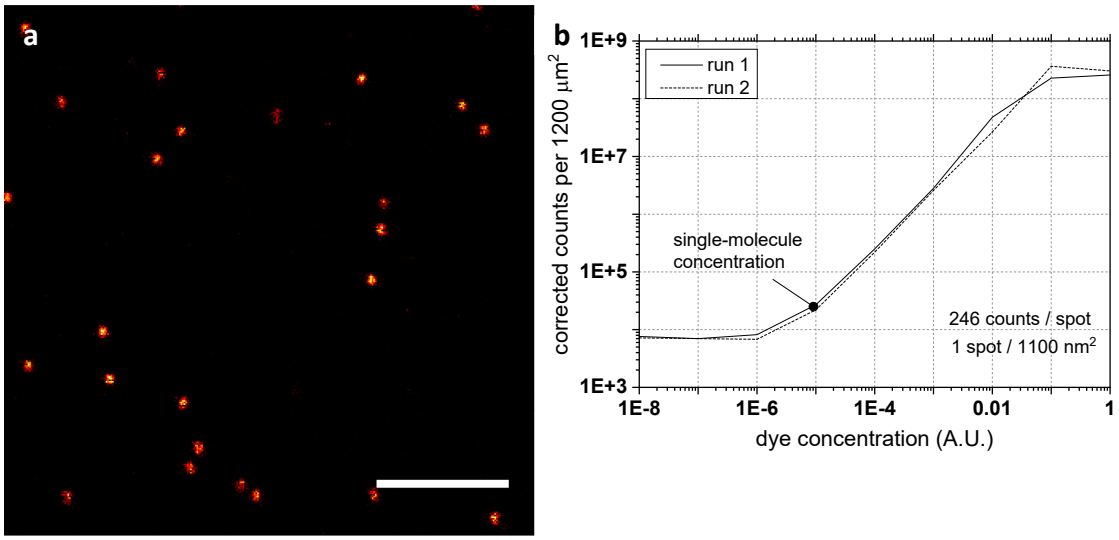

Supplementary Fig. 24: Estimating the neutravidin density on the surface. **a**) Atto647N-biotin in low concentration is added to a PEG-neutravidin functionalized surface to achieve single-molecule concentration. The average molecular brightness is determined from the number of emitters and the background-corrected intensity according to Supplementary Note 8. Scale bar is 5 µm. **b**) The solution is consequently exposed to higher concentration of Atto647N-biotin until surface saturation is reached (relative concentrations 0.1 and 1 A.U.). At higher dye concentrations the excitation power is reduced to avoid detector saturation. The counts are corrected for the lower excitation power assuming a linear dependence between brightness and excitation power. Two repetitions yield a saturation level of 300 and 250 Mcounts, of which the average has been taken. At saturation level individual spots can no longer be counted. The maximum spot density is calculated from the saturation brightness divided by the average brightness per emitter. Finally, the density is obtained by dividing with the surface area.

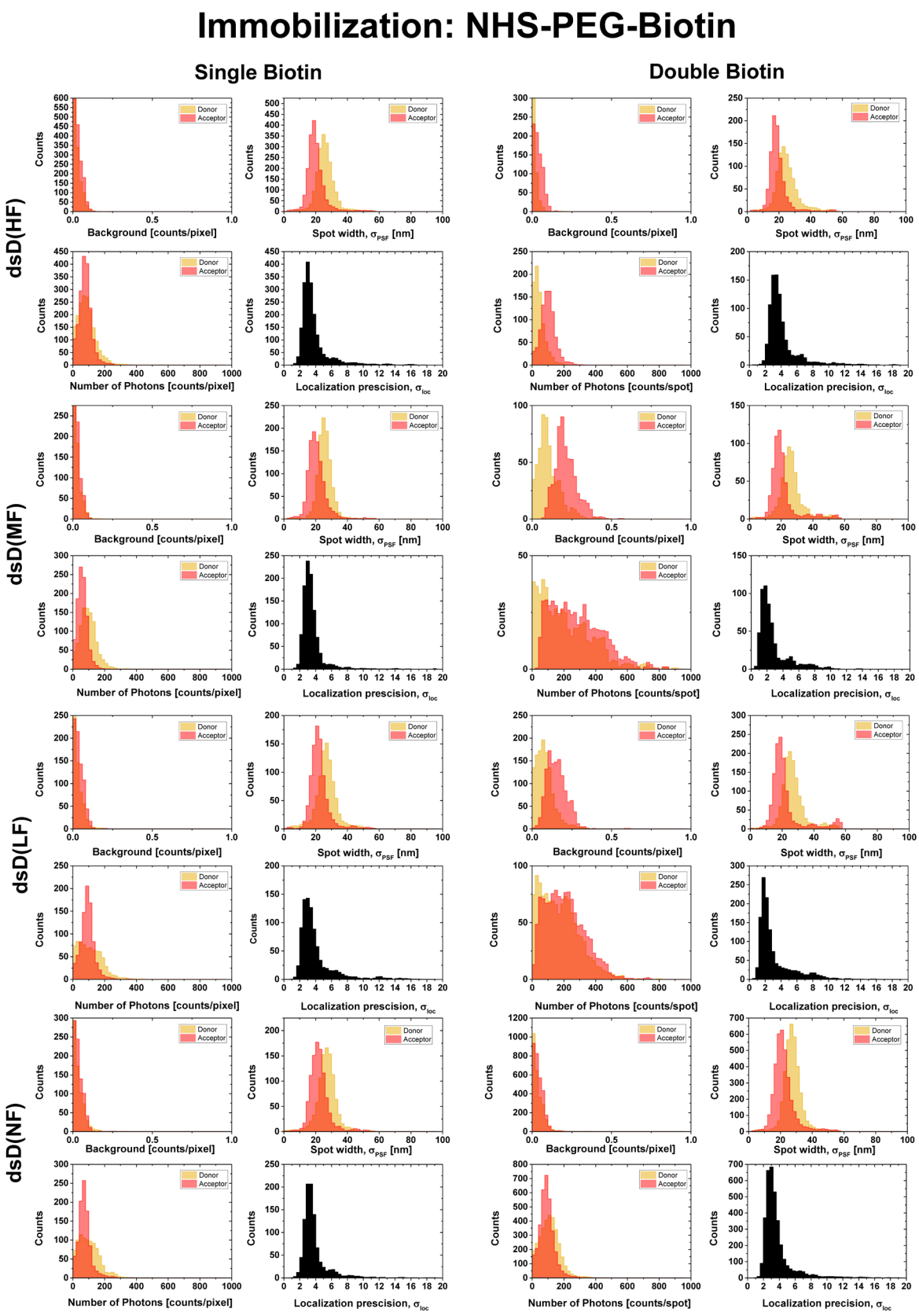
Immobilization: NHS-PEG-Biotin
Single Biotin
Double Biotin
dsD(HF)
dsD(MF)
dsD(LF)
dsD(NF)
Donor
Acceptor
Counts
Background [counts/pixel]
Spot width, σPSF [nm]
Number of Photons [counts/pixel]
Number of Photons [counts/spot]
Localization prescision, σloc
Localization precision, σloc

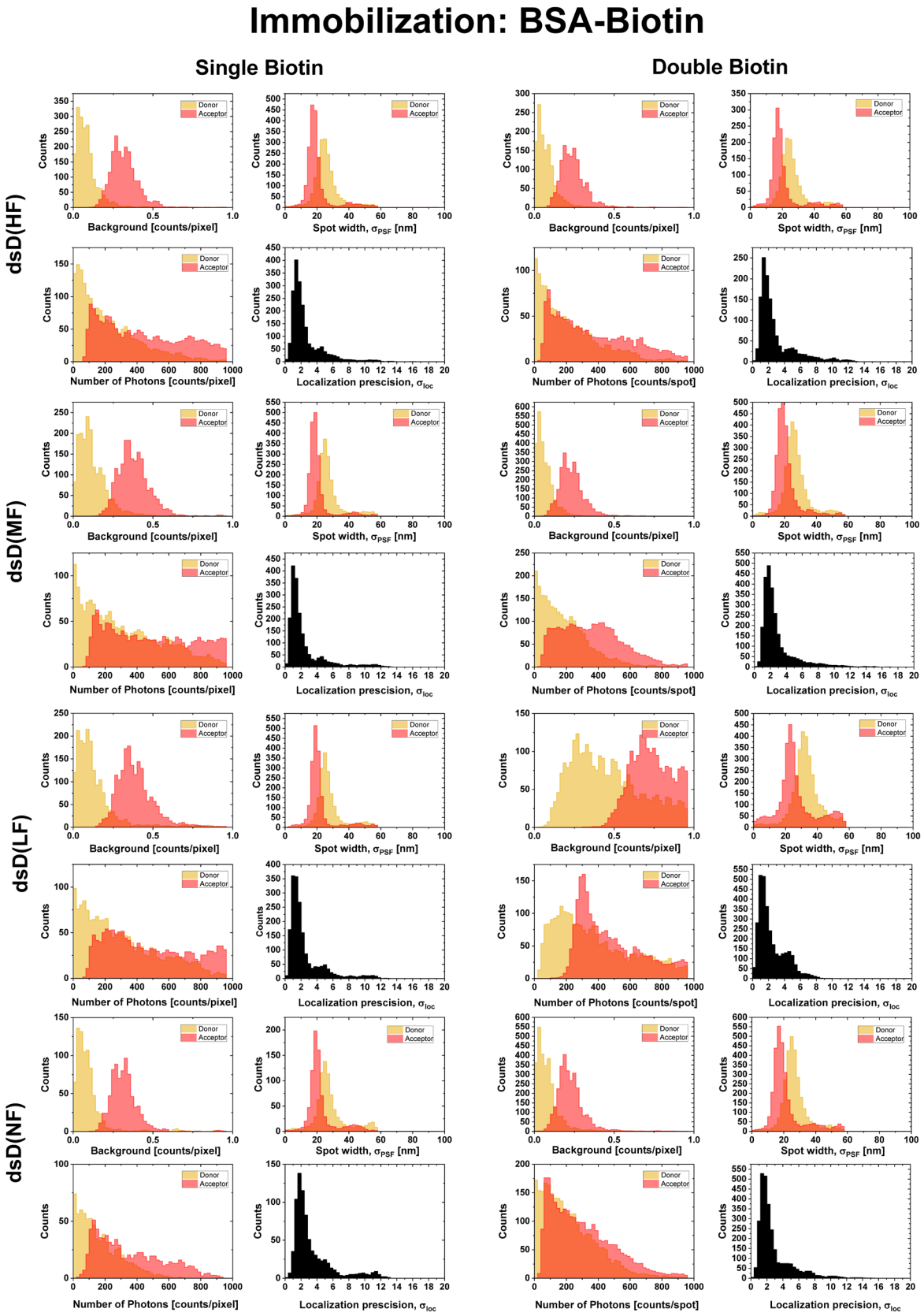

Supplementary Fig. 25: Localization precision for dsDNA rulers. Spot-wise localization characteristics for all dsDNA samples for BSA-Biotin and NHS-PEG-Biotin immobilization. The localization precision (bottom right) is calculated from equation S29 in the section 'Predicting the

localization precision' and depends on the number of photons per spot (bottom left), the background counts (top left) and the fitted spot width σ_{PSF} (top right). All data on microscope resolution and predicted precision are compiled in Supplementary Tab. 5.

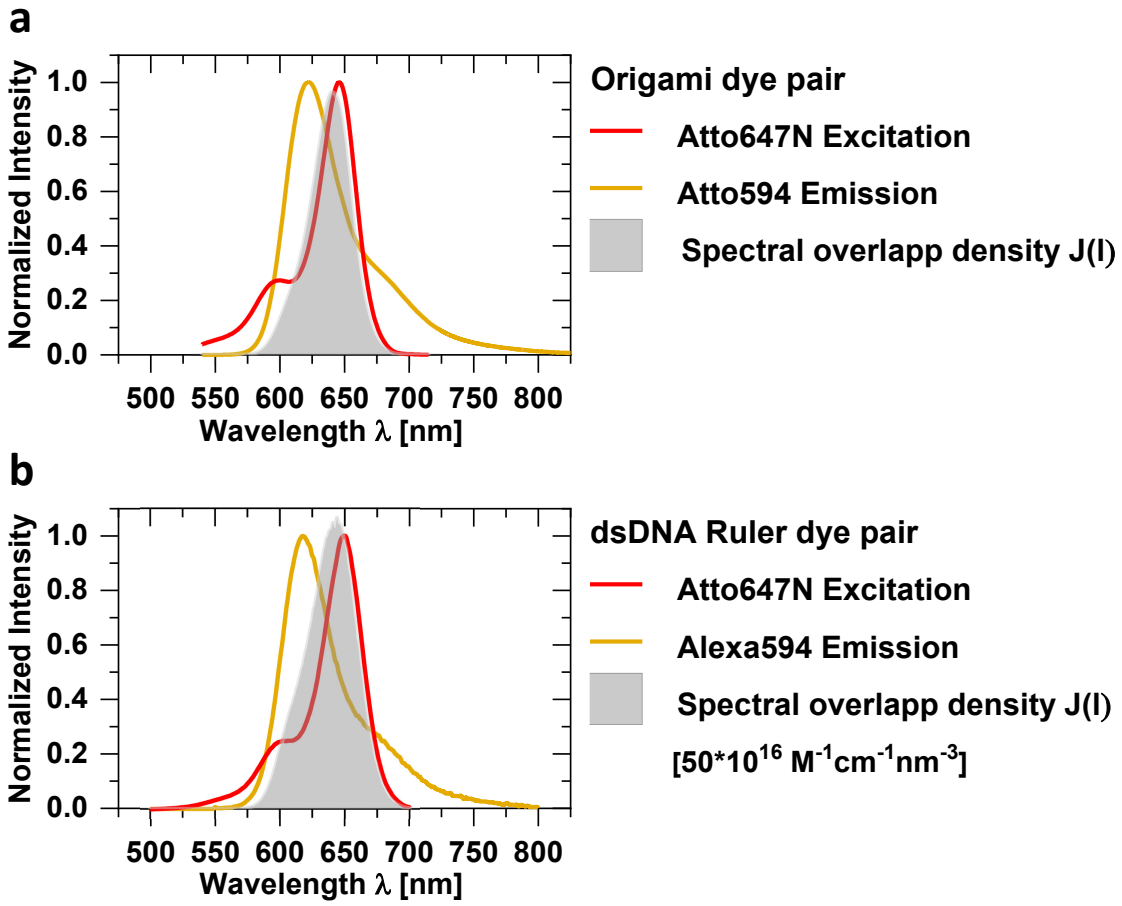

Supplementary Fig. 26: Spectral overlap integrals. Spectral overlap (grey area) of donor emission (orange) and acceptor excitation spectra (red) for **a)** origamis and **b)** dsDNA rulers. The calculated Förster radii R_0 are reported in Supplementary Tab. 4**.**

hGBP1 protein figures

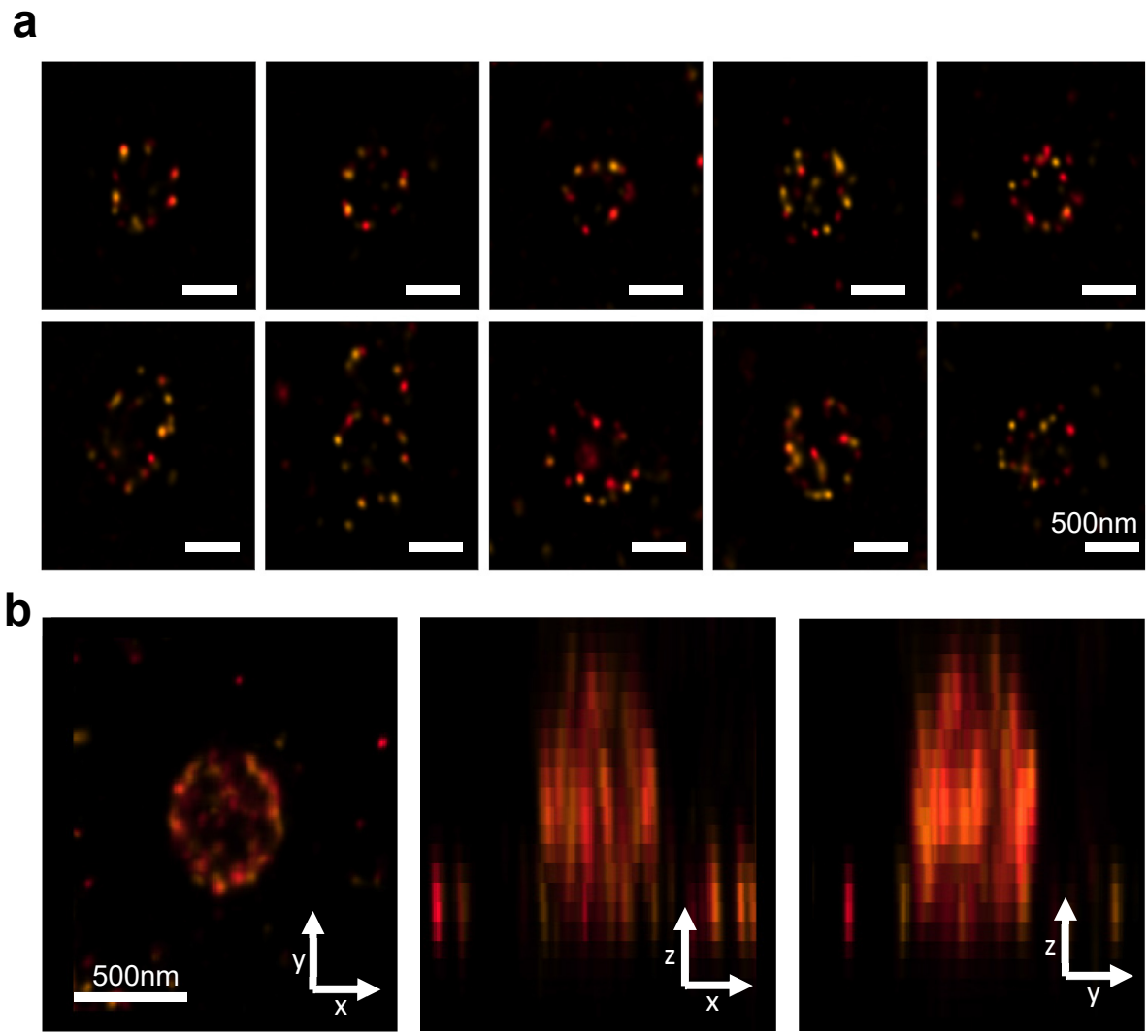

Supplementary Fig. 27: 3D STED images of hGBP1 fibers. a) Selection of deconvolved STED images. hGBP1 (18-577) was diluted 1:100 with unlabeled wild type hGBP1. The hGBP1 molecule is labeled with Alexa594 (donor) and Atto647N (acceptor). First row shows hGBP1 forming isolated ring-like structures, while the association of multiple ring structures is observed in second row. b) 3D illustration of hGBP1 ring structure in xy, xz and yz plane shows the 3D ring structure formed in oligomeric state. The procedures for the colocalization analysis of hGBP1 are described in Supplementary Note 10.

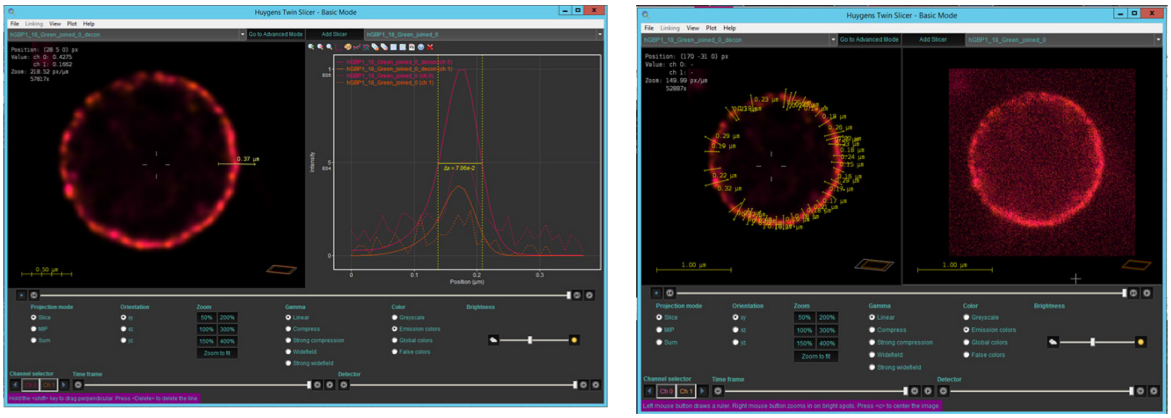

Supplementary Fig. 28: Determination of hGBP1 fiber diameter. Determination of fiber diameter using Huygens deconvolution software (see section 'Assessment of hGBP1 fiber diameter'). The measured lineprofile is drawn perpendicular to the ring profile.

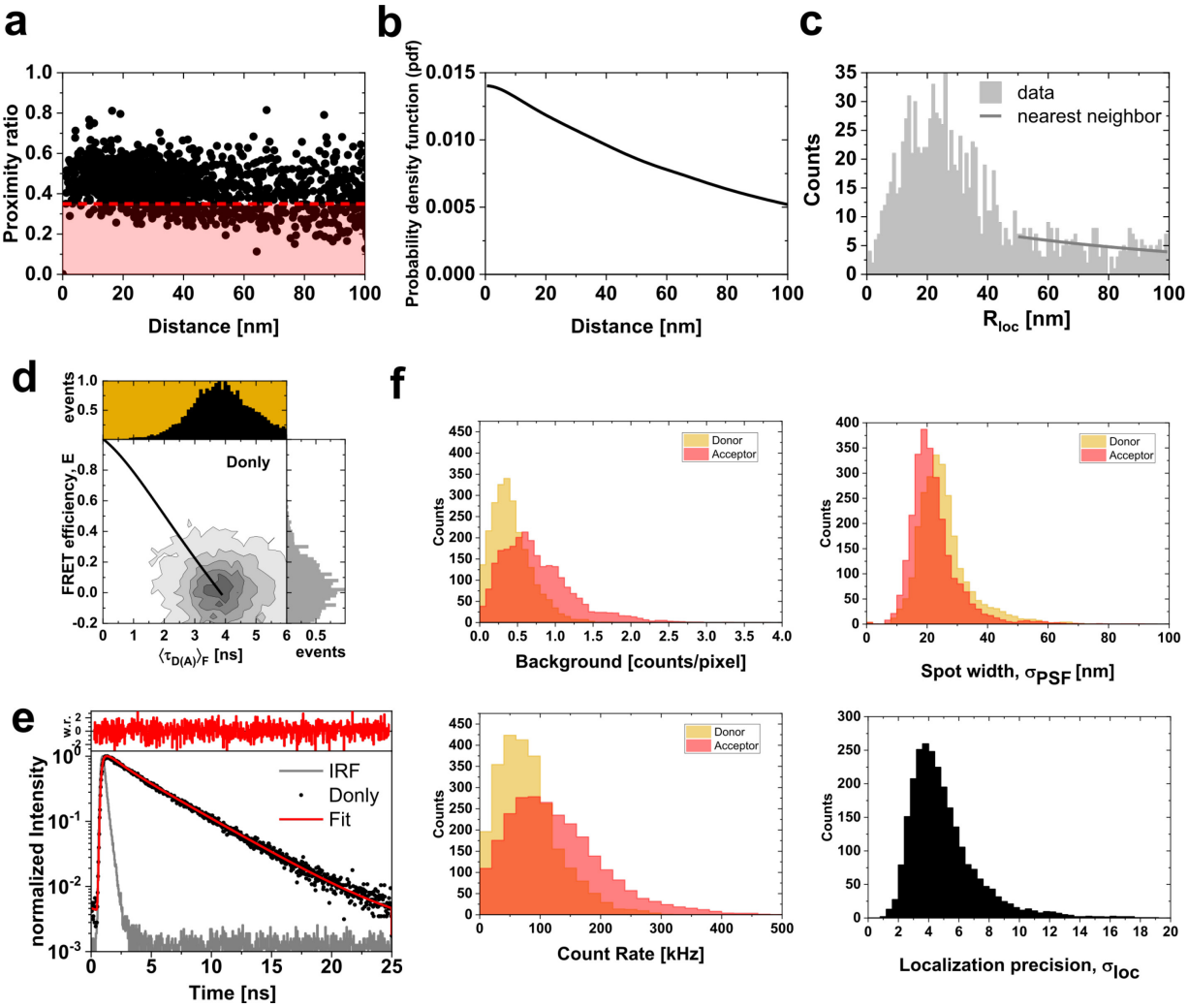

Supplementary Fig. 29: Colocalization analysis of hGBP1 by cSTED. **a)** A plot of the proximity ratio versus the localization-based interdye distance d_{loc}. Spots are filtered based on a proximity ratio threshold above 0.35. **b)** The probability density function of the localization-based interdye distance d_{loc} for randomly distributed spots on the ring. The curve is obtained by a Monte Carlo simulation of randomly distributed donors and acceptors along the hGBP1 ring, repeated 1000 times. See Supplementary Note 10 for details on the simulation procedure. **c)** hGBP1 interdye distance histogram used to determine the fraction of baseline (black line) by a fit for d_{loc} > 50 nm. See Supplementary Note 10 for details on the fitting procedure. **d)** Two-dimensional frequency histogram of the ROI-integrated intensity-based FRET efficiency, *E*, and the fluorescence-weighted average donor fluorescence lifetime, $\langle\tau_{\mathrm{D(A)}}\rangle_{\mathrm{F}}$ for the hGBP1 18-577 donor only (Alexa594) sample. The population lies on static FRET line (solid line, given by eq.10 in the Methods section of the main text using the parameters in Supplementary Tab. 19). **e)** The corresponding sub-ensemble lifetime decay. Measured data (black scatter) is fitted with a two-component model yielding a donor only lifetime of 3.9 ns, determined by fitting model eq. S18 in the section 'Sub-ensemble fluorescence decay analysis'. **f)** The histograms of donor and acceptor background photons, the fitted spot width, count rate and predicted precision are shown for the given ROI selection.

References

1. Vicidomini, G. *et al.* STED nanoscopy with time-gated detection: theoretical and experimental aspects. *PLoS One* **8**, e54421 (2013).
2. Szabelski, M. *et al.* Collisional quenching of erythrosine B as a potential reference dye for impulse response function evaluation. *Appl. Spectrosc.* **63**, 363-368 (2009).
3. Yang, H.-Y. & Moerner, W. E. Resolving mixtures in solution by single-molecule rotational diffusivity. *Nano Lett.* **18**, 5279-5287 (2018).
4. Schnitzbauer, J., Strauss, M. T., Schlichthaerle, T., Schueder, F. & Jungmann, R. Super-resolution microscopy with DNA-PAINT. *Nat. Protoc.* **12**, 1198-1228 (2017).
5. ACS NanoStahl, E., Martin, T. G., Praetorius, F. & Dietz, H. Facile and scalable preparation of pure and dense DNA origami solutions. *Angew. Chem. Int. Ed.* **53**, 12735-12740 (2014).
6. Douglas, S. *et al.* Rapid prototyping of 3D DNA-origami shapes with caDNAno. *Nucleic Acids Res.* **37**, 5001-5006 (2009).
7. Peulen, T.-O. *et al.* Integrative dynamic structural biology unveils conformers essential for the oligomerization of a large GTPase. *arXiv*, arxiv.org/abs/2004.04229 (2020).
8. Sistemich, L. *et al.* The molecular mechanism of polymer formation of farnesylated human guanylate-binding protein 1. *J. Mol. Biol.* **432**, 2164-2185 (2020).
9. Praefcke, G. J. K., Geyer, M., Schwemmle, M., Kalbitzer, H. R. & Herrmann, C. Nucleotide-binding characteristics of human guanylate-binding protein 1 (hGBP1) and identification of the third GTP-binding motif. *J. Mol. Biol.* **292**, 321-332 (1999).
10. Lee, N. K. *et al.* Accurate FRET measurements within single diffusing biomolecules using alternating-laser excitation. *Biophys. J.* **88**, 2939-2953 (2005).
11. Atto-Tec GmbH. *Fluorescent Labels and Dyes catalogue 2019/2020*, <https://www.atto-tec.com/images/ATTO/Katalog_Preisliste/Katalog_2019_2020.pdf> (2019).
12. Felekyan, S. *Computation of detection efficiencies*, <https://www.mpc.hhu.de/software/software-package.html> (2015).
13. Hellenkamp, B. *et al.* Precision and accuracy of single-molecule FRET measurements—a multi-laboratory benchmark study. *Nat. Methods* **15**, 669-676 (2018).
14. Förster, T. Zwischenmolekulare Energiewanderung und Fluoreszenz. *Ann.Phys.* **437**, 55-75 (1948).
15. Kalinin, S., Valeri, A., Antonik, M., Felekyan, S. & Seidel, C. A. M. Detection of structural dynamics by FRET: A photon distribution and fluorescence lifetime analysis of systems with multiple states. *J. Phys. Chem. B* **114**, 7983-7995 (2010).
16. Peulen, T.-O., Opanasyuk, O. & Seidel, C. A. M. Combining graphical and analytical methods with molecular simulations to analyze time-resolved FRET measurements of labeled macromolecules accurately. *J. Phys. Chem. B* **121**, 8211-8241 (2017).
17. Maus, M. *et al.* An experimental comparison of the maximum likelihood estimation and nonlinear least-squares fluorescence lifetime analysis of single molecules. *Anal. Chem.* **73**, 2078-2086 (2001).
18. D.A. Case, K. B., I.Y. Ben-Shalom, S.R. Brozell, D.S. Cerutti, T.E. Cheatham, III, V.W.D. Cruzeiro, T.A. Darden, R.E. Duke, G. Giambasu, M.K. Gilson, H. Gohlke, A.W. Goetz, R. Harris, S. Izadi, S.A. Izmailov, K. Kasavajhala, A. Kovalenko, R. Krasny, T. Kurtzman, T.S. Lee, S. LeGrand, P. Li, C. Lin, J. Liu, T. Luchko, R. Luo, V. Man, K.M. Merz, Y. Miao, O. Mikhailovskii, G. Monard, H. Nguyen, A. Onufriev, F.Pan, S. Pantano, R. Qi, D.R. Roe, A. Roitberg, C. Sagui, S. Schott-Verdugo, J. Shen, C. Simmerling, N.R.Skrynnikov, J. Smith, J. Swails, R.C. Walker, J. Wang, L. Wilson, R.M. Wolf, X. Wu, Y. Xiong, Y. Xue, D.M. York, P.A. Kollman. *AMBER*, <https://ambermd.org/doc12/Amber17.pdf> (2021).
19. Kalinin, S. *et al.* A toolkit and benchmark study for FRET-restrained high-precision structural modeling. *Nat. Methods* **9**, 1218-1225 (2012).
20. Lakowicz, J. R. *Principles of Fluorescence Spectroscopy*. (Springer US, 2006).

21. Mortensen, K. I., Churchman, L. S., Spudich, J. A. & Flyvbjerg, H. Optimized localization analysis for single-molecule tracking and super-resolution microscopy. *Nat. Methods* **7**, 377-381 (2010).
22. Smith, C. S., Joseph, N., Rieger, B. & Lidke, K. A. Fast, single-molecule localization that achieves theoretically minimum uncertainty. *Nat. Methods* **7**, 373-375 (2010).
23. Liu, D. C. & Nocedal, J. On the limited memory BFGS method for large scale optimization. *Math. Program.* **45**, 503-528 (1989).
24. Laurence, T. A. & Chromy, B. A. Efficient maximum likelihood estimator fitting of histograms. *Nat. Methods* **7**, 338-339 (2010).
25. Niekamp, S. *et al.* Nanometer-accuracy distance measurements between fluorophores at the single-molecule level. *Proc. Natl. Acad. Sci. U.S.A* **116**, 4275-4284 (2019).
26. Churchman, L. S., Flyvbjerg, H. & Spudich, J. A. A non-Gaussian distribution quantifies distances measured with fluorescence localization techniques. *Biophys. J.* **90**, 668-671 (2006).
27. Kabsch, W. A solution for the best rotation to relate two sets of vectors. *Acta Crystallographica Section A* **32**, 922-923 (1976).
28. Khara, D. C. *et al.* DNA bipedal motor walking dynamics: an experimental and theoretical study of the dependency on step size. *Nucleic Acids Res.* **46**, 1553-1561 (2018).
29. Bartnik, K. *et al.* A DNA origami platform for single-pair Förster Resonance Energy Transfer investigation of DNA–DNA Interactions and ligation. *J. Am. Chem. Soc.* **142**, 815-825 (2020).
30. JPK Instruments AG. *QI mode - Quantitative imaging with the NanoWizard 3 AFM*, <https://www.jpk.com/app-technotes-img/AFM/pdf/jpk-tech-quantitative-imaging.14-1.pdf> (2021).
31. Müller, B. K., Zaychikov, E., Bräuchle, C. & Lamb, D. C. Pulsed interleaved excitation. *Biophys. J.* **89**, 3508-3522 (2005).
32. Sisamakis, E., Valeri, A., Kalinin, S., Rothwell, P. J. & Seidel, C. A. M. Accurate single-molecule FRET studies using multiparameter fluorescence detection. *Methods Enzymol.* **475**, 455-514 (2010).
33. Fries, J. R., Brand, L., Eggeling, C., Köllner, M. & Seidel, C. A. M. Quantitative identification of different single molecules by selective time-resolved confocal fluorescence spectroscopy. *J. Phys. Chem. A* **102**, 6601-6613 (1998).
34. Weidtkamp-Peters, S. *et al.* Multiparameter fluorescence image spectroscopy to study molecular interactions. *Photochem. Photobiol. Sci.* **8**, 470-480 (2009).
35. Hübner, K. *et al.* Determining the in-plane orientation and binding mode of single fluorescent dyes in DNA origami structures. *ACS Nano* **15**, 5109-5117 (2021).
36. Sindbert, S. *et al.* Accurate distance determination of nucleic acids via Förster Resonance Energy Transfer: Implications of dye linker length and rigidity. *J. Am. Chem. Soc.* **133**, 2463-2480 (2011).
37. Livesey, A. K. & Skilling, J. Maximum entropy theory. *Acta Crystallogr. Sect. A* **41**, 113-122 (1985).
38. Brochon, J. C. Maximum entropy method of data analysis in time-resolved spectroscopy. *Methods Enzymol.* **240**, 262-311 (1994).
39. Skilling, J. & Bryan, R. K. Maximum entropy image reconstruction: general algorithm. *MNRAS* **211**, 111-124 (1984).
40. Vinogradov, S. A. & Wilson, D. F. Recursive maximum entropy algorithm and its application to the luminescence lifetime distribution recovery. *Appl. Spectrosc.* **54**, 849-855 (2000).
41. Hansen, P. C., Jensen, T. K. & Rodriguez, G. An adaptive pruning algorithm for the discrete L-curve criterion. *J. Comput. Appl. Math.* **198**, 483-492 (2007).
42. Höfig, H., Gabba, M., Poblete, S., Kempe, D. & Fitter, J. Inter-dye distance distributions studied by a combination of single-molecule FRET-filtered lifetime measurements and a weighted accessible volume (wAV) algorithm. *Molecules* **19**, 19269-19291 (2014).
43. Green, N. Avidin. 1. The use of [14C] biotin for kinetic studies and for assay. *Biochemical Journal* **89**, 585-591 (1963).

44. Wiseman, P. W., Squier, J. A., Ellisman, M. H. & Wilson, K. R. Two-photon image correlation spectroscopy and image cross-correlation spectroscopy. *J Microsc* **200**, 14-25 (2000).
45. Petersen, N. O., Hoddelius, P. L., Wiseman, P. W., Seger, O. & Magnusson, K. E. Quantitation of membrane receptor distributions by image correlation spectroscopy: concept and application. *Biophys J* **65**, 1135-1146 (1993).
46. *Welcome to Picasso's documentation!*, <https://picassosr.readthedocs.io/en/latest/index.html> (2021).
47. Castro, C. *et al.* A primer to scaffolded DNA origami. *Nat. Methods* **8**, 221-229 (2011).
48. Kim, D.-N., Kilchherr, F., Dietz, H. & Bathe, M. Quantitative prediction of 3D solution shape and flexibility of nucleic acid nanostructures. *Nucleic Acids Res.* **40**, 2862-2868 (2012).
49. Mathur, D. *et al.* Can a DNA origami structure constrain the position and orientation of an attached dye molecule? *J. Phys. Chem. C* **125**, 1509-1522 (2020).

Quantifying the Spatio-temporal Evolution of Protein Interactions using Cell Lifetime FRET Image Spectroscopy (CELFIS)

Authors:

Nicolaas T M van der Voort[1,†], Nina Bartels[2,†], Cornelia Monzel[2], Claus A M Seidel[1]

† contributed equally

* corresponding authors: cornelia.monzel@hhu.de, cseidel@hhu.de

[1]Molecular Physical Chemistry, Heinrich-Heine University, 40225 Düsseldorf

[2]Experimental Medical Physics, Heinrich-Heine University, 40225 Düsseldorf

Abstract

Like a Jungle, molecular interactions in live cells are characterized by a high inter-connectedness in space and time. We present Cell Lifetime FRET Image Spectroscopy (CELFIS) to measure time-evolution of pairwise homo- or hetero-interactions with 0.8% fraction precision and high statistics. We apply this method to the CD95 protein, showing passive and active single-cell response to ligand addition, and to CTLA4, showing concentration dependent dimerization. We deliver free-to-use analysis software.

Introduction

To study molecular interactions in live cells, new methods are needed that can determine the abundance of interacting molecular species in the cell accurately while obtaining sufficient statistics to characterize the vast variation in interaction conditions. Giving rise to cellular decision making and maintaining homeostasis in changing molecular surroundings, molecular interactions are the building block of interacting networks that are dynamically organized in time by rate kinetics and in space by means of cellular compartmentalization. An ideal research tool hence can 1) quantify the abundance of interacting species over time 2) is sufficiently accurate to measure small changes in binding fractions on a single-cell level 3) gather sufficient statistics to sample the inherent diversity in live cells while 4) measuring under biologically relevant conditions and 5) distinguishing subcellular compartments.

As a new candidate for such a research tool, we here introduce Cell Lifetime FRET Image Spectroscopy (CELFIS). It relies on FRET-sensitized fluorescence donor decays, an internally calibrated confocal lifetime-based FRET method, to quantify the fraction of FRET-capable molecules, x_{FRET} and the derived fraction of dimers/oligomers, $x_{\mathrm{dimer/oligomer}}$. Combined with single-molecule brightness calibrations, we can determine absolute concentrations and precise fractions of two interaction partners in the system of interest. Molecular interactions are heavily influenced by absolute molecular concentrations and we determine and probe receptor concentrations from 20 up to 7'000 receptors/μm². To access high receptor concentrations, we provide two novel approaches to correct for proximity FRET and compare them against an existing theoretical method. We follow the time evolution of x_{FRET} on the entire lower membrane over a time period of up to 7 hours. Our method is compatible with live-cells under endogenous expression levels and standard cell conditions. To gather sufficient statistics, we developed a python-based analysis toolkit reducing time

spent on operating analysis programs to a few minutes. We improve the conversion accuracy from x_{FRET} to $x_{\mathrm{dimer/oligomer}}$, by using Accessible Volume (AV) simulations that consider the linker length and anchoring position in addition to geometric restrictions due to e.g. the membrane to predict the FRET signal of a pure FRET sample. In summary, we show that our method fulfills the requirements listed above for homo-interactions on membranes while being easily expandable to homo- or hetero-interaction of up to two interacting species in any region of the cell.

Previously, Yeast-two-hybrid (Y2H)[1] or TAP-MS[2] were established as workhorses for quantitative interaction studies, but lack spatial, temporal and contextual information[3,4]. Recently, Fluorescence Intensity Fluctuation spectroscopy[5] was established to report on the oligomeric state of a protein complex, but works preferentially on fixed cells and low expression levels. FRET, especially based on genetically encoded fluorescent proteins (FPs), is ideally suited to report on molecular binding due to its biocompatibility and the ubiquity of fluorescently tagged proteins[6,7]. In recent years, a wealth of FRET-based biosensors was developed that report on context factors such as temperature sensing[8], pH sensing[9] and ATP sensing[10,11]. Multiparameter Fluorescence Image Spectroscopy (MFIS)-FRET obtains quantitative lifetime- and intensity-based FRET information in addition to anisotropy[12-14]. Quantitative Imaging (QI)-FRET[15,16] and its successor Fully-quantified Spectral Imaging (FSI)-FRET[17] use intensity-based FRET on a widefield microscope to measure dimer concentrations quantitatively. The latter two methods rely on vesiculation or osmotic swelling to produce flattened membranes, thus disturbing the endogenous state of the cell and are mostly used to detect large changes in FRET Efficiency. None of these methods have the sensitivity required to elucidate the subtle spatiotemporal dynamics of molecular interactions in live cells, underlining the importance of CELFIS (Figure 1 A).

To demonstrate the need of such a tool, we apply it to the highly complex and regulated signaling pathway of Cluster of Differentiation 95 (CD95), which induces apoptosis when triggered by the CD95 Ligand (CD95L)[18-20]. Signal initiation by CD95 activation classically results in apoptosis, a controlled form of cell death, albeit certain environments may also lead to its involvement in cell proliferation[21] or activation of the NFκB inflammatory signaling pathway[22]. Furthermore, the outcome of CD95 signaling must be mediated by spatiotemporal competition of the binding partners for the respective signaling pathways. Since CD95 signaling serves many functions during development and homeostasis, and is a central target in cancer therapy[23], understanding the precise spatiotemporal dynamics of the molecular interactions is critical. By following our methodology, we obtain a multi-variate dataset shown in Figure 1 B.1 that illustrates the FRET fraction against donor to acceptor concentration ratio as well as the temporal dynamics induced by ligand addition and the effect of proximity FRET. In our previous work applying CELFIS, we showed that CD95 is monomeric in absence of ligand and that ligand addition induces 6-15% oligomers sufficient to trigger apoptosis (N.B., N.v.d.V., A.G., A.B., C.W., C.A.M.S., C.M. *manuscript in preparation*). In this work, we elucidate the temporal-dynamics of ligand-induced CD95 oligomerization on a single-cell basis, achieving a sensitivity of 0.8% oligomer fraction (Figure 1 B.2, Supplementary Figure 1).

Further, we investigated the CTLA4 receptor which regulates T-cell activation by preferentially binding to its ligands compared to its competing receptor CD28[24]. Its importance is underlined by the interest in using CTLA4 derivatives as a therapeutic agent in auto-immune diseases[25,26] and cancer[27,28]. Crucial to the function of CTLA4 , binding affinities depend on the oligomeric state of the receptor, which were previously determined to be purely dimeric when probing at high concentrations[29-31]. Enabled by proximity FRET correction, we here study for the first time the influence of CTLA4 receptor concentrations from 60 up to 7’000 receptors/µm² on its oligomeric state.

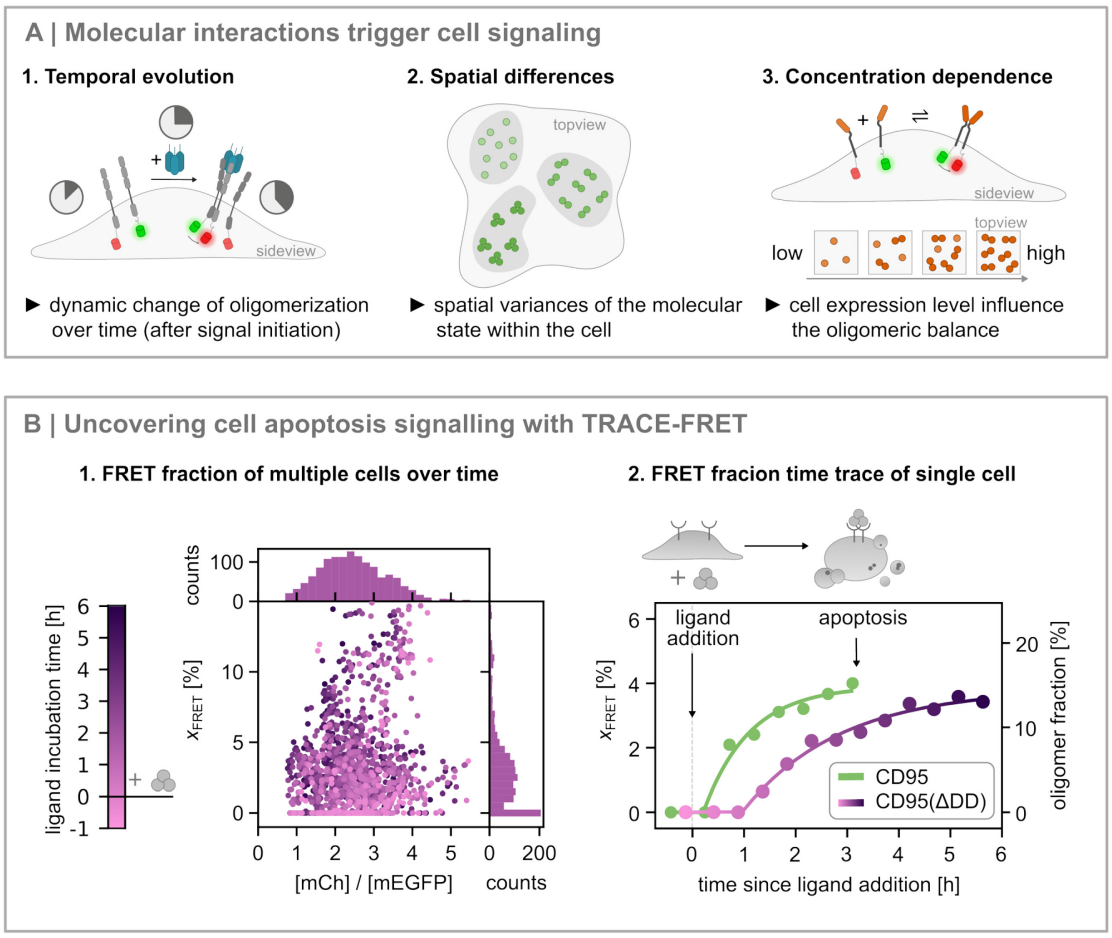

Figure 1: CELFIS unlocks sensitive molecular switches in cell signaling.
A | The signaling and interaction mechanisms in a cell are complex and refined processes depending on various parameters. To elucidate them in their entirety requires scanning multiple dimensions, which can be realized using CELFIS: 1. The time dimension elucidates interaction dynamics, for example after a ligand-induced signal initiation. 2. The spatial dimension helps to understand the involvement of different cellular compartments into the oligomerization process. 3. The concentration dimension uncovers the effect of cellular expression level on the fraction of oligomeric molecules. We illustrate all dimensions of our method here on homo-interactions of membrane proteins, but it is extendable to intracellular processes and hetero-interactions. **B** | 1. The FRET fraction x_{FRET} of apoptosis-incompetent CD95(ΔDD)-EGFP/mCherry expressing cells increases after ligand addition indicating ligand-induced homo-oligomerization. The measurement covers large statistics (n = 1328 from 116 cells measured in 4 independent experiments). The ratio of acceptor to donor concentrations ([mCh]/[mEGFP]) centers around a ratio or 2.5 : 1. 2. Evolution of x_{FRET} (left axes) and corresponding oligomer fraction (right axes) of single cells over time. Oligomer fraction is measured with high precision, showing the smooth evolution up to ~10% oligomers after which apoptosis can occur for apoptosis competed cells expression fill-length CD95.

Result

Configuration of the Microscope Setup. Our measurement setup consists of a confocal microscope with two excitation lines compatible with the excitation spectrum of the FRET pair and pulsed excitation combined with TCSPC (time-correlated single photon counting) readout to enable lifetime measurements (Figure 2 A). As an optional, but not required, addition to the setup, our setup detects emission in a polarization sensitized manner, giving us access to anisotropy and Multi-parameter Fluorescence Image Spectroscopy (MFIS)[13]. Alternating Line Excitation (ALEX) was used to determine acceptor concentrations, by measuring the emission in the acceptor channel due to FRET and donor crosstalk, on the one hand, and by measuring acceptor emission upon sole acceptor excitation, on the other hand.

High-throughput analysis via measurement automation. To sample large variations in the concentration in addition to the natural cell-to-cell variability, a high number of single-cell data is required. Here we achieve high throughput by implementing automation for data acquisition and analysis that can run overnight. The data acquisition is automated using an in-house built program that interfaces with the microscope control software using the python interface *specpy* for the control program imspector (methods). The program allows the user to identify regions of interest and to save them with a single mouse-click. After selecting the image acquisition settings, the user can choose to record each area once or repeatedly in a loop to acquire time-evolution data (Figure 2 B). Our measurement automation software is freely available on GitHub (https://github.com/Fluorescence-Tools/Abberior-Tools) and many modern microscope acquisition software now offer similar features. For the analysis, the researcher can segment the recorded images by generating binary masks. Depending on the experimental need, the researcher can select specific subcellular domains or select entire cells for analysis. Here we investigate the effect of local CD95 membrane concentration fluctuations on the oligomerization state (see below). In addition to automated data acquisition, we developed a python-based automated data analysis pipeline available on GitHub (https://github.com/Fluorescence-Tools/Seidel), requiring ~10 minutes for setting analysis settings after which data is batch-processed (Supplementary Table 1 and Supplementary Figure 2).

Determination of FRET fraction and FRET Efficiencies. We use the FRET sensitized donor decay analysis method previously established in our group[12,14,32], that is highly sensitive yet robust. The method measures changes in the donor decay due to FRET by measuring changes with respect to a donor only control (Figure 2 C.2). As the donor only control was recorded under identical circumstances as the FRET sample, this provides an internal calibration against temperature or pH induced lifetime changes. In contrast to intensity-based methods that measure the weighted average of FRET species, the FRET sensitized donor decay is more informative by distinguishing the fraction of FRET capable donors (x_{FRET}) and their average efficiency (k_{FRET}) in addition to the fraction of non-FRET capable donors (x_{noFRET}).

Determination of donor and acceptor concentrations. To transform the fluorescent brightness in a cell to a number of fluorophores, we obtain calibrations for the brightness of a single EGFP and a single mCherry molecule using a brightness calibration curve (Figure 2 D.1, Supplementary Figure 3). For a titration series of each fluorescent protein, the concentration was measured using absorption spectrometry (Supplementary Figure 4). Subsequently, the brightness per confocal volume was measured on the FRET measurement setup (methods Section). Accounting for the size of the confocal volume obtained with FCS calibration (Supplementary Table 2, Supplementary Figure 5), the brightness is transformed into a brightness per molecule [$\mathrm{kHz \cdot molecule^{-1} \cdot \mu W^{-1}}$] (methods, Supplementary Note 1). Indicated by Fluorescent images (N.B., N.v.d.V., A.G., A.B., C.W., C.A.M.S., C.M. *manuscript in preparation,* Supplementary Figures 1 and 12), a portion of fluorescent proteins exist in the cytoplasm. Using live-cell FCS, we determine the abundance of cytoplasmic and membrane-bound species when focusing on the membrane to be 37% and 63% respectively (Supplementary Table 3). To avoid a concentration bias due to a wrinkled membrane[15,17], we

measure the bottom of the cell membrane (Supplementary Figure 1), which is typically flat within 10 nm over a characteristic contour length of 500 nm[33].

Derivation of the oligomerization state from simulations and statistical analyses of the FRET fraction. To obtain a quantitative measure of the oligomerization state, we obtain a calibration for the FRET signal of a pure dimer sample, $x_{\mathrm{FRET,max}}$, which consists of three steps: 1) Although the monomeric constituents of a dimer are often spatially close within the FRET range (< 8 nm), the donor and acceptor are attached via long flexible peptide linkers (Figure 2 E.1) causing them to diffuse in and out of their FRET range, thus lowering the fraction of time they are FRET capable. The fluorescent protein as well as the labelled protein have flexible domains at the end of their peptide chains in addition to an artificial flexible linker added during plasmid design, leading to a 49 to 52 amino acid linker for our constructs (N.B., N.v.d.V., A.G., A.B., C.W., C.A.M.S., C.M. *manuscript in preparation,* Supplementary Table 4, see also Supplementary Figure 6). Truncation of the flexible domain is often not feasible as they are required for correct protein folding. As the fluorescent proteins diffuse on a tether, previous work in our group calculated the extension probability distribution for a given peptide length (Figure 2 E.1, colored area)[34,35]. To obtain the distribution of donor and acceptor distances (R_{DA} Figure 2 E.1, bottom), we perform Accessible Volume (AV) simulations using anchor points separated by 2.2 nm consistent with PDB structures 2NA7[36] for CD95. For CTLA4 no structural model of the transmembrane domain (amino acids 162-182) is available, hence all known information is captured using the CD95 model representing a dual helix across the membrane. Since lower FRET Efficiencies at high distances become indistinguishable from noFRET and very high FRET Efficiencies have very little photons in the donor channel, FRET can be measured for donor-acceptor distances from 2.0 to 8.2 nm, corresponding to 99 and 6% FRET Efficiency for our Förster radius of 5.2 nm, yielding that a FRET pair is FRET capable 46% of the time. 2) Furthermore, $x_{\mathrm{FRET,max}}$ is affected by the portion of mCherry molecules that is correctly folded such that the chromophore may accept a photon. While difficult to measure directly, we are informed by studies that measure the fraction of bright mCherry molecules[37] where we note that dark mCherry molecules may still accept a photon via FRET and emit it non-radiatively, yielding an informed estimate of 80% FRET capable acceptors. The fraction of bright mEGFP molecules affects the total concentration only, obtained from literature to be ~80%[37,38]. 3) For homotypical interactions, donor molecules can form donor-donor dimers that do not affect the lifetime. To correct for this effect, we calculate the abundance of donor-donor homo-dimers in addition to donor-acceptor hetero-dimers based on their abundance and assuming a binomial distribution (Figure 2 E.2). For CTLA4 the ratio between donor to acceptor was 1 : 3.5 yielding 78% hetero-dimers and for CD95 and CD86 variants the ratio was 1 : 2.5 yielding 71% hetero-dimers (Figure 1 B and Supplementary Figure 7). Further note that acceptor-acceptor dimers also form, but do not affect the lifetime measurement. Combining all elements, the maximum FRET fraction, $x_{\mathrm{FRET,max}}$, is obtained by multiplying the probability that the dyes are in the FRET range, the fraction of heterodimers and the fraction of FRET-capable acceptors, yielding 29% for CTLA4 and 26% for CD95, CD95(ΔDD) and CD86. An elaborate discussion of the advantages of using AV simulation to obtain $x_{\mathrm{FRET,max}}$ compared to previous methods is given is Supplementary Note 2. As the CD95 protein may form a mixture of monomers, dimers and trimers, we extend the calculation to the trimeric case in Supplementary Note 3 (see also Supplementary Figure 8) to yield $x_{\mathrm{FRET,max,trimer}}$ of 46% for CD95. While the final $x_{\mathrm{FRET,max}}$ can be obtained from the oligomer species weighted average, the latter is not known for CD95 (N.B., N.v.d.V., A.G., A.B., C.W., C.A.M.S., C.M. *manuscript in preparation*), noting that the overall oligomerization degree is low we make the simplest assumptions that CD95 consists of monomers and dimers. Combining all steps, CELFIS measures quantitative spatiotemporal donor and acceptor labelled receptor concentration and the quantitative fraction of complexes (Figure 2 F).

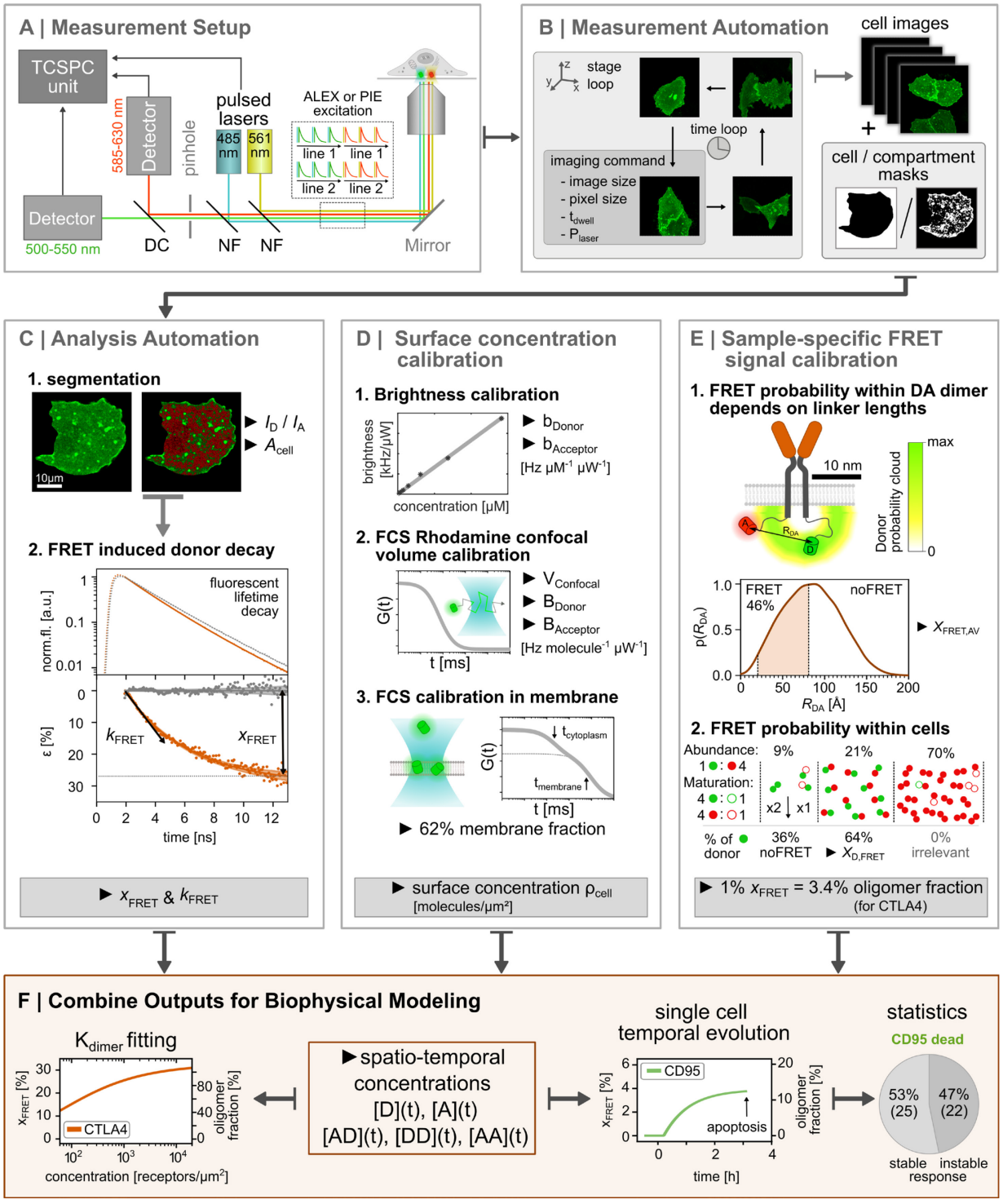

Figure 2: Method illustration.

A | The method requires a confocal setup with single photon counting ability (TCSPC) and Pulsed Interleaved - or Alternating Line Excitation (PIE/ALEX). **B** | Multi-cell images are recorded in an automated manner using stage- and time loops. The images can be segmented using cell- or cell compartment masks to select the regions of interest for analysis. **C** | The automated analysis obtains and fits the FRET induced donor lifetime decay, yielding the FRET fraction and rate, x_{FRET} and k_{FRET}, and derives image information like the channel intensities I_D/I_A and the segmented areas, A_{cell}. **D** | Precise calibration of the receptor surface concentration is achieved with 1. brightness vs. concentration

calibrations using the confocal setup and absorption spectroscopy, 2. confocal volume calibrations (FCS) with well-defined reference dyes (here: Rhodamines). 3. Sample-specific FCS calibrations to distinguish between membrane and intracellular signal. **E |** To derive the sample-specific maximal FRET fraction $x_{\mathrm{FRET,max}}$ three steps are required: 1. AV simulation of the constructs can determine the FRET probability due to linker lengths and anchor point distances. 2. The relative abundance of donor, acceptor and immature protein is used to determine the fraction of FRET-able oligomers (here: dimers). As a result, a sample-specific conversion factor from the FRET fraction to the oligomer fraction is achieved. **F |** All three pillars (**C,D,E**) converge to the highly accurate determination of absolute concentrations and precise oligomer fractions, that can be traced in time and space.

CTLA4 concentration dependent dimerization and proximity FRET correction Turning to the application of CELFIS on biological systems, our study of CTLA4 shows a clear increase of x_{FRET} as a function of total receptor surface concentration, indicating for the first time that the protein undergoes a concentration dependent monomer to dimer transition (Figure 3 B.1). Comparison to monomeric controls CD95, CD95(ΔDD) and CD86 clearly illustrates that in addition to FRET due to dimerization, the x_{FRET} signal is affected by unspecific interactions due to crowding at high concentrations, also known as proximity FRET (Figure 3 A). Our results show that proximity FRET arises already at common transfection conditions and hence accentuates the importance to test and correct for it. Supplementary Notes 4 and 5 introduce two new methods for estimating proximity FRET and compares against existing theoretical predictions[39]. Finally, we use the correction based on the CD95 monomer for its robustness and good fit quality to correct the CTLA4 data. The corrected data is fitted following a model for homo-dimerization (methods and Supplementary Note 6) yielding a dimerization constant, K_{dimer} to be 154 ± 14 receptors/μm^2 (Figure 3 B.1). The CTLA4 fit residuals have a standard deviation of 2.55% x_{FRET}. To ascertain the quality of our model, we visually inspect the fit residuals for systematic errors (Figure 3B.1) and quantify this using the Durbin-Watson test, yielding a good value of 1.48 close to the ideal value for random residuals of 2.0. Note that the χ^2_{red} parameter was not used as no reliable method was available to estimate the weights. As our model includes $x_{\mathrm{FRET,\,max}}$ as a fitting parameter (methods), we obtain an experimental value to be 32.6%, close to the predicted 29% from AV simulations.

Multivariate datasets of CD95 receptor induction reveal kinetics driven CD95 oligomerization, from ensemble statistics to single cells and subcellular membrane domains. CELFIS facilitates large, multivariate datasets of CD95 (Supplementary Figure 7), showing the proximity-corrected average oligomer fraction per cell and their time evolution after ligand addition. Our CELFIS method can be expanded to study protein interactions at the cellular compartment or organelle level by using masks to segment areas of interest (Figure 2 C.1). Here, we probe the oligomeric state of high- and low brightness membrane areas, as there were bright membrane domains of 0.5 – 3 μm² size consistently visible on the cell membrane indicating a local concentration of CD95 receptors. Using the pixel-based method MFIS[13], the FRET signal was homogeneous over the membrane within the noise level of 10% FRET Efficiency or ~40% oligomers (Supplementary Figure 9). Evolution of the oligomer fraction on a single cell level (Figure 3 C.2) shows that oligomerization occurs everywhere on the membrane, although slightly more oligomerization occurs in high brightness areas. Analysis of the full dataset from Figure 3 B shows that this trend is paradigmatic and occurs for all CD95 variants (Figure 3 C.1). Corroborating this result, oligomerization state increases with CD95 concentration at the single-cell level (Supplementary Figure 10). CELFIS enables to localize the changes in oligomeric states at different positions and time points in a spatial map of the cells (Figure 3 C.3) contributing to a full understanding of the CD95 signal initiation. Taken together, we conclude that CD95 oligomer formation is driven by kinetics and that bright membrane domains are not necessary for signaling. Supported by the observation that bright membrane domains are also found for CTLA4 and CD86 transfected cells, they may rather be an accidental by-product of other cellular processes.

Time evolution of CD95 receptor oligomer fractions in single-cells reveal temporal dynamics at 0.25% x_{FRET} precision. The ligand addition perturbs the steady-state of CD95 from purely monomeric to a mixture

of monomers and oligomers. We identify different characteristics of the time evolution. Several cells showed an asymptotic approach to a new steady-state corresponding to a purely kinetics driven, stable response (Figure 3D, Supplementary Figure 11), while others exhibit modulations of the oligomer fraction in time including jumps, fluctuations and continuous decreases (Figure 3D, Supplementary Figure 12). We obtain a conservative estimate of the measurement precision by considering the residuals of six selected CD95 and six selected CD95(ΔDD) cells corrected for the number of fit parameters, yielding 0.22% x_{FRET} or 0.8% oligomer fraction. We further characterize the error in the internal reference posed by the donor only control to be 0.36% x_{FRET} or 1.4% oligomer fraction caused by temperature changes (Supplementary Figure 13). This error represents an absolute offset to all x_{FRET} values recorded on that day, affecting accuracy but not precision.

In order to investigate traces exhibiting modulated response characteristics, we confirmed the absence of visible artifacts, such as cell movement and focus drift by visual inspection of selected cells. As the fluctuations clearly exceed our error, we suggest that these fluctuations indicate a rich multitude of underlying cellular processes that control the oligomerization state in a complex manner. Interestingly, some cells showed a temporal delay before responding to the ligand stimulus (Supplementary Figures 11 and 12). To classify the traces, we apply a model describing exponential convergence to steady-state after ligand addition (methods and Figure 3 D.1) and inspect the fit parameters for clusters (Supplementary Figure 14). We found that CD95 cells that died could more often be fitted with realistic rise times and decent fit quality ($11 < t_{\mathrm{rise}} < 500$ min, $\sigma_{xFRET} < 5\%$) than CD95 cells that stayed alive (p = 2.8%, Pearson's Chi-square test) and CD95(ΔDD) (p = 1.7%, Pearson's Chi-square test). Few cell traces (n = 6) had three or less datapoints and hence could not be fitted. Taking further advantage of the knowledge of our measurement error, we note that the residuals of the CTLA4 fit (2.55% x_{FRET} or 8.0% dimer fraction), represent biologically-relevant variability in single-cell dimerization fraction.

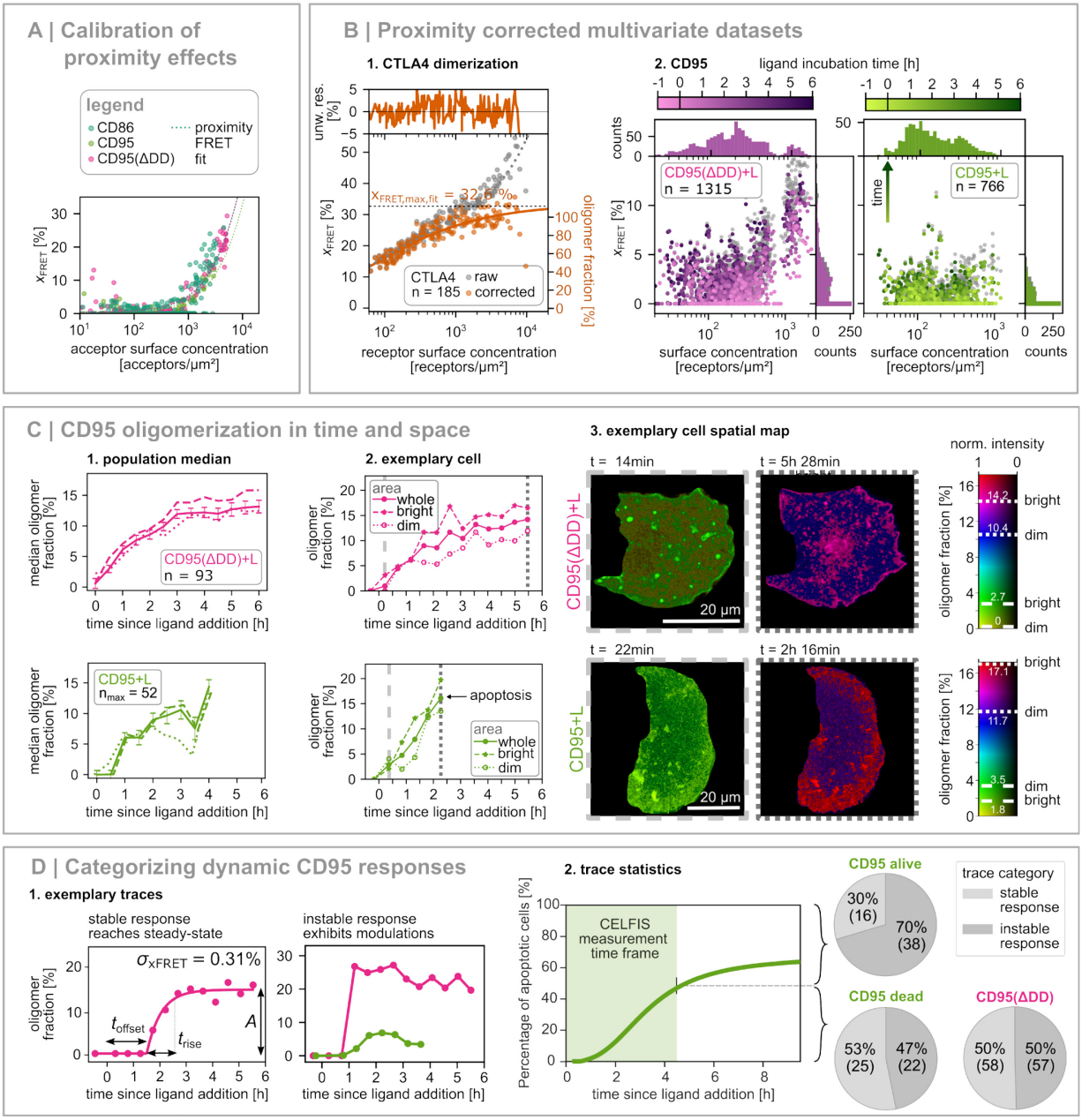

Figure 3: CELFIS probes proximity FRET and the evolution of oligomerization.
A | Proximity calibration of three different monomer controls. Data for each control was recorded in at least 4 experiments on at least 2 days with $n = 132$, $n = 143$, $n = 225$ independent cells for CD95, CD95(ΔDD) and CD86 respectively. **B |** Proximity corrected datasets. 1. CTLA4 dimerization: x_{FRET} increases with a cell's receptor surface concentration. The data can be corrected for proximity FRET using a monomer control and fitted with a K_{dimer}. The FRET fraction can be translated into an oligomer fraction (32.6% $x_{\mathrm{FRET}} = 100\%$ oligomers). 2. Proximity corrected high- statistical datasets of the variants CD95(ΔDD) (magenta) and CD95 (green) show the temporal and concentration dimension of the FRET fraction. CD95 and CD95(ΔDD) datasets were recorded in four independent experiments in 4 days. CTLA4 data was recorded in two days in 4 independent experiments. **C |** 1. Time-evolution of population median (> 50 cells/sample) of the oligomer fraction after ligand addition for cell expressing CD95 variants. The oligomer fraction is shown for the whole cell (all), and spatially-resolved in bright and dim membrane

surface areas (Figure 1 A.2). Note, CD95 cells die during this measurement. Dim and bright membrane areas show the same oligomerization trend. Error bars are obtained from standard error of the mean. 2. Exemplary single-cell time evolutions, spatially-resolved as before. Dashed lines indicate time points that are visualized in: 3. Exemplary spatial map of the measured cells, illustrating the differences in the oligomer fraction for bright and dim areas (hue) overlaid with the intensity image of the cell (brightness). Two time points shown for each cell, at the beginning of ligand addition and at the end of the measurement. **D |** Single-cell oligomerization responses to ligand addition are categorized. 1. Exemplary traces for the stable and instable response type. Steady-state responses can be described following a model (main text) and determine the precision of x_{FRET}. Dynamic responses show for example jumps, fluctuations/oscillations and decrease of x_{FRET}. 2. Statistical analysis of trace characteristics based on fitting parameters (methods). Apoptosis competent CD95 expressing cells that undergo apoptosis show more stable responses compared to CD95 cells that stay alive and CD95(ΔDD). As indicated by the schematic apoptosis dynamics (compare Figure 2 from N.B., N.v.d.V., A.G., A.B., C.W., C.A.M.S., C.M. *manuscript in preparation*), a fraction of CD95 cells that remained alive would be expected to die after the 4.5 h measurement time frame.

Conclusion

In conclusion, CELFIS paves the way for advanced interactome studies by 1) measuring dimer concentrations down to 1% precision in live cells at endogenous expression levels, 2) providing the architecture to obtain large datasets of single-cell dimer concentrations in time and 3) providing new solutions to correcting proximity FRET at high concentration levels and determining the FRET signal corresponding a pure dimer signal, $x_{\mathrm{FRET,max}}$, or pure timer, $x_{\mathrm{FRET,max,trimer}}$.

To perform CELFIS requires prerequisites that are now commonly available: First, fluorescent protein labelled biomolecules are a cornerstone of biomolecular research and thus are ubiquitously available, second, two-color confocal instruments with photon arrival time readout are commercially available and commonly found in imaging facilities, third, our python-based analysis software has no commercial dependencies and is now freely available. Due its relevance for a large problem class, measurement precision, biocompatibility and its ease of implementation, we expect that CELFIS will have a large impact on the study of molecular interactions. For example, it can be easily extended to cytoplasmic interactions, such as in the PI3K pathway, which triggers growth, proliferation or migration depending on time-modulation of the input signal[40,41]. Another example lies in the field of computational interaction modelling, where the limited availability of quantitative temporal data on protein-protein interactions in live cells is listed as a crucial limitation for the progression of the field[4,42].

Discussion

This work is the first to measure the concentration dependent dimerization of CTLA4. Early biochemical studies relied on Western Blot analysis of purified protein constructs, reporting a dimeric state at high concentrations (~2 mg/ml)[31,43] or predominantly dimeric (89 ± 13% dimers) state[30]. In an earlier FRET study[44], the total CTLA4 concentration is increased by additional acceptor expression. Within the accuracy of their results, the resulting increase in FRET is attributed completely to an increase of acceptor-donor ratio, although comparison to our results show that it is also consistent with concentration dependent dimerization. A recent STORM based approach[45] yielded the average fluorophore number in a cluster of 1.93 ± 0.02, or 93% dimers and 7% monomers, although they only measured at a single concentration. It is noteworthy that a purely monomeric CTLA4 variant remains competent to inhibit T-cells[30]. Further note that our cells do not express CTLA4 or any of its interaction partners natively (Supplementary Table 4). Summarizing our CTLA4 result, we conclude that we observe a transition because we can measure at a wide range of concentrations for the first time, whereas most previous studies[30,31,43] found dimers because they were performed at high concentrations. As endogenous CTLA4 expression level depends on the state of the

T-cell[46], our results shed new light on the interaction mechanisms of CTLA4 and underlines the importance of measuring the oligomeric state at different concentration levels.

We provide two new approaches to correct for proximity FRET, showing that we can measure up to 7'000 receptors/µm² with a theoretical limit of 25'000 receptors/µm², a detailed discussion is given in Supplementary Note 4. Similarly, the advantages of using AV-simulations to predict $x_{\mathrm{FRET,\,max}}$ is elaborated on in Supplementary Note 2.

Notable synergies for future improvements lie in the inclusion of the FRET rate, k_{FRET}. Although our analysis obtains k_{FRET} from the lifetime decay, it is used conservatively as the count-rate dependent shift in our detectors block accurate interpretation of k_{FRET}, but not of x_{FRET}. Hence, a change in detectors or a strategy to overcome this effect have the potential to resolve the oligomeric states of protein complexes (Supplementary Figure 15). Another synergy lies in the application of CRISPR Cas9 technology[47] to encode fluorescent proteins directly in the DNA, removing transfection stress and enabling studying the interaction at truly endogenous concentrations, while also being sensitive to protein translation regulation. Lastly, the analysis complexity can be reduced for homotypical interaction by measuring the reduction in fluorescence anisotropy due to homo-FRET (Supplementary Figure 16)[14,48].

Methods

Sample preparation

Plasmids and Stable cell line

For all measurements with transient transfections, a stable Hela cell line with knockout for CD95 was used (HeLa $CD95^{KO}$) generated using CRISPR/Cas9[49,50]. The sequences of CD86, CD95, CD95(ΔDD) and CTLA4 were fused C-terminally (intracellularly) via a linker to mEGFP (Donor only/D0) or mCherry in the pIRESpuro2 vector (Clontech)[50]. mCherry and mEGFP fused proteins were also available as bicistronic plasmid with a 2A peptide as linker between the two proteins[50] in order to ensure homogeneous co-expression. The stable cell line and all sequences were previously described in N.B., N.v.d.V., A.G., A.B., C.W., C.A.M.S., C.M. *manuscript in preparation*. Note, that HeLa cells naturally do not express CTLA4 or CD86 (Supplementary Table 4) as determined before[51,52].

Cell culture

Cells were maintained at 37 °C and in a 5% CO_2 humidified atmosphere in DMEM (Dulbecco's Modified Eagle Medium) + GlutaMAX™ (31966021, Gibco, Life Technologies Inc., Carlsbad, USA) containing 10% FBS (fetal bovine serum) (10500064, Gibco) and 1% penicillin/streptomycin (P/S) Solution (P0781, Sigma-Aldrich, Merck KGaA, Darmstadt, Germany).

Transfections and Sample Preparation

For live-cell CELFIS samples were prepared as follows:

Cells were trypsinated (T3924, Sigma-Aldrich) and replated in 8-well glass bottom slides (#80827, ibidi GmbH, Gräfelfing, Germany) with a density of 3-5 x 10^4 cells per well. Cells were transfected the day after using ViaFect™ Transfection Reagent (#E4981, Promega Corp., Madison, USA) following the manufacturer's protocol. The bicistronic and Donor only (D0) plasmids were transfected using varying amounts of target DNA to cover a wide range of expression levels: for a transfection in 2 wells, the combinations 25 ng target DNA + 975 ng empty vector, 100 ng target DNA + 900 ng empty vector, 250 ng target DNA + 750 ng empty vector as well as 1000 ng target DNA (no empty vector) were used. The empty vector helps to lower and control the expression levels by competing for transcription factors as it used the same promotor (cmv) as the target plasmids. FRET measurements were preformed 48-72 hours after transfection in imaging medium: Leibovitz's L-15 Medium (21083027, Gibco) without phenol red, supplemented with 10% FBS and 1% P/S (as before).

For signaling experiments, the CD95 Ligand (FasL, soluble (human) (recombinant) set, ALX-850-014-KI02, Enzo Life Sciences Inc., Loerrach, Germany) was used in a final concentration of 200 ng/ml + 100-fold Enhancer, diluted according to the manufacturers protocol. The Ligand was added to the cells on the microscope setup.

Data recording procedure

Live cells were mounted on the Abberior Expert Line setup and kept at 37 °C using an objective heater (microscope setups). A large concentration range was sampled by transfecting with 25, 100 or 250 ng/2 wells and selecting cells to cover the desired concentration level. Each day a donor only sample was recorded to serve as a reference, followed by multiple donor-acceptor samples. Data acquisition was highly accelerated by first manually selecting locations of interest and subsequently measuring those locations automatically using a home-written program that interfaces with the instrument control software Imspector using the python interface *specpy* (https://imspectordocs.readthedocs.io/en/latest/specpy.html, commit cbf00175, by A. Schönle, Max Planck Institute for Biopysical Chemistry, Göttingen and Abberior Instruments GmbH, Göttingen). The program is a major overhaul and extension of an original program used in[53]. In presence of a ligand, the home-written program was used to visit the same areas repeatedly, where

one round of recording 10 areas took 28.5 minutes. The focus of the microscope was kept stable on the cell bottom membrane over hours using the autofocus option. Statistics were improved by analyzing multiple cells per area. Images were recorded using Alternating Line Excitation (ALEX) with 485 nm excitation at 7.8 µW as prompt and 561 nm excitation at 7.5 µW as delay. Further data acquisition settings were an 80 µm x 80 µm image size, 100 nm pixel size, 100 µm pinhole corresponding to 1.25 Airy Units, 5 µs pixel integration time and 21 frames.

Generation of lifetime decays from live cell data

The photon stream was transformed into an (*x*, y, micro time) array where the first two dimensions correspond to the spatial coordinate and the last dimension contains the histogram of photon arrival times using 1024 bins with 32 ps/bin. Multiple frames were recorded and summed over to increase statistics. A lifetime decay was generated by integrating over a (x, y) mask as desired for the experiment. Masks were generated manually for each cell using the Freehand selection tool in imageJ[54]. Cell contact sites containing fluorescent signal from multiple cells were excluded. Additional masks containing only the bright or only the dark areas were subsequently generated automatically using self-written code.

FRET induced donor decay

FRET induced donor decays were fitted similar to the method described previously[12,14] with the difference that a tail fit was used without Instrument Response Function (IRF) convolution. The data was fitted from 1.92 ns at the IRF maximum up to 22.4 ns. The donor-only decay was fitted using two lifetimes,

$$f_{\mathrm{D|D}}^{(\mathrm{D0})}(t) = A_0\left(x_{\mathrm{D},1}e^{-t\,k_{\mathrm{D},1}} + \left(1-x_{\mathrm{D},1}\right)e^{-t\,k_{\mathrm{D},2}}\right) + bg_1 = A_0 f_{\mathrm{D|D}}^{(\mathrm{D0})'}(t) + bg_1. \quad (1)$$

The total amount of photons is used to constrain the fit and the normalized donor only decay $f_{D|D}^{(D0)'}$ can be accurately determined. The FRET induced donor decay was subsequently fitted assuming a donor only fraction and a FRET fraction,

$$f_{\mathrm{D|D}}^{(\mathrm{DA})}(t) = A_1\left((1-x_{\mathrm{FRET}})f_{\mathrm{D|D}}^{(\mathrm{D0})'}(t) + x_{\mathrm{FRET}}f_{\mathrm{D|D}}^{(\mathrm{D0})'}(t)e^{-t\,k_{\mathrm{FRET}}}\right) + bg_2, \quad (2)$$

$$f_{\mathrm{D|D}}^{(\mathrm{DA})}(t) = A_1 f_{\mathrm{D|D}}^{(\mathrm{D0})'}(t)\,\epsilon_{\mathrm{D}}(t) + bg_2, \quad (3)$$

where we substituted

$$\epsilon_{\mathrm{D}}(t) = x_{\mathrm{FRET}}e^{-t\,k_{\mathrm{FRET}}} + (1-x_{\mathrm{FRET}}). \quad (4)$$

As the normalized donor only decay is already known from the donor only fit and the amplitude is constrained by the total number of photons, only x_{FRET}, k_{FRET} and the background are free fit parameters, lending accuracy and robustness to the fit result. Data was fitted using the *optimize.curve_fit* function from the python *scipy* library version 1.7.3 using the Levenberg-Marquardt method.

Determining Surface Concentrations in Live Cells

To determine the fluorophore concentration in live cells, we obtain a calibration for the brightness of a single fluorophore using a titration series for EGFP (orb84840, Biorbyt Ltd, Cambridge, UK) and mCherry (TP790040, OriGene Technologies, Inc., Rockville, MD, USA) in DPBS (14190144, Gibco, Life Technologies Inc., Carlsbad, USA). First, the concentration was measured using an absorption spectrometer (Cary 4000 UV-Vis Spectrophotometer, Agilent Technologies, Inc., Santa Clara, CA, USA) and extinction coefficients of 55900 cm-1 M-1 and 72000 cm-1 M-1 for EGFP and mCherry, respectively. Subsequently,

the brightness per confocal volume was measured on the Abberior setup (methods: Microscope setup) at three different excitation powers for each sample. The variation of excitation powers is nessecary for a precise calibration in order to reduce a power-related bias due to triplet states and saturation effects. The brightness B [kHz/μW] was plotted against the concentration [μM] and fitted using a linear fit $b \cdot x$ (Supplementary Figure 3) resulting in the slopes $b_{\mathrm{D}} = 266.2$ kHz·μM^{-1}μW^{-1} or equivalent Hz·nM^{-1}μW^{-1} and $b_{\mathrm{A}} = 133.3$ Hz·nM^{-1}μW^{-1} for the donor D (EGFP) and acceptor A (mCherry), respectively.

In order to calculate a brightness per molecule, the confocal volume V was obtained from FCS (at identical pinhole settings) using Rhodamine 110 (Rh110, 83695, Sigma-Aldrich) as a calibration dye for excitation with 485 nm. The confocal volume was determined to be $V_{485} = 0.543$ fl by fitting a single diffusion time and triplet state while assuming $D_{\mathrm{Rh110}} = 470$ μm^2/s for the Rh110 diffusion constant at 25.8 °C lab room temperature[55-57]. The confocal volume at 561nm excitation was calculated based on V_{485} and the wavelength dependence of in all three dimensions. It results in:

$$V_{561} = 0.543\text{fl} \left(\frac{561\text{nm}}{485\text{nm}}\right)^3 = 0.840 \text{ fl.} \tag{5}$$

The size of the 561nm confocal volume was additionally confirmed by an FCS measurement of Rhodamine 101 (also Rh101 or Rhodamine 640 perchlorate, #06400, Exciton, Luxottica Group S.p.A., Lockbourne, Ohio, USA). The fit of a single diffusion time with triplet at a given confocal volume of 0.84 fl results in a diffusion constant $D_{\mathrm{Rh101}} = 431$ μm^2/s matching literature values for Rhodamine dyes of comparable structural size, for example Rhodamine 6G [55,57,58]. Supplementary Figure 5 shows the correlation curved for both Rhodamine dyes and Supplementary Table 2 shows the corresponding fitting parameters.

The molecular brightness can now be calculated as follows:

$$B_m = \frac{b}{NA \cdot V} \tag{6}$$

with the Avogadro constant NA, resulting in the molecular brightnesses $B_{\mathrm{m,\,D}} = 814$ Hz·molecule^{-1}μW^{-1} and $B_{m,A} = 264$ Hz·molecule^{-1}μW^{-1}. In order to validate the values, we calculated the expected ratio between $B_{\mathrm{m,\,A}}$ and $B_{\mathrm{m,\,D}}$ depending on the quantum yield of the fluorescent proteins and the setup detection efficiencies (Supplementary Note 1). The experimental ratio of $B_{\mathrm{m,\,A}}/B_{\mathrm{m,D}} = 0.324$ is confirmed by a theoretical value 0.34.

FCS studies on the same proteins used here performed in our group (N.B., N.v.d.V., A.G., A.B., C.W., C.A.M.S., C.M. *manuscript in preparation,* Supplementary Note 1 and Supplementary Figure 3) showed that while focusing the confocal volume strictly on the bottom cell membrane, there is still a fast diffusion component to be fitted. This diffusion was attributed to the presence of cytoplasmic mEGFP and mCherry, their presence confirmed by 3D confocal images of live cells (N.B., N.v.d.V., A.G., A.B., C.W., C.A.M.S., C.M. *manuscript in preparation,* Supplementary Figure 12). The analysis of >70 cells in this previous study resulted in a mean cytoplasmic fraction of $p_{\mathrm{cp}} = 38\%$ and $p_{\mathrm{mem}} = 62\%$ of the signal originating from the membrane (Supplementary Table 3). In these studies, care was taken to not bleach the fraction of proteins in the membrane before and during the FCS measurements.

Finally, the number of mEGFP and mCherry molecules per cell surface area – the average label surface concentration - was determined by:

$$\rho_{\mathrm{D}} = \frac{I_{\mathrm{cell,\,D|D}}\, p_{\mathrm{mem}}}{P_{485}\, A_{\mathrm{cell}}\, B_{\mathrm{m,D}}}\ ; \tag{7}$$

$$\rho_{\mathrm{A}} = \frac{I_{\mathrm{cell,\ A|A}}\, p_{\mathrm{mem}}}{P_{561}\, A_{\mathrm{cell}}\, B_{\mathrm{m,A}}}\,, \tag{8}$$

where $I_{\mathrm{cell,\ D|D}}$ and $I_{\mathrm{cell,A|A}}$ are the fluorescence intensities of the whole cell for the donor upon donor excitation and accepter upon acceptor excitation in Hertz, P_{485} and P_{561} are the excitation powers for the donor and acceptor lasers, respectively, and A_{cell} is the area of the respective cell. The area of the cell is determined from the images directly. Note that this the calculated surface concentration is the average per cell area, but a pixel-wise calculation would also be possible.

FRET Dependency on A:D ratio

In order to calculate the maximal possible FRET fraction $x_{\mathrm{FRET,max}}$, the fraction of FRET capable donors must be determined. For a purely dimeric sample, this is realized by calculating the probability of having a donor acceptor (DA) dimer and a donor donor (DD) dimer, whereas the abundance of acceptor acceptor (AA) dimers does not affect the outcome. The formation of the three possible dimer configurations (DD, DA, AA) follows a binomial probability with number of trials $n = 2$, depending on the initial probability p_{D} of a donor in the sample. This dimer probability depends on the expression ratio of acceptor to donor within the sample, e.g. if the ratio of donors to acceptors is 1:3, $p_{\mathrm{D}} = 25\%$ and $p_{\mathrm{A}} = 75\%$. The probability for a certain dimer configuration $p_{\mathrm{config}}(d|n,p)$ can be calculated with

$$P_{\mathrm{config}}(d|n,p_D) = \sum_{i=0}^{d} \binom{2}{i} {p_{\mathrm{D}}}^{i} (1-p_{\mathrm{D}})^{n-i}, \tag{9}$$

where d is the number of donors in the dimer.

For the FRET sensitized donor analysis, the fraction of donors able to FRET $x_{\mathrm{D,FRET}}$ (in DA dimers) compared to donors that are not able to FRET (in DD dimers) is relevant. This fraction equals the initial probability p_{A} of acceptors in the sample as it resembles the chance of one donor to find an acceptor as interaction partner. Analogous, the fraction of donors in DD dimers that cannot FRET $x_{\mathrm{D,noFRET}}$ is p_D:

$$x_{\mathrm{D,FRET}} = p_{\mathrm{A}}\,, \tag{10}$$

$$x_{\mathrm{D,noFRET}} = p_D. \tag{11}$$

Additionally, we must consider the fraction of matured acceptors in donor-acceptors dimers, $x_{\mathrm{A,mature}}$. Combined with $x_{\mathrm{FRET,AV}}$ from AV simulation, the overall max. FRET fraction results from

$$x_{\mathrm{FRET,max}} = x_{\mathrm{FRET,AV}} \cdot x_{\mathrm{D,FRET}} \cdot x_{\mathrm{A,mature}}. \tag{12}$$

AV Simulations

AV simulations were performed using the home-built program Olga[34]. To model a dimer in a membrane a plane was generated using a python script with two points 40 Å above the membrane surface and separated by 22 Å, following the geometry of the trimeric CD95 transmembrane domain described by[36]. The length of the linker was determined by adding up the flexible amino acids from the CD95 protein, the additional flexible linker and the flexible part of mEGFP. To additionally account for the flexible orientation of the death domain[59], 9 amino acids corresponding to a C-terminal N-terminal distance of 32 Å are added when

the death domain is present. All constructs had similar linker length between 46-53 amino acids, allowing the use of 51 amino acids to simulate all constructs. The contributions to the total linker length for each construct are found in Supplementary Table 4 in (N.B., N.v.d.V., A.G., A.B., C.W., C.A.M.S., C.M. *manuscript in preparation*). The result of the AV simulations is summarized in supplementary Figure 6.

Multiparameter Fluorescence Image Spectroscopy

Data analysis was performed as described previously [13].

Model for exponential convergence to steady state for single-cell traces (steady-state model)

A selection of single-cell traces was fitted according to a model where a system perturbed by ligand addition approaches a new steady-state (stable response). An additional time delay was allowed for:

$$oligomer\ fraction\ (t; A, t_{\text{offset}}, t_{\text{rise}}) = 0 \qquad \text{if } t < t_{\text{offset}} \tag{12}$$

$$oligomer\ fraction\ (t; A, t_{\text{offset}}, t_{\text{rise}}) = A\left(1 - e^{-\frac{t - t_{\text{offset}}}{t_{\text{rise}}}}\right) \qquad \text{if } t \geq t_{\text{offset}}. \tag{13}$$

A describes the amplitude of the response, t_{offset} the time before any response is registered and t_{rise} the rise time of the response.

Calculation of Weighted Lifetimes and Anisotropy

A description of anisotropy, g-factor, species- and fluorescence weighted lifetime τ_x and τ_f as well as a general introduction to fluorescence spectroscopy is given by Sisamakis et al.[60]. A good source describing magic angle decays is found in[61], Section 2.5.1.

Cell Segmentation in High and Low Brightness Areas

To segment cells in high and low brightness areas, two masks were generated per manual input mask using self-written software in the following steps. 1) the fluorescence image was smoothed using a gaussian filter with one-pixel sigma. 2) the fluorescent images were masked using the manual input mask. 3) the pixels values are sorted in a 1D array. 4) the cumulative sum is calculated. 5) the intensity at 50% cumulated sum is set as a threshold intensity. 6) All pixels with a lower intensity than the threshold are part of the low brightness mask whereas all pixels with a higher intensity become part of the high brightness mask. This approach ensures that both areas contain an equal number of photons which eliminated signal-to-noise effects in the resulting fluorescence decays.

CTLA4 K_{dimer} Model

The concentration dependent CTLA4 dimerization is fitted using:

$$x_{\text{dimer}}(K_{\text{dimer}}, c_0) = \frac{K_{\text{dimer}}}{4c_0}\left(1 + \frac{4[c_0]}{K_{\text{dimer}}} - \sqrt{1 + \frac{8\,[c_0]}{K_{\text{dimer}}}}\right). \tag{14}$$

Refer to Supplementary Note 6 for a derivation of this equation and explanation of the symbols.

Microscope setup: Abberior Expert Line

All measurements were performed on a custom Abberior Expert Line system as described before[53] (Abberior Instruments GmbH, Göttingen, Germany). The system is equipped with single-photon counting abilities (TCSPC) and a polarization-sensitive readout. Alternating line excitation was used to sequentially excite

the donor and acceptor fluorophores. mEGFP emission was filtered using ET 525/50 nm bandpass filters (Chroma Technology Corp., Below Falls, Vermont, USA) and mCherry using Brightline 615/20 filters (AHF analysentechnik AG, Tübingen, Germany). The instrument is operated using the customized Abberior microscope software Imspector (version 14.0.3060, Abberior Instruments GmbH). Cells were measured at 37 °C using a Heating Insert HP-LabTek (Pecon GmbH, Erbach, Germany) and an objective heater (Pecon GmbH).

Acknowledgement

This work was funded by the Deutsche Forschungsgemeinschaft (DFG, German Research Foundation) − project number 267205415-CRC 1208 (projects A08 and A12). We thank Joél Baudouin (formerly IBS, Grenoble) for providing plasmids and stable cell lines. In addition, C.M. is grateful for financial support by VolkswagenFoundation and Fonds der Chemischen Industrie.

Author Contributions

N.V. designed research under supervision of C.S. and C.M. N.B. and N.V. designed and performed the experiments and analyses. N.V. wrote the python code for automated data acquisition and analysis. N.B. established and prepared live cell samples. N.V and N.B. wrote the manuscript with the help of all authors. C.S. and C.M. initiated, supervised and coordinated the project.

All authors contributed to and approved the final version of the manuscript.

Declaration of interests

The authors declare no competing interests.

References

1 Fields, S. & Song, O.-k. A novel genetic system to detect protein–protein interactions. *Nature* **340**, 245-246, doi:10.1038/340245a0 (1989).

2 Collins, M. O. & Choudhary, J. S. Mapping multiprotein complexes by affinity purification and mass spectrometry. *Current Opinion in Biotechnology* **19**, 324-330, doi:https://doi.org/10.1016/j.copbio.2008.06.002 (2008).

3 Piehler, J. New methodologies for measuring protein interactions in vivo and in vitro. *Current Opinion in Structural Biology* **15**, 4-14, doi:https://doi.org/10.1016/j.sbi.2005.01.008 (2005).

4 Przytycka, T. M., Singh, M. & Slonim, D. K. Toward the dynamic interactome: it's about time. *Briefings in Bioinformatics* **11**, 15-29, doi:10.1093/bib/bbp057 (2010).

5 Stoneman, M. R. *et al.* A general method to quantify ligand-driven oligomerization from fluorescence-based images. *Nature Methods* **16**, 493-496, doi:10.1038/s41592-019-0408-9 (2019).

6 Pollok, B. A. & Heim, R. Using GFP in FRET-based applications. *Trends in cell biology* **9**, 57-60 (1999).

7 Clegg, R. M. in *Reviews in fluorescence 2006* 1-45 (Springer, 2006).

8 Kiyonaka, S. *et al.* Genetically encoded fluorescent thermosensors visualize subcellular thermoregulation in living cells. *Nature Methods* **10**, 1232-1238, doi:10.1038/nmeth.2690 (2013).

9 Esposito, A., Gralle, M., Dani, M. A. C., Lange, D. & Wouters, F. S. pHlameleons: A Family of FRET-Based Protein Sensors for Quantitative pH Imaging. *Biochemistry* **47**, 13115-13126, doi:10.1021/bi8009482 (2008).

10 Imamura, H. *et al.* Visualization of ATP levels inside single living cells with fluorescence resonance energy transfer-based genetically encoded indicators. *Proceedings of the National Academy of Sciences* **106**, 15651-15656, doi:doi:10.1073/pnas.0904764106 (2009).

11 Hochreiter, B., Pardo-Garcia, A. & Schmid, J. A. Fluorescent Proteins as Genetically Encoded FRET Biosensors in Life Sciences. *Sensors* **15**, 26281-26314 (2015).

12 Greife, A. *et al.* Structural assemblies of the di- and oligomeric G-protein coupled receptor TGR5 in live cells: an MFIS-FRET and integrative modelling study. *Scientific Reports* **6**, 36792, doi:10.1038/srep36792 (2016).

13 Weidtkamp-Peters, S. *et al.* Multiparameter fluorescence image spectroscopy to study molecular interactions. *Photochemical & Photobiological Sciences* **8**, 470-480, doi:10.1039/b903245m (2009).

14 Kravets, E. *et al.* Guanylate binding proteins directly attack Toxoplasma gondii via supramolecular complexes. *Elife* **5**, e11479, doi:10.7554/eLife.11479 (2016).

15 Chen, L., Novicky, L., Merzlyakov, M., Hristov, T. & Hristova, K. Measuring the energetics of membrane protein dimerization in mammalian membranes. *Journal of the American Chemical Society* **132**, 3628-3635 (2010).

16 Sarabipour, S., Del Piccolo, N. & Hristova, K. Characterization of membrane protein interactions in plasma membrane derived vesicles with quantitative imaging Forster resonance energy transfer. *Accounts of chemical research* **48**, 2262-2269 (2015).

17 King, C., Stoneman, M., Raicu, V. & Hristova, K. Fully quantified spectral imaging reveals in vivo membrane protein interactions. *Integrative Biology* **8**, 216-229 (2016).

18 Gülcüler Balta, G. S. *et al.* 3D Cellular Architecture Modulates Tyrosine Kinase Activity, Thereby Switching CD95-Mediated Apoptosis to Survival. *Cell Reports* **29**, 2295–2306, doi:10.1016/j.celrep.2019.10.054 (2019).

19 Peter, M. E. & Krammer, P. The CD95 (APO-1/Fas) DISC and beyond. *Cell Death & Differentiation* **10**, 26-35 (2003).

20 Lavrik, I. & Krammer, P. Regulation of CD95/Fas signaling at the DISC. *Cell Death & Differentiation* **19**, 36-41 (2012).

21 Martin-Villalba, A., Llorens-Bobadilla, E. & Wollny, D. CD95 in cancer: tool or target? *Trends in molecular medicine* **19**, 329-335 (2013).

22 Kreuz, S. *et al.* NFκB activation by Fas is mediated through FADD, caspase-8, and RIP and is inhibited by FLIP. *The Journal of cell biology* **166**, 369-380 (2004).

23 Bremer, E. Targeting of the tumor necrosis factor receptor superfamily for cancer immunotherapy. *ISRN Oncol* **2013**, 371854, doi:10.1155/2013/371854 (2013).

24 Collins, A. V. *et al.* The interaction properties of costimulatory molecules revisited. *Immunity* **17**, 201-210 (2002).

25 Gough, S. C., Walker, L. S. & Sansom, D. M. CTLA4 gene polymorphism and autoimmunity. *Immunological reviews* **204**, 102-115 (2005).

26 Hosseini, A., Gharibi, T., Marofi, F., Babaloo, Z. & Baradaran, B. CTLA-4: From mechanism to autoimmune therapy. *International Immunopharmacology* **80**, 106221 (2020).

27 Leach, D. R., Krummel, M. F. & Allison, J. P. Enhancement of antitumor immunity by CTLA-4 blockade. *Science* **271**, 1734-1736 (1996).

28 Du, X. *et al.* A reappraisal of CTLA-4 checkpoint blockade in cancer immunotherapy. *Cell research* **28**, 416-432 (2018).

29 Van Coillie, S., Wiernicki, B. & Xu, J. in *Regulation of Cancer Immune Checkpoints: Molecular and Cellular Mechanisms and Therapy* (ed Jie Xu) 7-32 (Springer Singapore, 2020).

30 Darlington, P. J., Kirchhof, M. G., Criado, G., Sondhi, J. & Madrenas, J. Hierarchical regulation of CTLA-4 dimer-based lattice formation and its biological relevance for T cell inactivation. *the Journal of Immunology* **175**, 996-1004 %@ 0022-1767 (2005).

31 Linsley, P. S. *et al.* Binding Stoichiometry of the Cytotoxic T Lymphocyte-associated Molecule-4 (CTLA-4): A DISULFIDE-LINKED HOMODIMER BINDS TWO CD86 MOLECULES (∗). *Journal of Biological Chemistry* **270**, 15417-15424 (1995).

32 Peulen, T.-O., Opanasyuk, O. & Seidel, C. A. Combining graphical and analytical methods with molecular simulations to analyze time-resolved FRET measurements of labeled macromolecules accurately. *The Journal of Physical Chemistry B* **121**, 8211-8241 (2017).

33 Zidovska, A. & Sackmann, E. Brownian motion of nucleated cell envelopes impedes adhesion. *Physical review letters* **96**, 048103 (2006).

34 Dimura, M. *et al.* Automated and optimally FRET-assisted structural modeling. *Nature Communications* **11**, 5394, doi:10.1038/s41467-020-19023-1 (2020).

35 Evers, T. H., van Dongen, E. M., Faesen, A. C., Meijer, E. & Merkx, M. Quantitative understanding of the energy transfer between fluorescent proteins connected via flexible peptide linkers. *Biochemistry* **45**, 13183-13192 (2006).

36 Fu, Q. S. *et al.* Structural Basis and Functional Role of Intramembrane Trimerization of the Fas/CD95 Death Receptor. *Molecular Cell* **61**, 602-613, doi:10.1016/j.molcel.2016.01.009 (2016).

37 Dunsing, V. *et al.* Optimal fluorescent protein tags for quantifying protein oligomerization in living cells. *Scientific reports* **8**, 1-12 (2018).

38 Ulbrich, M. H. & Isacoff, E. Y. Subunit counting in membrane-bound proteins. *Nature Methods* **4**, 319-321, doi:10.1038/Nmeth1024 (2007).

39 King, C., Sarabipour, S., Byrne, P., Leahy, D. J. & Hristova, K. The FRET signatures of noninteracting proteins in membranes: simulations and experiments. *Biophysical journal* **106**, 1309-1317 (2014).

40 Madsen, R. R. & Vanhaesebroeck, B. Cracking the context-specific PI3K signaling code. *Science Signaling* **13**, eaay2940 (2020).

41 He, J. *et al.* FRET biosensor-based kinase inhibitor screen for ERK and AKT activity reveals differential kinase dependencies for proliferation in TNBC cells. *Biochemical Pharmacology* **169**, 113640 (2019).

42 Wu, Z., Liao, Q. & Liu, B. A comprehensive review and evaluation of computational methods for identifying protein complexes from protein–protein interaction networks. *Briefings in bioinformatics* **21**, 1531-1548 (2020).

43 Greene, J. L. *et al.* Covalent dimerization of CD28/CTLA-4 and oligomerization of CD80/CD86 regulate T cell costimulatory interactions. *Journal of Biological Chemistry* **271**, 26762-26771 (1996).

44 Bhatia, S., Edidin, M., Almo, S. C. & Nathenson, S. G. Different cell surface oligomeric states of B7-1 and B7-2: implications for signaling. *Proceedings of the National Academy of Sciences* **102**, 15569-15574 %@ 10027-18424 (2005).

45 Fricke, F., Beaudouin, J., Eils, R. & Heilemann, M. One, two or three? Probing the stoichiometry of membrane proteins by single-molecule localization microscopy. *Scientific reports* **5**, 1-8 %@ 2045-2322 (2015).

46 Jago, C., Yates, J., Olsen Saraiva Câmara, N., Lechler, R. & Lombardi, G. Differential expression of CTLA-4 among T cell subsets. *Clinical & Experimental Immunology* **136**, 463-471 (2004).

47 Hsu, P. D., Lander, E. S. & Zhang, F. Development and applications of CRISPR-Cas9 for genome engineering. *Cell* **157**, 1262-1278 (2014).

48 Stahl, Y. *et al.* Moderation of Arabidopsis root stemness by CLAVATA1 and ARABIDOPSIS CRINKLY4 receptor kinase complexes. *Current Biology* **23**, 362-371 (2013).

49 Liesche, C. *et al.* Death receptor-based enrichment of Cas9-expressing cells. *Bmc Biotechnology* **16**, 17, doi:10.1186/s12896-016-0250-4 (2016).

50 Liesche, C. *et al.* CD95 receptor activation by ligand-induced trimerization is independent of its partial pre-ligand assembly. *bioRxiv*, 293530, doi:10.1101/293530 (2018).

51 Fricke, F., Beaudouin, J., Eils, R. & Heilemann, M. One, two or three? Probing the stoichiometry of membrane proteins by single-molecule localization microscopy. *Scientific Reports* **5**, 14072, doi:10.1038/srep14072 (2015).

52 Uhlén, M. *et al.* Tissue-based map of the human proteome. *Science* **347**, 1260419, doi:doi:10.1126/science.1260419 (2015).

53 Budde, J.-H. *et al.* FRET nanoscopy enables seamless imaging of molecular assemblies with sub-nanometer resolution. *arXiv*, 2108.00024 (2021).

54 Schneider, C. A., Rasband, W. S. & Eliceiri, K. W. NIH Image to ImageJ: 25 years of image analysis. *Nature Methods* **9**, 671-675, doi:10.1038/nmeth.2089 (2012).

55 Gendron, P. O., Avaltroni, F. & Wilkinson, K. J. Diffusion Coefficients of Several Rhodamine Derivatives as Determined by Pulsed Field Gradient-Nuclear Magnetic Resonance and Fluorescence Correlation Spectroscopy. *Journal of Fluorescence* **18**, 1093-1101, doi:10.1007/s10895-008-0357-7 (2008).

56 Weast, R. C. L., D. R. *CRC handbook of Chemistry and Physics*. 65 edn, (CRC Press, 1984).

57 Kapusta, P. Absolute diffusion coefficients: compilation of reference data for FCS calibration. *PicoQuant GmbH* **1**, 1-2 (2010).

58 Majer, G. & Melchior, J. P. Characterization of the fluorescence correlation spectroscopy (FCS) standard Rhodamine 6G and calibration of its diffusion coefficient in aqueous solutions. *Journal of Chemical Physics* **140**, doi:10.1063/1.4867096 (2014).

59 Scott, F. L. *et al.* The Fas-FADD death domain complex structure unravels signalling by receptor clustering. *Nature* **457**, 1019-1022, doi:10.1038/nature07606 (2009).

60 Sisamakis, E., Valeri, A., Kalinin, S., Rothwell, P. J. & Seidel, C. A. in *Methods in enzymology* Vol. 475 455-514 (Elsevier, 2010).

61 Lakowicz, J. R. *Principles of fluorescence spectroscopy*. third edition edn, (Springer, 2010).

Supplementary Information

Quantifying the Spatio-temporal Evolution of Protein Interactions using Cell Lifetime FRET Image Spectroscopy (CELFIS)

Authors:

Nicolaas T M van der Voort[1, †], Nina Bartels[2, †], Cornelia Monzel[2], Claus A M Seidel[1]

† contributed equally

* corresponding author:

1. Molecular Physical Chemistry, Heinrich-Heine University, 40225 Düsseldorf

2. Experimental Medical Physics, Heinrich-Heine University, 40225 Düsseldorf

Contents

Supplementary Notes

Supplementary Note 1: Brightness relation of mEGFP and mCherry

To confirm the experimentally determined values for the brightness of one fluorescent molecule of mEGFP and mCherry, we derived the theoretical ratio of the brightnesses using the relative extinction coefficients ϵ, quantum yields Φ and detection efficiencies g:

$$\frac{B_{\mathrm{m,A}}}{B_{\mathrm{m,D}}} = \frac{\epsilon_A}{\epsilon_D}\frac{\Phi_A}{\Phi_D}\frac{g_A}{g_D} \qquad (S1)$$

where the detection efficiency of the measurement setup was calculated using the homebuilt program *detection efficiencies* and other values obtained from literature[1,2]. Yielding:

$$\frac{B_{\mathrm{m,A}}}{B_{\mathrm{m,D}}} = \frac{1}{1.38}\frac{72000\ \mathrm{M^{-1}cm^{-1}}}{55900\ \mathrm{M^{-1}cm^{-1}}}\frac{0.22}{0.60} = 0.34. \qquad (S2)$$

Supplementary Note 2: Advantages of using AV simulation to predict $x_{\mathrm{FRET,max}}$

In previous publications[3,4] calibration of the maximum FRET fraction for a complete dimer was done using a donor-linker-acceptor construct of varying linker lengths. A perfect calibration sample should mimic the sample under investigation in having similar anchor points, linker lengths and geometry in which they are free to move. It is clear that donor-linker-acceptor constructs fulfill these conditions only approximately, as they are soluble and do not account for the position of the anchor points. Although a direct comparison has not been made to our knowledge, it is clear that significant deviations between a donor-linker-acceptor controls and a theoretical perfect control are to be expected based on studying systematic changes in the linker length[4].

By contrast, AV simulation can incorporate the geometry of the molecular environment. I.e., a plane was used to mimic the cell membrane resulting in Accessible Volumes resembling half-spheres. To provide a realistic representation, the anchoring positions were based on the crystal structure of the transmembrane domains of trimeric CD95 (structure id: 2NA7[5]). Importantly, the reliability of the result relies on the correct prediction of the expected linker extension distribution, which was thoroughly investigated by[6]. Furthermore, we are in the advantageous position of verifying our result from AV simulation against the CTLA4 protein, which, similar to CD95, is labelled on the intracellular side of the transmembrane domain. From the concentration dependency of CTLA4 and after including proximity FRET in our calculations, we are able to obtain the FRET fraction corresponding to a pure dimer sample, yielding 32.6 % x_{FRET}, corresponding closely to the 29% predicted by AV simulations in consideration of the donor: acceptor ratio.

Note that we used an average linker length of 51 amino acid for all linkers. This value can be used globally as the maximum linker length deviation of ± 5 amino acids (equal to 1.8 nm) results to a maximal error of ± 1% in $x_{\mathrm{FRET,AV}}$. This is lower than the uncertainty in linker flexibility and thus acceptable. Further, no molecular structure of the CTLA4 transmembrane and intracellular domain (amino acid sequence 162-200, last 23 amino acids truncated in our plasmid) is available at the time of writing. While the precise displacement of the anchor point is therefore unknown, it is reasonable to assume that they are in close proximity and the molecular surrounding is similarly well approximated using a half-sphere. This illustrates that even in absence of a molecular structure, AV simulations can yield reliable estimates, here based on the comparable CD95 anchor points and estimated linker lengths.

Supplementary Note 3: maximum FRET fraction in case of trimers

To calculate the maximum FRET fraction in case of trimers, $x_{\mathrm{FRET,max,trimer}}$, we list the abundance of trimer species and weight them according to their donor fluorescence, $p(F_D)$. For simplicity, we will consider non-fluorescent donors and non-fluorescent acceptors as the same category:

$$p_0 = p_{\mathrm{A}}\left(1 - p_{\mathrm{mature,A}}\right) + p_{\mathrm{D}}\left(1 - p_{\mathrm{mature,D}}\right). \quad (S3)$$

Similarly, we define the mature fractions of donor and acceptor as

$$p_{\mathrm{A,on}} = p_{\mathrm{A}} p_{\mathrm{mature,A}}, \quad (S4)$$

$$p_{\mathrm{D,on}} = p_D p_{\mathrm{mature,D}}. \quad (S5)$$

Supplementary Figure 8 provides a graphical representation of the different species, illustrating their combinatorial degeneracy, weighting by donor fluorescence and final probability. As before, the probability for FRET to occur when a single acceptor is present is obtained from AV simulations:

$$p(FRET|1A, \geq 1D) = x_{\mathrm{FRET,AV}}. \quad (S6)$$

When two acceptors are present, both acceptors move independently, such that FRET may occur if one of the two or both acceptors are within the FRET range. We simplify this calculation by considering that the chance for FRET to occur is 1 minus the chance that FRET does not occur, the latter only happens when both acceptors are outside of the FRET range, i.e.:

$$p(FRET|2A, F_{\mathrm{D}}) = 1 - p(noFRET|2A, F_{\mathrm{D}}), \quad (S7)$$

$$p(FRET|2A, F_{\mathrm{D}}) = 1 - (1 - x_{\mathrm{FRET.AV}})^2. \quad (S8)$$

Note that the probability for a donor to FRET is independent of the presence of other donors in the trimer. Using the definitions illustrated in Supplementary Figure XX, we arrive at our final expression:

$$x_{\mathrm{FRET,max,trimer}} = p(FRET|2A)p(2A|F_{\mathrm{D}}) + p(FRET|1A)p(1A|F_{\mathrm{D}}). \quad (S9)$$

Using the values from the main text for CD95, $p_{\mathrm{A}} = 0.71$, $p_{\mathrm{D}} = 0.29$, $p_{\mathrm{mature,A}} = 0.8$, $p_{\mathrm{mature,D}} = 0.8$, consequently $p_{\mathrm{A,on}} = 0.64$, $p_{\mathrm{D,on}} = 0.16$, $p_0 = 0.2$, with $x_{\mathrm{FRET.AV}} = 0.462$, this yields $x_{\mathrm{FRET,max,trimer}} = 0.46$.

Supplementary Note 4: Proximity FRET correction

At high expression levels, the molecular environment becomes crowded with acceptor molecules, causing FRET to occur due to proximity even if no specific interaction is present, obscuring the interpretation of the FRET signal. This effect is especially pronounced for membrane systems as a 2D surface can be more readily crowded. To study binding kinetics of membrane proteins at higher concentrations as is the case for CTLA4, it is therefore vital to correct for proximity FRET. A theoretical model to calculate proximity FRET quantitatively was published in 1979 by Wolber and Hudson[7] and was developed further and experimentally verified in the lab of K. Hristova[3,8,9]. The model depends on a single concentration parameter c_{prox}, describing the acceptor concentration at which proximity FRET is responsible for 63% FRET Efficiency. Note that the donor concentration does not contribute as homo-FRET between proximal donors does not affect lifetime measurements. A quantitative theoretical model calibrated on Widefield microscopy data was published in the group of K. Hristova[8]. Here, we present two new strategies to determine c_{prox} and compare against the theoretical model. Firstly, the proteins CD86, CD95 and a truncated variant CD95(ΔDD) are monomeric at low concentrations (N.B., N.v.d.V., A.G., A.B., C.W., C.A.M.S., C.M. *manuscript in preparation*) and their x_{FRET} dependency on concentration can be reliably modelled using monomers in

presence of proximity FRET, yielding c_{prox} to be $2.35 \pm 0.10 \cdot 10^4$, $2.34 \pm 0.07 \cdot 10^4$ and $3.14 \pm 0.15 \cdot 10^4$ receptors/µm² for CD86, CD95(ΔDD)and CD95, respectively, errors obtained from least-squared fit. Advantageously, this method works like an internal control which is robust and does not rely on any calibration factors. However, small deviations may occur if the control does not remain purely monomeric at very high concentrations. Secondly, we fit our CTLA4 data with a homo-dimerization model (see methods). The high quality of our data enables us to add a proximity contribution to the homo-dimerization fit, yielding a c_{prox} of $5.2 \pm 0.6 \cdot 10^4$ receptors/µm², errors obtained from least squared fit. Note that for this calculation the acceptor concentration was used to determine the proximity FRET distribution whereas the total concentration was used to determine the homo-dimerization constant K_{dimer}. This method is advantageous as it requires no further experimental data and can be used here as the data quality is high and no covariance between K_{dimer} and c_{prox} exists. Thirdly, we apply the WHH model applying our Förster radius of 52 Å and an exclusion radius corresponding to the long side of the EGFP beta barrel of EGFP of 30 Å, yielding c_{prox} to be $1.36 \cdot 10^4$ receptors/µm², no error estimate was included in the theoretical model. This method can be applied under any condition, but is less robust as it does not rely on experimental validation from within the same dataset.

In this study, receptor densities for the CTLA4 data up to 7'000 receptors/µm² were reliably corrected for proximity FRET and shown to match the dimerization model without excess features being visible in the residuals. Although often lethal to cells, for some applications it is worthwhile to increase the receptor concentration even further. To ascertain the theoretical upper limit for which proximity FRET can still be corrected, we take c_{prox} as the upper limit at which FRET can still be corrected, yielding ~25'000 receptors/µm² based on the CD95 corrections.

Overall, experimental approaches show excellent agreement and highlight that our CD86, CD95(ΔDD) and CD95 constructs are well suited to correct for proximity affects at high molecular densities in membranes. The theoretical prediction is lower than the theoretical result, but still shows good agreement considering that the former was calibrated on Widefield systems whereas the latter is based on confocal systems. A particular difference is lack of optical sectioning in Widefield systems creating a difficulty in estimating the membrane surface area that is contributing to the signal. By contrast, a confocal has optical sectioning and the area from which light is collected is accurately determined here using FCS.

Supplementary Note 5: Proximity FRET derivation

The first model for proximity FRET correction was generated by Wolber and Hudson based on theory and simulations[7]. It contained two exponential saturation terms

$$E_{\mathrm{prox,WH}}\left(x_1, c_{\mathrm{prox,E,1}}, c_{\mathrm{prox,E,2}} \middle| c_A\right) = 1 - x_1 e^{\frac{-c_{\mathrm{A}}}{c_{\mathrm{prox,E,1}}}} - (1 - x_1) e^{\frac{-c_{\mathrm{A}}}{c_{\mathrm{prox,E,2}}}}, \qquad (S10)$$

where c_{A} is the concentration of acceptors, $x_1$and $(1 - x_1)$ are the fraction of the exponentials, $c_{\mathrm{prox,E,1}}$ and $c_{\mathrm{prox,E,2}}$ are the characteristic acceptor concentrations for that species at which proximity FRET is responsible for 63% FRET Efficiency. The model can be approximated with a linear slope at low concentrations and saturates at higher concentrations. Later experimental work simplified the expression to a single exponential saturation term as the addition of a second term did not improve the fitting models[8].

$$E_{\mathrm{prox}}\left(c_{\mathrm{prox,E}} \middle| c_A\right) = 1 - e^{-\frac{c_{\mathrm{A}}}{c_{\mathrm{prox,E}}}} \qquad (S11)$$

FRET-sensitized donor decay analysis measures x_{FRET} and k_{FRET}, whereas previous models predicted FRET Efficiencies. They are related as follows:

$$E = x_{\mathrm{FRET}} \frac{k_{\mathrm{FRET}}}{k_{\mathrm{FRET}} + k_0}, \tag{S12}$$

where k_0 is the sum of decay rates in absence of FRET. From this relation it is clear that the proximity contribution to x_{FRET} is described by exponential saturation with a different weighting factor,

$$x_{\mathrm{FRET,prox}}(c_{\mathrm{prox}}|c_A) = 1 - e^{\frac{c_{\mathrm{A}}}{c_{\mathrm{prox}}}}. \tag{S13}$$

Note that this model has only a single fitting parameter and can hence be robustly determined. The corrected x_{FRET} can be straightforwardly determined using

$$x_{\mathrm{FRET,corr}} = x_{\mathrm{FRET}} - x_{\mathrm{FRET,prox}}. \tag{S14}$$

Alternatively, the proximity contribution can be directly included in the homo-dimerization fit model. For known pairs of acceptor and total concentrations, c_{A} and c_0 respectively, we write

$$x_{\mathrm{FRET}}(x_{\mathrm{FRET,max}}, K_{\mathrm{dimer}}, c_{\mathrm{prox}}|c_A, c_0) = x_{\mathrm{FRET,max}}\, x_{\mathrm{dimer}}(K_{\mathrm{dimer}}, c_0) + x_{\mathrm{FRET,p}}(c_{\mathrm{A}}, c_{\mathrm{prox}}), \tag{S15}$$

where x_{dimer} is described in Supplementary Note 6. This function is fitted to the CTLA4 data to obtain $x_{\mathrm{FRET,max}}$, K_{dimer} and c_0. Furthermore, we implemented a theoretical model using the formula and coefficients from equation 9 from[8]. As is clear from Supplementary Equation S12, x_{FRET} is always larger than E, hence the concentration at which 63% x_{FRET} occurs, c_{prox}, must be lower than its equivalent for Efficiency, $c_{\mathrm{prox,E}}$.

Supplementary Note 6: Derivation of homo-dimerization

We derive the fraction of homo-dimers from first principle for the reaction

$$[A_2] \rightleftharpoons [A] + [A], \tag{S16}$$

where $[A]$ and $[\mathrm{A}_2]$ are the concentration of monomers and homodimers of protein A respectively. Using the mass action law

$$K_{\mathrm{dimer}} = \frac{[A]^2}{[A_2]}, \tag{S17}$$

and assuming a total amount of proteins

$$c_0 = [A] + 2[A_2], \tag{S18}$$

we define the fraction of proteins that are part of a dimer

$$x_{\mathrm{dimer}}(K_{\mathrm{dimer}}, c_0) = \frac{2[A_2]}{c_0} \tag{S19}$$

and solve for $[A]$ and $[A_2]$ for given c_0, K_{dimer} to obtain

$$x_{\mathrm{dimer}}(K_{\mathrm{dimer}}, c_0) = \frac{K_{\mathrm{dimer}}}{4c_0}\left(1 + \frac{4c_0}{K_{\mathrm{dimer}}} \pm \sqrt{1 + \frac{8\,c_0}{K_{\mathrm{dimer}}}}\right), \tag{S20}$$

where the negative symbol in front of the root produces a physical result. The expression behaves similar to the commonly known Langmuir equation.

Supplementary Tables

parameter name	description	exemplary value, unit
data input		
ptu file	file containing the lifetime data	PQSpcm_2022-03-17_12-42-23area_0x_-4.299y_-8.368.ptu
mask	tiff file having non-zero values at pixels where photons have to be collected.	Mask2.tif
D0 G decay	magic angle lifetime decay generated in the same manner from a donor-only probe.	*lifetime decay of ntacs values*
Image reading parameters for whole dataset		
chan$_{P/S}$ G/R/Y	detection channel for parallel/perpendicular signal. coming from donor emission upon donor excitation (G), acceptor emission upon donor excitation (R) and acceptor emission upon acceptor excitation (Y).	chan$_P$ G = 2 chan$_S$ G = 0 chan$_P$ R = 3 chan$_S$ R = 1 chan$_P$ Y = 3 chan$_S$ Y = 1
linesteps G/R/Y	linesteps used for collecting a channel when operating in ALEX mode. 1 indicates line usage, whereas 0 indicated that the line is skipped.	line-step G = [1, 0] line-step R = [1, 0] line-step Y = [0, 1]
microtime G/R/Y	portion of the lifetime decay to be used when operating in PIE mode. Optional when operating in ALEX mode.	microtime G = [0 – 511] microtime R = [0 - 511] microtime Y = [512 - 1023] unit: tac channels
dwell time	pixel dwell time	5 µs
ntacs	number of tac channels in TAC decay. Usually the number of tac channels generated by the hardware exceeds the precision needed for the instrument. Hence it is down sampled to the number given here.	ntacs = 1024 tac channels
PS shift	A shift may occur between the parallel and perpendicular decays. The channels are shifted digitally to compensate.	PS shift = 5 tac channels
g-factor G/R/Y	ratio of detection efficiency for parallel channel relative to perpendicular channel. Usually determined using a small dye in solution calibration, e.g. Rhodamine 110.	g-factor G = 1.13 g-factor R = 1.22 g-factor Y = 1.22
fitrange	The range of tac channels to be fitted	fitrange = [55,700] tac channels
Experiment parameters		
molecular brightness, B D/A	Molecular brightness per molecule per µW excitation power. See methods for determination	B_D = 814 Hz/(molecule·µW) B_A = 264 Hz/(molecule·µW)
cell phenotype	short classification of the cell phenotype as judged by eye.	cell phenotype = dead
excitation power D/A	Power of the relevant excitation laser. Used to correct the brightness for day-to-day laser power fluctuations.	excitation power D = 6.7 µW excitation power A = 8.6 µW
time of ligand addition	time when an event occurred, for example ligand addition	2022-03-23_09-47-13 UTC±0
cell id	unique identifier of cell, useful when the same cell is measured repeatedly	2022-03-23 Batch 1 Area 4 Mask 2

batch id	unique identifier for data acquisition run	2022-03-23 Batch 1
p_{mem}	the probability that the protein is in the membrane, a correction factor to calculate the receptor concentration on the membrane. See Supplementary Table 3.	p_{mem}= 0.62
Intermediate results		
lifetime decay$_{P/S}$ G/R/Y	Lifetime decay consisting of ntacs tac channels for parallel, perpendicular.	*six lifetime decay of ntacs values*
magic angle decay G/R/Y	By combining parallel and perpendicular channels (see methods), a decay can be constructed that has no polarization effects.	*three lifetime decay of ntacs values*
anisotropy decay G/R/Y	The anisotropy decay is constructed from the parallel and perpendicular decays (see methods), which can be used for homo-FRET studies.	*three lifetime decay of ntacs values. All values between -0.2 and 0.4.*
intensity$_{P/S}$ G/R/Y	sum of pixels	intensity$_P$ G = 183448 counts intensity$_S$ G = 71712 counts intensity$_P$ R = 39085 counts intensity$_S$ R = 17650 counts intensity$_P$ Y = 168140 counts intensity$_S$ Y = 70861 counts
surface area G/R/Y	The area of non-zero values within the mask area. For samples studied here the surface area is typically equal for all channels.	surface area = 44091 surface area R = 43847 surface area Y = 40937
timestamp	time of data recorded obtained from the file name	2022-03-17_12-42-23
fit outputs		
D0 $\tau_{1/2}$	lifetimes from two-lifetime donor only fit for fitting EGFP decay.	D0 τ_1 = 2.05 ns D0 τ_2 = 3.17 ns
D0 $x_{1/2}$	fractions from two-lifetime donor only fit reported in total counts.	D0 x_1 = 52097 counts D0 x_2 = 19397 counts
D0 τ_x/τ_f	species-weighted and fluorescence weighted lifetimes of the donor-only decay, see methods.	D0 τ_x = 2.320 ns D0 τ_f = 2.417 ns
x_{FRET} or $x_{FRET1/2}$	Fraction of molecules showing FRET. For future robustness, a model with two species for describing the FRET decay is also implemented, in which case two fractions are reported.	x_{FRET} = 0.037
k_{FRET} or $k_{FRET1/2}$	average decay rate of molecules showing FRET. As above, two rates are reported if the two-species FRET decay model is used.	k_{FRET} = 0.69 ns^{-1}
Image analysis outputs		
surface/volume concentration Donor/Acceptor	concentration of fluorescent proteins per unit area in case of membrane bound proteins or per unit volume in case of soluble proteins.	donor surface concentration = 56 molecules/µm² Acceptor surface concentration = 113 molecules/µm²
ratio A to D	ratio of acceptor to donor molecules	ratio A to D = 2.5:1
total concentration	sum of donor and acceptor concentrations	total concentration = 169
time since ligand addition	the difference between the timestamp and the reference time.	time since ligand addition = 112 min

Supplementary Table 1: Description of parameters used in the analysis software

For accompanying flowchart and abbreviations, see Supplementary Figure 2.

Fit parameter	Rhodamine 110 485 nm excitation	Rhodamine 101 561 nm excitation
D [µm²/s]	470	431 ± 10
ρ (amplitude)	0.12550 ± 0.00076	0.12240 ± 0.00085
τ_{Diff} [µs]	29.12 ± 0.65	52.9 ± 3.3
T (triplet fraction)	0.1167 ± 0.0094	0.123 ± 0.026
τ_{Trip} [µs]	6.40 ± 0.84	20.0 ± 5.1
κ	7.60 ± 0.31	5.50 ± 0.49
N	9.00 ± 0.11	9.30 ± 0.37
$V_{confocal}$ [fl]	0.543 ± 0.011	**0.84**

Supplementary Table 2: FCS fit results for calibrations with Rh110 and Rh101.

Rhodamine 110 and 101 were used in order to determine the confocal volume under FRET measurement conditions. Both curves were fitted with a single diffusion time and triplet (Supplementary Figure 5). For Rhodamine 110 the diffusion constant was used as input value according to literature[10], for Rh101 the theoretically determined confocal volume was used as input parameter to determine D (methods, 'Determining Surface Concentrations in Live Cells').

Sample	Statistics [cells]	Membrane fraction	Cytoplasmic fraction
$CD86_{DO}$	9	0.589 ± 0.085	0.411 ± 0.085
$CD86_{DO}$	6	0.628 ± 0.052	0.372 ± 0.052
$CTLA4_{DA}$	10	0.703 ± 0.036	0.297 ± 0.036
$CD95_{D0}$	11	0.594 ± 0.045	0.406 ± 0.045
$CD95(\Delta DD)_{D0}$	12	0.598 ± 0.052	0.402 ± 0.052
$CD95_{D0}$ + Lig	11	0.597 ± 0.043	0.403 ± 0.043
$CD95(\Delta DD)_{D0}$ + Lig	14	0.637 ± 0.030	0.363 ± 0.030
Total	73	0.621 ± 0.062	0.379 ± 0.062

Supplementary Table 3: Membrane and cytoplasmic fraction of cell fluorescence signal determined with FCS

Fractions of fast cytoplasmic and slow membrane diffusion for different membrane proteins measured with FCS. Table reproduced from FCS studies performed previously in our group (Supplementary Table 1 in N.B., N.v.d.V., A.G., A.B., C.W., C.A.M.S., C.M. *manuscript in preparation*) which showed that there is a

fast diffusion component to be fitted in addition to the slow membrane component, even while focusing strictly on the bottom membrane due to the extent of the confocal volume.

Gene name	Alternative name	nTPM in HeLa cell line	URL
CD28		0.0	https://www.proteinatlas.org/ENSG00000178562-CD28/cell+line
CD80		0.0	https://www.proteinatlas.org/ENSG00000121594-CD80/cell+line
CD86		0.0	https://www.proteinatlas.org/ENSG00000114013-CD86/cell+line
CTLA4	CD152	0.0	https://www.proteinatlas.org/ENSG00000163599-CTLA4/cell+line
Fas	CD95	5.2	https://www.proteinatlas.org/ENSG00000026103-FAS/cell+line

Supplementary Table 4: Expression of various CD (Cluster of Differentiation) genes in Hela cells.

The Human Protein Atlas (HPA) quantifies the expression of proteins in the human genome, specified for tissues and cell lines. In the HPA an nTPM (normalized transcript per million) value of 1.0 is defined as a threshold for expression of the corresponding protein. Hela cells solely express one CD used in this study: CD95. They do not express CTLA4 or CD86 nor their natural interaction partners CD28 and CD80. Thus, we do not have to account for the endogenous expression of any of these CDs except for CD95 in our oligomerization studies. This is why we use a Hela CD95 knock out cell line for all experiments. Data available from v21.1.proteinatlas.org[11].

Supplementary Figures

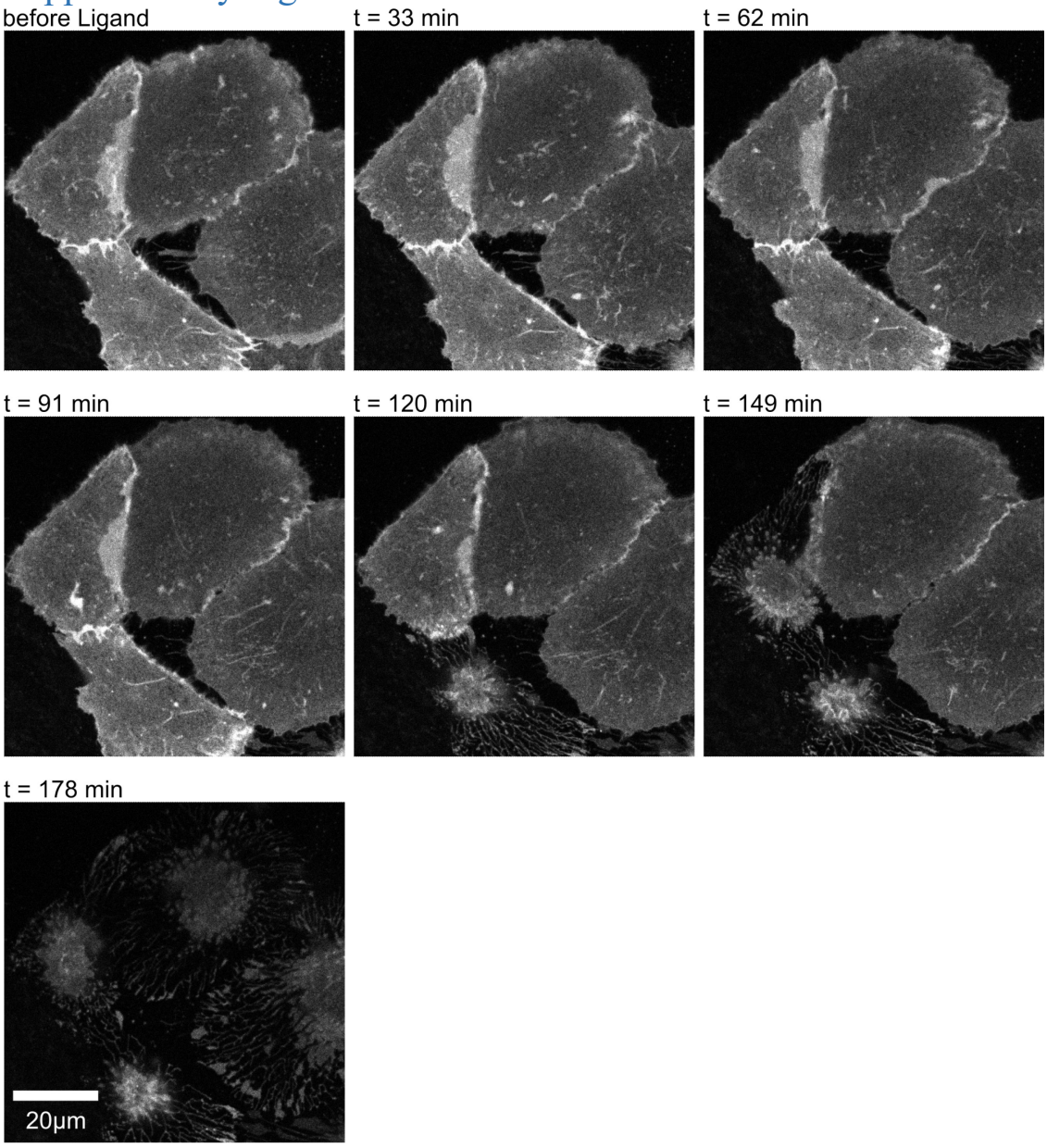

Supplementary Figure 1: Example FRET timelapse image data

Hela $CD95^{KO}$ transfected with the bicistronic plasmid CD95-mCherry-T2A-CD95-mEGFP. Confocal timelapse images were recorded during FRET measurements, all images of the time series included until cell death. The series show a consistent morphology and no movement of the cell up to the prominent shrinking effect of cell apoptosis. Images show the mEGFP channel.

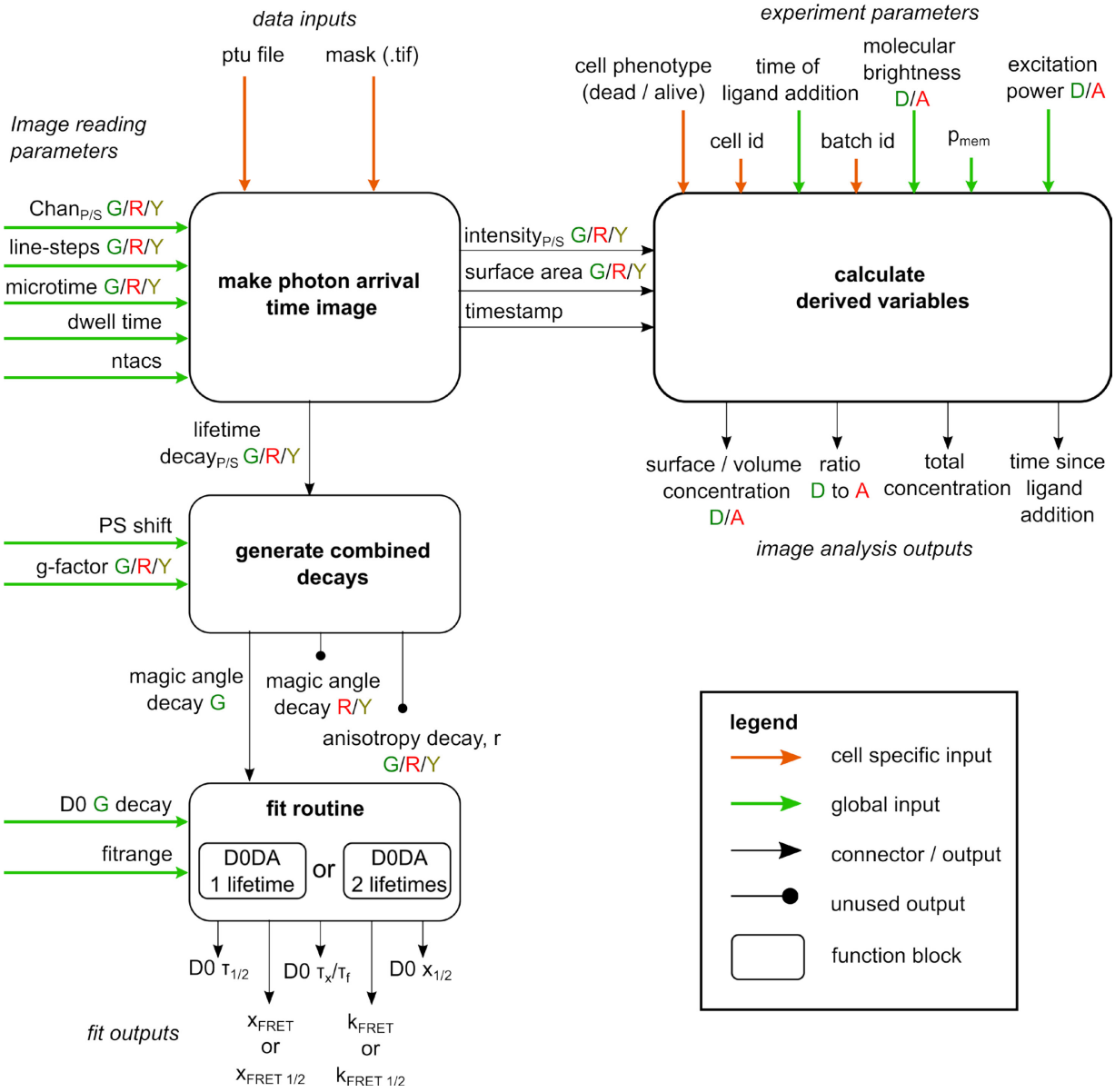

Supplementary Figure 2: Functional flowchart for CELFIS analysis software.

Detailed description of all fit parameters is found in Supplementary Table 1. Green (G) is shorthand for donor emission upon donor excitation, Red (R) for acceptor emission upon donor excitation and Yellow (Y) for acceptor emission upon acceptor excitation. Similarly, D is shorthand for the donor channel and A for the acceptor channel. Setting global inputs requires a one-time effort of ~20 minutes, while being typically constant over multiple days, only changing after instrument realignment. Time of Ligand addition and Donor only decay are exceptions that must be set per experiment and per measurement day respectively. Cell specific inputs must be set for each datapoint, where all ptu files are typically organized in a single folder and the cell id and batch id can be deduced from the file name or folder structure, requiring little time to setup. Most time is spent setting the cell phenotype and mask, which requires ~10 minutes per experiment. Although currently the latter two settings are set manually, they may be automated in the future using pattern recognition or counterstaining.

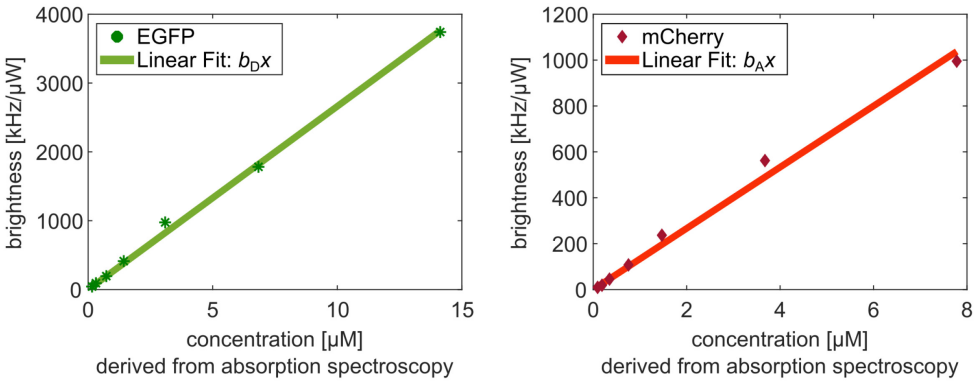

Supplementary Figure 3: Brightness calibration measurements.

Brightness vs. concentration calibration curves of fluorescent proteins EGFP (left) and mCherry (right) in solution. The concentration of the dilution series was measured with absorption spectroscopy (Supplementary Figure 4) while the brightness was obtained from confocal microscopy under the imaging conditions of the FRET measurements. The brightness of each dilution step was measured at three different laser powers. All data points were used for the linear fit $b \cdot x$, graphs show the mean of the three data points per sample. The fit results are shown given in the methods, section 'Determining Surface Concentrations in Live Cells'.

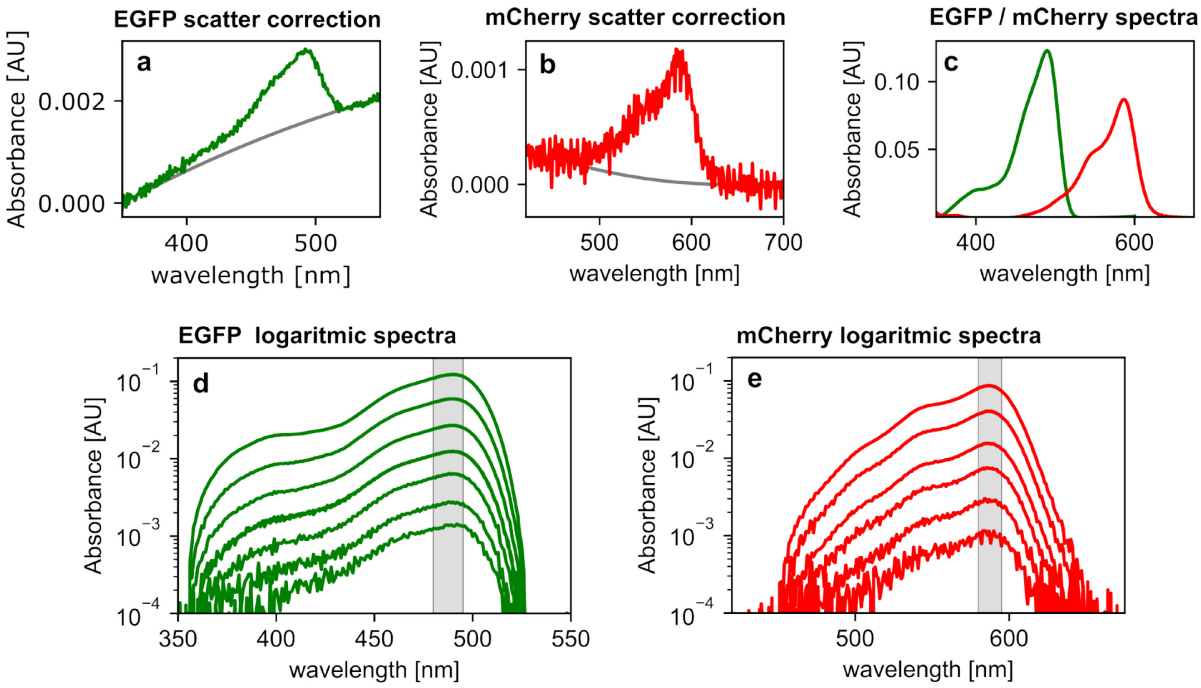

Supplementary Figure 4: Accurate concentration determination from absorption spectra.
a) Raw 0.16 µM EGFP spectra is affected by scatter which cannot be corrected for using a blank. Background signal is fitted outside the absorption peak from 350 – 360 nm and 520 – 600 nm with a parabolic function. The scatter contribution is subtracted to yield the corrected absorption curve. **b)** Same as in a) for 0.093 µM mCherry concentration using 350 – 450 nm and 620 – 700 nm for background fitting. **c)** Familiar linear representation of 14.1 µM EGFP and 7.8µM mCherry absorption spectra. d) Logarithmic representation of all corrected EGFP and **e)** mCherry spectra. Concentrations were determined by Lambert-Beer's law using the average absorption in the grey shaded area.

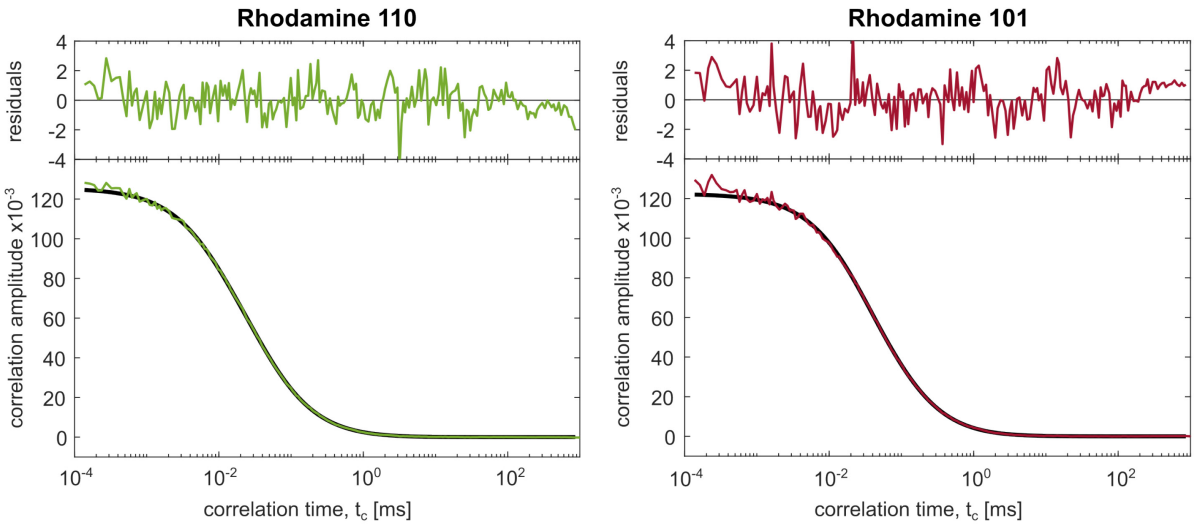

Supplementary Figure 5: FCS confocal volume calibration curves.

Rhodamine 110 and 101 were used in order to determine the confocal volume under FRET measurement conditions. The correlation curve of Rhodamine 110 excited with 485 nm was fitted using a single diffusion time plus triplet. The diffusion constant D_{110} was fixed to 470 µm²/s according to literature values [10,12] in order to determine the confocal volume precisely, resulting in $V_{485} = 0.543 \pm 11$ fl. Rhodamine 101 correlation excited at 561 nm was then fitted with the same model and the theoretically determined confocal volume of 0.84 fl (methods). The fit found a diffusion constant of $D_{110} = 431 \pm 10\ \mu m^2/s$, the reduced value matching the slightly larger size of Rhodamine 101 and literature values for comparable Rhodamines [10,13,14]. Supplementary Table 2 shows the fitting parameters of both fits.

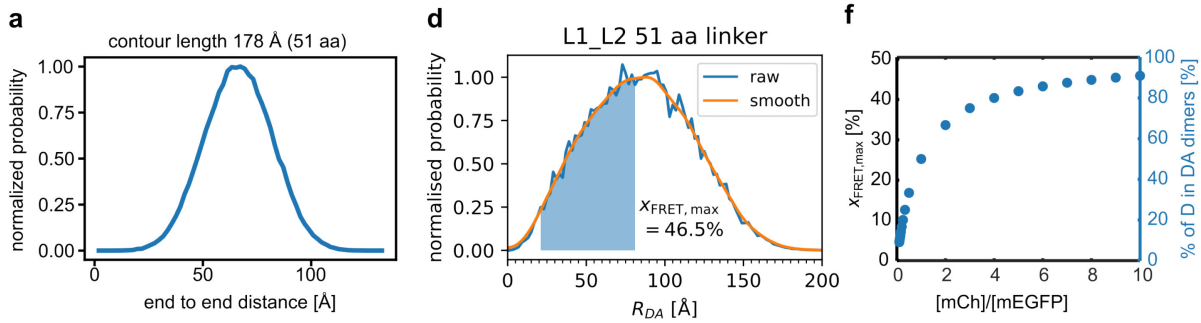

e

Dimer configuration	A:D ratio 1:1 p_D=0.50			A:D ratio 3:1 p_D=0.25		
	P_{config}	x_D	$x_{FRET,AV}$	P_{config}	x_D	$x_{FRET,AV}$
DD	0.25	0.50	0	0.06	0.25	0
AD	0.50	0.50	0.398	0.38	0.75	0.398
AA	0.25	0	0	0.56	0	0
Total $x_{FRET,max}$	x_D*$x_{FRET,AV}$ = 0.20			x_D*$x_{FRET,AV}$ = 0.30		

Supplementary Figure 6: AV simulations are used to obtain $x_{FRET,max}$.

Fluorescent proteins are linked via a flexible peptide chain with a total length of 51 amino acids (aa) or 178 Å contour length, 16 aa are part of the protein, 23 aa are cloned in for additional flexibility and 12 are part of the fluorescent protein. Linker lengths were very similar for mEGFP and mCherry and CD95 and CTLA4 samples. **a)** End-to-end distances are much shorter than the fully extended linker, graph based on data published in Greife et al.[15]. **b)** Top view and **c)** side view for the resulting accessible volume (AV) cloud. Only the AV cloud for the donor dye is shown. **d)** Donor-acceptor distance distribution, noise originates from limited sampling density. FRET Efficiencies lower than 6% are considered no FRET, corresponding to a distance of 82 Å for a Förster radius of 52 Å. Distances lower than 20 Å are also not considered as the donor is immediately quenched and hence is not detected. The area under the curve within the FRET range is used to predict the maximum x_{FRET} obtainable for a CTLA4 or CD95 dimer. **e)** Different ratios of donor D and acceptor A lead to different fractions of the possible dimer configurations: DD, DA and AA following binomial distributions. For the A:D ratios 1:1 and 3:1 the table shows the probability P_{config} for each configuration. x_D gives the fraction of donors D in the respective configuration and $x_{FRET,AV}$ the maximal possible FRET fraction resulting from AV simulations of a DA dimer. The bottom row shows the resulting $x_{FRET,max}$. **f)** Graph shows $x_{FRET,max}$ of the total donor signal depending on the A:D ratio [mCherry]/[mEGFP].

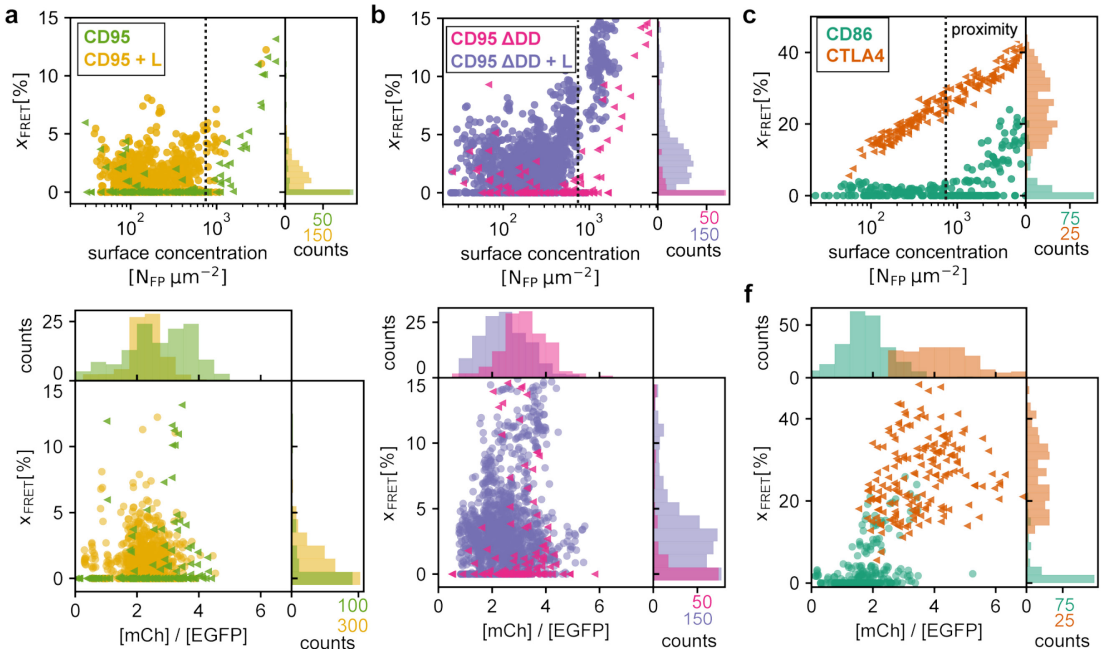

Supplementary Figure 7: Cellular FRET data.

a-c) x_{FRET} as a function of total receptor concentration for all variants. CD86 acts as a monomer control and shows increasing x_{FRET} for receptor densities higher than 1000/µm² (dashed line). The same pattern is found for all variants consistent with proximity FRET. **d-f)** x_{FRET} plotted against the concentration ratio of mCherry and EGFP with corresponding histograms.

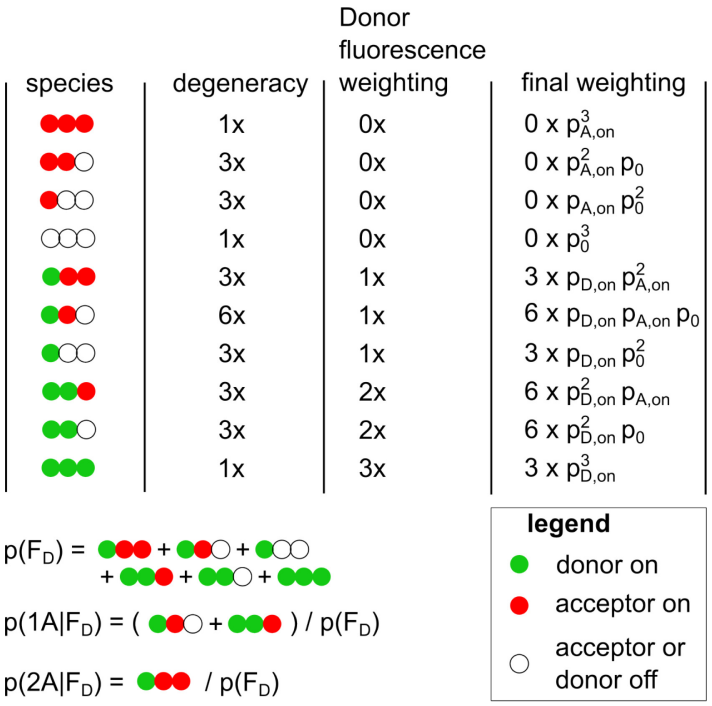

Supplementary Figure 8: trimeric Fluorescence Species:
A graphical representation of the different trimer configurations and their probabilities. The species are needed to calculate the maximum FRET fraction for a pure trimer species in Supplementary Note 3.

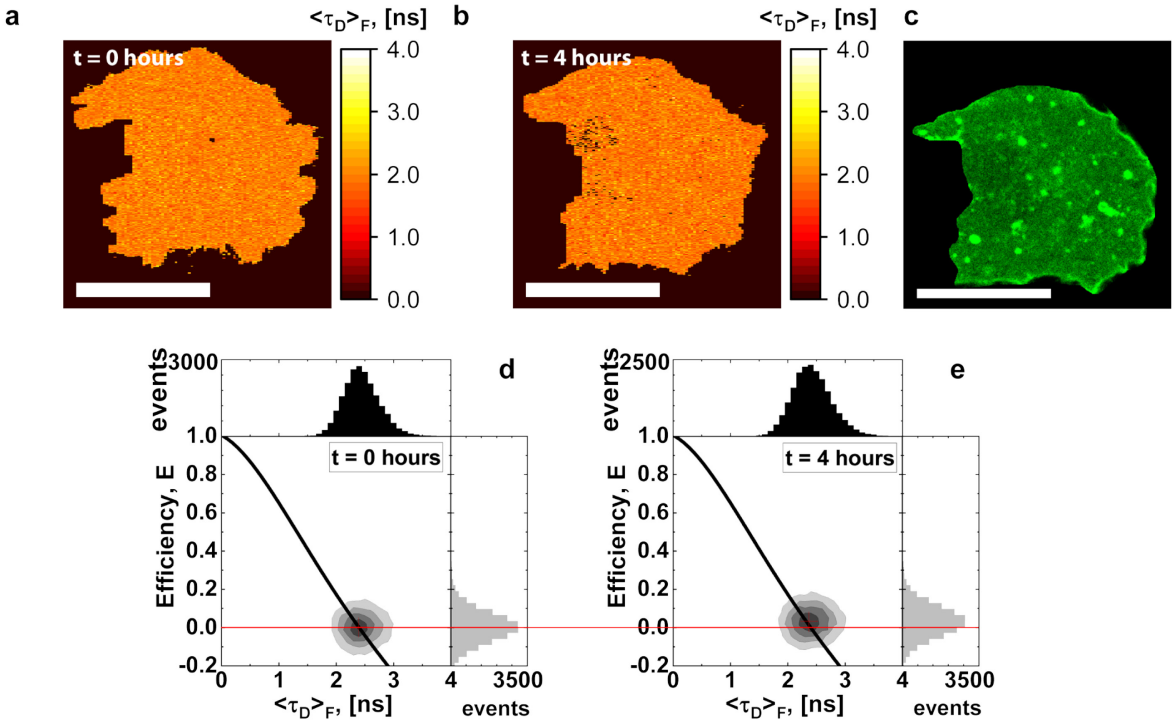

Supplementary Figure 9: MFIS shows homogeneous FRET in the cell membrane in the noise limit.

a) Donor lifetime image of the same CD95(ΔDD) cell shown in in Figure 3C top-right before ligand incubation and **b)** 4 hours after ligand incubation. Hints of correlation between cell organelle and lifetime can be seen, but a clear interpretation cannot be supported. Scale bar 20 µm. Data was binned 4 times in x to improve signal-to-noise. c) fluorescence image of the cell at 4 hours showing the bright and dim areas of the cell. **d,e)** Efficiency vs donor lifetime or the data shown in a,b). The horizontal red line guides the eye to show the very small increase in FRET Efficiency from no ligand (E = 0.00) to 4 hours after ligand incubation (E = 0.03), corresponding to an oligomer fraction of 10% from FRET-sensitized donor decay analysis. Data was recorded in PIE imaging mode and analyzed using home-built programs AnI and Margarita[16]. Correction parameters: relative detection efficiencies, $g_D/g_A = 1.01$, direct excitation,$\beta = 0.074$, donor quantum yield, $\Phi_{F,D} = 0.60$, acceptor quantum yield, $\Phi_{F,A} = 0.32$, crosstalk, $\alpha = 0.054$, backgrounds, $B_{G|G} = 0.5$ kHz, $B_{G|R} = 0.35$ kHz, $B_{R|R} = 0.25$ kHz.

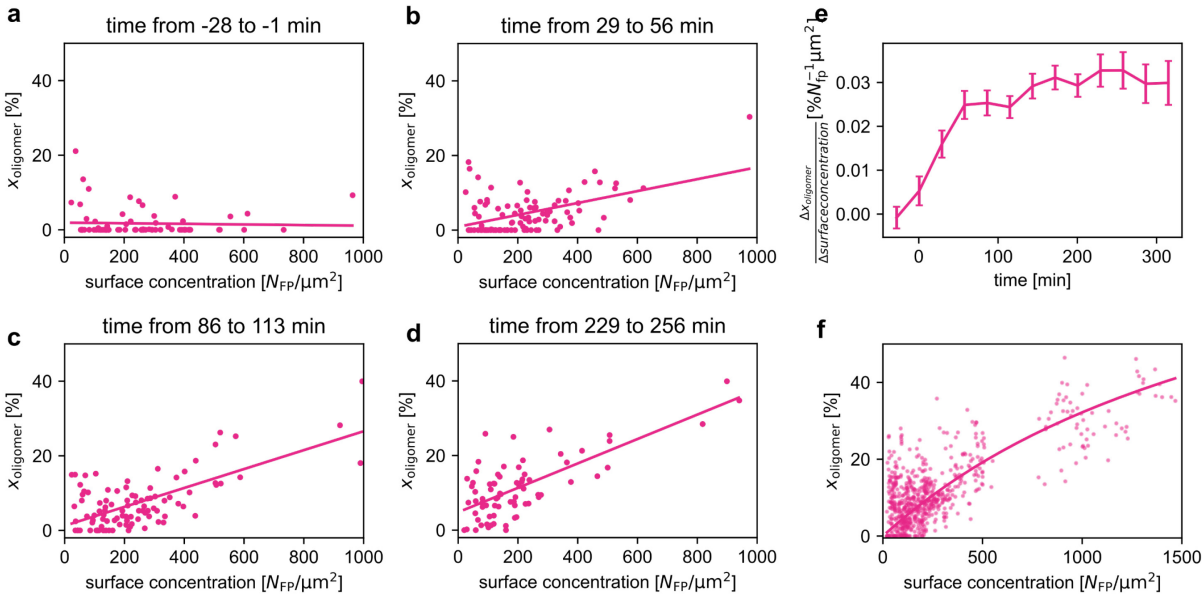

Supplementary Figure 10: Dissociation constant of CD95(ΔDD) in presence of ligand.
Data was corrected for proximity FRET and shown as oligomer fraction using $x_{\mathrm{FRET,max}}$. **a-d)** The oligomer fraction depends on the total receptor surface concentration. Measurements are grouped per time period where each cell was measured once and four exemplary time periods are shown. A simple linear fit is applied to obtain the initial characteristics. **e)** The slope and error from the linear fit is shown for each measurement round. Letters refer to the plots shown in a-d. As the graph indicates that the ensemble reached a steady-state after 120 minutes, all measurements taken after this time period (grey area) are used to determine K_{d}. **f)** CD95(ΔDD) live-cell data collected between 120 and 320 minutes after 200 ng/ml Ligand addition are fitted to the Langmuir equation to obtain a K_{dimer} of $2.10 \cdot 10^3 \pm 0.05 \cdot 10^3 N_{\mathrm{FP}}/\mu\mathrm{m}^2$.

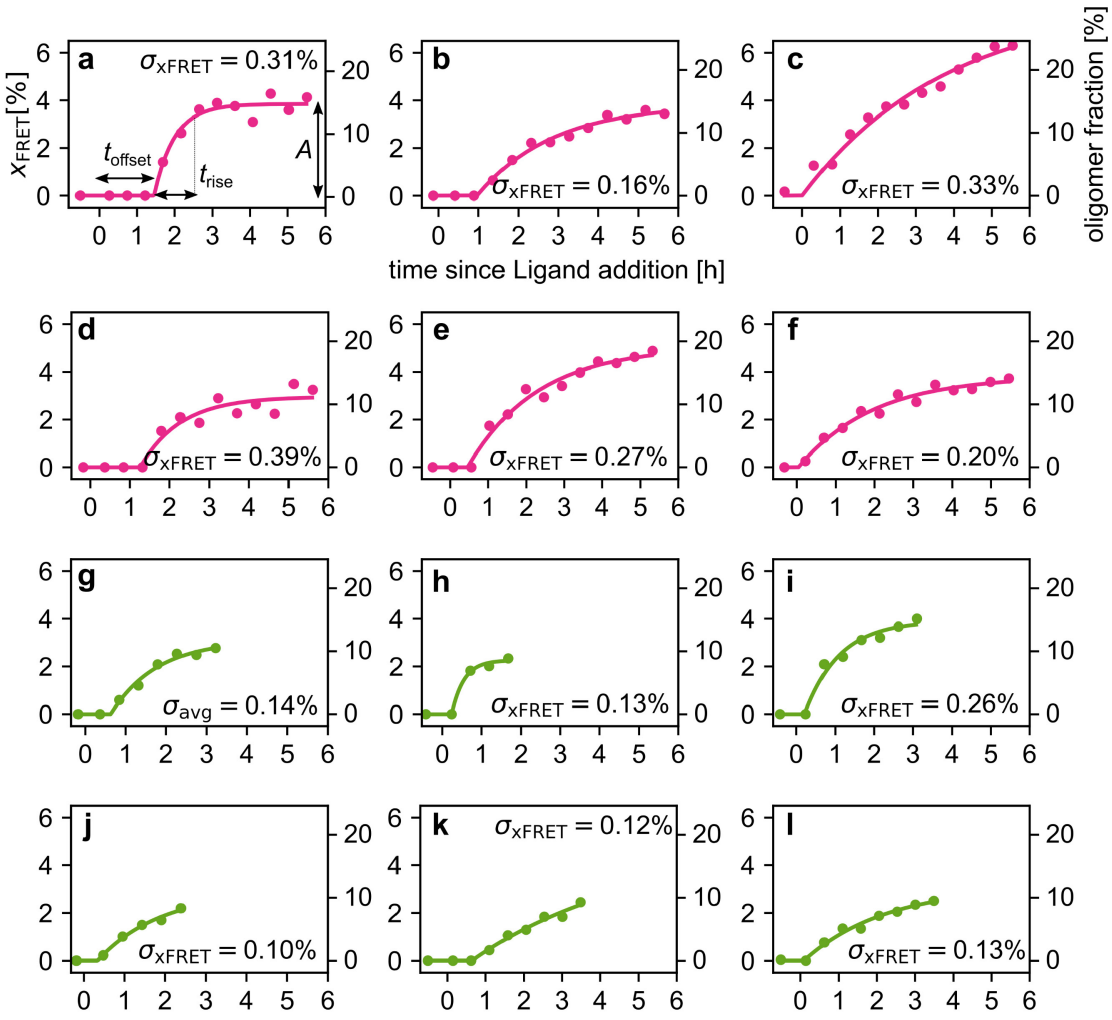

Supplementary Figure 11: Selected cells show time-dependent exponential convergence of the oligomer fraction to new steady state.

Time evolution is fitted according to the exponential convergence to a new steady state (methods). **a)** axes labels are valid for all panels. Fitting parameters are illustrated. **a-f)** Apoptosis incompetent CD95(ΔDD) sample. **g-l)** Apoptosis competent CD95 sample undergoes apoptosis after 2-3 hours. The fit residuals are corrected for the number of fit parameters to obtain the standard deviation of the measurement, σ_{xFRET}, for each cell.

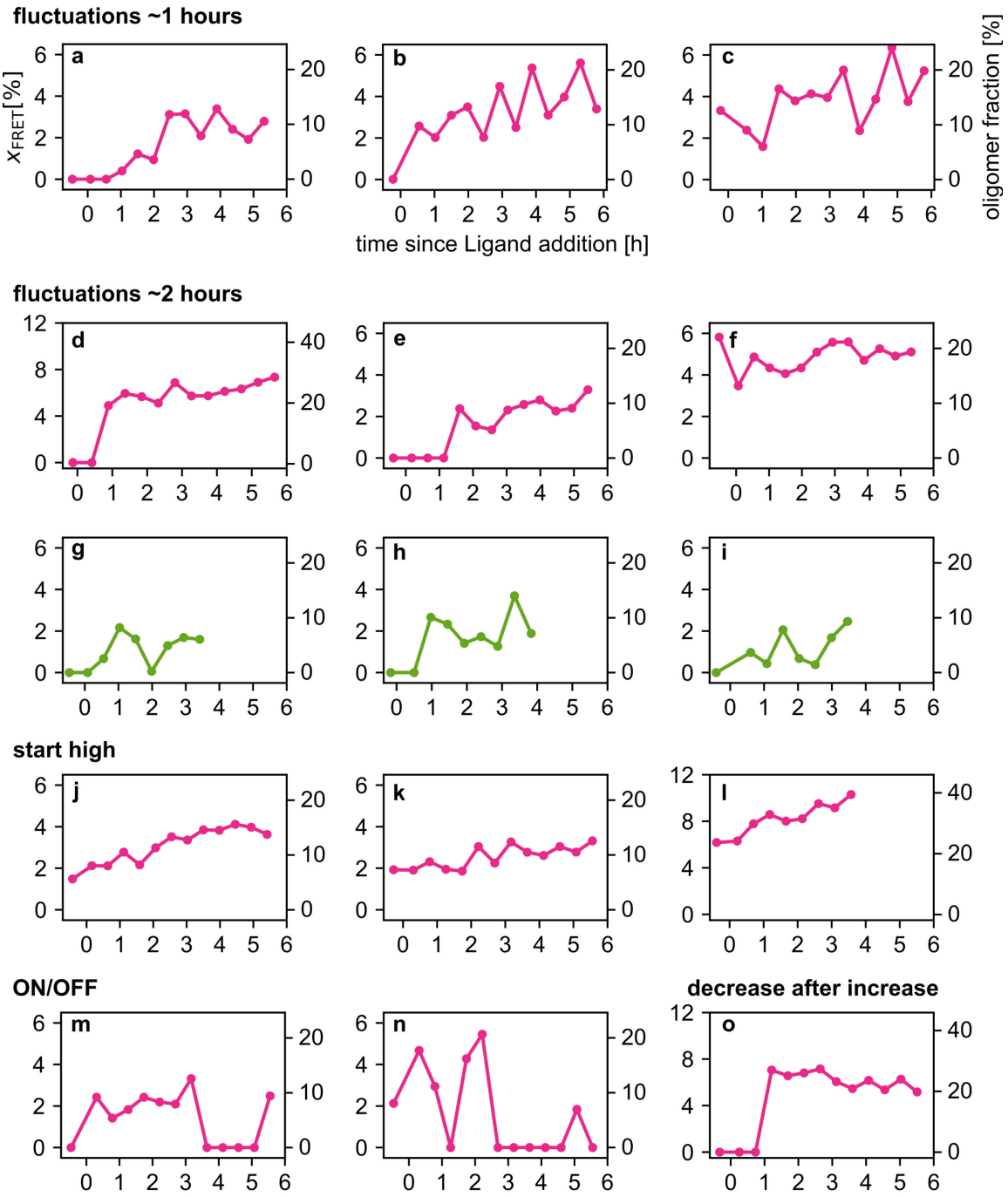

Supplementary Figure 12: Time evolution of oligomer fraction show variety in cellular response.

Exemplary cells show a variety of cellular responses to ligand stimulation. a-c) The oligomer fraction oscillates on the ~1 hour timescale after 120 minutes for equilibration. d-i) Oligomer fraction shows an oscillation on a ~2 hour timescale in addition to an overall increase. a,e) Oligomerization is delayed by a certain time. j-l) Before ligand addition the oligomer fraction is nonzero and ligand addition still increases the overall oligomer fraction. This was primarily observed for CD95(ΔDD) traces at high expression levels. m,n) After ligand addition initially triggered oligomerization, the oligomerization process is reversed

showing extended periods of absence of oligomers. Potentially this is an extreme case of the oscillations observed in a-i. o) After an initial rapid increase, the oligomer fraction slowly decreases again. Traces color code is the same as in Figure 3. Note that the majority of traces come from CD95(ΔDD) transfected cells as the truncation of the death domain prevented apoptosis and enabled longer measurement times.

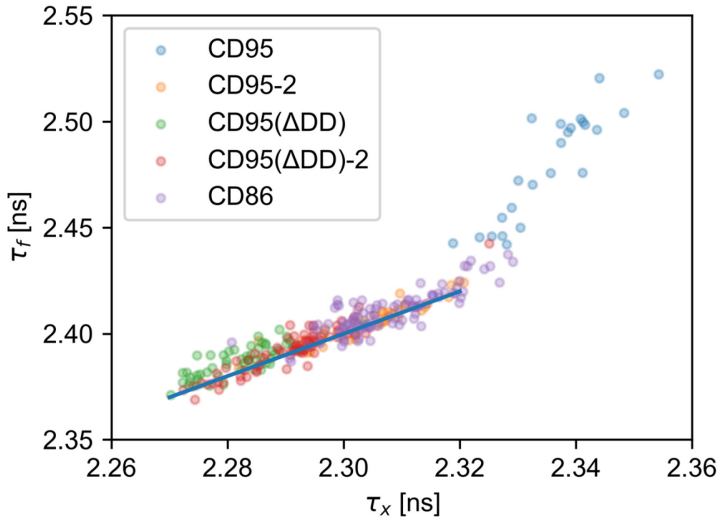

Supplementary Figure 13: Donor only lifetimes.

The species weighted average lifetime (τ_x) versus the fluorescence weighted average lifetime (τ_f) is shown. Five different control measurements recorded on five different days are shown. A selection criterion for receptor surface concentrations between 150 and 1000 receptors/µm² was applied to avoid noisy controls on one hand and controls affected by proximity-induced homo-FRET on the other hand. Center and standard deviation for τ_x of each population is 2.335 ± 0.008 ns, 2.304 ± 0.009 ns, 2.282 ± 0.007 ns, 2.290 ± 0.008 ns and 2.307 ± 0.009 ns for CD95, CD95-2, CD95(ΔDD), CD95(ΔDD) and CD86 donor only controls respectively, yielding a standard error of 0.36% within a control measurement and 0.79% between control measurements. Interestingly, we identify a population of constant τ_x/τ_f (blue line), indicating a change in lifetime but not in species fraction. An increased lifetime is consistent with a drop in the dielectric constant due to e.g. an increase in medium temperature. As such, these fluctuations are the consequence of minor temperature fluctuations between measurement days and within a calibration sample. In addition, the population located away from the blue line from mostly CD95 samples indicates a change in species fraction, consistent with a change in the preferred fluorescent state of EGFP.

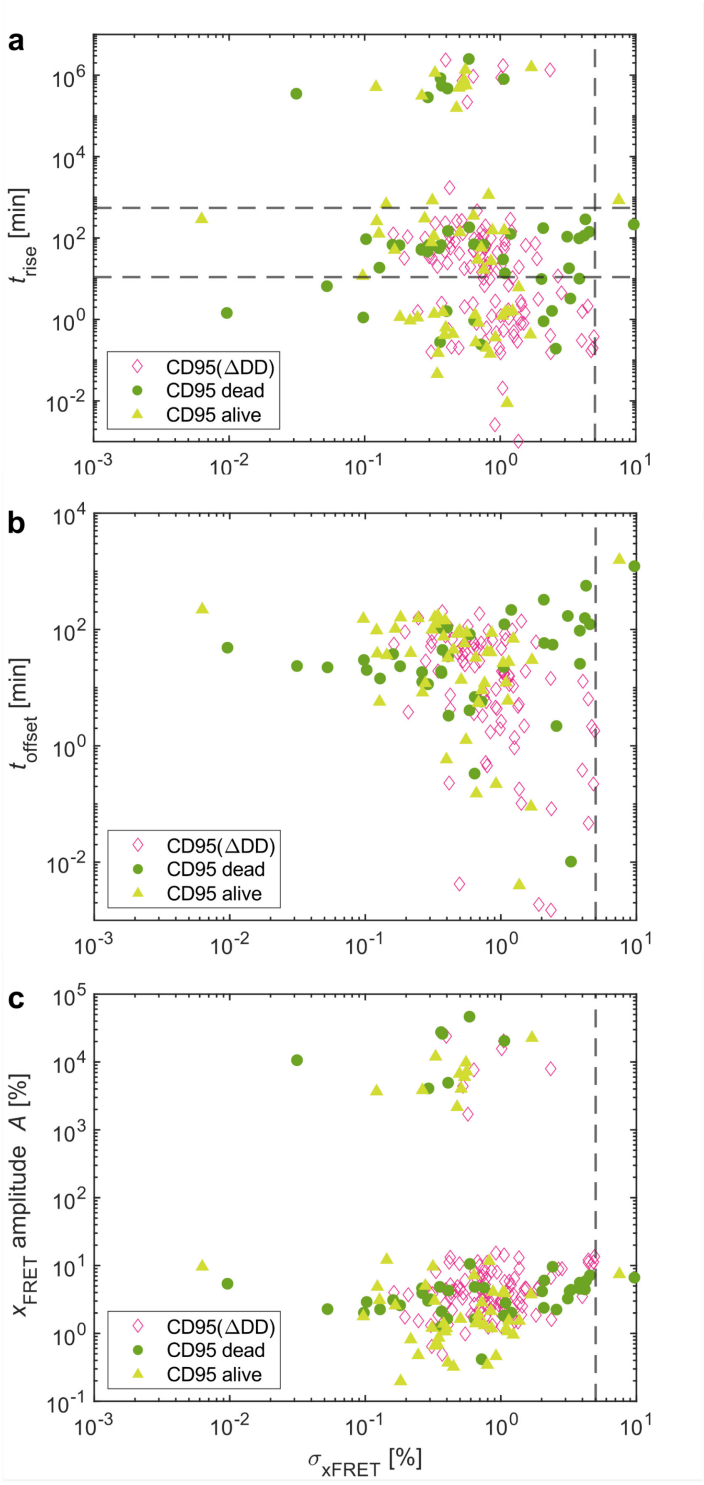

Supplementary Figure 14: Illustration of fitted parameters of the oligomer time evolution.
Oligomer time evolution of Hela CD95^{KO} cells expressing CD95(ΔDD) and CD95 were fitted according to the exponential convergence to a new steady state (methods). Fitting parameters are illustrated in Supplementary Figure 11a. The rise time t_{rise} (**a**), the offset time t_{offset} (**b**) and the x_{FRET} amplitude A plotted vs. the standard deviation of the measurement, σ_{xFRET}, for each cell. Dashed lines indicate the (min and

max) parameter value used for the trace classification (methods). For A, the x_{FRET} amplitude is shown but can be converted into the oligomer fraction amplitude by multiplication with the factor 3.6 for CD95 samples.

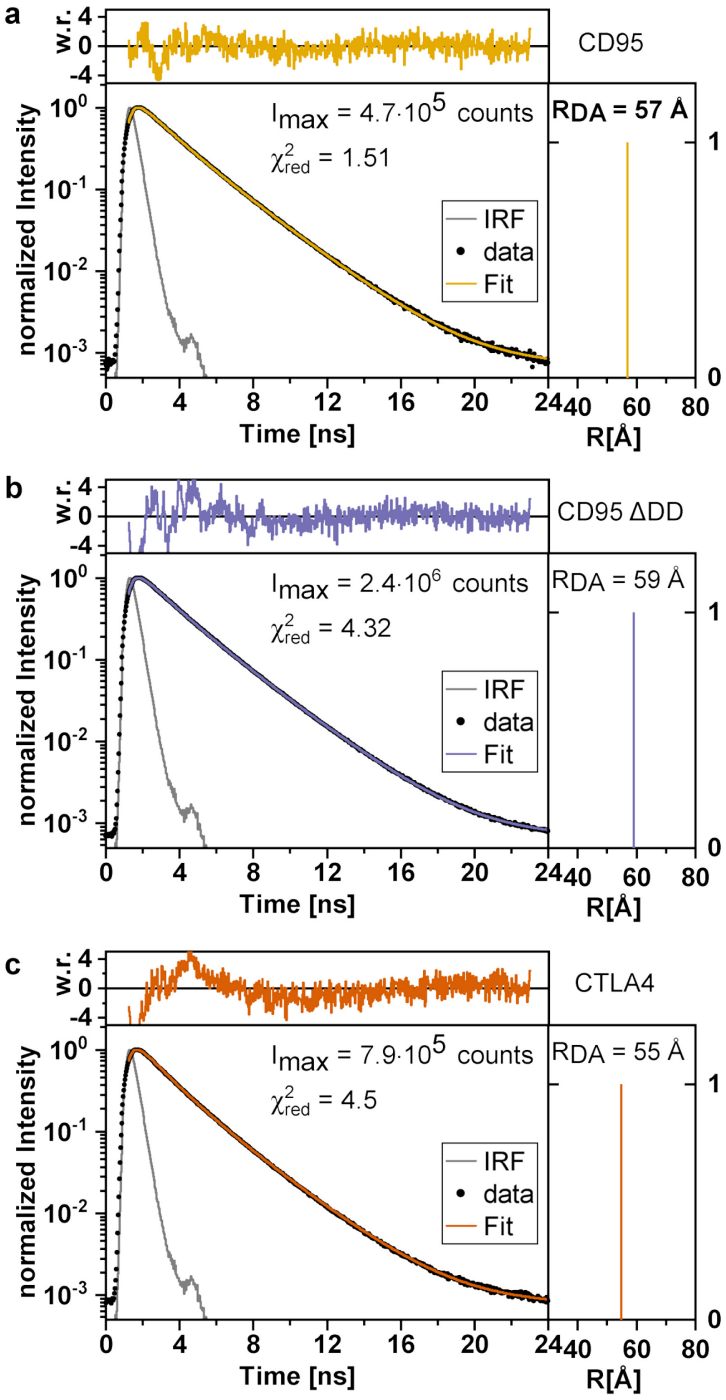

Supplementary Figure 15: Ensemble TCSPC of fluorescent protein in cells to obtain the FRET rate.

Decay histograms of multiple cells showing FRET were added to improve signal statistics. **a)** Reliability of FRET rate determination is improved when a significant portion of x_{FRET} is present. Hence, we select CD95 expressing cells transfected with 250 ng/2 wells transfection reagent with > 2% x_{FRET} and a time since

ligand addition >120 minutes. We further exclude proximity FRET by selecting cells with receptor concentrations between 500 and 1000 receptor/µm². **b)** CD95(ΔDD) using the same selection criteria as in a. **c)** CTLA4 cells were selected for surface concentrations between 500 and 1000 receptors/µm². Due to countrate dependent IRF shifts the decays show irregularities at the start, barring refined analysis. Based on our long-linkers we expect a continuous RDA distribution, hence the obtained R_{DA} represent the mode of the distance distribution in the FRET-sensitive range. All obtained RDA values are slightly larger than the Förster radius, matching the prediction of our AV simulations (Supplementary Figure 6).

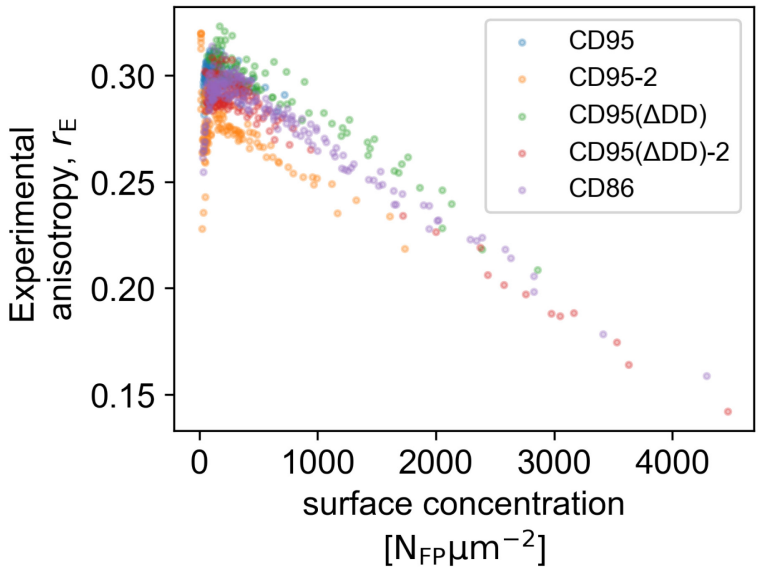

Supplementary Figure 16: Proof of principle for using homo-FRET

Experimental anisotropy (see methods) was calculated for monomeric donor only controls where only proximity-induced homo-FRET is expected to occur. Homo-FRET causes depolarization to occur that is measured by a decrease in anisotropy. The decrease in anisotropy with concentration is consistent with a proximity induced increasing FRET fraction. The analogous effect for hetero-FRET is shown in Figure 3A.

Bibliography

1 Patterson, G. H., Knobel, S. M., Sharif, W. D., Kain, S. R. & Piston, D. W. Use of the green fluorescent protein and its mutants in quantitative fluorescence microscopy. *Biophysical Journal* **73**, 2782-2790, doi:10.1016/s0006-3495(97)78307-3 (1997).

2 Shaner, N. C. *et al.* Improved monomeric red, orange and yellow fluorescent proteins derived from Discosoma sp red fluorescent protein. *Nature Biotechnology* **22**, 1567-1572, doi:10.1038/nbt1037 (2004).

3 Chen, L., Novicky, L., Merzlyakov, M., Hristov, T. & Hristova, K. Measuring the energetics of membrane protein dimerization in mammalian membranes. *Journal of the American Chemical Society* **132**, 3628-3635 (2010).

4 Evers, T. H., van Dongen, E. M., Faesen, A. C., Meijer, E. & Merkx, M. Quantitative understanding of the energy transfer between fluorescent proteins connected via flexible peptide linkers. *Biochemistry* **45**, 13183-13192 (2006).

5 Fu, Q. S. *et al.* Structural Basis and Functional Role of Intramembrane Trimerization of the Fas/CD95 Death Receptor. *Molecular Cell* **61**, 602-613, doi:10.1016/j.molcel.2016.01.009 (2016).

6 Dimura, M. *et al.* Automated and optimally FRET-assisted structural modeling. *Nature Communications* **11**, 5394, doi:10.1038/s41467-020-19023-1 (2020).

7 Wolber, P. & Hudson, B. S. An analytic solution to the Förster energy transfer problem in two dimensions. *Biophysical journal* **28**, 197-210 (1979).

8 King, C., Sarabipour, S., Byrne, P., Leahy, D. J. & Hristova, K. The FRET signatures of noninteracting proteins in membranes: simulations and experiments. *Biophysical journal* **106**, 1309-1317 (2014).

9 King, C., Raicu, V. & Hristova, K. Understanding the FRET signatures of interacting membrane proteins. *Journal of Biological Chemistry* **292**, 5291-5310 (2017).

10 Gendron, P. O., Avaltroni, F. & Wilkinson, K. J. Diffusion Coefficients of Several Rhodamine Derivatives as Determined by Pulsed Field Gradient-Nuclear Magnetic Resonance and Fluorescence Correlation Spectroscopy. *Journal of Fluorescence* **18**, 1093-1101, doi:10.1007/s10895-008-0357-7 (2008).

11 Uhlén, M. *et al.* Tissue-based map of the human proteome. *Science* **347**, 1260419, doi:doi:10.1126/science.1260419 (2015).

12 Weast, R. C. L., D. R. *CRC handbook of Chemistry and Physics*. 65 edn, (CRC Press, 1984).

13 Kapusta, P. Absolute diffusion coefficients: compilation of reference data for FCS calibration. *PicoQuant GmbH* **1**, 1-2 (2010).

14 Majer, G. & Melchior, J. P. Characterization of the fluorescence correlation spectroscopy (FCS) standard Rhodamine 6G and calibration of its diffusion coefficient in aqueous solutions. *Journal of Chemical Physics* **140**, doi:10.1063/1.4867096 (2014).

15 Greife, A. *et al.* Structural assemblies of the di- and oligomeric G-protein coupled receptor TGR5 in live cells: an MFIS-FRET and integrative modelling study. *Scientific Reports* **6**, 36792, doi:10.1038/srep36792 (2016).

16 Weidtkamp-Peters, S. *et al.* Multiparameter fluorescence image spectroscopy to study molecular interactions. *Photochemical & Photobiological Sciences* **8**, 470-480, doi:10.1039/b903245m (2009).

Determining Concentrations of Fluorescently Labelled Membrane Protein in live Cells using a Confocal Microscope

Nicolaas T M van der Voort[2,†], Nina Bartels[1,†], Claus A M Seidel[2], Cornelia Monzel[1,*]

† contributed equally

* corresponding author: cornelia.monzel@hhu.de

1. Experimental Medical Physics, Heinrich-Heine University, Düsseldorf, Germany

2. Molecular Physical Chemistry, Heinrich-Heine University, Düsseldorf, Germany

Keywords

Fluorescence, surface concentration, brightness calibration, FCS

Abstract

The surface concentration of fluorescently labelled membrane proteins images by a confocal microscope is determined by means of a brightness calibration via adsorption spectroscopy and a confocal volume calibration using FCS. When proteins localize in both the cytoplasm and membrane, we obtain the membrane-bound fraction from live-cell FCS. This protocol can be easily extended to include cytoplasmic concentrations.

Introduction

To transform the fluorescent brightness of FRET data to a number of fluorophores, we obtain calibrations for the brightness of single fluorescent proteins using a brightness calibration curve for the fluophores of interest – in our measurements mEGFP and mCherry. The procedure is composed of multiple steps:

1. Sample Preparation,
2. Determine Fluorophore Concentrations with Absorption Spectroscopy,
3. Fluorophore Brightness Measurements on the Confocal Microscope,
4. Determination of the Confocal Volume with FCS,
5. Calculation of the Molecular Brightness,
6. (Optional: Determine Receptor Membrane Fractions with FCS), and
7. Calculation of the Molecule (Surface) Concentrations.

Reagents and equipment

Equipment

- Absorption spectrometer, Here:
  - Cary 4000 UV-Vis Spectrophotometer (Agilent Technologies, Inc., Santa Clara, CA, USA)
- Confocal Microscopy with single-photon counting, here:
  - Customized Abberior Expert Line (Abberior Instruments GmbH, Göttingen, Germany)
- Powermeter, here:
  - PM400 optical power meter with S170C diode (Thorlabs GmbH, Bergkirchen, Germany)
- Software for image and data analysis, here:
  - MATLAB (R2019a, The MathWorks, Inc., Natick, Massachusetts, USA)

- Python 3.7 using the libraries python 3.7, numpy 1.20.3, pandas 1.3.5, matplotlib 3.5.0, scipy 1.7.3.

Reagents and Material

- Donor and Acceptor Fluorescent Proteins. Here:
  - EGFP (#orb84840, Biorbyt Ltd, Cambridge, UK)
  - mCherry (#TP790040, OriGene Technologies, Inc., Rockville, MD, USA)
- Buffer or deionized water. Here:
  - DPBS (#14190144, Gibco, Life Technologies Inc., Carlsbad, USA)
- Imaging slides. Here:
  - µ-Slide Angiogenesis Glass Bottom (#81507, ibidi GmbH, Gräfelfing, Germany)
- BSA for coating. Here:
  - Albumin (BSA) Fraktion V (pH 7,0) (A1391, ITW Reagents, AppliChem GmbH, Darmstadt, Germany)
- Reference Fluorophore for confocal volume calibration. Here:
  - Rhodamine 110 (#83695, Sigma-Aldrich, Merck KGaA, Darmstadt, Germany)
  - Rhodamine 101 (Rhodamine 640 perchlorate, #06400, Exciton, Luxottica Group S.p.A., Lockbourne, Ohio, USA)

Procedure

The following procedure is written for the use of one fluorescent protein. In case of FRET measurements with two fluorescent proteins – donor and acceptor – its needs to be repeated for both dyes.

Sample Preparation

1. Prepare BSA in Buffer in a concentration of 1 mg/ml
2. Cuvettes are cleaned by washing 10 times with ethanol, followed by 10 times washing with water.
3. Incubate all epis, cuvettes and imaging slides with the 1 mg/ml BSA in Buffer and incubate for >30 minutes to avoid adsorption of the fluorescent proteins to the walls of the respective vessel.
4. Prepare titration series of the fluorescent protein:
   a. Start with a highest concentration of ~10µM.
   b. Continuously dilute by a factor 2 two in PBS, prepare 7 dilution steps.
   c. Of each dilution prepare a sufficient volume to use for 1. the cuvettes of absorption spectrometry (here: 20 µl) and 2. the used imaging slide (here: 40 µl). For our measurement, we prepared 100µl per titration step.

Determine Fluorophore Concentrations with Absorption Spectroscopy

Experiment

1. As a concentration range use 350 – 600 nm for EGFP and 350-700 nm for mCherry. For other fluorophores, record a wide enough spectrum to include the whole absorption spectrum plus at least 20 nm on each side where no absorption occurs.
2. Record the blank solution.
3. Carefully Pipet out the blank solution and ensure no solution is left.
4. Add the next concentration. Work from low concentrations to higher concentration. Re-use the same cuvette as each cuvette has its own absorption spectrum.
5. Repeat steps 3-4 until all concentrations are measured.
6. In case of multiple fluorophores, such as for FRET, repeat steps 2-5 for each fluorophore.

Analysis

1. Subtract the blank spectrum from your measurement.
2. To correct for the scatter induced additional background, perform a parabolic fit to the background regions on either side of each spectrum.
    - Info: scatter is induced by the fluorescent protein itself and hence cannot be corrected using a blank. You need to fit the background for each spectrum separately as each time the spectrum is different.
    - For EGFP the fitted regions are 350-360 nm and 520-600, for mCherry 350 – 450 nm and 620 - 700 nm.
3. Subtract the scatter background.
4. Average the absorption in 15 nm around the absorption maximum to reduce noise.
    - For EGFP this range is 480-495nm, for mCherry 580-595nm
5. Calculate the concentration using Lambert-Beer's law

$$C = \frac{A}{\epsilon\, b},$$

where C is the concentration in M, A is the dimensionless absorption determined in step 4., b is the pathlength of your cuvette in cm and ε is the Extinction coefficient, reported in $M^{-1}cm^{-1}$.
    - As a calculation example: $A = 0.012$, $\varepsilon = 55900\ M^{-1}\ cm^{-1}$, $b = 0.15$ cm, yields 1.43µM.
    - The extinction coefficient for EGFP and mCherry is obtained from literature [1,2] (summarized here: www.fpbase.org) to be 55'900 $M^{-1}cm^{-1}$ and 72'000 $M^{-1}cm^{-1}$ respectively.
    - When averaging over a detection window, one may adjust the extinction coefficient to the average over that window. For example, EGFP detected from 480-495nm has an average 96.7% adsorption of the maximum, yielding $\epsilon_{avg} = 54'000\ M^{-1}cm^{-1}$.

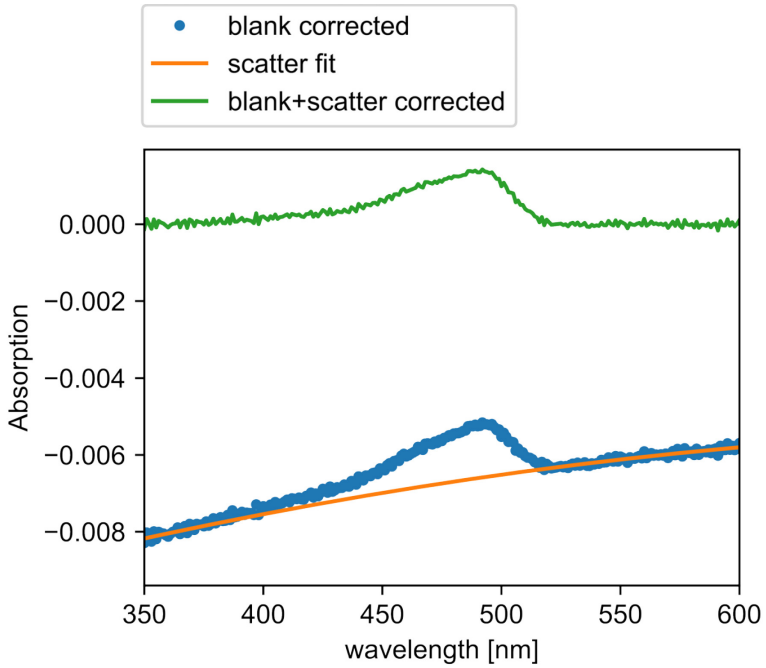

Figure 1: Scatter correction for 0.16µM EGFP concentration.

Tip: Steps 2-4 were automated in python. The code is included in appendix A with extensive commentary explaining how to use it. It requires the absorption data to be accessible as a *pandas Dataframe* type.

Fluorophore Brightness Measurements on the Confocal Microscope

1. Turn on / initiate confocal microscope.
2. Select the settings that are used in your experiment (objective, filters, pinhole).

3. Record the laser power at multiple power settings to create a calibration curve for the excitation wavelength.
4. Prepare the BSA-treated imaging slide:
    - Remove BSA solution completely
    - Fill wells with all prepared fluorophore dilution of the titration series (here: 40µl / well), label wells accordingly.
5. Mount imaging slide on the microscope.
6. For each dilution, focus into the middle of the solution and measure the countrate at three different laser powers to obtain countrates between 100kHz and 1 MHz. The variation of excitation powers is crucial for a precise calibration in order to reduce a power-related bias, e.g. due to triplet states.
    - Tip: when using an oil objective, measure close to the surface, or at the same height as your experiment is performed to account for the effects of refractive index mismatch.
7. Average and plot the measured power-normalized brightness (detector countrate per time and [kHz/µW]) against the obtained concentration [µM].
8. Fit a linear curve $b \cdot x$ to determine the slope b in kHz·µM^{-1}µW^{-1} or equivalent Hz·nM^{-1}µW^{-1}.

Determination of the Confocal Volume with FCS

1. Turn on / initiate confocal microscope.
2. Select the identical settings as for the brightness measurements (objective, filters, pinhole)
3. Check room temperature before measurement.
4. Dilute the reference fluorophore to a concentration between 3 and 10 molecules per confocal volume suitable for FCS.
5. Measure the used laser powers for the excitation laser .
6. Measure the auto-correlation curve of the reference fluorophore at three different laser powers (in case of a polarization-sensitized readout, the cross-correlation can be used)
    - Laser powers should lie between 5 and 30 µW measured at the objective
    - The confocal volume should be consistent between the measurements.
7. Fit the correlation curve with by fitting a single diffusion time and triplet state while assuming the literature diffusion constant of the reference fluorophore. Consider the temperature-dependance of the diffusion constant $D(T)$, which can be calculated following:
$$D(T) = D(T_0) \cdot \frac{T}{T_0} \cdot \frac{\eta(T_0)}{\eta(T)},$$
where $D(T_0)$ is the reference diffusion constant at a given Temperature T_0 in [K] and η is the viscosity of water at the respective temperatures T and T_0. (we use: $D_{\mathrm{Rh110}} = 470$ µm^2/s for the Rh110 diffusion constant at 25.8 °C lab room temperature [3-5]).
8. Determine the confocal volume of the device at the respective wavelength V_λ.

Calculation the Molecular Brightness

The molecular brightness can now be calculated as follows:

$$B_m = \frac{b}{N_\mathrm{A} \cdot V_\lambda}$$

with the Avogadro constant N_A, resulting in the molecular brightnesses B_m in [Hz·molecule^{-1}µW^{-1}].

(Optional: Determination of Receptor Membrane Fractions with FCS)

If the protein of interest is a membrane protein, one should additionally consider the cytoplasmic fraction of the signal. For transfected cells, there is usually a fast diffusion component detectable, even while focusing the confocal volume strictly on the (bottom) cell membrane. This diffusion is attributed to the

presence of cytoplasmic fluorescent proteins, originating from internal production and trafficking pathways.

Reliable FCS of membrane proteins is a complex application but not topic of this protocol, more information on it can be found in other publications [6].

1. Measure FCS on cells expressing the membrane protein of interest.
2. Fit cell FCS curves with two diffusion terms, corresponding to a cytoplasmic and a membrane component.
3. Determine the mean amplitude of the cytoplasmic fraction of at least 20 cells and average this value.

Calculation of Molecule (Surface) Concentrations

Finally, the number of fluorescent molecules per cell volume or surface area – the average label surface concentration – of a cell image can be determined with:

$$\rho_{\mathrm{FP}} = \frac{I_{\mathrm{cell,FP}}\, p_{\mathrm{mem}}}{P_{\mathrm{ex}}\, A_{\mathrm{cell}}\, B_{\mathrm{m}}} ;$$

where $I_{\mathrm{cell,FP}}$ and I are the fluorescence intensities of the whole cell of the fluorescent protein in [Hz], P_{ex} is the excitation power of the respective lasers, respectively, and A_{cell} is the area of the respective cell. The area of the cell is determined from the images directly. In case of a volume concentration, A_{cell} can be exchanged by V_{image} which is calculated by $V_{\mathrm{image}} = A_{\mathrm{cell}} \cdot h_{\mathrm{CV}}$, where h_{CV} is the height of the confocal volume. The analysis is analogous for all sub-compartments of the cell down to a single pixel.

Troubleshooting

- we avoid membrane roughness altogether by measuring the bottom of the cell membrane, which is flat to a high degree[7,8].
- Measuring a different confocal volume at different laser powers indicates one of the following: The confocal volume may increase at high excitation powers due to saturation. Lower your laser power to avoid this effect. Another option is the incorrect fitting of the FCS triplet therm. Try to improve the quality of your correlation by measuring longer or increasing the power. Make sure the starting parameters for the fit are proper.

Time taken

- Preparation: 1h
- Absorption measurements: 3h
- Fluorophore Brightness measurements: 3h
- Confocal Volume Calibration: 2h
  - ➔ Total: 9h

- (Optional: Determination of cytoplasmic fraction for membrane proteins): 8h

Anticipated results

A reliable conversion of an image count rate towards a reliable absolute protein (label) concentration.

References

1 Patterson, G. H., Knobel, S. M., Sharif, W. D., Kain, S. R. & Piston, D. W. Use of the green fluorescent protein and its mutants in quantitative fluorescence microscopy. *Biophysical Journal* **73**, 2782-2790, doi:10.1016/s0006-3495(97)78307-3 (1997).

2 Shaner, N. C. *et al.* Improved monomeric red, orange and yellow fluorescent proteins derived from Discosoma sp red fluorescent protein. *Nature Biotechnology* **22**, 1567-1572, doi:10.1038/nbt1037 (2004).

3 Gendron, P. O., Avaltroni, F. & Wilkinson, K. J. Diffusion Coefficients of Several Rhodamine Derivatives as Determined by Pulsed Field Gradient-Nuclear Magnetic Resonance and Fluorescence Correlation Spectroscopy. *Journal of Fluorescence* **18**, 1093-1101, doi:10.1007/s10895-008-0357-7 (2008).

4 Weast, R. C. L., D. R. *CRC handbook of Chemistry and Physics*. 65 edn, (CRC Press, 1984).

5 Kapusta, P. Absolute diffusion coefficients: compilation of reference data for FCS calibration. *PicoQuant GmbH* **1**, 1-2 (2010).

6 Kim, S. A., Heinze, K. G. & Schwille, P. Fluorescence correlation spectroscopy in living cells. *Nature Methods* **4**, 963-973, doi:10.1038/nmeth1104 (2007).

7 Zidovska, A. & Sackmann, E. Brownian motion of nucleated cell envelopes impedes adhesion. *Physical review letters* **96**, 048103 (2006).

8 Monzel, C. *et al.* Measuring fast stochastic displacements of bio-membranes with dynamic optical displacement spectroscopy. *Nature communications* **6**, 1-8 (2015).

Appendices

A)Code for absorption spectrum scatter correction

```
#tested in python 3.7, numpy 1.20.3, pandas 1.3.5, matplotlib 3.5.0, scipy 1.7.3
import numpy as np
import pandas as pd
import matplotlib.pyplot as plt
from scipy.optimize import curve_fit
def square(x, a, b, c):
    """parabolic function"""
    return a*x**2 + b*x + c
def calc_corrected_Abs(dfrm, key, verbose = False, plotout = None,
                       bgrange1 = (600,520), bgrange2 = (380,350), meanrange =
(495,480)):
    """
    Function takes a pandas dataframe object containing the absorption data and having
the wavelength as index.
    A parabolic fit is calculated to the background ranges 1 and 2.
    The fitted parabola as well as a corrected absorption spectrum is stored in the da-
taframe.
    Optionally: A plot of the fit and corrected data is generated.
    Finally, the average corrected absorption over the range indicated by meanrange is
returned.
    input parameters:
      dfrm      : the dataframe containing the absorption data
      key       : the name of the column containing the absorption data that has to be
corrected
      verbose   : if True, an insightful plot is generated, default False
      plotout   : if given, plot will be saved to the path plotout, the format    will
be inferred from
                  the extension. For example, plotout = r'/my/path/plot.svg'
      bgrange1  : The first background range where scatter, but no fluorescent absorp-
tion is present,
                  default 600-520 nm for EGFP
      bgrange2  : the second background range, default 380-350 nm for EGFP.
      meanrange : The spectrum range over which to calculate the average absorption, a
wider range is
                  needed in case of noisy spectra. Default 495-480 nm for EGFP
    returns:
      A         : the average corrected absorption over the meanrange
    """
    p0 = [0.01, 0.1, 0.1]  # for [amp, cen, wid]
    data = dfrm[key]
    bg = dfrm.loc[bgrange1[0]:bgrange1[1]].ap-
pend(dfrm.loc[bgrange2[0]:bgrange2[1]])[key]
    best_vals, covar = curve_fit(square, bg.index, bg.values, p0=p0)
    dfrm[key + ' corrModel'] = square(dfrm.index, *best_vals)
    dfrm[key + ' corr'] = dfrm[key] - dfrm[key + ' corrModel']
    if verbose:
        plt.plot(data.index, data.values, '.')
        plt.plot(data.index, square(data.index, *best_vals))
        plt.plot(dfrm[key + ' corr'])
        plt.xlabel('wavelength [nm]')
        plt.ylabel('Absorption')
        plt.xlim((bg.index.min(), bg.index.max()))
        plt.legend(loc = 4)
        if plotout: plt.savefig(plotout, transparent = True)
        plt.show()
    A = np.mean(dfrm[key + ' corr'].loc[meanrange[0]:meanrange[1]])
    print('corrected Absorption for %s is %.5f' % (key, A))
    return A
```

A Minimal Model of CD95 Signal Initiation Revealed by Advanced Super-resolution and Multiparametric Fluorescence Microscopy

Nina Bartels [1,†],Nicolaas T M van der Voort [2,†], Annemarie Greife[2], Arthur Bister[3], Constanze Wiek[3], Claus A M Seidel[2,*], Cornelia Monzel[1,*]

† contributed equally

* corresponding author: cornelia.monzel@hhu.de, cseidel@hhu.de

1. Experimental Medical Physics, Heinrich-Heine University, Düsseldorf, Germany

2. Molecular Physical Chemistry, Heinrich-Heine University, Düsseldorf, Germany

3. Department of Otorhinolaryngology, Head & Neck Surgery, Heinrich-Heine University, Düsseldorf, Germany

Abstract

Unraveling the spatiotemporal organization and dynamical interactions of receptors in the plasma membrane remains a key challenge for our mechanistic understanding of cell signal initiation. A paradigm of such process is the oligomerization of TNF receptor CD95 during apoptosis signaling, where molecular configurations are yet to be defined. Here, we scrutinize proposed oligomerization models in live cells, establishing a molecular sensitive imaging toolkit including time-resolved FRET spectroscopy, quantitative STED microscopy, confocal Photobleaching Step Analysis and FCS. CD95 interactions were probed over molecular concentrations of few to ~ 1000 molecules/μm^2, over ns to hours, and molecular to cellular scales. We further present high-fidelity monomer and dimer controls for quantitative benchmarking. Efficient apoptosis was already observed when ~ 8 to 17% monomeric CD95 oligomerize to dimers/trimers after ligand binding. Our multiscale study highlights the importance of molecular concentrations, of the native environment, and reveals a minimal oligomerization model of CD95 signal initiation.

Keywords

Cluster of Differentiation 95 (CD95), Tumor necrosis factor (TNF), oligomerization, single-molecule imaging, Förster Resonance Energy Transfer (FRET), Stimulated Emission Depletion (STED) nanoscopy, Photobleaching Step Analysis (PBSA), Fluorescence Correlation Spectroscopy (FCS)

Introduction

Identifying the spatiotemporal organization and dynamical interactions of receptors in the plasma membrane is key to our understanding of cell signal initiation. So far, we know about the molecules participating in distinct signaling cascades, however, insights about interaction

networks, assembly kinetics, the formation of supramolecular patterns, as well as the role of molecular concentration remain sparse.

A paradigm of signal initiation is given by the characteristic molecular organization proposed for tumor necrosis factor receptors (TNFR), with the most prominent molecular configurations described below. The understanding of TNFR induced signaling is important, as these receptors initiate signaling for cell proliferation, morphogenesis and most prominently, cell apoptosis[1-3]. TNFRs are further targets of therapeutic approaches for various diseases, including cancer, autoimmunity, or infectious diseases[4]. Of particular interest is, in this context, the TNF receptor Cluster of Differentiation 95 (CD95/ Fas / TNFR6), as it is exclusively activated by the trimeric ligand CD95L (FasL / TNFL6 / CD178), thus providing high control over the stimulation of the receptor (Figure 1a).

Two models of TNFR oligomerization are primarily discussed to explain the molecular mechanisms underlying signal initiation (Figure 1b)[5-8]: the first model proposes initially monomeric receptors which, upon binding of the trimeric TNF ligand, recruit further receptors to form small signaling units of up to trimer-trimer receptor-ligand configurations. Features of this 1st model comprise (i) a direct signal transduction from the extracellular to the intracellular side without the need for massive spatial molecular rearrangements as well as (ii) its occurrence already at low molecular expression levels. A second model proposes TNFRs to form inactive dimers prior to their activation, which in turn assemble into a supramolecular honeycomb lattice[9]. After TNF ligand binding and receptor activation the intracellular receptor domain is cross-linked to reestablish the honeycomb lattice on the intracellular membrane side. Features of this 2nd model are (i) a unique molecular complex permitting robust signal initiation and (ii) potential signal amplification by a factor of ~ 1.4[10].

Here, we scrutinize the two models, choosing CD95 as an example of TNFRs, as its exclusive activation by CD95L facilitates data quantification and interpretation. Moreover, qualitative observations of CD95 oligomerization in the cell plasma membrane have been reported[11], albeit a quantification of oligomer sizes in live cells is missing. This is most likely due to a lack of suitable techniques to discern different oligomerization states during the signaling process. To address this need, we here introduce a strategy based on complementary state-of-the art microscopy and spectroscopy[12,13] techniques and their further developments as multiscale approach to cover very large ranges in concentration, time, and space (Figure 1c). In particular, we advance and synergize the readouts of Cell Lifetime FRET Image Spectroscopy (CELFIS), Stimulated Emission Depletion (STED), polarization-resolved confocal Photobleaching Step Analysis (cPBSA), and use Fluorescence Correlation Spectroscopy (FCS). Our strategy also comprises a small library of CD95 variants with different signal initiation competency as well as high-fidelity monomer and dimer controls. In all cases, rigorous image analysis and benchmarking against control samples allowed us to identify concentration or photophysical effects and to quantify CD95 oligomeric states. Thus, we map the regulation of CD95 before and during the whole signaling process and derive a minimal model of CD95 signal initiation. Notably, the presented multiscale toolkit can also be applied to study the oligomerization of other membrane receptor systems quantitatively.

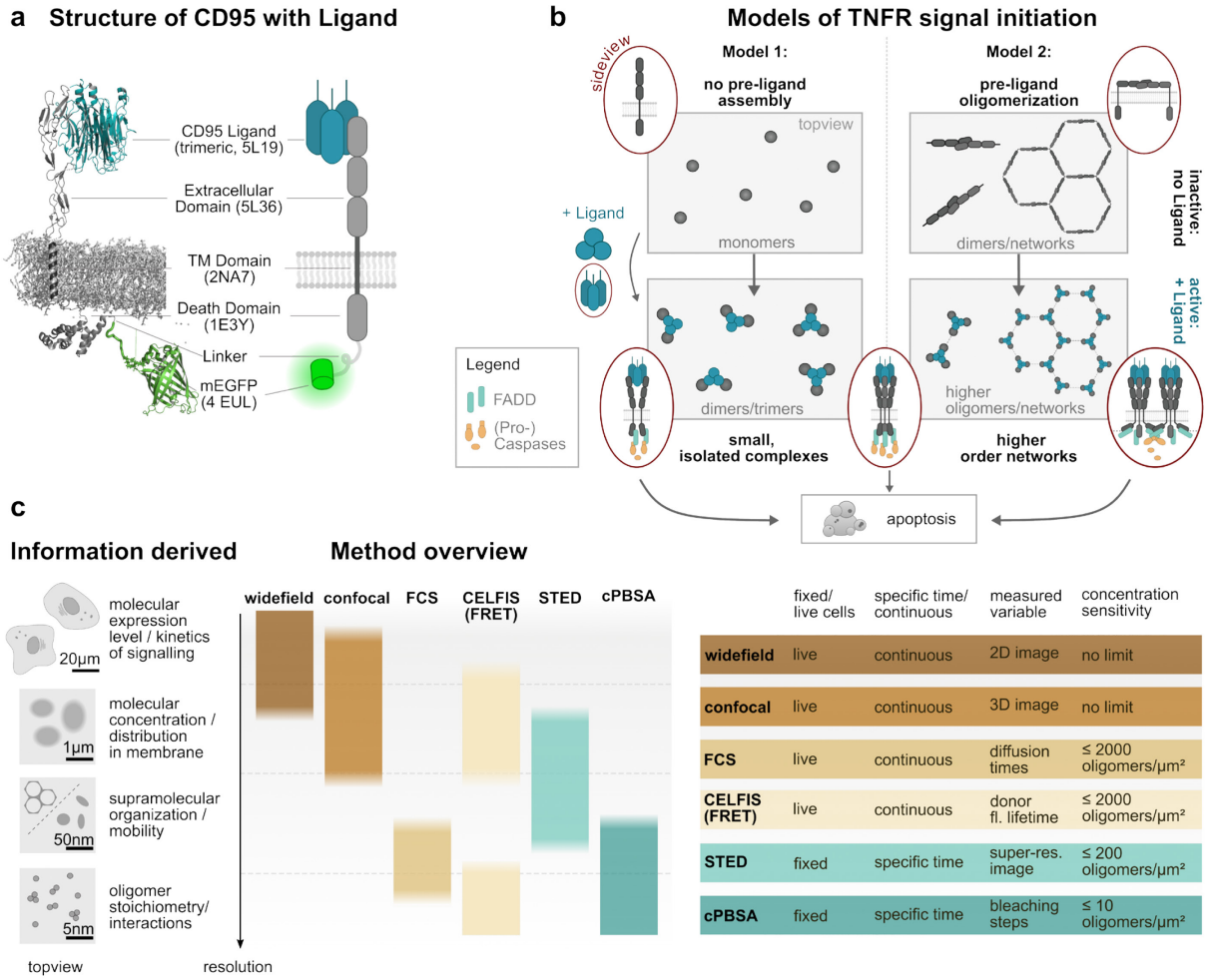

Figure 1: Probing Cluster of Differentiation 95 (CD95) signal initiation over a broad range of molecular concentrations and in space and time. a) Molecular structure and cartoon of CD95 receptor with genetically fused mEGFP and trimeric CD95 Ligand (CD95L). The four letter abbreviations refer to Protein Data Bank IDs. **b)** Schematic illustration of two proposed models of TNFR signal initiation. Left: monomeric receptors bind trimeric TNF ligands and form up to trimer-trimer receptor-ligand configurations. In the receptor activated state, the intracellular death domain (DD) opens and allows for recruitment of an adaptor molecule. The adapter molecule in case of CD95 is Fas-associated death domain protein (FADD, indicated in the sideview cartoons). A cascade of (Pro-)caspase binding and activation is initiated thereafter, resulting in intracellular protein cleavage followed by cell apoptosis. Right: TNFRs form inactive dimers prior to activation, which in turn assemble into a supramolecular honeycomb lattice consisting of hexagonal units of ~ 24 nm diameter (sizes may vary with TNF receptor)[9]. After ligand binding to the lattice, the receptor dimers decouple, turn into their active state, and recruit FADD to the opened DDs. In the following, FADD may crosslink the DDs to reestablish the honeycomb lattice on the intracellular membrane side from which the (Pro-)caspase cascade evolves as in Model 1. **c)** Overview of test strategy using a combination of super-resolution and multiparametric fluorescence microscopy techniques covering cellular to single molecule scales. Fixed cell analyses at specific time-points are complemented by live cell studies over several hours. A concentration range spanning few to several 1000 molecules / µm^2 is probed. Next to regular widefield, confocal time-lapse microscopy and FCS to monitor receptor and cell apoptosis dynamics, information about CD95 interaction dynamics, molecular distribution, and stoichiometries is obtained via Cell Lifetime FRET Image Spectroscopy (CELFIS),

quantitative spot analysis using STED, and confocal Photobleaching Step Analysis (cPBSA). For further details see text and Methods.

Results

Engineered plasma membrane receptors for molecular quantification in Super-resolution and Multiparametric Fluorescence Microscopy

We have collected a small library of mEGFP and mCherry labeled CD95 variants with different competency to recognize and transduce the signal initiated by CD95L (Figure 2a). Next to monocistronic plasmids, we used bicistronic constructs, combining mCherry and mEGFP labeled proteins, to ensure homogeneous co-expression of donor and acceptor fluorophores during FRET measurements. To quantify receptor oligomerization states, we established high-fidelity monomer and dimer controls using mEGFP or mCherry labeled CD86 and CTLA4 membrane receptors, respectively. As described below, generating a pseudo-dimer control from CD86 with two genetically fused mEGFP was necessary to determine the CTLA4 dimerization state. Further details on the design of the 13 plasmids are found in the Methods section. Prior to measurements, correct integration of all receptors into the plasma membrane was verified using confocal microscopy (see Supplementary Figure 1).

The efficiency of signal initiation relies on receptor expression levels and ligand concentrations

We first examined CD95 signal initiation and transduction on the cellular level to quantify effects of different ligand concentrations and receptor densities on the signaling kinetics and outcome. To this end, we recorded HeLa cell lines exhibiting different CD95 receptor expression levels of 0 to $4.5 \cdot 10^5$ receptors per cell, as quantified by flow cytometry. Cells were exposed to various ligand concentrations and the kinetics of the cellular fate decision was monitored. Several hours after CD95L incubation, the cells showed typical apoptosis characteristics such as initial blebbing followed by cell shrinkage (Figure 2b). In all cases, the kinetics of apoptosis signaling followed a sigmoidal progression. The initial onset just one hour after ligand addition indicated the minimal time the signal takes from apoptosis initiation until the eventual death of the cell. The predominant time interval of apoptosis events was between 1 to 5 hours after ligand addition, whereas the slowest signaling outcome was detected after 5 to 7 hours, depending on the experimental situation. The few apoptosis events recorded after this time were attributed to naturally occurring apoptosis. We observed a ligand dependent efficiency of apoptosis induction from 3% to 99% apoptotic cells, when the ligand concentration was increased from 2 to 200 ng/ml. Similarly, apoptosis initiation scaled with the number of receptors expressed on the cell surface, where a complete knockout of CD95 (0 receptors) led to no apoptosis, $2.5 \cdot 10^4$ CD95 molecules/cell led to 60-75% apoptotic cells and $4.5 \cdot 10^5$ CD95 molecules/cell led to 99% apoptosis (Figure 2c/d). A fit of the Hill function (see Methods) yielded the time after which half of all apoptotic cells had died. These half-times ranged from 1.5 h to 8 h and became shorter with higher CD95 ligand concentration or receptor cell surface expression (Figure 2d). Cells expressing CD95(ΔDD) and CD95(R102S) served as a negative control and showed apoptotic cells of less than 15% within 10 hours caused by natural apoptosis or potentially transfection stress (Supplementary Figure 2).

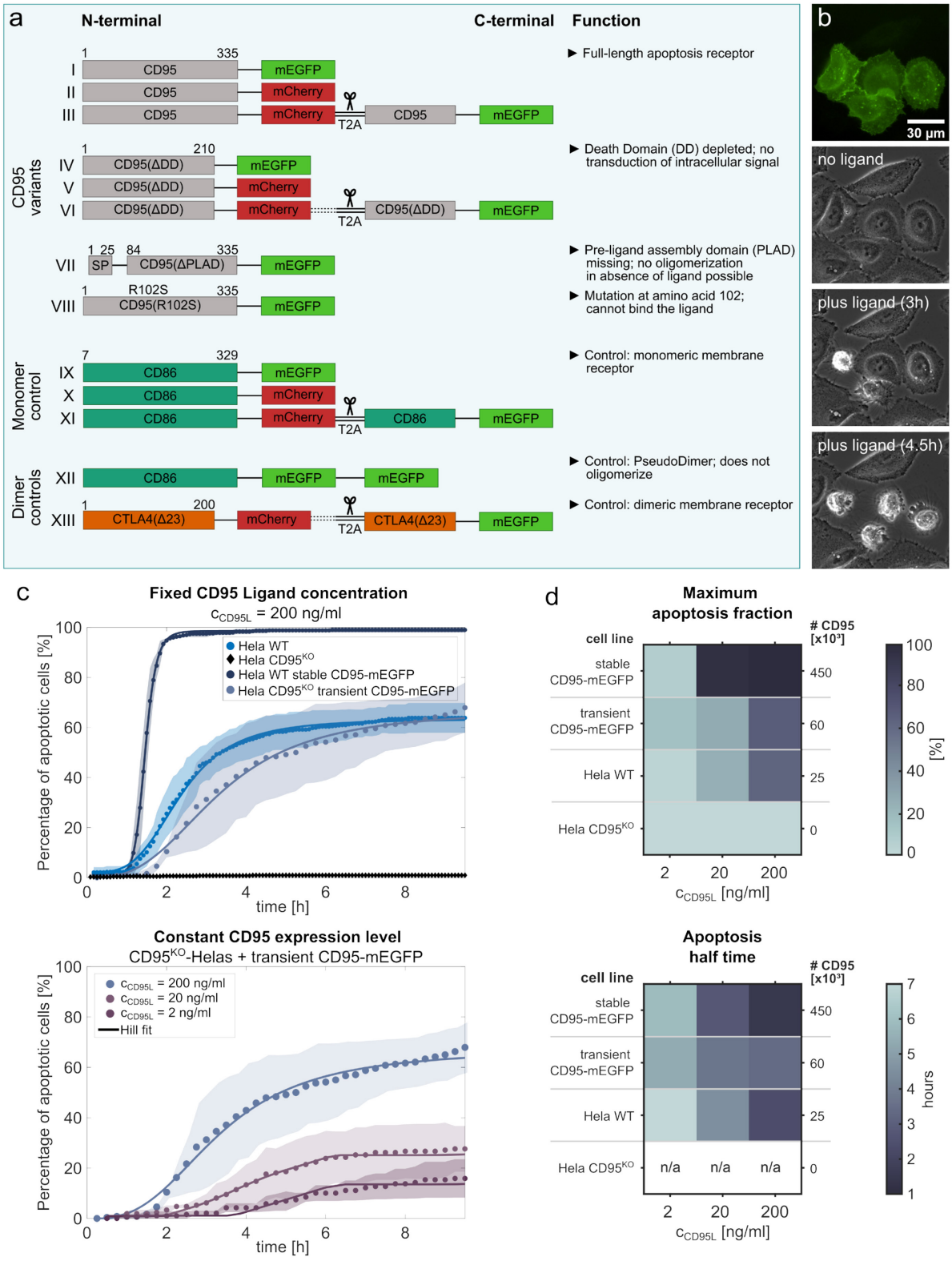

Figure 2: Engineered receptor variants for molecular quantification and characterization of molecular concentration dependent apoptosis dynamics. a) Schematic illustration of engineered CD95 variants of different signaling competency (I-VIII) as well as monomer (IX-XI) and dimer controls (XII-XIII). Bicistronic plasmids are used in CELFIS, mEGFP labeled monocistronic plasmids with all other techniques. Numbers refer to the amino acid sequence. Dashed lines indicate optional linkers. Blue panels illustrate the method. **b)** From top to bottom: mEGFP fluorescence and phase contrast microscopy of Hela $CD95^{KO}$ cells transiently

transfected with CD95-mEGFP before and after CD95 Ligand addition. 3 h and 4.5 h after 200 ng/ml CD95 Ligand addition apoptosis of transfected cells is observed. Non-transfected cells are unaffected by CD95 Ligand. **c)** Percentage of apoptotic cells over time after CD95 Ligand incubation. From a Hill equation fit (solid line, Equation (1) in Methods) characteristic apoptosis dynamics parameters shown in d) are derived. Top: comparison of cell lines with different CD95 expression level exposed to 200 ng/ml ligand concentration. Bottom: comparison of Hela $CD95^{KO}$ transient CD95-mEGFP cell line exposed to ligand concentrations of c_{CD95L} = 2, 20, 200 ng/ml. Data points show the weighted mean, shaded area the standard deviation of three independent measurements. N >180 cells per sample. **d)** Hill fit parameters: maximum apoptosis fraction (top) and apoptosis half time (bottom) of different cell lines and ligand concentrations c_{CD95L}. n/a indicates data where no Hill fit was possible due to a low percentage of apoptotic cells. For further details see text and Methods.

For CD95(ΔPLAD), the apoptosis dynamics slightly exceeded the negative controls with up to 25% of apoptotic cells (Supplementary Figure 2). Analyzing the apoptosis kinetics allowed us to define characteristic time points of the signaling process important for subsequent measurements with CELFIS, cPBSA, FCS or STED: (i) time points before signal initiation, (ii) directly after ligand addition, (iii) when most cells underwent apoptosis, and (iv) when all signaling events finished. Moreover, in all apoptosis experiments, the kinetics exhibited a strong correlation with ligand and receptor concentration, demonstrating that signal initiation is highly dependent on the absolute number of activated receptors. For this reason, we payed particular attention to the number of ligands and receptors in the system during the following measurements.

Ligand induced signal initiation does not affect receptor mobility in the plasma membrane as revealed by live-cell FCS

Prior to single-molecule analyses of CD95 oligomeric states, we tested if CD95 is sufficiently mobile and hence able to form (higher) oligomers using FCS (Supplementary Figures 3&4). Since FCS measurements are more sophisticated in live-cells, due to the natural variability and signal contributions of cytoplasm and plasma membranes, we elaborated an optimized laser power, pinhole and recording time to optimally balance signal-to-noise gains with recordings of less stable fluorophores, such as mEGFP (see Methods and Supplementary Notes 1&2). We recovered diffusion coefficients of CD95 and CD95(ΔDD) in membranes. The obtained diffusion coefficients $D = 0.23 \pm 0.02\,\mu m^2/s$ are typical of individually diffusing membrane proteins[14,15] and didn't change in the presence or absence of CD95L. The diffusion constants of CD95 were also comparable to those of our control constructs with single and double transmembrane helices, $CD86_{D0}$ and $CTLA4_{DA}$, respectively (Supplementary Figure 3, Supplementary Table 1). Overall, this data confirmed sustained CD95 mobility without significant changes in D during the whole signaling process.

Small spots of receptors below STED resolution and not large CD95 networks govern the distribution in the plasma membrane

We tested the CD95 membrane distribution for local accumulations or supramolecular cluster formation by STED nanoscopy. To this end, we fixed the transfected Hela cells 2h after ligand addition when the signaling was initiated in most cells. CD95-mEGFP was stained with GFP-nanobody Atto647N and the membrane surface was imaged with STED at 40 nm FWHM resolution. STED images revealed a distribution of CD95 in characteristic spots for which we

established a quantitative analysis using time-gating with maximum likelihood estimator-based deconvolution followed by a watershed object segmentation and determination of spot size and brightness (Figure 3a/b; see Methods).

To test for higher order pattern within the receptor spot distribution, we first calculated the pair correlation function $g(r)$ of the spot centers (Figure 3c). Our data and simulations revealed a random distribution of spots over the membrane surface for all receptors in absence and presence of the ligand. Note, that the decrease in correlation at radii below 130 nm arises from the size of the PSF (for CD95, dimer controls, and simulation see Supplementary Figure 5). From this data, an average concentration of 20 spots/μm^2 was derived, corresponding to an average distance of 224 nm between spots for an intermediate expression level of about $4 \cdot 10^4 - 8 \cdot 10^4$ receptors per cell. This estimate is in line with flow cytometry results when only few receptors are assumed for each spot. In addition, the size distribution of CD95(ΔDD) spots before and after ligand addition was comparable to the CD86 monomer control distribution. Simulation of a 6-mer illustrated the distribution expected for higher order clusters (Figure 3d). These data provided a first indication that the existence of higher oligomers/networks was rather unlikely (data of CD95 and dimer controls in Supplementary Figure 5).

To assess this readout further, we evaluated the spot brightness [photons/pixel] of round, resolution-limited spots before and after ligand addition (Figure 3e). Initially, the large spread in spot brightness of CD95 samples was interpreted as the existence of CD95 monomers as well as CD95 oligomers and few higher order networks. However, measurements of monomer and dimer control samples revealed similar distributions. Several reasons could cause spots with varying brightness or sizes exceeding the resolution limit, without the existence of any higher oligomers: (1) local concentration fluctuations, (2) limitations in staining efficiency, (3) photophysical effects, or (4) sample orientation in the membrane. In addition, the analysis of the registered polarization-resolved fluorescence revealed a wide range of fluorescence anisotropy values from 0 to 1. This is evidence for a wide distribution of static orientations of stained fixed receptors in the membrane (Supplementary Figure 6). Thus, the observed variations in brightness mainly arise from different orientations of the molecular absorption and emission transition dipole moments.
Under these circumstances, we used the median values of the spot brightness as a robust measure for the distinct samples (Figure 3e). The average monomer brightness was 1.91 photons per pixel (CD86), and the dimer samples were 2.04 ($CTLA4_{DA}$) and 2.08 (CD86-mEGFP-mEGFP) photons per pixel, respectively. The lower brightness of $CTLA4_{DA}$ compared to CD86-mEGFP-mEGFP can be understood from the fact that $CTLA4_{DA}$ dimers consisted of donor-donor as well as of donor-acceptor pairs. A CTLA4 donor only ($CTLA4_{D0}$) expression was not possible, since the plasmid did not localize to the membrane correctly. In addition, and in contrast to the state of knowledge, CTLA4 does not always build 100% dimers, but the dimer fraction depends on the total receptor concentration (as determined by us with CELFIS below). CD95 samples in the absence of a ligand exhibited a median close to the monomer value, whereas after ligand addition, a significant shift toward a median value of 2 was obtained. These results indicate that some oligomers, but no hexagonal networks, consisting of 18 receptors or more, would form. These analyses also highlight the importance of using high-fidelity monomer or dimer controls as molecular benchmarks. In order to determine the CD95 oligomerization state precisely, we then performed cPBSA and CELFIS measurements. These techniques also have the advantage that no additional staining is needed so that an overall higher label density is expected for fluorescent proteins.

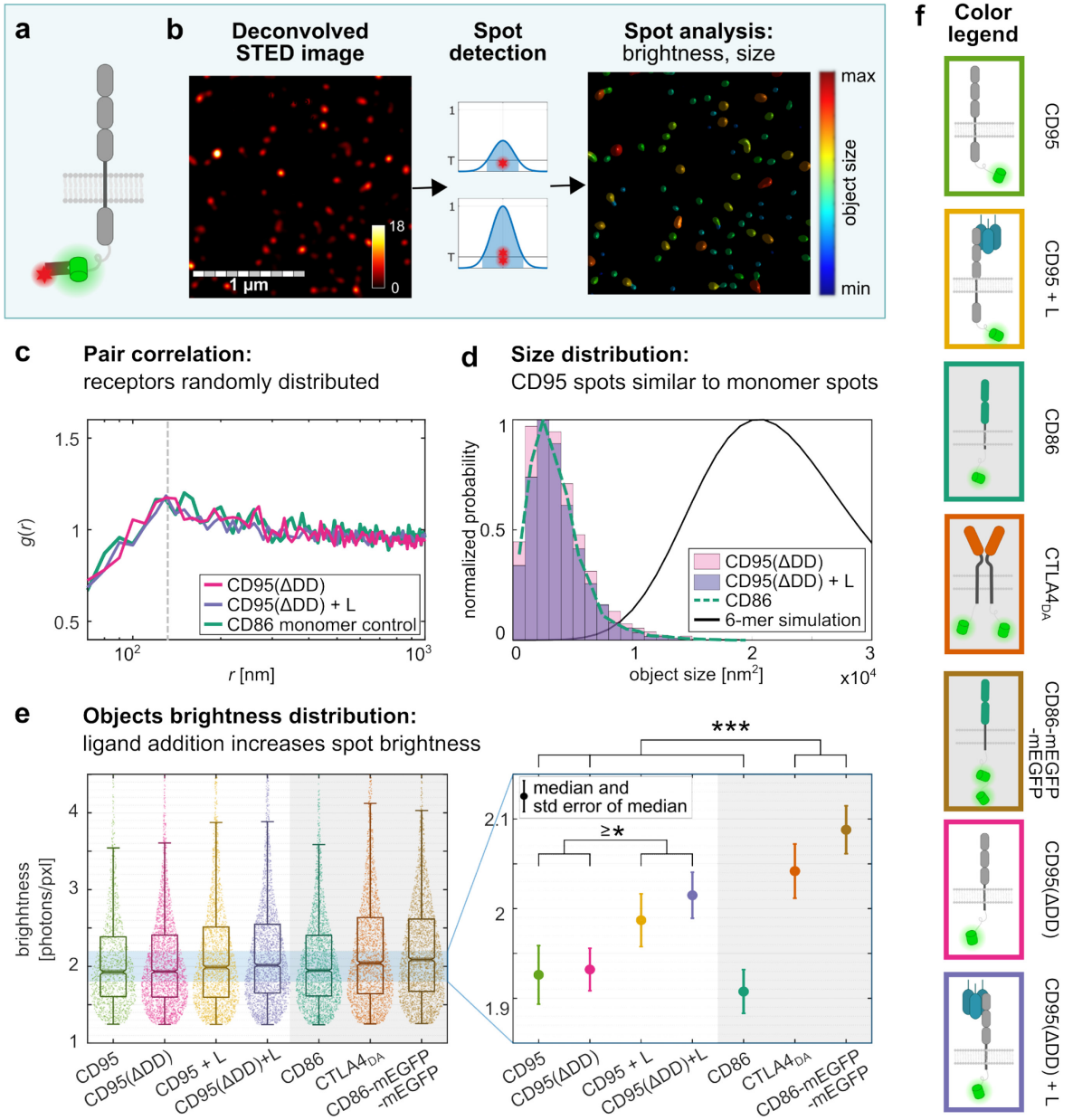

Figure 3: Quantitative STED imaging reveals randomly distributed CD95 spots and systematic changes in object brightness. a) Schematic representation of CD95-mEGFP with GFP-nanobody Atto647N labeling. **b)** Exemplary deconvolved STED image (left) of Hela $CD95^{KO}$ transiently transfected with CD95-mEGFP and threshold-based (T) spot detection and filtering (middle) followed by spot analysis (right) using Huygens SVI. Blue panels illustrate the method. **c)** Pair correlation function $g(r)$ (Equation (3) in Methods) of detected spots for CD95(ΔDD) with/without ligand as well as CD86 monomer control. Distances $r \geq 130$ nm (right of dashed line) with $g(r) \approx 1$ indicate a random distribution. The decrease in correlation for $r < 130$ nm arises from finite PSF size effects and no particular distribution (see also Supplementary Figure 5b). **d)** Size distribution of detected spots. CD95(ΔDD) object sizes in the presence and absence of CD95 ligand do not exceed the spot sizes adapted by the CD86 monomer control. Simulation of a 6-mer illustrates the distribution expected for higher order clusters. **e)** Violin - box plots show the distribution of object brightness up to 4.5 photons/pxl for all samples (left). Detail of median brightness (right) reveals a significantly higher value for dimer controls (>2 photons/pxl) compared to CD86, CD95, and CD95(ΔDD) in absence of

the ligand. Ligand addition shifts the median brightness of CD95 and CD95(ΔDD) towards the dimer controls. Mann-Whitney U-test with ***: $p < 0.001$, *: $p < 0.05$. **f)** Legend: cartoons illustrating the sample receptors. Box color code for each receptor used throughout the manuscript.

Confocal Photobleaching Step Analysis (cPBSA) identifies sensitive changes in ligand-induced receptor recruitment

Since STED and FCS are not sensitive enough to quantitatively determine the CD95 oligomer fraction and stoichiometry in resolution-limited spots, we also used Photobleaching Step Analysis (PBSA). In the past, PBSA was used to measure *in vitro* samples with photostable organic fluorophore labeling, to determine the number of membrane bound proteins[16], the degree of Quantum Dot labeling[17], or the number of fluorescent labels on DNA origami[18], amongst others. To apply PBSA to CD95, we advanced the technique to be compatible with widely available confocal microscopes and to use it with intracellular fluorescent labels with minimal background noise and without bleaching large areas of the cell (Figure 4a-c). Additionally, the confocal setup gave us full access to spectroscopic tools, which we used here to robustly interpret mEGFP bleaching steps despite the lower photostability and brightness of mEGFP compared to stable organic fluorophores (see Supplementary Note 3, Supplementary Tables 2-4**,** and Supplementary Figures 7-12). For example, signal fluctuations due to dark states were quantified by computing the cross-correlation function of the polarization-resolved intensity traces, $G_{\mathrm{ps}}(t)$, which allowed us to determine characteristic relaxation times for blinking, t_{b}, and bleaching, t_{bleach} (Figure 4d). Although we used circular polarized excitation, polarization effects arising from the presence of static emission dipoles caused variations in the single fluorophore brightness, similar to observations made with STED (Supplementary Figure 10). cPBSA was realized by a fast overview scan of the cell's lower membrane to identify receptor locations followed by placing a diffraction limited spot at the respective region of interest and recording the bleaching trace (Figure 4a-c; compare Methods). As the fluorophore brightness shifted slightly from day to day due to laser power changes, we calibrated the effect of brightness variations by changing the time bin sizes *in silico*, which is analogous to changing the laser power. This showed that the number of steps scaled with the laser power (Figure 4e). Subsequently, we correct for this effect by adjusting the minimal step size by the same factor (compare Methods, Supplementary Table 2 and Supplementary Figure 8). Thereafter, the Kalafut-Visscher (KV) algorithm[18,19] was used to derive the number of fluorophores per measurement spot.

In all cPBSA measurements mostly single, double or triple bleaching steps were detected. Only dimer controls exhibited bleaching traces with a higher number of fluorophores per spot. In case of CD95 and CD95(ΔDD) more than 70% of traces exhibited a single step, 23% two steps and about 2% three or more bleaching steps. Upon ligand addition, the fraction of monomers decreased to about 60%, whereas traces of two or three bleaching steps rose to 25% and 5%, respectively (Figure 4f). In absence of the ligand, CD95 and CD95(ΔDD) exhibited a similar distribution of detected fluorophore number compared to CD86 and also the average fluorophore number ($\langle N_{\mathrm{steps}} \rangle$) of 1.33 was identical for these cases. Hence, we concluded, that CD95 is monomeric in its inactive state.

Note, that an elevated average fluorophore number of $\langle N_{\mathrm{steps}} \rangle = 1.33$ instead of 1 was found, since also multi-step events corresponding to multiple fluorophores in a single confocal detection volume were recorded (Figure 4g). Intriguingly, these were found in all datasets,

including the monomer control dataset. As in case of our STED data, such events may arise from true oligomerization as well as molecular accumulation due to local concentration fluctuations. To estimate effects of molecular proximity within the confocal volume on the appearance of multi-step traces, we calculated an occupancy probability based on the signal density above a particular threshold (Supplementary Figure 8). For this, a weak correlation with $\langle N_{\text{steps}} \rangle$ was found, supporting the concentration fluctuation hypothesis. We further verified, that the occupancy probability distribution was comparable between samples, such that no additional correction of traces had to be introduced. After ligand incubation, a slight shift to higher oligomerization states was observed for CD95 (+7%) and CD95(ΔDD) (+6%) with an average fluorophore number rising to 1.42 (Figure 4f/g). To interpret this change in light of the appearance of local concentration fluctuations or photophysical effects, we rated it against the dimer controls CTLA4_{DA} and CD86-mEGFP-mEGFP. The two-step controls were significantly higher than all other measurements ($p < 0.001$) with CD86-mEGFP-mEGFP and CTLA4_{DA} exhibiting $\langle N_{\text{steps}} \rangle$ of 1.92 and 1.78, respectively. The value for CTLA4_{DA} was slightly lower than for CD86-mEGFP-mEGFP for the same reasons mentioned in case of STED. Both values were also smaller than the expected value of 2, most probably due to the maturation efficiency for mEGFP being $\lesssim 80\%$ [16,20]. Yet, on the other hand, the difference to the monomer control was higher than for nanobody staining because no additional preparation step was needed. Overall, cPBSA analyses showed that few CD95 receptors accumulating in spots are sufficient to trigger apoptosis effectively.

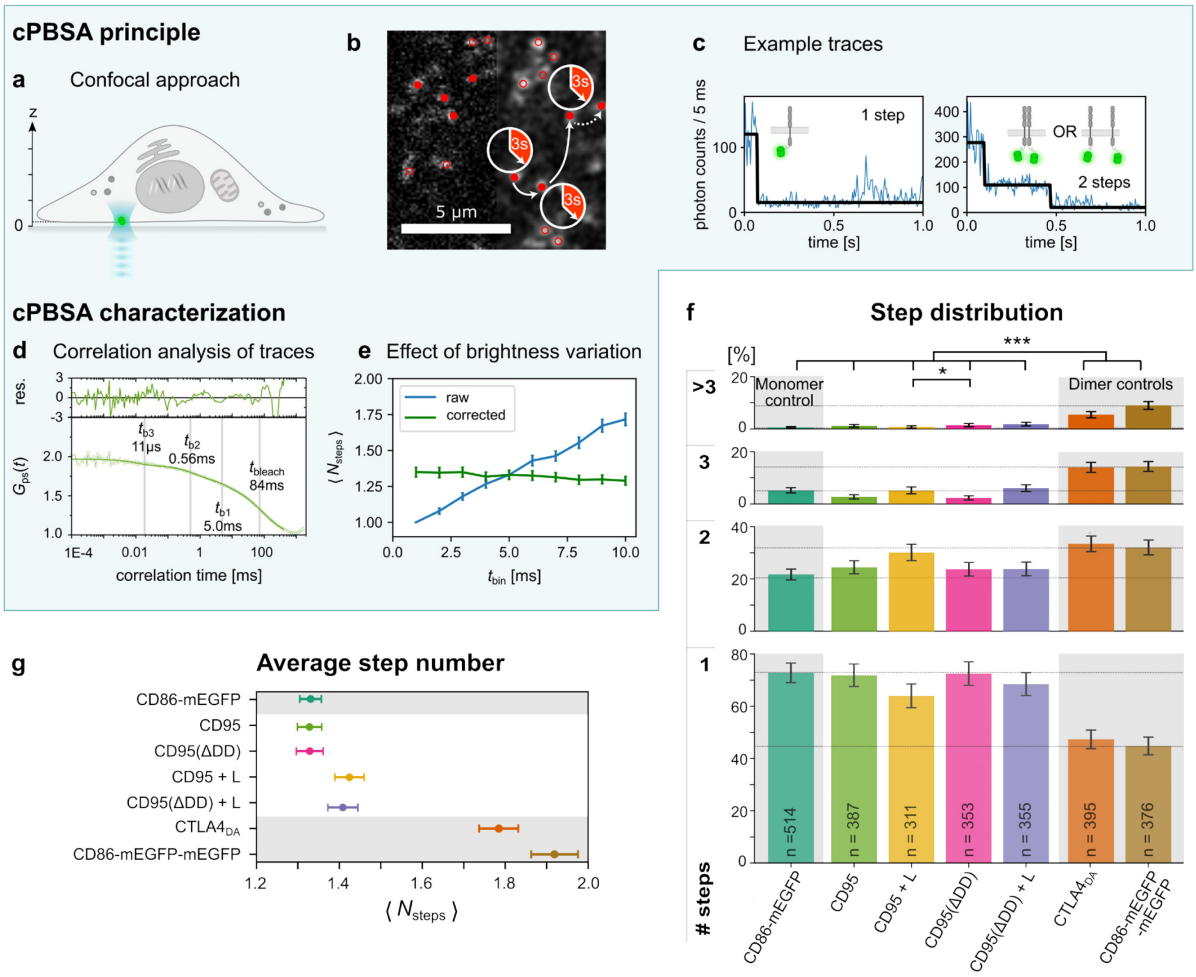

Figure 4: Confocal PBSA reveals the stoichiometry of CD95 in fluorescent spots. cPBSA principle: a) The confocal approach enables local trace analysis with minimal overall sample

bleaching. Traces may be recorded subsequently at different positions on or inside the cell. **b)** Confocal PBSA spot detection algorithm: acquired confocal overview image (left-half) is smoothed using a Gaussian filter with 1 pixel sigma (right-half). Fluorescent spots exhibiting maxima higher than 4 photons (red circles) and diffraction limited areas with no adjacent neighbors are selected (red dots). Bleaching traces are recorded from each red dot for 3 seconds. **c)** Left: exemplary trace of a monomer. Right: exemplary trace for either a dimer or two monomers in one confocal spot (crowding). **cPBSA characterization: d)** Cross-correlation function $G_{\mathrm{ps}}(t)$ (Equation (8) in Methods) of CD95 bleaching traces yield characteristic correlation times of mEGFP blinking and bleaching events in cells. Characteristic time scales are derived from a 4 term global fit (see Supplementary Figure 10). **e)** Increasing the time bins (which is analogous to an increased brightness) increases the number of steps found. This is corrected for by changing the minimal step size in the same proportion (see Supplementary Figure 8). **cPBSA results f)** Bar diagram of step occurrence. 1,2 and 3 photobleaching steps were primarily detected. The monomer and dimer controls are used to characterize the fraction of multimer events attributed to crowding. Errors bars are calculated from Poisson statistics. **g)** Mean number of fluorophores and standard error of the mean for data shown in f). A small increase in fluorophore number is detected for CD95 (* with $p = 0.026$) and CD95(ΔDD) (n.s. with $p = 0.169$, Mann-Whitney U-test with ***: $p < 0.001$, *: $p < 0.05$) in presence of the ligand. The average fluorophore number is significantly smaller compared to those of dimer controls.

CELFIS reveals for a large receptor concentration range that 8-17% monomers becoming part of dimers and trimers suffice for efficient apoptosis induction.

Finally, since the above techniques are not capable to distinguish molecular proximity from intermolecular interactions within diffraction- or STED resolution limited spots and have limited capacity to probe variability in biological phenotype, we used and advanced FRET to probe transfected cells with different receptor surface concentrations.

As before, CD95 and CD95(ΔDD) were measured in absence and presence of the ligand. The monomeric receptor CD86 served as a negative no-FRET control and CTLA4 as a dimeric positive control. In all cases, bicistronic plasmids were used to ensure homogeneous donor and acceptor expression. Figure 5a shows the localization of the CD95 receptor in live cells by confocal images on the lower cell membrane. The increased intensity at cell edges and cell-to-cell contacts confirms the primary integration of the receptor into the cell plasma membrane. Similar images were recorded for CD95(ΔDD), CD86 and CTLA4 (see Supplementary Figure 1).

To systematically tune the range of receptor surface concentrations and to thereby obtain insights about the molecular concentration fluctuations suggested by the above techniques, we titrated the amount of receptor DNA used for transfection against an empty vector, while keeping the total amount of DNA constant. We further determined the molecular brightness of the fluorophore to convert fluorescence intensities into surface densities, $N_{\mathrm{FP}}/\mu\mathrm{m}^2$. Here, changes of the donor fluorophore lifetime due to FRET only occurred, if receptors labeled with a mEGFP donor and a second receptor with a mCherry acceptor molecule were in close proximity due to binding (< 10 nm).

For Cell Lifetime FRET Image Spectroscopy (CELFIS*)*, we evaluated the data of receptors on the lower cell membrane and integrated all photons over the cell bottom surface in a single

fluorescence decay per cell to determine the average oligomerization state with great accuracy. Figure 5b illustrates the core principle of CELFIS: the fluorescence decay was measured in the FRET sample (DA) as well as the control sample, expressing the donor in absence of the acceptor (D0). Normalizing the DA fluorescence decay with respect to the average D0 decay allows one to extract the FRET-induced donor decay ($\varepsilon_{\mathrm{D}}(t)$), equations (9-12)[21-23]. Its amplitude drop directly corresponds to the donor fraction, x_{FRET}, which was quenched by FRET[22].

We determined x_{FRET} values for each cell individually and studied its dependence on the receptor surface concentration $N_{\mathrm{FP}}/\mu\mathrm{m}^2$ (Figure 5c). Thereafter, we benchmarked the data of CD95 against signals obtained from the CD86 and CTLA4 controls. As expected, we observed no FRET for CD86 which was predominantly monomeric up to a concentration of 1250 receptors/µm². At this point, a systematic increase in FRET indicates the onset of proximity FRET, which was also observed for CD95 and CD95(ΔDD) in absence of the ligand. For this reason, and since proximity FRET was suggested to lie in this concentration range[24], we evaluated the FRET data only up to the threshold of 1250 receptors/µm². FRET measurements of CD95 and CD95(ΔDD) without ligand likewise showed that both receptors are monomeric. Upon ligand addition, the value of x_{FRET} increased immediately by a few percent. Together with our cPBSA results, these values suggested formation of dimers and/or trimers (Figure 5c). Finally, we derived a relation to approximate the oligomer fraction from the measured x_{FRET} by calculating a sample-specific maximum FRET signal $x_{\mathrm{FRET,max}}$ for a purely dimeric sample (see Methods). This calibration accounts for i) the distance distribution between the two fluorescent proteins with long linkers[21,25] (see linker list in Supplementary Table 5), ii) the abundance of no-FRET species due to donor-donor dimers and iii) an estimated maturation efficiency of 80% for EGFP and mCherry[16,20], yielding a $x_{\mathrm{FRET,max}}$ of 29% and 26% for CTLA4 and CD95, respectively. Hence, for the CD95 protein, a pure dimer sample (100% dimers) corresponded to 26% x_{FRET} and, equally, 1% x_{FRET} corresponded to a ~ 3.8% oligomer fraction. The calculation for CTLA4 was analogous.

Equipped with these tools, we then probed how the oligomerization state changed over time until the point of apoptosis. Here, we recorded FRET data over 0 to 6 hours after ligand addition by repeated measurements of the same cells. Cells expressing the full-length CD95 were classified according to whether apoptosis occurred within the observation time of 4h (Figure 5d). For those that underwent apoptosis, the oligomer fraction started close-to-zero and increased quickly up to an 8% median value, whereas cells that did not show apoptosis exhibited a slower oligomer formation, reaching a ~ 5% median after 4h. CD95(ΔDD) expressing cells, where downstream signaling was suppressed, showed a slightly higher initial oligomer fraction and reached a population equilibrium of 12% median after ~ 3h. In individual cell traces rising and/or falling oligomer fractions were detected (Figure 5e), representing transient CD95 dimerization or binding/unbinding kinetics of CD95 to CD95L (see Methods for further analyses). As a measure of CD95 oligomerization needed to initiate apoptosis, the oligomerization fraction just prior to apoptotic blebbing and shrinkage was estimated, amounting to the interquartile range of ~ 8 to 17% with a median value of 12% (Figure 5f). Finally, we determined the oligomerization rate from the oligomer fraction change per time interval, which was faster in case of CD95 transfected cells that died (3.9% oligomers/h) compared to CD95 or CD95(ΔDD) transfected cells which stayed alive (with 1.3% and 1.8% oligomers/h respectively, Figure 5g). We further investigated the oligomeric state in membrane areas classified according to their brightness, revealing that the oligomerization is not limited

to certain areas and occurs according to its concentration dependence (see Supplementary Note 5 and Methods). Overall, our results demonstrate that oligomers form within 2 - 3 hours over the whole membrane. Oligomerization requires ligand addition and can develop in absence of a death domain, indicating that CD95 oligomerization may be mediated by the transmembrane domain only in the receptor activated state, as previously suggested[26], or simply via ligand binding. Finally, only about ~ 8 - 17% oligomers in the form of dimers or trimers are necessary for efficient signal initiation.

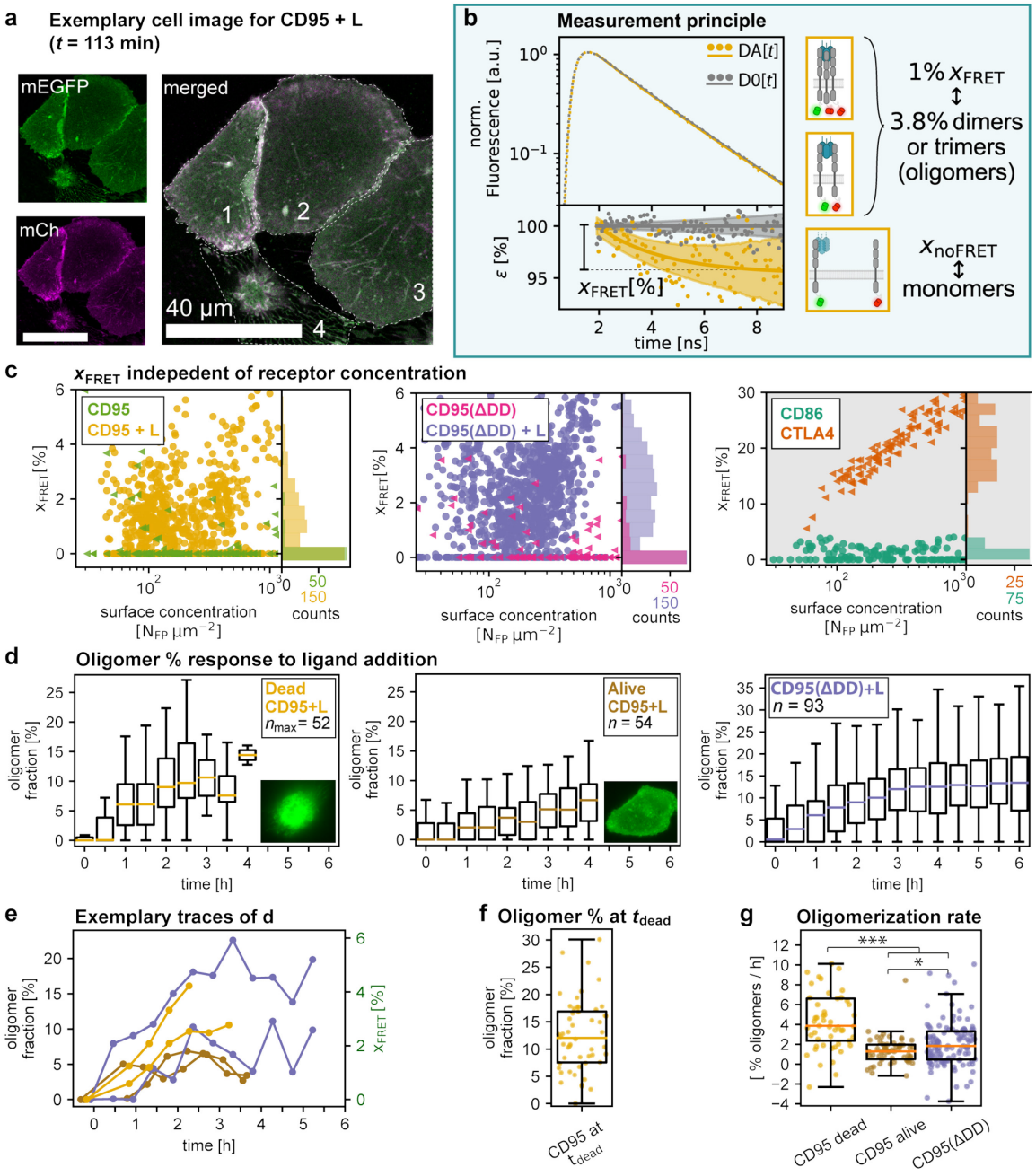

Figure 5: CELFIS quantifies the CD95 oligomerization state over a large concentration range. a) Confocal fluorescence image indicating correct integration and colocalization of mEGFP and mCherry labeled CD95 in the membrane. Cells 1, 2 and 3 are alive at the time of measurement, whereas cell 4 already underwent apoptosis. Fluorescence lifetimes were recorded over the whole cell membrane for each cell. **b) Measurement principle:** Top: fluorescence lifetime distribution for a live cell in absence (D0) and presence (DA) of FRET.

Bottom: normalized fluorescence decay ε shows the quenched fluorescence fraction (x_{FRET}) in presence of the acceptor due to FRET. Conversion of x_{FRET} into oligomer fraction was realized by a theoretical x_{FRET} determination of a pure dimer sample (see text). Blue panels illustrate the method. **c)** x_{FRET} histogram and scatter plot as a function of receptor surface density. CD95, CD95(ΔDD) and the monomer control CD86 are monomeric over the whole concentration range. After CD95 ligand incubation, a small fraction of CD95 and CD95(ΔDD) oligomerizes to dimers or trimers. Intriguingly, CTLA4 switches from a monomer to a dimer with increasing receptor concentration. N > 324 cells from at least 4 independent experiments were analyzed per condition. **d)** Dynamics of oligomer formation after CD95 ligand addition. The oligomer fraction was calculated from repeated measurement of the same cells and averaging over many traces. Boxplots are shown with colored medians. Oligomer fractions saturate after 3-4h. **e)** Exemplary evolution of the oligomer fraction in single cells over time. Legend same as in d). **f)** Boxplot of the oligomer fraction at the last time point before apoptosis. **g)** Oligomerization rate over the first 3 hours or less due to the timepoint of apoptosis. Legend same as in d). Mann-Whitney U-test with ***: $p < 0.001$, *: $p < 0.05$.

Discussion

Here, we present an advanced molecular sensitive imaging toolkit combined with multiscale analysis to decipher the spatiotemporal organization and dynamical interactions of CD95 during signaling in the cell plasma membrane. We determine CD95 oligomerization states and find receptors to be initially monomeric and homogeneously distributed on the cell plasma membrane. In previous studies TNFRs (including CD95) were reported to appear as monomers, dimers or trimers in the absence of a stimulus[8,27]. Pre-ligand dimer- and mostly trimerization of CD95 was reported in several works, where receptors were purified and reconcentrated (e.g. ~ 0.5 mg protein/ml[28]) from E.coli or mammalian cells and analyzed by gel filtration, western blot or crystallography[8,28-30]. In three further studies based on crystallography and NMR spectroscopy, CD95 was suggested to form higher oligomeric structures of penta- or hexagonal shape in bicelles (Figure 6a). In contrast to these biochemical *in vitro* approaches that can affect structural features in membrane proteins[31], molecular sensitive imaging of receptors directly in the cell plasma membrane revealed primarily monomer and dimer formation[27,32]. Our data obtained in live cells without fixation and staining confirms the latter results and suggests that the situation in the native membrane environment, with small or no oligomers developing, is significantly different from the purified receptor case (Figure 6).

After ligand addition, we find dimers and trimers forming within the first 2-3 hours with a final fraction of 8 to17% receptors exhibiting oligomerization. Interestingly, the majority of previous studies reports CD95 and other TNFRs to be trimeric after ligand addition. Among these, molecular sensitive techniques, such as crystallography, single molecule localization microscopy, and biochemical receptor cross-linking studies favor the trimeric state[3,6,7,27,33]. A general observation of molecular clustering was also reported in widefield fluorescence microscopy studies, albeit without quantifying molecular numbers or interactions[27,34,35]. Now, being equipped with the toolkit to quantify molecular oligomerization as presented herein, it would be interesting to also reconsider these cases.

From a structural point of view, three types of molecular interactions are currently discussed to give rise to TNFR signaling and to explain the reported observations: (i) the direct coupling of up to three receptors to the ligand, without the need of direct intermolecular interactions between receptors, (ii) interactions between CD95 transmembrane domains after ligand activation[26], and (iii) intracellular crosslinking of two CD95 DDs via FADD[36,37]. Cases (i) and (ii) would result in close packing of CD95 receptors with few nm intermolecular spacing around the ligand up to a trimer-trimer configuration[38]. Case (iii) suggests that recruitment of FADD and interaction with the DD results in crosslinking of two DDs. If a crosslinking between different trimer-trimer units occurs, also the higher oligomeric structure of hexagons could develop, placing the receptors some ~ 12 nm apart (with exact values varying between TNFRs)[9,10,36,39]. Yet, the DD-FADD interaction was reported to be weak[36] and may not occur at low CD95 and FADD concentrations. This may explain the appearance of higher oligomeric structures when purified and reconcentrated CD95 and FADD were investigated[39]. Moreover, as shown in our study, full length CD95 exhibited near identical oligomerization behavior compared to DD truncated receptors, demonstrating that efficient signaling is possible in the absence of DD-DD crosslinking (Figure 5c,d). This leads to the conclusion that the observed CD95 dimer/trimer formation is mediated via direct ligand (i) or ligand-induced transmembrane (ii) interactions.

The difference in oligomeric states found in case of purified receptors relative to cell membrane samples underscore the importance of the physical and molecular environment in which CD95 is measured. This is not surprising, as already molecular mobility and consequently any interaction probability is highly different in purified samples compared to CD95 embedded in the cell plasma membrane (e.g. protein membrane diffusion of $D \sim 0.2\ \mu m^2/s$ versus protein diffusion in solution $D \sim 50\ \mu m^2/s$[40]). More importantly, molecular concentration and environment will influence the oligomerization state. In case of the purified samples in presence of detergents a rather high sample concentration of ~ 100 µM was reported [36]. In cell lines, we determined molecular expressions to 10 to 1000 receptors / μm^2, where the lower limit marks the physiological expression level and the upper limit concentration regime is already found in *in vitro* studies. Despite this broad range of concentrations covered in live cells, our data did not show signatures of higher oligomers, suggesting that either concentrations are still too low or that CD95 in contrast to other TNFRs does not form any hexagonal network. Indeed, previous *in vitro* studies of purified TRAIL coupling to Death Receptors 4 and 5 reported changes of molecular stoichiometries in the protein complex only upon increasing molecular concentrations by orders of magnitude from 1 nM to 10 µM[41]. Hence, we conclude that higher oligomerization states of CD95 without ligand may only develop at very elevated receptor concentrations or under conditions, where the hydrophobic region of the receptor such as the transmembrane helix is not fully immersed in a lipid membrane layer, e.g. bicelles[26] or in a particular cell membrane environment[41].

While no significant changes in molecular oligomerization are detected, there is a remarkable change in signaling dynamics and the percentage of apoptosis events depending on the absolute ligand and receptor number. Here, as well as in previous studies[34,42], using different cell types and CD95 expression levels between $5 \cdot 10^3 - 450 \cdot 10^3$ receptors/cell, a significant acceleration of downstream signaling and systematic increase of apoptosis events was shown when receptor or ligand concentrations were increased. Hence, tuning the absolute number of activated receptors turns out to be a crucial aspect in apoptosis signal initiation.

To provide the above insights, we assembled a multiscale toolkit to cover spatial, stoichiometric and temporal resolution needed for studying receptor oligomerization. The toolkit consists of six techniques including super-resolution and multiparametric fluorescence imaging which were advanced to record data with single-molecule sensitivity. In particular, we established a quantitative spot analysis of STED data, verified receptor mobility with FCS, and determined CD95 stoichiometries in fluorescent spots from cPBSA. In case of the latter, mEGFP fluorescence labeling as well as confocal instead of Total Internal Reflection Fluorescence imaging was established, making cPBSA measurements applicable to common biological samples and more flexible in space, respectively. The automated workflow for time-resolved FRET image spectroscopy in live cells (CELFIS) was developed by the authors during the course of this study to measure and analyze large numbers of cells to obtain the required precision and sensitivity to determine oligomerization states over the whole cell and during the signaling process. Our study highlights the need for parallelized measurements using complementary techniques (in terms of their spatio-temporal resolution and molecular concentration detection) to probe a high dynamic range (µs to hours, nm to 100 µm scales, 1 to 10^4 molecules/µm^2) Finally, benchmarking CD95 data against robust monomer and dimer controls, revealed that intense regions on the membrane initially associated with higher oligomerization states may simply arise from molecular concentration fluctuations across the membrane.

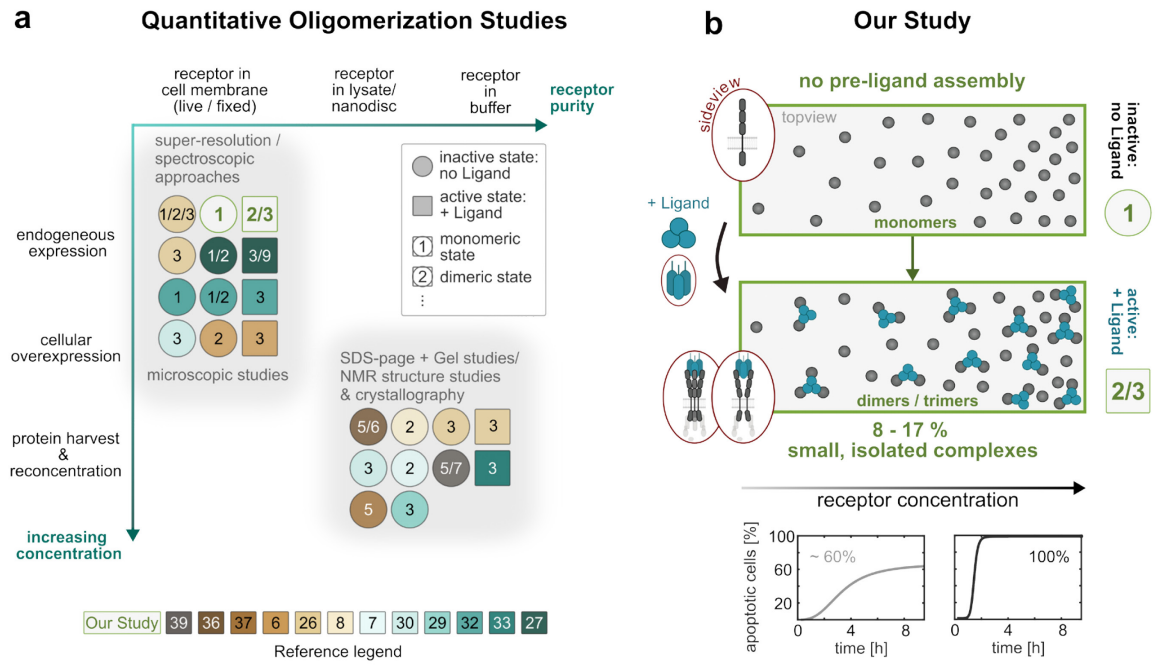

Figure 6: CD95 oligomerization state over a large concentration range. a) Summary of studies on quantitative TNFR oligomerization in context of the measurement parameters receptor concentration and receptor environment for different measurement technique. Numbers in circles or boxes indicate the measured oligomerization grade. Numbers in the reference legend correspond to publications in the reference list. **b)** Schematic illustration of the minimal model of CD95 signal initiation shown in this study: monomeric receptors (no pre-ligand CD95 assembly). After ligand binding 8 to 17% of receptors form small, isolated

complexes. Increasing receptor concentrations (surface expression level) do not lead to higher oligomer fractions. Since a higher number of apoptotic cells is obtained with increasing receptor concentration, the absolute number of active, oligomerized CD95 appears as a decisive parameter.

To our best knowledge, this study is the first to report a minimal model of CD95 signal initiation, identifying 8 - 17% CD95 monomers oligomerizing to dimers and trimers as efficient apoptosis signal inducers in live cells (Figure 6b). Our results do not exclude the existence of proposed higher order oligomeric states, but confirm that they are not necessary in the studied cellular context. In this respect, our study highlights the importance of molecular concentration level determination as well as the use of high-fidelity monomer and dimer controls for quantitative molecular imaging. Our study not only elucidates the debate about CD95 signal initiation mechanisms but also reports strategies of single molecule quantification in live cells, which are generally important for the study of cell signaling processes.

Methods

Sample preparation

Plasmids, molecular cloning and stable cell lines

For all measurements with transient transfections, a stable Hela cell line with knockout for CD95 was used (HeLa $CD95^{KO}$). It was generated using CRISPR/Cas9[43], the guide RNA was CATCTGGACCCTCCTACCTC[32]. For apoptosis dynamics, we additionally used Hela WT cells (purchased from the American Type Culture Collection (ATCC, Manassas, Virginia, USA)) and a stable, overexpressing cell line HeLa CD95-mEGFP, expressing CD95-mEGFP on top of endogenous CD95[32]. Hela $CD95^{KO}$ and Hela stable CD95-mEGFP cell lines were kindly provided from *Joël Beaudouin* (formerly IBS, Grenoble).

For CD95 constructs, four different sequences were used: the full-length protein CD95 (amino acids 1-335), a death domain truncated version CD95(ΔDD), CD95(R102S) and CD95(ΔPLAD). For CD95(ΔDD) amino acids 211-335 were truncated. CD95(ΔDD) is not capable to transduce the intracellular signal and is hence ideally suited for long-time observations after ligand incubation as well as to probe oligomerization mediated by the extracellular and transmembrane domain of CD95. CD95(ΔPLAD) is the PLAD (pre-ligand assembly domain) depleted variant, missing amino acids 26-83. It may be used to detect pre-oligomerization based on transmembrane and intracellular interactions. All amino acid numbers refer to the premature protein sequence (including signaling peptide). CD95(R102S) exhibits a mutation at amino acid 102 (pre-mature protein) and is suitable as control that cannot bind the ligand.

As monomer control plasmid, the full-length sequence of CD86[44] was used. For the dimer control CTLA-4, the last 23 amino acids of the sequence were removed in order to reduce the internalization of the receptor and to concentrate it at the plasma membrane[45]. As a second (pseudo-) dimer control, CD86 was fused to two consecutive mEGFPs. The UniProtKBs of CD95, CTLA4 and CD86 are P25445, P16410 and P42081-3, respectively.

All plasmids except CD86-mEGFP-mEGFP were as well kindly provided from *Joël Beaudouin* (formerly IBS, Grenoble). These plasmids were designed by fusing the coding sequences of the respective proteins C-terminal (intracellularly) via a linker to mEGFP (called D0 / Donor only) or mCherry in the pIRESpuro2 vector (Clontech)[32] (for more linker details see Supplementary Table 5). Besides these monocistronic constructs for CD86, CD95, CD95(ΔDD) and CTLA, we additionally used bicistronic plasmids combining the mCherry and mEGFP versions of a protein into one plasmid for FRET measurements to ensure homogeneous co-expression of donor and acceptor (called DA / donor-acceptor), where mCherry is first transcribed and thus more abundant. The bicistronic constructs with a 2A peptide use the sequence EGRGSLLTCGDVEENPGP as linker between the two proteins[32]. Note, that solely $CTLA4_{DA}$ was used instead of $CTLA4_{D0}$, as the latter did not localize to the membrane exclusively.

The CD86-mEGFP-mEGFP pseudo-dimer control was synthesized using a cloning service (*BioCat GmbH* Heidelberg, Germany) by fusing two linked mEGFP proteins C-terminally to the CD86 full-length sequence of CD86 in a pcDNA3.1(+) vector (*BioCat GmbH*).

Cell culture, transfections and ligand incubation
All cells were maintained in culture medium, consisting of DMEM (Dulbecco's Modified Eagle Medium) + GlutaMAX™ (31966021, Gibco, Life Technologies Inc., Carlsbad, California, USA) containing 10% FBS (fetal bovine serum) (10500064, Gibco) and 1% penicillin/streptomycin (P/S) Solution (P0781, Sigma-Aldrich, Merck KGaA, Darmstadt, Germany), in an environment with 5% CO_2 (v/v) at 37 °C.

For all live cell measurements as well as cPBSA, cells were trypsinized (T3924, Sigma-Aldrich) and seeded in an 8-well glass bottom slides (#80827, ibidi GmbH, Gräfelfing, Germany) with a density of 3-5 x 10^4 cells per well. For STED immunostaining, 100-150 x 10^4 cells were seeded on a sterile glass coverslip (13 mm diameter, No. 1.5H, 0117530, Paul Marienfeld GmbH & Co.KG, Lauda Königshofen, Deutschland).

Transfections were obtained using ViaFect™ Transfection Reagent (#E4981, Promega Corp., Madison, Wisconsin, USA) at a cell density of 60-70% following the manufacturer's protocol. For Apoptosis Dynamics, FCS, STED and cPBSA the cells were transfected with 25 ng of target DNA and 975 ng empty vector (pIRES-puro2 or pcDNA) for all used plasmids per two wells of an 8-well slide or one coverslip. For FRET measurements, the bicistronic plasmids were transfected using varying amounts of target DNA to cover a broad range of expression levels: for a transfection in 2 wells, the combinations 25 ng target DNA + 975 ng empty vector, 100 ng target DNA + 900 ng empty vector, 250 ng target DNA + 750 ng empty vector as well as 1000 ng target DNA (no empty vector) were used. Donor only controls (the monocistronic mEGFP fusion version of the proteins) were expressed at these varying concentrations as well.

Live experiments or fixations were done 48-72 hours after transfection. For all live-cell experiments (time-lapse imaging, FCS and FRET), the cells were incubated in Leibovitz's L-15 Medium (21083027, Gibco) without phenol red, supplemented with 10% FBS (10500064, Gibco) and 1% P/S (P0781, Sigma-Aldrich).

For all apoptosis experiments including the CD95 Ligand, the *FasL, soluble (human) (recombinant) set* (ALX-850-014-KI02, Enzo Life Sciences Inc., Loerrach, Germany) was used. The ligand was prepared according to the manufacturers protocol and further diluted in the respective cell culture or imaging medium. The provided enhancer was used for all experiments except FCS. For experiments using the Enhancer, the enhancer concentration was always 100-fold higher than the ligand concentration. For all apoptosis experiments except the apoptosis dynamics, the ligand concentration was 200 ng/ml.

CD95 Quantification by Flow Cytometry
The quantitative CD95 expression level of Hela WT, Hela $CD95^{KO}$ and Hela WT stable CD95-mEGFP was assessed using the QIFIKIT® for quantification of cell surface antigens by flow cytometry (K007811-8, Agilent Technologies, Inc., Santa Clara, California, USA) on a MACSQuant Analyzer 10 (Miltenyi Biotec) following the manufacturer's protocol accurately. For CD95 detection, a monoclonal CD95 antibody (130-108-066, Miltenyi Biotec B.V. & Co. KG, Bergisch Gladbach, Germany) was used. As negative control an antibody against CD28 was used (70-0281, Tonbo™ A Cytek® Brand, San Diego, California, USA). As the secondary FITC antibody provided with the QIFIKIT® interfered with the mEGFP of the stably expressing CD95-mEGFP HeLa cell line, a secondary anti-mouse antibody conjugated to APC (17-4010-82, eBioscience™, Invitrogen) was used for all samples instead. The measurement

was repeated two times independently. For Hela $CD95^{KO}$ with transient CD95-mEGFP, the number was not obtained from flow cytometry but from STED imaging spot density.

Cell fixation and Immunostaining

For cPBSA and STED immunostaining, cells were fixed after transfection within the respective seeding vessel (see Section *Cell culture and transfections*). For experiments including the CD95 Ligand (Enzo Life Sciences Inc.), the ligand was incubated for 2 hours at 37 °C before the fixation.

Before fixation, cells were washed three times with cold washing buffer (HBSS (14025050, Gibco) containing 0.1 M sucrose (57-50-1, Carl Roth GmbH + Co. KG, Karlsruhe, Germany) and 1% BSA (A1391, ITW Reagents, AppliChem GmbH, Darmstadt, Germany)). The fixation was obtained using 4% methanol-free formaldehyde (28906, Thermo Scientific, Life Technologies Inc.) in washing buffer for 10 minutes, shaking at RT. For STED, the fixation buffer additionally contained 0.1% Glutaraldehyde (25% in H_2O, G5882, Sigma-Aldrich), which was not used for PBSA in order to reduce the fixation related green autofluorescence of the sample. Afterwards, cells were washed three times again.

For cPBSA, as a last step, the cells were incubated with 750 mM Tris (Tris(hydroxymethyl)aminomethane, 103156X, VWR Chemicals, VWR International GmbH, Darmstadt, Germany) in DPBS (14190144, Gibco) to quench the autofluorescence of the formaldehyde. Afterwards, they were washed with DPBS (covered with DPBS for the experiment.

For STED immunostaining, the next step was permeabilization with the washing buffer including 0.2% Saponin (47036, Sigma-Aldrich) as permeabilizing reagent for 10 minutes. After 2x washing, the sample was blocked using a blocking buffer (HBSS with 0.1 M sucrose and 4% BSA) for one hour. For the staining step, the GFP-Booster Atto647N (gba647n-100, ChromoTek GmbH, Planegg-Martinsried, Germany) was diluted 1:200 in the blocking buffer and again incubated for 1 hour. Next, extensive washing was done using the washing buffer at least 3 times. As a last step, the coverslips were mounted upside down on a microscope slide using *ProLong™ Diamond Antifade Mountant* (P36965, Invitrogen, Life Technologies Inc., Carlsbad, California, USA) and stored over night before imaging.

Methods

Time-Lapse imaging for apoptosis dynamics
The time-laps measurements were performed on an IX83 inverted epi-fluorescence microscope system (Olympus Europa SE & CO. KG, Hamburg, Germany) (details in section *Microscope setups*) using either a 20x oil-objective (NA 0,85, UPLSAPO20xO) or a 60x oil-objective (NA 0.65–1.25, UPLFLN60XOIPH) on a temperature-controlled on-stage heating system (PeCon GmbH, Ulm, Germany) at 37 °C. The CD95 Ligand (Enzo Life Sciences Inc.) (Section *Cell culture, transfections and ligand incubation*) was added to the cells to the desired final concentration on the microscope. Time-lapse videos were acquired with the *CellSense Dimensions* Software (Olympus) by sequential imaging of the phase-contrast channel and, if available, the mEGFP channel (excitation 470/40 nm, emission 525/50 nm) at multiple positions every 5 to 15 minutes over 10 hours. Image analysis was performed with Fiji[46], using an intensity-based threshold to the fluorescence channel in order to detect successfully transfected cells. Apoptotic cells were manually identified via the phase-contrast channel.

For a mathematical description of the sigmoidal apoptosis dynamics curves $P(t)$, they were fitted (MATLAB R2019a, The MathWorks, Inc.) using the hill equation to characterize the dynamics and cooperativity of the cell response:

$$P(t) = P_{\max} - \frac{P_{\max} - P_{\min}}{1 + \left({}^{t}/_{t_{\text{half}}}\right)^{n}} \tag{1}$$

$P_{\min}$ and $P_{\max}$ are the minimal and maximal fractions of apoptotic cells and t_{half} is the characteristic time after that half of all apoptotic cells died. The hill coefficient (also cooperativity coefficient) n indicates the efficiency of the signal induction.

STED imaging and analysis
STED images were recorded on the Abberior Expert Line Setup (Abberior Instruments GmbH, details in section *Microscope setups*). All immunostained samples (section *Cell fixation and Immunostaining*) were imaged with a 640nm excitation laser (5.3 µW) and a 775 nm STED depletion laser (41 mW) using an oil-immersion objective (NA 1.4, UPLSAPO 100XO, Olympus Europa SE & CO. KG). Before the measurements, channel alignment was performed manually using TetraSpeck Microspheres (T7279, Invitrogen). ROIs of 5 µm x 5 µm (10 nm pixel size, 4.00 µs dwell time, 5 frames) of the bottom cell membrane were recorded.

Deconvolution & object analysis on STED data
As a first step of data processing, time-gating of the first 2.2 ns was employed to increase the achievable resolution using the home-built programm AnI. The sum of the parallel and perpendicular polarized images was used for further analysis. For deconvolution and image data analysis, Huygens Professional (HuPro Version 21.10.1p2 64b, Scientific Volume Imaging B.V., Hilversum, Netherlands) was used. The deconvolution was performed using the CMLE (Classic Maximum Likelihood Estimation) algorithm with a signal-to noise ratio (SNR) of 3. The convergence stop criterium was set to 0.01 or a maximum of 40 iterations. The automatic background estimation was used with a search area of 0.7 µm radius. After deconvolution, the Object Analyzer of Huygens was used to quantify the object properties of the membrane protein spots. The global object threshold was 1.2 with a seeding level of 1.3, the garbage volume was 2 voxels. Objects touching the image border were excluded from the analysis and only objects

with an aspect ratio $0.9 < D_x/D_y < 1.11$ of the diameters D in x and y were considered as elongated objects result from crowding. It was verified that this sphericity filter did not preferentially filters large objects.

The size distribution of a 6-mer was simulated by multiple (5x) convolution of the monomer control size distribution with itself.

Spot Anisotropy Analysis

The spot intensities of the parallel (P) and perpendicular (S) channel, I_P and I_S, were determined with an individual object analysis of both images (compare Chapter before). The steady state anisotropy r was calculated with

$$r = \frac{GI_P - I_S}{GI_P + 2I_S} \tag{2}$$

where the polarization correction factor $G = \eta_P/\eta_S$ corrects for the instrument's polarization dependent transmission. η_P and η_S are the detection efficiencies of the parallel and perpendicular detection channels. The polarization correction factor G was determined to be 0.905.

Pair correlation

The distribution of object points was analyzed using the pair correlation function $g(r)$[47]:

$$g(r) = \frac{1}{\pi\rho^2 r\gamma(r)} \sum_{i=1}^{N} \sum_{j=i+1}^{N} \mathrm{k}\left(r - \left|\mathrm{p}_i - \mathrm{p}_j\right|\right) \tag{3}$$

where ρ is the object density in the image, and $\left|\mathrm{p}_i - \mathrm{p}_j\right|$ is the distance between two object points p with two-dimensional position (x, y). The object positions were assumed to be planar. The covariance function γ and kernel k are defined in[48].

The pair correlation of the objects found by the Huygens Object Analyzer was calculated using a locally designed MATLAB script (R2019a, The MathWorks, Inc.) following the example of [48]. The correlation histogram $g(r)$ was calculated for binned distances with a bin with of 10 nm and a bandwidth of 5 nm. The data of all STED images per sample were averaged.

In order to compare the pair correlation of real STED images with a simulation of randomly distributed objects, we simulated images comparable to the real data. Using MATLAB (R2019a), 500x500 pixel images with randomly distributed object centers were created. The number of object points per image was selected randomly between 300 and 600 per image and the pixel value was adjusted to 4 (photons/pxl) to match the real data average. Next, the spots were filtered using a 2D Gaussian smoothing kernel with standard deviation of $\sigma = 2.5$ pixel. Subsequently, 20 simulated images were analyzed using the Huygens Object Analyzer similar to the real data (compare previous section) and finally the pair correlation $g(r)$ of simulated data was calculated.

FCS measurements

For sample preparation see method section Cell culture, transfections and ligand incubation.

Calibrations. Calibration of the LSM setup was performed according to established procedures in our research group[49]. Briefly, the optimal correction collar setting was found by minimizing the number of Rhodamine 110 (#83695, Sigma-Aldrich) molecules in the focus. For all our experiments the correction collar matched our coverslip thickness (170 µm). The instrument response function (IRF) was measured using a mirror to enable time-correlated-single-photon-counting (TCSPC) analyses. Next, we measure a Rhodamine 110 solution with 1-5 molecules in the focus to obtain 1) a calibration for the confocal spot shape factor, $\boldsymbol{z_0/\omega_0}$ or $\boldsymbol{\kappa}$, 2) the ratio of the parallel and perpendicular detection efficiencies, $\boldsymbol{\gamma}$, 3) the number and brightness of Rhodamine 110 molecules in the focus and 4) the confocal detection volume by inserting a Rhodamine 110 diffusion constant $D = 430\ \mu m^2/s$ when the calibration was recorded at room temperature (22.5 °C)[50] or 600 µm²/s when it was recorded at 37 °C considering the temperature dependence of $\boldsymbol{D}$.

The laser power was measured at the sample using an immersion S170C power meter head (Thorlabs GmbH, Lübeck, Germany) attached to a PM400 power meter body (Thorlabs GmbH, Lübeck, Germany). As the power varied by ~10% when translating in x, y and z, we avoid a systematic error by varying the position until maximum power is reached.

Recording procedure. A confocal microscope was used to bring the bottom membrane in focus. The diffraction limited focus was placed in a stationary position away from the edge of the cell and away from the endoplasmic reticulum (ER) and Golgi apparatus. FCS curves were recorded during 5 minutes using a 5 µW 488 nm pulsed excitation beam, a 200 µm or 2.1 AU pinhole, a 60X water objective and polarization sensitized readout (see Microscope setups – Confocal setup ('LSM')). Solution measurements were performed using identical settings except for placing the focus 50 µm above the glass surface and recording Rhodamine 110 and mEGFP for 1 minute and 5 minutes respectively.

FCS curve fitting. All cell measurements were fitted with two diffusion terms, corresponding to a cytoplasmic (cp) and a membrane (mem) component:

$$G(t_c) = 1 + \frac{\rho_{cp}}{\left(1 + \frac{t_c}{t_{diff,cp}}\right)\left(1 + \frac{t_c}{\kappa^2\, t_{diff,cp}}\right)^{0.5}} + \frac{\rho_{mem}}{\left(1 + \frac{t_c}{t_{diff,mem}}\right)\left(1 + \frac{t_c}{\kappa^2\, t_{diff,mem}}\right)^{0.5}} + G(\infty), \quad (4)$$

Where ρ denotes the species correlation amplitude, t_{diff} the species diffusion time, $G(\infty)$ the residual correlation at infinity, κ^2 the aspect ratio of the focus and t the correlation time. As the signal-to-noise was limited, the stability of the fit was improved by not fitting an additional bunching term to account for triplet as it did not affect the values of the diffusion times. To improve the stability of the fit further, a covariance between $t_{diff,cp}$ and $t_{diff,mem}$, $t_{diff,cp}$was fitted globally over a set of 11 points from 7 CD95 transfected cells, yielding a diffusion time of 0.60 ms to be kept fixed for all subsequent analyses. For more information on obtaining robust results from noisy live cell FCS data see Supplementary Note 2.

Curve weighting according to σ_{AV}[51] was preferred because of its ability to provide accurate weights at long correlation times. Our measurements fulfilled the requirement for that the recording can be divided in >10 chunks of 20 seconds each. FCS curves were created and fitted using the SymPhoTime software (PicoQuant GmbH, Berlin, Germany).

Confocal Photo Bleaching Step Analysis (cPBSA)
cPBSA measurements were performed on the Abberior setup (compare *Microscope setups*) using circular polarized light and a 100XO objective (NA 1.4, UPLSAPO, Olympus). Since the cell fixation which was needed to immobilize the receptors leads to a deflation of the cell, we ensured that a single membrane layer was in focus by measuring the area underneath the nucleus (see Supplementary Figure 7).

Automated data acquisition script. Data acquisition using a confocal microscope is generally slower than TIRF-based PBSA because only one molecular assembly can be measured simultaneously. To gather sufficient statistics, a data acquisition script was written that automates data acquisition after a manual area selection. The program uses the Python Application Programming Interface (API) from the Imspector acquisition software and contains a graphical user interface (GUI). Source code is available on request. Data acquisition works as follows:

1. A suitable area (20 x 20 μm^2) is selected on the lower membrane by the user.
2. An overview image is recorded using 50nm pixel size, 10 µs dwell time, 5% 488 nm excitation and summed over 3 frames. The output corresponding to 5% laser power fluctuated around 1.3 µW (see Supplementary Table 2).
3. The overview image is smoothened using a Gaussian filter with a standard deviation (sigma) of 1 pixel.
4. Molecular assemblies are identified from local maxima that exceed 3-5 counts on the smoothed image. The threshold level was adjusted per area as needed to select all spots while avoiding crowding by visual inspection.
5. Local maxima that are closer than 450 nm to any other local maxima are not considered for further analysis.
6. A photon trace is recorded for each remaining local maximum by placing the confocal beam there for a duration of 3 seconds.
7. A quick display is rendered for user feedback.

Data quality optimization. We established an experimental procedure to optimize the quality of our data. Firstly, our sample fixation procedure minimizes autofluorescence. Secondly, only molecular assemblies that are below the nucleus were recorded to ensure that the lower membrane was not in close proximity to the top membrane, as cells deflate upon fixation (see Supplementary Figure 7). To avoid deflation as far as possible, we forgo upside-down mounting on a cover slip and image cells in well slides instead. Thirdly, low excitation power and integration time was used for creating an overview image in order to avoid premature bleaching.

Data analysis. Data analysis was done using the Kalafut-Visscher (KV) algorithm[19] implemented by Hummert et al. in python[18]. The KV algorithm takes a minimal step size as a sole user input, limiting user bias. As our TCSPC modality records the arrival time of each photon, we can set the time binning of our data (t_{bin}(s)) post-acquisition. Due to the inherent noise level and varying fluorophore brightness a low threshold will count noise as events, overestimating the real number of Fluorophores, whereas a high threshold will discard bleaching events, underestimating the real number of Fluorophores. The threshold was chosen carefully to balance these two effects at 50 counts per t_{bin} of 5 ms, corresponding to 10 kHz at 1.36 µW. To compensate for variations in the laser power, the minimum step size was corrected according to:

$$\text{minimum step size} = 50\,\frac{p_{485}}{1.36\mu\mathrm{W}}, \tag{5}$$

where p_{485} is the laser power of the 485 excitation laser for that measurement in µW (see also Supplementary Table 2). Bleaching traces where no steps were found are disregarded from further analysis. No other selection criteria were applied.

Fluorescence polarization on traces. Intensities were calculated for traces that showed a single step by integrating fluorescence while the fluorophore was on. As circular polarization was used, fluorescence polarization was calculated using

$$p = \frac{I_{\mathrm{x}} - g\,I_{\mathrm{y}}}{I_{\mathrm{x}} + g\,I_{\mathrm{y}}}, \tag{6}$$

where I_{x} is the signal oriented along the x-axis and I_{y} was the signal along the y-axis and

$$g = \frac{g_{\mathrm{ox}}}{g_{\mathrm{oy}}}, \tag{7}$$

the relative detection efficiency along the x and y axis under circular polarization.

Cross-correlation of traces. The I_{x} and I_{y} signals of detector x- and y- polarization sensitized detectors were cross-correlated and analyzed using the home-built program Kristina[52]. All traces were used without any filtering. The signal-to-noise ratio was very high despite having a low total amount of photons as all photons correlate. Similar to FCS data, the correlation curve was fitted with one diffusion term and 3 bunching terms.

$$G_{\mathrm{ps}}(t_{\mathrm{c}}) = \frac{1}{N}\frac{1}{1+\frac{t_{\mathrm{c}}}{t_{\mathrm{bleach}}}}\frac{1}{\sqrt{1+\frac{t_{\mathrm{c}}}{\kappa^2 t_{\mathrm{bleach}}}}}\begin{pmatrix} 1 - A_{\mathrm{d1}} + A_{\mathrm{d1}}e^{\frac{\mathrm{t_c}}{t_{\mathrm{d1}}}} \\ -A_{\mathrm{d2}} + A_{\mathrm{d2}}e^{\frac{t_{\mathrm{c}}}{t_{\mathrm{d2}}}} - A_{\mathrm{d3}} + A_{\mathrm{d3}}e^{\frac{t_{\mathrm{c}}}{t_{\mathrm{d3}}}} \end{pmatrix}, \tag{8}$$

where $\kappa^2$was fixed to 100 such that the expression under the root is ~1, A indicate amplitudes, t correlation times. Results are summarized in Table 4. While the cross-correlation of a bleaching event is different from a diffusion event, no specialized model for this scenario was available. The resulting residuals around the bleaching time are acceptable as we are mainly interested in the bunching terms. The predicted variance from the cPBSA cross-correlation is discussed in Supplementary Note 3.

Cell Lifetime FRET Image Spectroscopy (CELFIS*)*,
The method is described in detail in [53]. First, we obtained the normalized donor only decay, $f_{\mathrm{D|D}}^{(\mathrm{D0})'}(t)$, from the donor emission upon donor excitation for a donor only reference sample, $f_{\mathrm{D|D}}^{(\mathrm{D0})}(t)$:[22]

$$f_{\mathrm{D|D}}^{(\mathrm{D0})}(t) = A_0\left(x_{\mathrm{D},1}e^{-t\,k_{\mathrm{D},1}} + \left(1 - x_{\mathrm{D},1}\right)e^{-t\,k_{\mathrm{D},2}}\right) + bg_1 = A_0 f_{\mathrm{D|D}}^{(\mathrm{D0})'}(t) + bg_1, \qquad (9)$$

where, $x_{\mathrm{D,i}}$ and $k_{\mathrm{D,i}}$ represent the fraction and decay rates of two fluorescence species, A_i represents the amplitude and bg_i represents the noise floor. This is subsequently used to fit the additional decay of the donor emission upon donor excitation for the donor-acceptor sample[22]

$$f_{\mathrm{D|D}}^{(\mathrm{DA})}(t) = A_1\left((1 - x_{\mathrm{FRET}})f_{\mathrm{D|D}}^{(\mathrm{D0})'}(t) + x_{\mathrm{FRET}}f_{\mathrm{D|D}}^{(\mathrm{D0})'}(t)e^{-t\,k_{\mathrm{FRET}}}\right) + bg_2, \qquad (10)$$

$$f_{\mathrm{D|D}}^{(\mathrm{DA})}(t) = A_1 f_{\mathrm{D|D}}^{(\mathrm{D0})'}(t)\,\epsilon_{\mathrm{D}}(t) + bg_2, \qquad (11)$$

where x_{FRET} and k_{FRET} are the FRET fraction and FRET rate and we substituted

$$\epsilon_{\mathrm{D}}(t) = x_{\mathrm{FRET}}e^{-t\,k_{\mathrm{FRET}}} + (1 - x_{\mathrm{FRET}}). \qquad (12)$$

All decays were tail fitted from 1.92 ns to 22.4 ns. Concentrations were determined using a molecular brightness of 814 and 264 Hz / molecule / µW for mEGFP and mCherry, respectively and a maturation factor of 0.8 for both mEGFP and mCherry. The oligomer fraction was obtained from x_{FRET} by calculating the FRET signal corresponding to a pure dimer, $x_{\mathrm{FRET,max}}$. To calculate the latter, we used 1) AV simulations were done in the program Olga[23] assuming a 51 amino acid linker and effective FRET range up to 80 Å using a solution NMR model of trimeric CD95 TM-domains (pdb id: 2NA7[26]) to set the anchor points for all structures. 2) a 78% and 71% abundance of the heterodimers compared to homodimers for CD95 variants and CD86 on one hand and CTLA4 on the other hand, derived from the abundance of mEGFP and mCherry. 3) an estimated maturation factor of 80%[16,20].

Microscope setups

Olympus IX83 widefield system

The IX83 P2ZF inverted epi-fluorescence microscope system (Olympus Europa SE & CO. KG, Hamburg, Germany) was used for all widefield and time-laps measurements. The microscope is equipped with the motorized TANGO Desktop stage (Märzhäuser Wetzlar GmbH & Co. KG, Wetzlar, Germany) and the Photometrics Prime BSI camera (Teledyne Photometrics, Tucson, Arizona, USA). An internal halogen lamp and the SOLA Light Engine (Lumencor Inc., Beaverton, Oregon, USA) served as light source for transmitted (brightfield, phase contrast) and reflected (fluorescence) illumination, respectively.

Abberior Expert Line setup
STED, cPBSA and FRET measurements were performed on an Abberior Expert Line system as described previously[54] (Abberior Instruments GmbH, Göttingen, Germany). Additionally, Polarization control for PBSA measurements was achieved using λ/2 and λ/4 waveplates (Abberior Instruments) and a SK010PA-vis 450-800 nm polarization analyzer (Schäfter Kirchhoff GmbH, Hamburg, Germany). Cells were kept at 37 °C using a Heating Insert HP-LabTek (Pecon GmbH, Erbach, Germany). The instrument is operated using the customized Abberior microscope software Imspector (version 14.0.3060, Abberior Instruments GmbH).

Confocal setup ('LSM')
Fluorescence Correlation Spectroscopy data was recorded using a confocal microscope modified with pulsed excitation and polarization-sensitized time correlated single photon counting readout. Excitation light was created using a Sepia II (PicoQuant GmbH, Berlin, Germany) driving an LDH-D-C-485 laser head (PicoQuant) and coupled to a FluoView1000 IX81 inverted microscope (Olympus, Shinjuku, Japan). Light was focused to a diffraction limited spot using an 60x water immersion UPLSAPO 1.2 NA objective (Olympus) and emitted light was separated using a DM405/488/559/635 quadband mirror (Olympus). Emitted fluorescence was split into perpendicular and parallel components using a polarizing beam splitter and measured using a BrightLine Fluorescence Filter 520/35 (Semrock Inc., Rochester, New York, USA) and PDM series avalanche photo diodes (Micro Photon Devices, Bolzano, Italy) for each channel. Electronic pulses were converted to photon events using a HydraHarp (PicoQuant). Cells were kept at 37 °C using a Heating Insert HP-LabTek (Pecon GmbH, Erbach, Germany).

Data availability

All data obtained in the study are available from the corresponding authors upon reasonable request.

Code availability

Code for PBSA trace segment variance prediction is included as a Supplementary Code. All other algorithms have been previously described elsewhere and are correspondingly cited. Analysis notebooks (python files, jupyter notebooks and MATLAB files) are available on reasonable request.

Author contributions

C.M. and C.A.M.S. conceived and supervised the project. N.B. and N.v.d.V. designed and performed the experiments and analyses. A.B. and C.W. organized and performed Flow Cytometry Measurements, A.G. contributed to the design of plasmids and provided substantial advice for FRET measurements. N.B., N.v.d.V., C.M. and C.A.M.S. discussed the results and wrote the manuscript.

Declaration of interests

The authors declare no competing interests.

Acknowledgement

This work was funded by the Deutsche Forschungsgemeinschaft (DFG, German Research Foundation) – project number 267205415 - CRC 1208 (projects A08 and A12). We thank Joél Baudouin (formerly IBS, Grenoble) for providing plasmids and stable cell lines. We thank Sebastian Hänsch and Stefanie Weidtkamp-Peters of the Centre of Advanced Imaging at HHU for fruitful discussions. We thank Suren Felekyan for support with cPBSA and general data analysis and Ralf Kühnemuth for technical support. We thank Hadeel Khalouf and Xiaoyue Shang for cloning initiatives of the pseudo-dimer. We are also in debt to Wolfgang Schulz, and Michèle Hoffmann both in the department of Urology, Heinrich Heine University, for the use of the MACSQuant Analyzer 10. A.G. is thankful for financial support from the HHU Stategischer Forschungsfonds. A.B. is thankful for financial support from the Medical Research School, DSO, Heinrich-Heine-University, Düsseldorf. C.M. is grateful for financial support by VolkswagenFoundation and Fonds der Chemischen Industrie

References

1 Aggarwal, B. B. Signalling pathways of the TNF superfamily: A double-edged sword. *Nature Reviews Immunology* **3**, 745-756 (2003). https://doi.org:10.1038/nri1184

2 Locksley, R. M., Killeen, N. & Lenardo, M. J. The TNF and TNF receptor superfamilies: Integrating mammalian biology. *Cell* **104**, 487-501 (2001). https://doi.org:10.1016/s0092-8674(01)00237-9

3 Bodmer, J. L., Schneider, P. & Tschopp, J. The molecular architecture of the TNF superfamily. *Trends in Biochemical Sciences* **27**, 19-26 (2002). https://doi.org:10.1016/s0968-0004(01)01995-8

4 Bremer, E. Targeting of the tumor necrosis factor receptor superfamily for cancer immunotherapy. *ISRN Oncol* **2013**, 371854 (2013). https://doi.org:10.1155/2013/371854

5 Chan, F. K. M. Three is better than one: Pre-ligand receptor assembly in the regulation of TNF receptor signaling. *Cytokine* **37**, 101-107 (2007). https://doi.org:10.1016/j.cyto.2007.03.005

6 Chan, F. K. M. *et al.* A domain in TNF receptors that mediates ligand-independent receptor assembly and signaling. *Science* **288**, 2351-2354 (2000). https://doi.org:10.1126/science.288.5475.2351

7 Boschert, V. *et al.* Single chain TNF derivatives with individually mutated receptor binding sites reveal differential stoichiometry of ligand receptor complex formation for TNFR1 and TNFR2. *Cellular Signalling* **22**, 1088-1096 (2010). https://doi.org:10.1016/j.cellsig.2010.02.011

8 Naismith, J. H., Devine, T. Q., Brandhuber, B. J. & Sprang, S. R. Crystallographic Evidence for Dimerization of Unliganded Tumor Necrosis Factor Receptor. *Journal of Biological Chemistry* **270**, 13303-13307 (1995). https://doi.org:10.1074/jbc.270.22.13303

9 Vanamee, E. S. & Faustman, D. L. Structural principles of tumor necrosis factor superfamily signaling. *Science Signaling* **11**, eaao4910 (2018). https://doi.org:10.1126/scisignal.aao4910

10 Vanamee, E. S., Lippner, G. & Faustman, D. L. Signal Amplification in Highly Ordered Networks Is Driven by Geometry. *Cells* **11**, 272 (2022). https://doi.org:10.3390/cells11020272

11 Siegel, R. M. *et al.* SPOTS: signaling protein oligomeric transduction structures are early mediators of death receptor-induced apoptosis at the plasma membrane. *Journal of Cell Biology* **167**, 735-744 (2004). https://doi.org:10.1083/jcb.200406101

12 Weidtkamp-Peters, S. *et al.* Multiparameter fluorescence image spectroscopy to study molecular interactions. *Photochemical & Photobiological Sciences* **8**, 470-480 (2009). https://doi.org:10.1039/b903245m

13 Lerner, E. *et al.* FRET-based dynamic structural biology: Challenges, perspectives and an appeal for open-science practices. *Elife* **10**, e60416 (2021).

14 Gerken, M. *et al.* Fluorescence correlation spectroscopy reveals topological segregation of the two tumor necrosis factor membrane receptors. *Biochimica Et Biophysica Acta-Biomembranes* **1798**, 1081-1089 (2010). https://doi.org:10.1016/j.bbamem.2010.02.021

15 Jaqaman, K., Galbraith, J. A., Davidson, M. W. & Galbraith, C. G. Changes in single-molecule integrin dynamics linked to local cellular behavior. *Molecular Biology of the Cell* **27**, 1561-1569 (2016). https://doi.org:10.1091/mbc.E16-01-0018

16 Ulbrich, M. H. & Isacoff, E. Y. Subunit counting in membrane-bound proteins. *Nature Methods* **4**, 319-321 (2007). https://doi.org:10.1038/Nmeth1024

17 Clarke, S. *et al.* Covalent Monofunctionalization of Peptide-Coated Quantum Dots for Single-Molecule Assays. *Nano Letters* **10**, 2147-2154 (2010). https://doi.org:10.1021/nl100825n

18 Hummert, J. *et al.* Photobleaching step analysis for robust determination of protein complex stoichiometries. *Molecular Biology of the Cell* **32**, ar35 (2021). https://doi.org:10.1091/mbc.E20-09-0568

19 Kalafut, B. & Visscher, K. An objective, model-independent method for detection of non-uniform steps in noisy signals. *Computer Physics Communications* **179**, 716-723 (2008). https://doi.org:10.1016/j.cpc.2008.06.008

20 Dunsing, V. *et al.* Optimal fluorescent protein tags for quantifying protein oligomerization in living cells. *Scientific reports* **8**, 1-12 (2018).

21 Greife, A. *et al.* Structural assemblies of the di- and oligomeric G-protein coupled receptor TGR5 in live cells: an MFIS-FRET and integrative modelling study. *Scientific Reports* **6**, 36792 (2016). https://doi.org:10.1038/srep36792

22 Peulen, T.-O., Opanasyuk, O. & Seidel, C. A. Combining graphical and analytical methods with molecular simulations to analyze time-resolved FRET measurements of labeled macromolecules accurately. *The Journal of Physical Chemistry B* **121**, 8211-8241 (2017).

23 Dimura, M. *et al.* Automated and optimally FRET-assisted structural modeling. *Nature Communications* **11**, 5394 (2020). https://doi.org:10.1038/s41467-020-19023-1

24 Clayton, A. H. A. & Chattopadhyay, A. Taking Care of Bystander FRET in a Crowded Cell Membrane Environment. *Biophysical Journal* **106**, 1227-1228 (2014). https://doi.org:10.1016/j.bpj.2014.02.004

25 Dimura, M. *et al.* Quantitative FRET studies and integrative modeling unravel the structure and dynamics of biomolecular systems. *Current opinion in structural biology* **40**, 163-185 (2016).

26 Fu, Q. S. *et al.* Structural Basis and Functional Role of Intramembrane Trimerization of the Fas/CD95 Death Receptor. *Molecular Cell* **61**, 602-613 (2016). https://doi.org:10.1016/j.molcel.2016.01.009

27 Karathanasis, C. *et al.* Single-molecule imaging reveals the oligomeric state of functional TNF alpha-induced plasma membrane TNFR1 clusters in cells. *Science Signaling* **13**, eaax5647 (2020). https://doi.org:10.1126/scisignal.aax5647

28 Rodseth, L. E. *et al.* 2 CRYSTAL FORMS OF THE EXTRACELLULAR DOMAIN OF TYPE-I TUMOR-NECROSIS-FACTOR RECEPTOR. *Journal of Molecular Biology* **239**, 332-335 (1994). https://doi.org:10.1006/jmbi.1994.1371

29 Papoff, G. *et al.* Identification and characterization of a ligand-independent oligomerization domain in the extracellular region of the CD95 death receptor. *Journal of Biological Chemistry* **274**, 38241-38250 (1999). https://doi.org:10.1074/jbc.274.53.38241

30 Siegel, R. M. *et al.* Fas preassociation required for apoptosis signaling and dominant inhibition by pathogenic mutations. *Science* **288**, 2354-2357 (2000). https://doi.org:10.1126/science.288.5475.2354

31 Frey, L., Lakomek, N. A., Riek, R. & Bibow, S. Micelles, Bicelles, and Nanodiscs: Comparing the Impact of Membrane Mimetics on Membrane Protein Backbone Dynamics. *Angew Chem Int Edit* **56**, 380-383 (2017). https://doi.org:10.1002/anie.201608246

32 Liesche, C. *et al.* CD95 receptor activation by ligand-induced trimerization is independent of its partial pre-ligand assembly. *bioRxiv*, 293530 (2018). https://doi.org:10.1101/293530

33 Banner, D. W. *et al.* Crystal structure of the soluble human 55 kd TNF receptor-human TNFβ complex: Implications for TNF receptor activation. *Cell* **73**, 431-445 (1993). https://doi.org:10.1016/0092-8674(93)90132-a

34 Gülcüler Balta, G. S. *et al.* 3D Cellular Architecture Modulates Tyrosine Kinase Activity, Thereby Switching CD95-Mediated Apoptosis to Survival. *Cell Reports* **29**, 2295–2306 (2019). https://doi.org:10.1016/j.celrep.2019.10.054

35 Henkler, F. *et al.* The extracellular domains of FasL and Fas are sufficient for the formation of supramolecular FasL-Fas clusters of high stability. *Journal of Cell Biology* **168**, 1087-1098 (2005). https://doi.org:10.1083/jcb.200501048

36 Scott, F. L. *et al.* The Fas-FADD death domain complex structure unravels signalling by receptor clustering. *Nature* **457**, 1019-1022 (2009). https://doi.org:10.1038/nature07606

37 Esposito, D. *et al.* Solution NMR Investigation of the CD95/FADD Homotypic Death Domain Complex Suggests Lack of Engagement of the CD95 C Terminus. *Structure* **18**, 1378-1390 (2010). https://doi.org:10.1016/j.str.2010.08.006

38 Levoin, N., Jean, M. & Legembre, P. CD95 Structure, Aggregation and Cell Signaling. *Frontiers in Cell and Developmental Biology* **8**, 314 (2020). https://doi.org:10.3389/fcell.2020.00314

39 Wang, L. W. *et al.* The Fas-FADD death domain complex structure reveals the basis of DISC assembly and disease mutations. *Nature Structural & Molecular Biology* **17**, 1324-U1176 (2010). https://doi.org:10.1038/nsmb.1920

40 Potma, E. O. *et al.* Reduced protein diffusion rate by cytoskeleton in vegetative and polarized Dictyostelium cells. *Biophysical Journal* **81**, 2010-2019 (2001). https://doi.org:10.1016/s0006-3495(01)75851-1

41 Reis, C. R., van Assen, A. H. G., Quax, W. J. & Cool, R. H. Unraveling the Binding Mechanism of Trivalent Tumor Necrosis Factor Ligands and Their Receptors. *Molecular & Cellular Proteomics* **10**, M110.002808 (2011). https://doi.org:10.1074/mcp.M110.002808

42 Berger, R. M. L. *et al.* Nanoscale FasL Organization on DNA Origami to Decipher Apoptosis Signal Activation in Cells. *Small* **17**, 2101678 (2021). https://doi.org:10.1002/smll.202101678

43 Liesche, C. *et al.* Death receptor-based enrichment of Cas9-expressing cells. *Bmc Biotechnology* **16**, 17 (2016). https://doi.org:10.1186/s12896-016-0250-4

44 Fricke, F., Beaudouin, J., Eils, R. & Heilemann, M. One, two or three? Probing the stoichiometry of membrane proteins by single-molecule localization microscopy. *Scientific Reports* **5**, 14072 (2015). https://doi.org:10.1038/srep14072

45 Qureshi, O. S. *et al.* Constitutive Clathrin-mediated Endocytosis of CTLA-4 Persists during T Cell Activation. *Journal of Biological Chemistry* **287**, 9429-9440 (2012). https://doi.org:10.1074/jbc.M111.304329

46 Schindelin, J. *et al.* Fiji: an open-source platform for biological-image analysis. *Nature Methods* **9**, 676-682 (2012). https://doi.org:10.1038/nmeth.2019

47 Stoyan, D. & Stoyan, H. Estimating pair correlation functions of planar cluster processes. *Biometrical Journal* **38**, 259-271 (1996). https://doi.org:10.1002/bimj.4710380302

48 Peckys, D. B., Korf, U. & de Jonge, N. Local variations of HER2 dimerization in breast cancer cells discovered by correlative fluorescence and liquid electron microscopy. *Science Advances* **1**, e1500165 (2015). https://doi.org:10.1126/sciadv.1500165

49 Felekyan, S. *et al.* Full correlation from picoseconds to seconds by time-resolved and time-correlated single photon detection. *Review of Scientific Instruments* **76**, 083104 (2005). https://doi.org:10.1063/1.1946088

50 Gendron, P. O., Avaltroni, F. & Wilkinson, K. J. Diffusion Coefficients of Several Rhodamine Derivatives as Determined by Pulsed Field Gradient-Nuclear Magnetic Resonance and

Fluorescence Correlation Spectroscopy. *Journal of Fluorescence* **18**, 1093-1101 (2008). https://doi.org:10.1007/s10895-008-0357-7

51 Wohland, T., Rigler, R. & Vogel, H. The standard deviation in fluorescence correlation spectroscopy. *Biophysical Journal* **80**, 2987-2999 (2001). https://doi.org:10.1016/s0006-3495(01)76264-9

52 Borst, J. W. *et al.* Structural Changes of Yellow Cameleon Domains Observed by Quantitative FRET Analysis and Polarized Fluorescence Correlation Spectroscopy. *Biophysical Journal* **95**, 5399-5411 (2008). https://doi.org:10.1529/biophysj.107.114587

53 van der Voort, N. T. M., Bartels, N., Monzel, C. & Seidel, C. A. M. Quantifying the Spatio-temporal Evolution of Protein Interactions using Cell Lifetime FRET Image Spectroscopy (CELFIS). *bioRxiv* (2022).

54 Budde, J.-H. *et al.* FRET nanoscopy enables seamless imaging of molecular assemblies with sub-nanometer resolution. *arXiv*, 2108.00024 (2021).

Supplementary Information

A Minimal Model of CD95 Signal Initiation Revealed by Advanced Super-resolution and Multiparametric Fluorescence Microscopy

Nina Bartels [1,†],Nicolaas T M van der Voort [2,†], Annemarie Greife[2], Arthur Bister[3], Constanze Wiek[3], Claus A M Seidel[2,*], Cornelia Monzel[1,*]

† contributed equally

* corresponding author: cornelia.monzel@hhu.de, cseidel@hhu.de

1. Experimental Medical Physics, Heinrich-Heine University, 40225 Düsseldorf

2. Molecular Physical Chemistry, Heinrich-Heine University, 40225 Düsseldorf

3. Department of Otorhinolaryngology, Head & Neck Surgery, Heinrich-Heine University, Düsseldorf, Germany

Contents

Supplementary Notes

Supplementary Note 1: Optimal instrument settings for live cell FCS

For method details see method section *FCS measurements*.

Live cell FCS measurements on mEGFP remain challenging due to the limited mEGFP photostability and limited mEGFP abundance in a cell. To nevertheless obtain a robust readout, we discuss optimal experimental settings along with a brief description of the photophysical effects governing the observations.

Pinhole setting

The optimal pinhole setting was determined experimentally to be 200 µm in diameter, or 492 nm backprojected pinhole radius[1], which corresponds to 2.1 Airy Units (AU). This setting optimally balances 1) a high photon collection efficiency 2) a sharp Point Spread Function (PSF) 3) the PSF shape to resemble a Gaussian. The tradeoff consists thereof that an open pinhole with high collection efficiency is needed to compensate for the poor photo-stability of mEGFP and resulting low signal-to-noise ratio (SNR). However, opening the pinhole transforms the shape of the PSF from a sinc², which is Gaussian-like to a sinc function, which in not Gaussian-like. As FCS theory (see Equation (4)) models a molecule diffusing through a 3D Gaussian volume, an open pinhole results in a mismatch between model and measurement visible in the fit residuals. As reported by others[2], a 2.1 AU pinhole leads to small but acceptable deviations between the model function and data.

Fluorescent molecule concentration changes during measurement

A change in fluorescent protein concentration is registered by the correlation function at long time scales, which complicates fitting slow membrane diffusion. For solution measurements, the dominant process for concentration decrease is adsorption of to the glass surface, which is easily prevented by coating the glass surfaces with BSA (incubate 1 mg/ml Bovine Serum Albumin for 10 minutes, BSA, Sigma-Aldrich Merck group, Taufkirchen, Germany). Bleaching does not significantly affect concentrations in solution measurements as the bleaching rate is small compared to the large fluorophore reservoir. In cells, a change in fluorescent protein concentration cannot be circumvented as photo-bleaching can readily deplete the reservoir of fluorescent proteins at an organelle or cellular scale. To mitigate the effects of a decreasing mEGFP concentration on the FCS curve, we divide the photon trace in chunks of approximately constant concentration and average the pieces[2].

We are able to gain additional insight in the photo-bleaching process from synergistically combining our read-out from FCS and cPBSA. From our FCS measurements we obtain diffusion times and fluorophore brightness, which we use to calculate the average number of photons per time the molecule diffuses through the focus to be ~1.5 for mEGFP[3]. From cPBSA we are able to obtain the total photon budget of mEGFP to be ~1000 photons. Taken together we conclude that the probability of mEGFP bleaching during a single pass through the detection volume is very low and that the mEGFP concentration decreases because a single molecule passes through the detection volume many times.

Power setting & photon budget

A higher laser power increases the signal-to-noise ratio for the FCS curve at the cost of a higher bleaching rate, which cause unwanted changes in local concentrations (see section above). In

this section, we explain the underlying processes and obtain a trade-off between the SNR level of the FCS curve and the bleaching rate.

Primarily, the SNR of an FCS curve must be sufficient to enable interpretation, which scales with the number of photons detected while a single molecule diffuses through the focus[4]. Interestingly, our results indicate that the average number of photons is ~1.5. On the condition that molecules diffuse independent from each other, at least two photons are needed to obtain a correlation. This apparent contradiction is resolved by realizing that the number of photons per event follows a distribution with a long tail at higher photon numbers. I.e., while some of the molecules emit zero or one photon, the fraction which emits two or more photons is responsible for the correlation in FCS[5].

To help understand bleaching processes, we introduce the concept of photon budget to mean the total amount of photons emitted by the fluorophore before bleaching. It is inversely proportional to the bleaching probability per excitation cycle. Work done by others[6-8] on decay pathway modelling reveals that the photon budget of mEGFP is constant at low irradiance but decreases after a transition regime. The decrease in photon budget is due to an additional photon being absorbed while the molecule is in the excited state, opening up additional photo-bleaching pathways and increasing the photo-bleaching probability per cycle. While a laser power lower than the transition irradiance maximizes the photon budget, a definite number was not found in literature by the authors, although an upper limit was reported by Cranfill et al.[7] to be 80 µW using 488 nm excitation in a diffraction limited focus. Based on our own experimental experience we estimate the transition point from mEGFP to be lower than ~10 µW.

To satisfy all the criteria above, the laser power was experimentally determined to be 5 µW corresponding to 3 kW/cm^2 for a calibrated 0.165 µm^2 focal area.

Recording time
Longer recording times improve the SNR of the FCS curve. However, to sample sufficient cell-to-cell variation during a measurement day it was limited to 5 minutes.

Supplementary Note 2: Live-cell Membrane FCS

To verify that CD95 is sufficiently mobile and hence able to form (higher) oligomers, we determined CD95 diffusion constants D during the whole signaling process using Fluorescence Correlation Spectroscopy (FCS). FCS was performed on live cells for $CD95_{D0}$ (Supplementary Figure 3a) and $CD95(\Delta DD)_{D0}$ (Supplementary Figure 3b) before and 100 - 200 minutes after ligand addition as well as for $CD86_{D0}$ and $CTLA4_{DA}$ as single and double transmembrane helix references, respectively (Supplementary Figure 3c). FCS curves were generated for each cell and fitted with two diffusion terms and no bunching term (see methods). The fast diffusion term was attributed to the presence of cytoplasmic mEGFP, which was confirmed by 3D confocal images of live cells. As the confocal detection volume extends halfway into the cytoplasm, FCS is sensitive to mEGFP present in the cytoplasm (see Supplementary Figure 12). To confirm that the fast diffusion component was of cytoplasmic origin, we fitted the fast diffusion term globally for all curves from the CD95 sample yielding a value of $t_{\mathrm{diff,cp}} = 0.60$ ms (corresponding to $D = 20$ μm²/s), reminiscent of soluble protein diffusion in eukaryotic cells, with typical values of 24 μm²/s[9]. In addition, we measured diffusion of free mEGFP in the cytoplasm and obtained two diffusion times, 0.27 ms and 2.2 ms, with a weighted average time of 0.50 ms (see Supplementary Figure 4) close to the cytoplasmic component of CD95. In the following, the fast diffusion term was kept fixed for all samples to improve the sensitivity of the fit for the slow diffusion time (see Supplementary Figure 3a-c). The time of the slow diffusion process turned out to lie in the range of 30-100ms and matches literature values for membrane proteins[10,11]. No difference in the diffusion constant was found between CD95 species within the measurement accuracy (see Supplementary Figure 3d), with absolute values of $D = 0.21$-0.24 μm²/s. Interestingly, $CTLA4_{DA}$ showed similar diffusion times of $D = 0.19$ μm²/s, but CD86 showed significantly slower diffusion times of $D = 0.15$ μm²/s indicating that the number of transmembrane helices is not the dominant factor of receptor diffusion. This result indicates that CD95 is sufficiently mobile to exhibit dynamic changes in its oligomeric state over time. In addition, comparison of the absolute values suggests that CD95 does not form supramolecular structures as this would result in a highly decreased diffusion constant. Finally, we tested whether the mobility of CD95 would change after ligand addition. To this end, CD95 and CD95(ΔDD) diffusion was monitored over 100-200 minutes after ligand addition (see Supplementary Figure 3e). Overall, our data confirm sustained CD95 mobility during the whole signaling process. Despite this possibility to accumulate into higher ordered structures CD95 did not show any systematic change in CD95 diffusion, thus indicating no excessive change in the receptor oligomerization state.

Supplementary Note 3: Predicted variance from cPBSA cross-correlation curves.

The cross-correlation of cPBSA traces is described in the method section on cPBSA.

To predict the variance, we assume a simple model where the mEGFP molecule can enter a dark state with rate k_{off} and return to the bright state with rate k_{on}. The latter can directly be obtained from the cross correlation fit as it is inversely proportional to t_{on}, the characteristic time from the cross-correlation bunching therm. To obtain k_{off}, we define the fraction of time spent in the on state, α as

$$\alpha = \frac{k_{\text{on}}}{k_{\text{on}} + k_{\text{off}}}, \tag{S1}$$

Where $(1 - \alpha)$ equals the amplitude of the bunching therm. Using the values from the fit listed in Supplementary Table 4, we obtain 1/5 ms and 1/30 ms for k_{on} and k_{off} for the slowest transition. To obtain a theoretical description of the variance on a trace segment, we define

$$n = t_{\text{bin}}(k_{\text{on}} + k_{\text{off}}), \tag{S2}$$

where n is the average number of transitions in some time period t_{bin}. For a fluorophore with fluorescence rate k_{fl}, the average signal in time period t_{bin} is given by

$$\langle S \rangle = t_{\text{bin}} \langle k_{\text{fl}} \rangle \alpha; \tag{S3}$$

$$\langle S \rangle = N_{\text{fl}} \alpha, \tag{S4}$$

where N_{fl} is defined as the average number of fluorophores emitted if there was no dark state. Note that the fluorophore brightness, k_{fl} is understood to include polarization effects, such that it differs per molecule. We may now write the variance of the signal as

$$Var(S) = \left|\frac{\partial S}{\partial \alpha}\right|^2 Var(\alpha) + \left|\frac{\partial S}{\partial N_{\text{fl}}}\right|^2 Var(N_{\text{fl}}), \tag{S5}$$

where the covariance between α and N_{fl} as a function of excitation power is not considered as the excitation was kept within the range 1.3 ± 0.2µW (Supplementary Table 2). From Barth et al.[12], we obtain the variance of alpha

$$Var(\alpha) = \alpha(1-\alpha)\frac{2}{n}\left(1 + \frac{e^{-n} - 1}{n}\right) \tag{S6}$$

To obtain the variance of N_{fl}, we consider that the average number of photons emitted follows a Poisson distribution

$$Var(N_{\text{fl}}) = \frac{N_{\text{fl}}}{\alpha}. \tag{S7}$$

Combining all formulas, we obtain a direct expression:

$$Var(S) = N_{\text{fl}}^2 \alpha(1-\alpha)\frac{2}{n}\left(1 + \frac{e^{-n} - 1}{n}\right) + \alpha N_{\text{fl}}. \tag{S8}$$

We check that in the limit of very fast fluctuations from the dark state, the variance due to α becomes zero and we obtain a Poisson distribution as expected

$$\lim_{n\to\infty} Var(S) = \alpha N_{\mathrm{fl}} \qquad (S9)$$

Intuitively, we understand that long dark state times with respect to t_{bin} cause fluctuations in α whose variance dominates the inherent Poisson noise, hence this result confirms that our initial model of considering only the longest dark states captures all essential features. To check our expression, we perform Monte Carlo simulations for all values of α, n and N_{fl} (see Supplementary Figure 11 and Supplementary Code 1) confirming that it correctly predicts the variance and showing that the variance per trace fluctuates with the stochastic number of blinks.

Supplementary Note 4: To investigate the possibility of higher oligomeric states further, we focus our attention on bright areas on the membrane of typically ~1µm diameter and ~5µm separation visible for all constructs including controls which cannot be related to intracellular organelles in close membrane proximity or membrane ruffling (Figure 5b and Supplementary Figure 1). We probe the oligomeric state of the bright areas by modifying our analysis to only consider signal originating from there, yielding a comparable although slightly higher oligomerization state from before, which is expected due to concentration driven kinetics (see (N.v.d.V., N.B., C.M., C.A.M.S., *manuscript in preparation*)). As the bright areas are not specific to CD95 variants and the FRET signature is similar before, we conclude that the bright areas are not higher oligomeric states, but simply local concentration of receptors ubiquitous to membrane receptors.

Supplementary Tables

Sample	Statistics [cells]	Membrane fraction	Cytoplasmic fraction
$CD86_{DO}$	9	0.589 ± 0.085	0.411 ± 0.085
$CD86_{DO}$	6	0.628 ± 0.052	0.372 ± 0.052
$CTLA4_{DA}$	10	0.703 ± 0.036	0.297 ± 0.036
$CD95_{D0}$	11	0.594 ± 0.045	0.406 ± 0.045
$CD95(\Delta DD)_{D0}$	12	0.598 ± 0.052	0.402 ± 0.052
$CD95_{D0}$ + Lig	11	0.597 ± 0.043	0.403 ± 0.043
$CD95(\Delta DD)_{D0}$ + Lig	14	0.637 ± 0.030	0.363 ± 0.030
Total	73	0.621 ± 0.062	0.379 ± 0.062

Supplementary Table 1: Membrane and cytoplasmic fraction of cell fluorescence signal determined with FCS

Fractions of fast cytoplasmic and slow membrane diffusion for different membrane proteins measured with FCS. See Supplementary Note 1 and Supplementary Figure 3.

dataset	date	laser power [µW]	minimum step size [counts]
CD95	22 July 2021	1.36	50
CD95 +L	23 July 2021	1.60	58
CD95(ΔDD)	22 July 2021	1.36	50
CD95(ΔDD) +L	23 July 2021	1.60	58
$CD86\text{-}mEGFP_1$	22 July 2021	1.36	50
$CD86\text{-}mEGFP_2$	24 November 2021	1.37	50
$CTLA4_{DA}$	2 February 2022	1.00	36
CD86-mEGFP-mEGFP	2 February 2022	1.00	36

Supplementary Table 2: Laser power fluctuations during measurement days for PBSA data.

The step threshold was adjusted such that the ratio of the power and the threshold remains constant (see Supplementary Figure 8).

model No. therms	$\chi^2_{red,avg}$	$t_{diff,1}$	$t_{bunch,1}$	$t_{bunch,2}$	$t_{bunch,3}$	$t_{bunch,4}$
1 diffusion, 1 bunching[1]	6.7	59.6 ms	0.85 ms	-	-	-
1 diffusion, 2 bunching[1]	2.1	73 ms	2.41 ms	0.09 ms	-	-
1 diffusion, 3 bunching	1.08	83 ms	5 ms	0.56 ms	0.011 ms	-
1 diffusion, 4 bunching[2]	0.78	95 ms	13.4 ms	1.4 ms	0.11 ms	0.006 ms

Supplementary Table 3: mEGFP bunching terms.

The correct model for fitting cross correlation of cPBSA traces was determined by best $\chi^2_{red,avg}$, the reduced chi-square averaged over the four cross correlations shown in Supplementary Figure 10a. Correlation times were fitted globally over the four cross correlations, the amplitudes were fitted individually. [1]Fit has too high χ^2_{red} to describe data well. [2] $\chi^2_{red} < 1$ indicates overfitting.

Parameter	CD95	CD95 + L	CD95(ΔDD)	CD86
G(∞)	0.95	1.01	0.95	0.98
N	0.78	0.72	0.98	0.77
t_{bleach} [ms]*	84	84	84	84
A_{bleach} [%]**	69.9	68.5	68.5	64.9
κ *	100	100	100	100
A_{d1} [%]	13.3	14.0	11.0	15.6
t_{d1} [ms]*	5.0	5.0	5.0	5.0
A_{d2} [%]	10.0	11.5	13.0	11.7
t_{d2} [ms]*	0.56	0.56	0.56	0.56
A_{d3} [%]	6.8	6.0	7.5	7.8
t_{d3} [ms]*	0.011	0.011	0.011	0.011

Supplementary Table 4: Fit parameters for cross-correlation fits on ensemble traces (see Supplementary Figure 10 and Equation (8)). *fitted globally ** calculated using $A_{\mathrm{bleach}} = 100 - A_{\mathrm{d1}} - A_{\mathrm{d2}} - A_{\mathrm{d3}}$.

plasmid id	sequence	linker sequence	flexible part protein #aa	linker length #aa	flexible part FP #aa	Total flexible #aa
1714	CD95(1-335)-mCherry T2A CD95(1-335)-mEGFP	GGGGGPVPQWEGFAALLATPVAT/ GGGGGPVPQWEGFAALLATPVGGAV	9[1]	23 / 25	16 / 12	48 / 46
1695	CD95-ΔDD(1-210)-mCherry T2A CD95-ΔDD(1-210)-mEGFP	GGGPVPQWEGFAALLATPVAT / GGGPVPQWEGFAALLATPVGGAV	16[4]	21 / 23	16 / 12	53 / 51
1693	CTLA4(1-200)-mCherry T2A CTLA4(1-200)-mEGFP	GGGPVPQWEGFAALLATPVAT / GGGPVPQWEGFAALLATPVGGAV	16[4]	21 / 23	16 / 12	53 / 51
1706	CD86-mCherry T2A CD86-mEGFP	GGGPVPQWEGFAALLATPVAT / GGGPVPQWEGFAALLATPVGGAV	-[2]	21 / 23	16 / 12	37 / 35
1531	CD95(1-335)-mEGFP	GGGGGPVPQWEGFAALLATPVGGAV	9[1]	25	12	46
1516	CD95-ΔDD(1-210)-mEGFP	GGGPVPQWEGFAALLATPVGGAV	16	23	12	51
1706	CD86-mEGFP	GGGPVPQWEGFAALLATPVGGAV	-[2]	23	12	35
88	CD86-*link*-mEGFP-mEGFP[3]	GGGPVPQWEGFAALLATPVGGAV	-[2]	23	12	35
88	CD86-mEGFP-*link*-mEGFP[3]	GSSGSSNAAIINAAGSSGSS	11	20	12	43

Supplementary Table 5: Specifications of linker lengths for used constructs.
[1]9 amino acids are used to model the flexible death domain, see methods. [2]flexible part could not be estimated because the structure of the CD86 TM domain is not known, taken as 0. [3]link indicates the position of the linker detailed. #aa: number of amino acids. CTLA-mEGFP control was not used as it did not localize near the membrane. [4] linker length based on the residual 16 intracellular amino acids after transmembrane domain.

Supplementary Codes

```
#all units in s, 1/s
#this code is fast in c, but slow in python
def simulateTrace(Nfl, alpha, n, tbin = 5e-3, tstep = 1e-4, timestop = 1):
  """
    Do a Monte Carlo simulation of a trace, assuming a single dark state.
    tstep is the time resolution of the simulation. It should be chosen such
  that the probability of multiple blinking events in 1 step is low, i.e.,
  pon and poff < 0.1
  Nfl:    average number of fluorophores in time tbin if the molecule is on,
        i.e. the molecule brightness (dimensionless)
  alpha:   the average fraction of time the molecule spends in the on state (dimensionless)
  n:      the average number of blinks in time tbin (dimensionless)
  tbin:    time period (s)
  tstep:   time resolution of simulation, see above (s)
  timestop: amount of time to simulate (s)"""
  #calculate derived variables
  Nevents = int(np.ceil(timestop / tstep))
  pfl = Nfl / tbin * tstep
  pon = n * alpha / tbin * tstep
  poff = n * (1-alpha) / tbin * tstep
  #fluorophore starts in the on state, compliant with physical conditions.
  state = 'on'
  #initialize arrays
  events = np.zeros(Nevents)
  #event loop
  for i in range(Nevents):
    if state == 'on':
      #add a poissonian number of photons
      events[i] = np.random.poisson(pfl)
      #switch off with probability poff
      if poff > np.random.random():
        state = 'off'
    elif state == 'off':
      #switch on with probability pon
      if pon > np.random.random():
        state = 'on'
  #downsample trace to tbin
  binfact = int(np.ceil(tbin / tstep))
  nbins = int(np.ceil(timestop / tbin))
  trace = np.sum(events.reshape((nbins, binfact)), axis = 1)
  #calculate variance
  variance = np.var(trace)
  return variance, trace
```

Supplementary Code 1: Code for Monte Carlo simulations on variance predictions. dark state Monte Carlo simulations for PBSA trace segment variance prediction. Code was tested in python 3.7, but should also run in Python 2.x and 3.x versions. The only dependency is the numpy library. Results are summarized in Figure 11.

Supplementary Figures

Supplementary Figure 1: Confocal images of transfected cells show the protein localization in the membrane.
Images show live Hela $CD95^{KO}$ cells transfected with bicistronic plasmids coding for donor (mEGFP) and acceptor (mCherry) bound CD95, CD95(ΔDD), CD86 or CTLA4 during FRET measurements, focused on the lower cell membrane. Higher intensities at cell edges and cell-to-cell contact points show the correct integration of the membrane proteins into the outer cell membrane. Scale bar applies for all images.

Supplementary Figure 2: Apoptosis dynamics of CD95 variants.
Apoptosis Dynamics of transiently transfected Hela $CD95^{KO}$ cells with the CD95 variants CD95(ΔDD), CD95(R102S) and CD95(Δ26-86). While the first two variants show apoptosis caused by natural apoptosis or transfection stress, the PLAD- depleted variant CD95(Δ26-86) (also called CD95(ΔPLAD)) shows an increased apoptosis efficiency up to 25% of dead cells. Statistics: > 25 cells for CD95(R102S) and CD95(Δ26-86), > 65 cells for CD95(ΔDD).

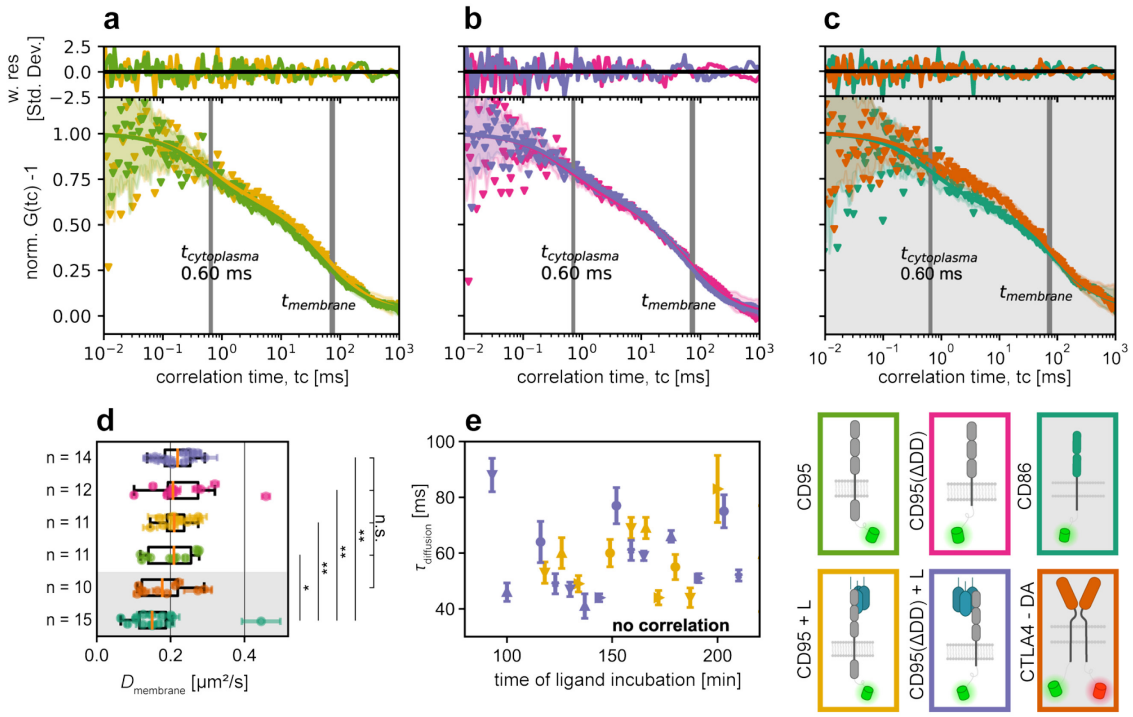

Supplementary Figure 3: Live cell FCS to obtain diffusion times.
Exemplary curves are shown for **a)** CD95 before (green) and 159 minutes after ligand addition (yellow) **b)** CD95(ΔDD) before (magenta) and 178 minutes after ligand addition (purple) **c)** CD86 monomeric control (teal) and CTLA4 dimer control (orange). All curves were fitted with two diffusion terms (compare methods and Equation (4)). The cytoplasmic diffusion term was fitted globally over 11 curves for the CD95 sample and fixed to this value for all other samples (see methods). **d)** Membrane diffusion constants were obtained from the membrane diffusion times. Mann-Whitney U-test was used to test for significance (*p < 0.05, **p < 0.01). **e)** Membrane diffusion time plotted against time since Ligand addition. No significant change was observed. At least ten different positions from at least 7 different cells were measured per sample and fitted subsequently. Legend: schematic representation of the samples used. Cytoplasmic and membrane fractions reported in Supplementary Table 1.

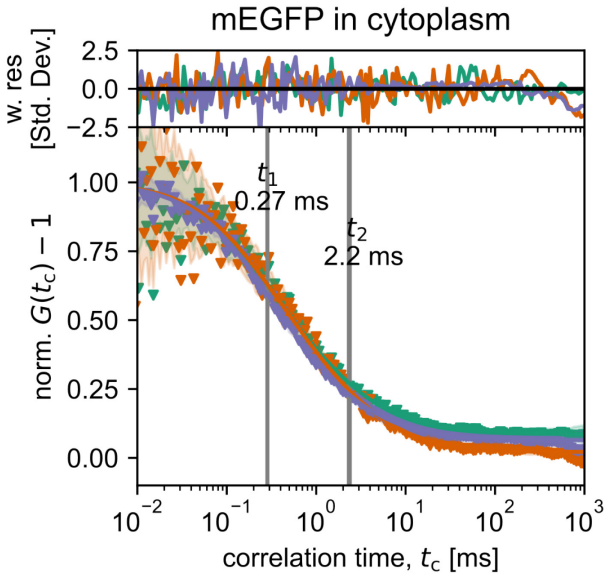

Supplementary Figure 4: FCS curves of free mEGFP in cytoplasm.
Free mEGFP in cytoplasm was fitted globally with two diffusion terms (Equation (4)), with a weighted average of 0.5 ms.

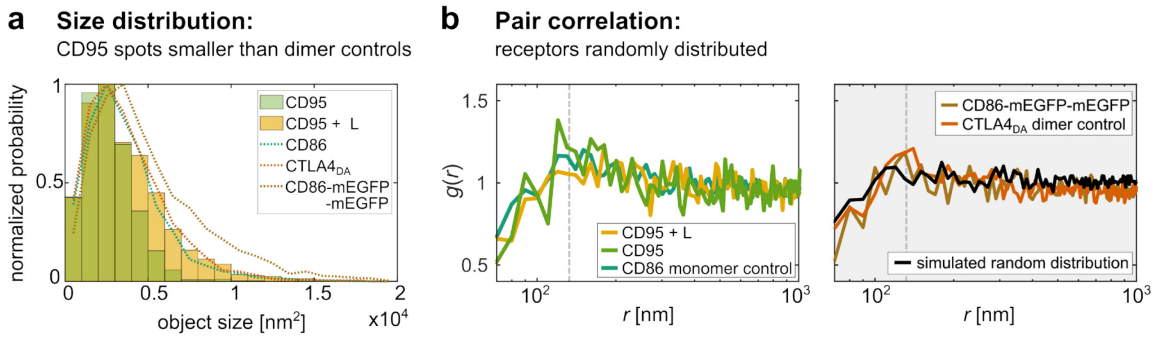

Supplementary Figure 5: STED spot analysis of CD95 variant.
a) Similar as for CD95(ΔDD) (Figure 3c), the distribution of full-length CD95 spot sizes (+/- ligand) is in the regime of monomer spot sizes. The slightly reduced size distribution of CD95 (no ligand) for larger spot sizes is correlating with a slightly lower expression level of the observed cells. The pseudo-dimer CD86-mEGFP-mEGFP show a slight shift to larger spot sizes. **b)** The pair correlation $g(r)$ (Equation (3)) of CD95 and dimer controls also shows a random distribution: Distances $r > 130$ nm (right of dashed line) with $g(r) \approx 1$ indicate a random distribution. A decrease in correlation for $r < 130$ nm arises from finite PSF size effects and not a particular distribution, as verified by simulations of randomly distributed spots with PSF (black curve, see *STED imaging and analysis* methods section).

Supplementary Figure 6: Polarization effect of STED samples.
a) Deconvolved STED images of Hela $CD95^{KO}$ CD86-mEGFP stained with Atto647N α-GFP nanobody in parallel (P) and perpendicular (S) channel. The comparison of both images shows, that the emission of different spots is not equally distributed to both channels. **b)** The histogram shows the measured anisotropy of n = 667 spots / objects (compare methods section and Equation (2) for details.). The spread in anisotropy confirms a strong polarization effect explaining the large spread in object intensities, even within one image.

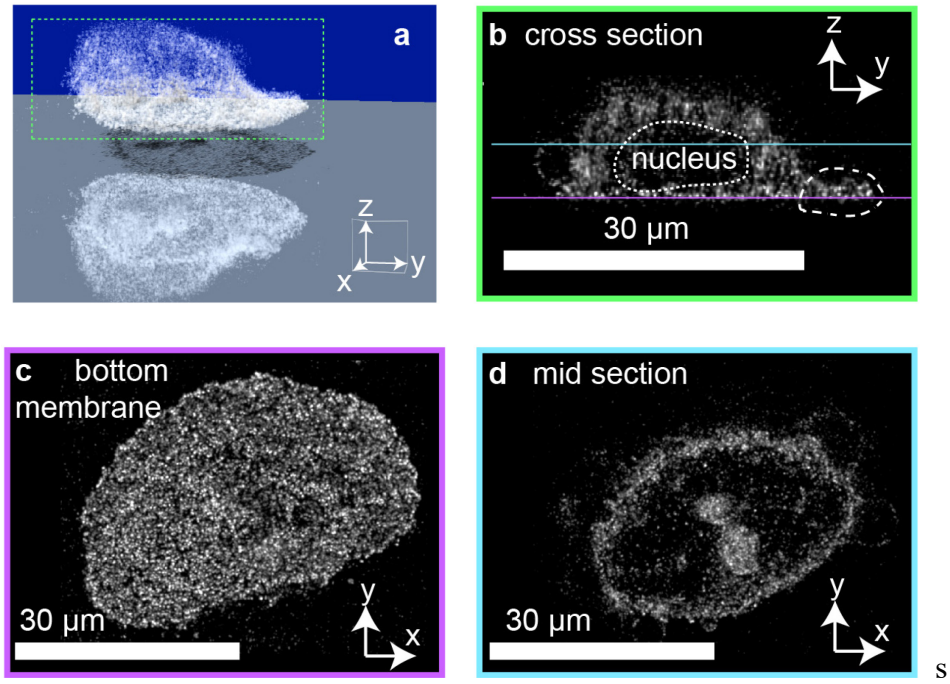

Supplementary Figure 7: 3D confocal image of CD95 transfected fixed cell.
a) Simulated fluorescence projection of 3D cell showing shadows on bottom plane. Cell was expressing mEGFP weakly and looks deflated due to the mounting process. **b)** xy cross section as indicated by dashed box in a. Dash-dotted line indicates the area where two membranes are in close proximity. Contour of nucleus is also shown. **c-d)** bottom and mid sections corresponding to colored planes in b. Figure highlights the need to measure cPBSA data below the nucleus to avoid having two membranes withing the confocal volume.

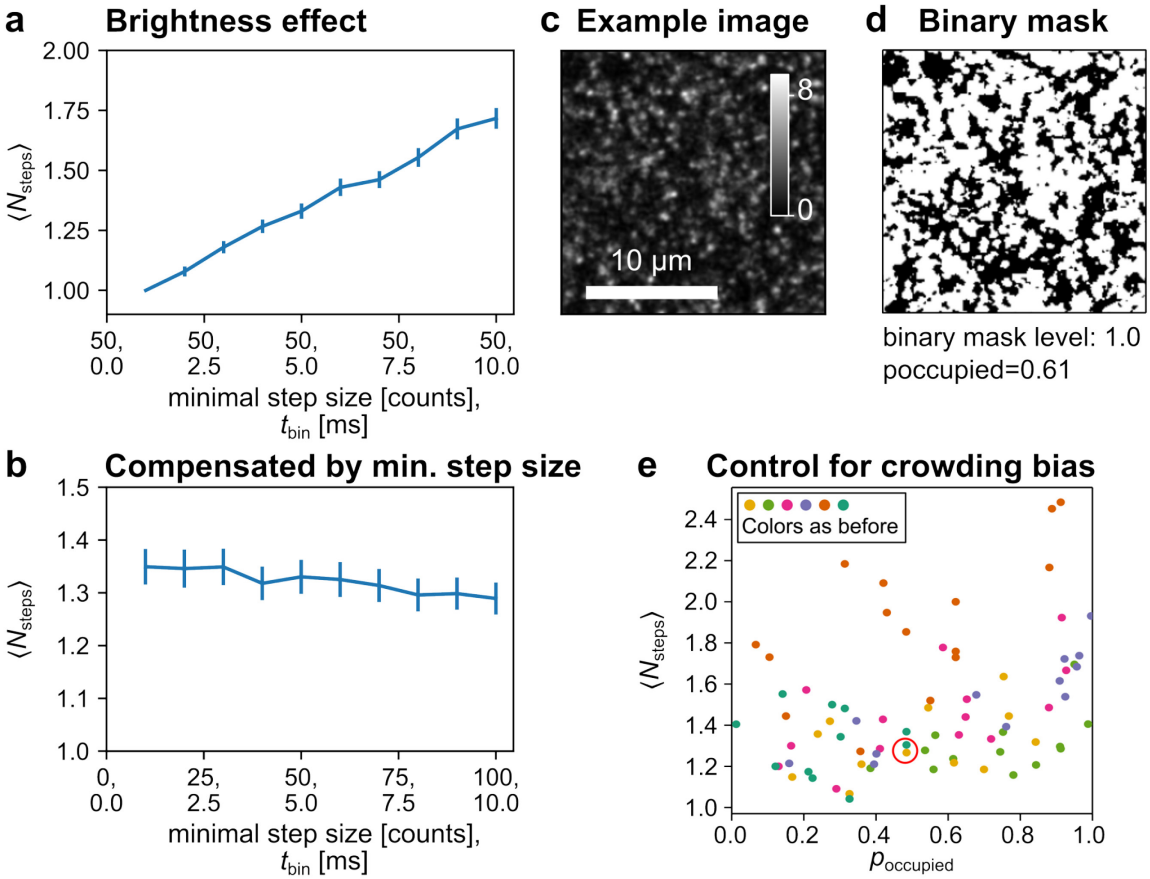

Supplementary Figure 8: Controls for Confocal Photo-Bleaching Step Analysis.
a) Effect of the brightness (effectively changed via t_{bin}) on cPBSA analysis on the average number of fluorophores for a CD86 dataset. **b)** Effect disappears when the threshold is increased in the same proportion as the t_{bin}. Data is obtained from the same dataset. **c)** Exemplary overview image smoothed with a 1 pixel sigma Gaussian filter from CD95 sample. **d)** Corresponding binary image illustrating p_{occupied} as an indicator of multi-molecule events due to crowding. p_{occupied} is determined as area fraction exceeding a signal intensity threshold of 1 pixel. **e)** To control for multi-step traces originating from multiple monomers or oligomers proximal in the confocal volume, the average numbers of bleaching steps $\langle N_{\mathrm{steps}} \rangle$ according to cPBSA of one area is plotted against p_{occupied}, for that area. A weak positive correlation between $\langle N_{\mathrm{steps}} \rangle$ and p_{occupied} is visible as expected. As the spread of the occupancy probability was similar over all samples, this created no systematic shift in the data, wherefore no additional correction had to be introduced. Colors indicate samples matching the main text. Red circle corresponds to the area shown in c-d.

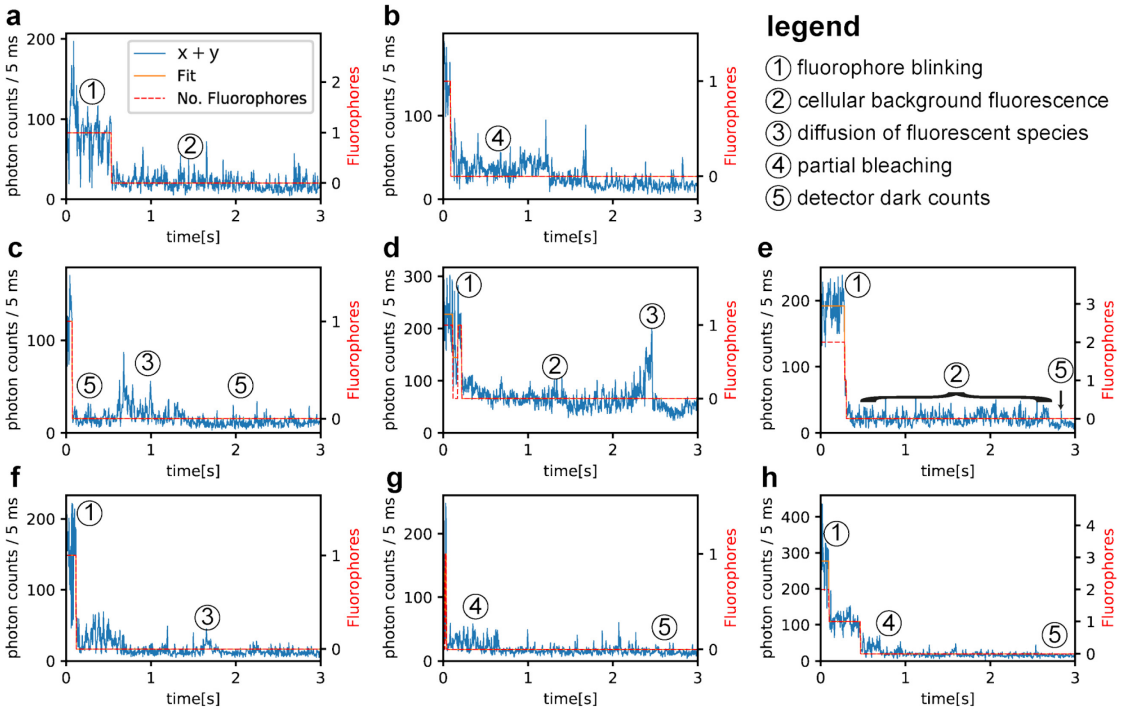

Supplementary Figure 9: Exemplary traces for confocal photo bleaching step analysis. **a-h)** Total fluorescent signal and fitted step trace, sources of noise are annotated. The most prominent sources of noise have been labelled in each graph for illustration purposes, although other sources are generally also present. **c-e)** Correlation curves of traces are plotted in Supplementary Figure 10, panels b-d, respectively. **h)** Two-step bleaching event show variation in step size. Traces were selected to illustrate noise sources and illustrate the overall data quality with little bias.

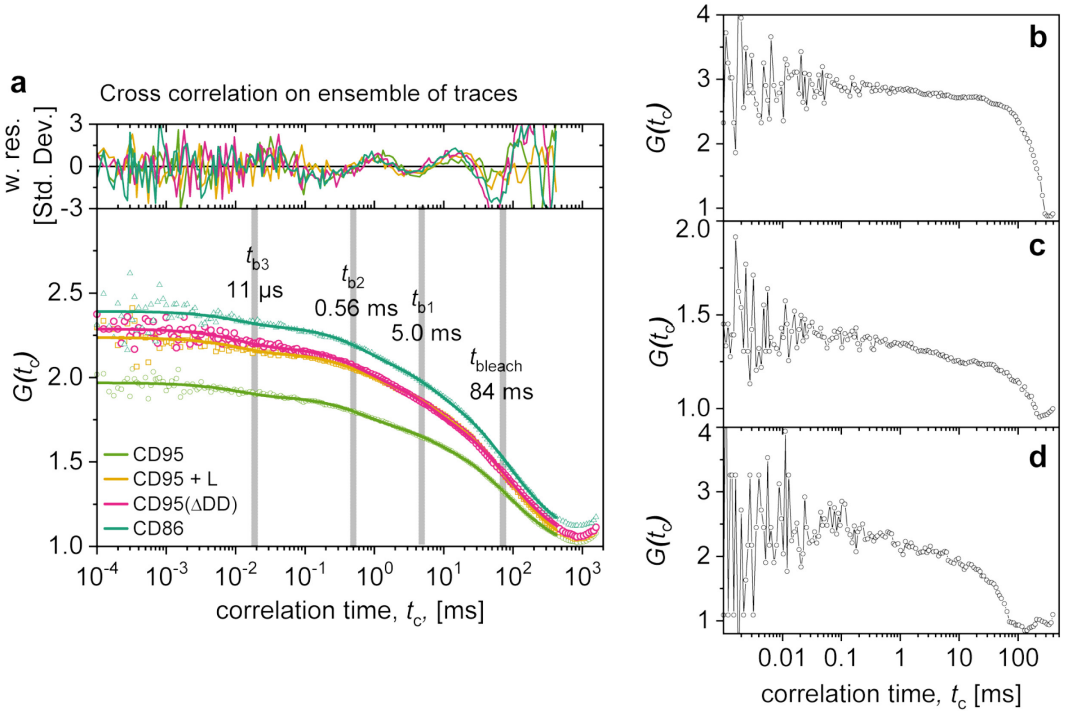

Supplementary Figure 10: Correlation analysis on photo bleaching traces.
a) Cross correlation curves of x- and y-polarization signals under circular polarization calculated for the ensemble of traces for each sample. Colors match the mainline figures. Curves were fitted with 3 bunching terms and 1 3D diffusion term as an approximation to model the bleaching behavior (see Equation (8)). As the bleaching statistics do not follow 3D diffusion statistics, we see a correlation in the residuals. All time parameters were fitted globally, whereas the fractions were left free (see Supplementary Table 4). We may obtain the parameters α and k_{on} from the bunching fraction and bunching times, respectively, and predict the variance of trace sections (see Supplementary Note 3). Note that the bunching fractions were similar over different samples, indicating that the photophysical properties of mEGFP over different samples were similar. **b-d)** CD86 correlation curves correspond to traces c-e respectively of Supplementary Figure 9. As all photons correlate, a high signal correlation curve can be generated based on only a few photons, allowing single-molecule based correlation fits. Whereas the correlation due to blinking looks similar to the ensemble fits, the bleaching correlation varies per molecular assembly, as also the bleaching time and amplitude varies.

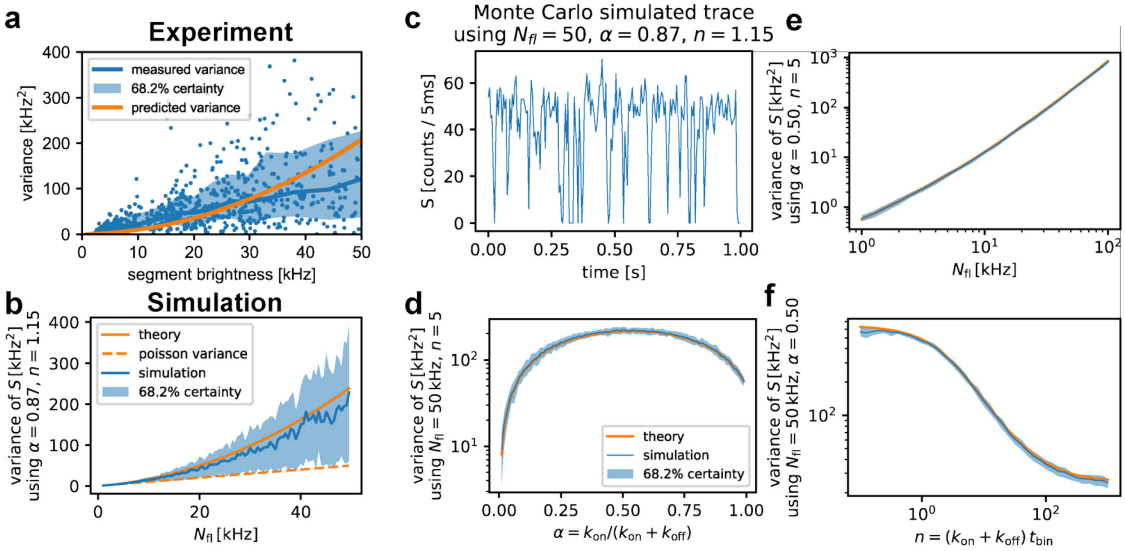

Supplementary Figure 11: A single dark state predicts trace variance.
A theoretical formula for the variance of an emitter under a single dark state (see Supplementary Note 3) is compared to measured and simulated trace variances. **a)** For each trace segment from CD86 traces measured on 22 July 2021 the segment intensity and variance was obtained from PBSA analysis (blue points). For each 50 consecutive intensities the median (blue line) and 15.9% - 84.1% quantiles (blue area) are determined to aid visualization. Supplementary Equation (S7) is used to predict the variance for each segment using α and n obtained from FCS[12] and N_{fl} for each segment. **b)** Monte Carlo traces using identical α, n , trace duration as in a) match the theoretical prediction. The short trace duration (84 ms, see Supplementary Figure 10) causes a large spread in the variance due to the varying number of blinks in this period, matching the spread observed in a). For reference the variance based on pure Poisson noise is shown. **c)** Exemplary Monte Carlo trace over 1 second under conditions typical to mEGFP measurements. **d-f)** Similar to b, but using a simulation time of 1 second and scanning the whole parameter space. Legend for all as given in d).

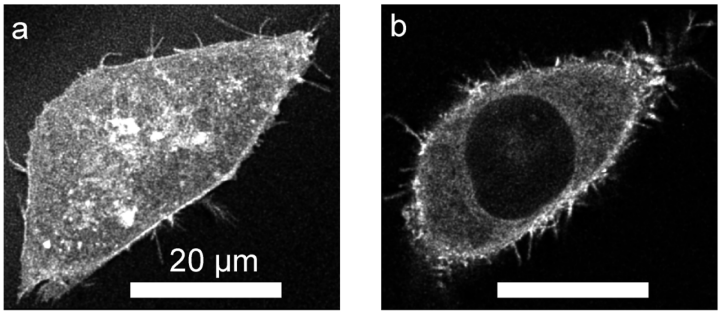

Supplementary Figure 12: CD95 transfected cells imaged by confocal microscopy.
a) Live cell transfected with CD95 bottom membrane of 3D stack. Image was recorded according to Nyquist sampling and deconvolved using Express Deconvolution Huygens Professional 21.10.0, SNR 6. **b)** mid-segment of same 3D, color scale same as in a. Signal is brightest in the membrane, but also cytoplasmic intensity is visible. No Fluorescent signal is present in the nucleus.

References

1 B.V., S. V. I. *Backprojected Pinhole Calculator*, <https://svi.nl/Olympus_FV1000> (2021).

2 Wohland, T., Rigler, R. & Vogel, H. The standard deviation in fluorescence correlation spectroscopy. *Biophysical Journal* **80**, 2987-2999 (2001). https://doi.org:10.1016/s0006-3495(01)76264-9

3 van der Voort, N. T. M., Bartels, N., Monzel, C. & Seidel, C. A. M. Quantifying the Spatio-temporal Evolution of Protein Interactions using Cell Lifetime FRET Image Spectroscopy (CELFIS). *bioRxiv* (2022).

4 Koppel, D. E. Statistical Accuracy in Fluorescence Correlation Spectroscopy. *Physical Review A* **10**, 1938-1945 (1974). https://doi.org:10.1103/PhysRevA.10.1938

5 Eggeling, C. *et al.* Data registration and selective single-molecule analysis using multi-parameter fluorescence detection. *Journal of Biotechnology* **86**, 163-180 (2001). https://doi.org:10.1016/s0168-1656(00)00412-0

6 Oracz, J., Westphal, V., Radzewicz, C., Sahl, S. J. & Hell, S. W. Photobleaching in STED nanoscopy and its dependence on the photon flux applied for reversible silencing of the fluorophore. *Scientific Reports* **7**, 11354 (2017). https://doi.org:10.1038/s41598-017-09902-x

7 Cranfill, P. J. *et al.* Quantitative assessment of fluorescent proteins. *Nature Methods* **13**, 557-562 (2016). https://doi.org:10.1038/nmeth.3891

8 Duan, C. X. *et al.* Structural Evidence for a Two-Regime Photobleaching Mechanism in a Reversibly Switchable Fluorescent Protein. *Journal of the American Chemical Society* **135**, 15841-15850 (2013). https://doi.org:10.1021/ja406860e

9 Potma, E. O. *et al.* Reduced protein diffusion rate by cytoskeleton in vegetative and polarized Dictyostelium cells. *Biophysical Journal* **81**, 2010-2019 (2001). https://doi.org:10.1016/s0006-3495(01)75851-1

10 Hennen, J., Hur, K. H., Saunders, C. A., Luxton, G. W. G. & Mueller, J. D. Quantitative Brightness Analysis of Protein Oligomerization in the Nuclear Envelope. *Biophysical Journal* **113**, 138-147 (2017). https://doi.org:10.1016/j.bpj.2017.05.044

11 Wenger, J. *et al.* Diffusion analysis within single nanometric apertures reveals the ultrafine cell membrane organization. *Biophysical Journal* **92**, 913-919 (2007). https://doi.org:10.1529/biophysj.106.096586

12 Barth, A. *et al.* Unraveling multi-state molecular dynamics in single-molecule FRET experiments. I. Theory of FRET-lines. *Journal of Chemical Physics* **156**, 141501 (2022). https://doi.org:10.1063/5.0089134